

Hydrodynamic regimes in autogenous fusion welding

by

Dmytro Havrylov

A thesis submitted in partial fulfillment of the requirements for the degree of

Doctor of Philosophy

in

Materials Engineering

Department of Chemical and Materials Engineering
University of Alberta

© Dmytro Havrylov, 2021

Abstract

The weld bead width and the penetration depth are major parameters that determine the mechanical strength of the weld joint. The analytic models, such as the Gaussian heat source model, may provide quite accurate estimations for the weld width and penetration; however, the model does not account for the weld pool convection which may significantly affect the weld shape. In “melt-in” mode, the principal driving forces for weld pool convection are buoyancy, electromagnetic forces, surface tension gradients and the arc pressure. The surface tension gradients on the melt surface have been reported in the literature to have the strongest effect on the weld pool convection. This effect is also known as the Marangoni effect. In case of a weld pool, the flow can be directed either outwards or inwards depending on the presence and the amount of surface active elements on the weld pool surface. In this work only the outward convective flows are analyzed. It is proposed that the effect of the Marangoni convection on the weld shape can be formulated in the form of correction factors to the solution for the Gaussian heat source. These correction factors are the objectives of this work. The scaling analysis of the Marangoni convection in weld pools identified five asymptotic hydrodynamic regimes for melts with both high and low Prandtl numbers. Scaling laws for the characteristic velocity of the convection and the Peclet number for the five asymptotic regimes were obtained and calibrated with the auxiliary numerical model and data from the literature. Correction factors for the weld width and depth predicted by the Gaussian heat source were proposed to account for the weld pool convection.

Preface

This thesis is an original work by Dmytro Havrylov. The material presented in it comprises the author's research project under supervision of Dr. Patricio F. Mendez. No part of this thesis has been previously published except conference presentations.

To my parents, for their encouragement, love and endless support

Acknowledgements

First and foremost I would like to express my gratitude to Prof. Patricio F. Mendez. Without his foresight, his guidance and patience this work would not have been possible. It was an invaluable experience for me and I am very lucky to have had the opportunity to work under his supervision that helped me develop my personality and scientific skills.

I would like to express my appreciation and thanks to Prof. Carlos F. Lange for his amazing course Introduction into computational fluid dynamics (CFD) for engineers and for his continuous support on the CFD aspects of my work.

I am very grateful to my Doctoral Final Examining Committee members: Prof. Leijun Li, Prof. Arman Hemmati, Prof. Carlos F. Lange and Prof. John Norrish from the University of Wollongong, Australia for their valuable comments on my work and the priceless conversation I had with them during my thesis defence.

I would like to thank Dr. Goetz Dapp for his support in all the administrative sides of my program.

A special gratitude to Dr. Gentry Wood for commenting on my thesis from the industrial point of view and for sharing his code for the Gaussian heat source model calculations.

I would like to thank my friends, the current and former members of the Canadian Centre for Welding and Joining: Vivek Sengupta, Syed Alam, Dr. Daniel Ramirez Rebollo, Dr. Gentry Wood, Dr. Nairn Barnes, Mitchell Grams, Alejandro Hintze Cesaro, Ying Wang, Yi “Louie” Lu, Cory McIntosh, Mackenzi Johnston, Steven Borle, Ata Kamyabi Gol, Matt Bell, Curtis Bell and many others. Thanks to the members of

the CWBA, AWS, IIW communities, especially to Dan Tadic, Ken McKen, Douglas Luciani and Dr. Eric Sjerne.

I would also like to express my special gratitude to Oleksii Semenov from The E.O. Paton Electric Welding Institute, Ukraine and Masaya Shigeta from Osaka University, Japan for their appreciation and support of my work.

I would like to gratefully acknowledge Cameron Serles, Xiris Automation and MITACS for financial support at the final stage of my program.

My parents have been my greatest source of support, endless inspiration and love, I would like to express my infinite gratitude to them.

Table of Contents

1	Introduction and Literature Review	1
1.1	Marangoni convection in welding	1
1.1.1	Introduction	1
1.1.2	Driving forces for convective flows in weld pools	2
1.1.3	Marangoni effect. Surface active elements	4
1.1.4	High-Prandtl-number materials. Polymers	9
1.1.5	Experimental studies	10
1.1.6	Numerical modelling	12
1.1.7	Scaling analysis	17
1.2	Problem statement	19
1.2.1	Prediction of weld bead width and penetration depth from moving heat source models	19
1.2.2	Asymptotic and intermediate regimes	19
1.2.3	Problem analysis from Buckingham π theorem	21
1.2.4	Main hypothesis	25
1.2.5	Objectives	28
1.2.6	Thesis outline	29
2	Scaling Analysis	30
2.1	Hydrodynamic regimes of thermocapillary flows in weld pools	30
2.2	Problem formulation for the scaling analysis	34
2.3	Regime I	37

2.4	Regime II	40
2.5	Regime III	45
2.6	Regime IV	51
2.7	Regime V	55
2.8	Summary	58
3	Auxiliary numerical model set-up	59
3.1	Model description	59
3.2	Reasons of the model choice. Limitations	61
3.3	Normalization scheme and boundary conditions	62
3.4	Mesh	64
3.5	Solver parameters	66
3.6	Convergence and grid independence	67
4	Results	70
4.1	Gaussian heat source model	70
4.2	Data used for the analysis	72
4.2.1	Numerical modeling results	72
4.2.2	Data from the literature	72
4.2.3	Dependence of γ_T on temperature	74
4.2.4	Adaptation of the Gaussian heat source model for stationary welds	75
4.2.5	Measurements of the weld width and depth	76
4.2.6	Top-hat and Gaussian heat sources	76
4.3	Characteristic velocities and the Peclet numbers	79
4.3.1	Regime I	79
4.3.2	Regime II	88
4.3.3	Regime III	97
4.3.4	Regime IV	109

4.3.5	Regime V	115
4.4	Weld width and penetration depth	123
4.4.1	Main assumption	123
4.4.2	Calculation results	123
4.4.3	Correlation between L_0 and D_0 and the Gaussian heat source predictions L_G and D_G	127
4.4.4	Verification with the experimental data	130
5	Discussion	135
6	Conclusions and Future Work	138
6.1	Conclusions	138
6.2	Recommendations for the future work	139
	Bibliography	141
	Appendix A: Parameters for the experiments from the literature	148
A.1	Saldi [22]	148
A.2	Wei <i>et al.</i> [95]	152
A.3	Mishra <i>et al.</i> [53]	154
A.4	Robert and DebRoy [97]	156
	Appendix B: Numerical modelling raw results	157
B.1	Regime I	157
B.2	Regime II	169
B.3	Regime III	221
B.4	Regime IV	255
B.5	Regime V	271

List of Tables

3.1	Dimensionless parameters	64
3.2	Boundary conditions	64
3.3	Details on the meshes	65
3.4	The parameters of the numerical model	67
3.5	Pseudo-transient explicit relaxation factors	67
4.1	Details on the literature used for the analysis.	72
4.2	Details on the literature used for the analysis (continuation).	74
4.3	Parameters for Eqs. 4.9 and 4.10 for γ_T from the works of Saldi [22] and Mishra <i>et al.</i> [53].	74
4.4	Approximated values of γ_T used for the scaling analysis for the data from the works of Saldi [22] and Mishra <i>et al.</i> [53].	75
4.5	Material properties for the data from [22].	78
4.6	Parameters of the heat source, weld width and depth from [22] and their counterparts calculated with the Gaussian heat source model.	79
4.7	Experiment parameters used for the analysis of the Regime I on the $Ri_{\mathcal{L}} - Pr$ plane as shown in the Fig. 4.9. The experimental points are located on the line set by Eq. 4.18.	83
4.8	The dimensionless parameters for the data from [22] sorted in group with approximately the same Pe	86

4.9	Experiment parameters used for the analysis of the Regime II on the $Ri_{\mathcal{L}} - Pr$ plane as shown in the Fig. 4.16. The experimental points are located on the line set by Eq. 4.25	92
4.10	Dimensionless parameters used for the analysis of the experimental results from [97].	96
4.11	Estimated characteristic velocities and the dimensionless parameters of the experimental results from [97] that are in the Regime II.	96
4.12	Experiment parameters used for the analysis of the Regime III on $Ri_{\mathcal{L}} - Pr$ plane as shown in the Fig. 4.26. The experimental points are located on the line set by Eq. 4.31	103
4.13	The dimensionless parameters for the data from [22]. The data points in the intermediate regime (considered as the Regime I) are separated in the bottom part of the table	105
4.14	The dimensionless parameters for the data from [95].	106
4.15	The dimensionless parameters for the data from [2].	106
4.16	The dimensionless parameters for the data from [53].	107
4.17	Experiment parameters used for the analysis of the Regime V on $Ri_{\mathcal{L}} - Pr$ plane as shown in the Fig. 4.42. The experimental points are located on the line set by Eq. 4.40	120
4.18	Measured weld pool widths and depths from [22] grouped according to \mathcal{R}_G	124
4.19	Calculated values of the exponents a , b , n and m	124
4.20	L_0 and D_0 compared with L_G and D_G for each group with the same \mathcal{R}_G	127
4.21	Welding parameters of the experiments from [53] and the corresponding characteristic velocity of convection u_{max}	130
4.22	Predicted and measured weld pool widths and depths from [53] and the corresponding Pe	134

4.23	Welding parameters of the experiments from [97] and the corresponding Pe.	134
4.24	Predicted and measured weld pool widths and depths from [97] and the corresponding Pe.	134
A.1	Physical parameters for the experiments in the work [22]	148
A.2	Parameters for the experiments from the work [22]	149
A.3	Parameters for the experiments from the work [22]	150
A.4	Parameters for the experiments from the work [22]	151
A.5	Physical parameters from the work of Wei [95]	152
A.6	Parameters from the work of Wei [95]	153
A.7	Parameters of the experiments from the work of Mishra <i>et al.</i> [53] . .	154
A.8	Parameters of the experiments from the work of Mishra <i>et al.</i> [53] . .	154
A.9	Parameters of the experiments from the work of Mishra <i>et al.</i> [53] . .	154
A.10	Parameters of the experiments from the work of Mishra <i>et al.</i> [53] . .	155
A.11	Parameters of the experiments from the work of Mishra <i>et al.</i> [53] . .	155
A.12	Parameters for the high speed steel experiments from the work of Robert and DebRoy [97]	156
A.13	Parameters of the high speed steel experiments from the work of Robert and DebRoy [97]	156

List of Figures

1.1	The orders of magnitude of the characteristic velocities for the principal convection driving forces in weld pools	3
1.2	Schematic of Marangoni convection in a weld pool	5
1.3	Surface tension as a function of temperature for two molten steels with and without surface active elements as shown in [17]. "Low d/w heat" labeled graph shows the surface tension of a high purity steel with no significant amount of surfactants. The data labeled "high d/w heat" represents the surface tension of a steel having approximately 160 ppm more sulfur than the latter material. The dashed lines show the suggested by [18] behaviour of the surface tension above the maximum studied temperature.	6
1.4	Surface tension temperature coefficient γ_T of Fe-S system as a function of temperature and surfactant activity	7
1.5	Schematics of the flow directions for various γ and γ_T temperature dependencies	8
1.6	Temperature dependence of surface tension of polyethylene samples (reprinted from Dee and Sauer [23]).	10
1.7	Weld pool shapes of NaNO_3 (Pr=9.1) from Limmaneevichitr and Kou [26] produced by CO_2 laser beams of the following: A — 4.5 W and 3.2 mm diameter; B — 12.4 W and 5.9 mm diameter; C — 12.4 W and 1.5 mm diameter.	11
1.8	Comparison of the weld pool shapes with flat and free deformable surface	13

1.9	Weld pool shapes at low Pr numbers of $10^{-2} < \text{Pr} < 1$ from Wei <i>et al.</i> [46].	14
1.10	Dimensionless weld penetration depth	23
1.11	Dimensionless leading length as a function of Ry from [92].	26
1.12	Typical welding conditions for various welding processes [89] ($n \equiv \text{Ry}$, $u \equiv \sigma^*$).	27
1.13	Width to depth ratio as a function of the Rykalin number and heat source distribution ($n \equiv \text{Ry}$, $u \equiv \sigma^*$) from [89].	27
2.1	Asymptotic flow regimes on the $\mathcal{R}_{\mathcal{L}}^4 \text{Ri}_{\mathcal{L}} - \text{Pr}$ plane map.	35
2.2	Schematics of the problem formulation	36
3.1	Schematics of the problem formulation.	60
3.2	Initial mesh #1 overview	65
3.3	Mesh at the domain corner (magnified).	66
3.4	A typical graph for u_{max} as a function of the number of nodes	68
4.1	Location of the numerical experiments on the $\text{Ri}_{\mathcal{L}} - \text{Pr}$ plane	73
4.2	The free surface, the axis of symmetry and the cutline at $r = \mathcal{L}$ ($r^* = 1$).	73
4.3	Surface tension temperature coefficient γ_T as a function of temperature for modelled samples with 20 and 150 ppm of sulfur	75
4.4	Example of a figure used to extract the weld width, depth and maximum surface velocity (reprinted from [22]).	77
4.5	Example of a figure used to determine the optimal estimation for the Gaussian heat source distribution (reprinted from [22]).	78
4.6	Location of the dimensionless parameters for Regime I on the $(D/\sigma)^2 \text{Re} - \text{Pr}$ plane.	80
4.7	Numerical experiments for the Regime I on the $\text{Ri}_{\mathcal{L}} - \text{Pr}$ plane (left) and the $\mathcal{R}_{\mathcal{L}}^4 \text{Ri} - \text{Pr}$ plane (right).	81

4.8	Calculated results for the Regime I (a - streamlines; b - temperature contour; c - radial velocity u^* along the cutline at $r = \mathcal{L}$ ($r^* = 1$) as indicated in Fig. 4.2 (abscissa is u^* , ordinate is z^*); d - u^* along the free surface; e - temperature T^* along the axis of symmetry (abscissa is T^* , ordinate is z^*); f - temperature T^* along the free surface). All the values are normalized. Note: the coordinate captions in the graphs are shown as noted in Ansys Fluent® and are not representative to the notations used in the work.	82
4.9	Location of the dimensionless parameters for Regime I and the experiment numbers on $Ri_{\mathcal{L}} - Pr$ plane.	84
4.10	Comparison of the calculated $Pe_{\mathcal{L}}$ with the scaling law $\widehat{Pe}_{\mathcal{L}}$ for the Regime I.	85
4.11	Pe for the data in the intermediate regime from [22] compared to the scaling law for the Regime I.	87
4.12	Location of the dimensionless parameters for the Regime II on the $(D/\sigma)^2 Re - Pr$ plane.	89
4.13	Location of the dimensionless parameters for the Regime II on $Ri_{\mathcal{L}} - Pr$ plane. Note: $\mathcal{R}_{\mathcal{L}} = 1$ in all the numerical experiments on this map.	89
4.14	Calculated results for the Regime II (a - streamlines; b - temperature contour; c - radial velocity u^* along the cutline at $r = \mathcal{L}$ ($r^* = 1$) as indicated in Fig. 4.2 (abscissa is u^* , ordinate is z^*); d - u^* along the free surface; e - temperature T^* along the axis of symmetry (abscissa is T^* , ordinate is z^*); f - temperature T^* along the free surface). All the values are normalized. Note: the coordinate captions in the graphs are shown as noted in Ansys Fluent® and are not representative to the notations used in the work.	90
4.15	Formation of the viscous boundary layer in the Regime II (dashed line) vs near-parabolic distribution in the Regime I (solid).	91

4.16	Location of the numerical experiments on the $Ri_{\mathcal{L}} - Pr$ used for the calibration of the scaling law for the Regime II.	93
4.17	Comparison of the calculated $Pe_{II_{\mathcal{L}}}$ with the scaling law $\widehat{Pe}_{II_{\mathcal{L}}}$ for the Regime II	94
4.18	Streamlines for a weld pool flow with a flow separation and the formation of a secondary vortex in the Regime II with high Re numbers corresponding to $Ri > 10^4$	95
4.19	Cross sections of the experimental and calculated weld pool of aluminum alloy 5182 at 1.5kW and 105.8 mm/s welding speed (reprinted from [97])	97
4.20	Location of the dimensionless parameters for the Regime III on the $(D/\sigma)^2 Re - Pr$ plane.	98
4.21	Location of the dimensionless parameters for Regime III on $Ri_{\mathcal{L}} - Pr$ plane. Note: $\mathcal{R}_{\mathcal{L}} = 1$ in all the numerical experiments on this map.	99
4.22	Calculated results for the Regime III (a - streamlines; b - temperature contour; c - radial velocity u^* along the cutline at $r = \mathcal{L}$ ($r^* = 1$) as indicated in Fig. 4.2 (abscissa is u^* , ordinate is z^*); d - u^* along the free surface; e - temperature T^* along the axis of symmetry (abscissa is T^* , ordinate is z^*); f - temperature T^* along the free surface). All the values are normalized. Note: the coordinate captions in the graphs are shown as noted in Ansys Fluent® and are not representative to the notations used in the work.	100
4.23	Normalized temperature T^* distributions along the axis of symmetry $r^* = 0$ in the Regime III (dashed line) and the Regime II (solid). The formation of a thermal boundary layer can be seen for the Regime III compared to a near-straight-line T^* distribution in the Regime II	101
4.24	Streamlines for a weld pool flow with a flow separation in Regime III at high Re numbers corresponding to $Ri > 10^4$	102

4.25	Temperature contour for a weld pool flow with a flow separation in Regime III at high Re numbers corresponding to $Ri > 10^4$	102
4.26	Location of the dimensionless parameters for Regime III and the experiment numbers.	104
4.27	An example illustrating that u_{max} is essentially independent from the weld pool size in the fully developed Regime III.	107
4.28	Measured Pe compared to the predicted \widehat{Pe}_{III} from the scaling law. . .	108
4.29	Location of the dimensionless parameters for the Regime IV on the $(D/\sigma)^2 Re - Pr$ plane.	109
4.30	Location of the dimensionless parameters for Regime IV on $Ri_{\mathcal{L}} - Pr$ plane. Note: $\mathcal{R}_{\mathcal{L}} = 1$ in all the numerical experiments on this map. .	110
4.31	Calculated results for the Regime IV (a - streamlines; b - temperature contour; c - radial velocity u^* along the cutline at $r = \mathcal{L}$ ($r^* = 1$) as indicated in Fig. 4.2 (abscissa is u^* , ordinate is z^*); d - u^* along the free surface; e - temperature T^* along the axis of symmetry (abscissa is T^* , ordinate is z^*); f - temperature T^* along the free surface). All the values are normalized. Note: the coordinate captions in the graphs are shown as noted in Ansys Fluent [®] and are not representative to the notations used in the work.	111
4.32	Formation of the viscous boundary layer in the Regime IV (dashed line) versus the viscous flow in the Regime V (solid line).	112
4.33	Formation of the viscous boundary layer in the Regime IV (dashed line) vs near-parabolic distribution in the Regime V (solid): comparison of the velocity profiles along the cutline normalized to their maximum value.	113
4.34	Formation of the thermal boundary layer in the Regime IV (dashed line) and V (solid line).	113
4.35	$NaNO_3$ (high Pr) weld pool at high Ma from Robert and DebRoy [97].	114

4.36	Location of the dimensionless parameters for the Regime V on the $(D/\sigma)^2 \text{Re} - \text{Pr}$ plane.	115
4.37	Location of the dimensionless parameters for Regime V on $\text{Ri}_{\mathcal{L}} - \text{Pr}$ plane. Note: $\mathcal{R}_{\mathcal{L}} = 1$ in all the numerical experiments on this map.	116
4.38	Calculated results for the Regime V (a - streamlines; b - temperature contour; c - radial velocity u^* along the cutline at $r = \mathcal{L}$ ($r^* = 1$) as indicated in Fig. 4.2 (abscissa is u^* , ordinate is z^*); d - u^* along the free surface; e - temperature T^* along the axis of symmetry (abscissa is T^* , ordinate is z^*); f - temperature T^* along the free surface). All the values are normalized. Note: the coordinate captions in the graphs are shown as noted in Ansys Fluent [®] and are not representative to the notations used in the work.	117
4.39	Near-parabolic velocity profile along the cutline at $r^* = 1$ in the Regime I (solid) and Regime V (dashed line).	118
4.40	Near-parabolic velocity profile along the cutline at $r^* = 1$ in the Regime I (solid) and Regime V (dashed line): comparison of the velocity profiles along the cutline normalized to their maximum value.	119
4.41	Formation of the thermal boundary layer in the Regime V (dashed line) vs near-straight-line distribution in the Regime I (solid).	119
4.42	Location of the dimensionless parameters for Regime V and the experiment numbers.	121
4.43	Measured $\text{Pe}_{\mathcal{L}}$ compared to the predicted $\widehat{\text{Pe}}_{\text{V}\mathcal{L}}$ from the scaling law (Eq. 4.42).	122
4.44	L/L_0 as a function of Pe for the data points from Saldi [22].	125
4.45	D/D_0 as a function of Pe	126
4.46	Comparison of the calculated L_0/σ against L_G/σ for the data points from Saldi [22]. The fitting curve is presented in Eq. 4.51	128

4.47	Comparison of the calculated D_0/σ against D_G/σ . The fitting curve is presented in Eq. 4.52.	129
4.48	An experimental example used for the verification of Eqs. 4.49 and 4.50 from [53].	130
4.49	Experimental examples used for the verification of Eqs. 4.49 and 4.50 from [97].	131
4.50	L/L_0 as a function of Pe for the modelling [22] and experimental [53], [97] data.	132
4.51	D/D_0 as a function of Pe for the modelling [22] and experimental [53], [97] data.	133

Chapter 1

Introduction and Literature Review

1.1 Marangoni convection in welding

1.1.1 Introduction

In fusion welding, the joining of two parts occurs by melting their edges with a high density heat source and merging them to form a continuous joint. Weld penetration depth and bead width, consequently, are the major parameters that determine the mechanical strength of the joint.

The penetration and width of the welds are governed by several physical mechanisms. There are two main penetration modes in welding: “melt-in” and keyhole mode. In high current GTA welding or high energy beam processes, arc or beam pressure is the dominant penetration mechanism representing the keyhole penetration mode. Arc pressure at currents over 250 A pushes the melt towards the weld pool rear, so that only a thin layer of molten metal appears below the arc [1]. However, in lower current arc or defocused laser or electron beam welding processes, the weld pool surface is not as depressed as in the high energy processes representing the “melt-in” mode. This work is focused on the “melt-in” penetration mode only. The results of the work are expected to be universal for various welding processes including GTAW, laser welding or electron beam welding as long as the process is autogenous and the penetration mechanism remains “melt-in” with no significant deformation of the weld

pool surface compared to the weld pool size.

In “melt-in” penetration mode, the energy from the heat source is transferred to the base metal through the weld pool. In this case, convection within the molten pool may play a dominant role in the heat distribution and weld formation and, therefore, have a strong effect on the properties of the resultant weld, such as the weld bead geometry, the cooling rate of the melt and the heat affected zone (HAZ), weld surface smoothness, microstructure, fumes formation, gas porosity in the weld, etc. [2–10]. Thereby, a quantitative understanding of the weld pool convection processes is important for the welding industry.

1.1.2 Driving forces for convective flows in weld pools

The principal driving forces for weld pool convection are buoyancy, electromagnetic forces, surface tension gradients and the arc pressure.

Density variations with temperature cause the buoyancy-driven flows. The top-centre area of the pool has a higher temperature than the areas closer to the liquid-solid interface. It causes the cooler and, consequently, heavier melt to sink down, whilst the lighter portion of the melt in the higher temperature regions floats upwards (Fig. 1.1 a). The velocities associated with the corresponding convective loop are of the order of mm/s [5].

The interaction between the magnetic flux induced in the weld pool and the divergent current flux coming from the electrode produces the Lorenz force ($\mathbf{J} \times \mathbf{B}$) and causes electromagnetically driven flow. The characteristic velocity of the electromagnetic flows is of the order of cm/s (Fig. 1.1 b).

The surface tension gradients on the melt surface are found to have the strongest effect on the weld pool convection causing flows with the velocities of the order of m/s (Fig. 1.1 c and d). Note that it is the surface tension gradient on the free surface that causes the flow, not the absolute value of the surface tension. The effect of the mass transfer along an interface between a liquid and a gas or two liquids is usually

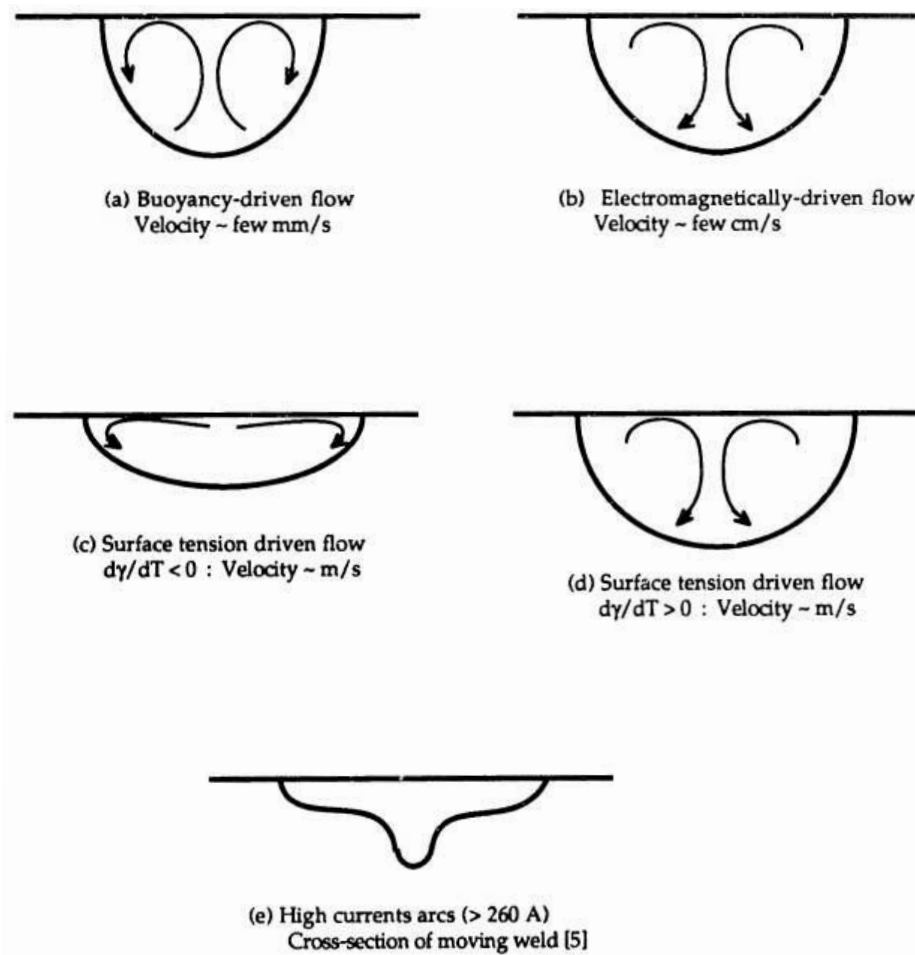


Figure 1.1: The orders of magnitude of the characteristic velocities for the principal convection driving forces in weld pools [5].

referred to as the Marangoni effect. It is named after an Italian physicist Carlo Marangoni who was one of the first to describe this effect in detail.

The surface tension gradients are caused by a temperature gradient or by a gradient of a surface active element concentration [11]. Due to the dynamics nature of welding, the weld pool surface is essentially never isothermal. The weld pool edge area is at the melting point, whilst the pool centre has a higher temperature due to the heat flux from the arc or laser heat source.

When the surface tension gradient is caused by the temperature gradient, the Marangoni convection in this case may also be called *thermocapillary*. When the surface tension gradient is caused by the variations in the concentration of surface active elements, it may be referred to as *solutocapillary*. In welding, both effects may occur at the same time, but since the temperature gradients are always present, in this work, this phenomenon is referred to as the Marangoni or thermocapillary convection as synonyms.

Pure materials normally have a negative surface tension temperature coefficient γ_T [6]. That means that the surface tension decreases as the surface temperature increases. In case of a weld pool that means that the cooler surface area at the pool edge has a higher surface tension than the hotter centre resulting in a recirculating flow directed from the centre to the edges. The schematic of such a flow is shown in the Fig. 1.2 a, b and c.

Surface active elements, also referred to as surfactants, besides changing the magnitude of γ_T , may also alternate the sign of the surface tension temperature coefficient changing the direction of the flow [12]. In this case, the hotter surface centre area has a greater tension causing flows directed inwards (Fig. 1.2 d, e and f).

1.1.3 Marangoni effect. Surface active elements

The dominance of Marangoni effect in weld pool convection was determined in the early 1980s. It had been noticed that in GTA welding different casts of the same

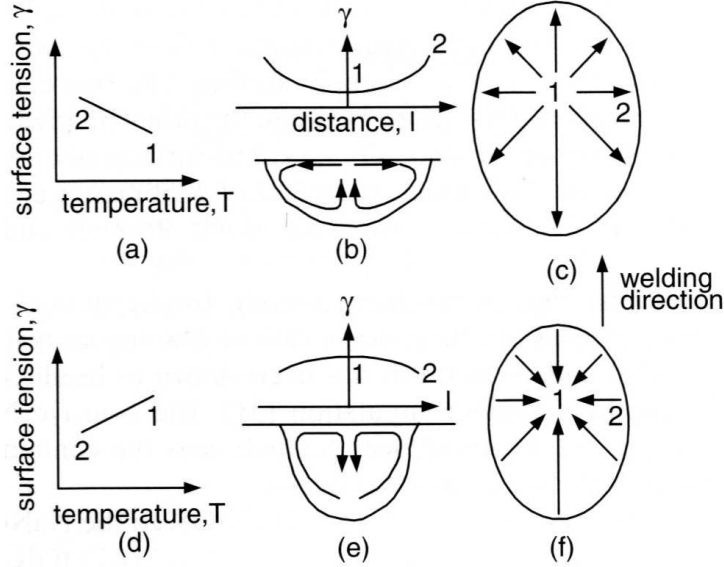


Figure 1.2: Schematic of Marangoni convection in a weld pool [6].

material which met the required material specifications could produce welds with various penetration and width that could significantly differ from the specified norm. It was found that where the correlation could be established, metal chemical composition had very small variations in the particular elements. Various theories were proposed to explain why such small differences in some elements had such a profound effect on the weld characteristics and weldability. Roper and Olson [13] proposed a model based on interfacial energies. Glickstein and Yeniscavich [14] and Savage *et al.* [15] suggested that the variations in the minor elements caused changes in the arc characteristics. However, a similar effect was found in laser and electron beam welding processes where no arc is present [16]. That proved that the changes in the arc characteristics cannot explain the ‘cast to cast’ weldability variations.

Heiple and Roper [4, 16] suggested that it was the thermocapillary weld pool flows that had the main influence on the shape of the fusion zone. They proposed that the major driving force for the flows was a surface tension gradient and that even low concentrations of surface active elements may have changed both the convection intensity and its direction.

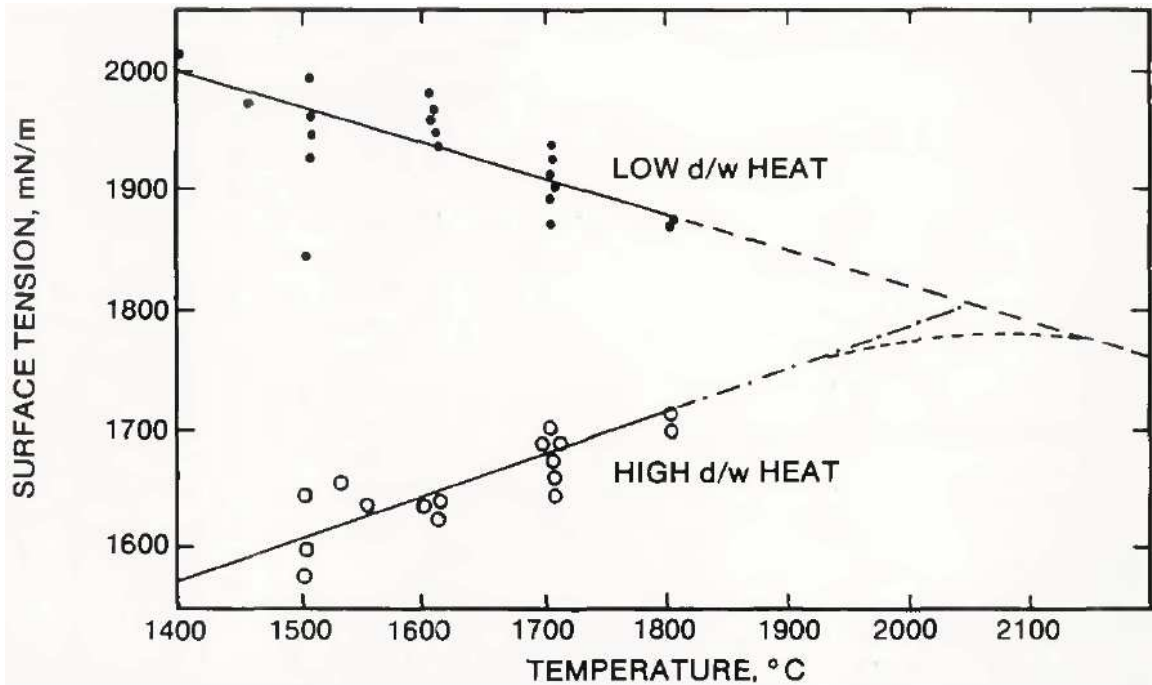


Figure 1.3: Surface tension as a function of temperature for two molten steels with and without surface active elements as shown in [17]. "Low d/w heat" labeled graph shows the surface tension of a high purity steel with no significant amount of surfactants. The data labeled "high d/w heat" represents the surface tension of a steel having approximately 160 ppm more sulfur than the latter material. The dashed lines show the suggested by [18] behaviour of the surface tension above the maximum studied temperature.

Surfactants lower the molten metal surface tension at the melting point. For example, the surface tension of molten iron was reported to drop by more than a factor of 2 near its melting point (1570 °C) by the addition of around 1 wt % of sulfur [19, 20]. At a higher temperature, however, the surfactant segregation diminishes due to the increase in entropy, thereby resulting in an increased surface tension (Fig. 1.3). Thus, when surface active elements are present, the hottest centre part of the pool may have the highest tension on the pool surface causing the flow to be directed inwards instead of outwards. The inward flow produced by this effect increases the depth-to-width ratio improving the penetration [4].

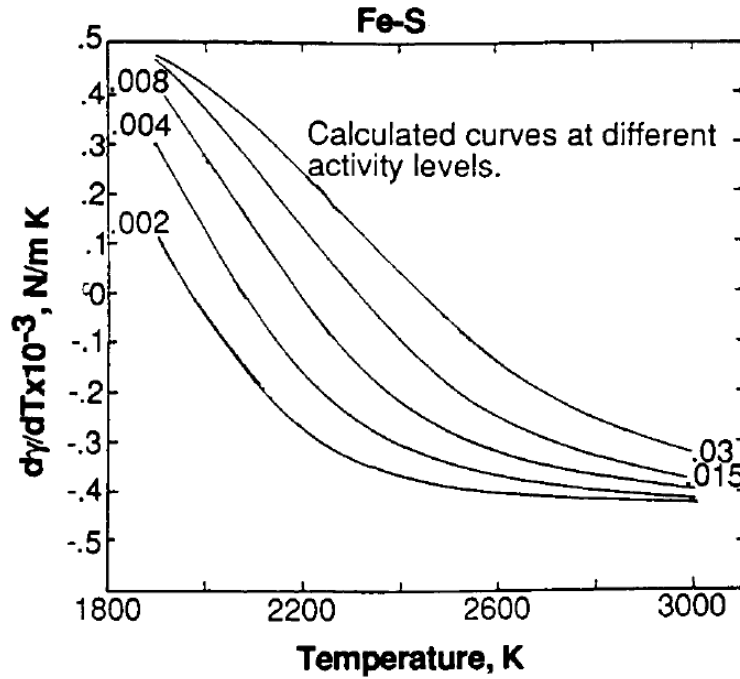


Figure 1.4: Surface tension temperature coefficient γ_T of Fe-S system as a function of temperature and surfactant activity (reprinted from [21]).

A general dependencies of the surface tension and surface tension temperature coefficient as functions of surfactant activities and temperature were established by Sahoo *et al.* [21] for Fe-O, Fe-S, Fe-Se, Cu-O, Cu-S, Cu-Se, Cu-Te, Ag-O and Sn-Te systems. Eq. 4.9 represents this dependence for surface tension temperature coefficient

γ_T .

$$\gamma_T = -A - R\Gamma_S \ln(1 + Ka_i) - \frac{Ka_i}{1 + Ka_i} \frac{\Gamma_S (\Delta H^0 - \Delta \bar{H}_i^M)}{T} \quad (1.1)$$

$$\text{where } K = k_1 \exp \left[\frac{-\Delta H^0}{RT} \right] \quad (1.2)$$

In Eqs. 4.9 and 4.10, A is the surface tension temperature coefficient for pure metal, Γ_S the surface excess of saturation, K the equilibrium constant for segregation, k_1 the entropy factor, ΔH^0 the standard heat of adsorption, $\Delta \bar{H}_i^M$ the partial molar enthalpy of species mixing in the solution, and a_i the activity of the element in wt %. As shown in the Fig. 1.4, surface tension temperature coefficient γ_T can change its

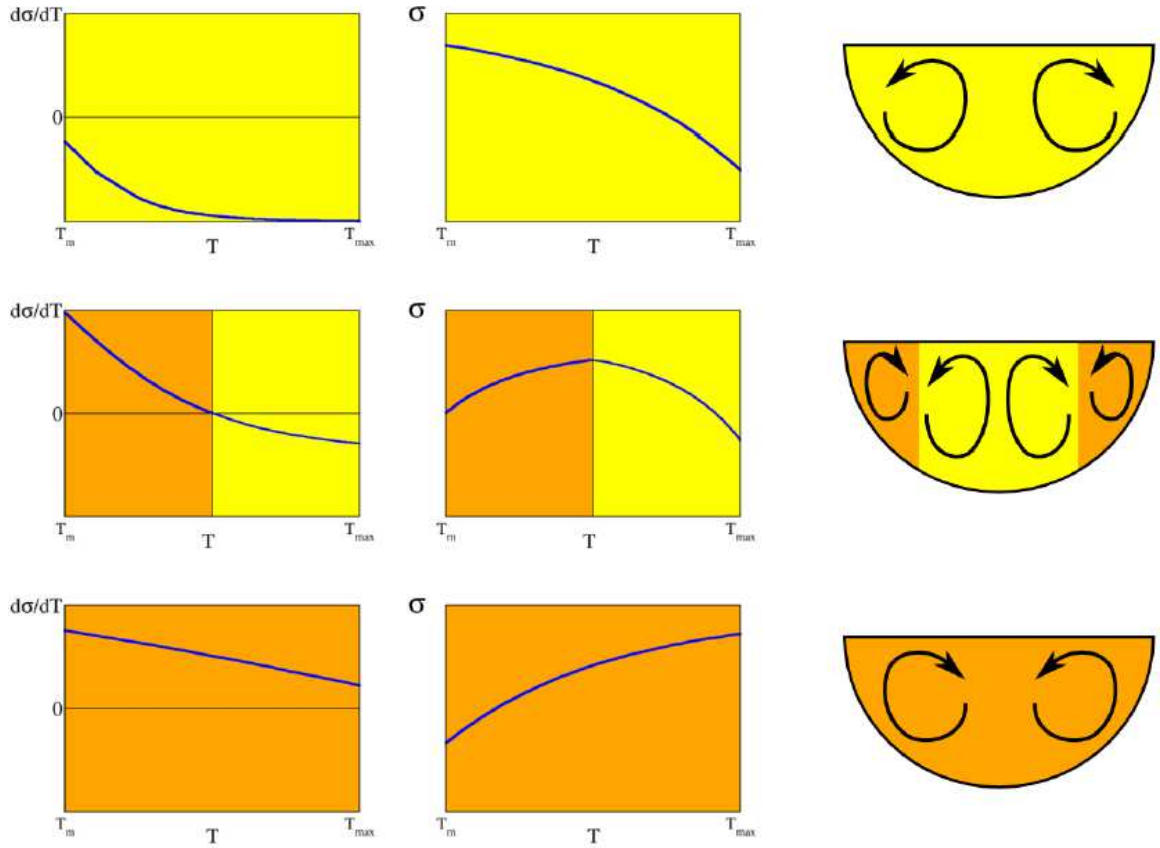


Figure 1.5: Schematics of the flow directions for various γ and γ_T temperature dependencies (reprinted from [22]).

sign depending on the temperature. Fig. 1.5 represents the possible resulting flows. In the case of a low amount of a surface active element in the metal, γ_T is negative

for all or most of the weld pool temperature range causing outward flows. On the contrary, in the case of an high surfactant activity, γ_T remains positive for most of the temperature range in the weld pool creating convective flows directed inwards. When an intermediate amounts of the surface active elements are present in the weld pool, a flow with two oppositely directed vortices occurs. This may lead to an unstable or oscillating weld pool convection.

In the current work, only the outwards directed convective flows are considered. Scaling analysis based on the fundamental physical formulation of the problem is used to provide the prediction formulae for the unknown characteristic values. Despite the seeming identity of the inwards and outwards directed weld pool flows, their mathematical treatment with scaling analysis is radically different. The outwards flows interaction with the weld pool liquid/solid interface normally takes place at a relatively far distance compared to the weld pool depth and the characteristic heat source size. If the weld pool width is significantly greater than the pool depth and the heat source size, its effect on the flow velocities may be insignificant and the dimensionless number associated with it may be omitted. In the case of the inwards directed convection, the flow constricts into a jet going vertically from the surface at approximately the weld pool center into the pool bottom. In this case the weld pool depth and the jet velocity are fully coupled and their mathematical treatment is significantly more complex. For this reason, due to the time limits this work had, only the outwards directed thermocapillary convective weld pool flows were considered in this work.

1.1.4 High-Prandtl-number materials. Polymers

High-Prandtl-number materials may also be subject to the Marangoni convection. Molten polymers are found to have surface tension decreasing with temperature similar to pure metals (Fig. 1.6) [23–25]. The effect of Marangoni convection during welding a high-Prandtl-number material was studied experimentally by Limmaneevi-

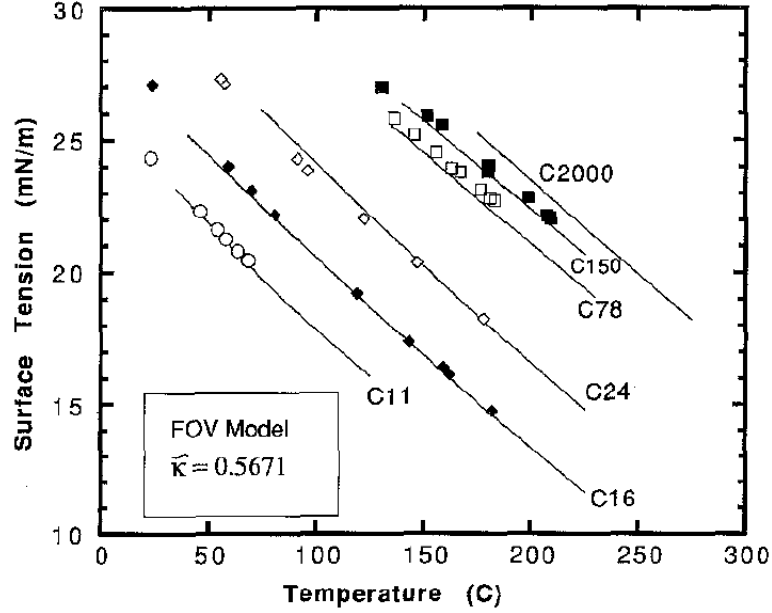


Figure 1.6: Temperature dependence of surface tension of polyethylene samples (reprinted from Dee and Sauer [23]).

chitr and Kou [26] on the example of sodium nitrate NaNO_3 . Molten sodium nitrate has the Prandtl number of $\text{Pr} = 9.15$. Stationary welds performed by a defocused laser beam. The thermocapillary convection promoted outward flows resulting in a range of welds from slightly concave to wide shallow convex shapes (Fig. 1.7) depending on the intensity of the beam and its diameter. Beam intensity being equal, smaller diameter beams were found to cause more intense convection.

1.1.5 Experimental studies

There are several obstacles to the experimental measurements of the convection velocities: opaqueness of the molten metal, high convection velocities in small volumes, high temperatures and their gradients, presence of a powerful heat and light source from the arc or laser beam. However, some experimental measurements of the weld convection velocities have been made.

Limmaneevichitr and Kou [26] used physical modelling technique for the analysis of thermocapillary weld pool convection. Transparent sodium nitrate molten

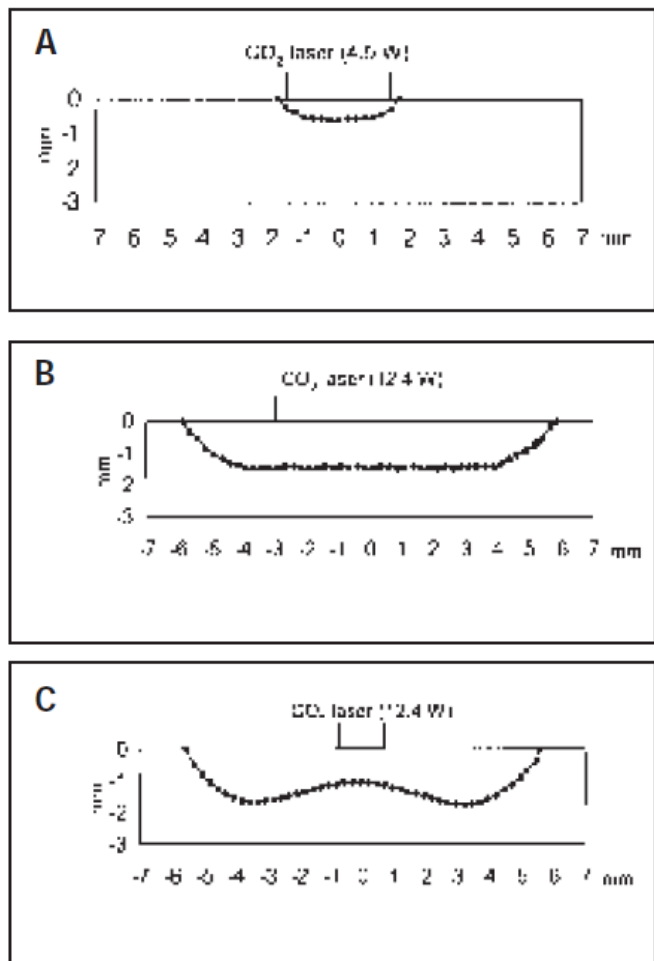


Figure 1.7: Weld pool shapes of NaNO_3 ($\text{Pr}=9.1$) from Limmaneevichitr and Kou [26] produced by CO_2 laser beams of the following: A — 4.5 W and 3.2 mm diameter; B — 12.4 W and 5.9 mm diameter; C — 12.4 W and 1.5 mm diameter.

pool heated from the top with a light source was used to represent a weld pool. Aluminum particles were added to trace the flow patterns. The results showed a principal agreement with the hypothesis that the surface tension temperature variations are a dominant driving force in the weld pool convection.

Recently, Delapp [27] and Zhao *et al.* [28, 29] performed high-speed videography of the weld pool surface. The surface flow of the oxide particles was then measured using Particle Image Velocimetry technique. Some work also has been done on X-ray weld pool velocity measurements [30, 31].

1.1.6 Numerical modelling

Flat and deformable surface

Many two-dimensional stationary models for Marangoni convection in weld pools assume that the free surface is flat and undeformable [2, 3, 32–37].

Tsai and Kou [38] studied the effect of a free deformable surface on Marangoni convection in stationary welds. The work was conducted for both positive and negative surface tension temperature coefficients. Pure aluminum properties were used to calculate the flow of a material with a negative surface tension temperature coefficient ($\gamma_T = -0.35 \cdot 10^{-3} \text{ kg s}^{-2} \text{ K}^{-1}$) and an artificial value of $\gamma_T = 0.1 \cdot 10^{-3} \text{ kg s}^{-2} \text{ K}^{-1}$ was used for a positive γ_T example. The authors found that the outward flows resulted in a depressed centre of the weld pool and an elevated edge portion of the surface. For the positive surface tension temperature coefficient, the trend is reversed: an elevated centre and a depressed surface at the edges. The authors conclude that in the case of a positive γ_T , the pool depth can be overestimated if the surface is assumed undeformable and flat; however, no justification was given for arc or beam pressure on the surface which usually has its maximum in the centre of the weld pool. Other works that calculated the surface-tension-driven flows in weld pool with a deformable surface include [39–42]. The difference in the weld pool shapes calculated using models with flat and deformable surfaces [22] for the outward flows are shown in the Fig. 1.8. Peng *et al.* [43] discussed the effect of the initial weld pool shape used as an initial guess for the transient two-dimensional modelling of Marangoni convection in welding. Ehlen *et al.* [44] focused on transient effects in an axisymmetrical two-dimensional transient model of laser melting. The molten pool shape changes were studied when a laser Gaussian heat source was applied to the surface, as well as the pool shape during cooling after the heat flux was switch off.

A two-dimensional laser welding process of steel and aluminum was modelled by Basu and Date [45]. The surface was exposed to an incident heat Gaussian flux. Two

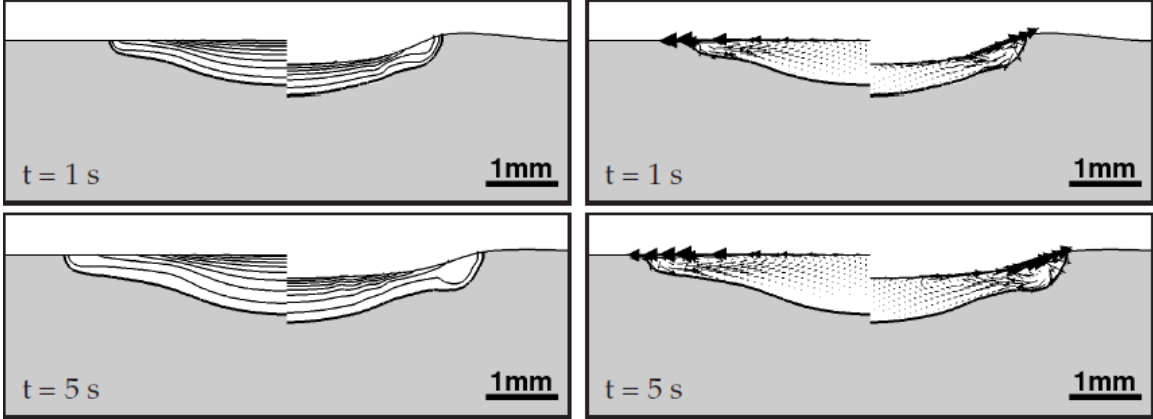


Figure 1.8: Comparison of the weld pool shapes and temperature (left) and velocity (right) fields for stationary welds in the models with flat and free deformable surface (reprinted from [22]).

convectational vortices occurred, a primary vortex cell near the surface at the edge of the weld pool, and an induced secondary vortex at the weld pool bottom. The pool shape was shallower for steel and deeper for aluminum.

The effect of the Marangoni convection on the formation of weld bead boundary was studied in [46]. The molten pool shapes with small Prandtl numbers can be identified by several regions: (i) the molten pool has a hemispherical shape for $Ma_f < 100$, (ii) the bottom of the pool is convex near the centerline for $0.1 < Pr < 1$ and $100 < Ma_f < 10^5$, (iii) the bottom is slightly convex near the centerline of the shallow pool for $0.3 < Pr < 1$ and $Ma_f > 10^5$, and (iv) the bottom exhibits a strong concave shape with concavity depth as high as one-half of the pool width for $Pr < 0.1$ and $Ma_f > 100$ and a concave shape for $0.1 < Pr < 0.3$ and $Ma_f > 10^5$. Corresponding weld pool shapes are shown in Fig. 1.9.

Three-dimensional models

Three-dimensional models were used by [3, 47–51]. Chan *et al.* [50] used a model of a stationary laser heat source that irradiated a flat semi-infinite surface of the workpiece. It was found that the cooling rate was higher at the pool edge gradually increasing along the melting line from the bottom to the edges, and it decreased with

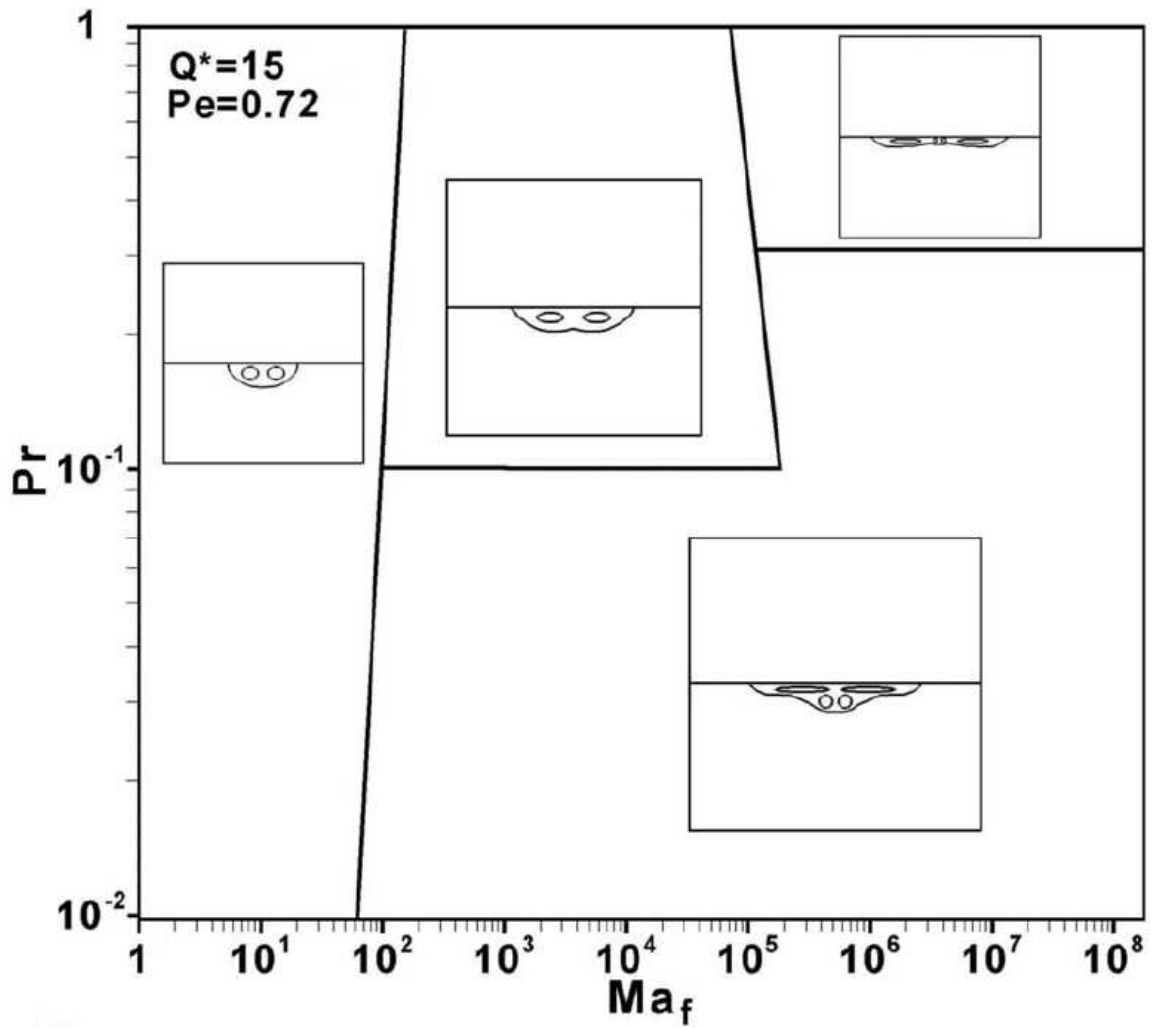


Figure 1.9: Weld pool shapes at low Pr numbers of $10^{-2} < Pr < 1$ from Wei *et al.* [46].

the elapsed time. The model did not consider latent heat nor the difference of the thermal conductivity for solid and liquid material.

Role of turbulence

The role of turbulence, i.e. chaotic variations in the flow velocity and pressure due to its high kinetic energy compared to the damping effect of the fluid viscosity, in the weld pool convection is not fully clear. Many researches that used laminar models, used modifications of transport coefficients such as viscosity and thermal conductivity, in order to obtain a better match with the experiments. These modifications are known as “enhancement”. There is no clear guide on how to perform these modifications. Dynamic viscosity and thermal conductivity were enhanced by a factor of 7 to 30 simultaneously or separately [52–54]. No physical explanation was provided.

The possible role of turbulence in the GTAW weld pool convection was discussed in [55]. The possibility of turbulent flow in the GTAW weld pools was also mentioned in [2]. The authors indicated a difference for the experimental results and those predicted with laminar models. The stationary GTAW welding of AISI 304 stainless steel was modelled using a k - ε turbulence model for 50, 100 and 150 A. The k - ε turbulence model is a CFD turbulence model that uses the concept of turbulent kinetic energy k and the rate of dissipation of turbulent kinetic energy ε and introduces two transport equations for these variables. The effect of turbulence on the GTAW weld pool convection was then numerically analyzed in [56]. The model includes buoyancy, Lorentz and Marangoni driven fluid flow, a large deformation model of the free surface, and a k - ε turbulence model. Other works on the effect of turbulence on the GTAW weld pool convection include [57, 58].

The differences between the predictions of laminar and turbulent models for laser welding of Fe and Cu are compared in [59]. It was concluded that unlike welding of Fe, for Cu convection has a marginal effect on the heat transport despite a vigorous mixing of the weld pool. A turbulent flow model was used in [60] in order to analyzed

the change in weld metal composition during laser welding of aluminum alloy 5182 in conduction mode.

The effect of thermocapillary convection on the weld pool length in keyhole laser welding was studied numerically in [61]. A turbulent flow in laser alloying is discussed in [62]; a turbulent flow in laser welding of copper-nickel dissimilar metals in [63]. The effect of turbulence in GMAW is discussed in [64–66]. The importance of turbulent flow on the bead formation in multi-pass hybrid gas metal arc laser welding is considered in [67]. A comprehensive overview of transport phenomena in both GMAW and GTAW is given in [68].

Most of the turbulence models used were Reynolds-Averaged Navier-Stokes (RANS), particularly often k - ε models. Since the k - ε models are based on the Boussinesq assumption which does not account for turbulence anisotropy and rotating flows, it is quite questionable how reliable are the results from these models in the case of complex recirculating flows in the weld pools with solid-liquid phase changes. The Boussinesq assumption is a hypothesis in CFD that relates the turbulence stresses to the mean flow. The model introduces the turbulence eddy viscosity, the concept that ignores the small-scale vortices (eddies) by estimating their effect on the large-scale motion with an effective viscosity or eddy viscosity.

There are few works on Large Eddy Scale (LES) models [69] or Direct Numerical Simulations (DNS) [70]. Chatterjee and Chakraborty [69] concluded that their LES model was more successful in capturing the experimental trends than k - ε . However, it was stressed that LES modeling for systems with phase transformation were in its infancy. A recent work [70] was performed using direct numerical simulations (DNS) to confirm the need for turbulence modelling for the numerical simulations of the laser welding. Only the case of 150 ppm of sulfur was studied. The calculated heat transfer increase due to the turbulence, however, was found insufficient for matching the experimental results.

1.1.7 Scaling analysis

Scaling, dimensional and asymptotic analyses are often used to obtain an approximate solution to a problem, mathematical treatment of which is difficult. These approaches has been widely used for various problems in physics and engineering [71–75]. For example, scaling approach was used in the well-known Blasius viscous boundary layer solution [76].

Scaling analysis is a powerful mathematical tool used to simplify mathematical equations with many terms by assessing their approximate magnitude and neglecting the small terms. Scaling approach has been used for various welding problems [77–79]. Order of Magnitude Scaling [80–83] has been applied for weld pool flows, arc behaviour, heat transfer and plastic deformation in friction stir welding [84].

Scaling laws for the characteristic values of the weld pool flows induced by Marangoni convection were proposed by Wei *et al.* for materials with the Prandtl numbers between $0.1 < Pr < 1$ [85] and $Pr > 1$ [86]. Both works provide scaling expressions for the six unknowns: the peak surface velocity and temperature, the secondary peak surface velocity and the temperature, the width and the depth of the weld pool as functions of Ma , Pr , Ste , the dimensionless heat input Q_0^* and the ratio of the thermal conductivities for solid and liquid metal k_s^* . The model used the melting efficiency equation that was obtained empirically and includes empirical constants. However, the numerical simulations results that were used for the optimization of the unknown functions for $0.1 < Pr < 1$ [85] used the variations of only the 2 parameters Ma , Pr out of presented 5. No justification was given to prove the dependencies on the other 3 dimensionless parameters. For the $Pr > 1$ model [86], the results of the numerical model used in the study were not presented.

Chakraborty [59] studied the effect of the Prandtl number on the momentum and heat transfer in a thermocapillary-driven weld pool convection. The authors concluded that for the materials with a very low Prandtl number the weld pool convection

does not significantly contribute to the formation of the weld shape.

Rivas and Ostrach [87] performed scaling analysis of thermocapillary flows in shallow rectangular cavities for low-Prandtl-number materials. The flow was analyzed in a rectangular cavity with its free surface exposed to a Gaussian distributed heat flux. As a result of the analysis, three regimes of the thermocapillary convection for $\text{Pr} < 1$ were identified. The Regime I represents a case of a viscous flow with conduction being the dominant heat transfer mechanism. Regime II is the case of a flow with the momentum boundary layer occurring at the surface (in this work also referred to as the “inertial flow”), but when conduction dominates as the heat transfer mechanism. Regime III represents the case when the flow is inertial with the momentum boundary layer at the surface, but when convection becomes dominant. The Regime III is characterized by both the momentum and temperature boundary layers.

Three dimensionless parameters were defined to govern the problem. The first was the ratio of the cavity depth to the heat source size $A = D/\mathcal{L}$; the second was the Prandtl number of the fluid $\text{Pr} = \nu/\alpha$. The third parameter was defined as a Reynolds number for the Regime I and called Re_σ :

$$\text{Re}_\sigma = \frac{\gamma_T Q_0 D^2}{\rho k \nu^2} \quad (1.3)$$

where γ_T is the absolute value of the temperature surface tension coefficient, Q_0 is the heat source peak intensity, D is the cavity depth, ρ is the fluid of density, k is the thermal conductivity of the fluid and ν is its kinematic viscosity. Note that this parameter Re_σ was used for all the regimes, although it is equal to the Reynolds number only for the Regime I. For the Regimes II and III this number is still used as a reference value, but it is not equal to Reynolds number which has to be calculated separately.

Mendez [80, 82, 83] analyzed the problem of the thermocapillary convection in a rectangular cavity defined in [87] using the Order of Magnitude Scaling methodology (OMS). OMS is a methodology that automatically makes selections of self-consistent

balances between dominant forces and provides estimated scaling laws based on the problem formulation.

1.2 Problem statement

1.2.1 Prediction of weld bead width and penetration depth from moving heat source models

The analytic model of a moving point heat source was proposed by Rosenthal [88] in 1946 and has still been widely used for the temperature distribution prediction in welding. It is simple to use, however, its predictions are accurate only far enough from the heat source.

Eagar [89] performed analysis of a more realistic distributed heat source approximated by a Gaussian function. Two dimensionless groups were found to govern the problem: the operating parameter n that includes the welding speed, the net heat input, the thermal diffusivity; and the dimensionless heat source distribution parameter u . The solution for Gaussian heat source can be obtained by taking an integral as proposed by Eagar. This is not as convenient as it would be if there were ready formulae, so additional work is continuing in this area [90].

It is proposed that the effect of the thermocapillary flows on the weld shape can be formulated in the form of correction factors to the solution for the Gaussian heat source. These correction factors are the objectives of this work.

1.2.2 Asymptotic and intermediate regimes

Many physical phenomena represent the cases of asymptotic behaviour of more complex systems. An example of a damped pendulum was discussed in [80, 83]. Another example of asymptotic and intermediate regimes could be a skydiver's free fall velocity as a function of time.

For this example let us assume the jump is performed from a stationary helicopter.

During the free fall, two forces are balancing each other: gravity and drag force.

$$mg - C_D A \frac{\rho V^2}{2} = ma \quad (1.4)$$

Here m is the skydiver's mass, g gravity acceleration, C_D is a drag coefficient, A is the skydiver's reference area, ρ is the air density, V is the velocity, a is the acceleration.

At the moment when the skydiver leaves the helicopter, the gravity force is the only force applied and, thus, it is equal to the product of the skydiver's mass to their acceleration. This situation represent the first asymptotic case, Regime I:

$$mg = ma_I \quad (1.5)$$

The skydiver's acceleration is equal to the gravity acceleration, thus, the fall velocity V increases with time t according to the simple law:

$$V_I(t) = gt, \quad (1.6)$$

i.e., the velocity in Regime I is proportional to the first order of time.

Along with the velocity, the drag force increases. Eventually, at a velocity V_{II} it becomes equal to the gravity force and there is no more velocity change:

$$mg = C_D A \frac{\rho V_{II}^2}{2} \quad (1.7)$$

This steady fall represents the second asymptotic regime, 'Regime II'. The velocity dependence on time is now expressed by the law:

$$V_{II}(t) = \sqrt{\frac{2mg}{C_D A \rho}} \quad (1.8)$$

In more formal way, the velocity in Regime II is proportional to the zeroth order of time. The obtained dependencies could be rewritten in a dimensionless form. Then the dimensionless velocity V^* would be a function of the dimensionless time in a form of scaling law, i.e. an exponent function:

$$V^* = t^{*c} \quad (1.9)$$

$$c_I = 1 \quad (1.10)$$

$$c_{II} = 0 \quad (1.11)$$

1.2.3 Problem analysis from Buckingham π theorem

In order to understand what parameters the weld pool width and depth depend on and what kind of dependencies these are, let us consider the problem from the perspective of the Buckingham π theorem starting from the model of point heat source.

Point heat source

First, let us consider a problem of the determination of the characteristic weld bead width $2L$ and penetration depth D during welding on a thick plate with a point heat source from Buckingham π theorem perspective [91]. The defining parameters are: the heat flux q ; travel velocity U ; material density ρ , thermal conductivity k_s and heat capacity c_P ; temperature difference between the melting point and the room temperature $\Delta T_m = T_m - T_\infty$.

The class of the parameter dimensions is chosen as $LMTQ\Theta$, where L represents the units of length, M - mass, T - time, Q - units of thermal heat and Θ for units of temperature. The number of independent dimensions in this case is $k = 5$, and the number of parameters in $n = 6$. Thus, the number of governing dimensionless parameters for the problem of a moving point heat source is $n - k = 1$. This conclusion agrees with the classic Rosenthal's solution [88].

The identified governing dimensionless parameter can be expressed in a form of the Rykalin number [92]:

$$\text{Ry} = \frac{qU}{4\pi k\alpha(T_m - T_\infty)}, \quad (1.12)$$

where $\alpha = k/(\rho c_P)$ is the thermal diffusivity. The coefficient of $1/4\pi$ is introduced to match the definition of the Rykalin number from [92]. Thus, the dimensionless weld bead width and penetration depth are functions of only Ry:

$$L^*, D^* = f(\text{Ry}), \quad (1.13)$$

where

$$L^* = \frac{UL}{2\alpha} \quad (1.14)$$

$$D^* = \frac{UD}{2\alpha} \quad (1.15)$$

Gaussian heat source

A more realistic Gaussian distributed heat source introduces another parameter: the heat source distribution size 2σ . Thus, it introduces another dimensionless parameter σ^* :

$$\sigma^* = \frac{U\sigma}{2\alpha} \quad (1.16)$$

$$L^*, D^* = f(\text{Ry}, \sigma^*) \quad (1.17)$$

This represents the solution proposed by Eagar and Tsai [89] shown in Fig. 1.10 ($n \equiv \text{Ry}$, $u \equiv \sigma^*$).

Melting and solidification

The Gaussian heat source model is considered to be quite accurate for predicting the weld bead width and penetration depth even though it does not account for the latent heat of melting and changes of the thermophysical properties with the phase transformations. It is assumed that due to the fast melting and re-solidification process the change in the properties is localized and can be neglected. There is a shift in the melting and solidification front line from the isotherm locations predicted by the model in the direction of welding; however, the prediction of weld width and depth can still be accurately predicted.

However, if melting is taken into consideration, then the latent heat i_{sl} of melting must be added to the problem parameters and, consequently, the Stefan number:

$$\text{Ste} = \frac{c_P \Delta T_m}{i_{sl}} \quad (1.18)$$

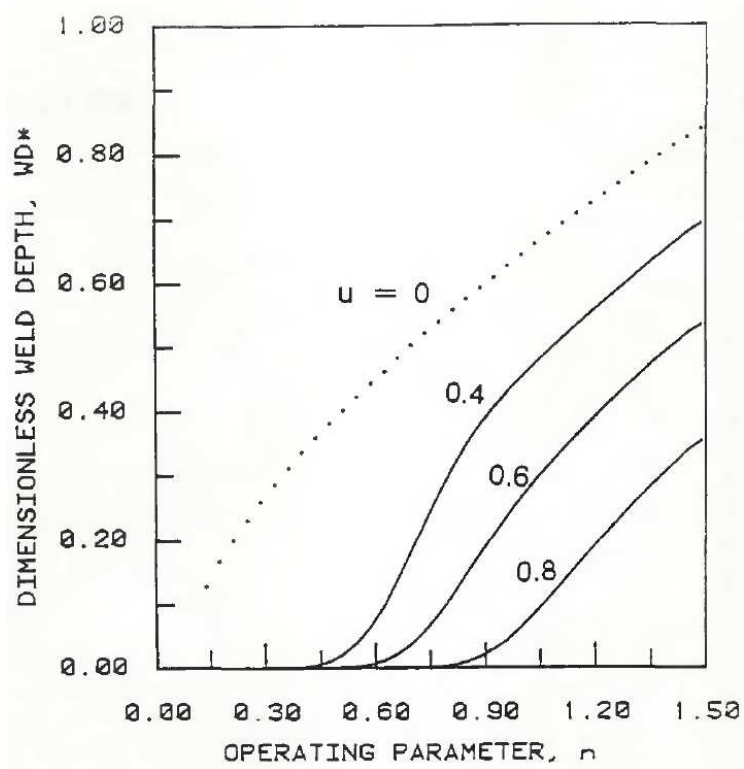


Figure 1.10: Dimensionless weld penetration depth from [89] ($n \equiv Ry$, $u \equiv \sigma^*$).

If the changes of the thermophysical parameters with the phase transformation are taken into account, then additional dimensionless parameters must be added, e.g., ratios of the considered parameters for solid to their liquid counterparts:

$$k_s^* = \frac{k_s}{k_l}, \alpha_s^* = \frac{\alpha_s}{\alpha_l}, \rho_s^* = \frac{\rho_s}{\rho_l}, \text{ etc.} \quad (1.19)$$

Since the material properties are also dependent on the temperature, the list of dimensionless groups related to the material properties that govern the problem is, generally speaking, infinite.

Effect of the Marangoni convection

Further, if the thermocapillary flows are taken into account, i.e., the convection inside the melt pool due to Marangoni effect, then the two important parameters must be added: the kinematic viscosity of the melt ν and the surface tension temperature coefficient γ_T . Consequently, they add two new dimensionless parameters. The first of them is the Prandtl number:

$$\text{Pr} = \frac{\nu}{\alpha_l} \quad (1.20)$$

The other dimensionless group must be a parameter that includes γ_T . Traditionally, the Marangoni number is used:

$$\text{Ma} = \frac{\gamma_T \Delta T_c L_c}{\rho_l \nu \alpha_l}, \quad (1.21)$$

where L_c is a characteristic length, ΔT_c is a characteristic temperature drop.

It makes the most sense to take ΔT_c as the difference between the maximum temperature in the melt pool T_{max} and the melting temperature T_m , and as the characteristic length L_c the half-width L of the weld pool. In this case, since the pool half-width is the distance between the point with the highest (T_{max}) and lowest (T_m) temperatures in the melt, the Marangoni number presented becomes essentially the Peclet number of the thermocapillary convection, i.e., the ratio of the heat transferred by thermocapillary convection to the heat transferred by conduction through the melt.

However, both the T_{max} and L are unknown parameters of the problem, which means other characteristic values must be used. Some researches use the difference between the melting point and the surrounding temperature $\Delta T_m = T_m - T_\infty$ and the heat source distribution size σ^* . The use of these parameters in Ma may cause confusion. Additionally, the physical meaning of the Marangoni number as the Peclet number for thermocapillary flows is lost in this case. For this reason, in this work the other dimensionless group Ri is used:

$$\text{Ri} = \frac{\gamma T q}{\rho_l \nu^2 k_l} \quad (1.22)$$

The physical meaning of this dimensionless number is described in Chapter 2.

Thus, the dimensionless weld pool width and the penetration depth are, strictly speaking, functions of the following dimensionless groups:

$$\frac{L}{\sigma}, \frac{D}{\sigma} = \Phi \left(\text{Ri}, \text{Pr}, \text{Ry}, \sigma^*, \text{Ste}, \frac{k_s}{k_l}, \frac{\alpha_s}{\alpha_l}, \frac{\rho_s}{\rho_l}, \dots \right) \quad (1.23)$$

1.2.4 Main hypothesis

Typical velocities of the thermocapillary convective flows in GTA weld pools are usually much greater than the weld torch travel speeds [5]. It allows to assume a relative independence of the thermocapillary convection in the weld pools and its effect on the weld geometry. One important parameter related to the moving heat source, however, must be considered: a ratio of the characteristic size of the weld pool to the heat source distribution parameter. Since the exact weld pool width and depth are unknowns and are subject to the convection, a ratio of the penetration depth from the Gaussian heat source solution D_G to its distribution parameter σ is proposed as such a parameter \mathcal{R}_G ('Aspect ratio Gaussian'):

$$\mathcal{R}_G = \frac{D_G}{\sigma} \quad (1.24)$$

The Peclet number Pe is proposed as the measure of convective heat transfer versus conduction through the melt. With the assumptions described above, it is possible

to assume that

$$\text{Pe} = C f(\text{Ri}, \text{Pr}, \mathcal{R}_G) \quad (1.25)$$

where C is a parameter related to the thermophysical material properties and is constant for a given material and the surrounding or preheat temperature:

$$C = g\left(\text{Ste}, \frac{k_s}{k_l}, \frac{\alpha_s}{\alpha_l}, \frac{\rho_s}{\rho_l}, \dots\right) \quad (1.26)$$

The Gaussian aspect ratio, in its turn, is a function of the Rykalin number and the heat source distribution parameter:

$$\mathcal{R}_G = g(\text{Ry}, \sigma^*) \quad (1.27)$$

For stationary GTAW welds, the parameter \mathcal{R}_G can be considered as the dimensionless time. When a system is in an asymptotic regime, it is likely that the unknowns

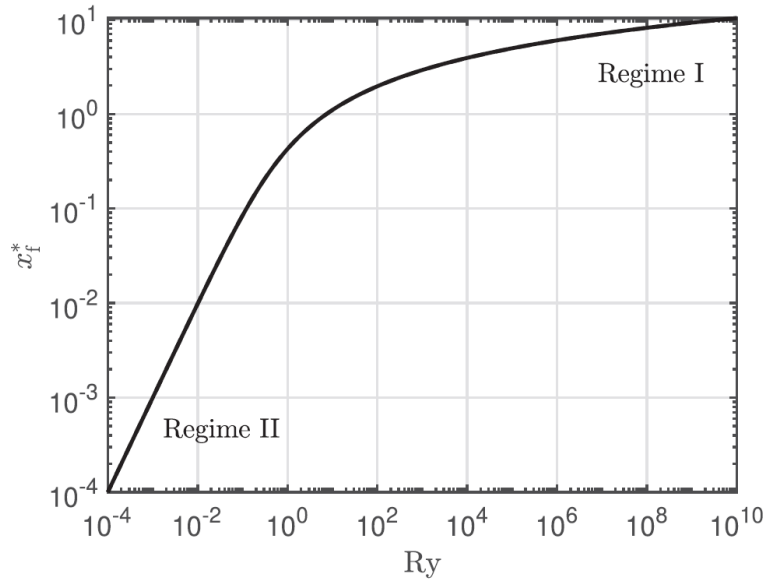


Figure 1.11: Dimensionless leading length as a function of Ry from [92].

can be expressed in a form of a scaling law. Analogously to [87], it is reasonable to assume that for each asymptotic regime of the thermocapillary flow the dependence 1.25 has a form of a scaling law, too:

$$\text{Pe} = C \text{Ri}^a \text{Pr}^b \mathcal{R}_G^c \quad (1.28)$$

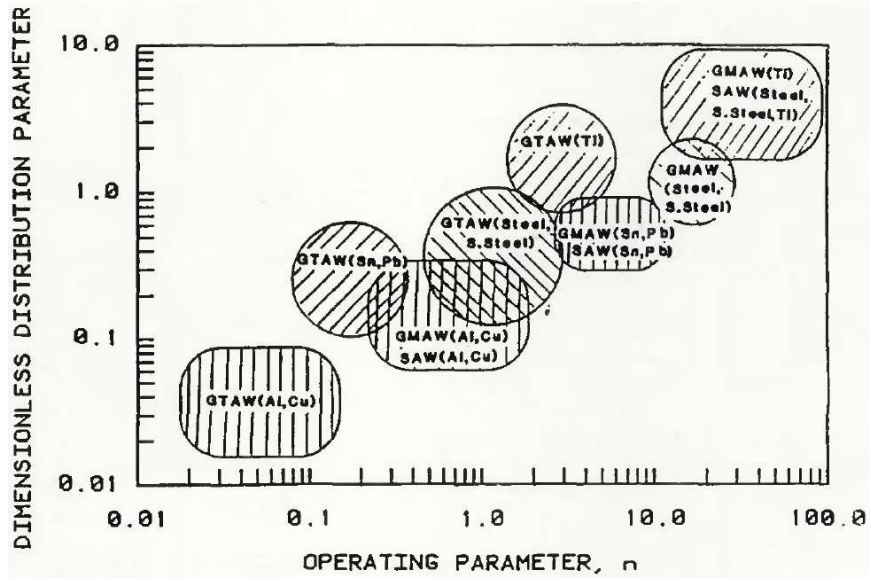


Figure 1.12: Typical welding conditions for various welding processes [89] ($n \equiv Ry$, $u \equiv \sigma^*$).

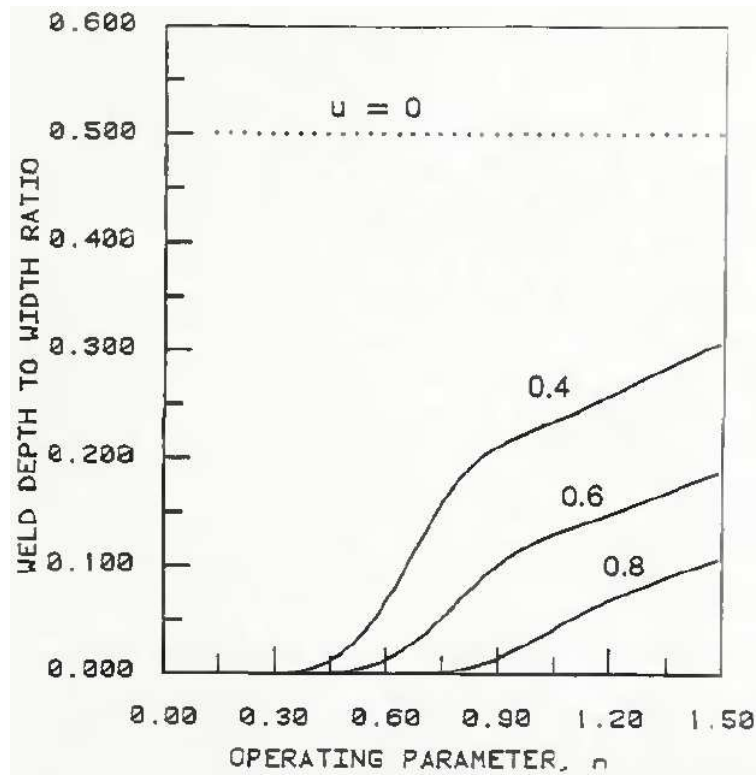


Figure 1.13: Width to depth ratio as a function of the Rykalin number and heat source distribution ($n \equiv Ry$, $u \equiv \sigma^*$) from [89].

However, if a system is in the intermediate state between two asymptotic regimes, then such a dependence may be more complex. For example, Fig. 1.11 shows the dimensionless leading length for the point heat source problem as a function of the Rykalin number from [92]. It can be seen that in the asymptotic Regime I of a fast moving heat source for $Ry > 10^3$, the dependence of the unknown value is linear in the logarithmic scale, i.e., can be expressed in the form of a scaling law. Analogously, the dimensionless leading length in the Regime II of the slow point heat source for $Ry < 10^{-3}$ can be presented as an exponent function. For $0.1 < Ry < 10$, however, the exponent function is not applicable.

This intermediate state between fast and slow moving heat source is also applicable for the Gaussian heat source model. Typical GTAW processes parameters lie within $0.1 < Ry < 10$ range of the Rykalin number (Fig. 1.12). It can be seen from, for example, Fig. 1.13 that for the Gaussian heat source model the dependencies of the unknown parameters, for example, the width-to-depth ratio on this range of the Rykalin number cannot be expressed in the form of a scaling law.

Thus, the proposed separation of variables allows the non-asymptotic dependency of the unknowns from Ry and σ^* to be excluded, as well as travel speed from the focus of the Marangoni flow problem.

1.2.5 Objectives

The objectives of this work are to:

1. Identify asymptotic regimes of the thermocapillary flows in weld pools, criteria that set the demarcation between them, the flow patterns and other features of the identified regimes for both low-Prandtl-number and high-Prandtl-number melts.
2. Define the scaling laws for the dependencies of the characteristic convection velocity u_T and, consequently, the Peclet number Pe from Ri , Pr and \mathcal{R}_G for

each asymptotic flow regime.

3. Verify and calibrate the obtained scaling laws.
4. Create correction factors for weld width and penetration depth calculated with the Gaussian heat source model that would account for the effect of the thermocapillary convection.

1.2.6 Thesis outline

Chapter 2 describes the identified regimes of the thermocapillary flows in weld pools, the scaling analysis of these regimes and the obtained scaling laws for the characteristic velocities and the Peclet numbers.

Chapter 3 describes the numerical model used to verify and calibrate the obtained scaling laws.

Chapter 4 includes the calibration of the scaling laws for the Peclet number with the use of the results from the numerical model and the literature data, as well as the calculation of the correction factors for the weld bead width and penetration depth compared to the predicted ones by the Gaussian heat source model.

Chapter 2

Scaling Analysis

2.1 Hydrodynamic regimes of thermocapillary flows in weld pools

Rivas and Ostrach [87] proposed that there are three flow regimes for thermocapillary flows in shallow enclosures filled with a low-Prandtl-number fluid. The flow can be either viscous or inertial. By inertial flow the authors meant the flow with a formation of a viscous boundary layer at the free surface where the driving Marangoni shear occurs, while the viscous flow mean that the viscous shear is distributed evenly throughout the fluid. The heat transfer can be dominated by either conduction or convection. In case of convection-dominated flow, a thermal boundary layer occur at the free surface.

The three regimes identified in [87] represent combinations of the types of flow and heat transfer mechanisms. The Regime I stands for a viscous flow with conduction being dominant heat transfer mechanism. The Regime II represents the case when the flow is inertial, but conduction still dominates the heat transfer. This regime represents, for example, the cases reported in the literature of aluminum weld pools not having their shape noticeably affected by the flow due to the very low Prandtl number of molten aluminum. The Regime III represents the case of an inertial flow with convection dominating over conduction in the pool. This regime is the most common flow regime in steel weld pools.

To quantify the effect of the thermocapillary shear stress on the flow, Rivas and Ostrach [87] proposed a dimensionless number Re_σ defined as

$$\text{Re}_\sigma = \frac{\gamma_T Q_0 D^2}{\rho k \nu^2} \quad (2.1)$$

where γ_T is the surface tension temperature coefficient, Q_0 is the peak intensity of the heat source, D is the weld pool depth, ρ is the fluid density, k is the thermal conductivity and ν is the kinematic viscosity. This number represents the scaling law for the Reynolds number of the Regime I.

From the scaling analysis it was identified that $A^2 \text{Re}_\sigma$ is a representative dimensionless number that identifies the transition from a viscous to inertial flow in the weld pool. A is the aspect ratio defined as $A = D/\mathcal{L}$, where D is the pool depth and \mathcal{L} is the characteristic size of the heat source. The width of the weld pool is assumed much greater than both D and \mathcal{L} .

Thus, the criterion for the Regime I was stated as:

$$\text{Pr} < 1 \quad (2.2)$$

$$A^2 \text{Re}_\sigma < 1 \quad (2.3)$$

Since $\text{Pe} = \text{RePr}$, for the melts with $\text{Pr} < 1$ this criterion automatically confirms that conduction is dominant.

Due to formation of the viscous boundary layer when the flow is inertial, Re_σ is no longer valid as an approximation for the Reynolds number in the Regimes II and III. Two characteristic velocities are identified in the Regime II: the characteristic velocity in the viscous boundary layer and the characteristic velocity of the core of the bulk of the melt. The approximation for the Reynolds number based on the core velocity in the Regime II is:

$$\text{Re}_{\text{II}} = A^{2/3} \text{Re}_\sigma^{1/3} \quad (2.4)$$

Thus, the transition criterion for convection being negligible in the Regimes II is

$$A^{2/3} \text{Re}_\sigma^{1/3} \text{Pr} < 1 \quad (2.5)$$

The full criteria for the Regime II are:

$$\text{Pr} < 1 \quad (2.6)$$

$$A^2 \text{Re}_\sigma > 1 \quad (2.7)$$

$$A^{2/3} \text{Re}_\sigma^{1/3} \text{Pr} < 1 \quad (2.8)$$

Thus, the criteria for the Regime III are:

$$\text{Pr} < 1 \quad (2.9)$$

$$A^2 \text{Re}_\sigma > 1 \quad (2.10)$$

$$A^{2/3} \text{Re}_\sigma^{1/3} \text{Pr} > 1 \quad (2.11)$$

The use of the weld pool depth D in the governing dimensionless number Re_σ , may lead to over-complication when the depth of the weld pool is an unknown. Also the notation Re_σ is found confusing, since it is used in all the regimes, but represents the Reynolds number only for the Regime I. To avoid the confusion and inconvenience, two novel dimensionless numbers Ri and $\text{Ri}_\mathcal{L}$ are proposed in this work. $\text{Ri}_\mathcal{L}$ is defined as:

$$\text{Ri}_\mathcal{L} = \frac{\gamma_T Q_0 \mathcal{L}^2}{\rho k \nu^2} \quad (2.12)$$

The index \mathcal{L} indicates that the number is defined based on the peak intensity of the heat source Q_0 and its characteristic size \mathcal{L} . This number is used for the scaling analysis in this chapter.

Since the product $Q_0 \mathcal{L}^2$, in fact, represents the heat source power, the other dimensionless number Ri is defined as:

$$\text{Ri} = \frac{\gamma_T q}{\rho k \nu^2} \quad (2.13)$$

where q is the power of the heat source in Watts. For a Gaussian heat source

$$q = \frac{\pi}{\ln 2} Q_0 \mathcal{L}^2 \approx 4.53 Q_0 \mathcal{L}^2 \quad (2.14)$$

Also, in this work the notation $\mathcal{R}_{\mathcal{L}}$ will be used for the aspect ratio defined as:

$$\mathcal{R}_{\mathcal{L}} = D/\mathcal{L} \quad (2.15)$$

Since

$$\text{Re}_{\sigma} = \mathcal{R}_{\mathcal{L}}^2 \text{Ri}_{\mathcal{L}} \quad (2.16)$$

then, the criteria for the flow regimes can be represented with the Ri number in the following way. The criteria for the Regime I are:

$$\text{Pr} < 1 \quad (2.17)$$

$$\mathcal{R}_{\mathcal{L}}^4 \text{Ri}_{\mathcal{L}} < 1 \quad (2.18)$$

The criteria for the Regime II are:

$$\text{Pr} < 1 \quad (2.19)$$

$$\mathcal{R}_{\mathcal{L}}^4 \text{Ri}_{\mathcal{L}} > 1 \quad (2.20)$$

$$\mathcal{R}_{\mathcal{L}}^{4/3} \text{Ri}_{\mathcal{L}}^{1/3} \text{Pr} < 1 \quad (2.21)$$

And the criteria for the Regime III are as follows:

$$\text{Pr} < 1 \quad (2.22)$$

$$\mathcal{R}_{\mathcal{L}}^4 \text{Ri}_{\mathcal{L}} > 1 \quad (2.23)$$

$$\mathcal{R}_{\mathcal{L}}^{4/3} \text{Ri}_{\mathcal{L}}^{1/3} \text{Pr} > 1 \quad (2.24)$$

Another three regimes can be identified for the high-Prandtl-number melt similarly to the Regimes I, II and III.

Since $\text{Pe} = \text{RePr}$, for a melt with a $\text{Pr} > 1$, inertial flow automatically means that convection dominates the heat transfer. This regime is introduced as the Regime IV and defined as:

$$\text{Pr} > 1 \quad (2.25)$$

$$\mathcal{R}_{\mathcal{L}}^4 \text{Ri}_{\mathcal{L}} > 1 \quad (2.26)$$

For a high-Prandtl-number fluid, in a viscous flow both convection and conduction may be dominant as the heat transfer mechanism. The case when conduction dominates in the viscous flow can be also referred as the Regime I and share the scaling laws with the predictions for low-Prandtl-number melts. The criteria for the flow to fall into the Regime I for $\text{Pr} > 1$ is:

$$\text{Pr} > 1 \quad (2.27)$$

$$\mathcal{R}_{\mathcal{L}}^4 \text{Ri}_{\mathcal{L}} < 1 \quad (2.28)$$

$$\mathcal{R}_{\mathcal{L}}^4 \text{Ri}_{\mathcal{L}} \text{Pr} < 1 \quad (2.29)$$

The regime with the viscous type of flow, but convection being dominant, is identified in the Regime V. Its criteria are, then:

$$\text{Pr} > 1 \quad (2.30)$$

$$\mathcal{R}_{\mathcal{L}}^4 \text{Ri}_{\mathcal{L}} < 1 \quad (2.31)$$

$$\mathcal{R}_{\mathcal{L}}^4 \text{Ri}_{\mathcal{L}} \text{Pr} > 1 \quad (2.32)$$

Thus, five regimes of the thermocapillary-driven weld pool flows are identified for the melts with both high and low Prandtl numbers. The schematic map of the regimes on $\mathcal{R}_{\mathcal{L}}^4 \text{Ri}_{\mathcal{L}} - \text{Pr}$ plane is shown in the Fig. 2.1.

2.2 Problem formulation for the scaling analysis

For the scaling analysis, the flow is analyzed in a simplified axisymmetric rectangular cavity with the free surface exposed to a Gaussian heat flux as shown in the Fig. 2.2 (a half of the enclosure is shown) analogously to the flat two-dimensional problem formulation in [87]. The rectangular cavity with the width $2L$ and the depth D is filled with a fluid of density ρ , thermal diffusivity α and kinematic viscosity ν . The half-width of the cavity L is considered much greater than both the depth D and the characteristic size of the heat source \mathcal{L} . The walls are at the melting temperature

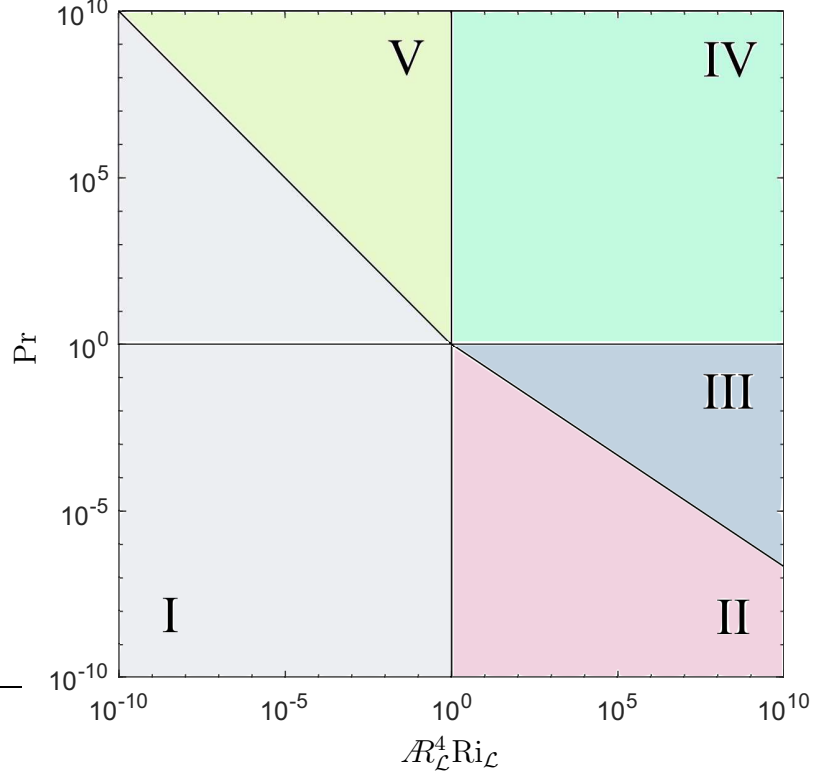


Figure 2.1: Asymptotic flow regimes on the $\mathcal{R}_L^4 \text{Ri}_L - \text{Pr}$ plane map.

T_m . The free surface is exposed to a Gaussian heat flux $Q(r)$ with peak intensity of Q_0 and characteristic width \mathcal{L} .

The following simplifications are used: steady state, non-deformable free-surface, heat source stationary with respect to solid boundaries, axisymmetric two-dimensional rectangular geometry, lack of electromagnetic or buoyancy body forces in the melt, no gas shear on the surface, no frictional heating (including the heating by viscous dissipation of kinematic energy), and width of solid boundaries much larger than width of heat source. The fluid is considered laminar, incompressible, with constant thermophysical properties. The surface pressure far from the heat source is atmospheric. The free surface is associated with surface tension γ that decreases linearly with temperature:

$$\gamma = \gamma_0 - \gamma_T (T - T_m) \quad (2.33)$$

The temperature surface tension coefficient γ_T , as well as all the other parameters

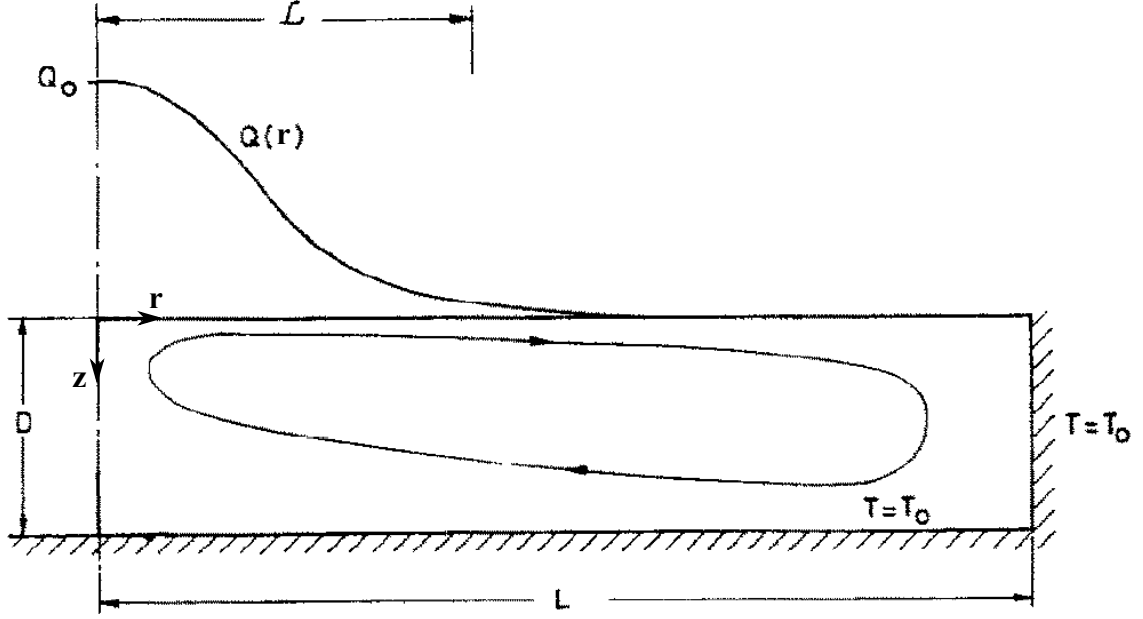


Figure 2.2: Schematics of the problem formulation (modified from [87])

are assumed constant.

Based on the above considerations, the mathematical formulation of the problem involves the equation of mass conservation (Eq. 2.34), two Navier-Stokes equations for the radial (Eq. 2.35) and axial (Eq. 2.36) directions, and the conservation of the thermal energy equation (Eq. 2.37):

$$\frac{1}{r} \frac{\partial}{\partial r} (ru) + \frac{\partial w}{\partial z} = 0 \quad (2.34)$$

$$u \frac{\partial u}{\partial r} + w \frac{\partial u}{\partial z} = -\frac{1}{\rho} \frac{\partial p}{\partial r} + \nu \left[\frac{1}{r} \frac{\partial}{\partial r} \left(r \frac{\partial u}{\partial r} \right) - \frac{u}{r^2} + \frac{\partial^2 u}{\partial z^2} \right] \quad (2.35)$$

$$u \frac{\partial w}{\partial r} + w \frac{\partial w}{\partial z} = -\frac{1}{\rho} \frac{\partial p}{\partial z} + \nu \left[\frac{1}{r} \frac{\partial}{\partial r} \left(r \frac{\partial w}{\partial r} \right) + \frac{\partial^2 w}{\partial z^2} \right] \quad (2.36)$$

$$u \frac{\partial T}{\partial r} + w \frac{\partial T}{\partial z} = \alpha \left[\frac{1}{r} \frac{\partial}{\partial r} \left(r \frac{\partial T}{\partial r} \right) + \frac{\partial^2 T}{\partial z^2} \right] \quad (2.37)$$

The boundary conditions on the free surface involve the Marangoni boundary condition and the input heat flux condition:

$$\rho \nu \frac{\partial u}{\partial z} = \gamma_T \frac{\partial T}{\partial r} \quad (2.38)$$

$$k \frac{\partial T}{\partial z} = -Q(r) \quad (2.39)$$

The independent variables are $\{X\} = \{r, z\}$. The dependent variables are $\{U\} = \{u(r, z), w(r, z), p(r, z), T(r, z)\}$, representing the r and z components of the velocity field, the pressure field, and the temperature field; and the parameters are $\{P\} = \{\mathcal{L}, \rho, \alpha, k, Q_0, \gamma_T, \nu, D\}$ representing a characteristic half width of the heat source, the melt density, the melt thermal diffusivity, the melt thermal conductivity, the peak intensity of the heat source, the surface tension temperature coefficient, the kinematic viscosity, and the depth of the melt respectively.

2.3 Regime I

The governing equations and the boundary conditions at the free surface are non-dimensionalized using the traditional approach. The heat source distribution parameter \mathcal{L} is taken as the characteristic value to normalize the coordinate r , and the depth of the cavity D is considered as the characteristic length for the coordinate z :

$$r^* = r/\mathcal{L} \quad (2.40)$$

$$z^* = z/D \quad (2.41)$$

The temperature, pressure and velocity components are normalized with their unknown characteristic maximum values ΔT , p_c , u_c and w_c .

Since in the Regime I the flow is viscous and conduction is dominant, the derivatives of the independent variables u , w , p and T are normalized with the ratios of their characteristic maximum values over the characteristic lengths of the respective coordinates, e.g.:

$$\frac{\partial p}{\partial z} = \frac{p_c}{D} \left(\frac{\partial p}{\partial z} \right)^* \quad (2.42)$$

$$\frac{1}{r} \frac{\partial}{\partial r} (ru) = \frac{u_c}{\mathcal{L}} \frac{1}{r^*} \frac{\partial^*}{\partial r^*} (r^* u^*) \quad (2.43)$$

The second derivatives are non-dimensionalized similarly, e.g.:

$$\frac{\partial^2 T}{\partial z^2} = \frac{\Delta T}{D^2} \left(\frac{\partial^2 T}{\partial z^2} \right)^* \quad (2.44)$$

$$\frac{1}{r} \frac{\partial}{\partial r} \left(r \frac{\partial w}{\partial r} \right) = \frac{w_c}{\mathcal{L}^2} \frac{1}{r^*} \frac{\partial^*}{\partial r^*} \left(r^* \frac{\partial w^*}{\partial r^*} \right) \quad (2.45)$$

Thus, the normalized continuity and Navier-Stokes equations for the Regime I are:

$$\frac{u_c}{\mathcal{L}} \frac{1}{r^*} \frac{\partial^*}{\partial r^*} (r^* u^*) + \frac{w_c}{D} \frac{\partial w^*}{\partial z^*} = 0 \quad (2.46)$$

$$\begin{aligned} \frac{u_c^2}{\mathcal{L}} u^* \frac{\partial u^*}{\partial r^*} + \frac{u_c w_c}{D} w^* \frac{\partial u^*}{\partial z^*} = -\frac{p_c}{\rho \mathcal{L}} \frac{\partial p^*}{\partial r^*} + \\ + \frac{\nu u_c}{\mathcal{L}^2} \frac{\partial^*}{\partial r^*} \left(\frac{1}{r^*} \frac{\partial^*}{\partial r^*} (r^* u^*) \right) + \frac{\nu u_c}{D^2} \frac{\partial^2 u^*}{\partial z^{*2}} \end{aligned} \quad (2.47)$$

$$\begin{aligned} \frac{u_c w_c}{\mathcal{L}} u^* \frac{\partial w^*}{\partial r^*} + \frac{w_c^2}{D} w^* \frac{\partial w^*}{\partial z^*} = -\frac{p_c}{\rho D} \frac{\partial p^*}{\partial z^*} + \\ + \frac{\nu w_c}{\mathcal{L}^2} \frac{1}{r^*} \frac{\partial^*}{\partial r^*} \left(r^* \frac{\partial w^*}{\partial r^*} \right) + \frac{\nu w_c}{D^2} \frac{\partial^2 w^*}{\partial z^{*2}} \end{aligned} \quad (2.48)$$

The thermal energy equation is:

$$\begin{aligned} \frac{u_c \Delta T}{\mathcal{L}} u^* \frac{\partial T^*}{\partial r^*} + \frac{w_c \Delta T}{D} w^* \frac{\partial T^*}{\partial z^*} = \\ = \frac{\alpha \Delta T}{\mathcal{L}^2} \frac{1}{r^*} \frac{\partial^*}{\partial r^*} \left(r^* \frac{\partial T^*}{\partial r^*} \right) + \frac{\alpha \Delta T}{D^2} \frac{\partial^2 T^*}{\partial z^{*2}} \end{aligned} \quad (2.49)$$

The normalized Marangoni boundary condition is:

$$\frac{\rho \nu u_c}{D} \frac{\partial u^*}{\partial z^*} = \frac{\gamma_T \Delta T}{\mathcal{L}} \frac{\partial T^*}{\partial r^*} \quad (2.50)$$

The input heat flux boundary condition is normalized as:

$$\frac{k \Delta T}{D} \frac{\partial T^*}{\partial z^*} = -Q_0 Q^*(r^*) \quad (2.51)$$

The estimation of unknown characteristic values was performed with the use of the Order of Magnitude Scaling (OMS) methodology described in detail in [82]. The methodology involves a computer algorithm which automatically exhausts all the possible balances of the dominant terms and makes selections based on self-consistency of the selected balances. The methodology uses the linear algebra matrix operations and provides the scaling laws for the unknowns as the functions of the problem parameters.

Since the approach is based on the linear algebra operations, the normalized coefficients are rewritten in the form of the Matrix of Coefficients $[C_I]$ with each row corresponding to the exponents of the parameters and the unknown characteristic values. The Matrix of Coefficients for the Regime I is:

$$[C_I] = \begin{array}{c} \begin{array}{cccccccc} \mathcal{L} & D & \rho & \nu & \alpha & k & \sigma_T & Q_0 & u_c & w_c & p_c & \Delta T \end{array} \\ \left[\begin{array}{cccccccc|cccc} -1 & & & & & & & & 1 & & & \\ & -1 & & & & & & & & 1 & & \\ \hline -1 & & & & & & & & 2 & & & \\ & -1 & & & & & & & 1 & 1 & & \\ -1 & & -1 & & & & & & & & 1 & \\ -2 & & & 1 & & & & & 1 & & & \\ & -2 & & 1 & & & & & 1 & & & \\ \hline -1 & & & & & & & & 1 & 1 & & \\ & -1 & & & & & & & & 2 & & \\ -1 & -1 & -1 & & & & & & & & 1 & \\ -2 & & & 1 & & & & & 1 & & & \\ & -2 & & 1 & & & & & 1 & & & \\ \hline -1 & & & & & & & & 1 & & & 1 \\ & -1 & & & & & & & & 1 & & 1 \\ -2 & & & & 1 & & & & & & & 1 \\ & -2 & & & 1 & & & & & & & 1 \\ \hline & -1 & 1 & 1 & & & & & 1 & & & \\ -1 & & & & & & 1 & & & & & 1 \\ \hline & -1 & & & & & & & & & & 1 \\ & & & & & 1 & & & & & & \\ & & & & & & & 1 & & & & \end{array} \right] \end{array} \quad (2.52)$$

The obtained Matrix of Coefficients $[C_I]$ (Eq. 2.52) matches the Matrix of Coefficients for the Regime I formulated in [82] for the flat two-dimensional problem. Since the solution of the problem is described in detail in [82], the detailed description of the final choice of the scaling laws is omitted in the present work. The resulting matrix of the scaling factors is shown in the Eq. 2.53:

$$[S_I] = \begin{array}{c} \begin{array}{cccccccc} \mathcal{L} & D & \rho & \nu & \alpha & k & \sigma_T & Q_0 \end{array} \\ \left[\begin{array}{cccccccc|c} -1 & 2 & -1 & -1 & & -1 & 1 & 1 & \widehat{u}_c \\ -2 & 3 & -1 & -1 & & -1 & 1 & 1 & \widehat{w}_c \\ & & & & & -1 & 1 & 1 & \widehat{p}_c \\ & 1 & & & & -1 & & 1 & \widehat{\Delta T} \end{array} \right] \end{array} \quad (2.53)$$

The radial velocity estimation presented in the first row of the matrix of the scaling

factors $[S_I]$ can be rewritten in the traditional form as:

$$\widehat{u}_c = \frac{D^2 \gamma_T Q_0}{\mathcal{L} \rho k \nu} \quad (2.54)$$

This scaling law is exactly the same as the one obtained manually in [87]. The obtained estimation for the characteristic velocity of the thermocapillary convection in the Regime I yields the following estimation for the Peclet number:

$$\widehat{\text{Pe}}_{I_{\mathcal{L}}} = \frac{D^2 \gamma_T Q_0}{\rho k \nu \alpha} \quad (2.55)$$

or as a function of the dimensionless numbers:

$$\widehat{\text{Pe}}_{I_{\mathcal{L}}} = \mathcal{R}_{\mathcal{L}}^2 \text{Ri}_{\mathcal{L}} \text{Pr} \quad (2.56)$$

2.4 Regime II

The Regime II represents the case of inertial flow with negligible convection. Unlike the Regime I where the viscous shear is significant throughout the entire depth of the pool, in the Regime II the viscous shear is significant only in a thinner layer close to the free surface: the viscous boundary layer. The thickness of the viscous boundary layer δ is one of the unknown characteristic values.

The characteristic values of the velocity components and pressure are different for the viscous boundary layer and the weld pool core, as well as the characteristic lengths used to normalize the terms in these two sub-domains. The characteristic length along z -axis for the viscous boundary layer is the thickness of the layer δ , whilst for the core this value is D . This fact requires two sets of the continuity and momentum equations normalized separately for the viscous boundary layer and the core of pool.

The normalized equations for the viscous boundary layer and the core are presented in Eqs. 2.57 - 2.62. The subscript s indicates the characteristic values of the unknowns in the viscous boundary layer and the subscript c applies for the core of the pool.

The normalized continuity and momentum equations for the viscous boundary layer are:

$$\frac{u_s}{\mathcal{L}} \frac{1}{r^*} \frac{\partial^*}{\partial r^*} (r^* u^*) + \frac{w_s}{\delta} \frac{\partial w^*}{\partial z^*} = 0 \quad (2.57)$$

$$\begin{aligned} \frac{u_s^2}{\mathcal{L}} u^* \frac{\partial u^*}{\partial r^*} + \frac{u_s w_s}{\delta} w^* \frac{\partial u^*}{\partial z^*} &= -\frac{p_s}{\rho \mathcal{L}} \frac{\partial p^*}{\partial r^*} + \\ &+ \frac{\nu u_s}{\mathcal{L}^2} \frac{\partial^*}{\partial r^*} \left(\frac{1}{r^*} \frac{\partial^*}{\partial r^*} (r^* u^*) \right) + \frac{\nu u_s}{\delta^2} \frac{\partial^2 u^*}{\partial z^{*2}} \end{aligned} \quad (2.58)$$

$$\begin{aligned} \frac{u_s w_s}{\mathcal{L}} u^* \frac{\partial w^*}{\partial r^*} + \frac{w_s^2}{\delta} w^* \frac{\partial w^*}{\partial z^*} &= -\frac{p_s}{\rho \delta} \frac{\partial p^*}{\partial z^*} + \\ &+ \frac{\nu w_s}{\mathcal{L}^2} \frac{1}{r^*} \frac{\partial^*}{\partial r^*} \left(r^* \frac{\partial w^*}{\partial r^*} \right) + \frac{\nu w_s}{\delta^2} \frac{\partial^2 w^*}{\partial z^{*2}} \end{aligned} \quad (2.59)$$

The normalized continuity and momentum equations for the core are:

$$\frac{u_c}{\mathcal{L}} \frac{1}{r^*} \frac{\partial^*}{\partial r^*} (r^* u^*) + \frac{w_c}{D} \frac{\partial w^*}{\partial z^*} = 0 \quad (2.60)$$

$$\begin{aligned} \frac{u_c^2}{\mathcal{L}} u^* \frac{\partial u^*}{\partial r^*} + \frac{u_c w_c}{D} w^* \frac{\partial u^*}{\partial z^*} &= -\frac{p_c}{\rho \mathcal{L}} \frac{\partial p^*}{\partial r^*} + \\ &+ \frac{\nu u_c}{\mathcal{L}^2} \frac{\partial^*}{\partial r^*} \left(\frac{1}{r^*} \frac{\partial^*}{\partial r^*} (r^* u^*) \right) + \frac{\nu u_c}{D^2} \frac{\partial^2 u^*}{\partial z^{*2}} \end{aligned} \quad (2.61)$$

$$\begin{aligned} \frac{u_c w_c}{\mathcal{L}} u^* \frac{\partial w^*}{\partial r^*} + \frac{w_c^2}{D} w^* \frac{\partial w^*}{\partial z^*} &= -\frac{p_c}{\rho D} \frac{\partial p^*}{\partial z^*} + \\ &+ \frac{\nu w_c}{\mathcal{L}^2} \frac{1}{r^*} \frac{\partial^*}{\partial r^*} \left(r^* \frac{\partial w^*}{\partial r^*} \right) + \frac{\nu w_c}{D^2} \frac{\partial^2 w^*}{\partial z^{*2}} \end{aligned} \quad (2.62)$$

The thermal energy equation is normalized with the characteristic radial velocity component for the viscous boundary layer u_s , however, since in the Regime II conduction is dominant, the pool depth D is used as the characteristic thermal length in the z -direction:

$$\begin{aligned} \frac{u_s \Delta T}{\mathcal{L}} u^* \frac{\partial T^*}{\partial r^*} + \frac{w_s \Delta T}{D} w^* \frac{\partial T^*}{\partial z^*} &= \\ &= \frac{\alpha \Delta T}{\mathcal{L}^2} \frac{1}{r^*} \frac{\partial^*}{\partial r^*} \left(r^* \frac{\partial T^*}{\partial r^*} \right) + \frac{\alpha \Delta T}{D^2} \frac{\partial^2 T^*}{\partial z^{*2}} \end{aligned} \quad (2.63)$$

The Marangoni boundary condition is normalized with the boundary layer characteristic values u_s and δ :

$$\frac{\rho \nu u_s}{\delta} \frac{\partial u^*}{\partial z^*} = \frac{\gamma_T \Delta T}{\mathcal{L}} \frac{\partial T^*}{\partial r^*} \quad (2.64)$$

The input heat flux boundary condition is normalized using D as the characteristic thermal length:

$$\frac{k\Delta T}{D} \frac{\partial T^*}{\partial z^*} = -Q_0 Q^*(r^*) \quad (2.65)$$

The unknown characteristic velocities for the momentum boundary layer and the core require a link between them. To match the velocities in the two sub-domains the following equation is proposed based on the mass conservation:

$$u_s \delta = u_c D \quad (2.66)$$

The Matrix of Coefficients $[C_{II}]$ corresponding to the obtained normalized equations is presented in the Eq. 2.67:

maximum) spot size is 1 mm ($\mathcal{L}=0.5$ mm), and the travel velocity is 10 mm/s. The beam efficiency is taken as $\eta=15\%$. The welding is performed without keyhole with a penetration of $D=0.5$ mm. The thermophysical parameters of aluminum 5083 melt at 800°C are $\rho=2309$ kg/m³, $\nu=4.33 \cdot 10^{-7}$ m²/s, $\alpha=2.4 \cdot 10^{-5}$ m²/s, and $k=68$ W/mK. An artificial surface tension temperature coefficient of $\gamma_T=3.5 \cdot 10^{-8}$ N/mK is used in order for the solution to comply with the criteria for the Regime II.

For the matrix of coefficients $[C_{II}]$ (Eq. 2.67), the OMS algorithm tried 777,600 combinations of 8 pairs of balancing terms. This exhaustive analysis identified 682,325 incompatible balances, 94,223 inconsistent balances and 1,052 self-consistent balances. The 1,052 self-consistent balances correspond to 79 classes, with each class made of all balances that result in the same estimation. Of the 79 classes of self-consistent balances, only 2 are consistent with mass conservation for both the boundary layer and the core region (Eqs. 2.57 and 2.60), the Navier-Stokes equations for both axes for the boundary layer (Eqs. 2.58 and 2.59), the Navier-Stokes equation for the r -axis for the core region (Eq. 2.61), the boundary conditions (Eqs. 2.64 and 2.65) and the matching condition for the characteristic velocities in the core and the boundary layer (Eq. 2.66). However, one of these two classes provides the estimation:

$$\delta = \mathcal{L} \quad (2.68)$$

that contradicts the assumption that $\delta \ll \mathcal{L}$. Thus, this class is not representative for the Regime II.

The selected matrix of scaling factors is:

$$[S_{II}] = \begin{bmatrix} \mathcal{L} & D & \rho & \nu & \alpha & k & \gamma_T & Q_0 \\ 1/3 & -2/3 & -1/3 & 1/3 & & -1/3 & 1/3 & 1/3 \\ -2/3 & 1/3 & -1/3 & 1/3 & & -1/3 & 1/3 & 1/3 \\ 2/3 & -4/3 & 1/3 & 2/3 & & -2/3 & 2/3 & 2/3 \\ & 1 & & & & -1 & & 1 \\ 2/3 & -1/3 & 1/3 & 2/3 & & 1/3 & -1/3 & -1/3 \\ -1/3 & 2/3 & -2/3 & -1/3 & & -2/3 & 2/3 & 2/3 \\ -2/3 & 1/3 & -1/3 & 1/3 & & -1/3 & 1/3 & 1/3 \\ -4/3 & 2/3 & 1/3 & 2/3 & & -2/3 & 2/3 & 2/3 \end{bmatrix} \begin{bmatrix} \widehat{u}_c \\ \widehat{w}_c \\ \widehat{p}_c \\ \widehat{\Delta T} \\ \widehat{\delta} \\ \widehat{u}_s \\ \widehat{w}_s \\ \widehat{p}_s \end{bmatrix} \quad (2.69)$$

The obtained estimation for the characteristic radial velocity component for the viscous boundary layer is:

$$\widehat{u}_s = \left(\frac{D^2 \gamma_T^2 Q_0^2}{\mathcal{L} \rho^2 \nu k^2} \right)^{1/3} \quad (2.70)$$

yielding the estimation for the Peclet number for the Regime II:

$$\widehat{\text{Pe}}_{\text{II}\mathcal{L}} = \frac{\gamma_T^{2/3} Q_0^{2/3} D^{2/3} \mathcal{L}^{2/3}}{\rho^{2/3} k^{2/3} \nu^{1/3} \alpha} \quad (2.71)$$

or as a function of the dimensionless numbers:

$$\widehat{\text{Pe}}_{\text{II}\mathcal{L}} = \mathcal{R}\mathcal{L}^{2/3} \text{Ri}_{\mathcal{L}}^{2/3} \text{Pr} \quad (2.72)$$

2.5 Regime III

The Regime III represents the case of the recirculating weld pool flows of a low-Pr-number melt when convection is dominant and the flow is inertial. This means that both the thermal and viscous boundary layers are formed at the free surface and, since $\text{Pr} < 1$, the thermal boundary layer is thicker than the viscous boundary layer. The thickness of the thermal boundary layer δ_T is added as an unknown characteristic value.

The normalization scheme for the equations of mass conservation and momentum is the same as used for the Regime II.

Thus, the normalized continuity and momentum equations for the viscous boundary layer are:

$$\frac{u_s}{\mathcal{L}} \frac{1}{r^*} \frac{\partial^*}{\partial r^*} (r^* u^*) + \frac{w_s}{\delta} \frac{\partial w^*}{\partial z^*} = 0 \quad (2.73)$$

$$\begin{aligned} \frac{u_s^2}{\mathcal{L}} u^* \frac{\partial u^*}{\partial r^*} + \frac{u_s w_s}{\delta} w^* \frac{\partial u^*}{\partial z^*} &= -\frac{p_s}{\rho \mathcal{L}} \frac{\partial p^*}{\partial r^*} + \\ &+ \frac{\nu u_s}{\mathcal{L}^2} \frac{\partial^*}{\partial r^*} \left(\frac{1}{r^*} \frac{\partial^*}{\partial r^*} (r^* u^*) \right) + \frac{\nu u_s}{\delta^2} \frac{\partial^2 u^*}{\partial z^{*2}} \end{aligned} \quad (2.74)$$

$$\begin{aligned} \frac{u_s w_s}{\mathcal{L}} u^* \frac{\partial w^*}{\partial r^*} + \frac{w_s^2}{\delta} w^* \frac{\partial w^*}{\partial z^*} &= -\frac{p_s}{\rho \delta} \frac{\partial p^*}{\partial z^*} + \\ &+ \frac{\nu w_s}{\mathcal{L}^2} \frac{1}{r^*} \frac{\partial^*}{\partial r^*} \left(r^* \frac{\partial w^*}{\partial r^*} \right) + \frac{\nu w_s}{\delta^2} \frac{\partial^2 w^*}{\partial z^{*2}} \end{aligned} \quad (2.75)$$

The normalized continuity and momentum equations for the core are:

$$\frac{u_c}{\mathcal{L}} \frac{1}{r^*} \frac{\partial^*}{\partial r^*} (r^* u^*) + \frac{w_c}{D} \frac{\partial w^*}{\partial z^*} = 0 \quad (2.76)$$

$$\begin{aligned} \frac{u_c^2}{\mathcal{L}} u^* \frac{\partial u^*}{\partial r^*} + \frac{u_c w_c}{D} w^* \frac{\partial u^*}{\partial z^*} = & -\frac{p_c}{\rho \mathcal{L}} \frac{\partial p^*}{\partial r^*} + \\ & + \frac{\nu u_c}{\mathcal{L}^2} \frac{\partial^*}{\partial r^*} \left(\frac{1}{r^*} \frac{\partial^*}{\partial r^*} (r^* u^*) \right) + \frac{\nu u_c}{D^2} \frac{\partial^2 u^*}{\partial z^{*2}} \end{aligned} \quad (2.77)$$

$$\begin{aligned} \frac{u_c w_c}{\mathcal{L}} u^* \frac{\partial w^*}{\partial r^*} + \frac{w_c^2}{D} w^* \frac{\partial w^*}{\partial z^*} = & -\frac{p_c}{\rho D} \frac{\partial p^*}{\partial z^*} + \\ & + \frac{\nu w_c}{\mathcal{L}^2} \frac{1}{r^*} \frac{\partial^*}{\partial r^*} \left(r^* \frac{\partial w^*}{\partial r^*} \right) + \frac{\nu w_c}{D^2} \frac{\partial^2 w^*}{\partial z^{*2}} \end{aligned} \quad (2.78)$$

In order to provide the correct approximation for the thermal energy equation, the characteristic velocity of the thermal boundary layer u_T is introduced defined as:

$$u_T = u_s \frac{\delta}{\delta_T} \quad (2.79)$$

The thermal energy equation is normalized with the characteristic velocity of the thermal boundary layer u_T and the thermal boundary layer thickness δ_T :

$$\begin{aligned} \frac{u_T \Delta T}{\mathcal{L}} u^* \frac{\partial T^*}{\partial r^*} + \frac{w_T \Delta T}{\delta_T} w^* \frac{\partial T^*}{\partial z^*} = \\ = \frac{\alpha \Delta T}{\mathcal{L}^2} \frac{1}{r^*} \frac{\partial^*}{\partial r^*} \left(r^* \frac{\partial T^*}{\partial r^*} \right) + \frac{\alpha \Delta T}{\delta_T^2} \frac{\partial^2 T^*}{\partial z^{*2}} \end{aligned} \quad (2.80)$$

The velocity component w_T is assumed:

$$w_T = w_s \quad (2.81)$$

Since $(w_T \Delta T) / \delta_T$ is much smaller than the coefficient of the dominant terms in Eq. 2.80, this term will be omitted in the matrix of coefficients $[C_{III}]$, as well as the term with the coefficient $(\alpha \Delta T) / \mathcal{L}^2$. Thus, for the scaling analysis, Eq. 2.80 is simplified as:

$$\frac{u_T \Delta T}{\mathcal{L}} u^* \frac{\partial T^*}{\partial r^*} = \frac{\alpha \Delta T}{\delta_T^2} \frac{\partial^2 T^*}{\partial z^{*2}} \quad (2.82)$$

The Marangoni boundary condition is normalized with the viscous boundary layer characteristic values:

$$\frac{\rho \nu u_s}{\delta} \frac{\partial u^*}{\partial z^*} = \frac{\gamma_T \Delta T}{\mathcal{L}} \frac{\partial T^*}{\partial r^*} \quad (2.83)$$

The input heat flux boundary condition is normalized with the thermal boundary layer thickness δ_T :

$$\frac{k\Delta T}{\delta_T} \frac{\partial T^*}{\partial z^*} = -Q_0 Q^*(r^*) \quad (2.84)$$

Analogously to the Regime II, the characteristic velocities of the viscous boundary layer and the core are to be matched:

$$u_s \delta = u_c D \quad (2.85)$$

The resultant matrix of coefficients $[C_{III}]$ is presented in Eq. 2.86.

in order for the flow to fall into the pronounced Regime III. For the same purpose, an artificial value of $\gamma_T=1 \cdot 10^{-3} \text{ Nm}^{-1}\text{K}^{-1}$ is taken for the analysis. The heat source parameters are $\mathcal{L}=0.8 \text{ mm}$, $Q_0=1 \cdot 10^7 \text{ W/m}^{-2}$. The weld pool depth is $D=0.8 \text{ mm}$.

For the matrix of coefficients $[C_{\text{III}}]$ (Eq. 2.86), the OMS algorithm tried 74,000 combinations of balancing terms. The analysis identified 60,255 incompatible balances, 6,432 inconsistent balances and 7,313 self-consistent balances corresponding to 311 classes, with each class made of all balances that result in the same estimation.

Of the 311 classes of self-consistent balances, similarly to the Regime II only 2 are consistent with mass conservation for both the boundary layer and the core region (Eqs. 2.73 and 2.76), the Navier-Stokes equations for both axes for the boundary layer (Eqs. 2.74 and 2.75), the Navier-Stokes equation for the r -axis for the core region (Eq. 2.77), the boundary conditions (Eqs. 2.83 and 2.84), the matching condition for the characteristic velocities in the core and the boundary layer (Eq. 2.85), the thermal energy equation (Eq. 2.82) and the equation for the characteristic velocity for the thermal boundary layer (Eq. 2.79).

Analogously to the solution for the Regime II, one of the obtain classes provides a non-physical estimation:

$$\delta = \mathcal{L} \tag{2.87}$$

which contradicts the assumption that $\delta \ll \mathcal{L}$. Thus, there is only one solution class that is representative for the Regime III. The corresponding matrix of scaling factors is shown in the Eq. 2.88.

$$[S_{\text{III}}] = \begin{bmatrix} \mathcal{L} & D & \rho & \nu & \alpha & k & \gamma_T & Q_0 & \\ -1/2 & & -1/2 & -1/2 & 1/2 & -1/2 & 1/2 & 1/2 & \\ -1 & & -1/4 & 1/4 & 1/4 & -1/4 & 1/4 & 1/4 & \\ 1/2 & -1 & 1/2 & 1/2 & 1/2 & -1/2 & 1/2 & 1/2 & \\ -1/2 & & -1/4 & 1/4 & 1/4 & -1/4 & 1/4 & 1/4 & \\ 1 & -2 & 1/2 & 1/2 & 1/2 & -1/2 & 1/2 & 1/2 & \\ 1/2 & & 1/4 & -1/4 & 3/4 & -3/4 & -1/4 & 3/4 & \\ 1/2 & & 1/4 & 3/4 & -1/4 & 1/4 & -1/4 & -1/4 & \\ 1/2 & & 1/4 & -1/4 & 3/4 & 1/4 & -1/4 & -1/4 & \\ & & -1/2 & 1/2 & -1/2 & -1/2 & 1/2 & 1/2 & \end{bmatrix} \begin{bmatrix} \widehat{u}_s \\ \widehat{w}_s \\ \widehat{p}_s \\ \widehat{u}_c \\ \widehat{w}_c \\ \widehat{p}_c \\ \widehat{\Delta T} \\ \widehat{\delta} \\ \widehat{\delta}_T \\ \widehat{u}_T \end{bmatrix} \quad (2.88)$$

The obtained estimation for the characteristic surface velocity is:

$$\widehat{u}_s = \left(\frac{\gamma_T Q_0 \alpha}{\rho k \nu} \right)^{1/2} \quad (2.89)$$

This estimation is the same that obtained manually in [87]. It yields the estimation for the Peclet number of the Regime III as presented in Eq. 2.91:

$$\widehat{\text{Pe}}_{\text{III}_{\mathcal{L}}} = \left(\frac{\gamma_T Q_0 \mathcal{L}^2}{\rho k \nu \alpha} \right)^{1/2} \quad (2.90)$$

or formulated as a function of the dimensionless numbers:

$$\widehat{\text{Pe}}_{\text{III}_{\mathcal{L}}} = \text{Ri}_{\mathcal{L}}^{1/2} \text{Pr}^{1/2} \quad (2.91)$$

The estimated $\widehat{\text{Pe}}_{\text{III}_{\mathcal{L}}}$ does not depend on the aspect ratio $\mathcal{R}_{\mathcal{L}}$. Moreover, since $\text{Ri}_{\mathcal{L}}$ is, in fact, the function of the heat source power, in case of the fully developed Regime III the obtained $\text{Pe}_{\text{III}_{\mathcal{L}}}$ is independent of the heat source size. However, it is important to remember that the criteria for the flow to represent the Regime III include the aspect ratio $\mathcal{R}_{\mathcal{L}}$ as shown in Eq. 2.24 and for the weld pool with small D/\mathcal{L} ratio the flow may not be in the fully developed Regime III. In that case, the characteristic velocity of the convection is still dependent on $\mathcal{R}_{\mathcal{L}}$. This phenomenon is illustrated in Chapter 4 Subsection 4.3.3.

2.6 Regime IV

The Regime IV represents the inertial flow with the convection being dominant analogously to the Regime III, but for the melts with $\text{Pr} > 1$. In the Regime IV the thermal boundary layer is thinner than the viscous boundary layer, thus, the assumption for the characteristic velocity of the thermal boundary layer proposed for the Regime III are no longer valid and the regime requires different scaling laws.

Since the thermal boundary layer is thinner than the viscous boundary layer, the characteristic velocity for the thermal boundary layer may be taken as the characteristic surface velocity u_s .

The normalized continuity and momentum equations for the viscous boundary layer remain analogous to the ones for the Regimes II and III:

$$\frac{u_s}{\mathcal{L}} \frac{1}{r^*} \frac{\partial^*}{\partial r^*} (r^* u^*) + \frac{w_s}{\delta} \frac{\partial w^*}{\partial z^*} = 0 \quad (2.92)$$

$$\begin{aligned} \frac{u_s^2}{\mathcal{L}} u^* \frac{\partial u^*}{\partial r^*} + \frac{u_s w_s}{\delta} w^* \frac{\partial u^*}{\partial z^*} &= -\frac{p_s}{\rho \mathcal{L}} \frac{\partial p^*}{\partial r^*} + \\ &+ \frac{\nu u_s}{\mathcal{L}^2} \frac{\partial^*}{\partial r^*} \left(\frac{1}{r^*} \frac{\partial^*}{\partial r^*} (r^* u^*) \right) + \frac{\nu u_s}{\delta^2} \frac{\partial^2 u^*}{\partial z^{*2}} \end{aligned} \quad (2.93)$$

$$\begin{aligned} \frac{u_s w_s}{\mathcal{L}} u^* \frac{\partial w^*}{\partial r^*} + \frac{w_s^2}{\delta} w^* \frac{\partial w^*}{\partial z^*} &= -\frac{p_s}{\rho \delta} \frac{\partial p^*}{\partial z^*} + \\ &+ \frac{\nu w_s}{\mathcal{L}^2} \frac{1}{r^*} \frac{\partial^*}{\partial r^*} \left(r^* \frac{\partial w^*}{\partial r^*} \right) + \frac{\nu w_s}{\delta^2} \frac{\partial^2 w^*}{\partial z^{*2}} \end{aligned} \quad (2.94)$$

The normalized equations continuity and momentum for the core are:

$$\frac{u_c}{\mathcal{L}} \frac{1}{r^*} \frac{\partial^*}{\partial r^*} (r^* u^*) + \frac{w_c}{D} \frac{\partial w^*}{\partial z^*} = 0 \quad (2.95)$$

$$\begin{aligned} \frac{u_c^2}{\mathcal{L}} u^* \frac{\partial u^*}{\partial r^*} + \frac{u_c w_c}{D} w^* \frac{\partial u^*}{\partial z^*} &= -\frac{p_c}{\rho \mathcal{L}} \frac{\partial p^*}{\partial r^*} + \\ &+ \frac{\nu u_c}{\mathcal{L}^2} \frac{\partial^*}{\partial r^*} \left(\frac{1}{r^*} \frac{\partial^*}{\partial r^*} (r^* u^*) \right) + \frac{\nu u_c}{D^2} \frac{\partial^2 u^*}{\partial z^{*2}} \end{aligned} \quad (2.96)$$

$$\begin{aligned} \frac{u_c w_c}{\mathcal{L}} u^* \frac{\partial w^*}{\partial r^*} + \frac{w_c^2}{D} w^* \frac{\partial w^*}{\partial z^*} &= -\frac{p_c}{\rho D} \frac{\partial p^*}{\partial z^*} + \\ &+ \frac{\nu w_c}{\mathcal{L}^2} \frac{1}{r^*} \frac{\partial^*}{\partial r^*} \left(r^* \frac{\partial w^*}{\partial r^*} \right) + \frac{\nu w_c}{D^2} \frac{\partial^2 w^*}{\partial z^{*2}} \end{aligned} \quad (2.97)$$

As mentioned above, the characteristic velocity for the viscous boundary layer u_s is

used to scale the equation of the thermal energy. The equation is simplified to:

$$\frac{u_s \Delta T}{\mathcal{L}} u^* \frac{\partial T^*}{\partial r^*} = \frac{\alpha \Delta T}{\delta_T^2} \frac{\partial^2 T^*}{\partial z^{*2}} \quad (2.98)$$

The Marangoni boundary condition is normalized with the boundary layer characteristic values:

$$\frac{\rho \nu u_s}{\delta} \frac{\partial u^*}{\partial z^*} = \frac{\gamma_T \Delta T}{\mathcal{L}} \frac{\partial T^*}{\partial r^*} \quad (2.99)$$

The input heat flux boundary condition is normalized with the thickness of the thermal boundary layer δ_T as the characteristic length in the z -direction:

$$\frac{k \Delta T}{\delta_T} \frac{\partial T^*}{\partial z^*} = -Q_0 Q^*(r^*) \quad (2.100)$$

Analogously to the Regimes II and III, a matching condition for the characteristic velocities of the the core and the viscous boundary layers is required:

$$u_s \delta = u_c D \quad (2.101)$$

The resultant matrix of coefficients $[C_{IV}]$ is presented in Eq. 2.102:

an artificial value of $\gamma_T=1 \cdot 10^{-3} \text{ Nm}^{-1}\text{K}^{-1}$ is taken for the analysis. The heat source parameters are $\mathcal{L}=0.8 \text{ mm}$, $Q_0=1 \cdot 10^7 \text{ W/m}^{-2}$. The weld pool depth is $D=0.8 \text{ mm}$.

For the matrix of coefficients $[C_{IV}]$ (Eq. 2.102), the OMS algorithm tried 64,000 combinations of balancing terms. The analysis identified 50,925 incompatible balances, 6,925 inconsistent balances and 6,150 self-consistent balances corresponding to 258 classes, with each class made of all balances that result in the same estimation.

Of the 258 classes of self-consistent balances, similarly to the Regime II and III only 2 are consistent with mass conservation for both the boundary layer and the core region (Eqs. 2.92 and 2.95), the Navier-Stokes equations for both axes for the boundary layer (Eqs. 2.93 and 2.94), the Navier-Stokes equation for the r -axis for the core region (Eq. 2.96), the boundary conditions (Eqs. 2.99 and 2.100), the matching condition for the characteristic velocities in the core and the boundary layer (Eq. 2.101) and the thermal energy equation (Eq. 2.98).

Analogously to the solution for the Regime II and III, one of the obtain classes provides a non-physical estimation:

$$\delta = \mathcal{L} \tag{2.103}$$

which contradicts the assumption that $\delta \ll \mathcal{L}$. Thus, there is only one solution class that is representative for the Regime IV. The corresponding matrix of scaling factors is shown in the Eq. 2.104.

$$[S_{IV}] = \begin{bmatrix} \mathcal{L} & D & \rho & \nu & \alpha & k & \gamma_T & Q_0 \\ -1/2 & & -1/2 & -1/4 & 1/4 & -1/2 & 1/2 & 1/2 \\ -1 & & -1/4 & 3/8 & 1/8 & -1/4 & 1/4 & 1/4 \\ 1/2 & -1 & 1/2 & 3/4 & 1/4 & -1/2 & 1/2 & 1/2 \\ -1/2 & & -1/4 & 3/8 & 1/8 & -1/4 & 1/4 & 1/4 \\ 1 & -2 & 1/2 & 3/4 & 1/4 & -1/2 & 1/2 & 1/2 \\ 1/2 & & 1/4 & 1/8 & 3/8 & -3/4 & -1/4 & 3/4 \\ 1/2 & & 1/4 & 5/8 & -1/8 & 1/4 & -1/4 & -1/4 \\ 1/2 & & 1/4 & 1/8 & 3/8 & 1/4 & -1/4 & -1/4 \end{bmatrix} \begin{bmatrix} \widehat{u}_s \\ \widehat{w}_s \\ \widehat{p}_s \\ \widehat{u}_c \\ \widehat{w}_c \\ \widehat{p}_c \\ \widehat{\Delta T} \\ \widehat{\delta} \\ \widehat{\delta}_T \end{bmatrix} \tag{2.104}$$

The obtained estimation for the characteristic surface velocity is:

$$\widehat{u}_s = \frac{\gamma_T^{1/2} Q_0^{1/2} \alpha^{1/4}}{\rho^{1/2} k^{1/2} \nu^{1/4}} \quad (2.105)$$

This estimation yields the estimation for the Peclet number of the Regime IV:

$$\widehat{\text{Pe}}_{\text{IV}\mathcal{L}} = \frac{\gamma_T^{1/2} Q_0^{1/2} \mathcal{L}}{\rho^{1/2} k^{1/2} \nu^{1/6} \alpha^{3/4}} \quad (2.106)$$

or formulated as a function of the dimensionless numbers:

$$\widehat{\text{Pe}}_{\text{IV}\mathcal{L}} = \text{Ri}_{\mathcal{L}}^{1/2} \text{Pr}^{3/4} \quad (2.107)$$

Similarly to the Peclet number estimation for the Regime III, the estimated $\widehat{\text{Pe}}_{\text{IV}\mathcal{L}}$ is independent from the aspect ratio $\mathcal{R}_{\mathcal{L}}$.

2.7 Regime V

The Regime V represents the case of viscous flow with convection being dominant for the melts with $\text{Pr} > 1$. In the Regime V the thermal boundary layer is formed, however, there is no viscous boundary layer. Since the thermal boundary layer is thinner than the depth of the weld pool, the characteristic velocity for the thermal boundary layer may be taken as the characteristic surface velocity u_c .

The normalized continuity and momentum equations remain analogous to the ones for the Regimes I:

$$\frac{u_c}{\mathcal{L}} \frac{1}{r^*} \frac{\partial^*}{\partial r^*} (r^* u^*) + \frac{w_c}{D} \frac{\partial w^*}{\partial z^*} = 0 \quad (2.108)$$

$$\begin{aligned} \frac{u_c^2}{\mathcal{L}} u^* \frac{\partial u^*}{\partial r^*} + \frac{u_c w_c}{D} w^* \frac{\partial u^*}{\partial z^*} &= -\frac{p_c}{\rho \mathcal{L}} \frac{\partial p^*}{\partial r^*} + \\ &+ \frac{\nu u_c}{\mathcal{L}^2} \frac{\partial^*}{\partial r^*} \left(\frac{1}{r^*} \frac{\partial^*}{\partial r^*} (r^* u^*) \right) + \frac{\nu u_c}{D^2} \frac{\partial^2 u^*}{\partial z^{*2}} \end{aligned} \quad (2.109)$$

$$\begin{aligned} \frac{u_c w_c}{\mathcal{L}} u^* \frac{\partial w^*}{\partial r^*} + \frac{w_c^2}{D} w^* \frac{\partial w^*}{\partial z^*} &= -\frac{p_c}{\rho D} \frac{\partial p^*}{\partial z^*} + \\ &+ \frac{\nu w_c}{\mathcal{L}^2} \frac{1}{r^*} \frac{\partial^*}{\partial r^*} \left(r^* \frac{\partial w^*}{\partial r^*} \right) + \frac{\nu w_c}{D^2} \frac{\partial^2 w^*}{\partial z^{*2}} \end{aligned} \quad (2.110)$$

kinematic viscosity $\nu=8.32 \cdot 10^{-7} \text{ m}^2/\text{s}$, thermal conductivity $k=18 \text{ Wm}^{-1}\text{K}^{-1}$ [82]. For the thermal diffusivity, the artificial value of $\alpha=8.32 \cdot 10^{-9} \text{ m}^2/\text{s}$ is taken, as well as the artificial value of $\gamma_T=1 \cdot 10^{-8} \text{ Nm}^{-1}\text{K}^{-1}$. The heat source parameters are $\mathcal{L}=0.8 \text{ mm}$, $Q_0=1 \cdot 10^7 \text{ W/m}^{-2}$. The weld pool depth is $D=0.8 \text{ mm}$.

For the matrix of coefficients $[C_V]$ (Eq. 2.114), the OMS algorithm tried 420 combinations of balancing terms. The analysis identified 255 incompatible balances, 35 inconsistent balances and 130 self-consistent balances corresponding to 32 classes, with each class made of all balances that result in the same estimation.

Of the 32 classes of self-consistent balances, only 2 are consistent with mass conservation (Eq. 2.108), the Navier-Stokes equation for the r -axis (Eq. 2.109), the boundary conditions (Eqs. 2.112 and 2.113) and the thermal energy equation (Eq. 2.111). The only difference in the two classes is the estimation for the pressure. The chosen matrix of the scaling factors is shown in Eq. 2.115:

$$[S_V] = \begin{bmatrix} \mathcal{L} & D & \rho & \nu & \alpha & k & \gamma_T & Q_0 \\ -1/3 & 2/3 & -2/3 & -2/3 & 1/3 & -2/3 & 2/3 & 2/3 \\ -4/3 & 5/3 & -2/3 & -2/3 & 1/3 & -2/3 & 2/3 & 2/3 \\ -4/3 & 2/3 & 1/3 & 1/3 & 1/3 & -2/3 & 2/3 & 2/3 \\ 2/3 & -1/3 & 1/3 & 1/3 & 1/3 & -2/3 & -1/3 & 2/3 \\ 2/3 & -1/3 & 1/3 & 1/3 & 1/3 & 1/3 & -1/3 & -1/3 \end{bmatrix} \begin{bmatrix} \widehat{u}_c \\ \widehat{w}_c \\ \widehat{p}_c \\ \widehat{\Delta T} \\ \widehat{\delta}_T \end{bmatrix} \quad (2.115)$$

The obtained estimation for the characteristic surface velocity is:

$$\widehat{u}_c = \frac{\gamma_T^{2/3} Q_0^{2/3} \alpha^{1/3} D^{2/3}}{\rho^{2/3} k^{2/3} \nu^{2/3} \mathcal{L}^{1/3}} \quad (2.116)$$

This estimation yields the estimation for the Peclet number of the Regime V:

$$\widehat{\text{Pe}}_{V_{\mathcal{L}}} = \frac{\gamma_T^{2/3} Q_0^{2/3} \mathcal{L}^{2/3} D^{2/3}}{\rho^{2/3} k^{2/3} \nu^{2/3} \alpha^{2/3}} \quad (2.117)$$

or formulated as a function of the dimensionless numbers:

$$\widehat{\text{Pe}}_{V_{\mathcal{L}}} = \mathcal{R}_{\mathcal{L}}^{2/3} \text{Ri}_{\mathcal{L}}^{2/3} \text{Pr}^{2/3} \quad (2.118)$$

2.8 Summary

Scaling analysis is a powerful tool for the prediction of the unknown characteristic values by capturing their trend in the form of a scaling law in an asymptotic regime. The analysis is based on the fundamental physical formulation of the problem rather than on empirical formulae. If done properly, the results of the scaling are general and comprehensive; however, they provide an order of magnitude approximation. It means that the scaling laws obtained should be verified and calibrated using a different approach. In this work, both literature data and an auxiliary numerical simulations performed by the author were used for this verification and calibrations. The auxiliary numerical model set-up is described in Chapter 3.

Chapter 3

Auxiliary numerical model set-up

Auxiliary numerical modelling of the Marangoni-driven recirculating flows were performed in order to preliminary test the scaling laws and provide insight into the mechanics of the recirculating flows at the identified regimes. Since the presence of turbulent flows in weld pools is not defined yet and laminar models with enhancement factors for the melt thermal conductivity and viscosity are widely used to simulate the possible role of turbulence, a laminar model of a semi-elliptical axisymmetric pool was used with a flat non-deformable surface, constant temperature wall representing liquid-solid interface and the parameters independent from temperature. The assumptions of the flat surface and axisymmetric geometry were used since at the representative “melt-in” welding mode the weld is slow which also means that its geometry is close to axisymmetric and its surface has minimal deformation from the arc pressure.

3.1 Model description

The flows were modelled in an axisymmetric semi-elliptical weld pool with a flat non-deformable surface heated by the arc. The modelling was performed in ANSYS Fluent® software package. The liquid-solid interface was pre-imposed as a constant temperature boundary condition. Melting and solidification were not modelled. Due to the axial symmetry, a two-dimensional axisymmetric model was used. The domain

was taken as a quarter of an ellipse with the longer ellipse axis representing the weld pool free surface heated by the arc and the shorter ellipse axis being the axis of symmetry (Fig 3.1). The input heat flux was represented with a Gaussian function. The fluid flow and the heat transfer were decoupled from each other and connected only through the Marangoni surface boundary condition. All other physical phenomena were neglected, including buoyancy, electromagnetic forces, free surface deformations, etc. All the properties were considered independent of temperature. The problem was solved in dimensionless form and, thus, the parameter values and boundary conditions were dimensionless.

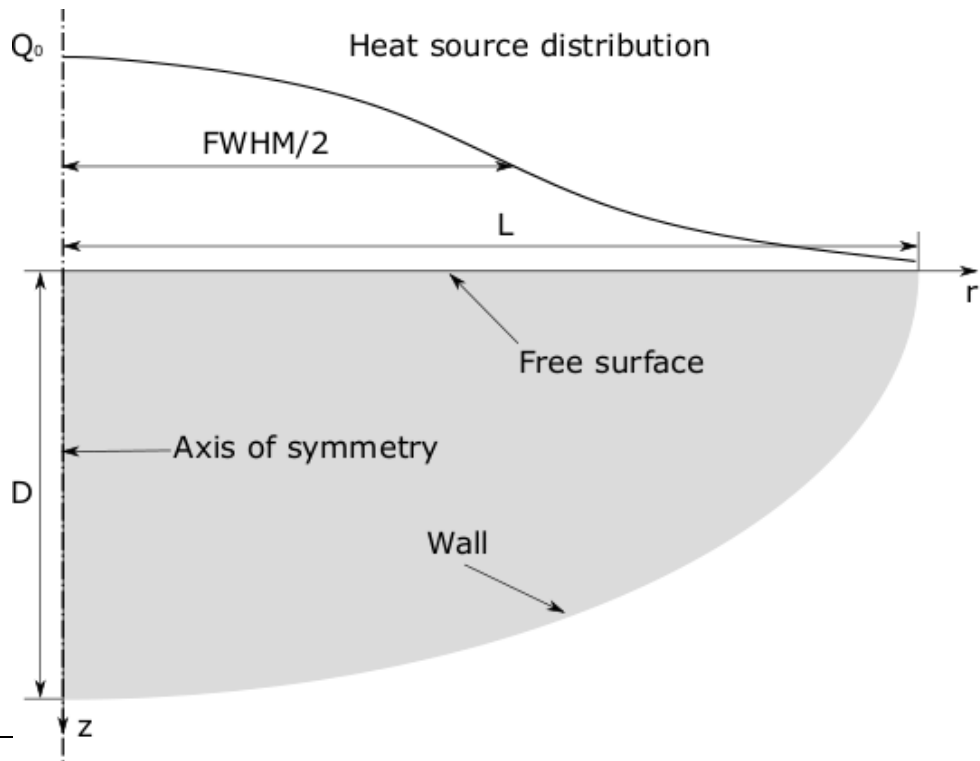


Figure 3.1: Schematics of the problem formulation.

The proportions of the modelled weld pool width and depth were chosen to correspond to a typical proportions of a GTAW weld. According to Eagar and Tsai [89], the typical GTAW steel weld parameters fell within the range of the Rykalin number (in [89] noted as the operating parameter n) of approximately $0.5 < Ry < 2$ and

the dimensionless heat source distribution size (noted as u in [89]) of $0.1 < \sigma^* < 1$. The values of $Ry = 1.1$ and $\sigma^* = 0.4$ were chosen as the middle ones. A $1/2$ of the Full Width Half Maximum (FWHM) \mathcal{L} was taken as the characteristic size of the heat source. The half-value of the FWHM was related to the Gaussian distribution parameter σ by $\sigma = \mathcal{L}/\sqrt{2 \ln 2}$.

For the dimensionless welding parameters chosen, the weld pool depth D calculated using a Gaussian heat source assumption was equal to $1.02 \mathcal{L}$. The weld pool width corresponding to these parameters was equal to $1.66 \mathcal{L}$. To be used in the numerical model, the weld pool depth and width were rounded to:

$$D = \mathcal{L} \tag{3.1}$$

$$L = 2 \mathcal{L} \tag{3.2}$$

The reason for that was that the Gaussian heat source intensity at $r = 1.66 \mathcal{L}$ was still significant and may create a sharp gradient near the corner of the constant temperature wall. A wider pool with its width equal to $r = 2 \mathcal{L}$ would reduce this gradient without changing the characteristic pattern of the flow behaviour.

3.2 Reasons of the model choice. Limitations

The model requirements for this project were (1) universality for all the identified regimes, (2) usability for a large number of the numerical experiments with a wide range of the input parameters, (3) calculation speed and set up simplicity. The model was chosen out of this balance.

Such a simple model had both advantages and limitations. This model was representative for the Regimes I and II, since in these regimes the weld pool shape was governed by conduction and was not affected by the flow. On the other hand, the fixed liquid-solid interface limited the accuracy of the results for the Regimes III, IV and V, i.e., the regimes with dominant convection. However, the model could still correctly represent the typical flow patterns and the expected characteristics of each

flow Regime and was able to reveal the characteristic features of each regime.

3.3 Normalization scheme and boundary conditions

The governing equations were normalized to be suitable for the numerical modelling. Since the normalization scheme can be, generally speaking, arbitrary as long as characteristic values for normalization are linearly independent, the characteristic values proposed for the Regime I as shown in Section 2 were chosen to normalize the problem. Thus, the independent variables were normalized in the following way:

$$r^* = r/\mathcal{L} \quad (3.3)$$

$$z^* = z/\mathcal{L} \quad (3.4)$$

$$u^* = u/U_R \quad (3.5)$$

$$w^* = w/U_R \quad (3.6)$$

$$p^* = p/P_R \quad (3.7)$$

$$T^* = (T - T_m)/T_R \quad (3.8)$$

where

$$U_R = \frac{\gamma_T Q_0 \mathcal{L}}{\rho k \nu} \quad (3.9)$$

$$T_R = \frac{Q_0 \mathcal{L}}{k} \quad (3.10)$$

$$P_R = \rho U_R^2 = \frac{\mathcal{L}^2 \gamma_T^2 Q_0^2}{\rho k^2 \nu^2} \quad (3.11)$$

$Q_0 = q/2\pi\sigma^2$ was the maximum heat intensity of the heat source of the power of q .

$$Q = \frac{q}{2\pi\sigma^2} \exp \frac{-r^2}{2\sigma^2} \quad (3.12)$$

Since $\sigma = \mathcal{L}/\sqrt{2 \ln 2}$, the heat source power q was related to $Q_0 \mathcal{L}$ as:

$$q = \frac{\pi}{\ln 2} Q_0 \mathcal{L}^2 \approx 4.53 Q_0 \mathcal{L}^2 \quad (3.13)$$

Introduce dimensionless numbers:

$$\text{Ri}_{\mathcal{L}} = \frac{\gamma_T Q_0 \mathcal{L}^2}{\rho k \nu^2} \quad (3.14)$$

$$\text{Pr} = \frac{\nu}{\alpha} \quad (3.15)$$

$$\mathcal{R}_{\mathcal{L}} = \frac{D}{\mathcal{L}} \quad (3.16)$$

The numbers $\text{Ri}_{\mathcal{L}}$ and $\mathcal{R}_{\mathcal{L}}$ were based on the FWHM \mathcal{L} as the characteristic length and relate to Ri and \mathcal{R}_G that were based on σ as:

$$\text{Ri} = \frac{\pi}{\ln 2} \text{Ri}_{\mathcal{L}} \approx 4.53 \text{Ri}_{\mathcal{L}} \quad (3.17)$$

$$\mathcal{R}_G = \sqrt{2 \ln 2} \mathcal{R}_{\mathcal{L}} \approx 1.2 \mathcal{R}_{\mathcal{L}} \quad (3.18)$$

The governing equations normalized using $\text{Ri}_{\mathcal{L}}$ and Pr dimensionless numbers were as follows:

$$\frac{1}{r^*} \frac{\partial^*}{\partial r^*} (r^* u^*) + \frac{\partial w^*}{\partial z^*} = 0 \quad (3.19)$$

$$u^* \frac{\partial u^*}{\partial r^*} + w^* \frac{\partial u^*}{\partial z^*} = -\frac{\partial p^*}{\partial r^*} + \frac{1}{\mathcal{R}_{\mathcal{L}}^2 \text{Ri}_{\mathcal{L}}} \left[\frac{1}{r^*} \frac{\partial^*}{\partial r^*} \left(r^* \frac{\partial u^*}{\partial r^*} \right) - \frac{u^*}{r^{*2}} \right] + \frac{1}{\mathcal{R}_{\mathcal{L}}^2 \text{Ri}_{\mathcal{L}}} \frac{\partial^2 u^*}{\partial z^{*2}} \quad (3.20)$$

$$u^* \frac{\partial w^*}{\partial r^*} + w^* \frac{\partial w^*}{\partial z^*} = -\frac{\partial p^*}{\partial z^*} + \frac{1}{\mathcal{R}_{\mathcal{L}}^2 \text{Ri}_{\mathcal{L}}} \left[\frac{1}{r^*} \frac{\partial^*}{\partial r^*} \left(r^* \frac{\partial w^*}{\partial r^*} \right) \right] + \frac{1}{\mathcal{R}_{\mathcal{L}}^2 \text{Ri}_{\mathcal{L}}} \frac{\partial^2 w^*}{\partial z^{*2}} \quad (3.21)$$

$$u^* \frac{\partial T^*}{\partial r^*} + w^* \frac{\partial T^*}{\partial z^*} = \frac{1}{\mathcal{R}_{\mathcal{L}}^2 \text{Ri}_{\mathcal{L}} \text{Pr}} \left[\frac{1}{r^*} \frac{\partial^*}{\partial r^*} \left(r^* \frac{\partial T^*}{\partial r^*} \right) + \frac{\partial^2 T^*}{\partial z^{*2}} \right] \quad (3.22)$$

with the normalized boundary conditions at the free surface ($r^* = [0; 2]$, $z^* = 0$):

$$\frac{\partial u^*}{\partial z^*} = \frac{\partial T^*}{\partial r^*} \quad (3.23)$$

$$\frac{\partial T^*}{\partial z^*} = -Q^*(r) \quad (3.24)$$

where

$$Q^*(r) = \exp \left(-r^{*2} \frac{\mathcal{L}^2}{2\sigma^2} \right) = \exp (-0.69 r^{*2}) \quad (3.25)$$

The modelling was performed in ANSYS Fluent® software package. Since this software supported only dimensional parameters, the parameters were set in the SI system with their values equal to the values of the dimensionless parameters.

Table 3.1 lists the dimensionless values used in the numerical model. Since for the parameters chosen, the aspect ratio is $\mathcal{R}_{\mathcal{L}} = 1$, it is omitted in the values formulation. Table 3.2 lists the boundary conditions.

Table 3.1: Dimensionless parameters

Parameter	Value
\mathcal{L}^*	1
D^*	1
Q_0^*	1
ρ^*	1
ν^*	$1/\text{Ri}_{\mathcal{L}}$
k^*	1
α^*	$1/\text{Ri}_{\mathcal{L}}\text{Pr}$
γ_T^*	$1/\text{Ri}_{\mathcal{L}}$

Table 3.2: Boundary conditions

Region	Velocity B. C.	Thermal B. C.
Wall	$u^* = 0$	$T^* = 0$
Axis of symmetry	$\partial w^*/\partial r^* = 0; u^* = 0$	$\partial T^*/\partial r^* = 0$
Free surface	Eq. 3.23	Eq. 3.25

3.4 Mesh

A two-dimensional axisymmetric coordinate system was used. To confirm the grid independence of the solutions, each numerical simulation was calculated using four systematically refined meshes. The coarsest initial mesh #1 used in the analysis is shown in the Fig. 3.2. Tetragonal linear elements with inclusion of triangular elements were used. Every next mesh had approximately twice more nodes than the previous one. Each mesh had the inflation layers on the free surface and the no-slip wall of the

fixed thickness 0.15 and the growth rate of 1.2 (Fig. 3.3). The mesh details are listed in the Table 3.3. The quadrilateral elements with the inflation layers at the wall and the free surface were chosen since the geometry was relatively simple and did not require the complex meshing algorithms to create the grid. Moreover, in case of tetragonal elements, for the majority of elements their faces were approximately perpendicular to the expected flow direction (Fig. 3.2). That reduced the discretization error when the upwind discretization scheme was used compared to triangular unstructured mesh. The change in the inflation layer number in the meshes used was taken so that any part of the mesh would be systematically refined in all the meshes including the inflation layer areas.

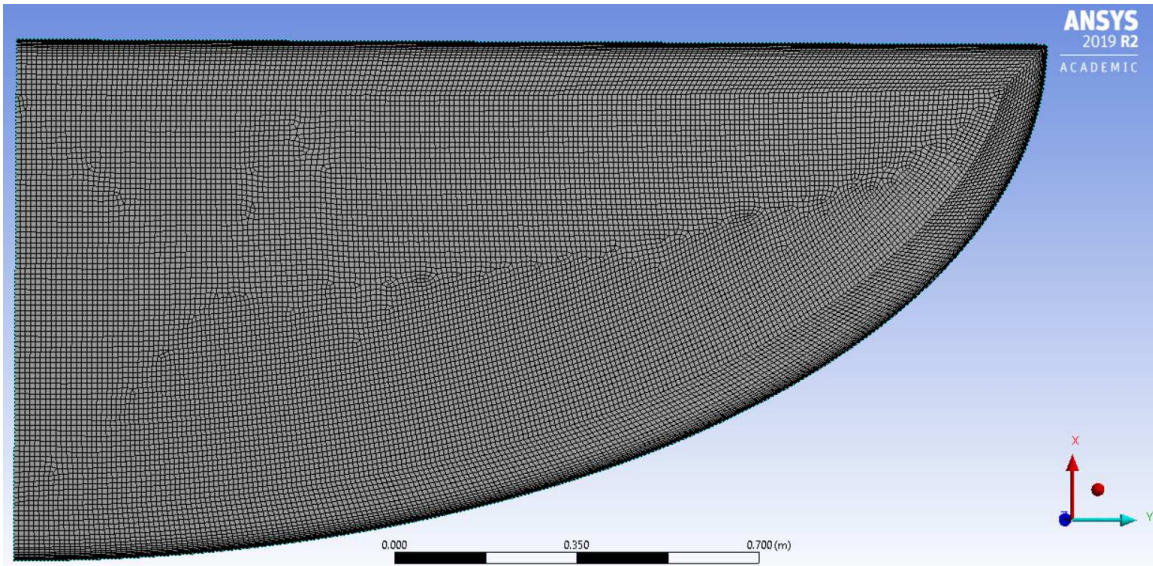


Figure 3.2: Initial mesh #1 overview

Table 3.3: Details on the meshes

Mesh #	# of nodes	Element size	# of inflation layers
1	21,590	0.01	20
2	43,903	0.007071	28
3	89,637	0.005	40
4	182,898	0.003536	56

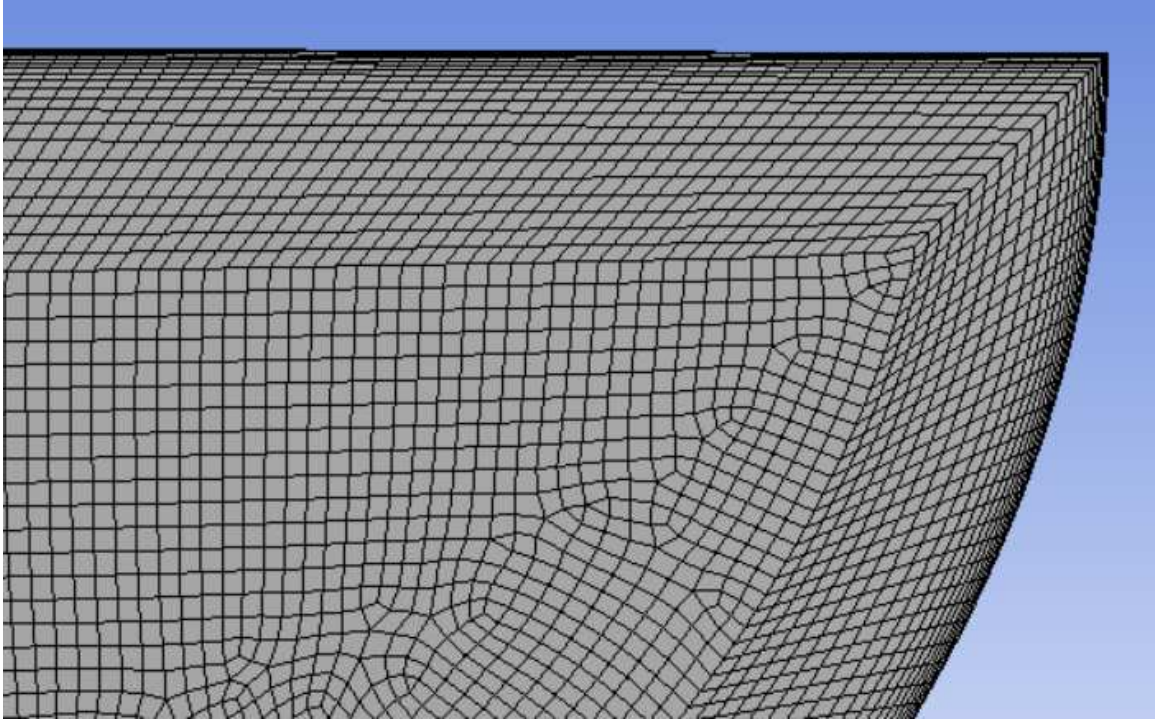


Figure 3.3: Mesh at the domain corner (magnified).

3.5 Solver parameters

As mentioned above, the simulations were performed in the ANSYS Fluent® software which is based on the Finite Volume Method (FVM). The problem was solved in a steady state using the Pseudo-Transient approach. The heat and momentum equations were solved using the second order upwind discretization scheme, i.e. the discretization scheme biased in the direction determined by the sign of the characteristic flow speeds. The discretization scheme for pressure was second order. Since the set of meshes was used for the numerical experiments with a wide set of input parameters and the resulting flow patterns, the second order schemes were chosen to decrease the numerical discretization error (numerical diffusion), particularly in the case when the flow was not aligned with the grid. The equations were solved with pressure and velocity fully coupled. The parameters of the numerical model are listed in the Table 3.4. The relaxation factors for the Pseudo-Transient terms are listed in

the Table 3.5.

Table 3.4: The parameters of the numerical model

Model type	2D axisymmetric
Element order	All linear
Element type	Tetragonal dominant
Solution type	Pseudo-transient steady-state
Flow model	Laminar
Heat transfer	Included
Pressure-velocity coupling scheme	Coupled
Momentum discretization scheme	Second Order Upwind
Heat energy discretization scheme	Second Order Upwind
Pressure discretization scheme	Second Order
Residuals	All 10^{-4}
Precision	Double precision

Table 3.5: Pseudo-transient explicit relaxation factors

Pressure	0.5
Momentum	0.5
Density	1
Energy	0.75

3.6 Convergence and grid independence

All the solutions were obtained with all the residuals converging below 10^{-4} . The generally accepted criteria for scientific accurate CFD calculations are in 10^{-6} - 10^{-8} . However, due to the large number of simulations, the simple geometry used and the compliance of the observed flow patterns with the expected ones, the flow behaviour and the characteristic parameters were expected not to be significantly different at both the higher and lower residuals. For this reason, the higher residuals of 10^{-4} were chosen.

The order of truncation p was calculated using the following formulae:

$$a = \left(\frac{N_2}{N_1} \right)^{1/2} \quad (3.26)$$

$$p \approx \frac{\ln \left(\frac{u_3^{max} - u_2^{max}}{u_4^{max} - u_3^{max}} \right)}{\ln a} \quad (3.27)$$

The three finest meshes were used for the order of truncation calculations: Mesh #2, #3, and #4. The ratio of the number of nodes was approximately $(N_4/N_3) \approx (N_3/N_2) \approx 2.04$, thus, $a = 1.428$.

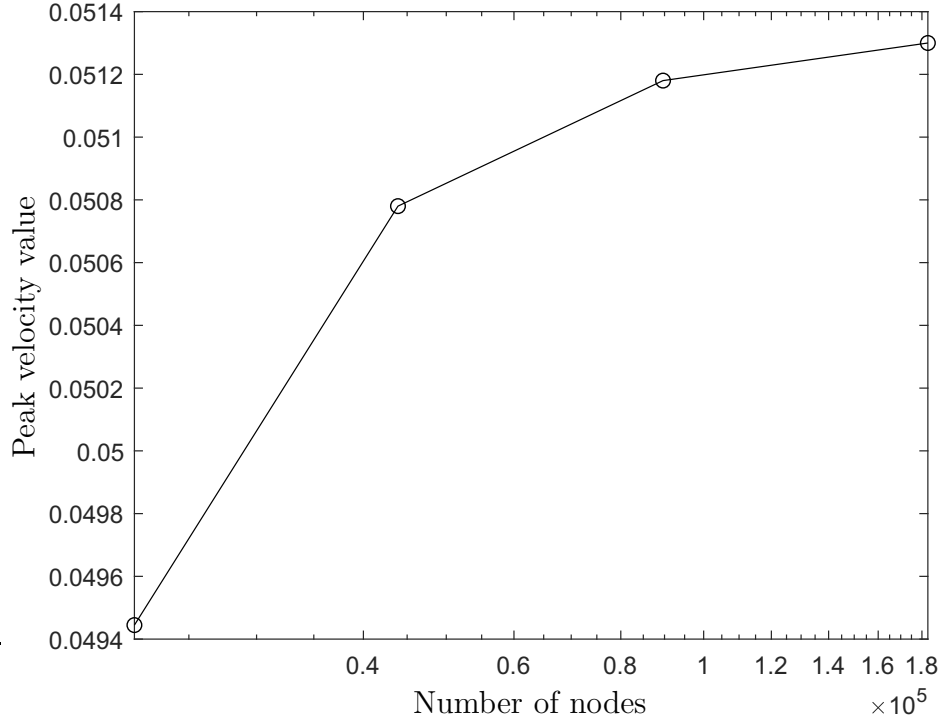


Figure 3.4: A typical graph for u_{max} as a function of the number of nodes

Maximum surface velocity u_{max} was used in the grid independence analysis, since it was dependent on the solution in the whole domain. For the calculated values of u_{max} , typical order of truncation p lied within the range of 4 to 6. These values were higher than expected $0.8 \leq p \leq 2.2$ for the second-order pressure, momentum and heat energy discretization schemes used. It means that the asymptotic behaviour

of the solution values was not reached, however, the exact solution was expected to be within a reasonable distance from the obtained values. The difference between the calculated velocity values at the sensitive point was found negligible for all the calculations. The absence of a noticeable variation in the velocity profile and values allow us to consider the finest Mesh 4 as the optimum grid system for the simulations.

Chapter 4

Results

The state-of-the-art analytic model for prediction weld width and penetration depth is the Gaussian heat source model described in the work by Eagar and Tsai [89]. As mentioned in Chapter 1, this model accounts for the spatial distribution of the welding heat source flux, but does not account for the convective flows in the weld pool. Chapter 4 summarizes the results on the predictions of the Peclet number of the thermocapillary convection in weld pools (Section 4.3) and the obtained correction factors for the predictions of the weld width and depth from the Gaussian heat source that account for the thermocapillary convection (Section 4.4).

4.1 Gaussian heat source model

The general solution of the temperature field for the moving Gaussian heat source was proposed by Eagar and Tsai [89]. This solution is presented in Eq. 4.1 with the notations used in the works by Wood *et al.* [93] and Wood [94].

$$T^* = \frac{1}{\sqrt{2\pi}} \int_0^\infty d\tau \frac{\tau^{-1/2}}{\tau + \sigma^{*2}} \exp\left(-\frac{x^{*2} + y^{*2} + 2x^*\tau + \tau^2}{2\tau + 2\sigma^{*2}} - \frac{z^{*2}}{2\tau}\right) \quad (4.1)$$

where T^* is the dimensionless temperature as defined in Eq. 4.2, τ is the dimensionless time (Eq. 4.3), σ^* is the dimensionless heat source size (Eq. 4.4), x^* , y^* , z^* are the dimensionless Cartesian coordinates as defined in Eqs. 4.5-4.7.

$$T^* = \frac{4\pi k_{eff}\alpha_{eff}(T - T_0)}{\eta_{th}q_{eff}U} \quad (4.2)$$

$$\tau = \frac{U^2 t}{2\alpha_{eff}} \quad (4.3)$$

$$\sigma^* = \frac{U\sigma}{2\alpha_{eff}} \quad (4.4)$$

$$x^* = \frac{Ux}{2\alpha_{eff}} \quad (4.5)$$

$$y^* = \frac{Uy}{2\alpha_{eff}} \quad (4.6)$$

$$z^* = \frac{Uz}{2\alpha_{eff}} \quad (4.7)$$

In Eqs. 4.1-4.7, k_{eff} is the effective thermal conductivity (W/mK), α_{eff} is the effective thermal diffusivity (m²/s), T is the temperature (K), T_0 is the preheat temperature (K), η_{th} is the effective thermal efficiency of the heat source, q_{eff} is the effective heat source power (W), U is the weld travel speed (m/s).

The Rykalin number is defined as the reciprocal of T^* (Eq. 4.8):

$$\text{Ry} = \frac{\eta_{th} q_{eff} U}{4\pi k_{eff} \alpha_{eff} (T - T_0)} \quad (4.8)$$

The algorithm for the calculation of the estimations for the weld width L_G and depth D_G is the following. L_G and D_G are calculated as the maximum width and the maximum depth of the melting temperature isotherm T_m . The calculation of the dimensionless maximum isotherm width corresponds to solving Eq. 4.1 as a function of y^* at $z^* = 0$ and the search of its maximum value. Analogously, the calculation of the dimensionless maximum isotherm depth corresponds to solving Eq. 4.1 as a function of z^* at $y^* = 0$ and finding its maximum. Then the obtained dimensionless values are recalculated into dimensional L_G and D_G using Eqs. 4.6 and 4.7.

The calculations of L_G and D_G were performed with the help of the optimization algorithm in the form of a MATLAB® code written by Gentry Wood and published in his PhD thesis [94].

4.2 Data used for the analysis

In order to perform the analysis two main sources of data were used: the results from the numerical model described in Chapter 3 and the literature.

4.2.1 Numerical modeling results

The numerical modelling was performed for the dimensionless parameter sets shown in the Fig. 4.1 on the $Ri_{\mathcal{L}} - Pr$ plane. The overall number of experimental points was 103 with 4 calculations for each experiments with the 4 meshes used for the grid independence analysis. Thus, 412 calculations were performed. The obtained temperature and velocity fields were analyzed along three lines: the free surface line, the axis of symmetry and the cut line parallel to z -axis located at $r = \mathcal{L}$ ($r^* = 1$) as shown in the Fig. 4.2. Since weld pool geometry change with melting was not modelled, the results of these numerical simulations were used only for the analysis of flow velocities and the Peclet numbers. The details on the dimensionless parameters and the obtained results are presented in Section 4.3.

4.2.2 Data from the literature

For the analysis of the flow behaviour, several publications were used as the data sources [2, 22, 53, 95, 96]. The details on the literature data used in the analysis are summarized in the Tables 4.1 and 4.2

Table 4.1: Details on the literature used for the analysis.

#	Reference	Year	Type of study	Heat source
1	Saldi [22]	2012	Numerical only	Top hat
2	Wei <i>et al.</i> [95]	2012	Numerical; scaling	Gaussian
3	Oreper <i>et al.</i> [2]	1983	Numerical only	Gaussian
4	Robert and DebRoy [97]	2001	Numerical; experimental	Gaussian; top hat
5	Mishra <i>et al.</i> [53]	2008	Numerical; experimental	Gaussian
6	Mundra <i>et al.</i> [96]	1992	Numerical only	Gaussian

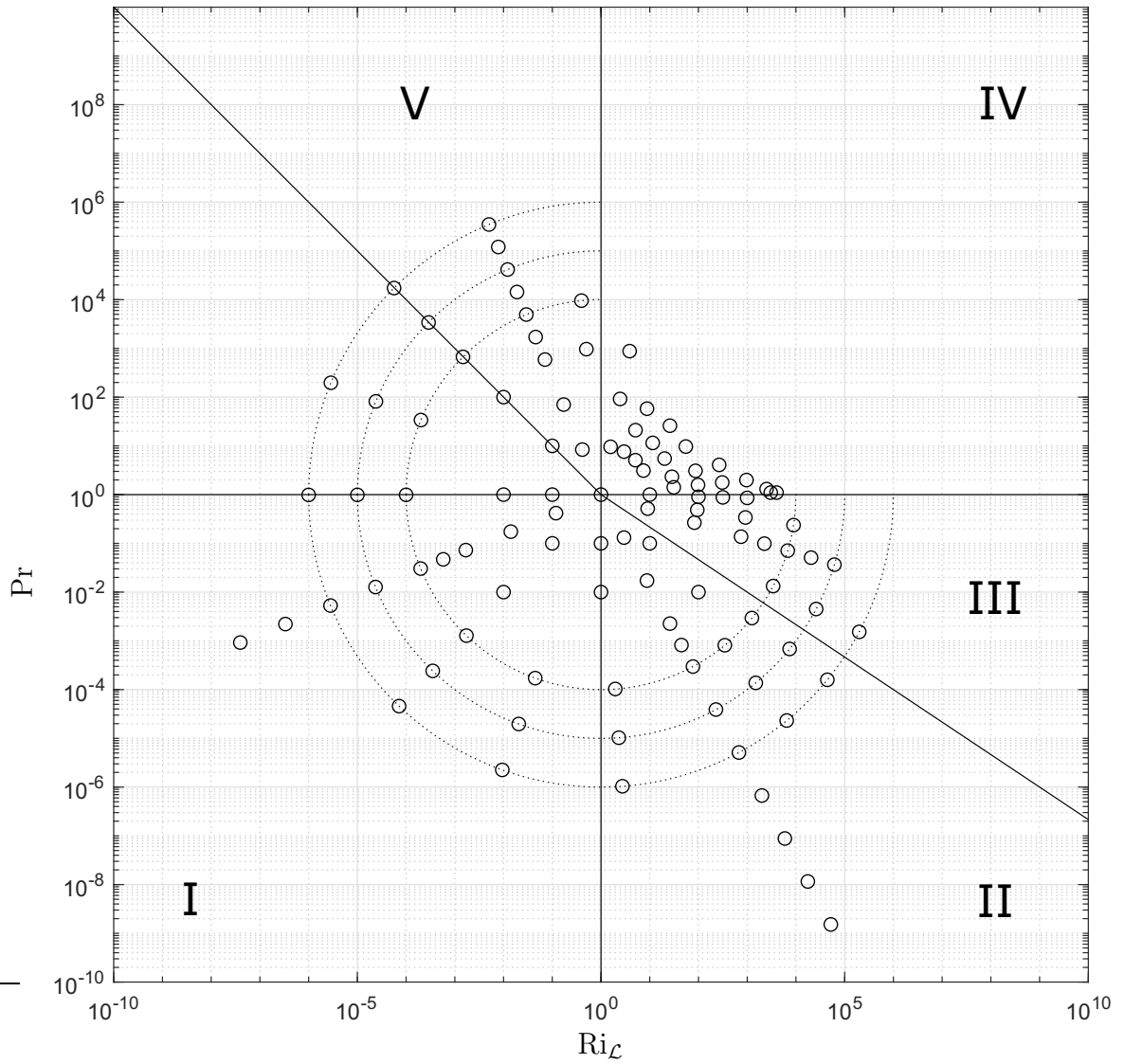


Figure 4.1: Location of the numerical experiments on the $Ri_{\mathcal{L}} - Pr$ plane

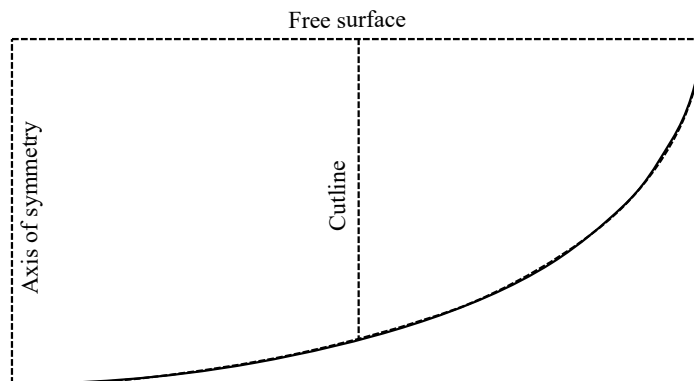


Figure 4.2: The free surface, the axis of symmetry and the cutline at $r = \mathcal{L}$ ($r^* = 1$).

Table 4.2: Details on the literature used for the analysis (continuation).

#	$\gamma_T = f(T)$	Weld type	Model type
1	yes	Stationary	Transient 2D axisymmetric
2	no	Moving	Transient 2D
3	no	Stationary	Transient 2D axisymmetric
4	no	Moving and stationary	Transient 2D axisymmetric
5	yes	Moving	Transient 2D (Pseudo-steady-state)
6	no	Stationary	Steady-state 2D axisymmetric

Table 4.3: Parameters for Eqs. 4.9 and 4.10 for γ_T from the works of Saldi [22] and Mishra *et al.* [53].

Parameters	Values	Units
A	$5.0 \cdot 10^{-4}$	N/mK
Γ_S	$1.3 \cdot 10^{-8}$	kmole/m ²
k_1	0.00318	-
ΔH^0	$-1.66 \cdot 10^{-8}$	J/kmole
$\Delta \bar{H}_i^M$	0	J/kmole

4.2.3 Dependence of γ_T on temperature

As shown in Table 4.2, the calculations by Saldi [22] and Mishra *et al.* [53] accounted for the temperature variations of the surface tension temperature coefficient γ_T . The dependence of γ_T on temperature complies with the law proposed by Sahoo *et al.* [21] (Eq. 4.9). For example, the behaviour of γ_T for a stainless steel with 20 ppm of sulfur modelled in [22] is shown in Fig. 4.3.

$$\gamma_T = -A - R\Gamma_S \ln(1 + Ka_i) - \frac{Ka_i}{1 + Ka_i} \frac{\Gamma_S (\Delta H^0 - \Delta \bar{H}_i^M)}{T} \quad (4.9)$$

$$\text{where } K = k_1 \exp \left[\frac{-\Delta H^0}{RT} \right] \quad (4.10)$$

In Eqs. 4.9 and 4.10, A is the surface tension temperature coefficient for pure metal, Γ_S the surface excess of saturation, K the equilibrium constant for segregation, k_1 the entropy factor, ΔH^0 the standard heat of adsorption, $\Delta \bar{H}_i^M$ the partial molar enthalpy of species mixing in the solution, and a_i the activity of the element in wt %.

The scaling model, however, requires a constant approximation for the surface

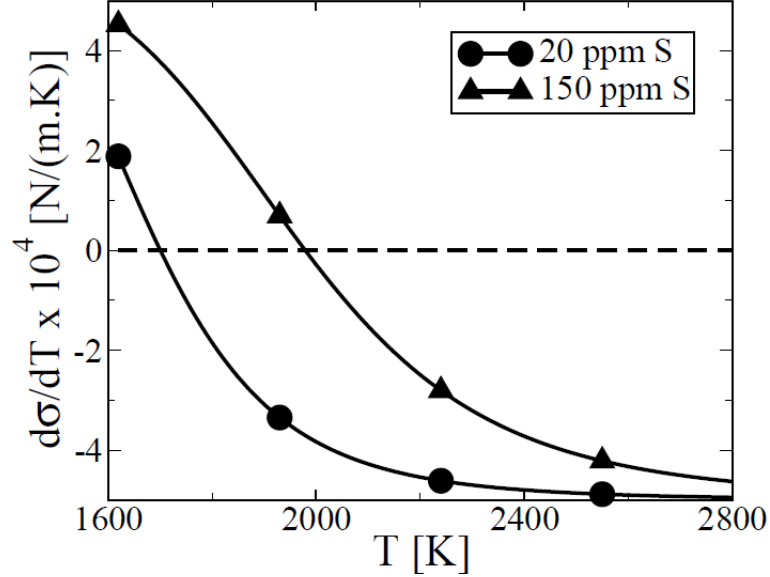


Figure 4.3: Surface tension temperature coefficient γ_T as a function of temperature for modelled samples of Böhler S705 steel with 20 and 150 ppm of sulfur (reprinted from [22]).

Table 4.4: Approximated values of γ_T used for the scaling analysis for the data from the works of Saldi [22] and Mishra *et al.* [53].

Reference	Sulfur content, ppm	$-\gamma_T$, N/mK
Saldi [22]	20	$4 \cdot 10^{-4}$
Mishra <i>et al.</i> [53]	30	$3 \cdot 10^{-4}$

tension temperature coefficient. According to the approximate surface temperature ranges, the approximate values of γ_T chosen for the data from [22, 53] are shown in Table 4.4.

4.2.4 Adaptation of the Gaussian heat source model for stationary welds

The weld simulations from the works [2, 22, 96, 97] used for the analysis were performed for stationary welds. Prediction formulae for the weld width and penetration depth from the Gaussian heat source [89] (Eqs. 4.1-4.7) are originally developed for moving, not stationary, welds and require the welding travel speed as an input parameter. For the stationary weld models, the travel speed was assessed as the ratio

of the heat source distribution size σ to the weld time t (Eq. 4.11).

$$U = \sigma/t \quad (4.11)$$

4.2.5 Measurements of the weld width and depth

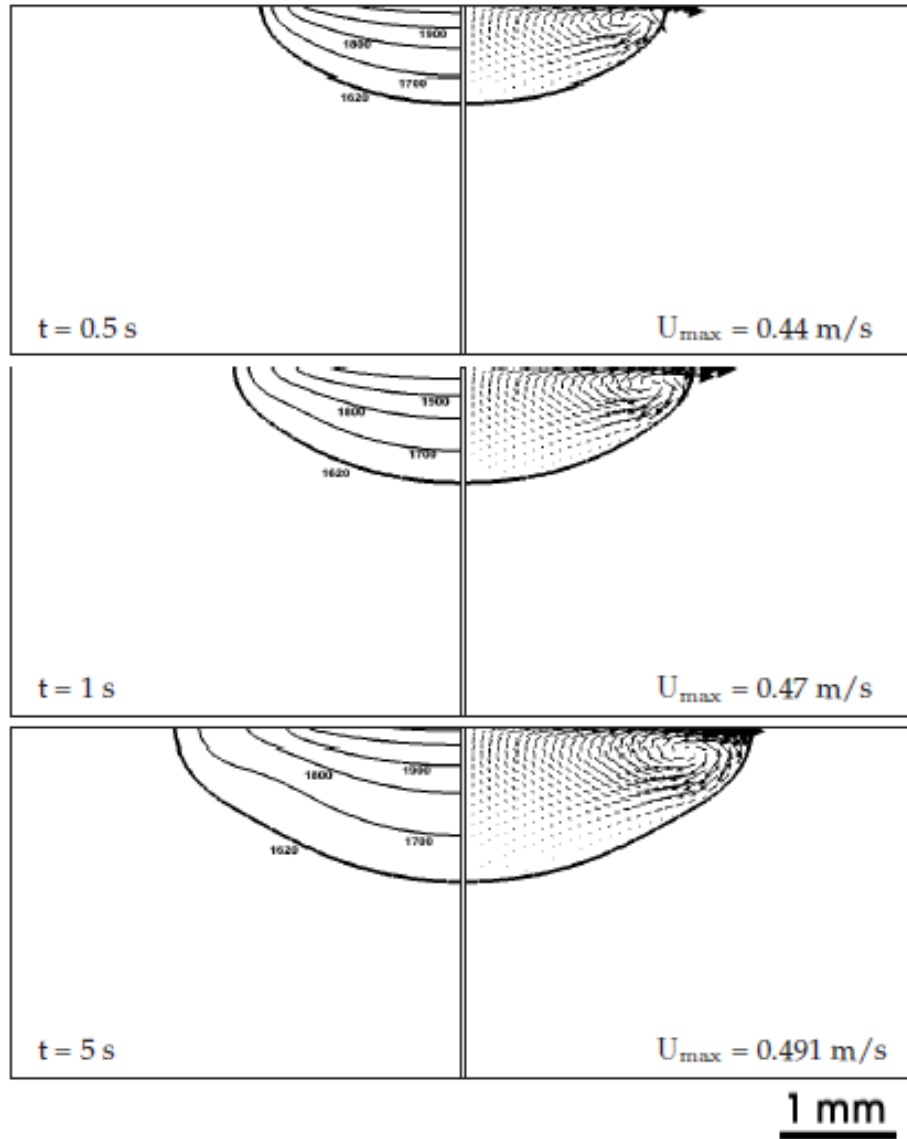
Some of the literature works presented the calculated or measured weld widths and depths explicitly; however, in some of the works only the figures of the weld profiles were presented, e.g., as shown in Fig. 4.4. The numerical values of the widths and depths in those cases were obtained with ImageJ software which counted the pixels between two selected points on the figure. The length in pixels was then compared with the pixel length of the image scale bar and converted into the actual length.

4.2.6 Top-hat and Gaussian heat sources

The models from the literature used the surface heat source with both the Gaussian [2, 53, 95–97] and the top-hat distribution profiles [22, 97] (Table 4.1). The top-hat surface heat flux boundary condition from [22] is:

$$k \frac{\partial T}{\partial n} = q''_{in} = \begin{cases} \eta Q / \pi r_q^2 & \text{for } r \leq r_q \\ 0 & \text{for } r > r_q \end{cases} \quad (4.12)$$

To obtain an estimation of the weld pool width and depth from the Gaussian heat source model, an estimated the Gaussian distribution factor σ as a function of the top-hat beam radius r_q was required. To determine the optimal σ , a comparative analysis of the weld pool sizes calculated with the top-hat model and the Gaussian heat source model was performed. As the reference top-hat heat source solution, an experiment from [22] was chosen (Fig. 4.5). This numerical experiment was chosen as the one having a low Peclet number of the convective flows to confirm that the effect of the thermocapillary convection could be neglected. The material properties of the experiment are listed in Table 4.5. The details on the heat source parameters and the measured and calculated weld width and depth are listed in Table 4.6.



(c) 3850 W, 20 ppm, $f = 4$.

Figure 4.4: Example of a figure used to extract the weld width, depth and maximum surface velocity (reprinted from [22]).

(a) 1900 W, 20 ppm S

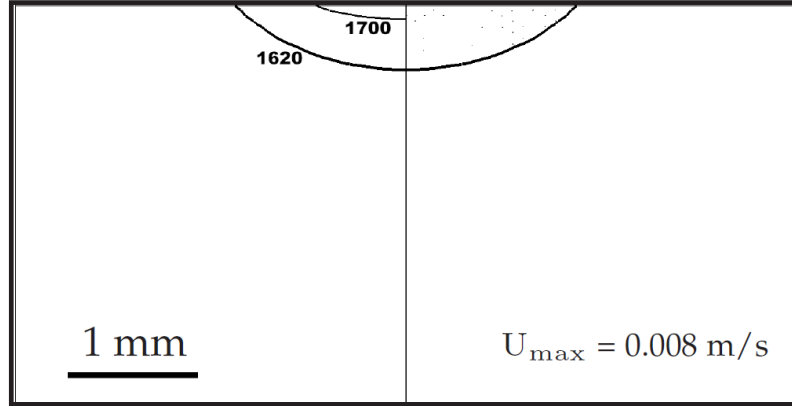


Figure 4.5: Example of a figure used to determine the optimal estimation for the Gaussian heat source distribution (reprinted from [22]).

Table 4.5: Material properties for the data from [22].

Properties	Values	Units
Density ρ	8100	kg/m ³
Melting temperature T_m	1620	K
Dynamic viscosity μ	0.006	kg/m s
Thermal conductivity of solid k_s	22.9	J/m s K
Thermal conductivity of liquid k_l	22.9	J/m s K
Enhancement factor for viscosity and liquid thermal conductivity	7.0	-
Specific heat of solid c_{ps}	627	J/kg K
Specific heat of liquid c_{pl}	723.14	J/kg K
Latent heat of melting i_{sl}	$2.508 \cdot 10^5$	J/kg

Table 4.6: Parameters of the heat source, weld width and depth from [22] and their counterparts calculated with the Gaussian heat source model.

Properties	Values	Units
Heat source power q	1900	W
Efficiency η	0.13	-
Irradiation time t	5	s
Beam radius r_q	1.4	mm
Convective Peclet number Pe	0.41	-
Assessed travel speed U	$2.8 \cdot 10^{-4}$	m/s
Gaussian heat source size σ	1.162	mm
Modified efficiency η_m	0.13689	-
Weld width L	1.40	mm
Weld depth D	0.57	mm
Calculated weld width L_G	1.4471	mm
Calculated weld depth D_G	0.5679	mm

As the result of the analysis, the Gaussian heat source distribution size σ was assessed as the 0.83 fraction of the top-hat beam radius r_q (Eq. 4.13):

$$\sigma = 0.83 r_q \quad (4.13)$$

The Gaussian heat source flux is distributed over the surface, generally speaking, infinitely, unlike the top-hat model which is fully concentrated within a particular radius. To minimize this effect, a correction factor for the heat source power was used in the form of a modified efficiency as shown in Eq. 4.14.

$$\eta_m = 1.053 \eta \quad (4.14)$$

4.3 Characteristic velocities and the Peclet numbers

4.3.1 Regime I

Criteria

The Regime I represents a case of the viscous flow with negligible convection and no boundary layers present. The Regime I exists in both high and low-Pr-number melts. Since for a low-Pr-number liquid the Peclet number does not exceed the Reynolds

number, the criterion for a melt with $\text{Pr} < 1$ to fall in Regime is $(D/\sigma)^2 \text{Re} < 1$ as shown in the Chapter 2, where $\text{Re} = u_{max}\sigma/\nu$. For a high-Pr-number fluid, the Peclet number may exceed the Reynolds number if its product with Pr is greater than unity. Thus, the criterion for melts with $\text{Pr} > 1$ is $(D/\sigma)^2 \text{Re Pr} < 1$:

$$(D/\sigma)^2 \text{Re} < 1, \quad \text{for } \text{Pr} < 1 \quad (4.15)$$

$$(D/\sigma)^2 \text{Re Pr} < 1, \quad \text{for } \text{Pr} > 1 \quad (4.16)$$

Schematically, the Regime I can be presented on $(D/\sigma)^2 \text{Re} - \text{Pr}$ map as shown in the Fig. 4.6.

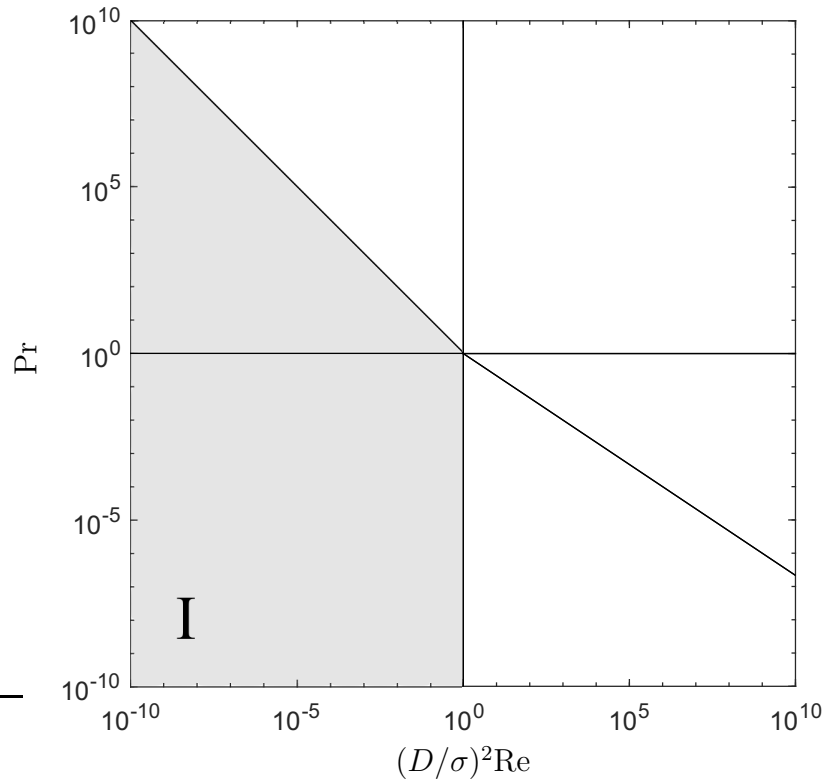


Figure 4.6: Location of the dimensionless parameters for Regime I on the $(D/\sigma)^2 \text{Re} - \text{Pr}$ plane.

Results of the numerical model

As shown in Chapter 2, the expression $\mathcal{R}_G^4 \text{Ri}$ can be used as an estimation for $(D/\sigma)^2 \text{Re}$ for the Regime I. However, the numerical model described in Chapter 3

uses the dimensionless numbers based on \mathcal{L} as the characteristic length, such as $\mathcal{R}_{\mathcal{L}}$ and $\text{Ri}_{\mathcal{L}}$. The analysis of the literature data, on the contrary, is based on σ as the characteristic length and, consequently, $\mathcal{R}_{\mathcal{G}}$ and Ri . The comparison of the locations of the numerical experiment parameters on the $\text{Ri}_{\mathcal{L}} - \text{Pr}$ ($\mathcal{R}_{\mathcal{L}}^4 \text{Ri}_{\mathcal{L}} = \text{Ri}_{\mathcal{L}}$ since $\mathcal{R}_{\mathcal{L}} = 1$ for all the numerical experiments) and the $\mathcal{R}_{\mathcal{G}}^4 \text{Ri} - \text{Pr}$ planes is shown in Fig. 4.7. From Eqs. 3.18 and 3.18:

$$\mathcal{R}_{\mathcal{L}}^4 \text{Ri}_{\mathcal{L}} = \frac{\mathcal{R}_{\mathcal{G}}^4 \text{Ri}}{4\pi \ln 2} \approx 0.11 \mathcal{R}_{\mathcal{G}}^4 \text{Ri} \quad (4.17)$$

Since the area of interest in every regime is where the regime is fully developed

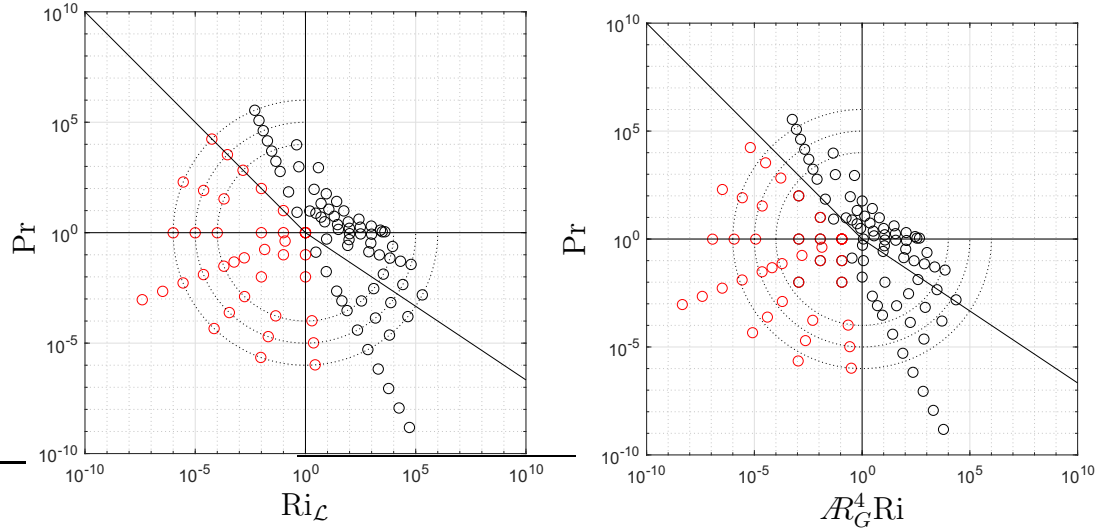


Figure 4.7: Numerical experiments for the Regime I on the $\text{Ri}_{\mathcal{L}} - \text{Pr}$ plane (left) and the $\mathcal{R}_{\mathcal{G}}^4 \text{Ri} - \text{Pr}$ plane (right).

rather than the intermediate stages and the conversion is clearly defined in Eq. 4.17, the results will be plotted either on the $\text{Ri}_{\mathcal{L}} - \text{Pr}$ or on the $\mathcal{R}_{\mathcal{G}}^4 \text{Ri} - \text{Pr}$ plane. The numerical experiments from the model described in Chapter 3 will be shown on the $\text{Ri}_{\mathcal{L}} - \text{Pr}$ plane. The literature data will be plotted on the $\mathcal{R}_{\mathcal{G}}^4 \text{Ri} - \text{Pr}$ plane. The graphs containing the results for both the literature data and the numerical model will be plotted on the $\mathcal{R}_{\mathcal{G}}^4 \text{Ri} - \text{Pr}$ plane.

The locations of the data presented in the Fig. 4.8 are the free surface, the axis of symmetry for the temperature field and $r^* = 1$ for the radial velocity profile as shown

in the Fig. 4.2. The radial velocity u^* profile along the cutline at $r^* = 1$ represents a near parabolic velocity distribution, as expected in a viscous flow. The discrepancy from a pure parabola are due to the curvature of the bottom wall. The temperature profile along the axis of symmetry is a near straight line. The discrepancy from the straight line are due to the fact that the bottom wall is not parallel to the free surface and, thus, a portion of the heat flow is directed radially. Since the normalization scheme used for all the simulations were based on scaling expressions for the Regime I, all the results within the Regime are identical.

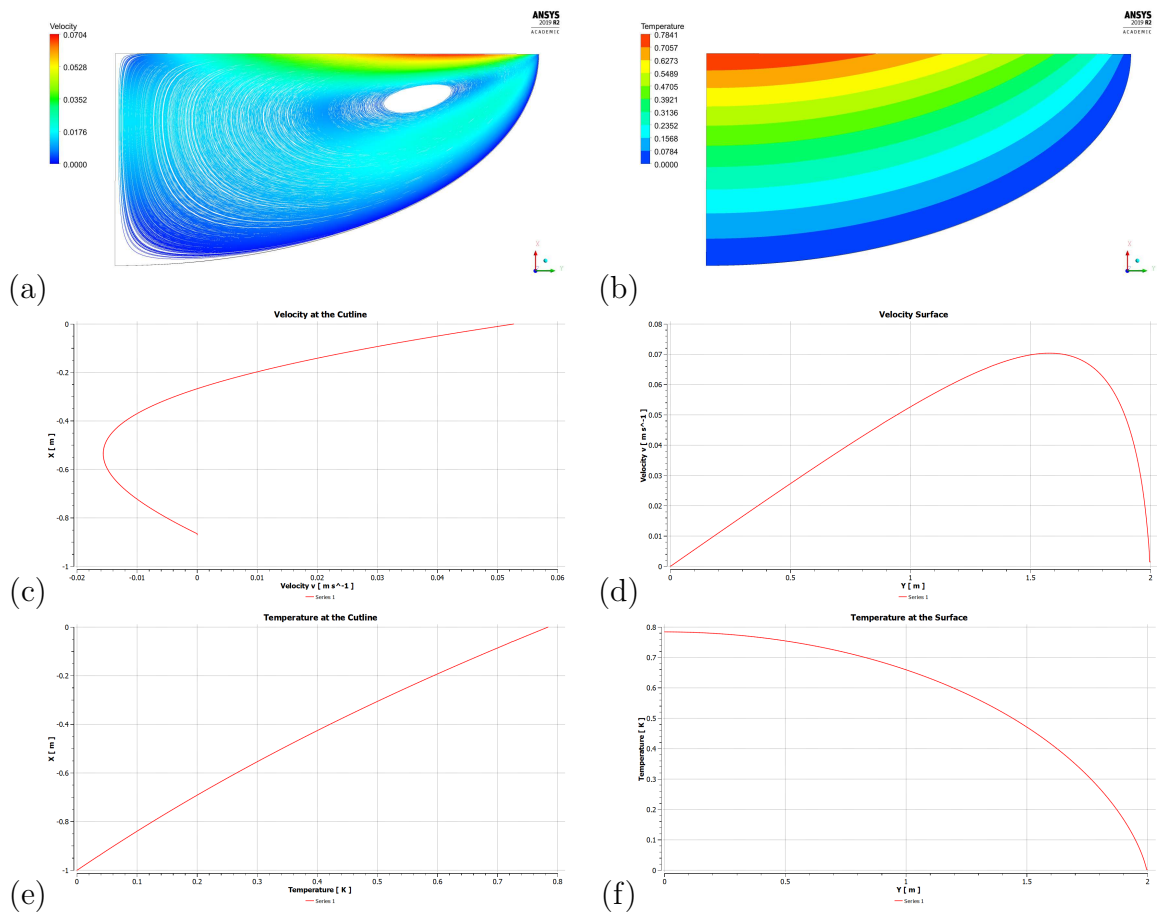


Figure 4.8: Calculated results for the Regime I (a - streamlines; b - temperature contour; c - radial velocity u^* along the cutline at $r = \mathcal{L}$ ($r^* = 1$) as indicated in Fig. 4.2 (abscissa is u^* , ordinate is z^*); d - u^* along the free surface; e - temperature T^* along the axis of symmetry (abscissa is T^* , ordinate is z^*); f - temperature T^* along the free surface). All the values are normalized. Note: the coordinate captions in the graphs are shown as noted in Ansys Fluent® and are not representative to the notations used in the work.

Table 4.7: Experiment parameters used for the analysis of the Regime I on the $Ri_{\mathcal{L}} - Pr$ plane as shown in the Fig. 4.9. The experimental points are located on the line set by Eq. 4.18.

Exp. number	Pr	$Ri_{\mathcal{L}}$	$\widehat{Pe}_{I_{\mathcal{L}}}$	$Pe_{I_{\mathcal{L}}}$
1.01	$4.17 \cdot 10^{-1}$	$1.19 \cdot 10^{-1}$	$4.96 \cdot 10^{-2}$	$2.61 \cdot 10^{-3}$
1.02	$1.74 \cdot 10^{-1}$	$1.41 \cdot 10^{-2}$	$2.46 \cdot 10^{-3}$	$1.30 \cdot 10^{-4}$
1.1	$7.28 \cdot 10^{-2}$	$1.68 \cdot 10^{-3}$	$1.22 \cdot 10^{-4}$	$6.43 \cdot 10^{-6}$
1.2	$4.70 \cdot 10^{-2}$	$5.78 \cdot 10^{-4}$	$2.72 \cdot 10^{-5}$	$1.43 \cdot 10^{-6}$
1.3	$3.04 \cdot 10^{-2}$	$1.99 \cdot 10^{-4}$	$6.05 \cdot 10^{-6}$	$3.19 \cdot 10^{-7}$
1.4	$1.27 \cdot 10^{-2}$	$2.36 \cdot 10^{-5}$	$3.00 \cdot 10^{-7}$	$1.58 \cdot 10^{-8}$
1.5	$5.30 \cdot 10^{-3}$	$2.81 \cdot 10^{-6}$	$1.49 \cdot 10^{-8}$	$7.84 \cdot 10^{-10}$
1.6	$2.21 \cdot 10^{-3}$	$3.34 \cdot 10^{-7}$	$7.38 \cdot 10^{-10}$	$3.89 \cdot 10^{-11}$
1.7	$9.23 \cdot 10^{-4}$	$3.96 \cdot 10^{-8}$	$3.66 \cdot 10^{-11}$	$1.93 \cdot 10^{-12}$

Since the asymptotic trend may reveal at some distance of the centre point on the $Ri_{\mathcal{L}} - Pr$ plane, a set of points that lay on the line in the middle of the Regime I was used to compare the calculated $Pe_{I_{\mathcal{L}}}$ with $\widehat{Pe}_{I_{\mathcal{L}}}$ predicted from the scaling approach. The line in the middle of the Regime I is set by Eq. 4.18:

$$Pr = Ri_{\mathcal{L}}^a \tag{4.18}$$

$$\text{where } a = \tan(\pi/8) = 0.41 \tag{4.19}$$

The parameters of the chosen set are presented in Tab. 4.7 and are schematically presented on the $Ri_{\mathcal{L}} - Pr$ plane in Fig. 4.9.

The trend was captured well with the scaling formula as can be seen in Fig. 4.10. The calibration coefficient connecting the scaling formula with the calculated values of Pe is shown in Eq. 4.20.

$$Pe_{I_{\mathcal{L}}} = 0.0527 \widehat{Pe}_{I_{\mathcal{L}}} \tag{4.20}$$

Analysis of literature data

The analysis of the literature data showed that for some of the numerical experiments from the work of Saldi [22] $(D/\sigma)^2 Re \sim 1$ or $(D/\sigma)^2 Re \lesssim 10$ as shown in Table 4.8,

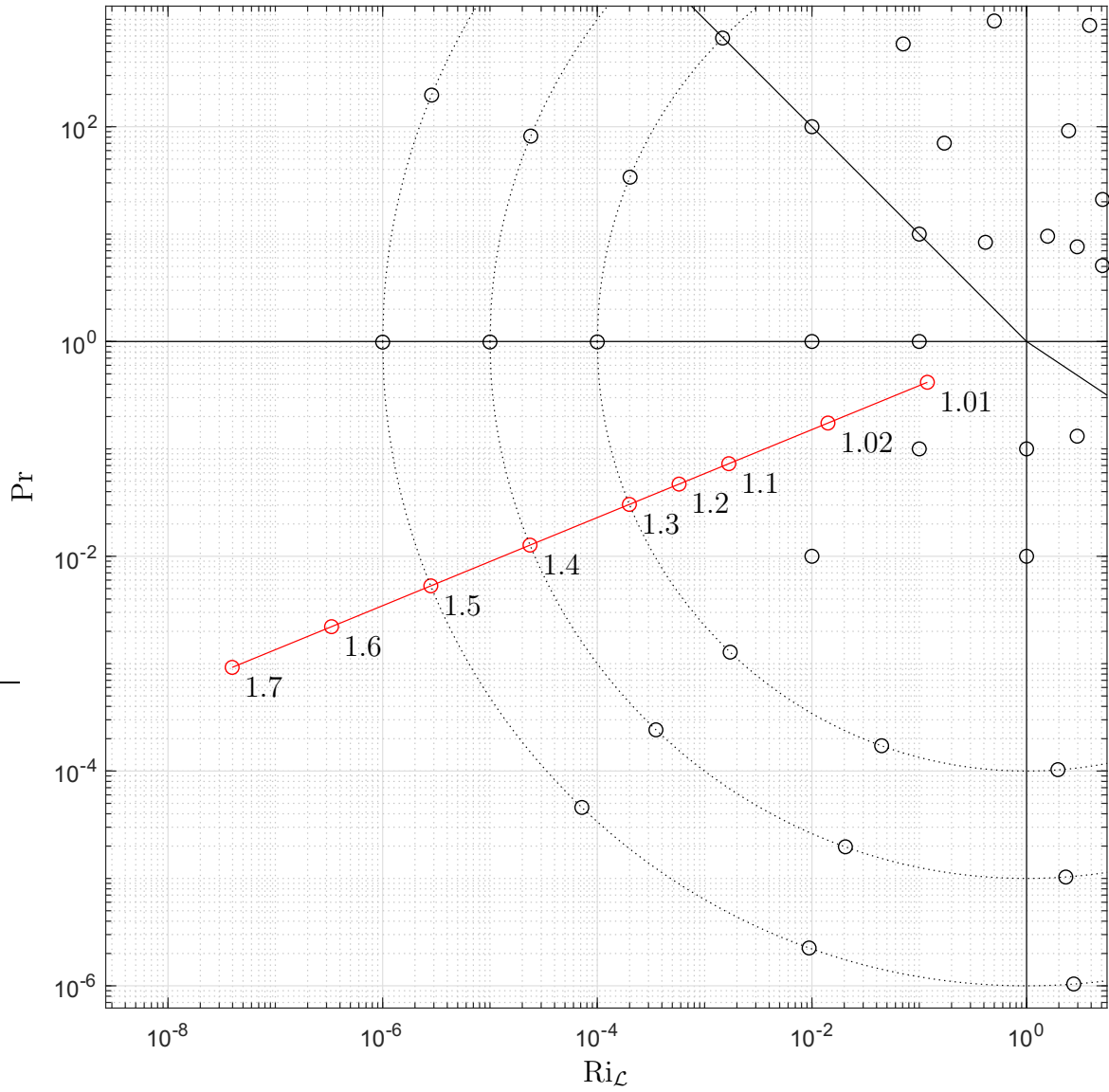


Figure 4.9: Location of the dimensionless parameters for Regime I and the experiment numbers on $Ri_L - Pr$ plane.

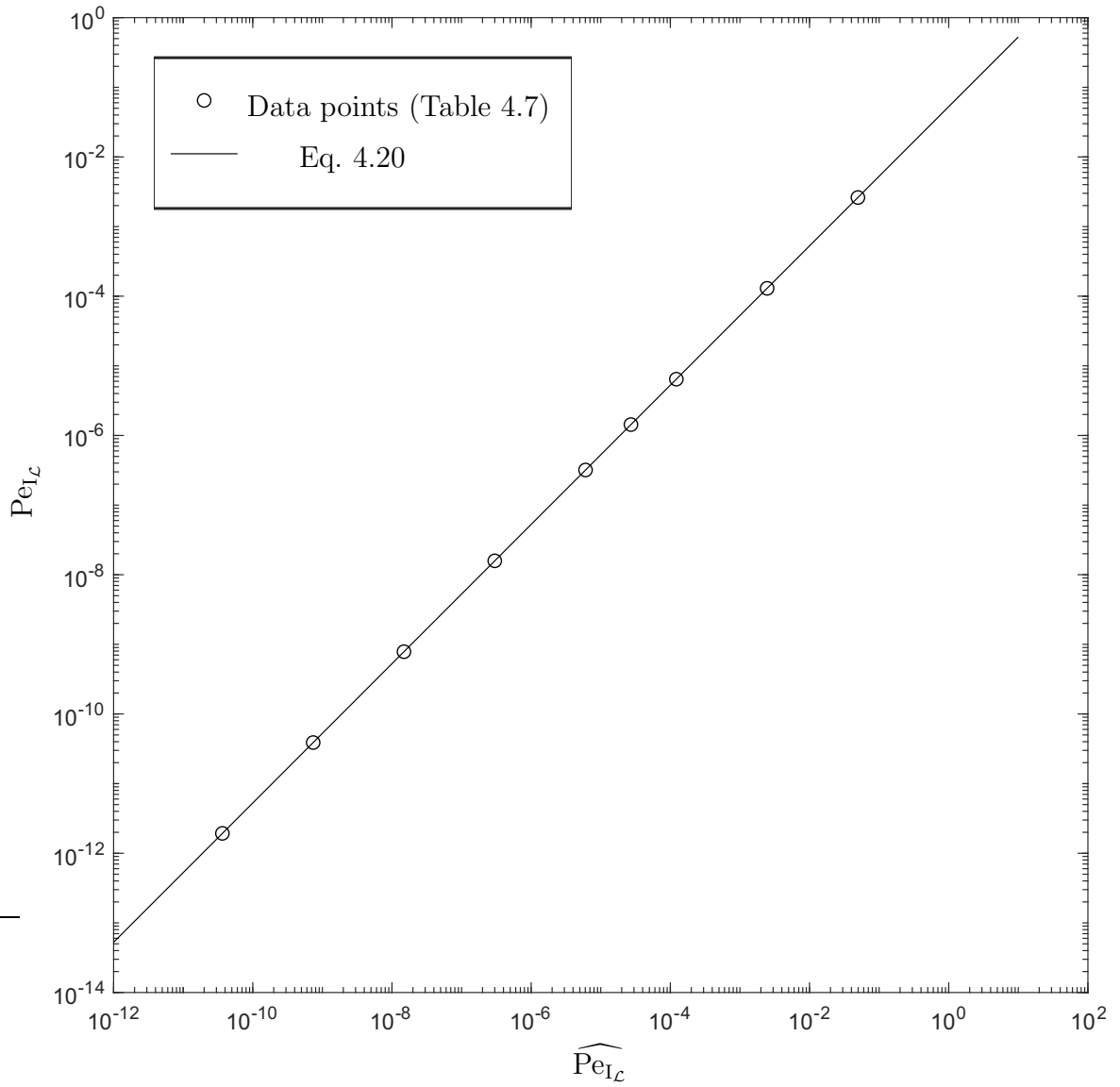


Figure 4.10: Comparison of the calculated Pe_{I_L} with the scaling law \widehat{Pe}_{I_L} for the Regime I.

which means that those experiments are in the intermediate regime between the Regimes I and III and not in the fully developed Regime III.

Table 4.8: The dimensionless parameters for the data from [22] sorted in group with approximately the same Pe.

#	Ri	\mathcal{R}_G	Pe	$(D/\sigma)^2\text{Re}$	Regime
1	2797577.293	1.5004	675.7279101	578.624579	III
2	2797577.293	1.9156	676.0860065	1029.211051	
3	2797577.293	2.6065	669.9983677	1568.265573	
4	2071283.188	1.0511	537.8607954	367.5547071	
5	2071283.188	1.3549	545.7389163	558.6182535	
6	2071283.188	1.8179	548.6036875	886.0039653	
7	349697.1616	1.5004	198.9225512	341.5448607	
8	349697.1616	1.9156	199.4596958	545.1535798	
9	349697.1616	2.6065	197.6692138	866.8170289	
10	258910.3985	1.0511	150.7585851	173.7092927	
11	258910.3985	1.3549	157.2043204	268.8925079	
12	258910.3985	1.8179	160.0690916	505.2833157	
13	43712.1452	1.5004	55.32589407	158.14817	
14	43712.1452	1.9156	56.48970738	240.5710781	
15	43712.1452	2.6065	57.29542428	428.5714286	
16	32363.79981	1.0511	39.39060419	78.12400551	
17	32363.79981	1.3549	42.07632721	115.0009796	
18	32363.79981	1.8179	43.95633331	220.7597107	
19	2980.150738	0.4887	0.409253031	0.357087308	
20	6038.726495	1.8179	10.23132576	54.8089775	
21	8156.202019	2.6065	15.34698865	129.3593769	
22	683.0022687	1.5004	0.917622029	4.508345176	I
23	683.0022687	1.9156	1.298099456	9.767877033	
24	683.0022687	2.6065	2.10381636	29.54247386	
25	505.684372	1.0511	0.335715377	1.00244083	
26	505.684372	1.3549	0.335715377	1.552820847	
27	505.684372	1.8179	0.626668703	5.578512397	

The analysis of the intermediate data showed that it comply with the trend proposed with the scaling law for Pe in the Regime I (Fig. 4.11) and represents a behaviour different from the the data point that lie in the fully developed Regime III. The calibration coefficient and the resultant calibrated scaling law for this set of data is shown in Eq. 4.21.

$$\text{Pe}_{I_c} = 0.0025 \widehat{\text{Pe}}_{I_c} \quad (4.21)$$

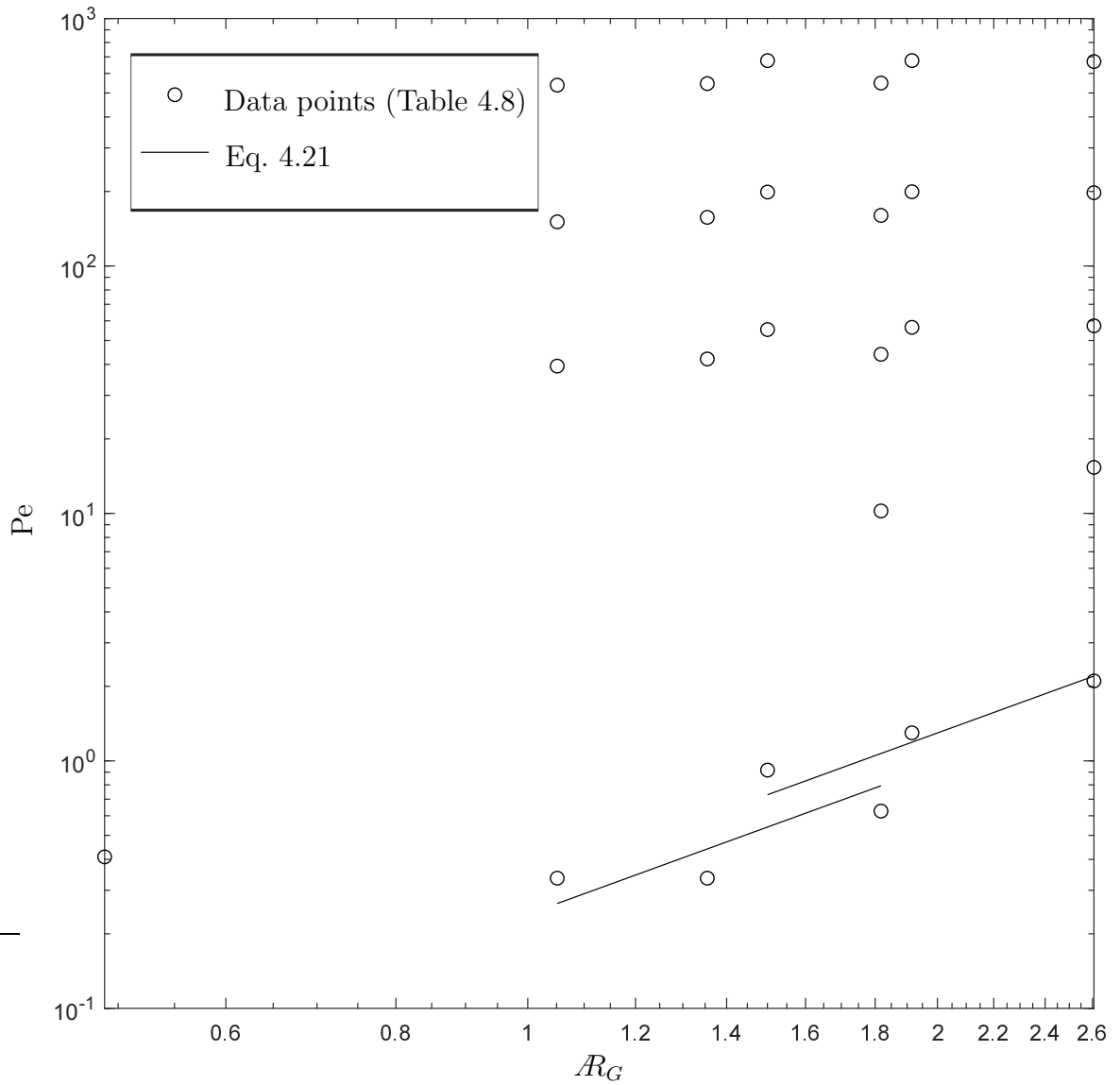


Figure 4.11: Pe for the data in the intermediate regime from [22] compared to the scaling law for the Regime I.

4.3.2 Regime II

The Regime II represents a case of the inertial flow with negligible convection, i.e., a viscous boundary layer is formed at the free surface, but there is no thermal boundary layer. The Regime II is a flow regime that may be present only in low Pr number fluids.

Criteria

Since the flow is inertial, the criterion for a flow to fall into the regime is $(D/\sigma)^2 \text{Re} \gg 1$, where $\text{Re} = u_{max}\sigma/\nu$. However, the Peclet number must not exceed unity in order for convection to be negligible. Thus, the criterion for $\text{Pr} > 1$ is $(D/\sigma)^2 \text{Re Pr} \leq 1$:

$$(D/\sigma)^2 \text{Re} \gg 1 \quad (4.22)$$

$$(D/\sigma)^2 \text{Re Pr} \leq 1 \quad (4.23)$$

As shown in Chapter 2, Eq. 4.29 can be approximated as:

$$\mathcal{R}_G^{4/3} \text{Ri}^{1/3} \text{Pr} \leq 1 \quad (4.24)$$

In Eq. 4.24, the aspect ratio and the Ri number based on σ as the characteristic length were used, unlike Eq. 2.21. This approximation can be considered valid since the intermediate regime zones lie within 1-2 orders of magnitude. Schematically, the Regime II can be presented on $(D/\sigma)^2 \text{Re} - \text{Pr}$ map as shown in the Fig. 4.12.

Results of the numerical model

The locations of the numerical experiments within this regime on $\text{Ri}_L - \text{Pr}$ are highlighted in red colour in the Fig. 4.13.

The locations of the data presented in the Fig. 4.14 are the free surface, the axis of symmetry for the temperature field and $r^* = 1$ for the radial velocity profile as shown in the Fig. 4.2. The radial velocity u^* profile along the cutline at $r^* = 1$ indicates the formation of the viscous boundary layer at the free surface (Fig. 4.14). A comparison

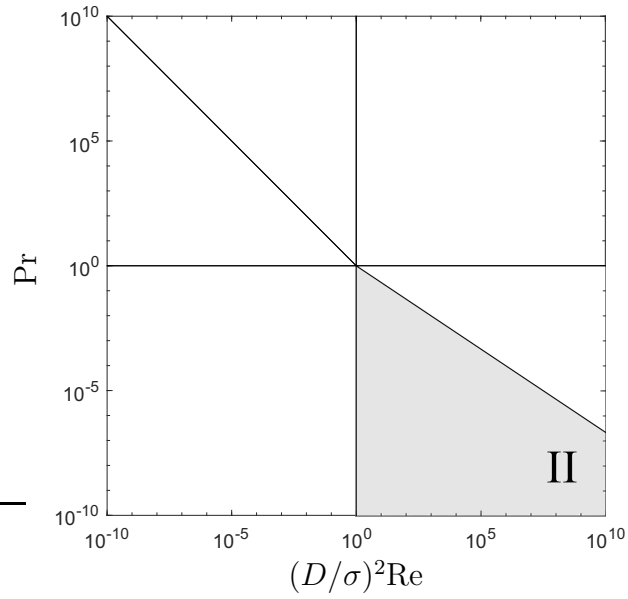


Figure 4.12: Location of the dimensionless parameters for the Regime II on the $(D/\sigma)^2 \text{Re} - \text{Pr}$ plane.

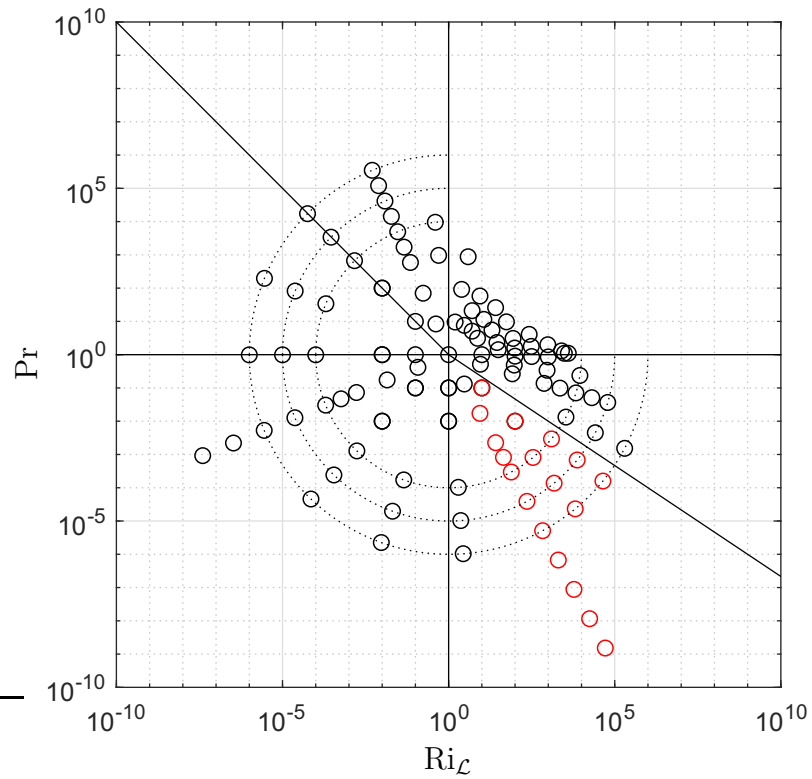


Figure 4.13: Location of the dimensionless parameters for the Regime II on $\text{Ri}_L - \text{Pr}$ plane. Note: $\mathcal{R}_L = 1$ in all the numerical experiments on this map.

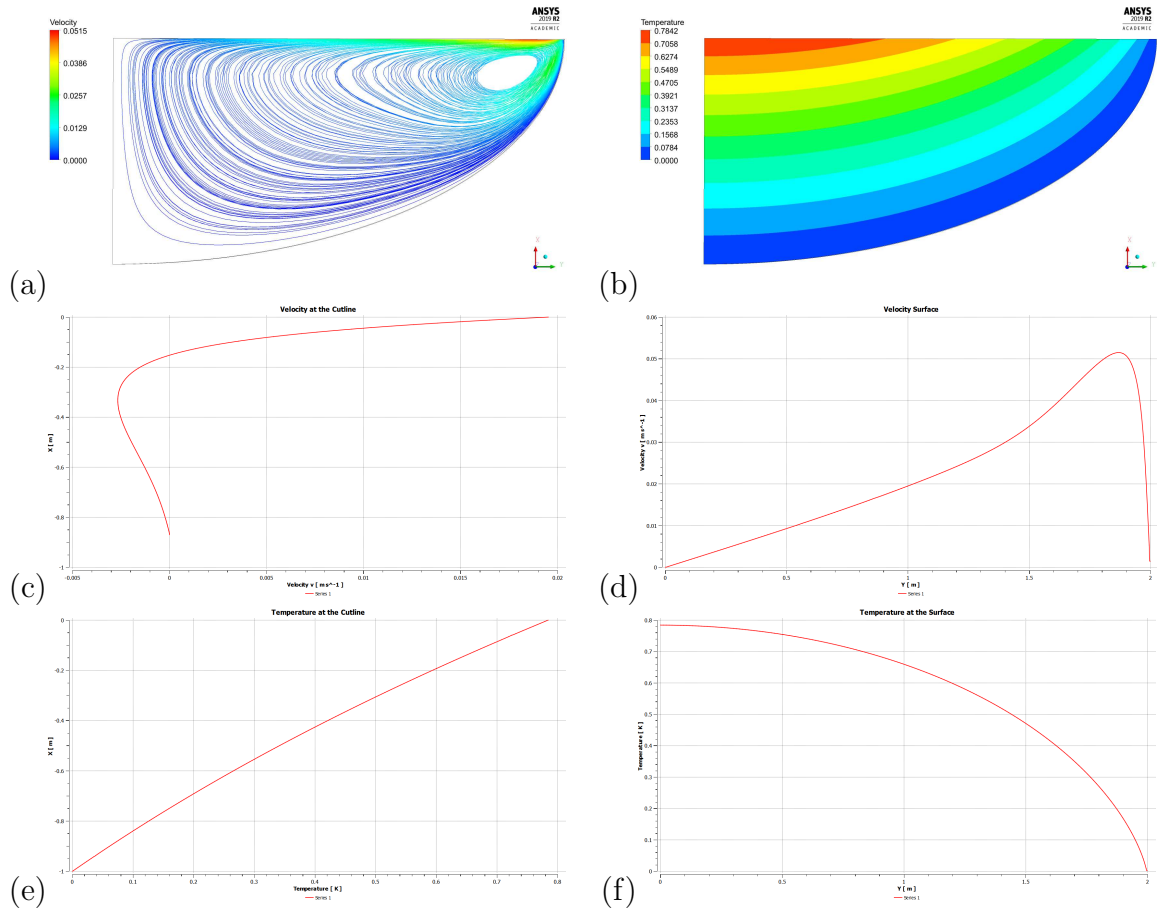


Figure 4.14: Calculated results for the Regime II (a - streamlines; b - temperature contour; c - radial velocity u^* along the cutline at $r = \mathcal{L}$ ($r^* = 1$) as indicated in Fig. 4.2 (abscissa is u^* , ordinate is z^*); d - u^* along the free surface; e - temperature T^* along the axis of symmetry (abscissa is T^* , ordinate is z^*); f - temperature T^* along the free surface). All the values are normalized. Note: the coordinate captions in the graphs are shown as noted in Ansys Fluent® and are not representative to the notations used in the work.

graph of u^* profile along $r^* = 1$ for Regimes I and II are shown in the Fig. 4.15. The center of the recirculation vortex is shifted towards the edge of the weld pool (Fig. 4.14 a) compared to the Regime I. This shift can be seen at the free surface velocity profiles (Fig. 4.14 d). The temperature profile along the axis of symmetry is a near straight line coinciding with the one for the Regime I indicating that the convective heat transfer is negligible in the Regime II (Fig. 4.14 e). The temperature distribution along the free surface coincide with the one from the Regime I, too (Fig. 4.14 f).

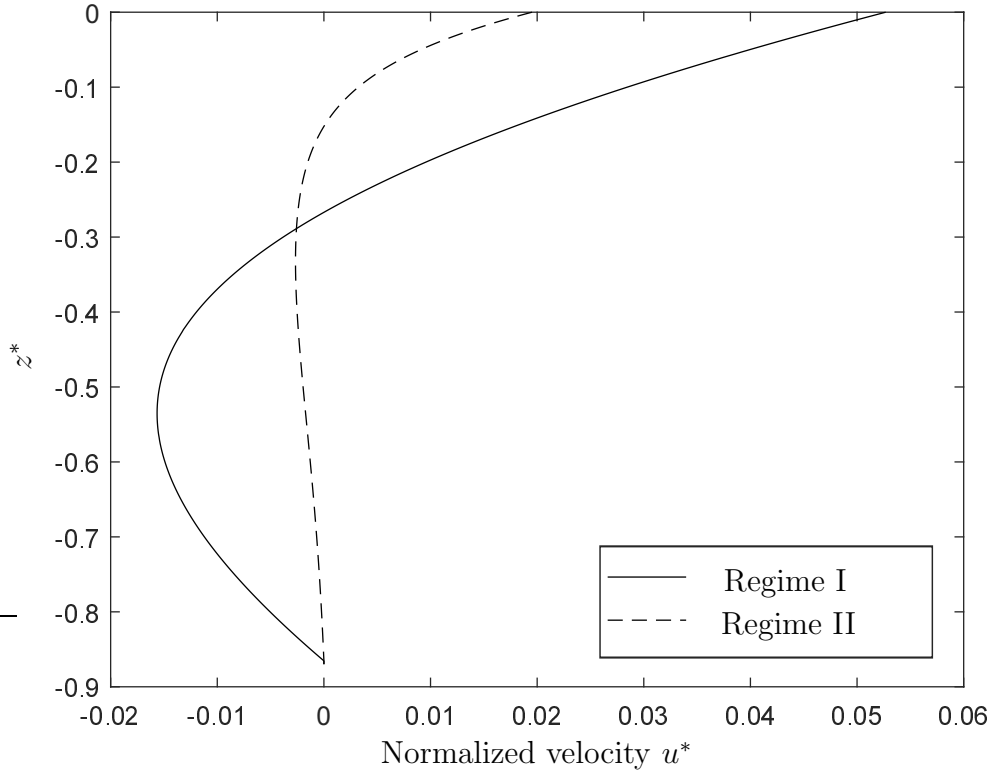


Figure 4.15: Formation of the viscous boundary layer in the Regime II (dashed line) vs near-parabolic distribution in the Regime I (solid).

A set of the numerical experiments with their parameters lying on the line defined in Eq. 4.25 was used to verify that the asymptotic behaviour of the calculated Pe_{II} matches the corresponding scaling law (Eq. 2.72). Eq. 4.25 defines a line that lies in

Table 4.9: Experiment parameters used for the analysis of the Regime II on the $Ri_{\mathcal{L}} - Pr$ plane as shown in the Fig. 4.16. The experimental points are located on the line set by Eq. 4.25

Exp. number	Pr	$Ri_{\mathcal{L}}$	$\widehat{Pe}_{II_{\mathcal{L}}}$	$Pe_{II_{\mathcal{L}}}$
2.01	$1.31 \cdot 10^{-1}$	2.96	$2.71 \cdot 10^{-1}$	$2.04 \cdot 10^{-2}$
2.02	$1.72 \cdot 10^{-2}$	8.77	$7.33 \cdot 10^{-2}$	$7.92 \cdot 10^{-3}$
2.1	$7.28 \cdot 10^{-2}$	$2.60 \cdot 10^1$	$1.98 \cdot 10^{-2}$	$3.05 \cdot 10^{-3}$
2.2	$8.20 \cdot 10^{-4}$	$4.47 \cdot 10^1$	$1.03 \cdot 10^{-2}$	$1.88 \cdot 10^{-3}$
2.3	$2.97 \cdot 10^{-4}$	$7.70 \cdot 10^1$	$5.37 \cdot 10^{-3}$	$1.15 \cdot 10^{-3}$
2.4	$3.90 \cdot 10^{-5}$	$2.28 \cdot 10^2$	$1.45 \cdot 10^{-3}$	$4.47 \cdot 10^{-4}$
2.5	$5.12 \cdot 10^{-6}$	$6.75 \cdot 10^2$	$3.94 \cdot 10^{-4}$	$1.31 \cdot 10^{-4}$
2.6	$6.72 \cdot 10^{-7}$	$2.00 \cdot 10^3$	$1.07 \cdot 10^{-4}$	$3.72 \cdot 10^{-5}$
2.7	$8.82 \cdot 10^{-8}$	$5.92 \cdot 10^3$	$2.89 \cdot 10^{-5}$	$1.02 \cdot 10^{-5}$
2.8	$1.16 \cdot 10^{-8}$	$1.75 \cdot 10^4$	$7.82 \cdot 10^{-6}$	$2.78 \cdot 10^{-6}$
2.9	$1.52 \cdot 10^{-9}$	$5.20 \cdot 10^4$	$2.12 \cdot 10^{-6}$	$7.58 \cdot 10^{-7}$

the middle of the Regime II.

$$Pr = Ri_{\mathcal{L}}^a \quad (4.25)$$

$$\text{where } a = -\tan(\pi/3) = -1.87 \quad (4.26)$$

The dimensionless parameters of the chosen experiment set are listed in Table 4.9. Their locations on the $Ri_{\mathcal{L}} - Pr$ plane is shown in Fig. 4.16.

The comparison of the calculated $Pe_{II_{\mathcal{L}}}$ with the the scaling law $\widehat{Pe}_{II_{\mathcal{L}}}$ for the Regime II proposed in Eq. 2.72 is shown in Fig. 4.17. The fully developed Regime II in Fig. 4.17 corresponds to the low values of $\widehat{Pe}_{II_{\mathcal{L}}}$ on the left side of the figure, whereas the right part of the higher $\widehat{Pe}_{II_{\mathcal{L}}}$ corresponds to the intermediate zone between the Regimes I and II. The correction coefficient for the scaling law of Eq. 2.72 is shown in Eq. 4.27:

$$Pe_{II_{\mathcal{L}}} = 0.36 \widehat{Pe}_{II_{\mathcal{L}}} \quad (4.27)$$

Formation of a secondary vortex

In the Regime II there was observed the formation of a secondary vortex at $Ri > 10^4$ (Fig. 4.18). Since in the Regime II the temperature field is essentially independent

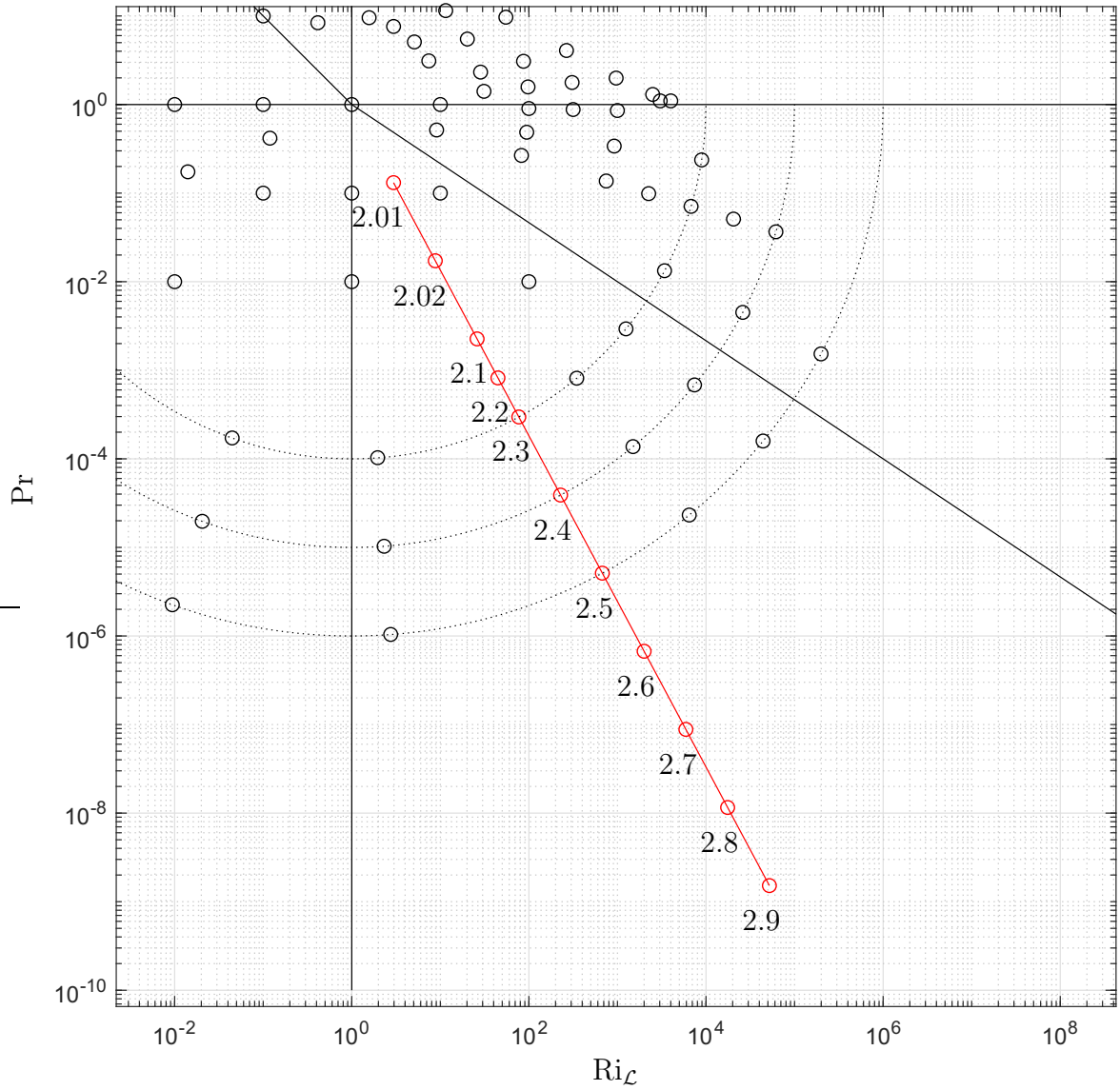


Figure 4.16: Location of the numerical experiments on the $Ri_C - Pr$ used for the calibration of the scaling law for the Regime II.

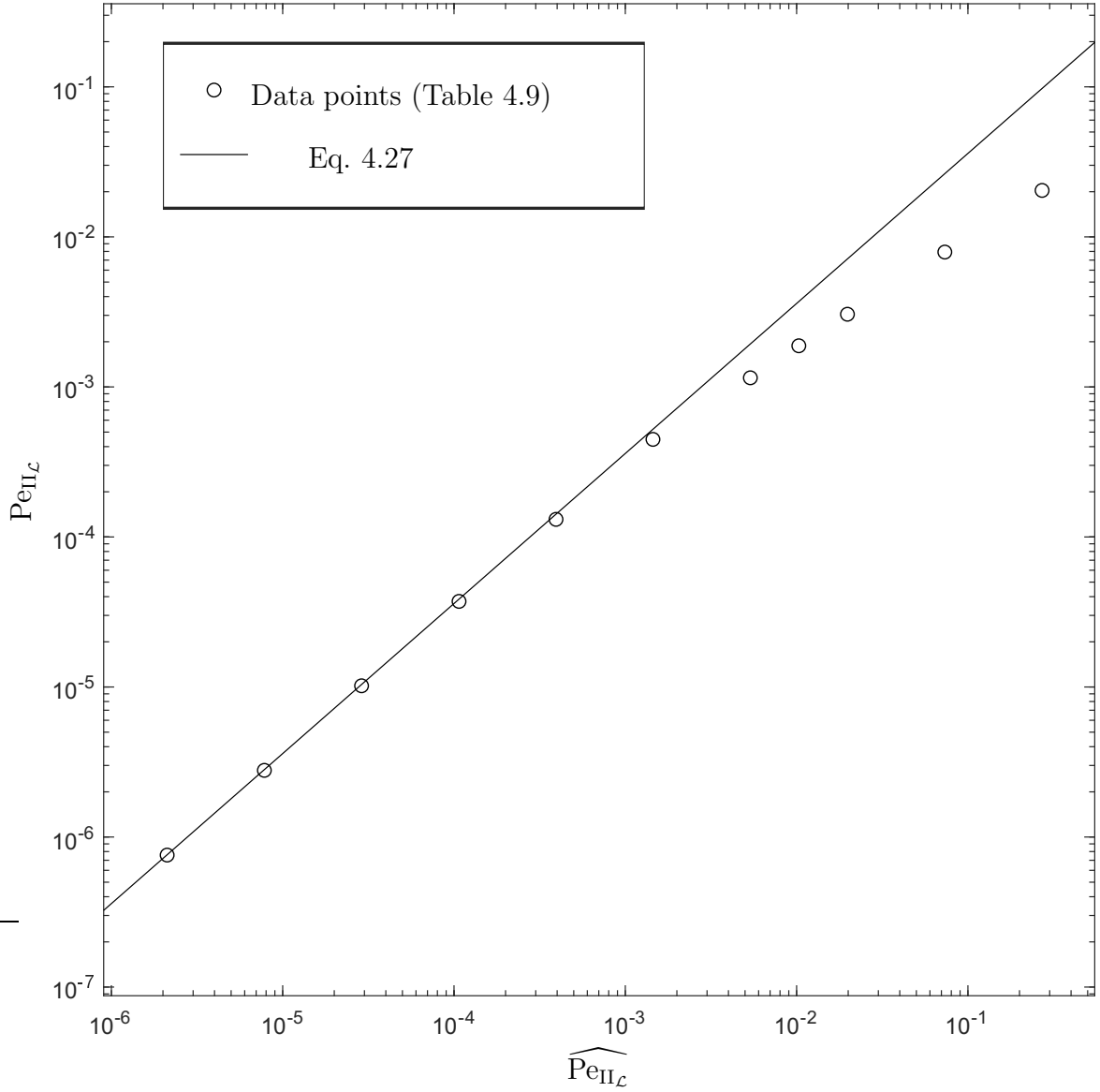


Figure 4.17: Comparison of the calculated Pe_{II_L} with the scaling law \widehat{Pe}_{II_L} for the Regime II. Note: the fully developed Regime II corresponds to the low values of \widehat{Pe}_{II_L} on the left of the figure, whereas the right part of the higher \widehat{Pe}_{II_L} corresponds to the intermediate zone between the Regimes I and II.

from the flow, the formed secondary vortex was not found to have a significant effect on the characteristic flow velocities.

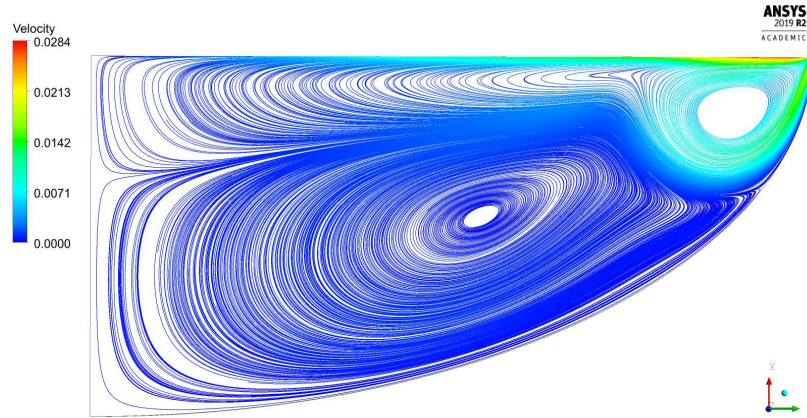


Figure 4.18: Streamlines for a weld pool flow with a flow separation and the formation of a secondary vortex in the Regime II with high Re numbers corresponding to $Ri > 10^4$.

Experimental example from the literature

Weld pool flows of metals with a very low Prandtl numbers such as aluminum alloys, gallium, etc., may fall into the Regime II. Tables 4.10 and 4.11 summarize the experimental examples of the weld pool flows in the Regime II. Two welds of the aluminum alloy 5182 and one weld of gallium were characterized with both the estimated Re and $(D/\sigma)^2 Re$ numbers being two orders of magnitude above unity, which means that the flows were inertial and the viscous boundary layers were formed at the weld pool free surfaces (Table 4.11). However, as shown in Table 4.11, the estimated Pe numbers were of the order of unity or lower indicating that convection heat transfer was negligible. The negligence of convection is also confirmed with the criterion defined in Eq. 4.24. Despite of large Ri numbers (Table 4.10), the criterion $\mathcal{R}_G^{4/3} Ri^{1/3} Pr$ was of the order of magnitude of unity for all the four welds. The cross section of one of the aluminum welds considered is shown in Fig. 4.19. As indicated in Table 4.11, the measured weld width L and depth D were within the calculation tolerance with their

Table 4.10: Dimensionless parameters used for the analysis of the experimental results from [97].

#	Material	Pr	Ri	\mathcal{R}_G	$\mathcal{R}_G^{4/3} \text{Ri}^{1/3} \text{Pr}$ (Eq. 4.24).
1	Al alloy 5182	0.012	$1.78 \cdot 10^6$	0.78	1.05
2	Al alloy 5182	0.012	$2.79 \cdot 10^6$	0.99	1.68
3	Ga	0.024	$1.47 \cdot 10^4$	1.2	0.75
4	Ga	0.024	$1.29 \cdot 10^4$	5.64	5.65

Table 4.11: Estimated characteristic velocities and the dimensionless parameters of the experimental results from [97] that are in the Regime II.

#	u_{est} , m/s	Pe_{est}	Re_{est}	$(D/\sigma)^2 \text{Re}_{est}$	D/D_G	L/L_G
1	0.15	1.94	97.23	89.02	1.22	0.94
2	0.15	1.19	131.73	120.89	0.96	0.84
3	0.001	0.01	9.28	17.05	1.14	0.91
4	0.002	0.45	4.72	149.31	1.00	0.98

counterparts L_G and D_G predicted with the Gaussian heat source model, confirming that weld pool convection was negligible in the four welds.

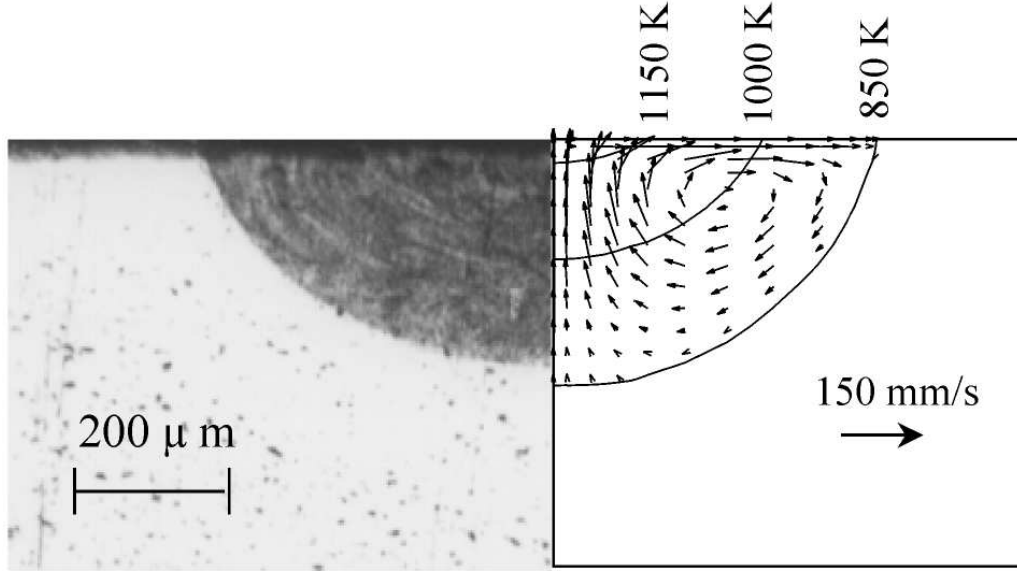


Figure 4.19: Cross sections of the experimental and calculated weld pool of aluminum alloy 5182 at 1.5kW and 105.8 mm/s welding speed (reprinted from [97])

4.3.3 Regime III

The Regime III represents the case of an inertial flow of a low-Prandtl-number melt with significant convection, i.e., both the viscous boundary layer and the thermal boundary layer are formed at the free surface. The Regime III is a flow regime that is defined only for low-Pr-number fluids. In case of $Pr > 1$ the thermal boundary layer is thinner than the viscous boundary layer which requires different scaling laws; this analogous regime for high-Pr-number melts is defined as the Regime IV.

Criteria

Since the flow is inertial, the criterion to fall in the regime is $(D/\sigma)^2 Re \gg 1$, where $Re = u_{max}\sigma/\nu$. Moreover, the Peclet number is greater than unity:

$$(D/\sigma)^2 Re \gg 1 \quad (4.28)$$

$$(D/\sigma)^2 Re Pr > 1 \quad (4.29)$$

As shown in Chapter 2, Eq. 4.29 can be approximated as:

$$\mathcal{R}_G^{4/3} Ri^{1/3} Pr > 1 \quad (4.30)$$

Schematically, the Regime III can be presented on $(D/\sigma)^2\text{Re} - \text{Pr}$ map as shown in the Fig. 4.20. The locations of the numerical experiments within this regime on $\text{Ri}_{\mathcal{L}} - \text{Pr}$ are highlighted in red colour in the Fig. 4.21.

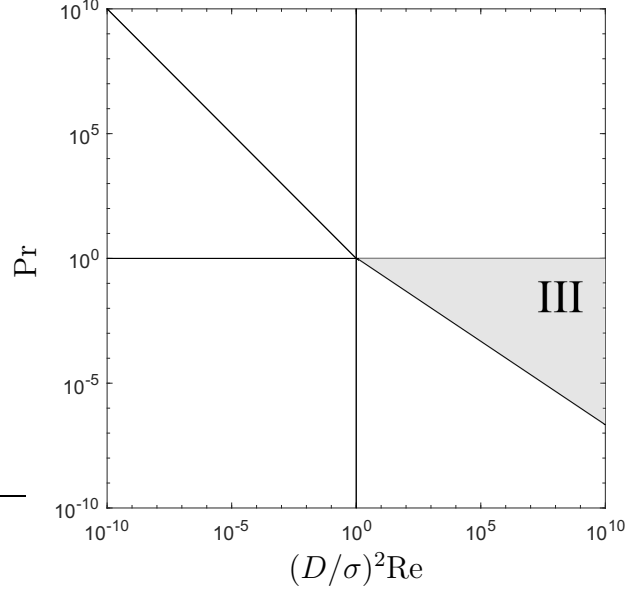


Figure 4.20: Location of the dimensionless parameters for the Regime III on the $(D/\sigma)^2\text{Re} - \text{Pr}$ plane.

Results of the numerical model

The locations of the data presented in the Fig. 4.22 are the free surface, the axis of symmetry for the temperature field and $r^* = 1$ for the radial velocity profile as shown in the Fig. 4.2. The radial velocity u^* profile along the cutline at $r^* = 1$ indicates the formation of the viscous boundary layer at the free surface similar to the Regime II (Fig. 4.22 c). The center of the recirculation vortex is shifted towards the edge of the weld pool (Fig. 4.22 a). This shift can be seen at the free surface velocity profiles (Fig. 4.22 d). The temperature profile along the axis of symmetry indicates the formation of a thermal boundary layer at the free surface indicating that the convective heat transfer is not negligible in the Regime III unlike in the Regime II. A comparative graph of the temperature distribution along the axis of symmetry is shown in Fig. 4.23.

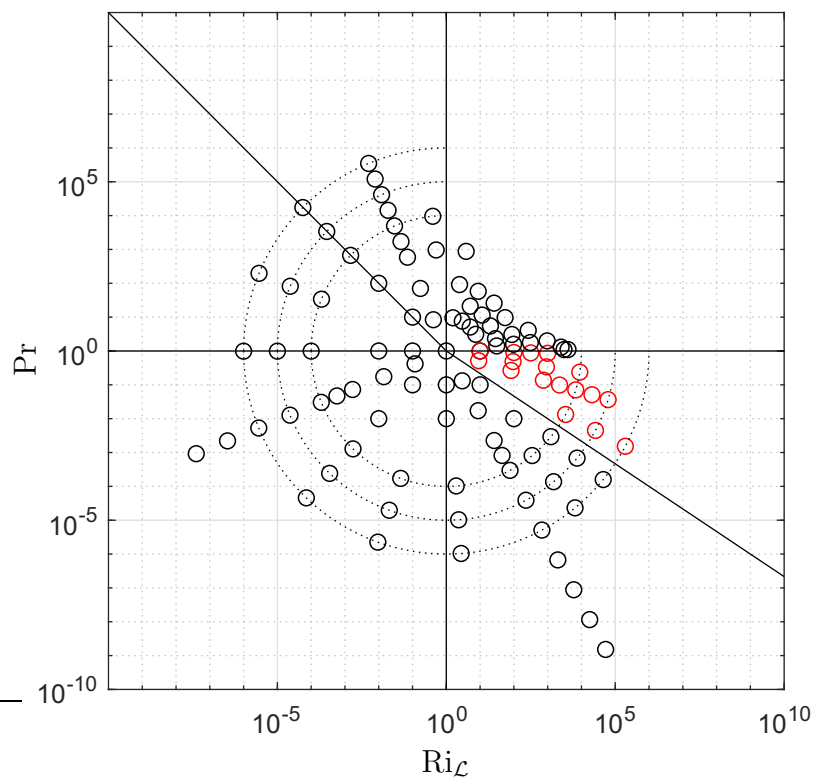


Figure 4.21: Location of the dimensionless parameters for Regime III on $Ri_{\mathcal{L}} - Pr$ plane. Note: $\mathcal{R}_{\mathcal{L}} = 1$ in all the numerical experiments on this map.

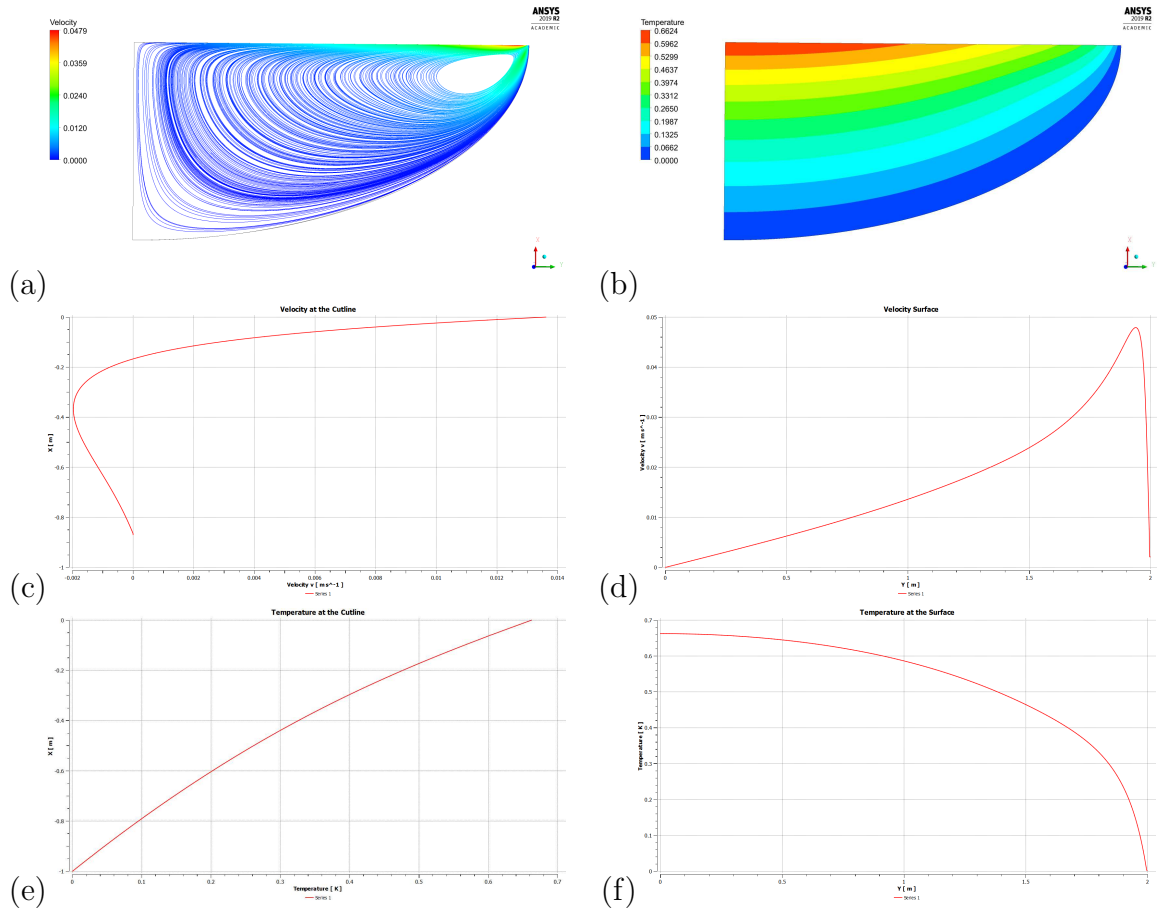


Figure 4.22: Calculated results for the Regime III (a - streamlines; b - temperature contour; c - radial velocity u^* along the cutline at $r = \mathcal{L}$ ($r^* = 1$) as indicated in Fig. 4.2 (abscissa is u^* , ordinate is z^*); d - u^* along the free surface; e - temperature T^* along the axis of symmetry (abscissa is T^* , ordinate is z^*); f - temperature T^* along the free surface). All the values are normalized. Note: the coordinate captions in the graphs are shown as noted in Ansys Fluent® and are not representative to the notations used in the work.

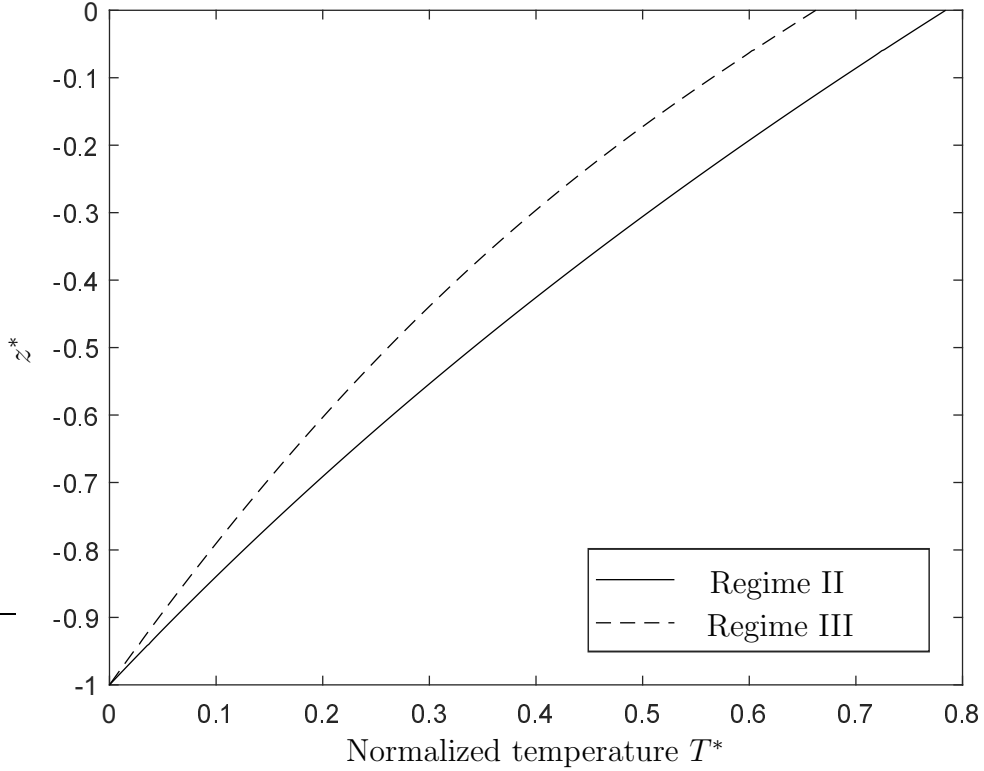


Figure 4.23: Normalized temperature T^* distributions along the axis of symmetry $r^* = 0$ in the Regime III (dashed line) and the Regime II (solid). The formation of a thermal boundary layer can be seen for the Regime III compared to a near-straight-line T^* distribution in the Regime II

Secondary vortex formation

At high Reynolds numbers, a secondary vortex of the weld pool recirculating flow may form as shown in Fig. 4.24. For the model used in this work, the secondary vortex was found to form at $Ri > 10^4$. This number depends on the weld pool shape, and the number obtained for the model with a different shape and/or variations of the weld pool shape due to melting may not be representative.

The secondary vortex, however, may significantly effect the weld pool temperature field as shown in Fig. 4.25. Since it is not clear whether the flow with the secondary vortex in the stationary walls model is representative and physical, for the Regime III only the numerical experiments resulting in a single vortex flow were considered.

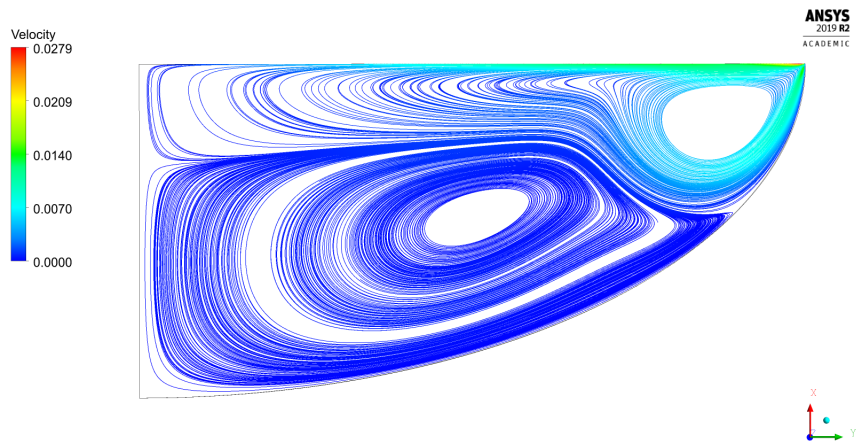


Figure 4.24: Streamlines for a weld pool flow with a flow separation in Regime III at high Re numbers corresponding to $Ri > 10^4$.

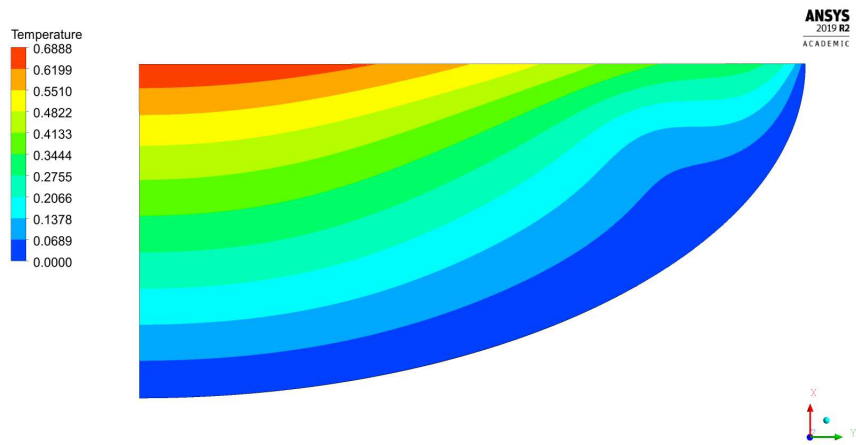


Figure 4.25: Temperature contour for a weld pool flow with a flow separation in Regime III at high Re numbers corresponding to $Ri > 10^4$.

Table 4.12: Experiment parameters used for the analysis of the Regime III on $Ri_{\mathcal{L}} - Pr$ plane as shown in the Fig. 4.26. The experimental points are located on the line set by Eq. 4.31

Exp. #	Pr	$Ri_{\mathcal{L}}$	$\widehat{Pe}_{III_{\mathcal{L}}}$	$Pe_{III_{\mathcal{L}}}$	$(D/\sigma)^2 Re$
3.01	$1.31 \cdot 10^{-1}$	2.96	0.48	0.20	0.54
3.02	$1.72 \cdot 10^{-2}$	8.77	1.03	0.82	4.24
3.1	$7.28 \cdot 10^{-2}$	25.98	2.24	2.37	23.83
3.2	$8.20 \cdot 10^{-4}$	44.72	3.29	3.63	50.85
3.3	$2.97 \cdot 10^{-4}$	76.96	4.84	5.56	108.58
3.4	$3.8981 \cdot 10^{-5}$	227.95	7.12	9.46	257.15

Scaling law validation and calibration

A set of the numerical experiments with their parameters lying on the line defined in Eq. 4.31 was used to verify that the asymptotic behaviour of the calculated Pe_{III} matches the corresponding scaling law (Eq. 2.91). Eq. 4.31 defines a line that lies in the middle of the Regime III.

$$Pr = Ri_{\mathcal{L}}^a \quad (4.31)$$

$$\text{where } a = -\tan(\pi/12) = -0.3 \quad (4.32)$$

The dimensionless parameters of the chosen experiment set are listed in Table 4.12. Their locations on the $Ri_{\mathcal{L}} - Pr$ plane is shown in Fig. 4.26.

Various literature resources were used for the analysis as well. Tables 4.13-4.16 summarize the dimensionless parameters from the literature data.

The comparison of the experimental results with the predicted values is shown in the Fig. 4.28. The graph includes both the numerical modelling data from this work and the literature data. It can be also seen from Fig. 4.27 that in the fully developed Regime III the characteristic velocity is independent from the weld pool size.

The scaling law for the Peclet number for Regime III, as discussed in the Chapter 2, is:

$$\widehat{Pe}_{III} = Ri^{1/2} Pr^{1/2} \quad (4.33)$$

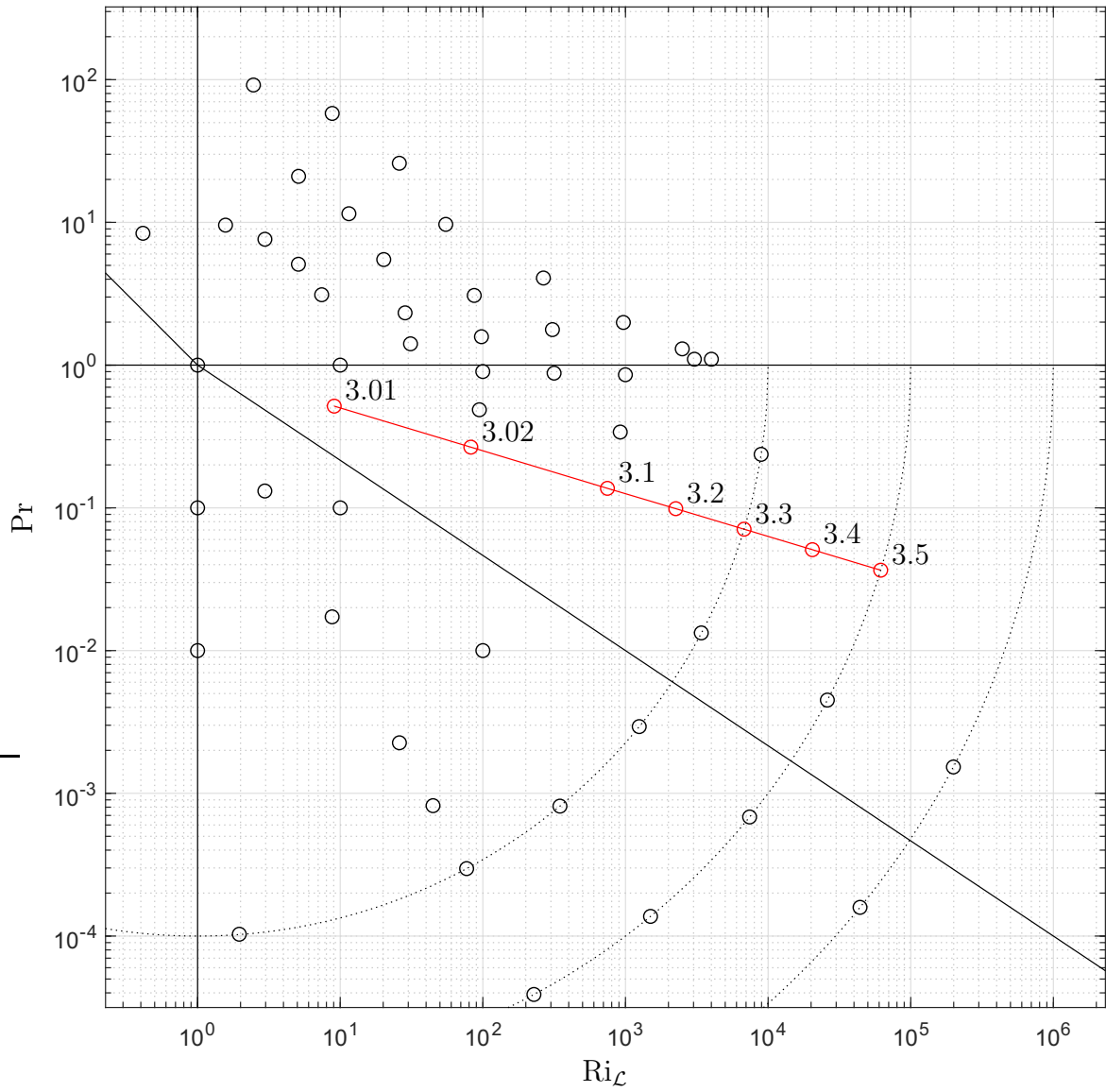


Figure 4.26: Location of the dimensionless parameters for Regime III and the experiment numbers.

Table 4.13: The dimensionless parameters for the data from [22]. The data points in the intermediate regime (considered as the Regime I) are separated in the bottom part of the table

#	Pr	Ri	\mathcal{R}_G	$\widehat{\text{Pe}}_{\text{III}}$ (Eq. 4.33)	Pe	$(D/\sigma)^2 \text{Re}$	Regime
1	0.189	$2.80 \cdot 10^6$	1.50	728.05	675.73	578.62	III
2	0.189	$2.80 \cdot 10^6$	1.92	728.05	676.09	1029.21	
3	0.189	$2.80 \cdot 10^6$	2.61	728.05	670.00	1568.27	
4	0.189	$2.07 \cdot 10^6$	1.05	626.45	537.86	367.55	
5	0.189	$2.07 \cdot 10^6$	1.35	626.45	545.74	558.62	
6	0.189	$2.07 \cdot 10^6$	1.82	626.45	548.60	886.00	
7	0.189	$3.50 \cdot 10^5$	1.50	257.40	198.92	341.54	
8	0.189	$3.50 \cdot 10^5$	1.92	257.40	199.46	545.15	
9	0.189	$3.50 \cdot 10^5$	2.61	257.40	197.67	866.82	
10	0.189	$2.59 \cdot 10^5$	1.05	221.48	150.76	173.71	
11	0.189	$2.59 \cdot 10^5$	1.35	221.48	157.20	268.89	
12	0.189	$2.59 \cdot 10^5$	1.82	221.48	160.07	505.28	
13	0.189	$4.37 \cdot 10^4$	1.50	91.01	55.33	158.15	
14	0.189	$4.37 \cdot 10^4$	1.92	91.01	56.49	240.57	
15	0.189	$4.37 \cdot 10^4$	2.61	91.01	57.30	428.57	
16	0.189	$3.24 \cdot 10^4$	1.05	78.31	39.39	78.12	
17	0.189	$3.24 \cdot 10^4$	1.35	78.31	42.08	115.00	
18	0.189	$3.24 \cdot 10^4$	1.82	78.31	43.96	220.76	
19	0.189	$6.04 \cdot 10^3$	1.82	33.83	10.23	54.81	
20	0.189	$8.16 \cdot 10^3$	2.61	39.31	15.35	129.36	
21	0.189	$2.98 \cdot 10^3$	0.49	23.76	0.41	0.36	I
22	0.189	683.00	1.50	11.38	0.92	4.51	
23	0.189	683.00	1.92	11.38	1.30	9.77	
24	0.189	683.00	2.61	11.38	2.10	29.54	
25	0.189	505.68	1.05	9.79	0.34	1.00	
26	0.189	505.68	1.35	9.79	0.34	1.55	
27	0.189	505.68	1.82	9.79	0.63	5.58	

Table 4.14: The dimensionless parameters for the data from [95].

#	\mathcal{R}_G	Pr	Ri	$\widehat{\text{Pe}}_{\text{III}}$ (Eq. 4.33)	Pe
1	0.19	0.30	$5.20 \cdot 10^4$	58.47	51.19
2	0.19	0.30	$1.56 \cdot 10^5$	101.28	86.90
3	0.19	0.30	$2.60 \cdot 10^5$	130.75	111.90
4	0.19	0.30	$5.20 \cdot 10^5$	184.91	155.95
5	0.19	0.40	$2.91 \cdot 10^4$	50.59	45.24
6	0.19	0.40	$8.74 \cdot 10^4$	87.63	80.95
7	0.19	0.40	$1.46 \cdot 10^5$	113.13	101.19
8	0.19	0.40	$2.91 \cdot 10^5$	159.99	142.86
9	0.19	0.50	$1.86 \cdot 10^4$	45.23	40.48
10	0.19	0.50	$5.58 \cdot 10^4$	78.34	73.81
11	0.19	0.50	$9.30 \cdot 10^4$	101.14	95.24
12	0.19	0.50	$1.86 \cdot 10^5$	143.03	133.33
13	0.19	0.60	$1.29 \cdot 10^4$	41.27	39.29
14	0.19	0.60	$3.87 \cdot 10^4$	71.49	67.86
15	0.19	0.60	$6.45 \cdot 10^4$	92.29	90.48
16	0.19	0.60	$1.29 \cdot 10^5$	130.52	127.38
17	0.19	0.70	$9.52 \cdot 10^3$	38.26	36.90
18	0.19	0.70	$2.86 \cdot 10^4$	66.27	66.67
19	0.19	0.70	$4.76 \cdot 10^4$	85.55	84.52
20	0.19	0.70	$9.52 \cdot 10^4$	120.99	120.24
21	0.19	0.80	$7.28 \cdot 10^3$	35.78	34.52
22	0.19	0.80	$2.18 \cdot 10^4$	61.97	61.90
23	0.19	0.80	$3.64 \cdot 10^4$	80.00	82.14
24	0.19	0.80	$7.28 \cdot 10^4$	113.13	114.29
25	0.19	0.90	$5.75 \cdot 10^3$	33.72	30.95
26	0.19	0.90	$1.72 \cdot 10^4$	58.40	59.52
27	0.19	0.90	$2.87 \cdot 10^4$	75.40	75.00
28	0.19	0.90	$5.75 \cdot 10^4$	106.63	107.14

Table 4.15: The dimensionless parameters for the data from [2].

#	\mathcal{R}_G	Pr	Ri	$\widehat{\text{Pe}}_{\text{III}}$ (Eq. 4.33)	Pe
1	1.620255091	0.11295	$2.80 \cdot 10^6$	179.0191136	181.732032
2	0.72155022	0.11295	$2.80 \cdot 10^6$	179.031545	195.204708
3	2.2991898	0.11295	$3.73 \cdot 10^6$	206.742175	206.078028
4	1.183812731	0.11295	$3.74 \cdot 10^6$	206.7565276	208.9270487
5	2.298870601	0.11295	$1.91 \cdot 10^6$	147.683234	144.2746494

Table 4.16: The dimensionless parameters for the data from [53].

#	\mathcal{R}_G	Pr	Ri	$\widehat{\text{Pe}}_{\text{III}}$ (Eq. 4.33)	Pe	$(D/\sigma)^2 \text{Re}$
1	1.11	0.043	$3.72 \cdot 10^5$	27.94	19.59	263.33
2	1.02	0.043	$3.72 \cdot 10^5$	27.94	22.85	225.71
3	1.33	0.043	$3.72 \cdot 10^5$	27.94	22.85	225.71
4	1.33	0.043	$4.46 \cdot 10^5$	30.61	22.85	225.71

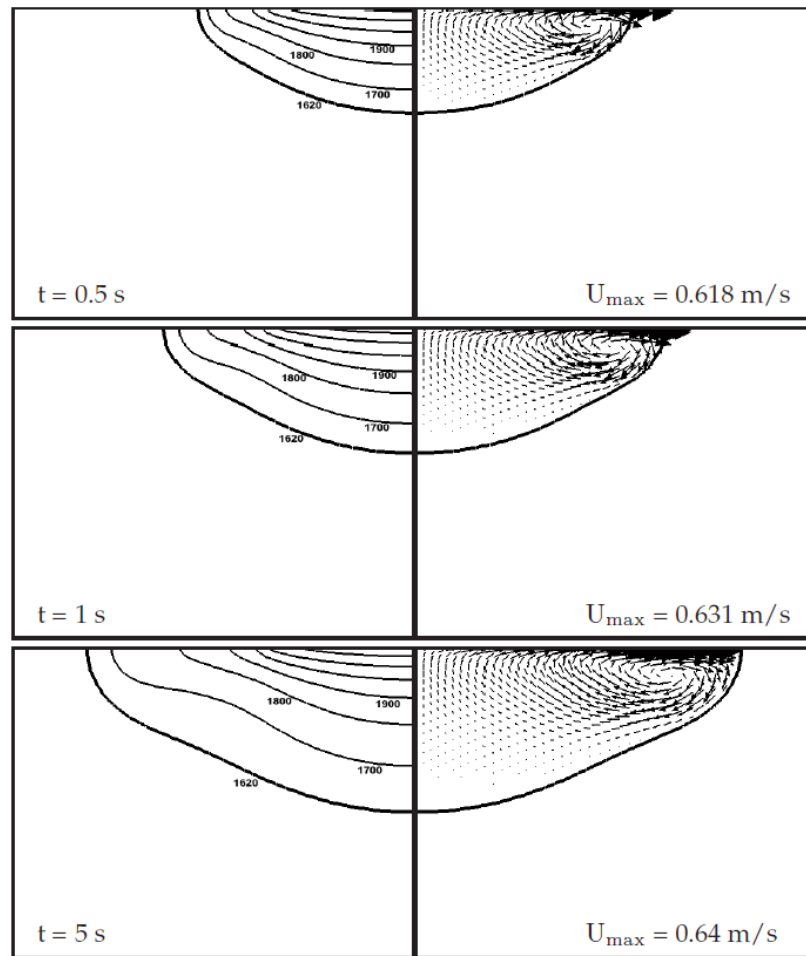


Figure 4.27: An example illustrating that u_{max} is essentially independent from the weld pool size in the fully developed Regime III.

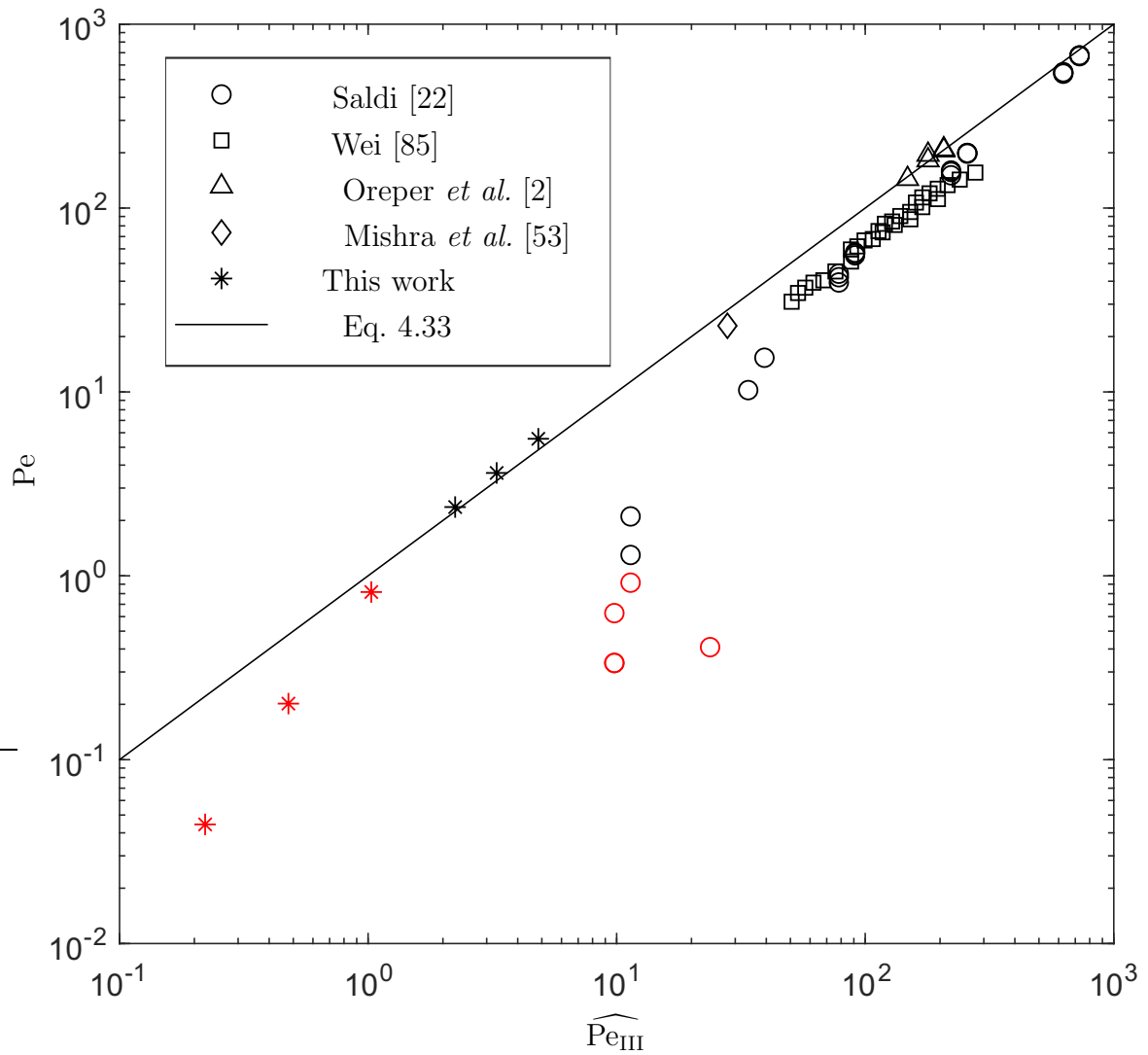


Figure 4.28: Measured Pe compared to the predicted \widehat{Pe}_{III} from the scaling law.

4.3.4 Regime IV

The Regime IV represents a case of the inertial flow with convection, i.e., both a viscous boundary layer and a thermal boundary layer are formed at the free surface, for the case of $\text{Pr} > 1$. Since the flow is inertial, the criterion to fall in the regime is $(D/\sigma)^2 \text{Re} \gg 1$, where $\text{Re} = u_{max}\sigma/\nu$.

$$(D/\sigma)^2 \text{Re} > 1 \quad (4.34)$$

$$\text{Pr} > 1 \quad (4.35)$$

As discussed in Chapter 2, Eq. 4.34 can be approximated as:

$$\mathcal{Ri}_G^4 \text{Pr} > 1 \quad (4.36)$$

Schematically, the Regime IV can be presented on $(D/\sigma)^2 \text{Re} - \text{Pr}$ map as shown in the Fig. 4.29. The locations of the numerical experiments within this regime on $\text{Ri}_L - \text{Pr}$ are highlighted in red colour in the Fig. 4.30.

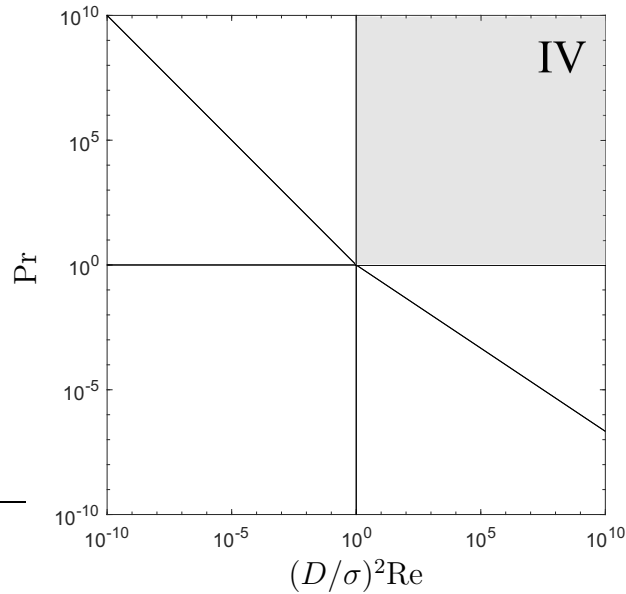


Figure 4.29: Location of the dimensionless parameters for the Regime IV on the $(D/\sigma)^2 \text{Re} - \text{Pr}$ plane.

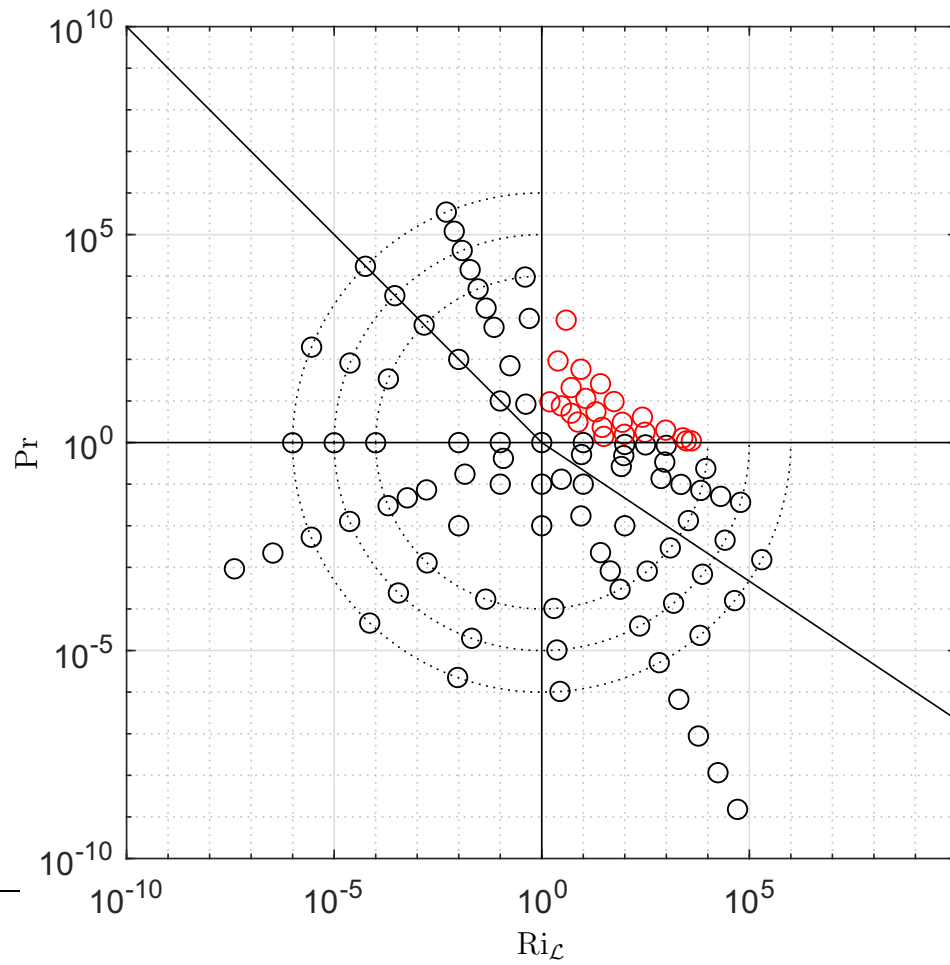


Figure 4.30: Location of the dimensionless parameters for Regime IV on $Ri_L - Pr$ plane. Note: $\mathcal{R}_L = 1$ in all the numerical experiments on this map.

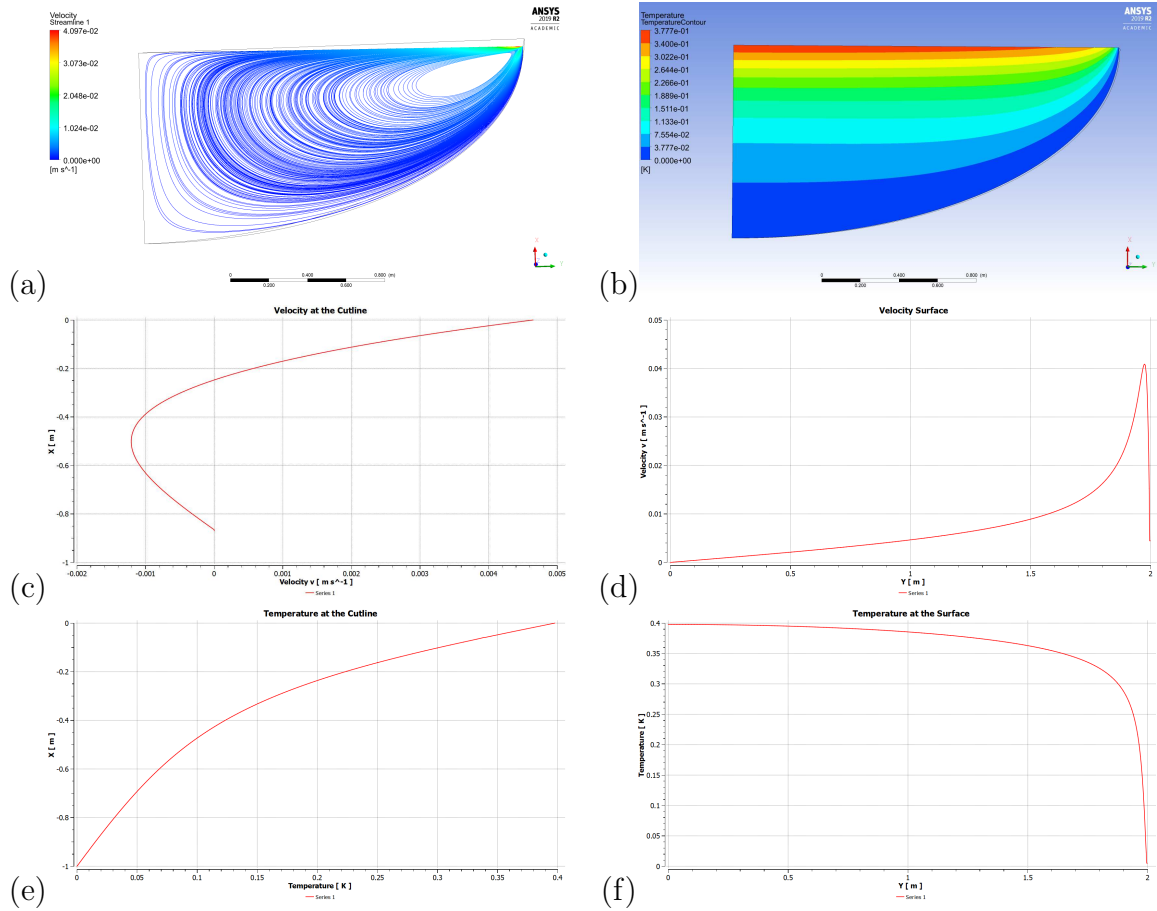


Figure 4.31: Calculated results for the Regime IV (a - streamlines; b - temperature contour; c - radial velocity u^* along the cutline at $r = \mathcal{L}$ ($r^* = 1$) as indicated in Fig. 4.2 (abscissa is u^* , ordinate is z^*); d - u^* along the free surface; e - temperature T^* along the axis of symmetry (abscissa is T^* , ordinate is z^*); f - temperature T^* along the free surface). All the values are normalized. Note: the coordinate captions in the graphs are shown as noted in Ansys Fluent® and are not representative to the notations used in the work.

The locations of the data presented in the Fig. 4.31 are the free surface, the axis of symmetry for the temperature field and $r^* = 1$ for the radial velocity profile as shown in the Fig. 4.2. The radial velocity u profile along the cutline at $r^* = 1$ indicates the formation of the viscous boundary layer at the free surface and now does not have a near parabolic distribution as appeared in the Regime V (Section 4.3.5). The temperature profile along the axis of symmetry shows the formation of a thermal boundary layer in the Regime IV.

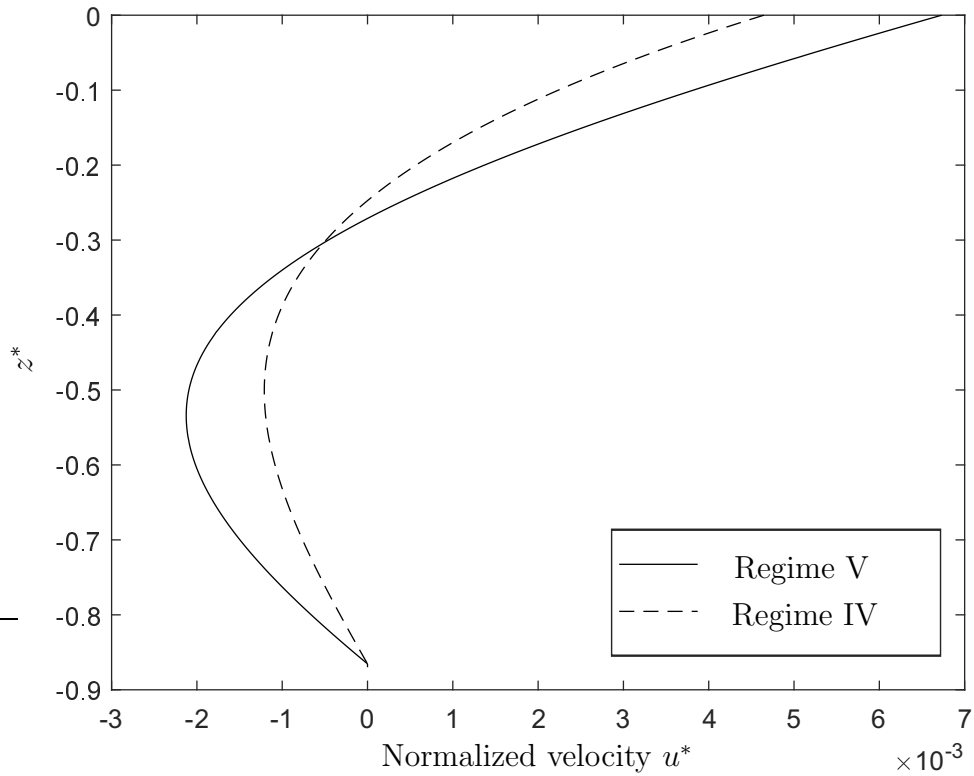


Figure 4.32: Formation of the viscous boundary layer in the Regime IV (dashed line) versus the viscous flow in the Regime V (solid line).

The velocity profile along the cutline at $r^* = 1$ for the Regime IV is shown in comparison with its counterpart for the Regime V in Fig. 4.32. The same profiles but normalized with their maximum value as shown in Fig. 4.33 allow to notice a small discrepancy between the Regime IV and the near-parabolic profile of the Regime V. This mismatch indicates the beginning of the viscous boundary layer formation in

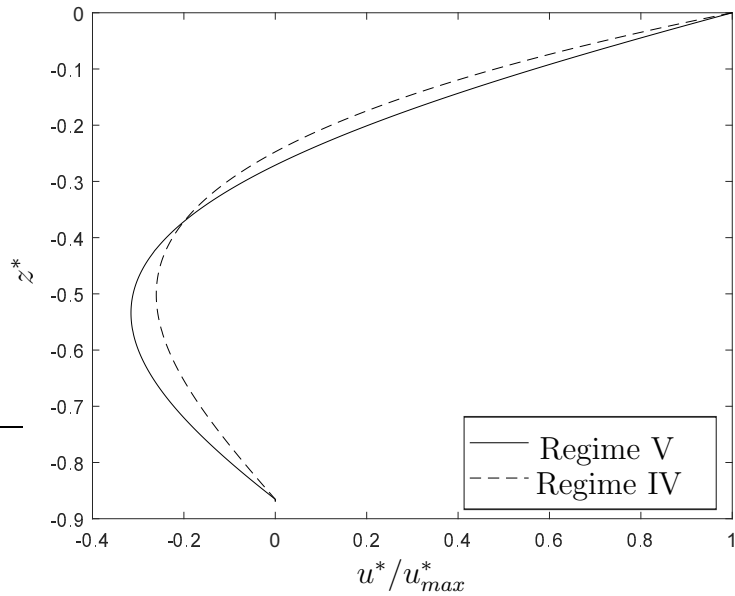


Figure 4.33: Formation of the viscous boundary layer in the Regime IV (dashed line) vs near-parabolic distribution in the Regime V (solid): comparison of the velocity profiles along the cutline normalized to their maximum value.

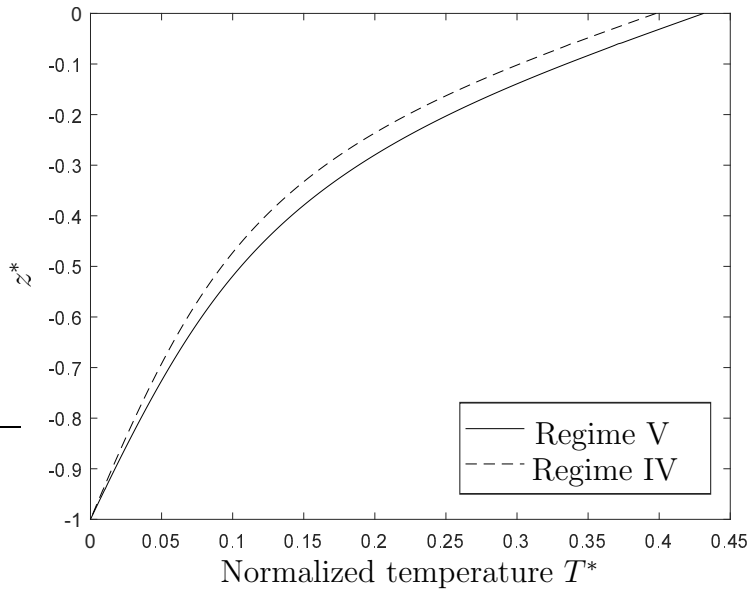


Figure 4.34: Formation of the thermal boundary layer in the Regime IV (dashed line) and V (solid line).

the Regime IV profile (dashed line).

The temperature distribution along the axis of symmetry represents a clearly formed thermal boundary layer for both the Regimes.

The numerical model's mesh used for the analysis did not allow to solve the problem of the Regime IV to obtain high Re values. The stationary wall model used is not representative for the high-Pr-number melts since their flow is highly coupled with the geometry of the weld pool. Due to this fact, it was decided not to refine the mesh more in order to obtain a more detailed result, since it would be not more representative to the reality.

In the literature there is also a very limited amount of the experimental or numerical simulation results for the weld pool flows of a high-Pr-number melts in the Regime IV. One of the very few examples is the NaNO_3 model of welding reported by [97] as shown in Fig. 4.35.

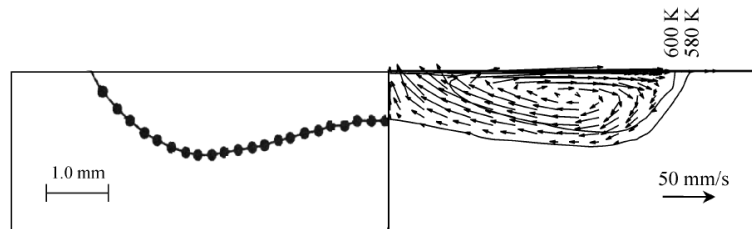


Figure 4.35: NaNO_3 (high Pr) weld pool at high Ma from Robert and DebRoy [97].

4.3.5 Regime V

The Regime V represents a case of the viscous flow with convection, i.e., a thermal boundary layer is formed at the free surface. The Regime V is a flow regime that may be present only in high-Pr-number fluids. Since the flow is inertial, the criterion to fall in the regime is $(D/\sigma)^2 \text{Re} \gg 1$, where $\text{Re} = u_{max}\sigma/\nu$. Moreover, the Peclet number is greater than unity:

$$(D/\sigma)^2 \text{Re} < 1 \quad (4.37)$$

$$(D/\sigma)^2 \text{Re} \text{Pr} > 1 \quad (4.38)$$

According to [87], Eq. 4.38 can be approximated as:

$$\mathcal{R}_G^4 \text{Ri} \text{Pr} > 1 \quad (4.39)$$

Schematically, the Regime V can be presented on $(D/\sigma)^2 \text{Re} - \text{Pr}$ map as shown in the Fig. 4.36. The locations of the numerical experiments within this regime on $\text{Ri}_L - \text{Pr}$ are highlighted in red colour in the Fig. 4.37.

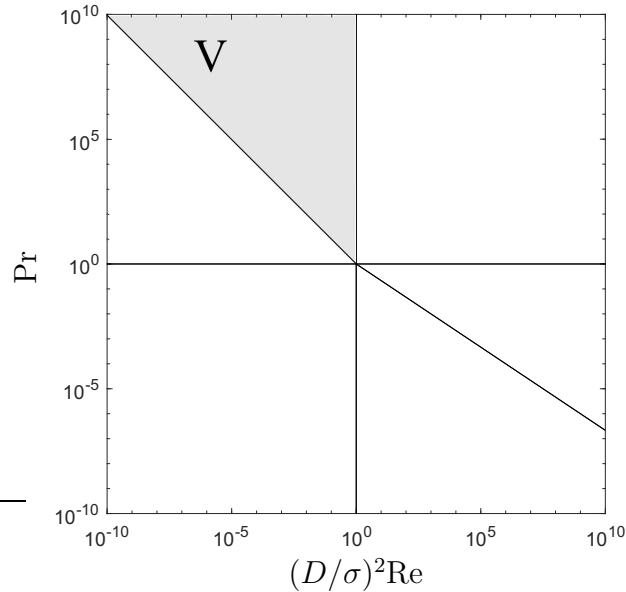


Figure 4.36: Location of the dimensionless parameters for the Regime V on the $(D/\sigma)^2 \text{Re} - \text{Pr}$ plane.

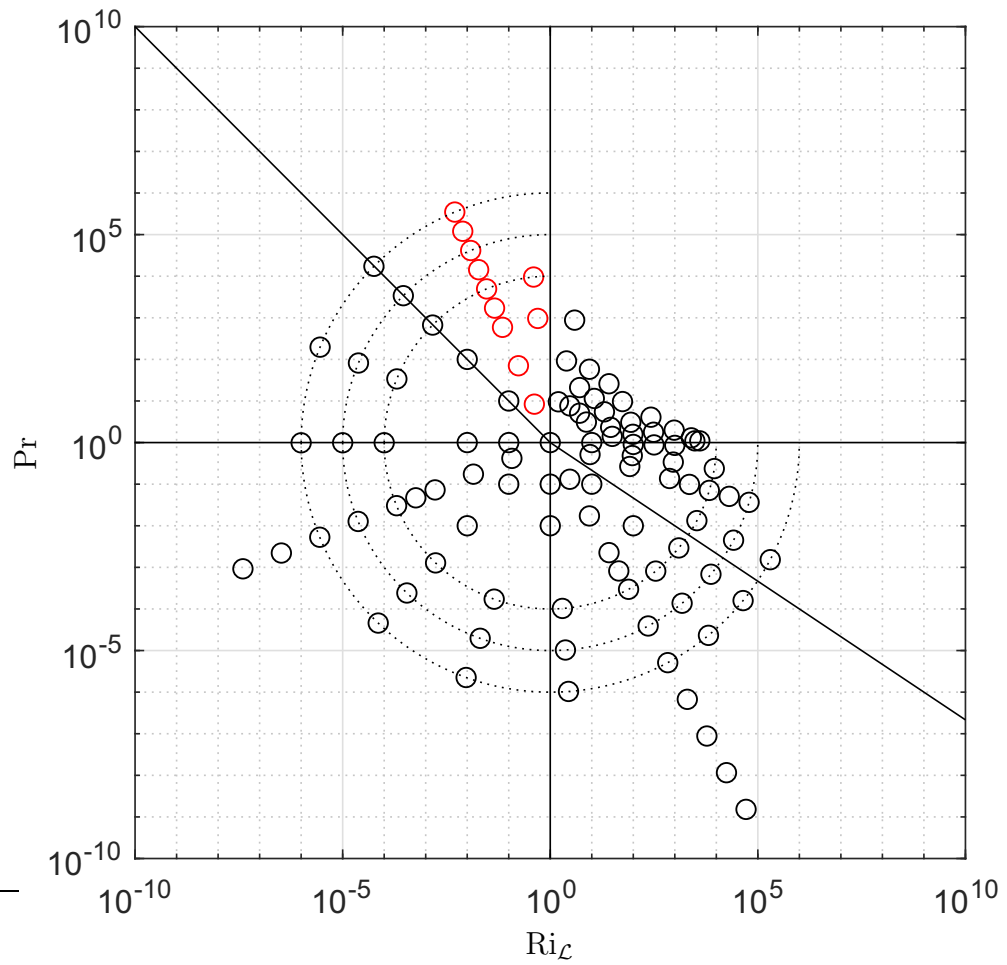


Figure 4.37: Location of the dimensionless parameters for Regime V on $Ri_{\mathcal{L}} - Pr$ plane. Note: $\mathcal{R}_{\mathcal{L}} = 1$ in all the numerical experiments on this map.

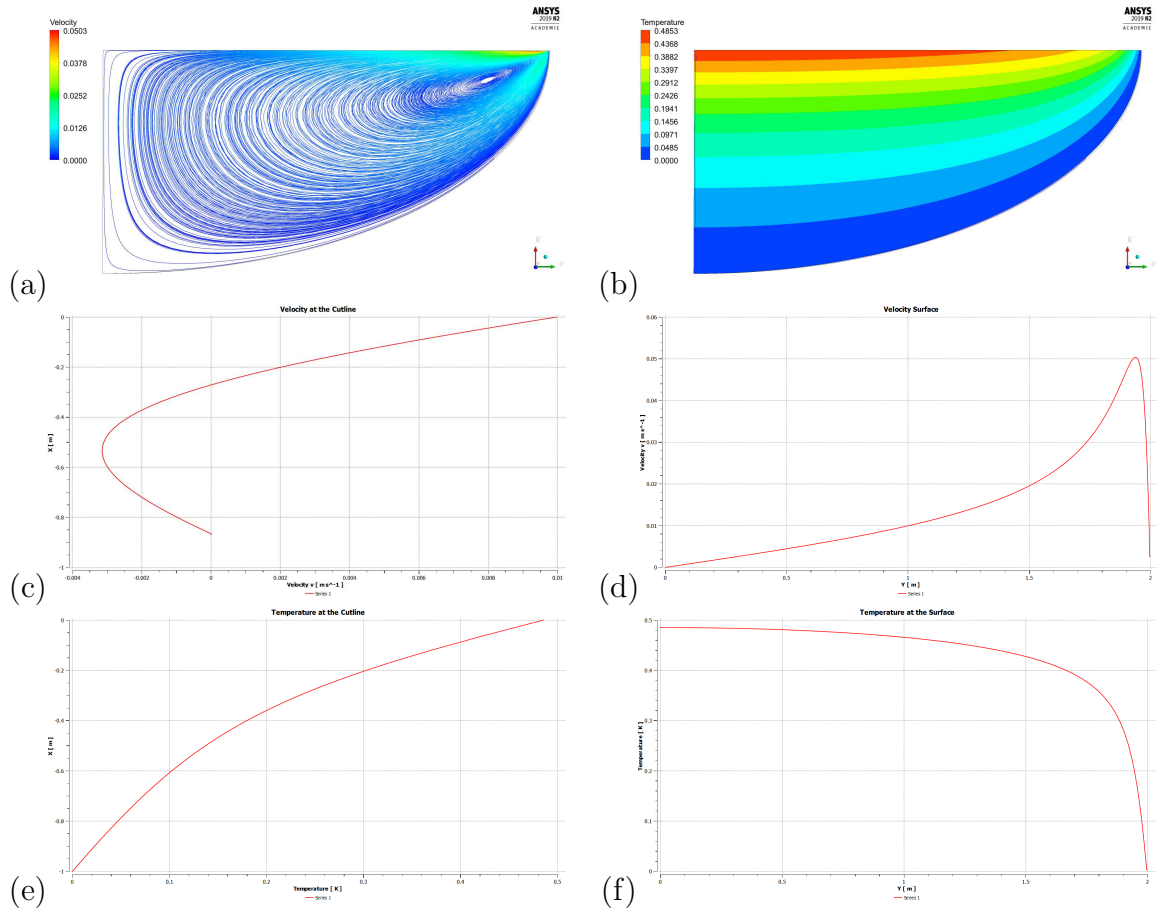


Figure 4.38: Calculated results for the Regime V (a - streamlines; b - temperature contour; c - radial velocity u^* along the cutline at $r = \mathcal{L}$ ($r^* = 1$) as indicated in Fig. 4.2 (abscissa is u^* , ordinate is z^*); d - u^* along the free surface; e - temperature T^* along the axis of symmetry (abscissa is T^* , ordinate is z^*); f - temperature T^* along the free surface). All the values are normalized. Note: the coordinate captions in the graphs are shown as noted in Ansys Fluent® and are not representative to the notations used in the work.

The locations of the data presented in the Fig. 4.38 are the free surface, the axis of symmetry for the temperature field and $r^* = 1$ for the radial velocity profile as shown in the Fig. 4.2. The radial velocity u^* profile along the cutline at $r^* = 1$ represents the near parabolic behaviour analogously to the Regime I (Figs. 4.39 and 4.40). The temperature profile along the axis of symmetry, however, indicates the presence of a thermal boundary layer at the free surface (Fig. 4.41), which means that the convective heat transfer is significant in the Regime V.

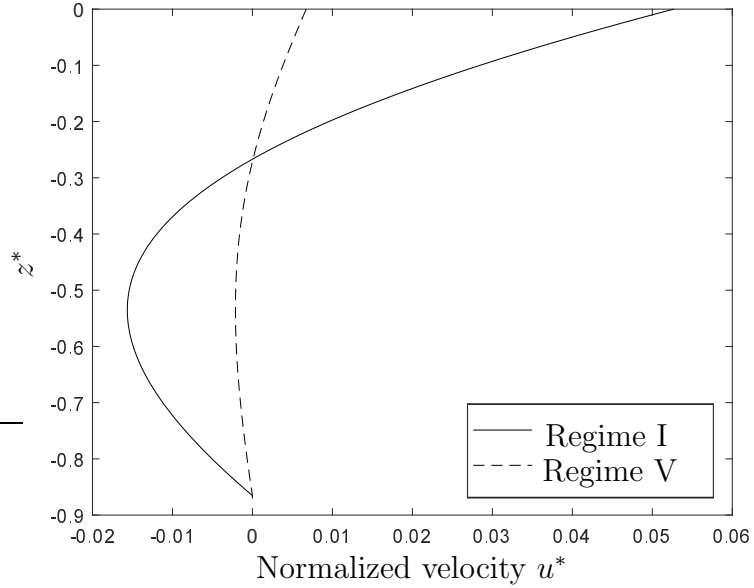


Figure 4.39: Near-parabolic velocity profile along the cutline at $r^* = 1$ in the Regime I (solid) and Regime V (dashed line).

Since the asymptotic trend may reveal at some distance of the centre point on the $\text{Ri}_{\mathcal{L}} - \text{Pr}$ plane, a set of points that lay on the line in the middle of the Regime V was used to compare the calculated $\text{Pe}_{\text{V}_{\mathcal{L}}}$ with $\widehat{\text{Pe}}_{\text{V}_{\mathcal{L}}}$ predicted from the scaling approach. The line in the middle of the Regime V is set by Eq. 4.40:

$$\text{Pr} = \text{Ri}_{\mathcal{L}}^a \quad (4.40)$$

$$a = -\tan(5\pi/8) = -2.41 \quad (4.41)$$

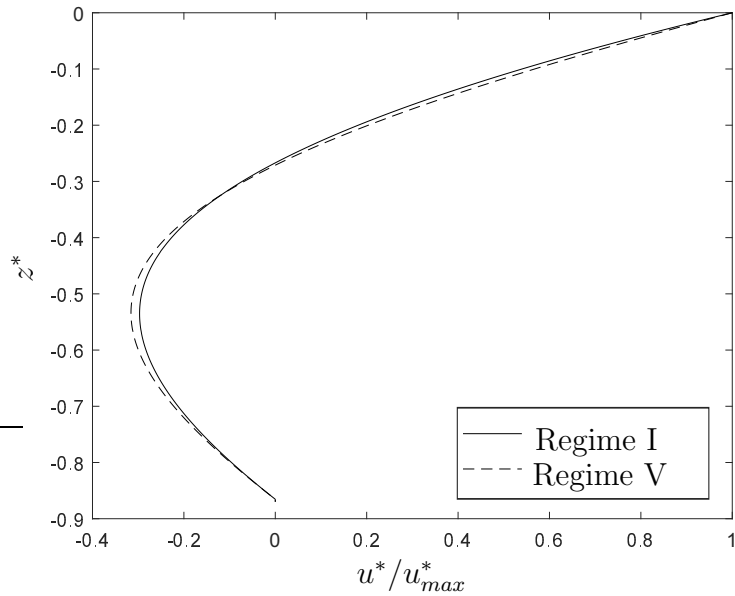


Figure 4.40: Near-parabolic velocity profile along the cutline at $r^* = 1$ in the Regime I (solid) and Regime V (dashed line): comparison of the velocity profiles along the cutline normalized to their maximum value.

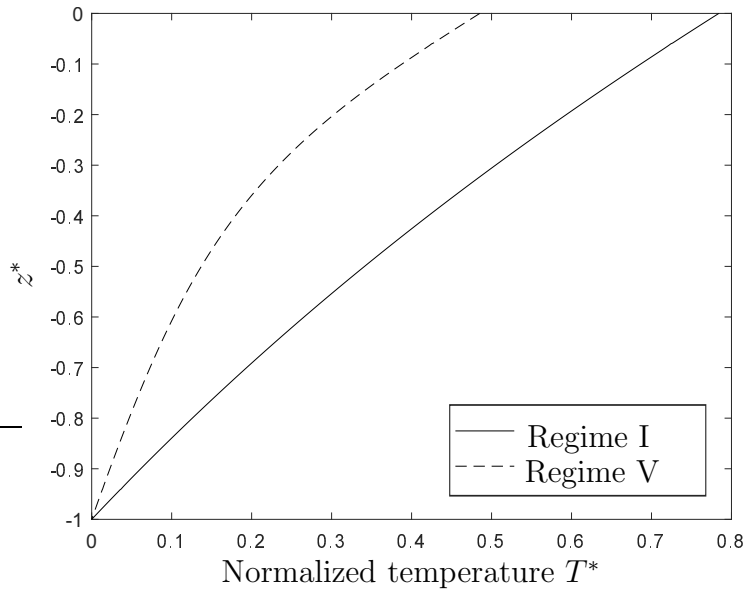


Figure 4.41: Formation of the thermal boundary layer in the Regime V (dashed line) vs near-straight-line distribution in the Regime I (solid).

Table 4.17: Experiment parameters used for the analysis of the Regime V on $\text{Ri}_{\mathcal{L}} - \text{Pr}$ plane as shown in the Fig. 4.42. The experimental points are located on the line set by Eq. 4.40

$\mathcal{R}_{\mathcal{L}}$	Pr	$\text{Ri}_{\mathcal{L}}$	$\text{Pe}_{\mathcal{L}}$	$\widehat{\text{Pe}}_{\text{V}_{\mathcal{L}}}$
1	8.39	0.41	0.18	1.51
1	70.35	0.17	0.58	2.29
1	$5.90 \cdot 10^2$	0.07	1.69	3.47
1	$1.71 \cdot 10^3$	0.05	2.65	4.27
1	$4.95 \cdot 10^3$	0.03	3.89	5.25
1	$1.43 \cdot 10^4$	0.02	5.40	6.47
1	$4.15 \cdot 10^4$	0.01	7.25	7.96
1	$1.20 \cdot 10^5$	0.01	9.35	9.79
1	$3.48 \cdot 10^5$	0.01	11.76	12.04

The parameters of the chosen set are presented in Table 4.17 and are schematically presented on the $\text{Ri}_{\mathcal{L}} - \text{Pr}$ plane in Fig. 4.42. The trend was captured well with the scaling formula as can be seen in Fig. 4.43. The scaling law for the Peclet number for the Regime V, is found to be:

$$\widehat{\text{Pe}}_{\text{V}_{\mathcal{L}}} = \mathcal{R}_{\mathcal{L}}^{2/3} \text{Ri}_{\mathcal{L}}^{1/3} \text{Pr}^{1/3} \quad (4.42)$$

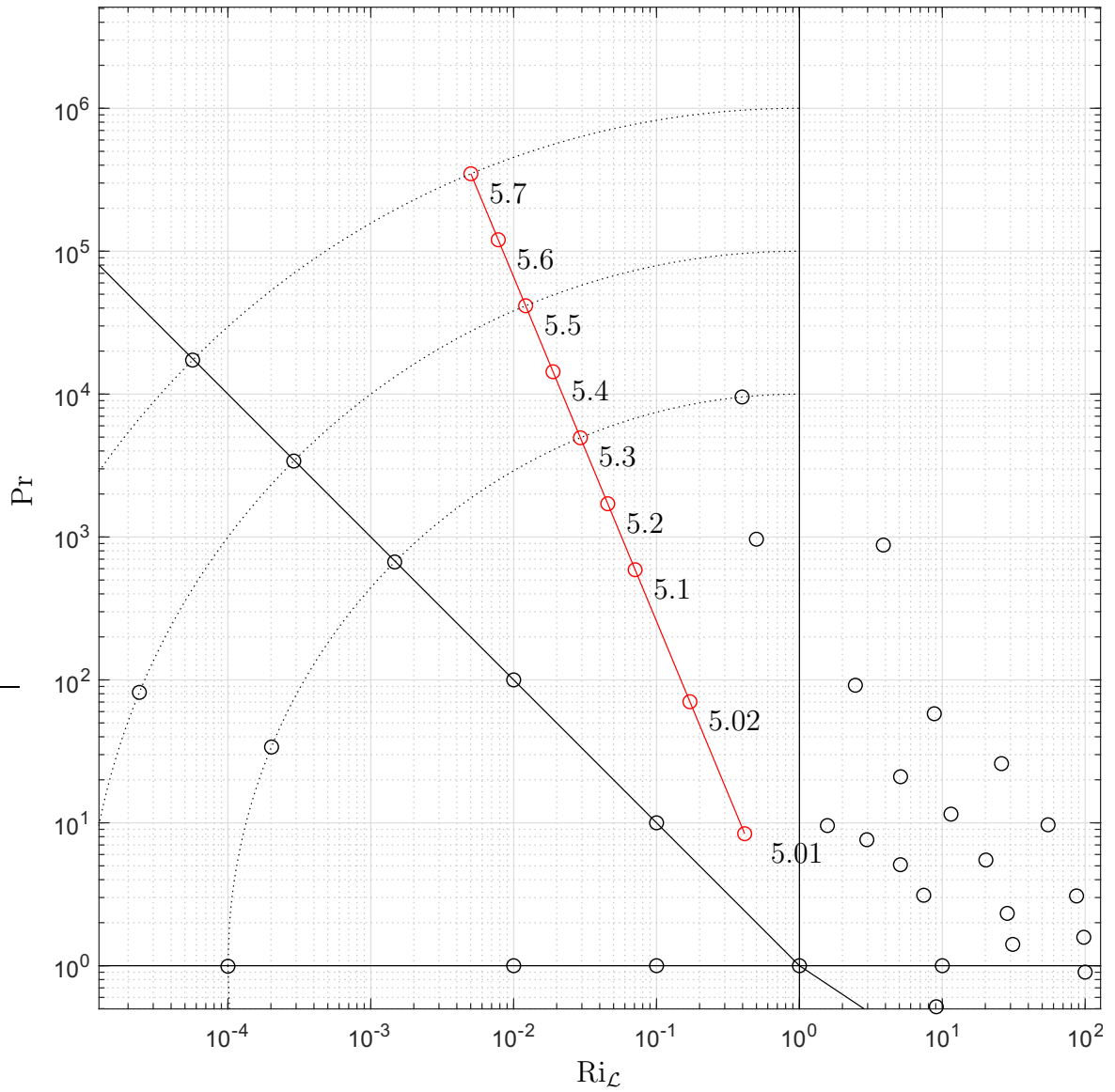


Figure 4.42: Location of the dimensionless parameters for Regime V and the experiment numbers.

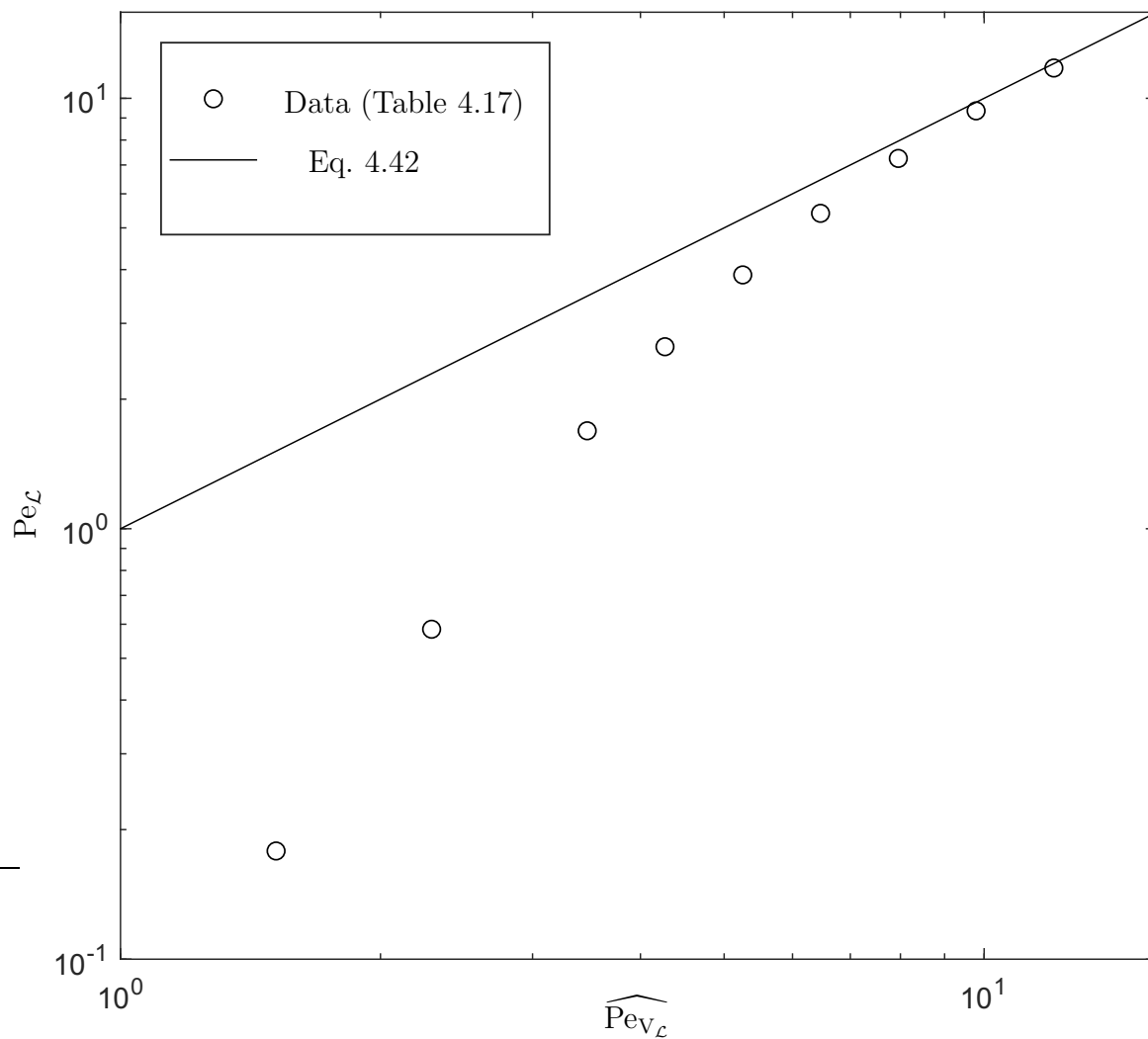


Figure 4.43: Measured $Pe_{\mathcal{L}}$ compared to the predicted $\widehat{Pe}_{V_{\mathcal{L}}}$ from the scaling law (Eq. 4.42).

4.4 Weld width and penetration depth

4.4.1 Main assumption

It is assumed that the weld pool width L and depth D are affected by the convective flow proportionally to the Peclet number to some power when the Peclet number is significant. On the other hand, if the Peclet number is small, the width L and depth D should tend to an “undisturbed” value, i.e. the width and depth the weld would have if there was no melt pool convection. Thus, two asymptotic regimes for the weld width L as a function of Pe are expected:

$$L = L_0 Pe^a, Pe \rightarrow \infty \quad (4.43)$$

$$L = L_0, Pe \rightarrow 0 \quad (4.44)$$

Analogously, the two regimes for the weld depth as function of Pe are:

$$D = \frac{D_0}{Pe^b}, Pe \rightarrow \infty \quad (4.45)$$

$$D = D_0, Pe \rightarrow 0 \quad (4.46)$$

The weld depth D is expected to decrease with high Pe as shown in Eq. 4.45.

The Churchill-Usagi [98] blending technique can be used to provide a single formula for both regimes:

$$L^n = L_0^n + (L_0 Pe^a)^n \quad (4.47)$$

$$\left(\frac{1}{D}\right)^m = \left(\frac{1}{D_0}\right)^m + \left(\frac{Pe^b}{D_0}\right)^m \quad (4.48)$$

In Eqs. 4.47 and 4.48 L_0 and D_0 are the “undisturbed” weld width and depth, n and m are the blending exponents, a and b are the proportionality exponents for Pe .

4.4.2 Calculation results

In order to obtain the exponents a , b , n and m , the optimization problem was solved. The data from [22] was split into 6 groups according to \mathcal{R}_G . Each group was assigned with “undisturbed” weld pool width L_0 and depth D_0 which were assumed constant

for each group. The exponents a , b were assumed constant for all the groups. The blending exponents n and m were adjusted to minimize the error. Table 4.18 summarizes the data used for the analysis. The graphs of L/L_0 and D/D_0 as functions

Table 4.18: Measured weld pool widths and depths from [22] grouped according to \mathcal{R}_G .

#	Group	\mathcal{R}_G	Pe	L, m	D, m	L_0, m	D_0, m	L/L_0	D/D_0
1	I	1.05	537.86	$2.08 \cdot 10^{-3}$	$5.04 \cdot 10^{-4}$	$1.52 \cdot 10^{-3}$	$1.38 \cdot 10^{-3}$	1.37	0.36
2		1.05	150.76	$2.00 \cdot 10^{-3}$	$6.54 \cdot 10^{-4}$	$1.52 \cdot 10^{-3}$	$1.38 \cdot 10^{-3}$	1.32	0.47
3		1.05	39.39	$1.82 \cdot 10^{-3}$	$8.58 \cdot 10^{-4}$	$1.52 \cdot 10^{-3}$	$1.38 \cdot 10^{-3}$	1.20	0.62
4		1.05	0.34	$1.68 \cdot 10^{-3}$	$1.05 \cdot 10^{-3}$	$1.52 \cdot 10^{-3}$	$1.38 \cdot 10^{-3}$	1.11	0.76
5	II	1.35	545.74	$2.53 \cdot 10^{-3}$	$6.17 \cdot 10^{-4}$	$1.72 \cdot 10^{-3}$	$1.69 \cdot 10^{-3}$	1.46	0.37
6		1.35	157.20	$2.23 \cdot 10^{-3}$	$7.97 \cdot 10^{-4}$	$1.72 \cdot 10^{-3}$	$1.69 \cdot 10^{-3}$	1.29	0.47
7		1.35	42.08	$2.04 \cdot 10^{-3}$	$1.01 \cdot 10^{-3}$	$1.72 \cdot 10^{-3}$	$1.69 \cdot 10^{-3}$	1.19	0.60
8		1.35	0.34	$1.85 \cdot 10^{-3}$	$1.31 \cdot 10^{-3}$	$1.72 \cdot 10^{-3}$	$1.69 \cdot 10^{-3}$	1.07	0.78
9	III	1.50	675.73	$2.65 \cdot 10^{-3}$	$5.64 \cdot 10^{-4}$	$1.79 \cdot 10^{-3}$	$1.74 \cdot 10^{-3}$	1.48	0.32
10		1.50	198.92	$2.39 \cdot 10^{-3}$	$7.99 \cdot 10^{-4}$	$1.79 \cdot 10^{-3}$	$1.74 \cdot 10^{-3}$	1.33	0.46
11		1.50	55.33	$2.20 \cdot 10^{-3}$	$1.03 \cdot 10^{-3}$	$1.79 \cdot 10^{-3}$	$1.74 \cdot 10^{-3}$	1.23	0.59
12		1.50	0.92	$1.90 \cdot 10^{-3}$	$1.35 \cdot 10^{-3}$	$1.79 \cdot 10^{-3}$	$1.74 \cdot 10^{-3}$	1.06	0.78
13	IV	1.82	548.60	$3.02 \cdot 10^{-3}$	$7.74 \cdot 10^{-4}$	$2.12 \cdot 10^{-3}$	$2.28 \cdot 10^{-3}$	1.43	0.34
14		1.82	160.07	$2.78 \cdot 10^{-3}$	$1.08 \cdot 10^{-3}$	$2.12 \cdot 10^{-3}$	$2.28 \cdot 10^{-3}$	1.32	0.47
15		1.82	43.96	$2.61 \cdot 10^{-3}$	$1.37 \cdot 10^{-3}$	$2.12 \cdot 10^{-3}$	$2.28 \cdot 10^{-3}$	1.23	0.60
16		1.82	0.63	$2.23 \cdot 10^{-3}$	$1.82 \cdot 10^{-3}$	$2.12 \cdot 10^{-3}$	$2.28 \cdot 10^{-3}$	1.05	0.80
17	V	1.92	676.09	$2.99 \cdot 10^{-3}$	$7.52 \cdot 10^{-4}$	$2.05 \cdot 10^{-3}$	$2.22 \cdot 10^{-3}$	1.46	0.34
18		1.92	199.46	$2.73 \cdot 10^{-3}$	$1.01 \cdot 10^{-3}$	$2.05 \cdot 10^{-3}$	$2.22 \cdot 10^{-3}$	1.33	0.45
19		1.92	56.49	$2.55 \cdot 10^{-3}$	$1.26 \cdot 10^{-3}$	$2.05 \cdot 10^{-3}$	$2.22 \cdot 10^{-3}$	1.24	0.57
20		1.92	1.30	$2.18 \cdot 10^{-3}$	$1.67 \cdot 10^{-3}$	$2.05 \cdot 10^{-3}$	$2.22 \cdot 10^{-3}$	1.06	0.75
21	VI	2.61	670.00	$3.85 \cdot 10^{-3}$	$9.32 \cdot 10^{-4}$	$2.64 \cdot 10^{-3}$	$2.91 \cdot 10^{-3}$	1.46	0.32
22		2.61	197.67	$3.58 \cdot 10^{-3}$	$1.28 \cdot 10^{-3}$	$2.64 \cdot 10^{-3}$	$2.91 \cdot 10^{-3}$	1.36	0.44
23		2.61	57.30	$3.35 \cdot 10^{-3}$	$1.67 \cdot 10^{-3}$	$2.64 \cdot 10^{-3}$	$2.91 \cdot 10^{-3}$	1.27	0.57
24		2.61	2.10	$2.75 \cdot 10^{-3}$	$2.28 \cdot 10^{-3}$	$2.64 \cdot 10^{-3}$	$2.91 \cdot 10^{-3}$	1.04	0.79

of Pe are presented in Figs. 4.44 and 4.45 respectively. The resultant values of the exponents a , b , n and m are shown in Table 4.19: Thus, the proposed formulae to

Table 4.19: Calculated values of the exponents a , b , n and m .

a	n	b	m
0.0549	11.5438	0.1515	3.1759

calculate the effect of Pe of thermocapillary convection on the weld pool width and

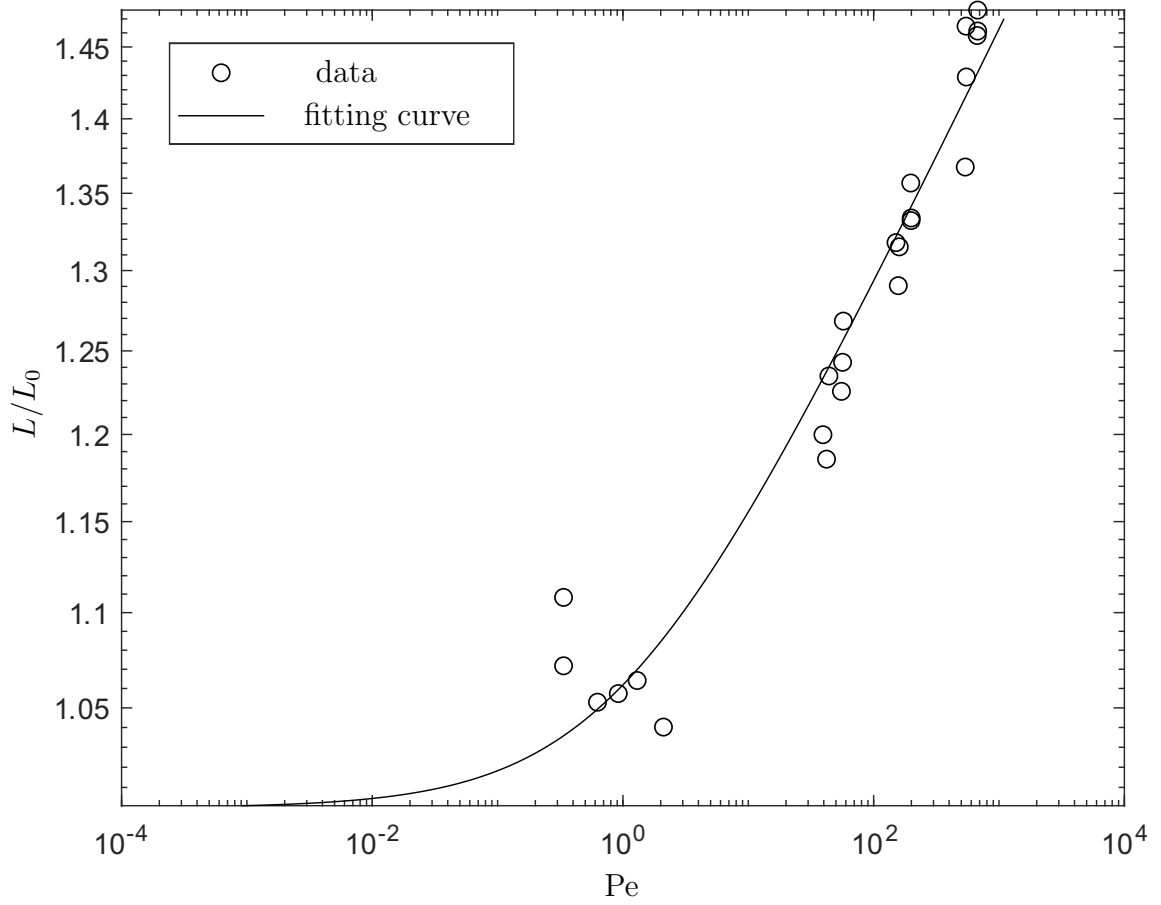


Figure 4.44: L/L_0 as a function of Pe for the data points from Saldi [22].

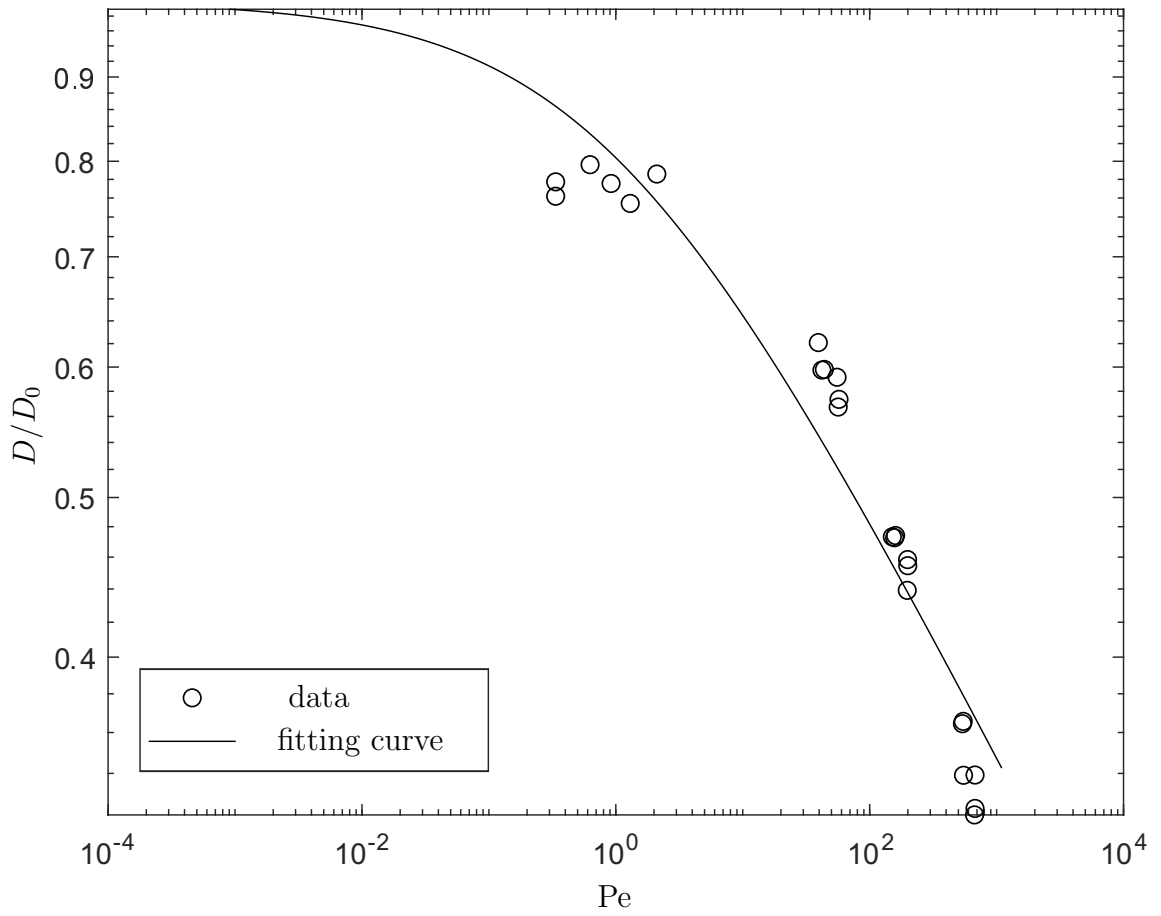


Figure 4.45: D/D_0 as a function of Pe .

depth are as follows:

$$L = (L_0^{11.5438} + (L_0 \text{Pe}^{0.0549})^{11.5438})^{0.0866} \quad (4.49)$$

$$D = \left(\left(\frac{1}{D_0} \right)^{3.1759} + \left(\frac{\text{Pe}^{0.1515}}{D_0} \right)^{3.1759} \right)^{-0.3149} \quad (4.50)$$

4.4.3 Correlation between L_0 and D_0 and the Gaussian heat source predictions L_G and D_G

The basis source of data for the weld width and depth correction factors analysis [22] used the top-hat distributed heat source for their modelling. The “undisturbed” weld proportions from the Gaussian heat source model might not match those by the top-hat source, particularly when the when the weld pool width and depth are comparable to the heat source radius.

The obtained L_0 and D_0 correlate with the Gaussian heat source model predictions L_G and D_G as shown in Figs. 4.46 and 4.47. The data used for the plots is summarized in Table 4.20. The correlation formulae for L_0 and L_G and D_0 and D_G are Eqs. 4.51 and 4.52.

Table 4.20: L_0 and D_0 compared with L_G and D_G for each group with the same R_G .

Group	L_G , m	D_G , m	L_G/σ	D_G/σ	L_0/σ	D_0/σ
I	0.0021	0.0012	1.81	1.03	1.31	1.19
II	0.0024	0.0016	2.07	1.38	1.48	1.45
III	0.0026	0.0017	2.24	1.46	1.54	1.50
IV	0.0029	0.0021	2.50	1.81	1.82	1.97
V	0.003	0.0022	2.58	1.89	1.76	1.91
VI	0.0036	0.003	3.10	2.58	2.27	2.50

$$L_0/\sigma = 0.7399L_G/\sigma - 0.0668 \quad (4.51)$$

$$D_0/\sigma = 0.8706D_G/\sigma + 0.2805 \quad (4.52)$$

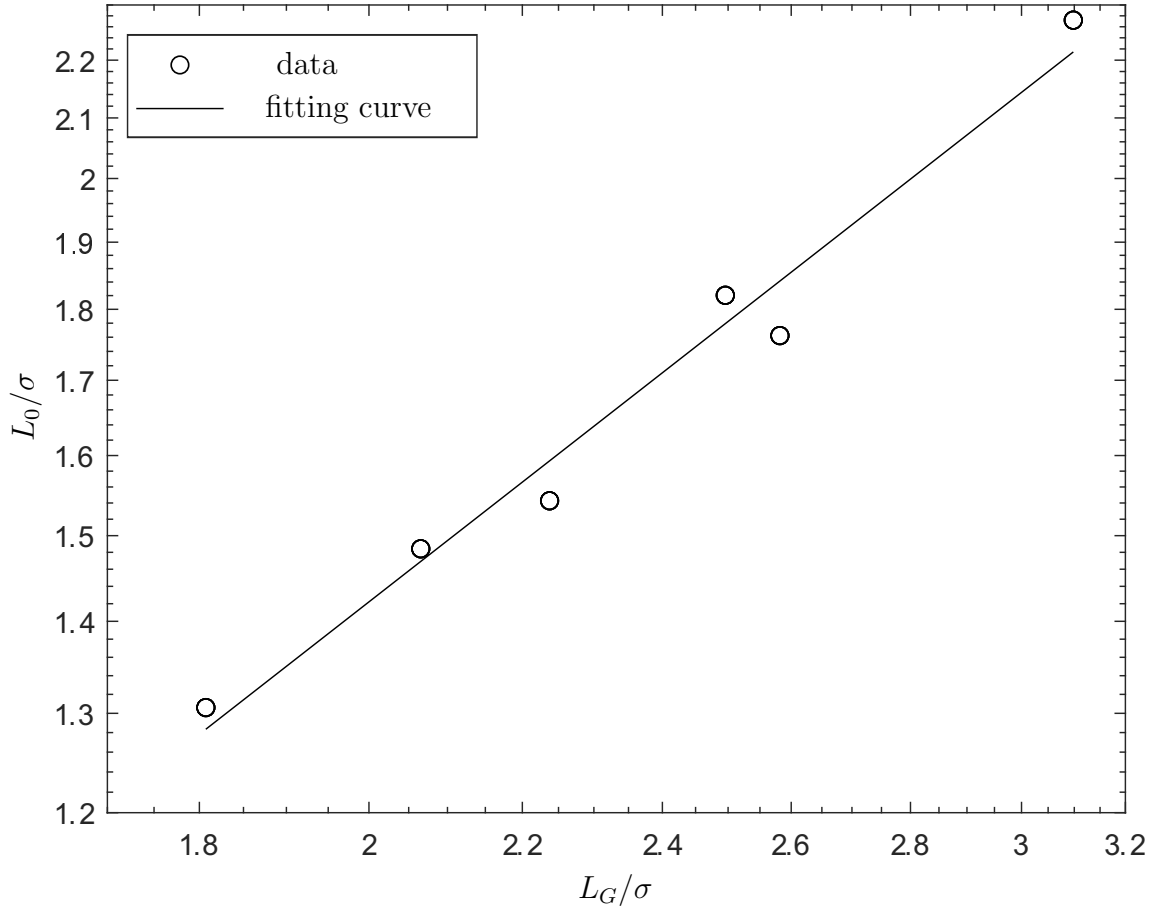


Figure 4.46: Comparison of the calculated L_0/σ against L_G/σ for the data points from Saldi [22]. The fitting curve is presented in Eq. 4.51

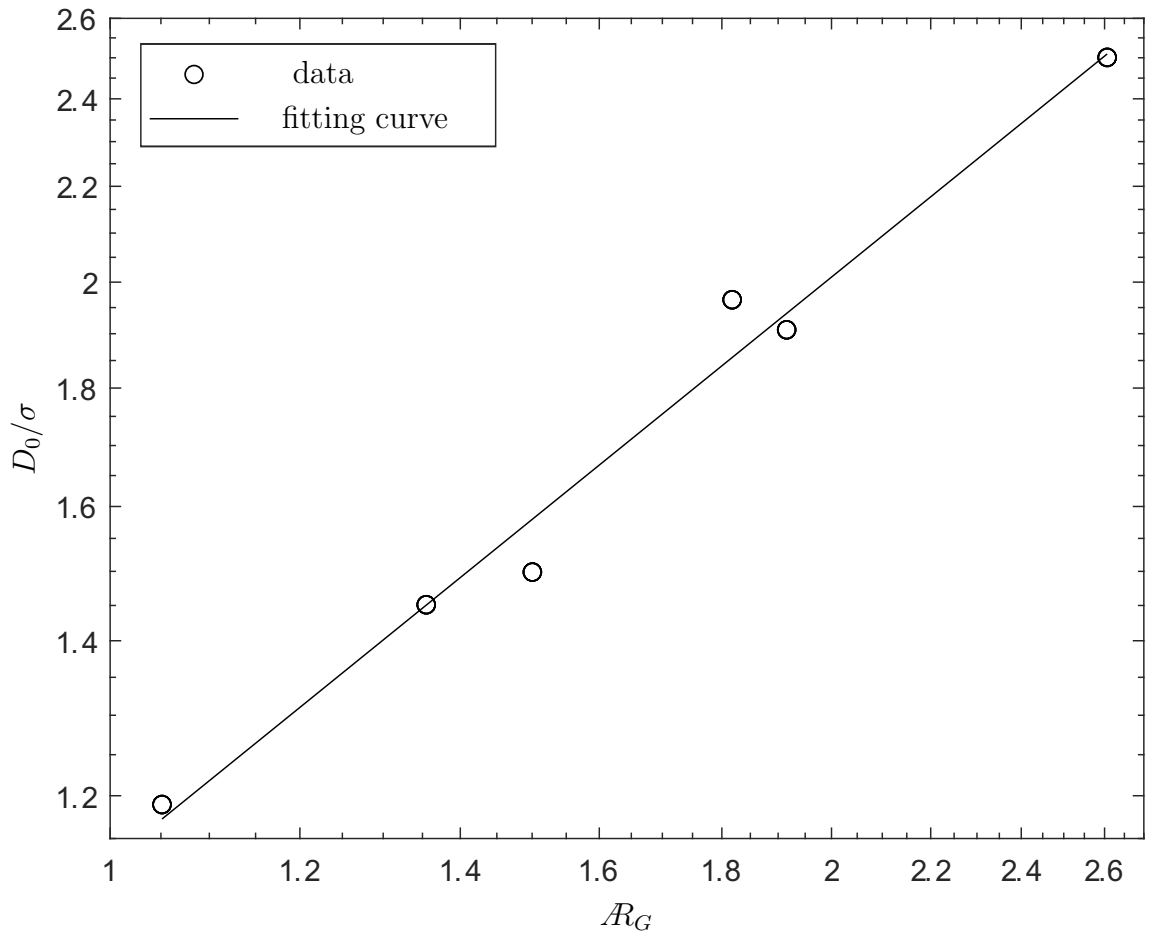


Figure 4.47: Comparison of the calculated D_0/σ against D_G/σ . The fitting curve is presented in Eq. 4.52.

4.4.4 Verification with the experimental data

To verify the obtained formulae, the experimental data from the works by Mishra *et al.* [53] and Robert and DebRoy [97] were used (Figs. 4.48, 4.49). The parameters of the two experiments of welding 304 stainless steel with 30 ppm of sulfur from [53] are listed in Tables 4.21 and 4.22. In [53] the arc welding process was used. For this work, the heat source is considered Gaussian. In the work [97] the laser welding was performed with the top hat laser beam distribution. Thus, the “undisturbed” weld width L_G and depth D_G estimations calculated with the Gaussian heat source model are not representative and may produce extra error. The “undisturbed” weld width L_0 and depth D_0 were recalculated for the top hat source model from L_G and D_G with Eqs. 4.51 and 4.52. The obtained parameters are listed in Tables 4.23 and 4.24. The graphs of the correction factors for the weld width L/L_0 and depth D/D_0 as a function of Pe for the experimental data [53], [97] and the data from the numerical model [22] (Table 4.18) are shown in Figs. 4.50 and 4.51.

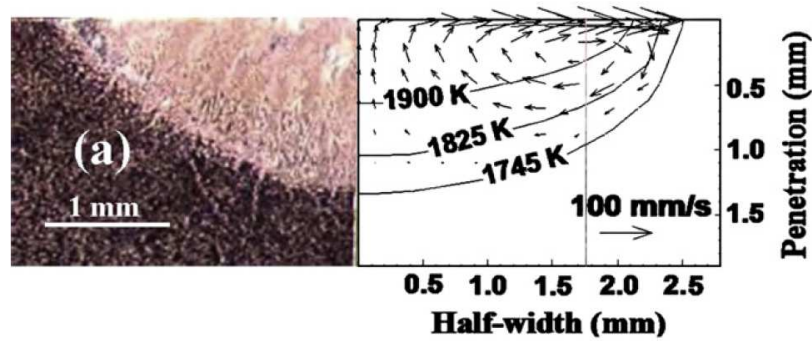
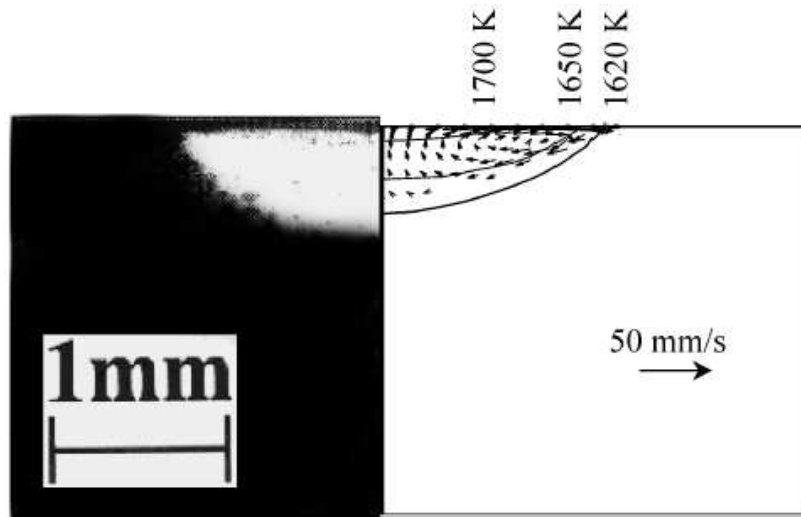


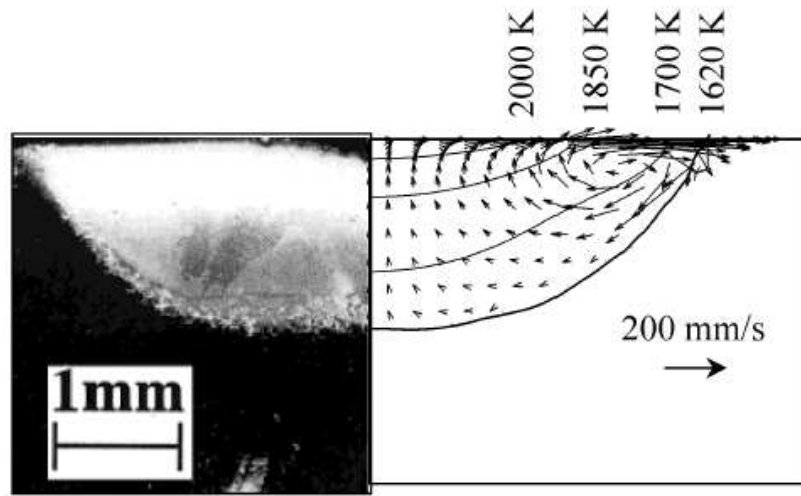
Figure 4.48: An experimental example used for the verification of Eqs. 4.49 and 4.50 from [53].

Table 4.21: Welding parameters of the experiments from [53] and the corresponding characteristic velocity of convection u_{max} .

Mishra <i>et al.</i> [53]	I , A	V , V	U , m/s	σ , m	u_{max} , m/s
Exp. 1	101	9.6	$1.70 \cdot 10^{-3}$	0.0018	0.235
Exp. 3	150	9.9	$1.70 \cdot 10^{-3}$	0.00235	0.384



(a)



(b)

Figure 4.49: Experimental examples used for the verification of Eqs. 4.49 and 4.50 from [97].

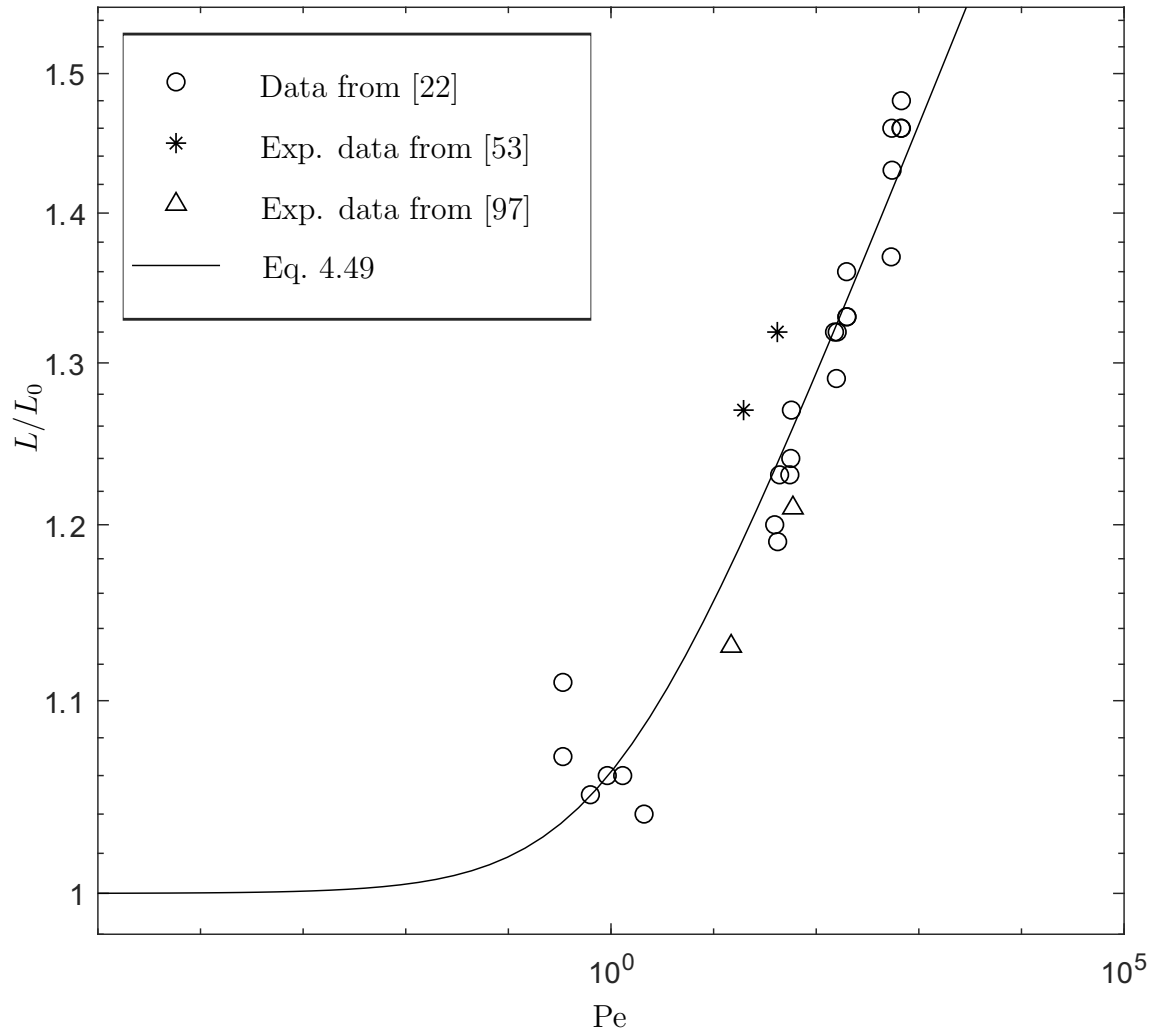


Figure 4.50: L/L_0 as a function of Pe for the modelling [22] and experimental [53], [97] data.

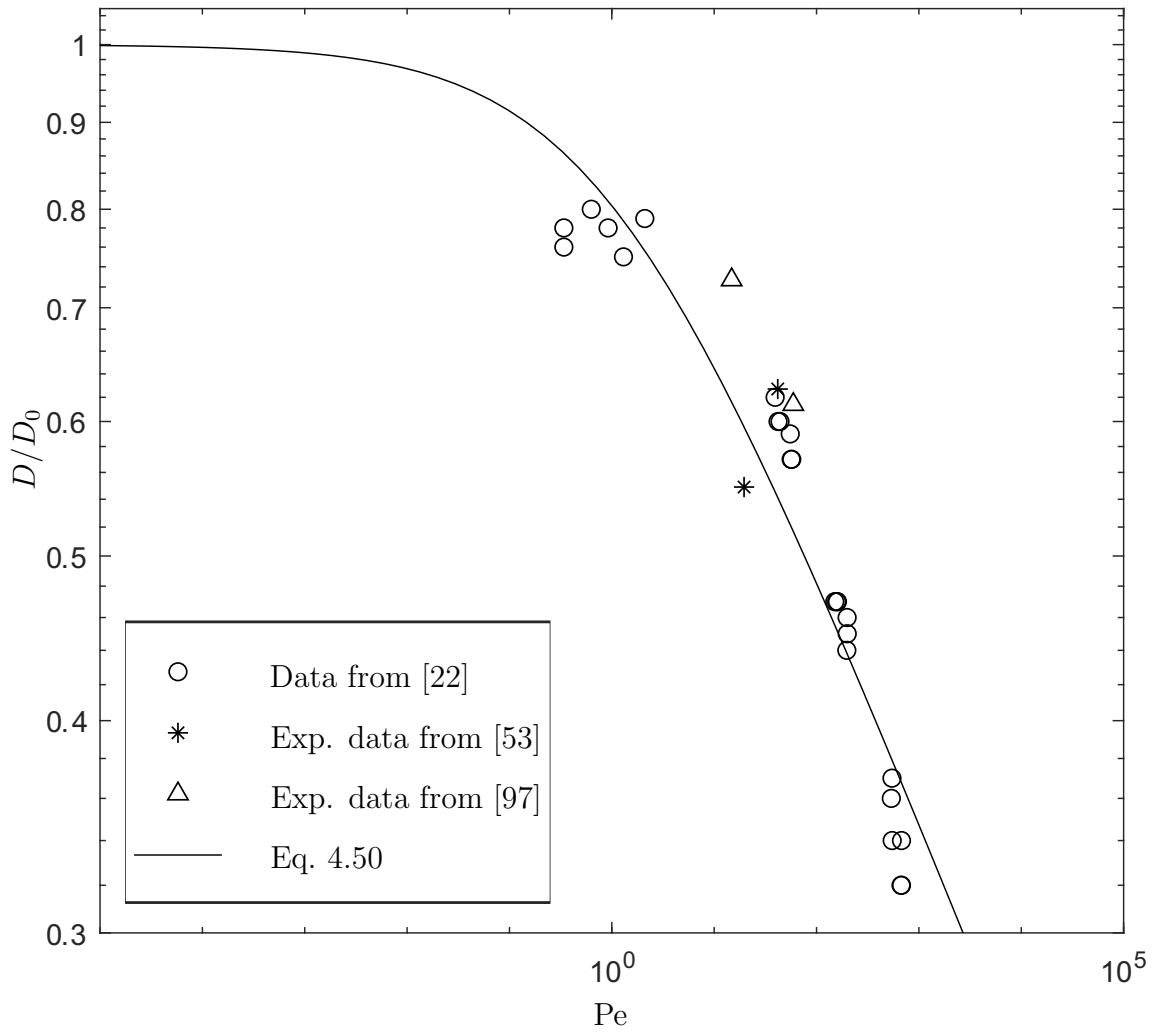


Figure 4.51: D/D_0 as a function of Pe for the modelling [22] and experimental [53], [97] data.

Table 4.22: Predicted and measured weld pool widths and depths from [53] and the corresponding Pe.

Mishra <i>et al.</i> [53]	Pe	L_G , m	D_G , m	L , m	D , m	L/L_G	D/D_G
Exp. 1	19.59	$3.81 \cdot 10^{-3}$	$2.50 \cdot 10^{-3}$	$4.83 \cdot 10^{-3}$	$1.37 \cdot 10^{-3}$	1.27	0.55
Exp. 3	41.78	$5.14 \cdot 10^{-3}$	$3.48 \cdot 10^{-3}$	$6.80 \cdot 10^{-3}$	$2.18 \cdot 10^{-3}$	1.32	0.63

Table 4.23: Welding parameters of the experiments from [97] and the corresponding Pe.

#	q , W	η	σ , m	U , m/s	u_{est} , m/s	Pe_{est}
1	1900	0.14	$1.16 \cdot 10^{-3}$	$2.32 \cdot 10^{-4}$	0.05	14.82
2	5200	0.12	$1.16 \cdot 10^{-3}$	$2.32 \cdot 10^{-4}$	0.20	59.29

Table 4.24: Predicted and measured weld pool widths and depths from [97] and the corresponding Pe.

#	L , m	D , m	L_G , m	D_G , m	L_0 , m	D_0 , m	L/L_0	D/D_0
1	$1.17 \cdot 10^{-3}$	$6.23 \cdot 10^{-4}$	$1.50 \cdot 10^{-3}$	$6.10 \cdot 10^{-4}$	$1.03 \cdot 10^{-3}$	$8.57 \cdot 10^{-4}$	1.13	0.73
2	$2.85 \cdot 10^{-3}$	$1.60 \cdot 10^{-3}$	$3.30 \cdot 10^{-3}$	$2.62 \cdot 10^{-3}$	$2.36 \cdot 10^{-3}$	$2.60 \cdot 10^{-3}$	1.21	0.61

Chapter 5

Discussion

An auxiliary CFD model was created to verify and calibrate the scaling laws. The model requirements for this project were (1) universality for all the identified regimes, (2) usability for a large number of the numerical experiments with a wide range of the input parameters, (3) calculation speed and set-up simplicity.

Since for the Regimes I and II the convection was expected to be negligible and for the Regime III from the scaling laws the Peclet number was expected to be independent from the weld pool depth and width (Eq. 2.91), a laminar fixed-wall cavity model was used. Since the welds with a relatively flat undeformed surface are present at low heat input processes, the welds also are normally slow, the axysimmetric elliptical weld pool geometry was chosen.

Such a simple model had both advantages and limitations. This model was fully representative for the Regimes I and II, since in these regimes the weld pool shape was governed by conduction and was not affected by the flow. For the Regimes III, IV and V, i.e., the regimes with dominant convection, on the other hand, the fixed liquid-solid interface was not fully representative. However, the comparative analysis showed the agreement of the numerical modelling results with the proposed scaling laws. The model could correctly represent the typical flow patterns and the expected characteristics of each flow Regime and was able to reveal the characteristic features of each regime. The literature data was also found to be in a good agreement with

the proposed prediction.

The Peclet numbers were calculated based on characteristic velocities proposed by the scaling laws for each regime. The observed flow behaviour confirmed the validity of the fixed-wall simplification for the low-Prandtl-number regimes and its ability to capture the characteristic flow behaviour in the case of the high-Prandtl-number regimes.

The analysis was performed for the case of negative γ_T , i.e., the convective flows directed outwards. The variations of γ_T with temperature were not considered; γ_T was assumed constant for the purposes of the scaling analysis.

Despite the seeming identity of the inwards and outwards directed weld pool flows, their mathematical treatment with scaling analysis is radically different. The outwards flows interaction with the weld pool liquid/solid interface normally takes place at a relatively far distance compared to the weld pool depth and the characteristic heat source size. If the weld pool width is significantly greater than the pool depth and the heat source size, its effect on the flow velocities may be insignificant and the dimensionless number associated with it may be omitted.

In the case of the inwards directed convection, the flow constricts into a jet going vertically from the surface at approximately the weld pool center into the pool bottom. In this case the weld pool depth and the jet velocity are fully coupled and their mathematical treatment is significantly more complex. For this reason, due to the time limits this work had, only the outwards directed thermocapillary convective weld pool flows were considered in this work.

The results of the numerical modelling were found to be in a good agreement with the trends of the obtained scaling laws. However, the calibration coefficients for the scaling laws from the numerical model results and the literature data were more than one order of magnitude different for the Regimes I and II. The main reason for these discrepancies is the traditional approach used for the estimation of the characteristic values of the partial derivatives present in the governing equations. This approach

allows to capture the behavioral trends well, however, the numerical values could be off by an order of magnitude for some characteristic values and the product of these values could be more than one order of magnitude off. The other reason for the coefficient discrepancy of the proposed scaling laws from the literature data was due to the inability of the scaling law model to account for the surface tension temperature coefficient γ_T variations with temperature. This led to overestimation of γ_T for smaller and, consequently, cooler weld pools.

In Regimes II and III, at high flow velocities calculated with the numerical model a formation of the secondary vortex was observed at $Ri > 10^4$ with the separation of the flow from the solid boundary. Since the numerical model used did not calculate the liquid/solid interface variations and the separation of the flow is highly dependent on the boundary geometry, it was impossible to confirm whether the calculated feature was physical and quantitatively representative. For this reason, the numerical experiments having the flow separation and the secondary vortex in Regime III were discarded from consideration.

Chapter 6

Conclusions and Future Work

6.1 Conclusions

The Gaussian heat source model [89] is the state-of-the-art analytic solution for the predictions of the weld bead width and penetration depth. However, this model does not account for the weld pool convection. To fix this drawback, a fundamental study of the asymptotic hydrodynamic regimes of the weld pool convection was performed using the scaling analysis methodology to provide correction factors for the Gaussian heat source model.

In addition to the three asymptotic regimes proposed by [87] for the low-Prandtl-number fluids, two novel regimes were proposed for the melts with $\text{Pr} > 1$. The scaling laws to estimate the Peclet number of the thermocapillary flows Pe were proposed for the two novel regimes. The qualitative features of the two novel regimes were identified with an auxiliary numerical model. The scaling laws for Pe were verified for four regimes with the numerical model and the data from the literature.

As a result of the analysis, a novel dimensionless number Ri was proposed for the analysis of the thermocapillary convection in weld pools (Eq. 2.13). The proposed dimensionless group Ri embeds the dimensional parameters associated with the surface tension temperature coefficient and together with the melt Prandtl number Pr and the ratio of the heat source size to the weld pool depth D/σ fully defines the problem of thermocapillary weld pool convection. Unlike the dimensionless groups proposed

in the literature, the Ri defined in this work does not include unknown parameters such as weld pool width, depth, temperature variation within the weld pool, etc. The proposed number includes only the known parameters of the heat source and material properties, which makes it more intuitive and easy to use for the calculations.

For the first time, the correction factors that account for the effect of the thermocapillary convective flows in weld pools were proposed for the weld bead width and depth predicted by the Gaussian heat source model [89]. Eq. 4.49 and Eq. 4.50 represent the correction factors for the weld width L and depth D obtained for the flow with a negative surface tension temperature coefficient γ_T . The correction factors were calculated as functions of the Peclet number of thermocapillary flows Pe as the measure of convective heat transfer versus conduction through the melt.

The obtained correction factors were verified with experimental data (Figs. 4.50 and 4.51) that used both Gaussian and top-hat heat sources, as well as laser beam and GTA welding. The good agreement of the proposed dependencies with the various literature data allows to consider them universal.

6.2 Recommendations for the future work

Considering the potentials and limitations of the obtained results, some future developments are recommended:

- Perform scaling analysis to obtain the correction factors for the case of the inward flows ($\gamma_T > 0$), for example, the case of a high sulfur content in stainless steel.
- Analyze the convective weld pool flows in the case when γ_T changes the sign (Fig. 1.5) within the weld pool temperature range.
- Perform a deep experimental study in order to calibrate and enhance the proposed correction factors; study the potential dependence of the correction factors on the Stefan number and other dimensionless groups.

- Investigate and confirm the presence or absence of turbulence in weld pool flows.

Bibliography

- [1] P. F. Mendez and T. W. Eagar, “Penetration and defect formation in high-current arc welding,” *Welding Journal*, vol. 82, no. 10, p. 296, 2003.
- [2] G. Oreper, T. Eagar, and J Szekely, “Convection in arc weld pools,” *Welding journal*, vol. 62, no. 11, pp. 307–312, 1983.
- [3] S Kou, Y. Wang, *et al.*, “Weld pool convection and its effect,” *Welding Journal*, vol. 65, no. 3, pp. 63–70, 1986.
- [4] C. Heiple, H. CR, *et al.*, “Mechanism for minor element effect on gta fusion zone geometry,” *Weld. J.*, vol. 61, no. 4, pp. 97–102, 1982.
- [5] T. C. Choo, “Mathematical modelling of heat and fluid flow phenomena in a mutually coupled welding arc and weld pool,” PhD thesis, Massachusetts Institute of Technology, 1991.
- [6] S Kou, “Welding metallurgy, 1987,” *A Wiley-Interscience Publication, New York*, pp. 29–59,
- [7] T. DebRoy and S. David, “Physical processes in fusion welding,” *Reviews of modern physics*, vol. 67, no. 1, p. 85, 1995.
- [8] J. Elmer, S. Allen, and T. Eagar, “Microstructural development during solidification of stainless steel alloys,” *Metallurgical transactions A*, vol. 20, no. 10, pp. 2117–2131, 1989.
- [9] P. Mohanty and J Mazumder, “Solidification behavior and microstructural evolution during laser beam—material interaction,” *Metallurgical and materials transactions B*, vol. 29, no. 6, pp. 1269–1279, 1998.
- [10] W. Liu and J. DuPont, “Effects of melt-pool geometry on crystal growth and microstructure development in laser surface-melted superalloy single crystals: Mathematical modeling of single-crystal growth in a melt pool (part i),” *Acta materialia*, vol. 52, no. 16, pp. 4833–4847, 2004.
- [11] L. Scriven and C. Sternling, “The marangoni effects,” *Nature*, vol. 187, no. 4733, pp. 186–188, 1960.
- [12] K. Mills, B. Keene, R. Brooks, and A Shirali, “Marangoni effects in welding,” *Philosophical Transactions of the Royal Society of London. Series A: Mathematical, Physical and Engineering Sciences*, vol. 356, no. 1739, pp. 911–925, 1998.

- [13] J Roper and D Olson, "Capillarity effects in the gta weld penetration of 21-6-9 stainless steel," *Welding Journal, Research Supplement*, vol. 57, 103s–108s, 1978.
- [14] S. Glickstein and W. Yeniscavich, "A review of minor element effects on the welding arc and weld penetration," Tech. Rep., 1977.
- [15] W. Savage, E. Nippes, and G. Goodwin, "Effect of minor elements on fusion zone dimensions of inconel 600," *Welding Journal*, vol. 56, no. 4, 1977.
- [16] C. Heiple, J. Roper, R. Stagner, and R. Aden, "Surface active element effects on the shape of gta, laser and electron beam welds," *Weld. J.*, vol. 62, no. 3, p. 72, 1983.
- [17] K. Mills, B. Keene, R. Brooks, and A Olusanya, "The surface tensions of 304 and 316 type stainless steels and their effect on weld penetration," *Report of the National Physical Laboratory, Teddinton, Middlesex, UK*, 1984.
- [18] P Burgardt, C. Heiple, *et al.*, "Interaction between impurities and welding variables in determining gta weld shape," *Weld. J.*, vol. 65, no. 6, p. 150, 1986.
- [19] F. Halden and W. Kingery, "Surface tension at elevated temperatures. ii. effect of c, n, o and s on liquid iron surface tension and interfacial energy with al₂o₃," *The Journal of Physical Chemistry*, vol. 59, no. 6, pp. 557–559, 1955.
- [20] B. F. Dyson, "Surface tension of iron and some iron alloys," *Transactions of the Metallurgical Society of AIME*, vol. 227, no. 5, p. 1098, 1963.
- [21] P Sahoo, T. Debroy, and M. McNallan, "Surface tension of binary metal—surface active solute systems under conditions relevant to welding metallurgy," *Metallurgical transactions B*, vol. 19, no. 3, pp. 483–491, 1988.
- [22] Z. S. Saldi, "Marangoni driven free surface flows in liquid weld pools," PhD thesis, TU Delft, 2012.
- [23] G. T. Dee and B. B. Sauer, "The molecular weight and temperature dependence of polymer surface tension: Comparison of experiment with interface gradient theory," *Journal of colloid and interface science*, vol. 152, no. 1, pp. 85–103, 1992.
- [24] R.-J. Roe, "Surface tension of polymer liquids," *The Journal of Physical Chemistry*, vol. 72, no. 6, pp. 2013–2017, 1968.
- [25] S. Wu, "Surface and interfacial tensions of polymer melts: I. polyethylene, polyisobutylene, and polyvinyl acetate," *Journal of Colloid and Interface Science*, vol. 31, no. 2, pp. 153–161, 1969.
- [26] C Limmaneevichitr and S Kou, "Experiments to simulate effect of marangoni convection on weld pool shape," *WELDING JOURNAL-NEW YORK-*, vol. 79, no. 8, 231–S, 2000.
- [27] D Delapp, G Cook, A Strauss, and W Hofmeister, "Quantitative observations of surface flow and solidification on autogenous gta weld pools," *ASM Proceedings of International Conference of Trends in Welding Research*, 2005.

- [28] C. Zhao, V. van Steijn, I. M. Richardson, C. R. Kleijn, S. Kenjeres, and Z Saldi, “Unsteady interfacial phenomena during inward weld pool flow with an active surface oxide,” *Science and Technology of Welding and Joining*, vol. 14, no. 2, pp. 132–140, 2009.
- [29] C. Zhao, C Kwakernaak, Y Pan, I. Richardson, Z Saldi, S Kenjeres, and C. Kleijn, “The effect of oxygen on transitional marangoni flow in laser spot welding,” *Acta Materialia*, vol. 58, no. 19, pp. 6345–6357, 2010.
- [30] M. Mizutani, S. Katayama, and A. Matsunawa, “Observation of molten metal behavior during laser irradiation: Basic experiment to understand laser welding phenomena,” in *First International Symposium on High-Power Laser Macroprocessing*, International Society for Optics and Photonics, vol. 4831, 2003, pp. 208–213.
- [31] Y. Naito, M. Mizutani, and S. Katayama, “Effect of oxygen in ambient atmosphere on penetration characteristics in single yttrium–aluminum–garnet laser and hybrid welding,” *Journal of laser applications*, vol. 18, no. 1, pp. 21–27, 2006.
- [32] K. Tsao, C. Wu, *et al.*, “Fluid flow and heat transfer in gma weld pools,” *Welding journal*, vol. 67, no. 3, 70s–75s, 1988.
- [33] G. Oreper and J Szekely, “Heat-and fluid-flow phenomena in weld pools,” *Journal of Fluid Mechanics*, vol. 147, pp. 53–79, 1984.
- [34] C. Chan, J Mazumder, and M. Chen, “A two-dimensional transient model for convection in laser melted pool,” *Metallurgical Transactions A*, vol. 15, no. 12, pp. 2175–2184, 1984.
- [35] S. Kou and D. Sun, “Fluid flow and weld penetration in stationary arc welds,” *Metallurgical Transactions A*, vol. 16, no. 1, pp. 203–213, 1985.
- [36] S. Kou and Y. Wang, “Three-dimensional convection in laser melted pools,” *Metallurgical transactions A*, vol. 17, no. 12, pp. 2265–2270, 1986.
- [37] S Kou and Y. Wang, “Computer simulation of convection in moving arc weld pools,” *Metallurgical Transactions A*, vol. 17, no. 12, pp. 2271–2277, 1986.
- [38] M. Tsai and S. Kou, “Marangoni convection in weld pools with a free surface,” *International Journal for Numerical Methods in Fluids*, vol. 9, no. 12, pp. 1503–1516, 1989.
- [39] T Zacharia, A. Eraslan, D. Aidun, *et al.*, “Modeling of non-autogenous welding,” *Welding journal*, vol. 67, no. 1, 18s–27s, 1988.
- [40] T Zacharia, A. Eraslan, D. Aidun, *et al.*, “Modeling of autogenous welding,” *Welding journal*, vol. 67, no. 3, 53s–62s, 1988.
- [41] A Paul and T DebRoy, “Prediction of marangoni convection heat transfer and surface profiles during laser welding,” *Modeling and Control of Casting and Welding processes IV, The Metallurgical Society, Warrendale, PA*, pp. 421–431, 1988.

- [42] R McLay and G. Carey, “Coupled heat transfer and viscous flow, and magnetic effects in weld pool analysis,” *International Journal for Numerical Methods in Fluids*, vol. 9, no. 6, pp. 713–730, 1989.
- [43] X. Peng, X. Lin, D. Lee, Y Yan, and B. Wang, “Effects of initial molten pool and marangoni flow on solid melting,” *International journal of heat and mass transfer*, vol. 44, no. 2, pp. 457–470, 2001.
- [44] G. Ehlen, A. Ludwig, and P. R. Sahn, “Simulation of time-dependent pool shape during laser spot welding: Transient effects,” *Metallurgical and materials transactions A*, vol. 34, no. 12, pp. 2947–2961, 2003.
- [45] B. Basu and A. Date, “Numerical study of steady state and transient laser melting problems—i. characteristics of flow field and heat transfer,” *International journal of heat and mass transfer*, vol. 33, no. 6, pp. 1149–1163, 1990.
- [46] P. Wei, C. Ting, J. Yeh, T. DebRoy, F. Chung, and G. Yan, “Origin of wavy weld boundary,” *Journal of Applied Physics*, vol. 105, no. 5, p. 053 508, 2009.
- [47] Y Wang, Q Shi, and H.-L. Tsai, “Modeling of the effects of surface-active elements on flow patterns and weld penetration,” *Metallurgical and Materials Transactions B*, vol. 32, no. 1, pp. 145–161, 2001.
- [48] T Zacharia, “Weld pool development during gta and laser beam welding of type 304 stainless steel, part i-theoretical analysis,” *Welding Journal*, vol. 68, no. 12, 499s–509s, 1989.
- [49] T Zacharia, S. David, J. Vitek, and T. Debroy, “Weld pool development during gta and laser beam welding of type 304 stainless steel, part ii—experimental correlation,” *Welding journal*, vol. 68, no. 12, 510s–519s, 1989.
- [50] C. Chan, J Mazumder, and M. Chen, “Effect of surface tension gradient driven convection in a laser melt pool: Three-dimensional perturbation model,” *Journal of applied physics*, vol. 64, no. 11, pp. 6166–6174, 1988.
- [51] S Mishra, S Chakraborty, and T. DebRoy, “Probing liquation cracking and solidification through modeling of momentum, heat, and solute transport during welding of aluminum alloys,” *Journal of Applied Physics*, vol. 97, no. 9, p. 094 912, 2005.
- [52] T. Anderson, J. DuPont, and T. DebRoy, “Origin of stray grain formation in single-crystal superalloy weld pools from heat transfer and fluid flow modeling,” *Acta Materialia*, vol. 58, no. 4, pp. 1441–1454, 2010.
- [53] S Mishra, T. Lienert, M. Johnson, and T. DebRoy, “An experimental and theoretical study of gas tungsten arc welding of stainless steel plates with different sulfur concentrations,” *Acta Materialia*, vol. 56, no. 9, pp. 2133–2146, 2008.
- [54] W Pitscheneder, T DebRoy, K Mundra, and R Ebner, “Role of sulfur and processing variables on the temporal evolution of weld pool geometry during multikilowatt laser beam welding of steels,” *Welding Journal (Miami, Fla)*, vol. 75, no. 3, 71s–80s, 1996.

- [55] R. Choo and J Szekeley, “The possible role of turbulence in gta weld pool behavior,” *WELDING JOURNAL-NEW YORK-*, vol. 73, 25–s, 1994.
- [56] K Hong, D. Weckman, A. Strong, and W Zheng, “Modelling turbulent thermofluid flow in stationary gas tungsten arc weld pools,” *Science and Technology of Welding and Joining*, vol. 7, no. 3, pp. 125–136, 2002.
- [57] N. Chakraborty, S. Chakraborty, and P. Dutta, “Modelling of turbulent transport in arc welding pools,” *International Journal of Numerical Methods for Heat & Fluid Flow*, vol. 13, no. 1, pp. 7–30, 2003.
- [58] N. Chakraborty and S. Chakraborty, “Influences of sign of surface tension coefficient on turbulent weld pool convection in a gas tungsten arc welding (gtaw) process: A comparative study,” *Journal of heat transfer*, vol. 127, no. 8, pp. 848–862, 2005.
- [59] N. Chakraborty, “Thermal transport regimes and effects of prandtl number in molten pool transport in laser surface melting processes,” *Numerical Heat Transfer, Part A: Applications*, vol. 53, no. 3, pp. 273–294, 2007.
- [60] H Zhao and T DebRoy, “Weld metal composition change during conduction mode laser welding of aluminum alloy 5182,” *Metallurgical and materials transactions B*, vol. 32, no. 1, pp. 163–172, 2001.
- [61] W Sudnik, D Radaaj, S Breitschwerdt, and W Erofeew, “Numerical simulation of weld pool geometry in laser beam welding,” *Journal of Physics D: Applied Physics*, vol. 33, no. 6, p. 662, 2000.
- [62] N. Chakraborty, D. Chatterjee, and S. Chakraborty, “Modeling of turbulent transport in laser surface alloying,” *Numerical Heat Transfer, Part A*, vol. 46, no. 10, pp. 1009–1032, 2004.
- [63] N. Chakraborty and S. Chakraborty, “Modelling of turbulent molten pool convection in laser welding of a copper–nickel dissimilar couple,” *International Journal of Heat and Mass Transfer*, vol. 50, no. 9-10, pp. 1805–1822, 2007.
- [64] J Hu and H.-L. Tsai, “Heat and mass transfer in gas metal arc welding. part ii: The metal,” *International Journal of Heat and Mass Transfer*, vol. 50, no. 5-6, pp. 808–820, 2007.
- [65] J. Hu, H Guo, and H.-L. Tsai, “Weld pool dynamics and the formation of ripples in 3d gas metal arc welding,” *International Journal of Heat and Mass Transfer*, vol. 51, no. 9-10, pp. 2537–2552, 2008.
- [66] J Jaidi and P Dutta, “Three-dimensional turbulent weld pool convection in gas metal arc welding process,” *Science and Technology of Welding and Joining*, vol. 9, no. 5, pp. 407–414, 2004.
- [67] O. Desmaison, G. Guillemot, and M. Bellet, “Modelling of the bead formation during multi pass hybrid laser/gas metal arc welding,” in *LASERAP’7, Séminaire européen recherche-industrie et Ecole CNRS sur les applications des lasers de puissance*, 2012, 17–pages.

- [68] P. Jönsson, J Szekely, R. Choo, and T. Quinn, “Mathematical models of transport phenomena associated with arc-welding processes: A survey,” *Modelling and Simulation in Materials Science and Engineering*, vol. 2, no. 5, p. 995, 1994.
- [69] D. Chatterjee and S. Chakraborty, “Large-eddy simulation of laser-induced surface-tension-driven flow,” *Metallurgical and Materials Transactions B*, vol. 36, no. 6, pp. 743–754, 2005.
- [70] A. Kidess, S. Kenjereš, B. W. Righolt, and C. R. Kleijn, “Marangoni driven turbulence in high energy surface melting processes,” *International Journal of Thermal Sciences*, vol. 104, pp. 412–422, 2016.
- [71] E. d. S. Q. Isaacson and M. d. S. Q. Isaacson, *Dimensional methods in engineering and physics: reference sets and the possibilities of their extension*. John Wiley & Sons, 1975.
- [72] G. I. Barenblatt, *Scaling, self-similarity, and intermediate asymptotics: dimensional analysis and intermediate asymptotics*. Cambridge University Press, 1996, vol. 14.
- [73] F. David and H Nolle, *Experimental modelling in engineering*. Elsevier, 2013.
- [74] D. I. Barr, “Consolidation of basics of dimensional analysis,” *Journal of Engineering Mechanics*, vol. 110, no. 9, pp. 1357–1376, 1984.
- [75] L. I. Sedov, *Similarity and dimensional methods in mechanics*. CRC press, 2018.
- [76] H. Schlichting and K. Gersten, *Boundary-layer theory*. Springer, 2016.
- [77] P. Mendez, M. Ramirez, G Trapaga, and T. Eagar, “Scaling laws in the welding arc,” *Book-Institute of Materials*, vol. 784, pp. 43–62, 2002.
- [78] P. F. Mendez, “Scaling laws in welding modeling,” 2005.
- [79] P. F. Mendez, K. E. Tello, and S. S. Gajapathi, “Generalization and communication of welding simulations and experiments using scaling analysis,” in *Ninth International Conference on Trends in Welding Research, Chicago, IL, June, 2012*, pp. 4–8.
- [80] P. F. Mendez, “Order of magnitude scaling of complex engineering problems, and its application to high productivity arc welding,” PhD thesis, Massachusetts Institute of Technology, 1999.
- [81] P. F. Mendez and T. W. Eagar, “The matrix of coefficients in order of magnitude scaling,” in *Fourth International Workshop on Similarity Methods*, 2001, pp. 51–67.
- [82] P. F. Mendez and N. Stier, “Oms: A computer algorithm to develop closed-form solutions to multicoupled, multiphysics problems,” *Mathematical Modelling of Weld Phenomena*, vol. 10, pp. 219–54, 2013.
- [83] P. F. Mendez and T. W. Eagar, “Order of magnitude scaling: A systematic approach to approximation and asymptotic scaling of equations in engineering,” *Journal of Applied Mechanics*, vol. 80, no. 1, 2013.

- [84] P. F. Mendez, K. E. Tello, and T. J. Lienert, “Scaling of coupled heat transfer and plastic deformation around the pin in friction stir welding,” *Acta Materialia*, vol. 58, no. 18, pp. 6012–6026, 2010.
- [85] P. Wei, H. Liu, and C. Lin, “Scaling weld or melt pool shape induced by thermocapillary convection,” *International journal of heat and mass transfer*, vol. 55, no. 9-10, pp. 2328–2337, 2012.
- [86] P. Wei, C. Lin, H. Liu, and T. DebRoy, “Scaling weld or melt pool shape affected by thermocapillary convection with high prandtl numbers,” *Journal of heat transfer*, vol. 134, no. 4, 2012.
- [87] D. Rivas and S. Ostrach, “Scaling of low-prandtl-number thermocapillary flows,” *International Journal of Heat and Mass Transfer*, vol. 35, no. 6, pp. 1469–1479, 1992.
- [88] D. Rosenthal, “The theory of moving sources of heat and its application of metal treatments,” *Transactions of ASME*, vol. 68, pp. 849–866, 1946.
- [89] T. Eagar, N. Tsai, *et al.*, “Temperature fields produced by traveling distributed heat sources,” *Welding journal*, vol. 62, no. 12, pp. 346–355, 1983.
- [90] Y. Wang, Y. Lu, and P. F. Mendez, “Scaling laws to predict isotherm width under gaussian heat source,” 2019.
- [91] E. Buckingham, “On physically similar systems; illustrations of the use of dimensional equations,” *Physical review*, vol. 4, no. 4, p. 345, 1914.
- [92] Y. Wang, Y. Lu, and P. F. Mendez, “Scaling expressions of characteristic values for a moving point heat source in steady state on a semi-infinite solid,” *International Journal of Heat and Mass Transfer*, vol. 135, pp. 1118–1129, 2019.
- [93] G. Wood, S. A. Islam, and P. F. Mendez, “Calibrated expressions for welding and their application to isotherm width in a thick plate,” *Soldagem & Inspeção*, vol. 19, no. 3, pp. 212–220, 2014.
- [94] G. D. Wood, “Heat and mass transfer aspects of coaxial laser cladding and its application to nickel-tungsten carbide alloys,” PhD thesis, University of Alberta, 2017.
- [95] P. Wei, H. Liu, and C. Lin, “Scaling weld or melt pool shape induced by thermocapillary convection,” *International Journal of Heat and Mass Transfer*, vol. 55, no. 9-10, pp. 2328–2337, 2012.
- [96] K. Mundra, T. Debroy, T. Zacharia, and S. David, “Role of thermophysical properties in weld pool modeling,” *Welding Journal(USA)*, vol. 71, no. 9, p. 313, 1992.
- [97] A. Robert and T. Debroy, “Geometry of laser spot welds from dimensionless numbers,” *Metallurgical and materials transactions B*, vol. 32, no. 5, pp. 941–947, 2001.
- [98] S. Churchill and R. Usagi, “A general expression for the correlation of rates of transfer and other phenomena,” *AIChE Journal*, vol. 18, no. 6, pp. 1121–1128, 1972.

Appendix A: Parameters for the experiments from the literature

A.1 Saldi [22]

Table A.1: Physical parameters for the experiments in the work [22]

Parameter	Symbol	Dimension	Value
Thermal efficiency	η	-	0.13689
Density	ρ	kg/m ³	8100
Kinematic viscosity	ν	m ² /s	7.407 10 ⁻⁷
Thermal conductivity (liquid)	k	W/m K	22.9
Thermal conductivity (solid)	k_s	W/m K	22.9
Heat source size	σ	m	0.0014
Surface tension temperature coeff.	γ_T	N/m K	4.00 10 ⁻⁴
Dynamic viscosity	μ	Pa s	6.00 10 ⁻³
Heat capacity (liquid)	c_{pl}	J/kg K	723.14
Heat capacity (solid)	c_{ps}	J/kg K	627
Thermal diffusivity (solid)	α_s	m ² /s	4.51 10 ⁻⁶
Latent heat of melting	i_{sl}	J/kg	2.51 10 ⁵
Melting temperature	T_m	K	1620
Preheat temperature	T_∞	K	300
Stefan number	Ste	-	3.3
Prandtl number	Pr	-	0.19

Table A.2: Parameters for the experiments from the work [22]

#	Image in [22]	q , W	u_{max} , m/s	t , s	f	# in Table 4.8	# in Tables 4.13 and 4.18
1	4.7 a	1900	0.008	5	7	19	-
2	4.7 b	3850	0.2	5	7	20	-
3	4.7 c	5200	0.3	5	7	21	-
4	4.10 a	3850	1.502	0.5	1	4	1
5	4.10 a	3850	1.524	1	1	5	5
6	4.10 a	3850	1.532	5	1	6	13
7	4.10 b	3850	0.842	0.5	2	10	2
8	4.10 b	3850	0.878	1	2	11	6
9	4.10 b	3850	0.894	5	2	12	14
10	4.10 c	3850	0.44	0.5	4	16	3
11	4.10 c	3850	0.47	1	4	17	7
12	4.10 c	3850	0.491	5	4	18	15
13	4.10 d	3850	0.015	0.5	16	25	4
14	4.10 d	3850	0.015	1	16	26	8
15	4.10 d	3850	0.028	5	16	27	16
16	4.12 a	5200	1.887	0.5	1	1	9
17	4.12 a	5200	1.888	1	1	2	17
18	4.12 a	5200	1.871	5	1	3	21
19	4.12 b	5200	1.111	0.5	2	7	10
20	4.12 b	5200	1.114	1	2	8	18
21	4.12 b	5200	1.104	5	2	9	22
22	4.12 c	5200	0.618	0.5	4	13	11
23	4.12 c	5200	0.631	1	4	14	19
24	4.12 c	5200	0.64	5	4	15	23
25	4.12 d	5200	0.041	0.5	16	22	12
26	4.12 d	5200	0.058	1	16	23	20
27	4.12 d	5200	0.094	5	16	24	24

Table A.3: Parameters for the experiments from the work [22]

#	Pe	1mm in pixels	L , pixels	D , pixels	L , m	D , m
1	0.41	65	91	37	$1.40 \cdot 10^{-3}$	$5.69 \cdot 10^{-4}$
2	10.23	67	140	94.5	$2.09 \cdot 10^{-3}$	$1.41 \cdot 10^{-3}$
3	15.35	65	178	115	$2.74 \cdot 10^{-3}$	$1.77 \cdot 10^{-3}$
4	537.86	66.5	138	33.5	$2.08 \cdot 10^{-3}$	$5.04 \cdot 10^{-4}$
5	545.74	66.5	168	41	$2.53 \cdot 10^{-3}$	$6.17 \cdot 10^{-4}$
6	548.60	66.5	201	51.5	$3.02 \cdot 10^{-3}$	$7.74 \cdot 10^{-4}$
7	150.76	66.5	133	43.5	$2.00 \cdot 10^{-3}$	$6.54 \cdot 10^{-4}$
8	157.20	66.5	148	53	$2.23 \cdot 10^{-3}$	$7.97 \cdot 10^{-4}$
9	160.07	66.5	185	72	$2.78 \cdot 10^{-3}$	$1.08 \cdot 10^{-3}$
10	39.39	67	122	57.5	$1.82 \cdot 10^{-3}$	$8.58 \cdot 10^{-4}$
11	42.08	67	137	67.5	$2.04 \cdot 10^{-3}$	$1.01 \cdot 10^{-3}$
12	43.96	67	175	91.5	$2.61 \cdot 10^{-3}$	$1.37 \cdot 10^{-3}$
13	0.34	66	111	69.5	$1.68 \cdot 10^{-3}$	$1.05 \cdot 10^{-3}$
14	0.34	66	122	86.5	$1.85 \cdot 10^{-3}$	$1.31 \cdot 10^{-3}$
15	0.63	66	147	120	$2.23 \cdot 10^{-3}$	$1.82 \cdot 10^{-3}$
16	675.73	66.5	176	37.5	$2.65 \cdot 10^{-3}$	$5.64 \cdot 10^{-4}$
17	676.09	66.5	199	50	$2.99 \cdot 10^{-3}$	$7.52 \cdot 10^{-4}$
18	670.00	66.5	256	62	$3.85 \cdot 10^{-3}$	$9.32 \cdot 10^{-4}$
19	198.92	67	160	53.5	$2.39 \cdot 10^{-3}$	$7.99 \cdot 10^{-4}$
20	199.46	67	183	67.5	$2.73 \cdot 10^{-3}$	$1.01 \cdot 10^{-3}$
21	197.67	67	240	85.5	$3.58 \cdot 10^{-3}$	$1.28 \cdot 10^{-3}$
22	55.33	66	145	68	$2.20 \cdot 10^{-3}$	$1.03 \cdot 10^{-3}$
23	56.49	66	168	83	$2.55 \cdot 10^{-3}$	$1.26 \cdot 10^{-3}$
24	57.30	66	221	110	$3.35 \cdot 10^{-3}$	$1.67 \cdot 10^{-3}$
25	0.92	67	127	90.5	$1.90 \cdot 10^{-3}$	$1.35 \cdot 10^{-3}$
26	1.30	67	146	112	$2.18 \cdot 10^{-3}$	$1.67 \cdot 10^{-3}$
27	2.10	67	184	153	$2.75 \cdot 10^{-3}$	$2.28 \cdot 10^{-3}$

Table A.4: Parameters for the experiments from the work [22]

#	Ry	σ^*	L_G , m	D_G , m	\mathcal{R}_G	Ri
1	0.04	0.04	$1.40 \cdot 10^{-3}$	$5.68 \cdot 10^{-4}$	0.49	$2.98 \cdot 10^3$
2	0.09	0.04	$2.90 \cdot 10^{-3}$	$2.10 \cdot 10^{-3}$	1.82	$6.04 \cdot 10^3$
3	0.12	0.04	$3.60 \cdot 10^{-3}$	$3.00 \cdot 10^{-3}$	2.61	$8.16 \cdot 10^3$
4	0.86	0.36	$2.10 \cdot 10^{-3}$	$1.20 \cdot 10^{-3}$	1.05	$2.07 \cdot 10^6$
5	0.43	0.18	$2.40 \cdot 10^{-3}$	$1.60 \cdot 10^{-3}$	1.35	$2.07 \cdot 10^6$
6	0.09	0.04	$2.90 \cdot 10^{-3}$	$2.10 \cdot 10^{-3}$	1.82	$2.07 \cdot 10^6$
7	0.86	0.36	$2.10 \cdot 10^{-3}$	$1.20 \cdot 10^{-3}$	1.05	$2.59 \cdot 10^5$
8	0.43	0.18	$2.40 \cdot 10^{-3}$	$1.60 \cdot 10^{-3}$	1.35	$2.59 \cdot 10^5$
9	0.09	0.04	$2.90 \cdot 10^{-3}$	$2.10 \cdot 10^{-3}$	1.82	$2.59 \cdot 10^5$
10	0.86	0.36	$2.10 \cdot 10^{-3}$	$1.20 \cdot 10^{-3}$	1.05	$3.24 \cdot 10^4$
11	0.43	0.18	$2.40 \cdot 10^{-3}$	$1.60 \cdot 10^{-3}$	1.35	$3.24 \cdot 10^4$
12	0.09	0.04	$2.90 \cdot 10^{-3}$	$2.10 \cdot 10^{-3}$	1.82	$3.24 \cdot 10^4$
13	0.86	0.36	$2.10 \cdot 10^{-3}$	$1.20 \cdot 10^{-3}$	1.05	$5.06 \cdot 10^2$
14	0.43	0.18	$2.40 \cdot 10^{-3}$	$1.60 \cdot 10^{-3}$	1.35	$5.06 \cdot 10^2$
15	0.09	0.04	$2.90 \cdot 10^{-3}$	$2.10 \cdot 10^{-3}$	1.82	$5.06 \cdot 10^2$
16	1.16	0.36	$2.60 \cdot 10^{-3}$	$1.70 \cdot 10^{-3}$	1.50	$2.80 \cdot 10^6$
17	0.58	0.18	$3.00 \cdot 10^{-3}$	$2.20 \cdot 10^{-3}$	1.92	$2.80 \cdot 10^6$
18	0.12	0.04	$3.60 \cdot 10^{-3}$	$3.00 \cdot 10^{-3}$	2.61	$2.80 \cdot 10^6$
19	1.16	0.36	$2.60 \cdot 10^{-3}$	$1.70 \cdot 10^{-3}$	1.50	$3.50 \cdot 10^5$
20	0.58	0.18	$3.00 \cdot 10^{-3}$	$2.20 \cdot 10^{-3}$	1.92	$3.50 \cdot 10^5$
21	0.12	0.04	$3.60 \cdot 10^{-3}$	$3.00 \cdot 10^{-3}$	2.61	$3.50 \cdot 10^5$
22	1.16	0.36	$2.60 \cdot 10^{-3}$	$1.70 \cdot 10^{-3}$	1.50	$4.37 \cdot 10^4$
23	0.58	0.18	$3.00 \cdot 10^{-3}$	$2.20 \cdot 10^{-3}$	1.92	$4.37 \cdot 10^4$
24	0.12	0.04	$3.60 \cdot 10^{-3}$	$3.00 \cdot 10^{-3}$	2.61	$4.37 \cdot 10^4$
25	1.16	0.36	$2.60 \cdot 10^{-3}$	$1.70 \cdot 10^{-3}$	1.50	$6.83 \cdot 10^2$
26	0.58	0.18	$3.00 \cdot 10^{-3}$	$2.20 \cdot 10^{-3}$	1.92	$6.83 \cdot 10^2$
27	0.12	0.04	$3.60 \cdot 10^{-3}$	$3.00 \cdot 10^{-3}$	2.61	$6.83 \cdot 10^2$

A.2 Wei *et al.* [95]

Table A.5: Physical parameters from the work of Wei [95]

Parameter	Symbol	Dimension	Value
Heat source power	q	W	1800
Density	ρ	kg/m ³	5710
Thermal conductivity (liquid)	k_l	W/m K	43
Thermal conductivity (solid)	k_s	W/m K	97
Heat source size	σ	m	0.001
Heat capacity	c_p	J/kg K	890
Thermal diffusivity (liquid)	α_l	m ² /s	8.40 10 ⁻⁶
Thermal diffusivity (solid)	α_s	m ² /s	8.40 10 ⁻⁶
Latent heat of melting	i_{sl}	J/kg	3.10 10 ⁻⁵
Melting temperature	T_m	K	1546
Preheat temperature	T_∞	K	300
Stefan number	Ste	-	3.58
Rykalin number	Ry	-	0.37
Dimensionless heat source size	σ^*	-	0.16
Estimation for L from the Gaussian model	L_G	m	2.10 10 ⁻³
Estimation for D from the Gaussian model	D_G	m	1.40 10 ⁻³
Travel speed	U	m/s	6.00 10 ⁻³
Aspect ratio for the Gaussian model	\mathcal{R}_G	-	1.39

Table A.6: Parameters from the work of Wei [95]

#	$\nu, \text{m}^2/\text{s}$	$\sigma, \text{N}/\text{m K}$	Pr	Ri	Pe	$\widehat{\text{Pe}}_{\text{III}}$ (Eq. 4.33)
1	$2.50 \cdot 10^{-6}$	$1.00 \cdot 10^{-4}$	0.30	$1.17 \cdot 10^5$	51.19	87.71
2	$2.50 \cdot 10^{-6}$	$3.00 \cdot 10^{-4}$	0.30	$3.51 \cdot 10^5$	86.90	151.92
3	$2.50 \cdot 10^{-6}$	$5.00 \cdot 10^{-4}$	0.30	$5.84 \cdot 10^5$	111.90	196.12
4	$2.50 \cdot 10^{-6}$	$1.00 \cdot 10^{-3}$	0.30	$1.17 \cdot 10^6$	155.95	277.36
5	$3.35 \cdot 10^{-6}$	$1.00 \cdot 10^{-4}$	0.40	$6.55 \cdot 10^4$	45.24	75.89
6	$3.35 \cdot 10^{-6}$	$3.00 \cdot 10^{-4}$	0.40	$1.97 \cdot 10^5$	80.95	131.45
7	$3.35 \cdot 10^{-6}$	$5.00 \cdot 10^{-4}$	0.40	$3.28 \cdot 10^5$	101.19	169.70
8	$3.35 \cdot 10^{-6}$	$1.00 \cdot 10^{-3}$	0.40	$6.55 \cdot 10^5$	142.86	239.99
9	$4.19 \cdot 10^{-6}$	$1.00 \cdot 10^{-4}$	0.50	$4.18 \cdot 10^4$	40.48	67.84
10	$4.19 \cdot 10^{-6}$	$3.00 \cdot 10^{-4}$	0.50	$1.26 \cdot 10^5$	73.81	117.51
11	$4.19 \cdot 10^{-6}$	$5.00 \cdot 10^{-4}$	0.50	$2.09 \cdot 10^5$	95.24	151.70
12	$4.19 \cdot 10^{-6}$	$1.00 \cdot 10^{-3}$	0.50	$4.18 \cdot 10^5$	133.33	214.54
13	$5.03 \cdot 10^{-6}$	$1.00 \cdot 10^{-4}$	0.60	$2.90 \cdot 10^4$	39.29	61.91
14	$5.03 \cdot 10^{-6}$	$3.00 \cdot 10^{-4}$	0.60	$8.71 \cdot 10^4$	67.86	107.23
15	$5.03 \cdot 10^{-6}$	$5.00 \cdot 10^{-4}$	0.60	$1.45 \cdot 10^5$	90.48	138.44
16	$5.03 \cdot 10^{-6}$	$1.00 \cdot 10^{-3}$	0.60	$2.90 \cdot 10^5$	127.38	195.78
17	$5.85 \cdot 10^{-6}$	$1.00 \cdot 10^{-4}$	0.70	$2.14 \cdot 10^4$	36.90	57.39
18	$5.85 \cdot 10^{-6}$	$3.00 \cdot 10^{-4}$	0.70	$6.43 \cdot 10^4$	66.67	99.40
19	$5.85 \cdot 10^{-6}$	$5.00 \cdot 10^{-4}$	0.70	$1.07 \cdot 10^5$	84.52	128.33
20	$5.85 \cdot 10^{-6}$	$1.00 \cdot 10^{-3}$	0.70	$2.14 \cdot 10^5$	120.24	181.48
21	$6.69 \cdot 10^{-6}$	$1.00 \cdot 10^{-4}$	0.80	$1.64 \cdot 10^4$	34.52	53.66
22	$6.69 \cdot 10^{-6}$	$3.00 \cdot 10^{-4}$	0.80	$4.91 \cdot 10^4$	61.90	92.95
23	$6.69 \cdot 10^{-6}$	$5.00 \cdot 10^{-4}$	0.80	$8.19 \cdot 10^4$	82.14	120.00
24	$6.69 \cdot 10^{-6}$	$1.00 \cdot 10^{-3}$	0.80	$1.64 \cdot 10^5$	114.29	169.70
25	$7.53 \cdot 10^{-6}$	$1.00 \cdot 10^{-4}$	0.90	$1.29 \cdot 10^4$	30.95	50.58
26	$7.53 \cdot 10^{-6}$	$3.00 \cdot 10^{-4}$	0.90	$3.88 \cdot 10^4$	59.52	87.61
27	$7.53 \cdot 10^{-6}$	$5.00 \cdot 10^{-4}$	0.90	$6.46 \cdot 10^4$	75.00	113.10
28	$7.53 \cdot 10^{-6}$	$1.00 \cdot 10^{-3}$	0.90	$1.29 \cdot 10^5$	107.14	159.95

A.3 Mishra *et al.* [53]

Table A.7: Parameters of the experiments from the work of Mishra *et al.* [53]

#	# in Mishra <i>et al.</i> [53]	I , A	V , V	q_{eff} , W	σ , m	U , m/s	ρ , kg/m ³
1	Exp. 1	101	9.6	969.6	$1.80 \cdot 10^{-3}$	$1.70 \cdot 10^{-3}$	7200
2	Exp. 3	150	9.9	1485	$2.35 \cdot 10^{-3}$	$1.70 \cdot 10^{-3}$	7200

Table A.8: Parameters of the experiments from the work of Mishra *et al.* [53]

#	ν , m ² /s	k_l , W/m K	k_s , W/m K	γ_T , N/m K	c_{pl} , J/kg K	c_{ps} , J/kg K
1	$9.31 \cdot 10^{-7}$	125.5	25.08	$3.00 \cdot 10^{-4}$	807.1	702.24
2	$9.31 \cdot 10^{-7}$	125.5	25.08	$3.00 \cdot 10^{-4}$	807.1	702.24

Table A.9: Parameters of the experiments from the work of Mishra *et al.* [53]

#	α_s , m ² /s	α_l , m ² /s	T_m , K	T_∞ , K	i_{sl} , J/kg	Ste	u_{max} , m/s	Pe
1	$4.96 \cdot 10^{-6}$	$2.16 \cdot 10^{-5}$	1745	300	$2.51 \cdot 10^5$	4.05	0.235	19.59
2	$4.96 \cdot 10^{-6}$	$2.16 \cdot 10^{-5}$	1745	300	$2.51 \cdot 10^5$	4.05	0.384	41.78

Table A.10: Parameters of the experiments from the work of Mishra *et al.* [53]

#	L , m	D , m	Ry	σ^*	Ri	Pr
1	$4.83 \cdot 10^{-3}$	$1.37 \cdot 10^{-3}$	0.88	0.31	$3.72 \cdot 10^5$	0.04
2	$6.80 \cdot 10^{-3}$	$2.18 \cdot 10^{-3}$	1.34	0.31	$5.69 \cdot 10^5$	0.04

Table A.11: Parameters of the experiments from the work of Mishra *et al.* [53]

#	\mathcal{R}_G	L_G , m	D_G , m
1	1.11	$3.81 \cdot 10^{-3}$	$2.50 \cdot 10^{-3}$
2	1.11	$5.14 \cdot 10^{-3}$	$3.48 \cdot 10^{-3}$

A.4 Robert and DebRoy [97]

Table A.12: Parameters for the high speed steel experiments from the work of Robert and DebRoy [97]

Parameter	Symbol	Dimension	Value
Density	ρ	kg/m ³	8100
Kinematic viscosity	ν	m ² /s	7.41 10 ⁻⁷
Thermal conductivity (liquid)	k	W/m K	22.9
Thermal conductivity (solid)	k_s	W/m K	22.9
Heat source size	σ	m	1.16 10 ⁻³
Surface tension temperature coeff.	σ_T	N/m K	5.00 10 ⁻⁴
Dynamic viscosity	μ	Pa s	6.00 10 ⁻³
Heat capacity (liquid)	c_{pl}	J/kg K	723.14
Heat capacity (solid)	c_{ps}	J/kg K	627
Thermal diffusivity (solid)	α_s	m ² /s	4.51 10 ⁻⁶
Latent heat of melting	i_{sl}	J/kg	2.51 10 ⁵
Melting temperature	T_m	K	1620
Preheat temperature	T_∞	K	300
Stefan number	Ste	-	3.3
Prandtl number	Pr	-	0.19
Rivas number	Ri	-	1.31 10 ⁶
Welding time	t	s	5
Heat source distribution	-	-	Top hat

Table A.13: Parameters of the high speed steel experiments from the work of Robert and DebRoy [97]

#	q , W	η	D , m	L , m	U_{est} , m/s	Pe_{est}
1	1900	0.14	6.23 10 ⁻⁴	1.17 10 ⁻³	0.05	14.82
2	5200	0.12	1.60 10 ⁻³	2.85 10 ⁻³	0.2	59.29

Appendix B: Numerical modelling raw results

B.1 Regime I

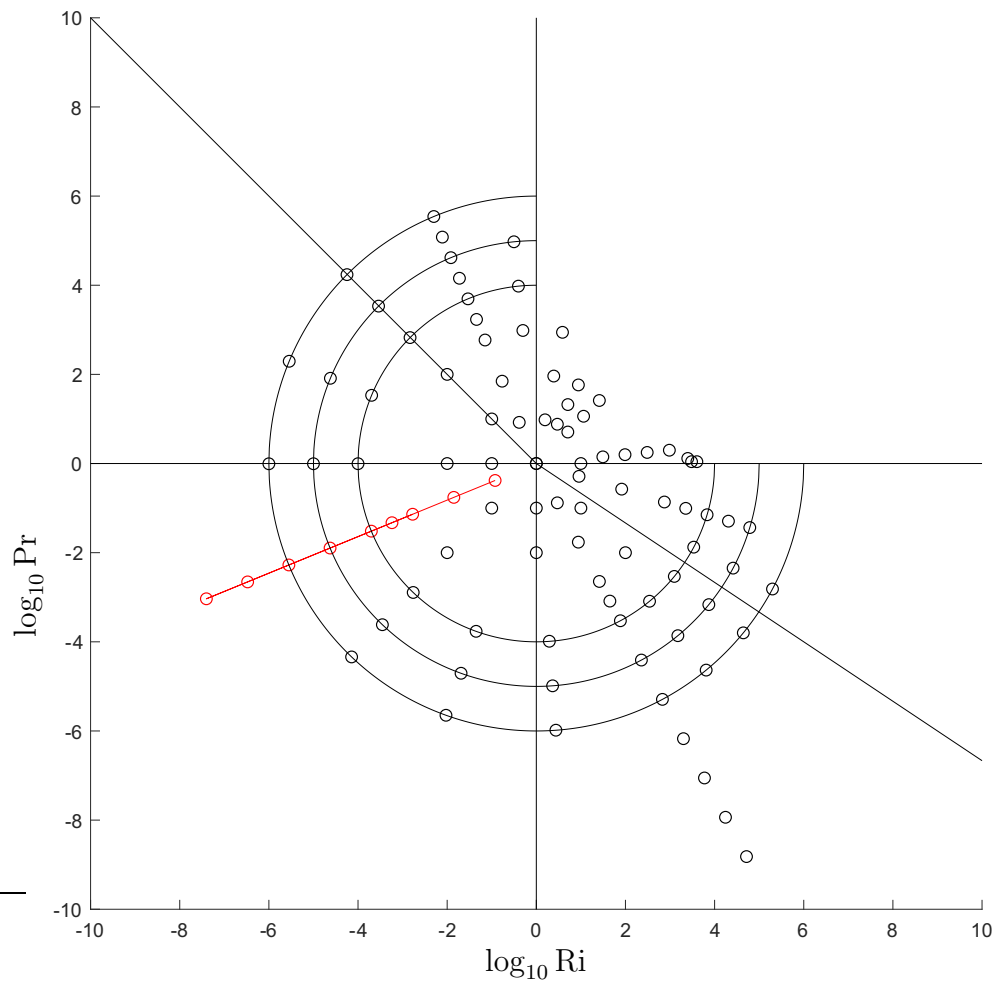


Figure B.1: Location of the dimensionless parameters for Regime I.

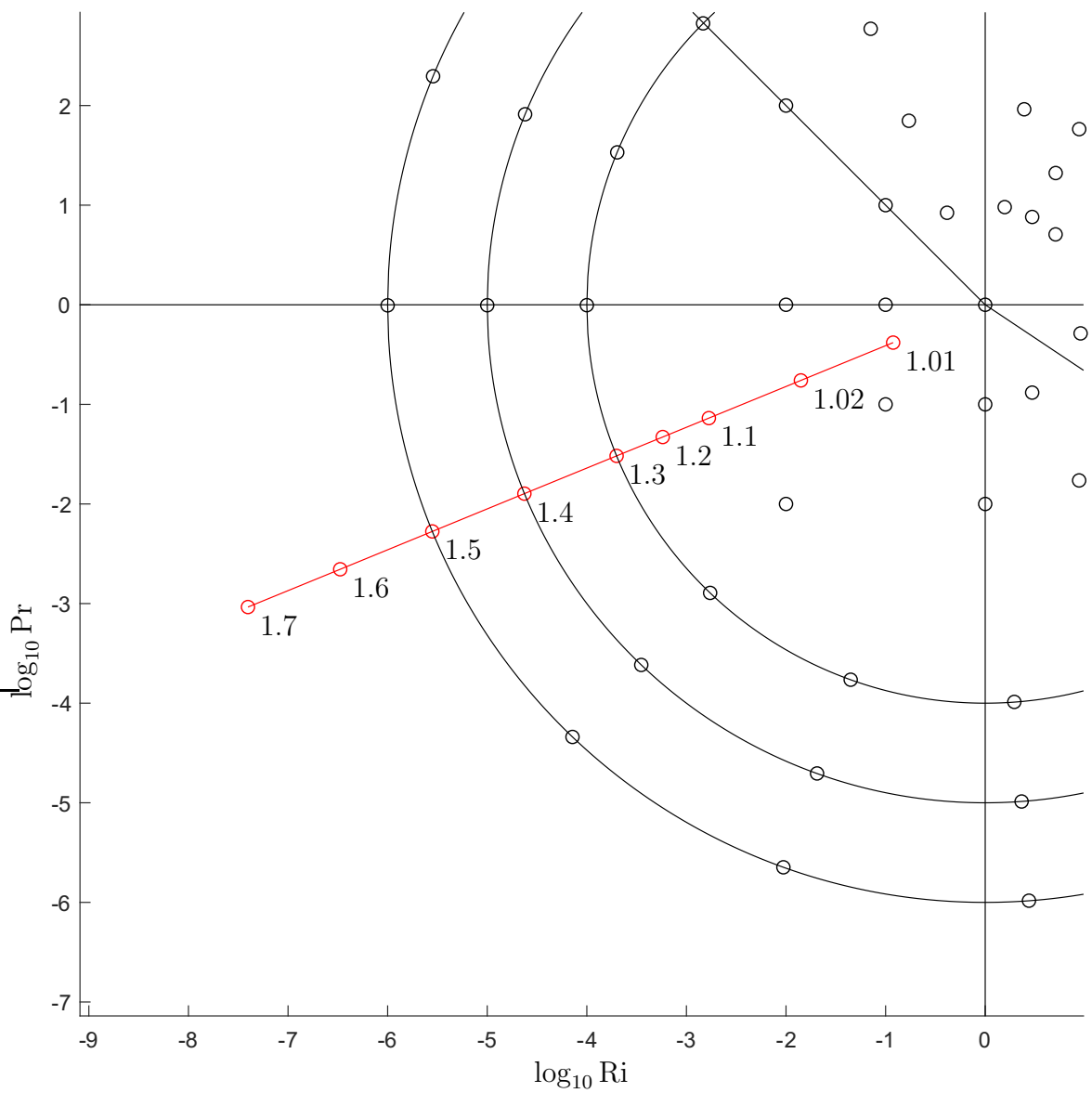


Figure B.2: Location of the dimensionless parameters for Regime I and the experiment numbers.

Exp 1.01

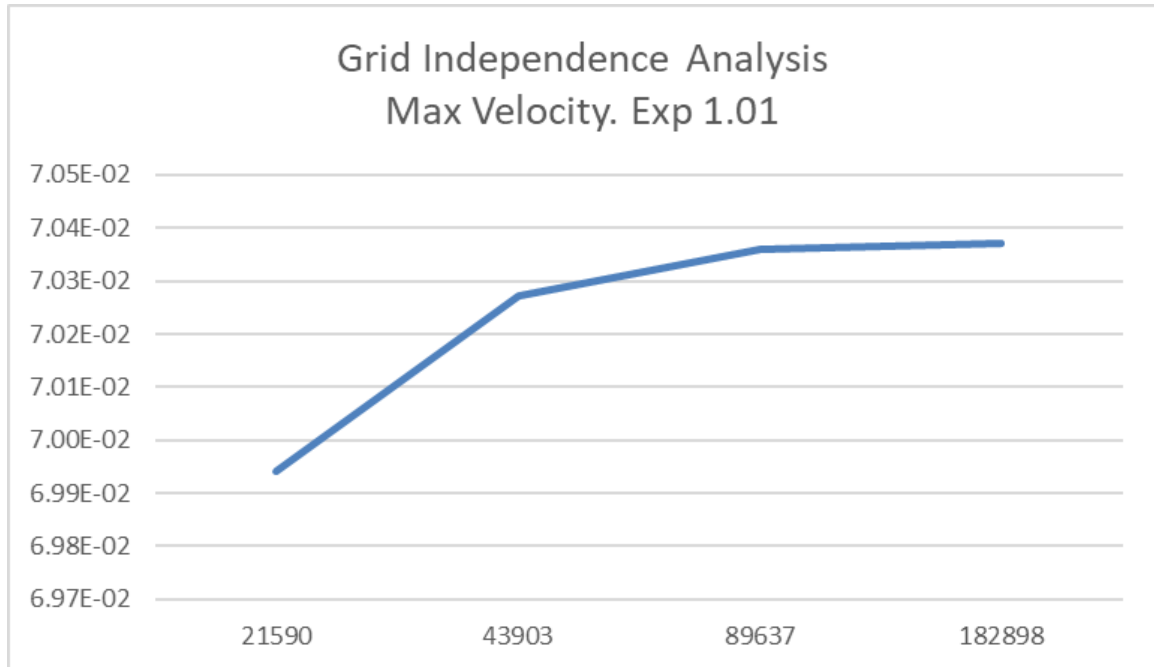


Figure B.3: Convergence for Exp 1.01: peak velocity values vs number of nodes in logarithmic scale.

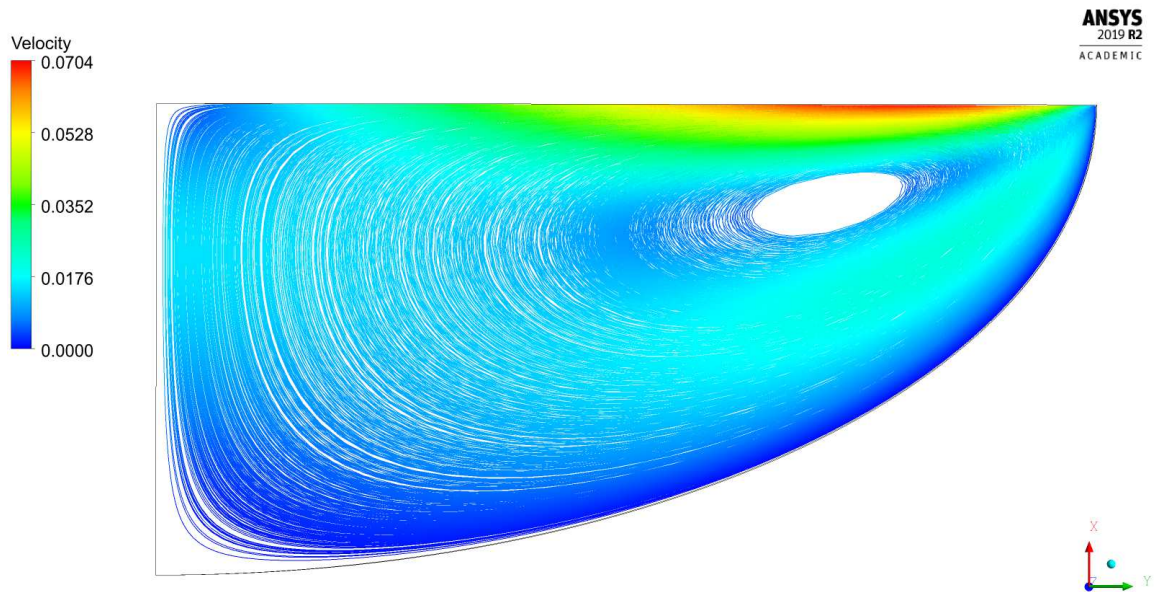


Figure B.4: Streamlines for Exp 1.01.

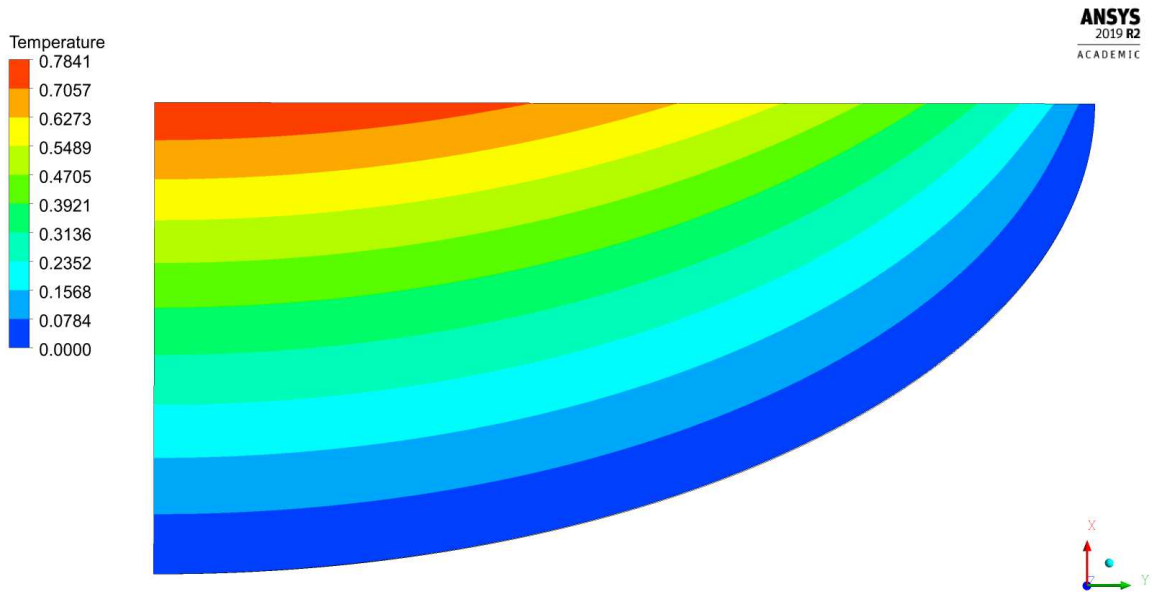


Figure B.5: Temperature field for Exp 1.01.

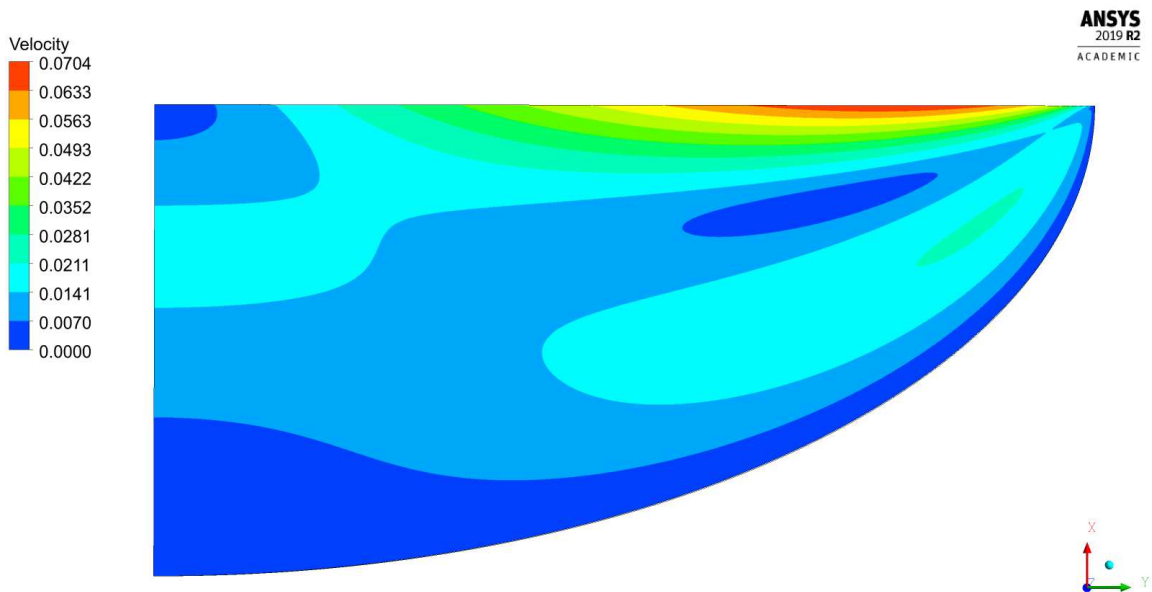


Figure B.6: Velocity magnitude contour for Exp 1.01.

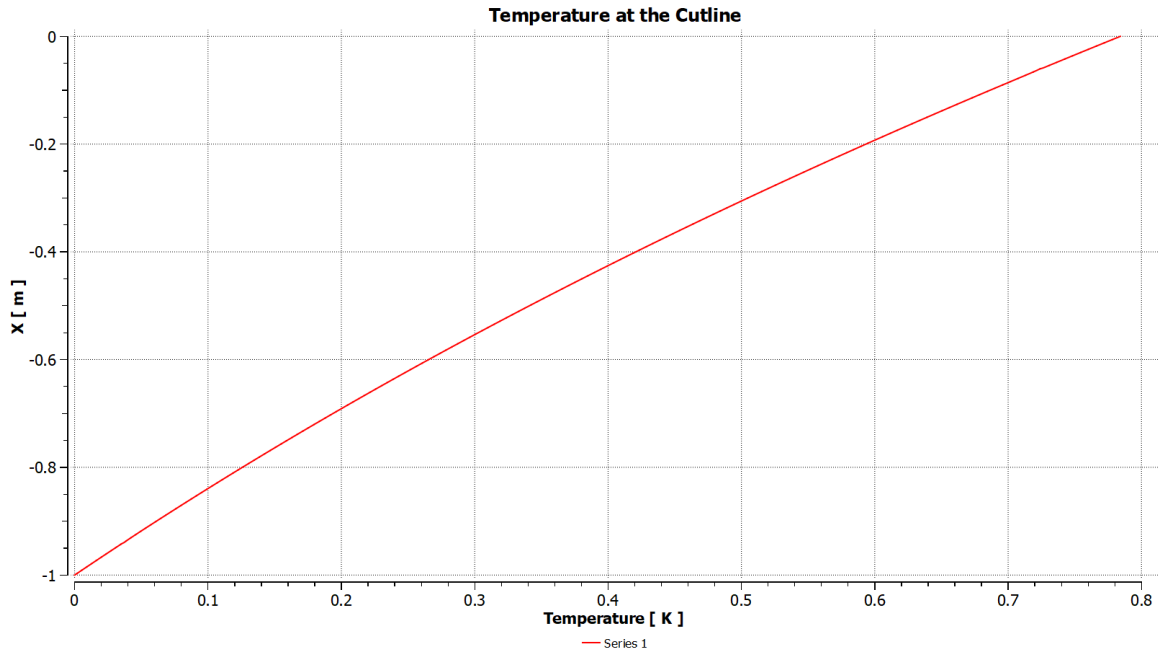


Figure B.7: Temperature at the axis of symmetry for Exp 1.01.

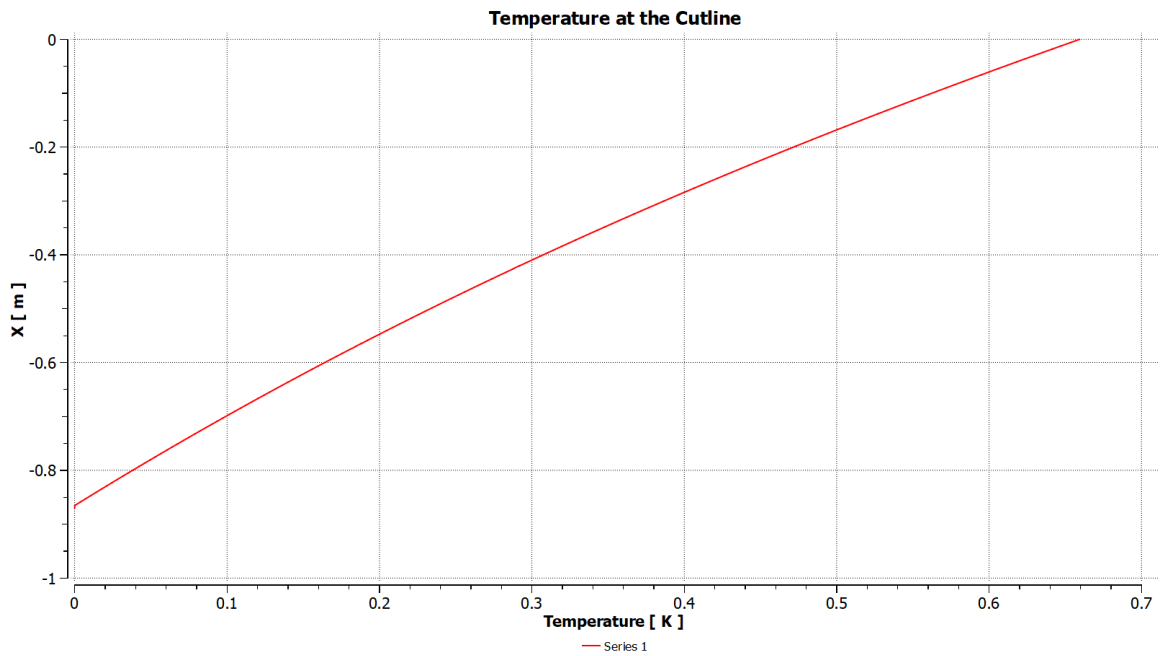


Figure B.8: Temperature at the cutline at $r^*=1$ for Exp 1.01.

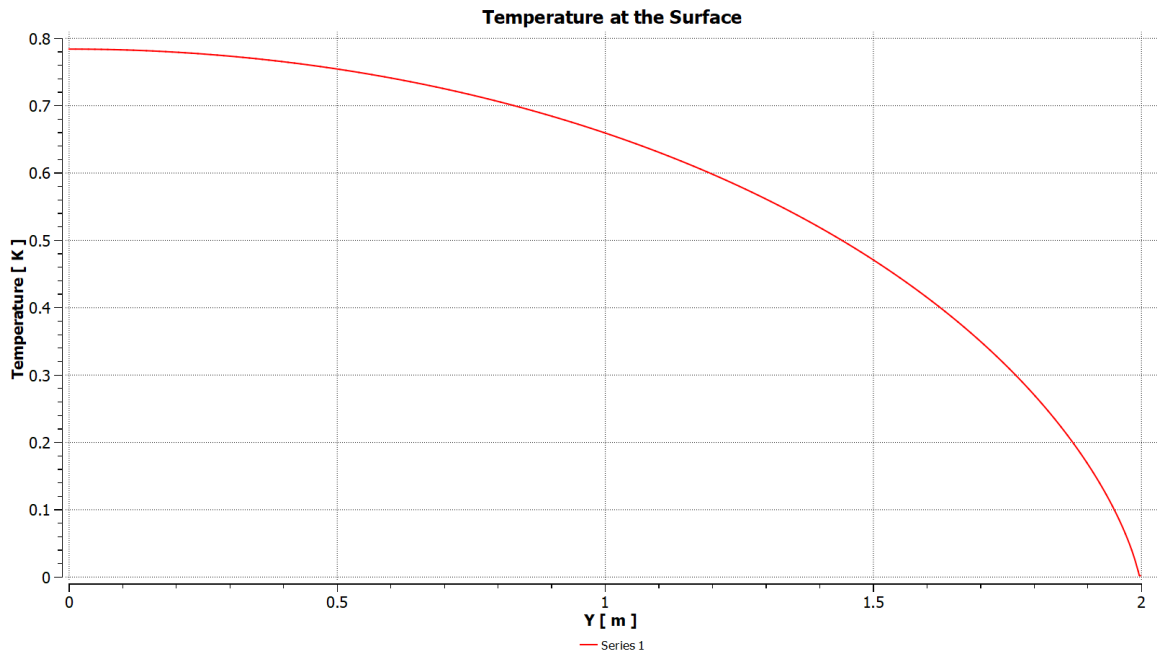


Figure B.9: Temperature at the free surface for Exp 1.01.

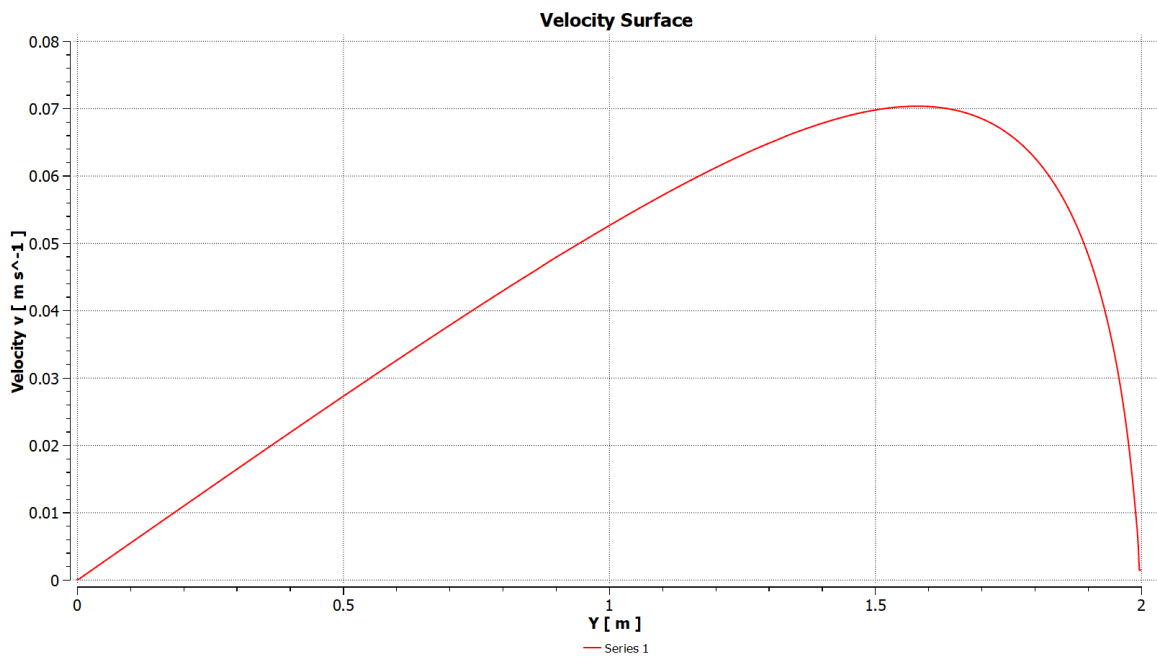


Figure B.10: Velocity at the free surface for Exp 1.01.

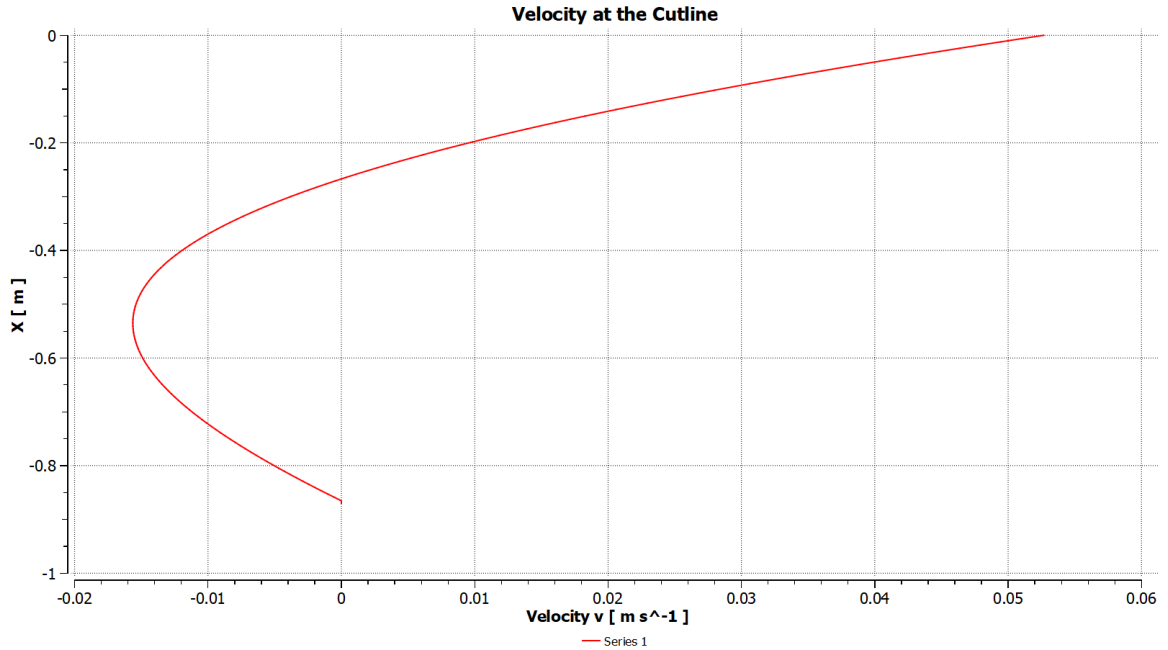


Figure B.11: Radial velocity u at the cutline at $r^*=1$ for Exp 1.01.

Exp 1.02-1.7

The results for Exp 1.02, Exp 1.1-1.7 are identical up to 5th digit after decimal point. Because of this fact, only one set of graphs and data is present here for these experiments. The difference between peak velocity magnitude for Exp 1.01 and 1.02-1.7 is quite negligible, too, and is not greater than $1 \cdot 10^{-5}$.

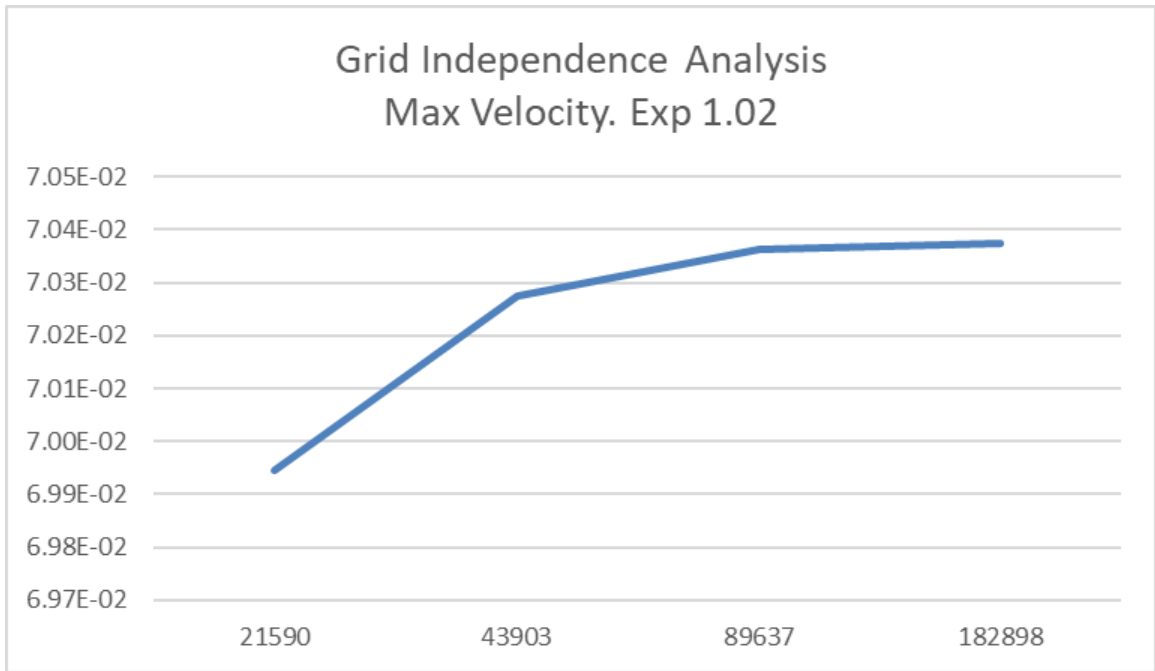


Figure B.12: Convergence for Exp 1.02-1.7: peak velocity values vs number of nodes in logarithmic scale.

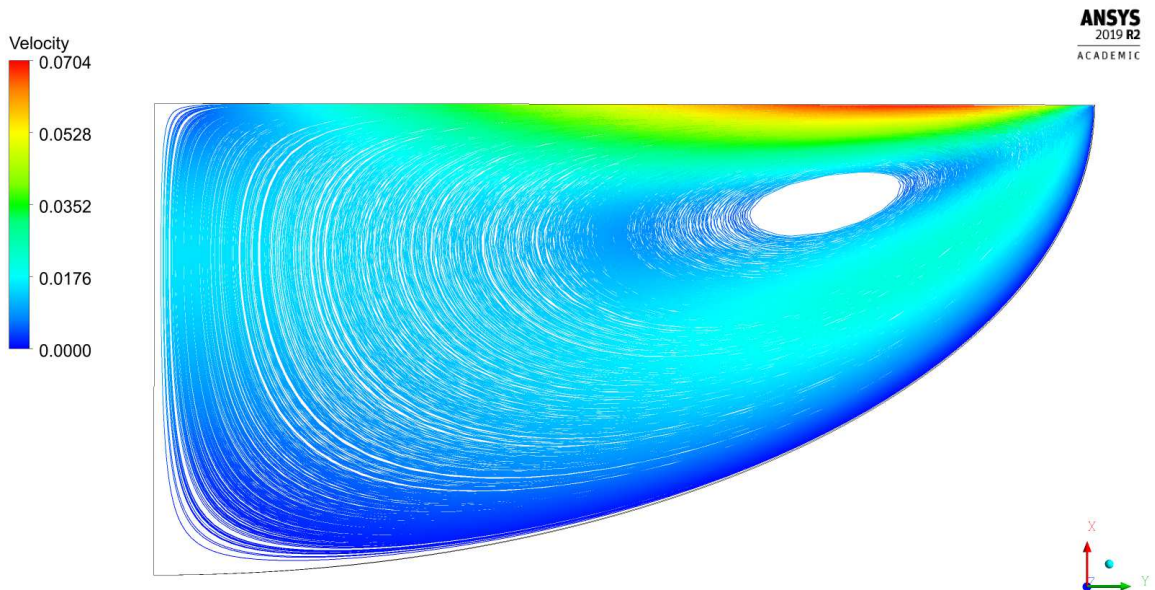


Figure B.13: Streamlines for Exp 1.02-1.7.

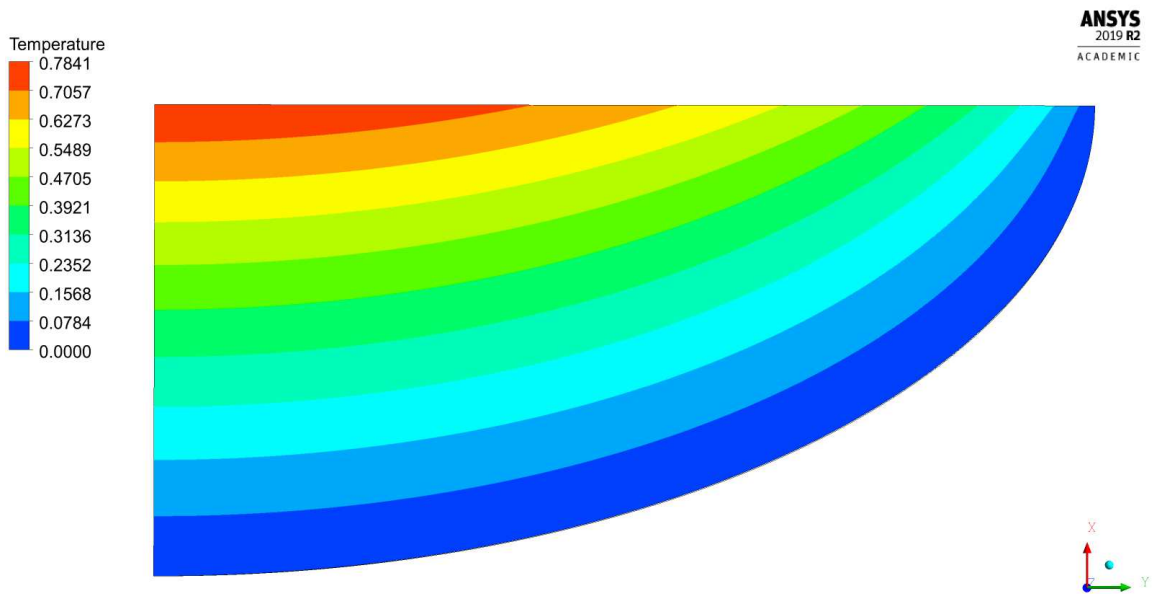


Figure B.14: Temperature field for Exp 1.02-1.7.

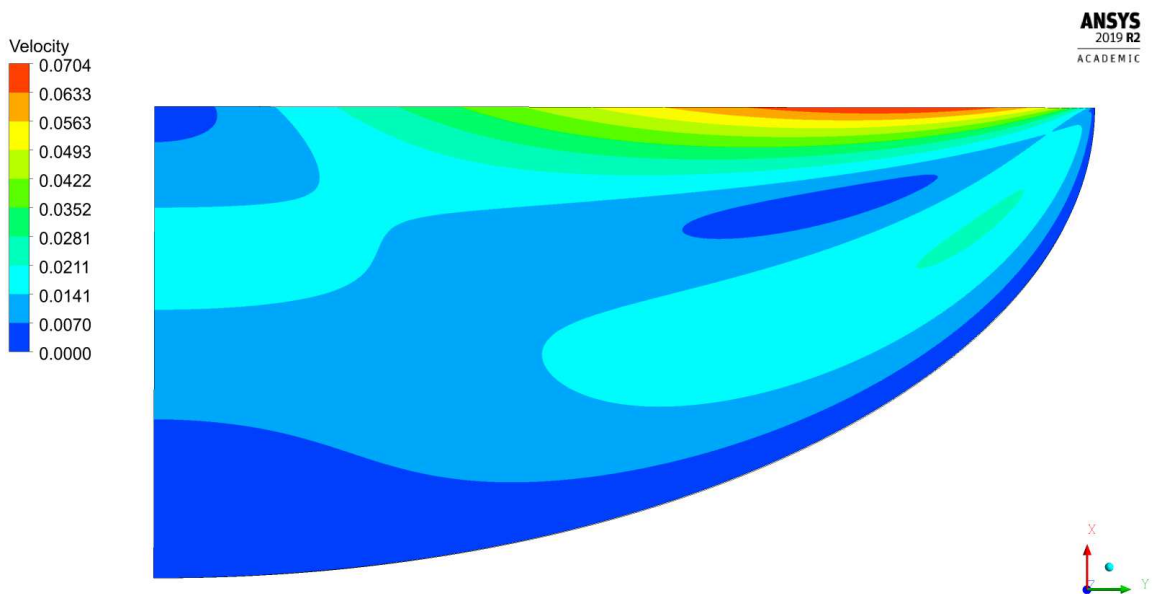


Figure B.15: Velocity magnitude contour for Exp 1.02-1.7.

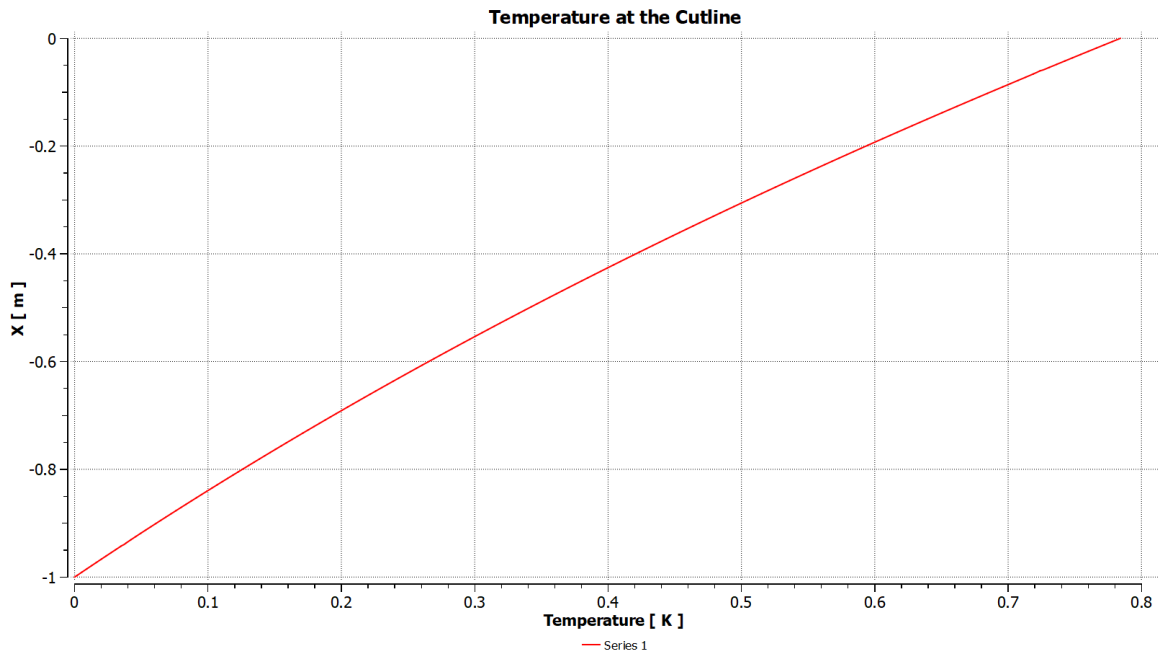


Figure B.16: Temperature at the axis of symmetry for Exp 1.02-1.7.

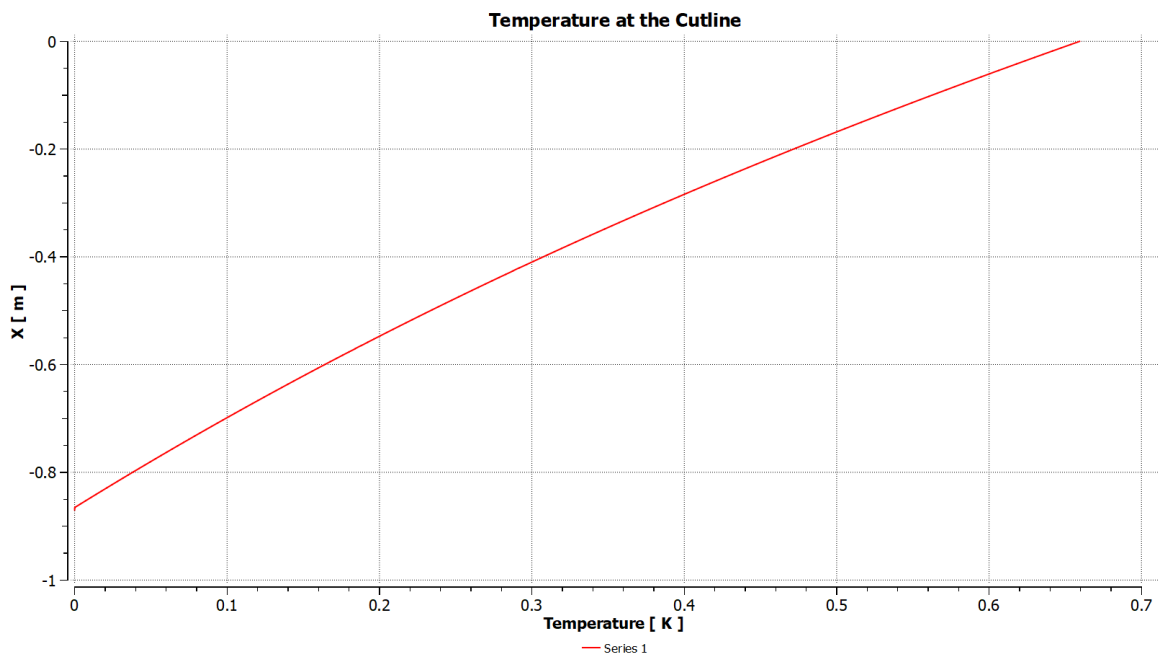


Figure B.17: Temperature at the cutline at $r^*=1$ for Exp 1.02-1.7.

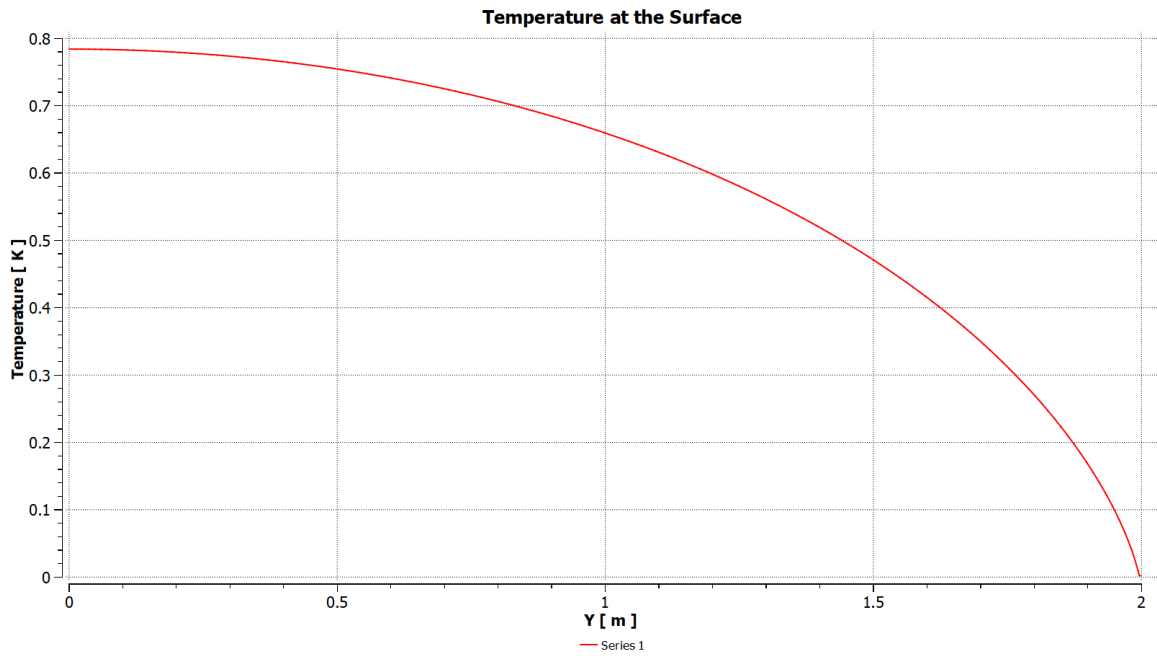


Figure B.18: Temperature at the free surface for Exp 1.02-1.7.

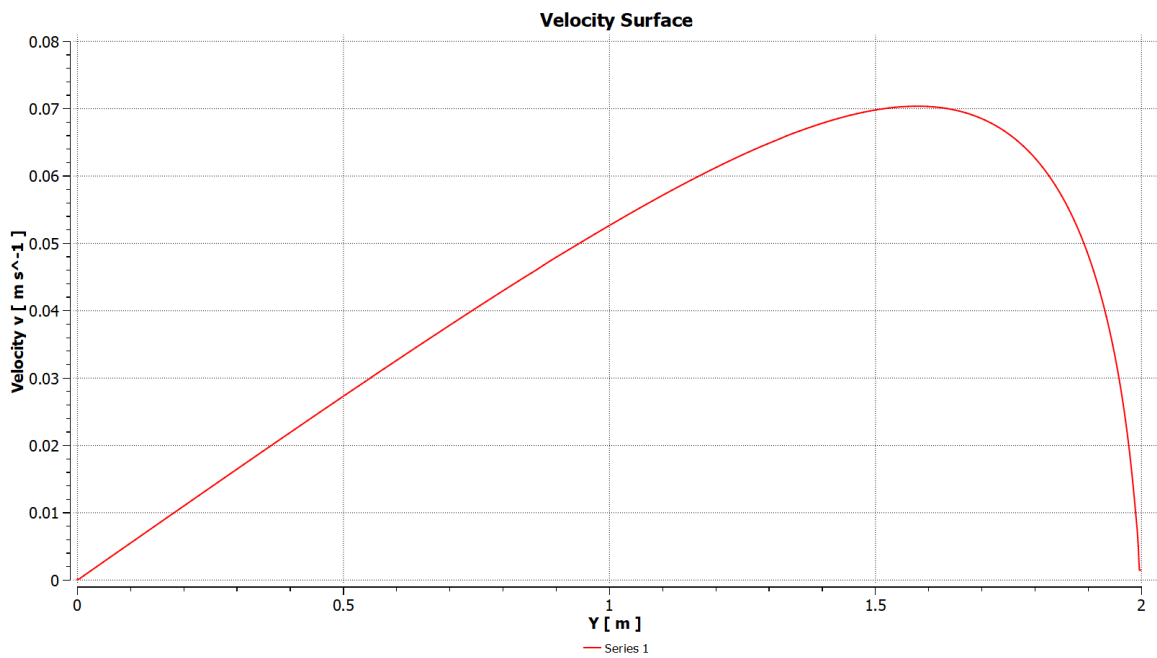


Figure B.19: Velocity at the free surface for Exp 1.02-1.7.

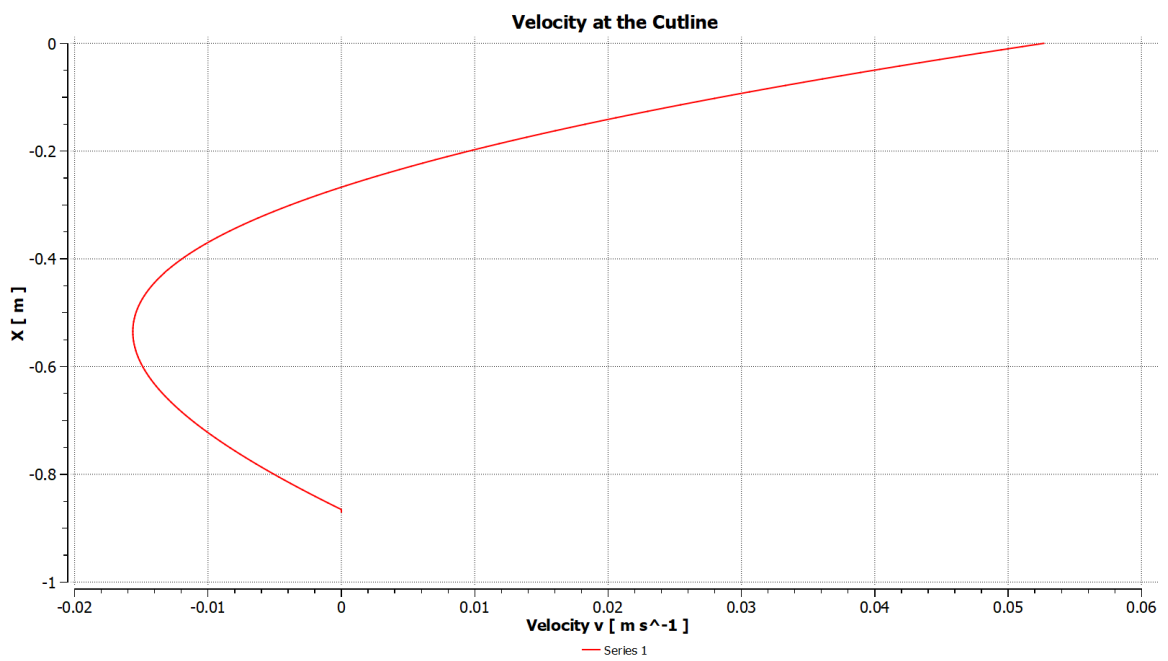


Figure B.20: Radial velocity u at the cutline at $r^*=1$ for Exp 1.02-1.7.

B.2 Regime II

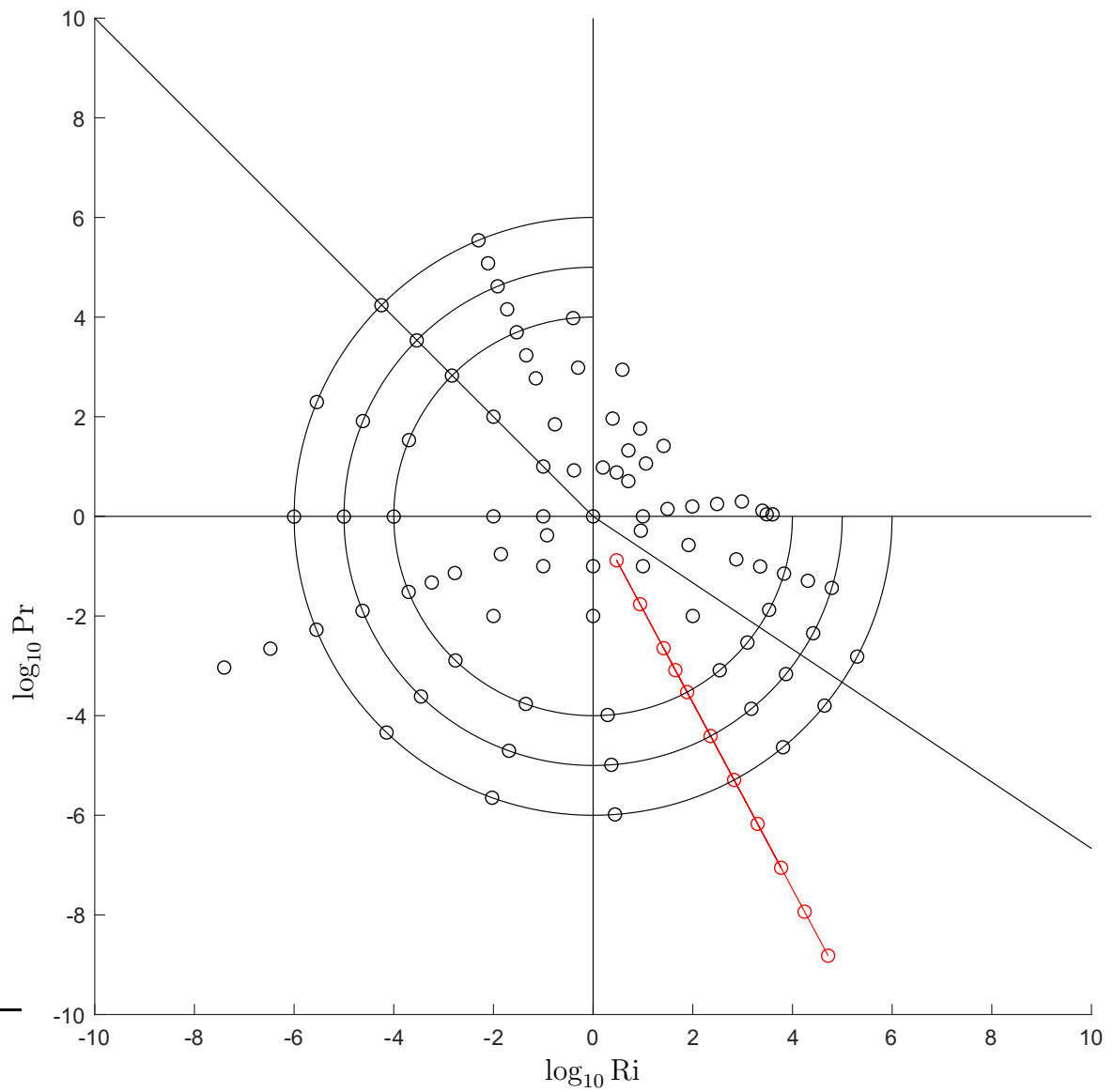


Figure B.21: Location of the dimensionless parameters for Regime II.

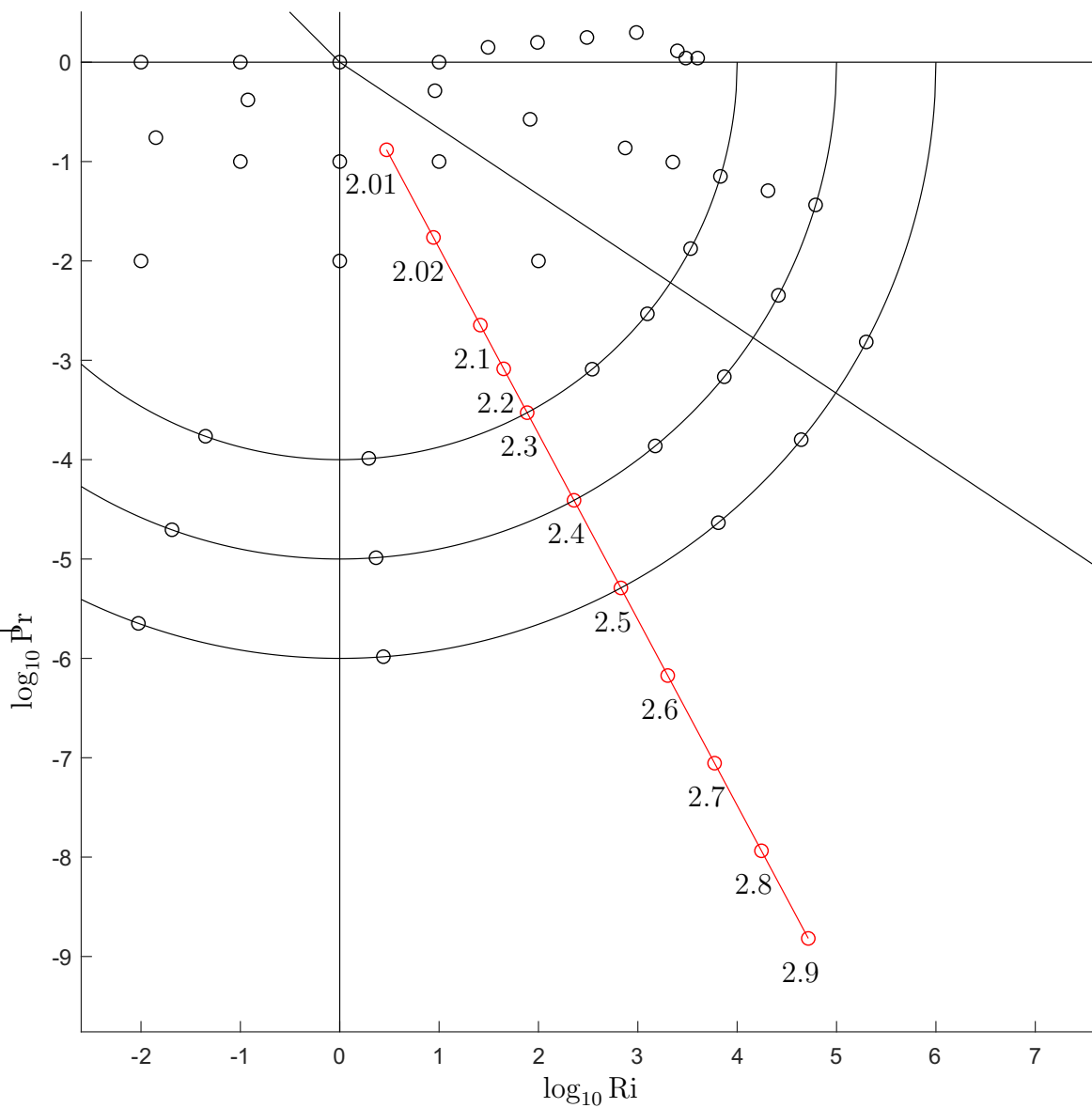


Figure B.22: Location of the dimensionless parameters for Regime II and the experiment numbers.

Exp 2.01

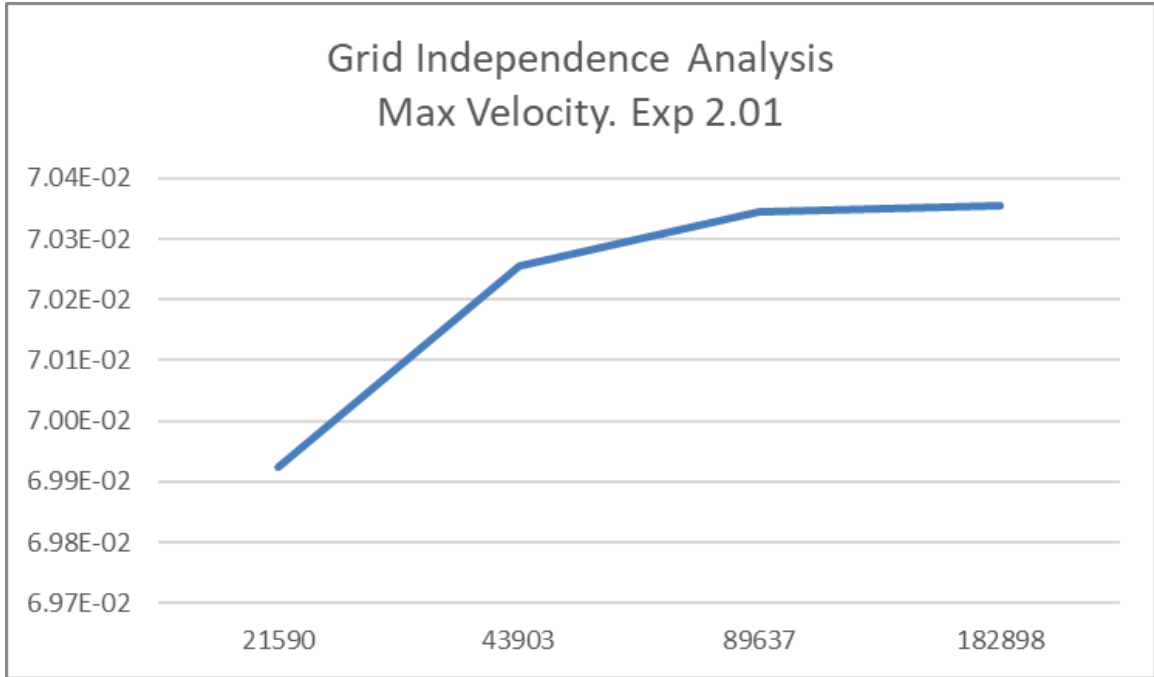


Figure B.23: Convergence for Exp 2.01: peak velocity values vs number of nodes in logarithmic scale.

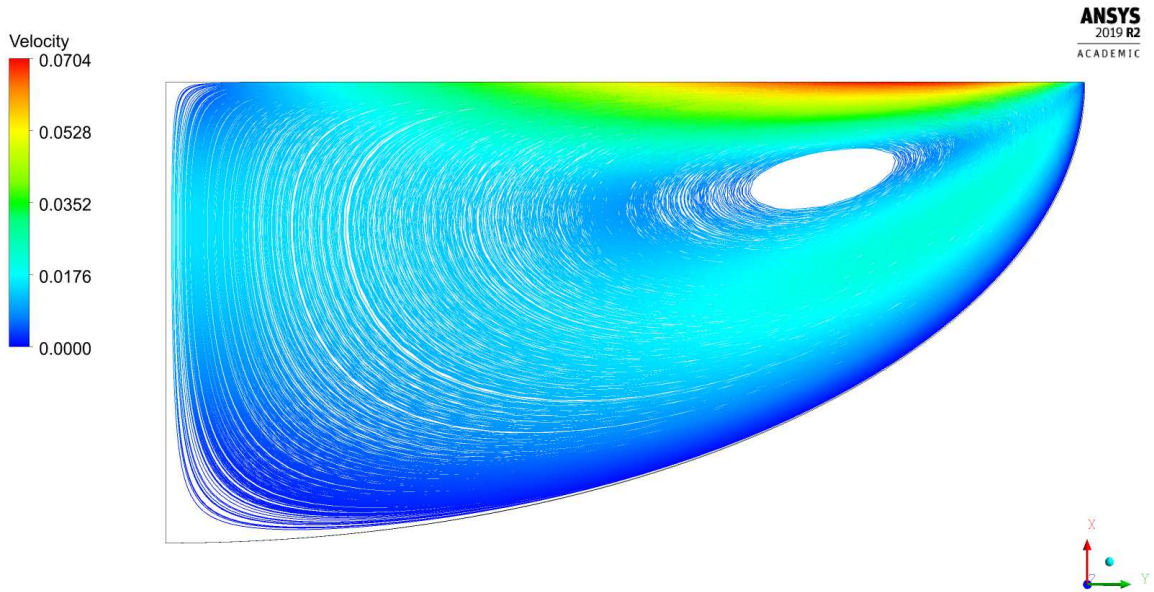


Figure B.24: Streamlines for Exp 2.01.

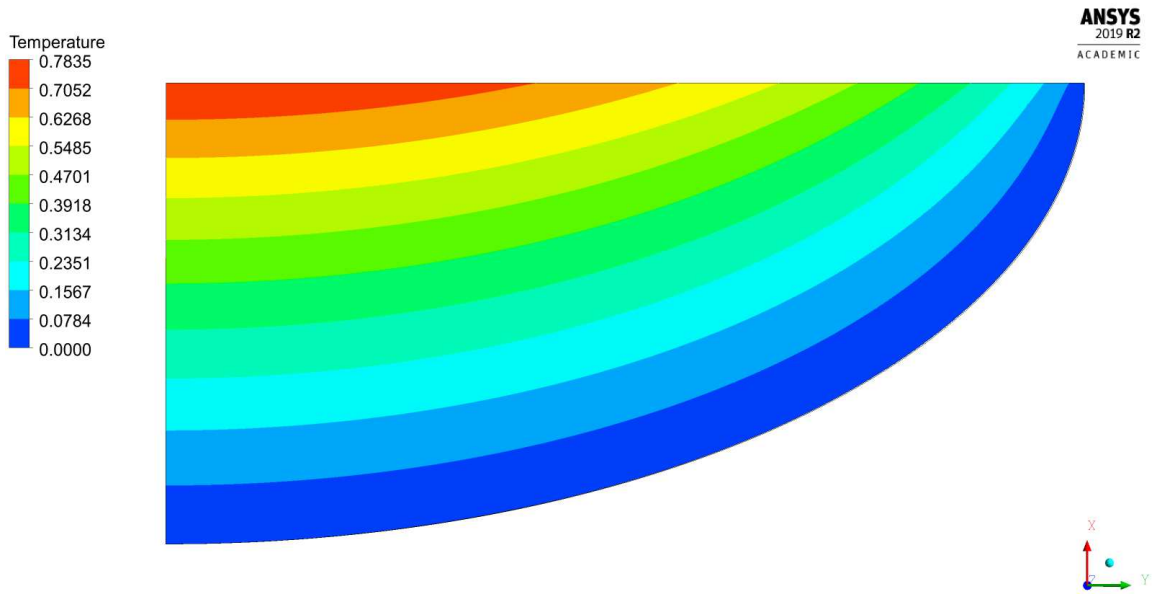


Figure B.25: Temperature field for Exp 2.01.

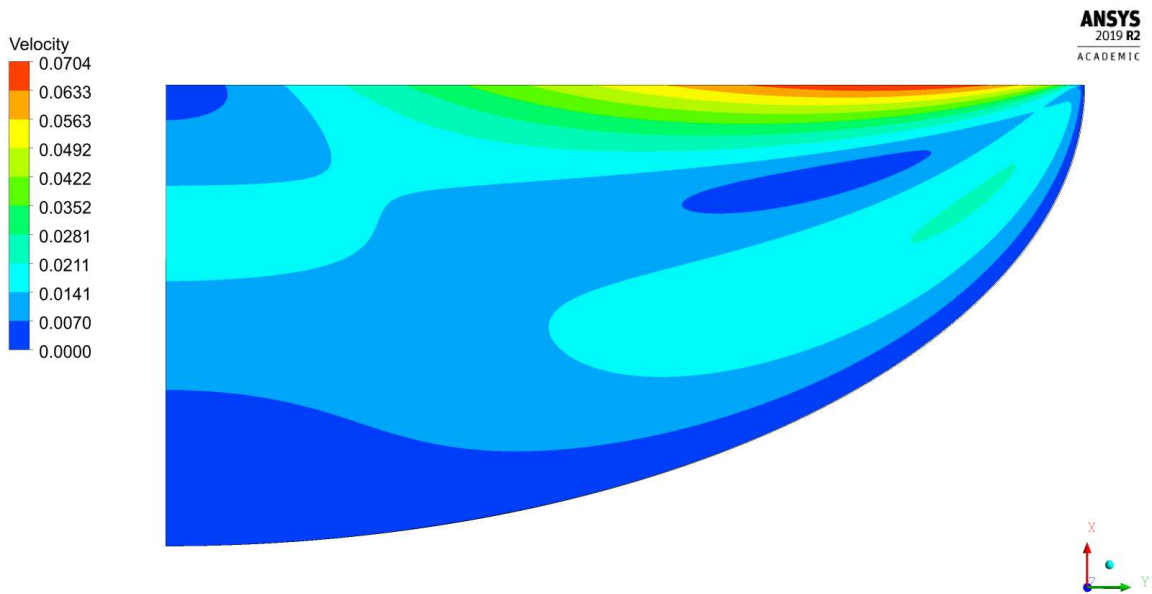


Figure B.26: Velocity magnitude contour for Exp 2.01.

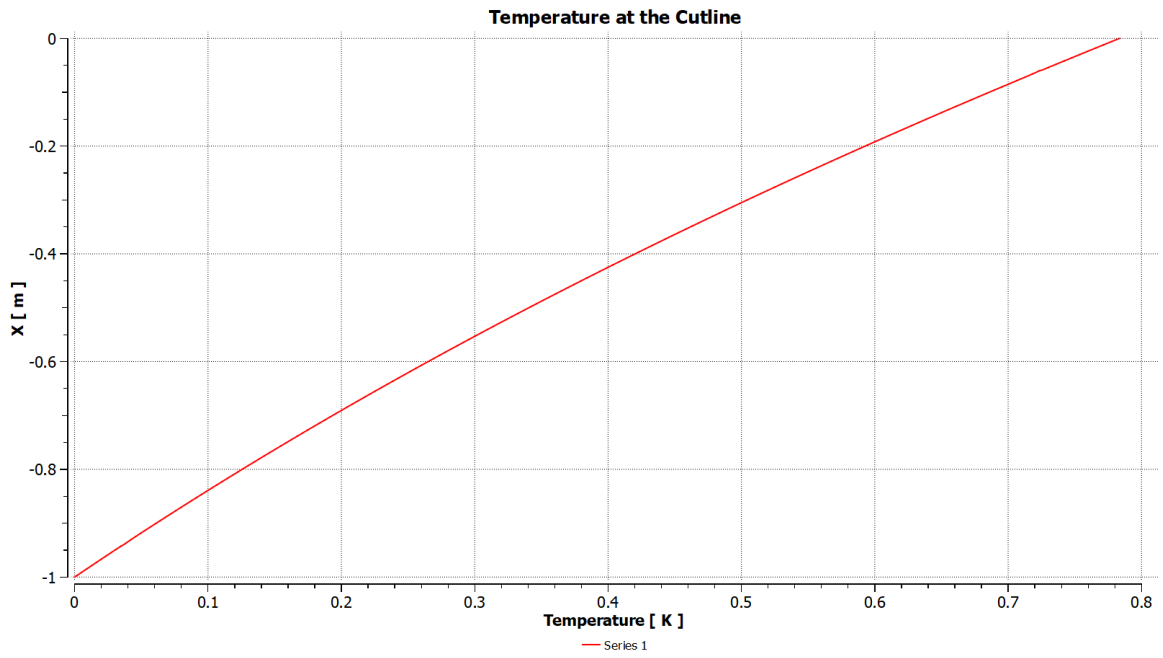


Figure B.27: Temperature at the axis of symmetry for Exp 2.01.

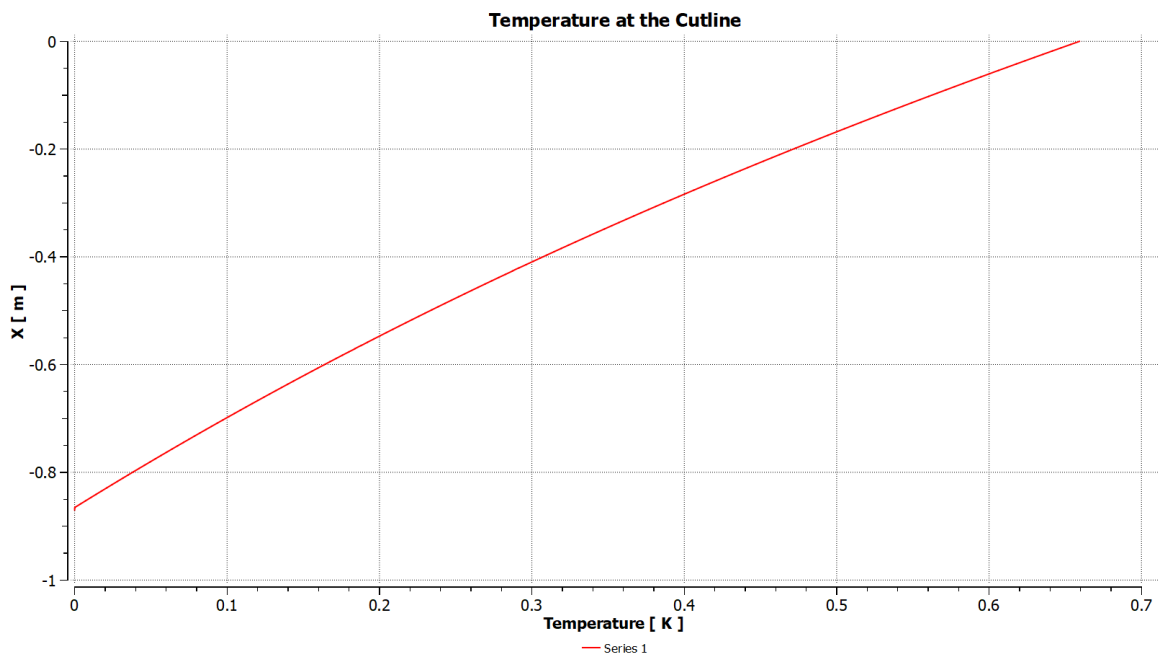


Figure B.28: Temperature at the cutline at $r^*=1$ for Exp 2.01.

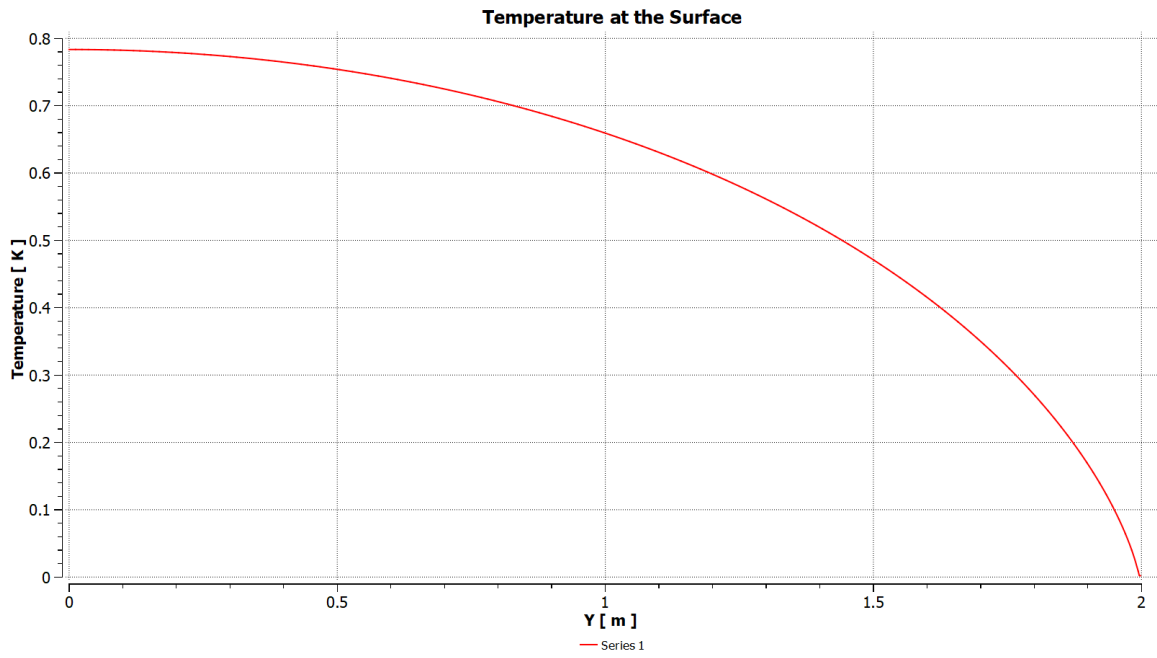


Figure B.29: Temperature at the free surface for Exp 2.01.

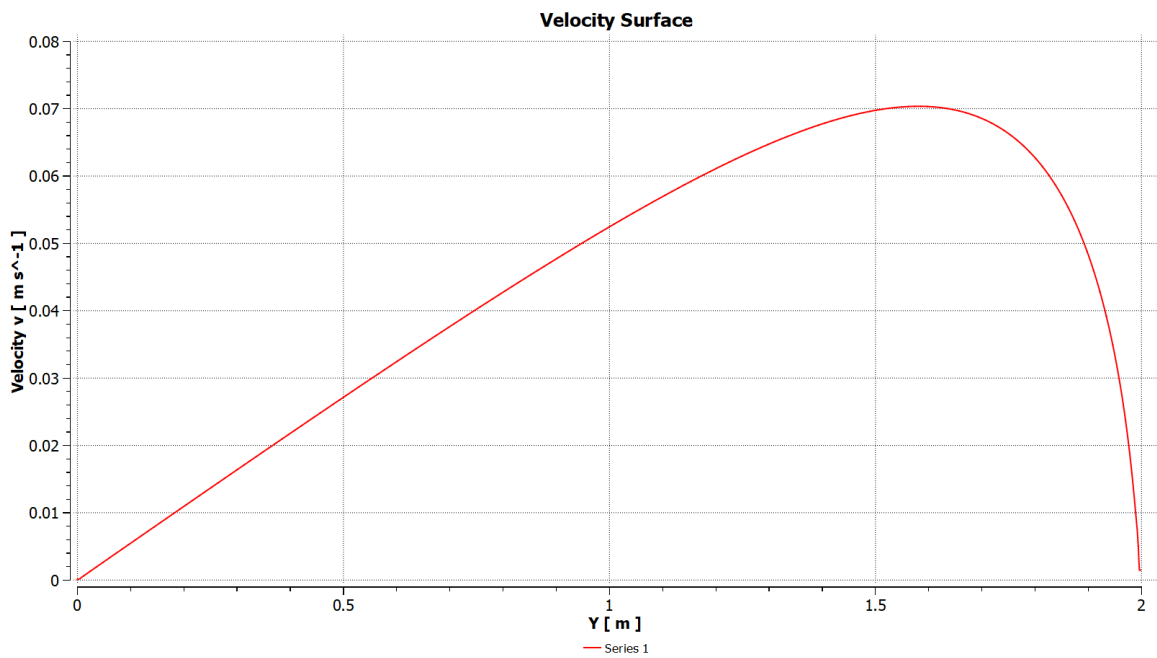


Figure B.30: Velocity at the free surface for Exp 2.01.

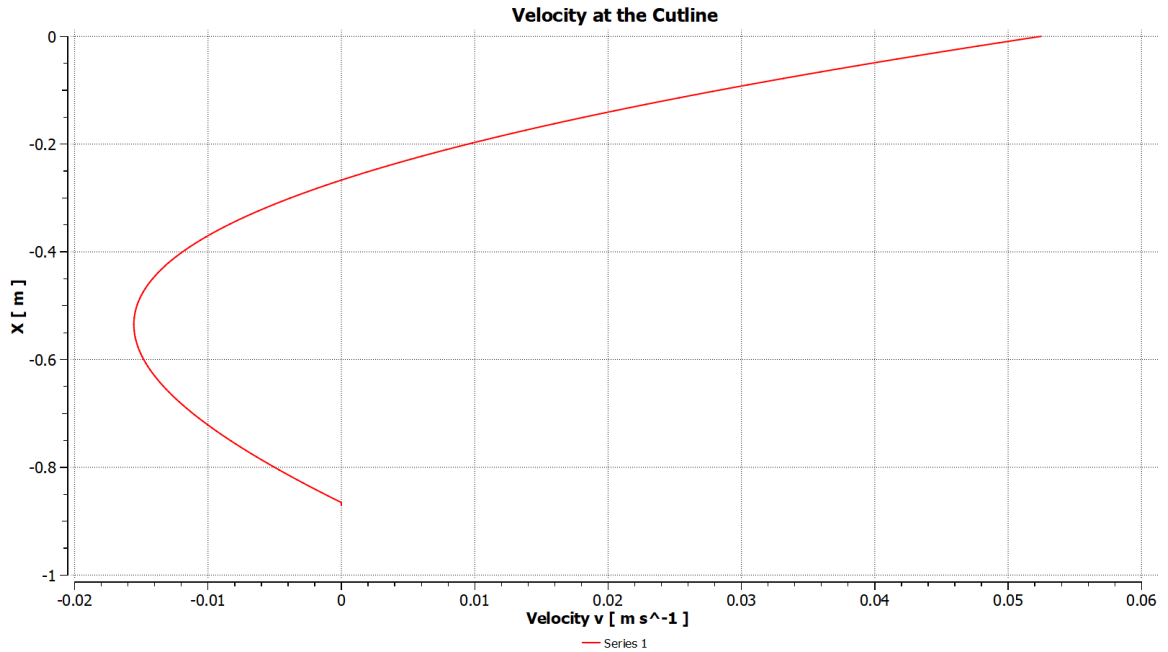


Figure B.31: Radial velocity u at the cutline at $r^*=1$ for Exp 2.01.

Exp 2.02

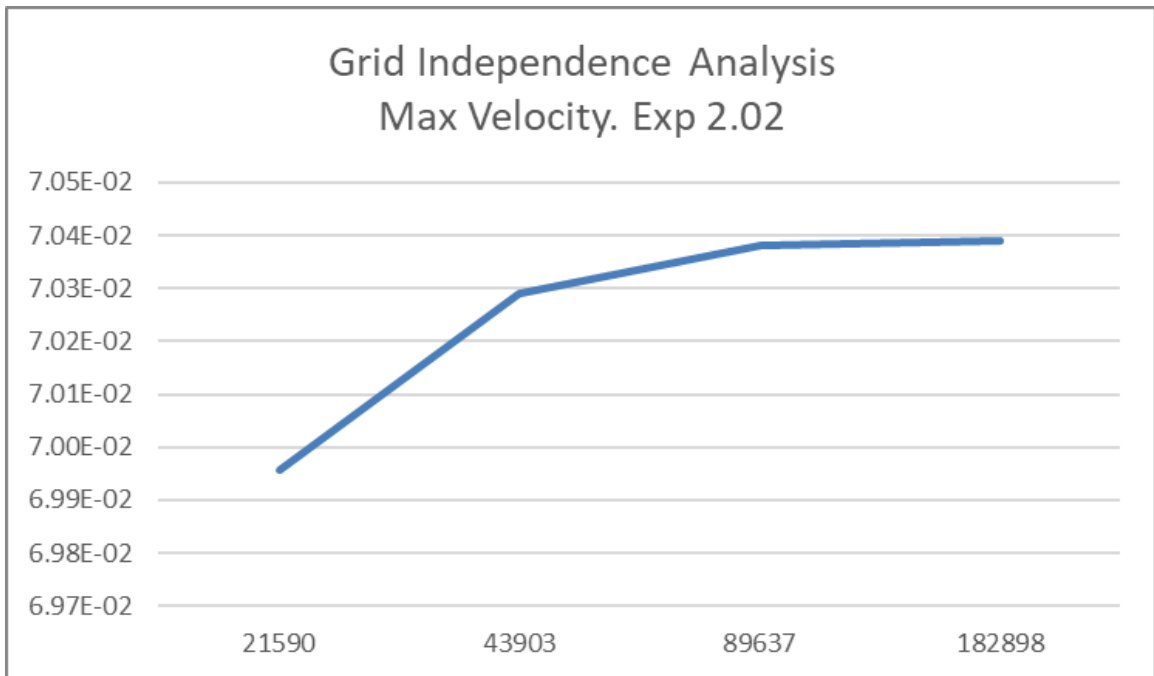


Figure B.32: Convergence for Exp 2.02: peak velocity values vs number of nodes in logarithmic scale.

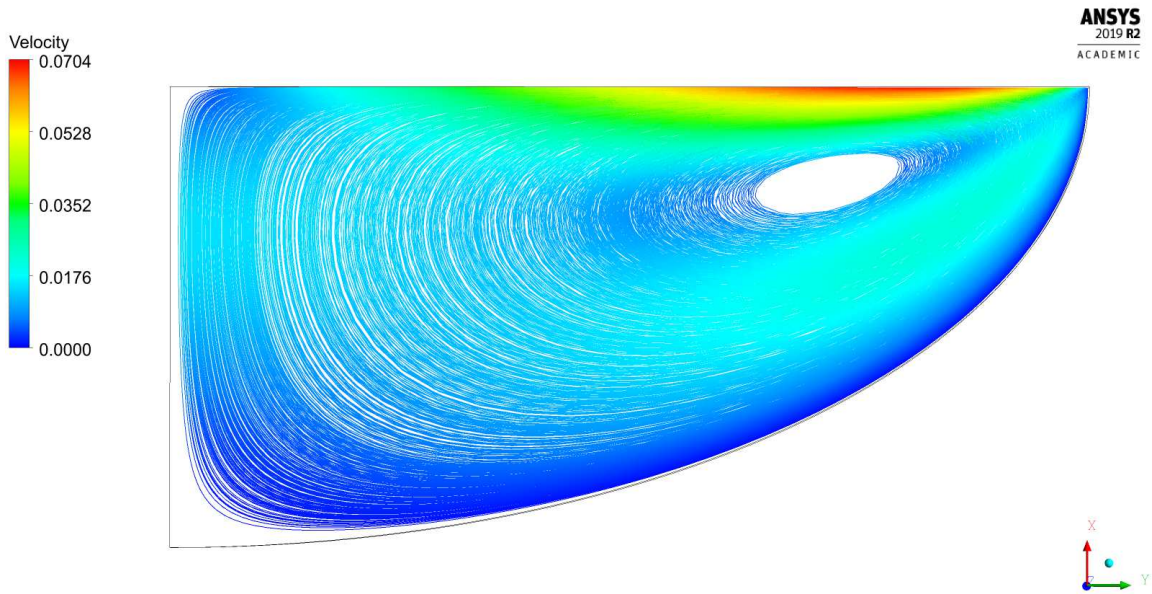


Figure B.33: Streamlines for Exp 2.02.

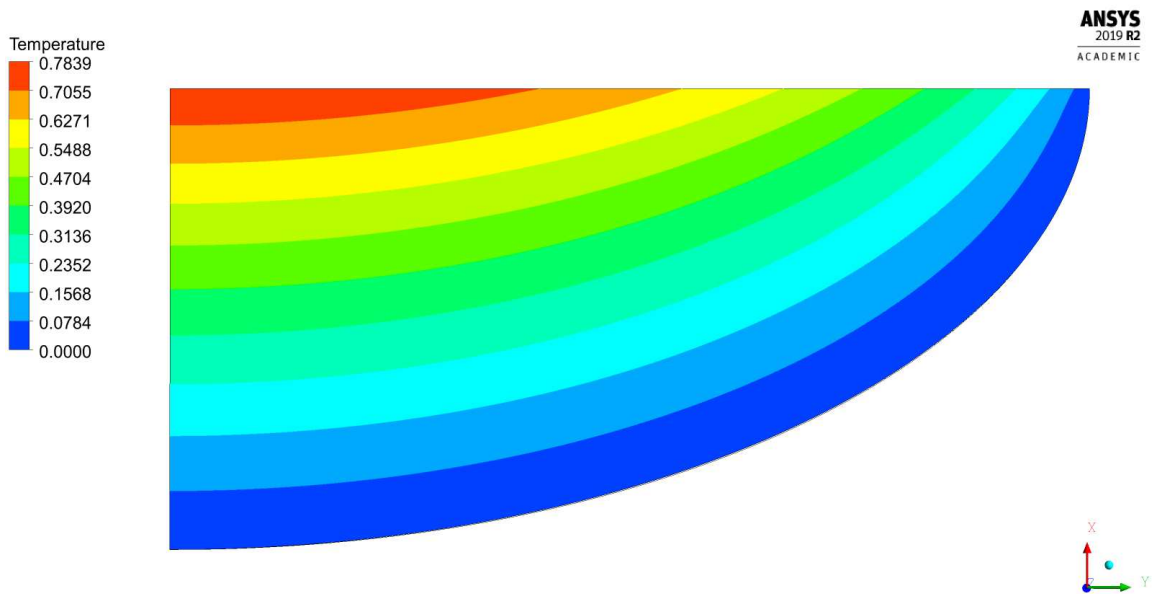


Figure B.34: Temperature field for Exp 2.02.

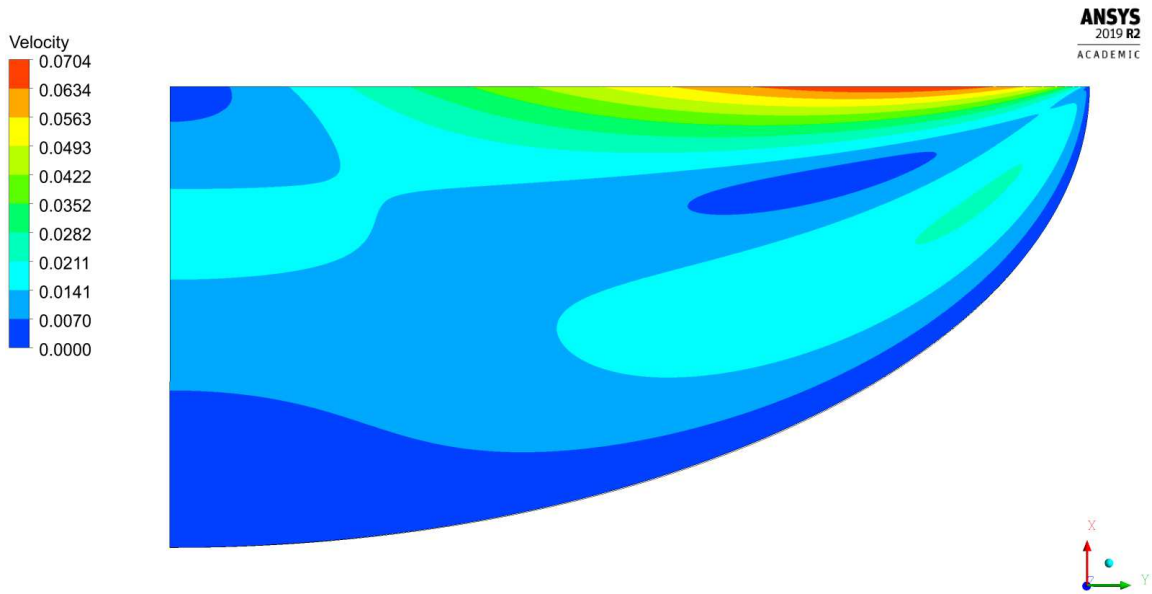


Figure B.35: Velocity magnitude contour for Exp 2.02.

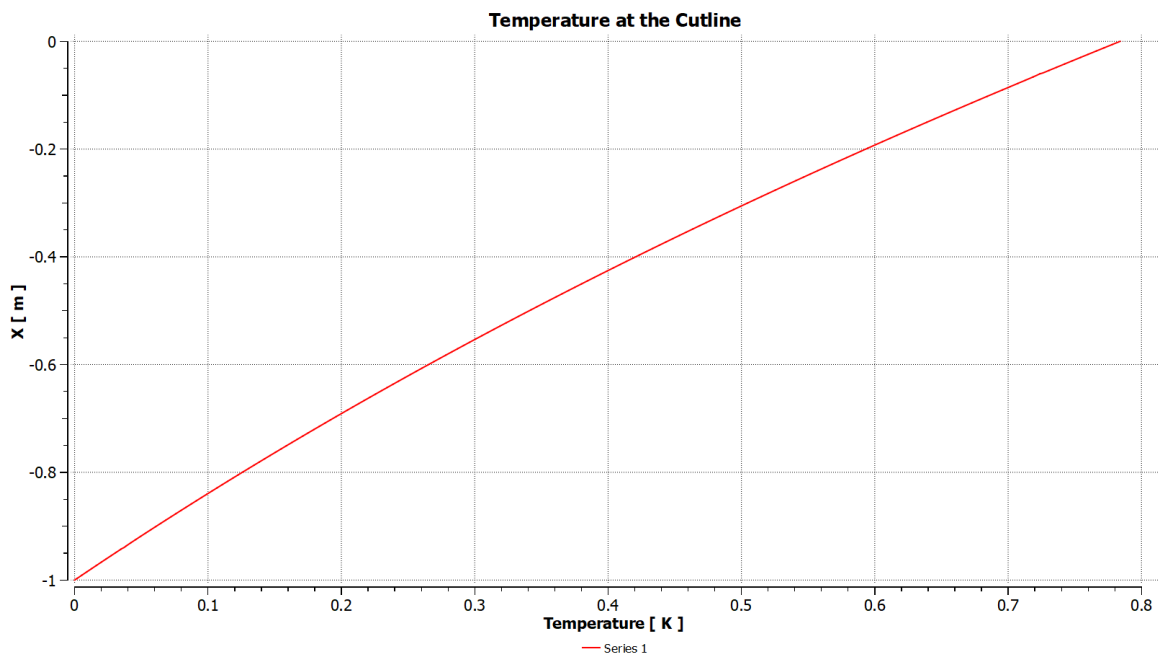


Figure B.36: Temperature at the axis of symmetry for Exp 2.02.

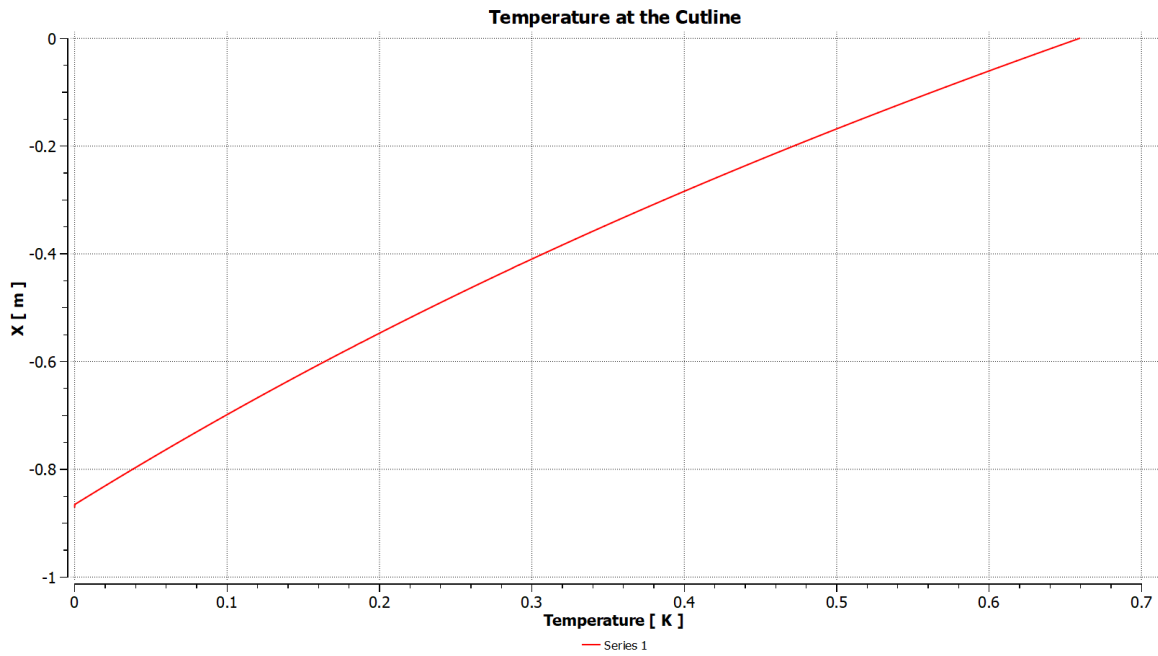


Figure B.37: Temperature at the cutline at $r^*=1$ for Exp 2.02.

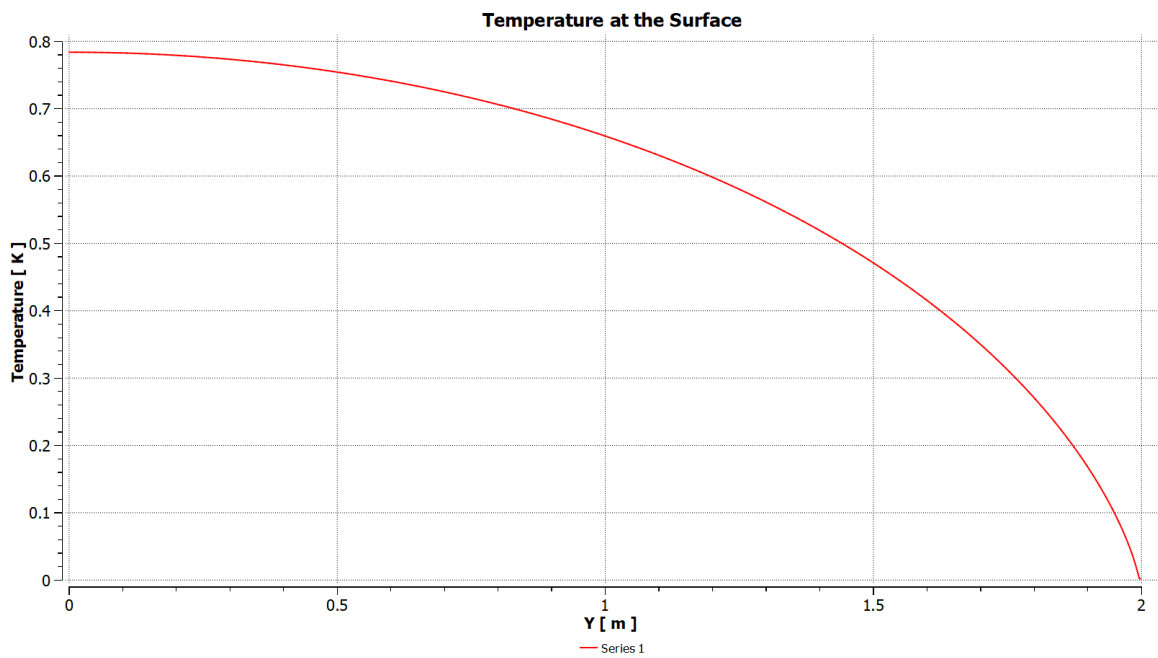


Figure B.38: Temperature at the free surface for Exp 2.02.

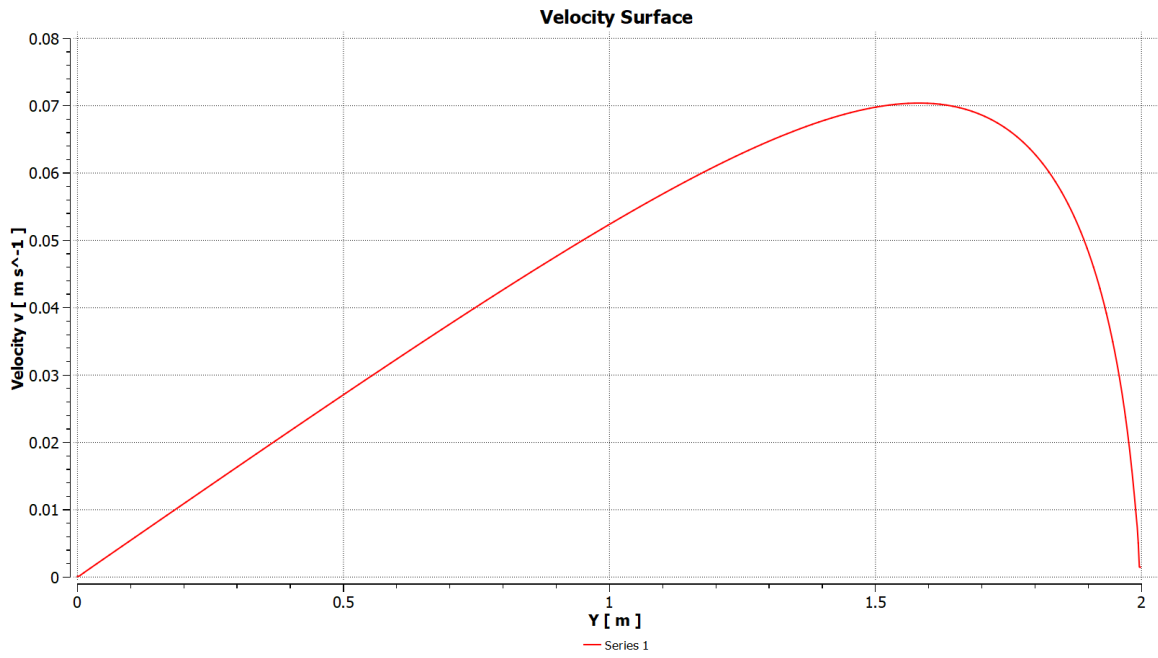


Figure B.39: Velocity at the free surface for Exp 2.02.

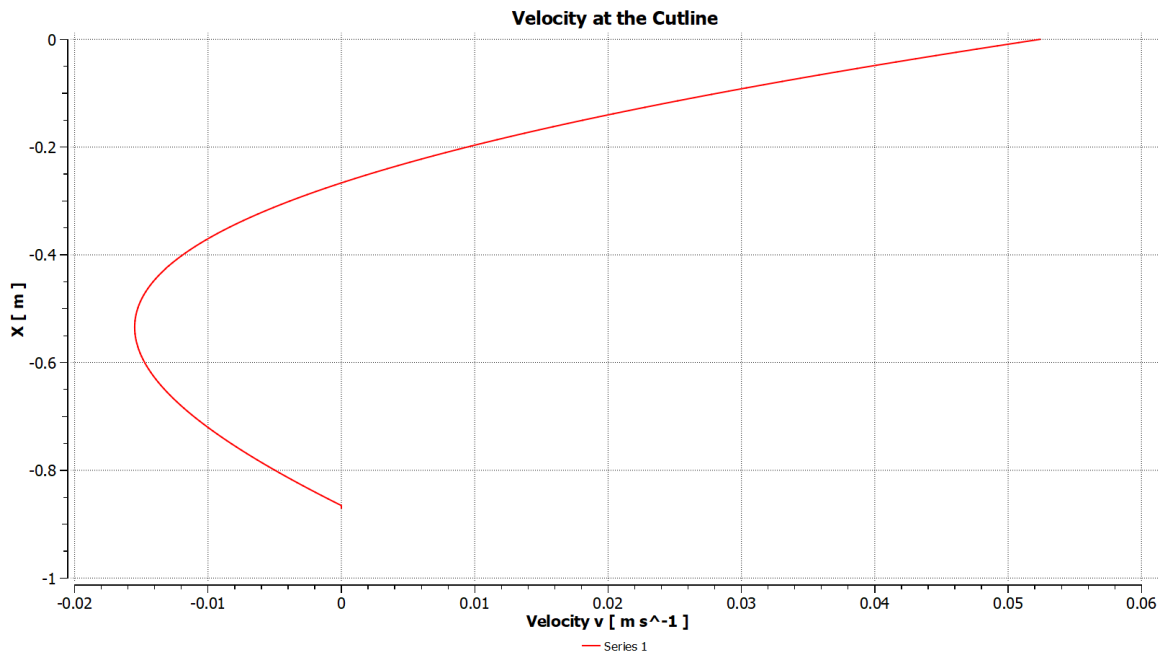


Figure B.40: Radial velocity u at the cutline at $r^*=1$ for Exp 2.02.

Exp 2.1

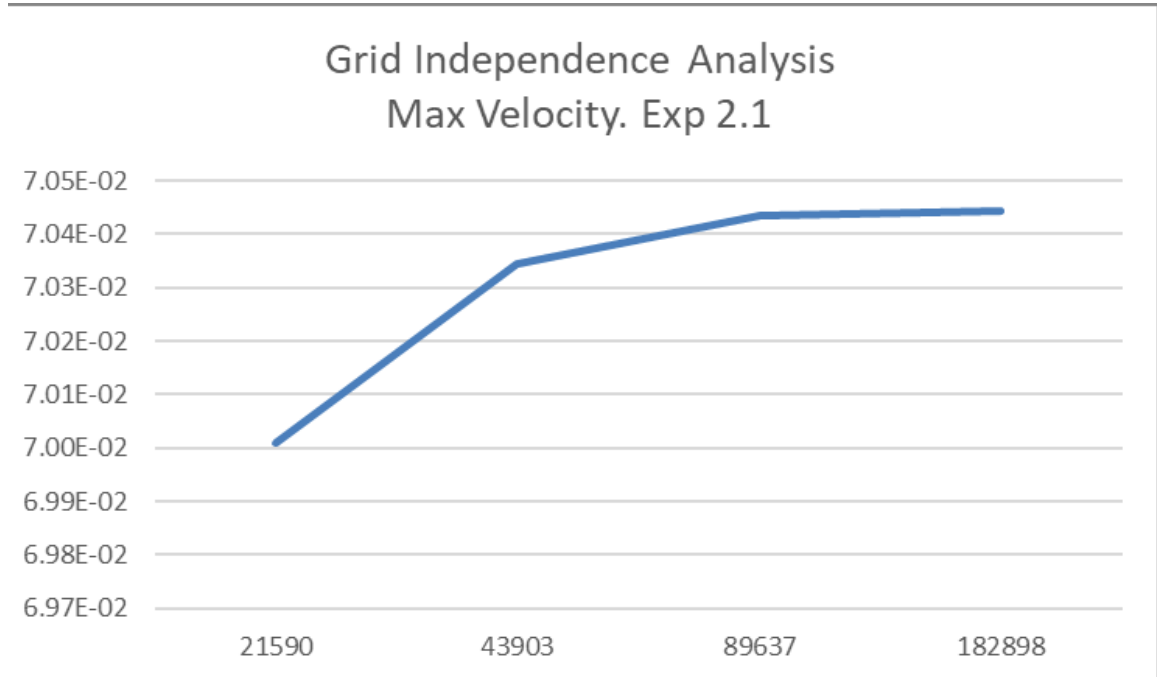


Figure B.41: Convergence for Exp 2.1: peak velocity values vs number of nodes in logarithmic scale.

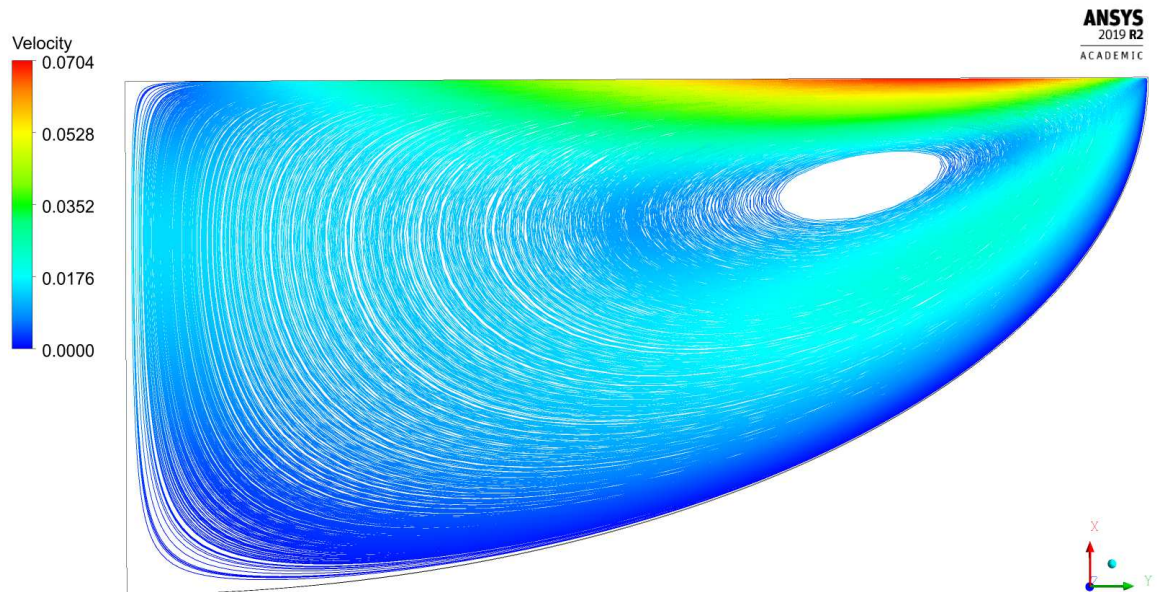


Figure B.42: Streamlines for Exp 2.1.

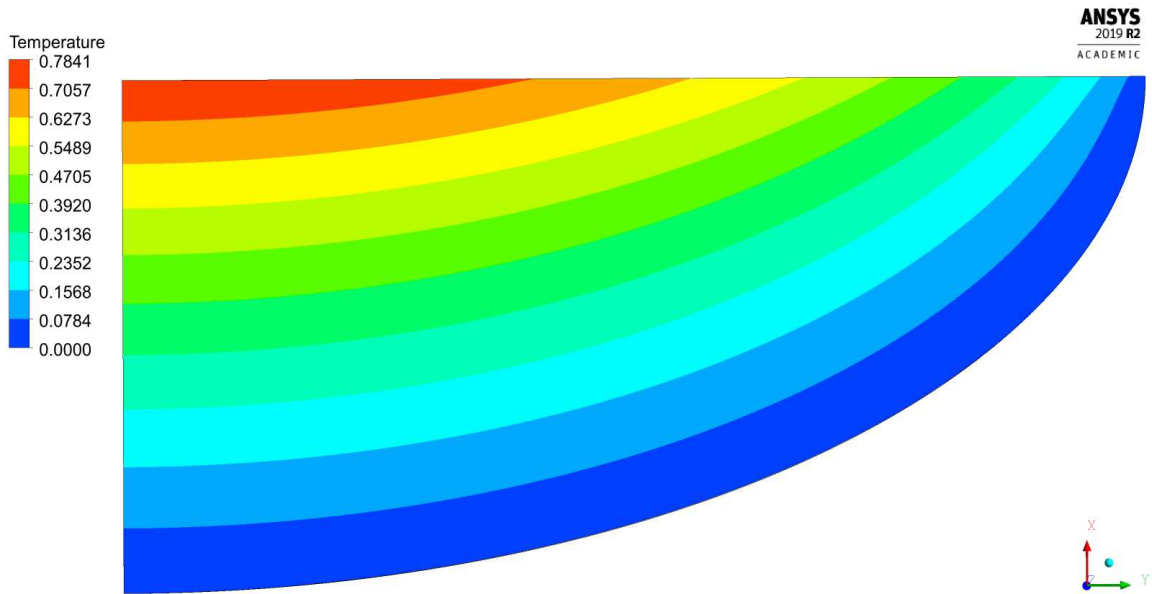


Figure B.43: Temperature field for Exp 2.1.

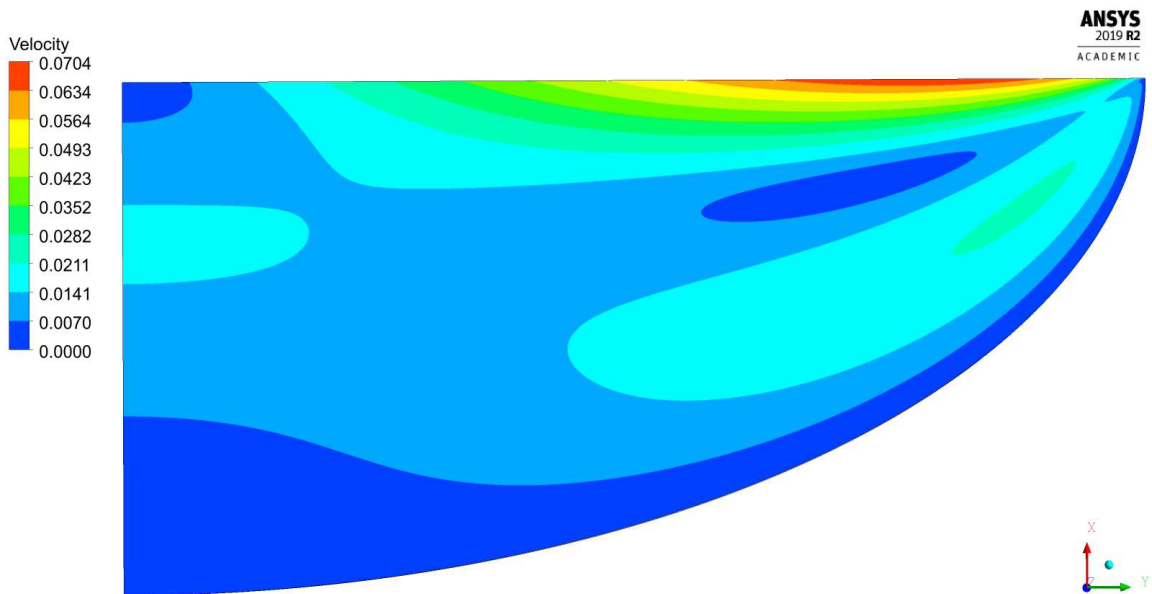


Figure B.44: Velocity magnitude contour for Exp 2.1.

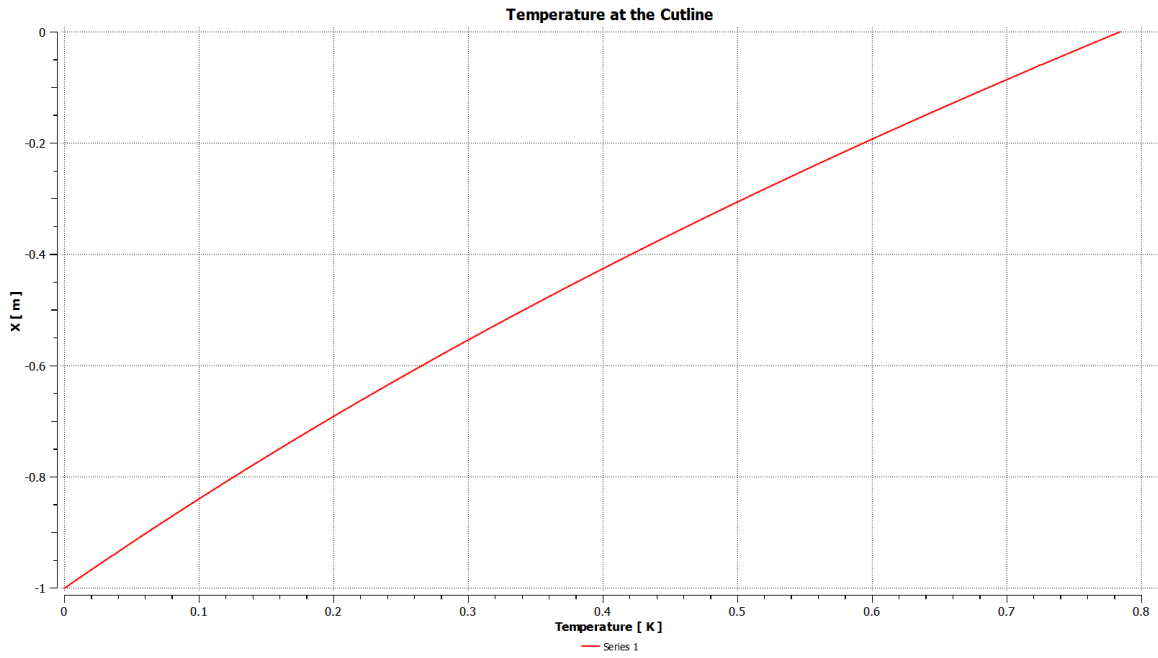


Figure B.45: Temperature at the axis of symmetry for Exp 2.1.

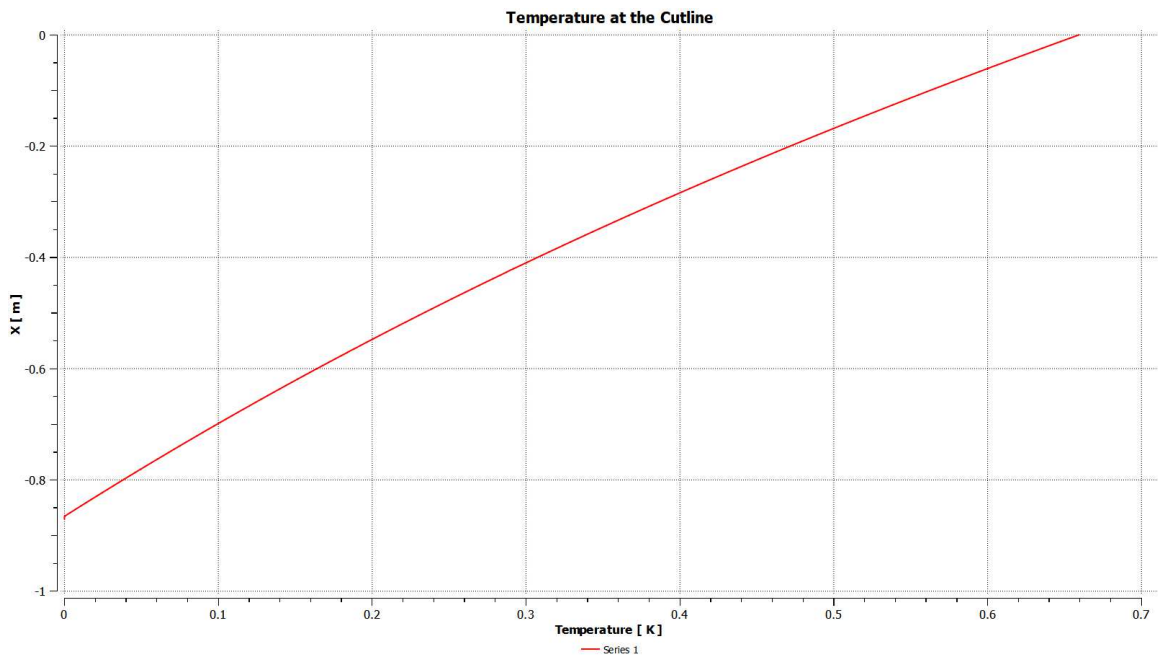


Figure B.46: Temperature at the cutline at $r^*=1$ for Exp 2.1.

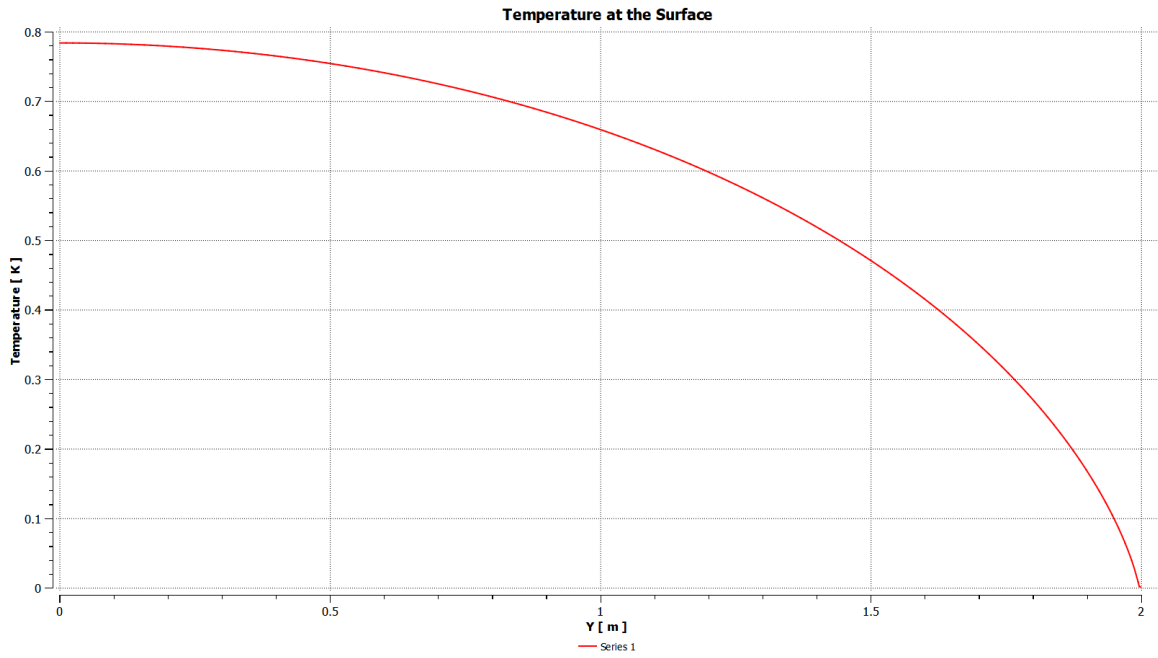


Figure B.47: Temperature at the free surface for Exp 2.1.

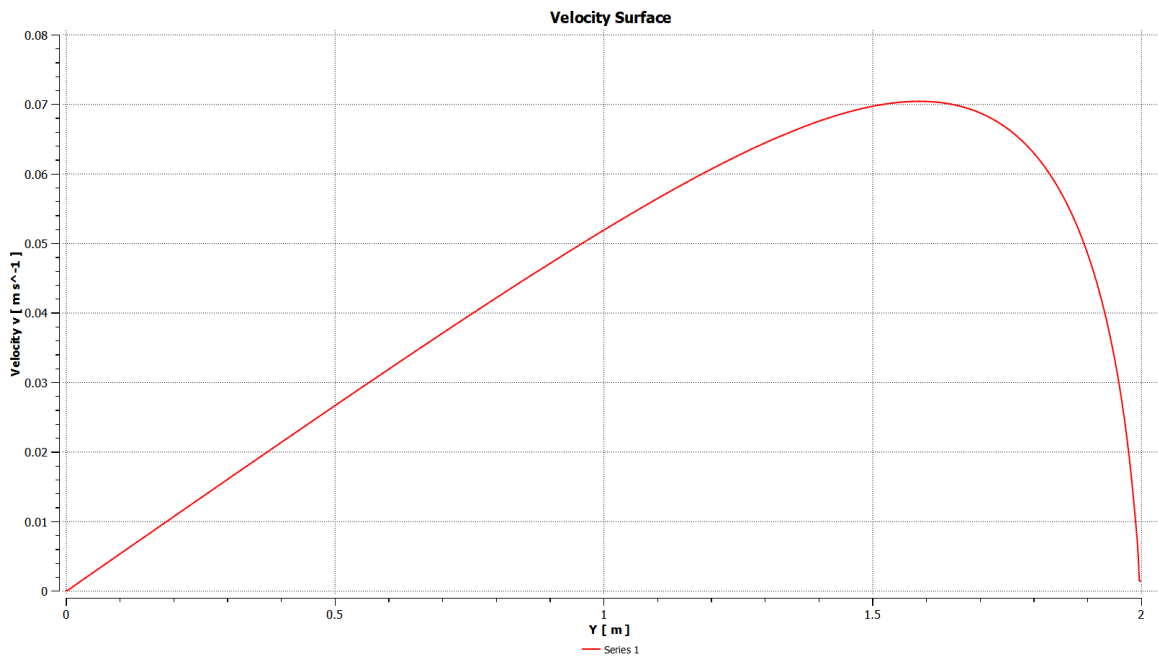


Figure B.48: Velocity at the free surface for Exp 2.1.

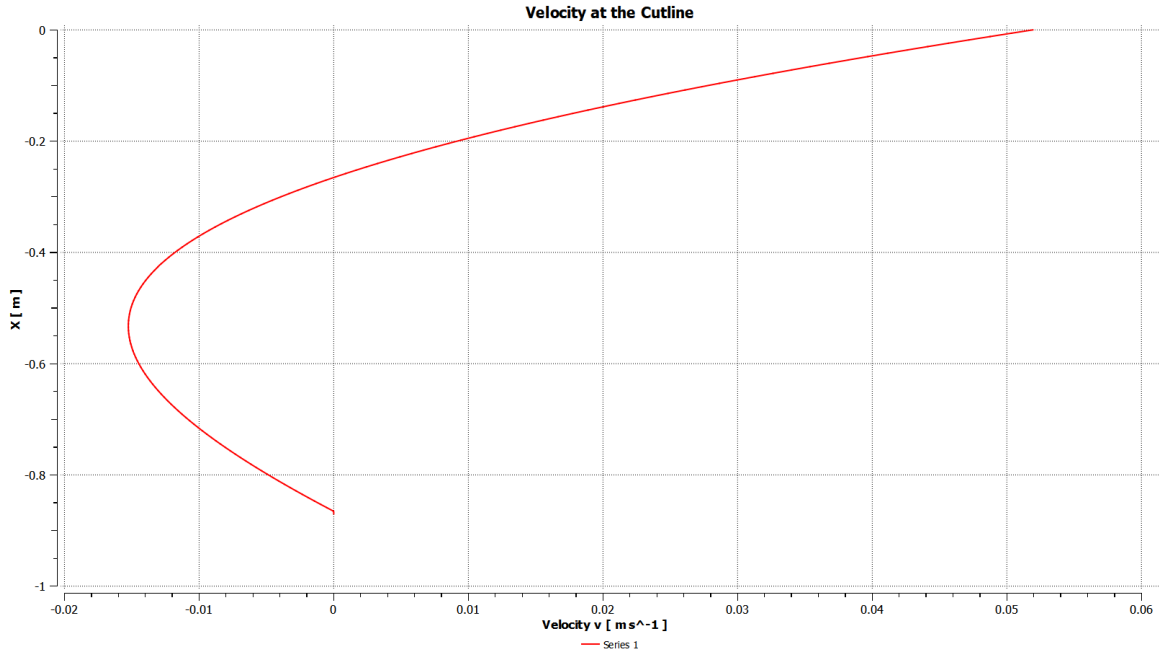


Figure B.49: Radial velocity u at the cutline at $r^*=1$ for Exp 2.1.

Exp 2.2

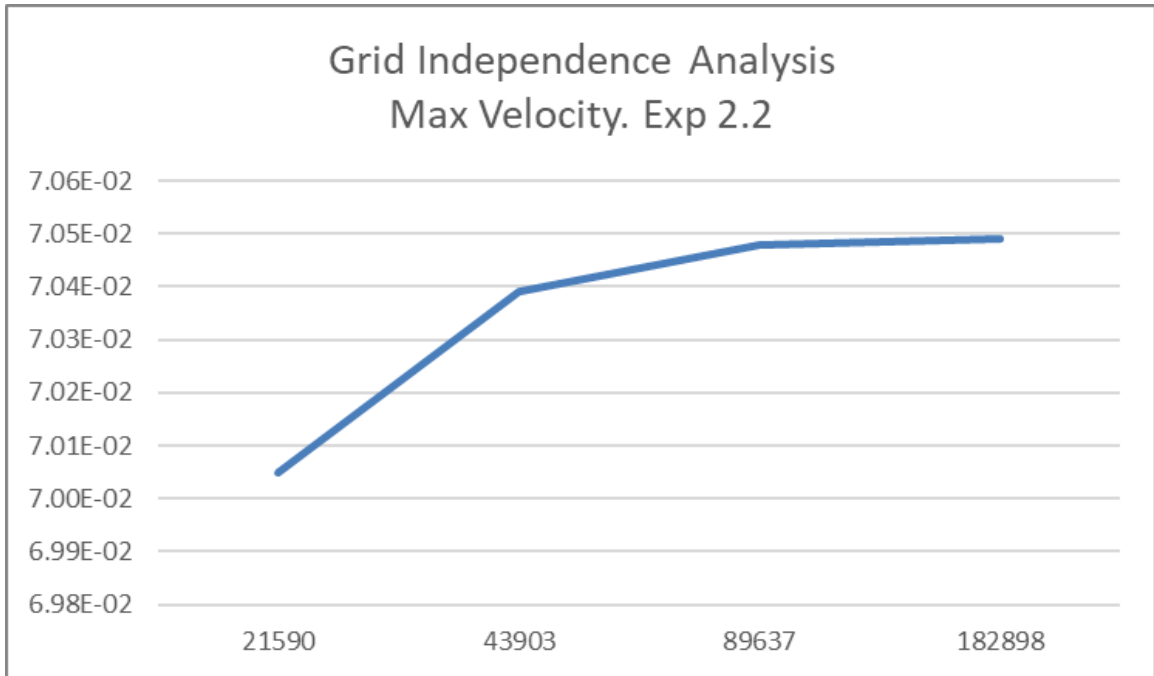


Figure B.50: Convergence for Exp 2.2: peak velocity values vs number of nodes in logarithmic scale.

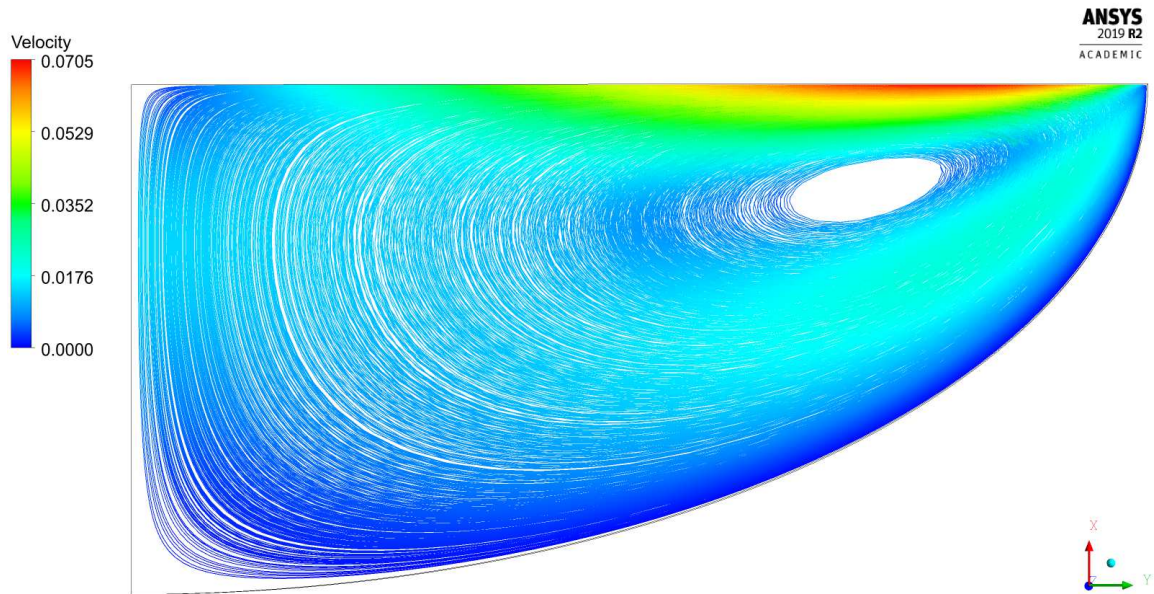


Figure B.51: Streamlines for Exp 2.2.

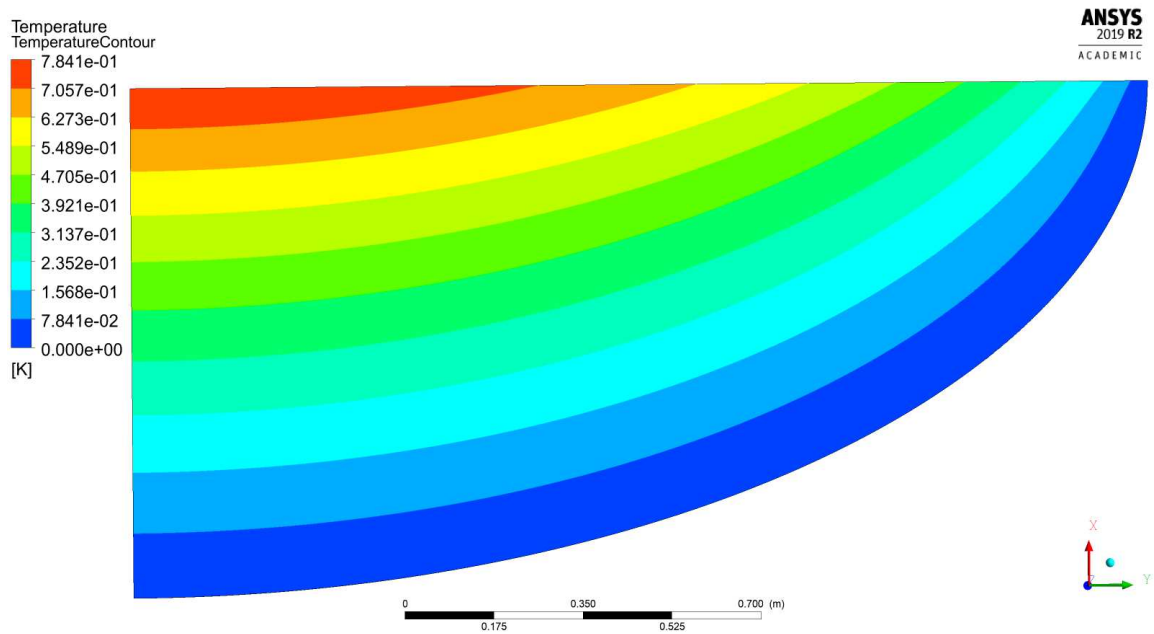


Figure B.52: Temperature field for Exp 2.2.

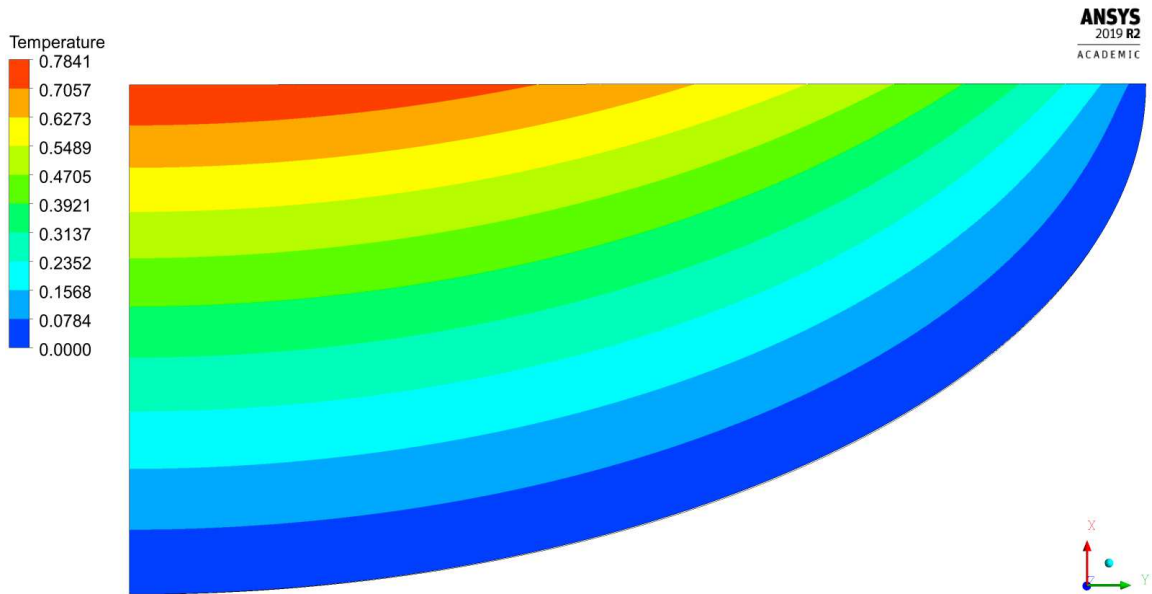


Figure B.53: Velocity magnitude contour for Exp 2.2.

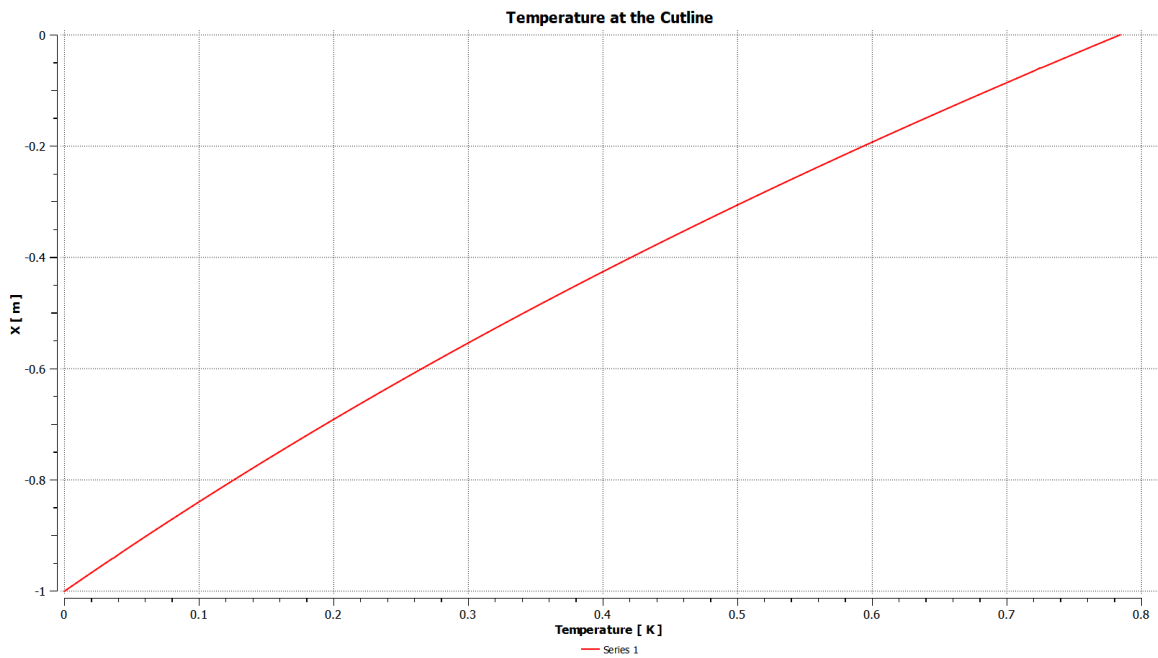


Figure B.54: Temperature at the axis of symmetry for Exp 2.2.

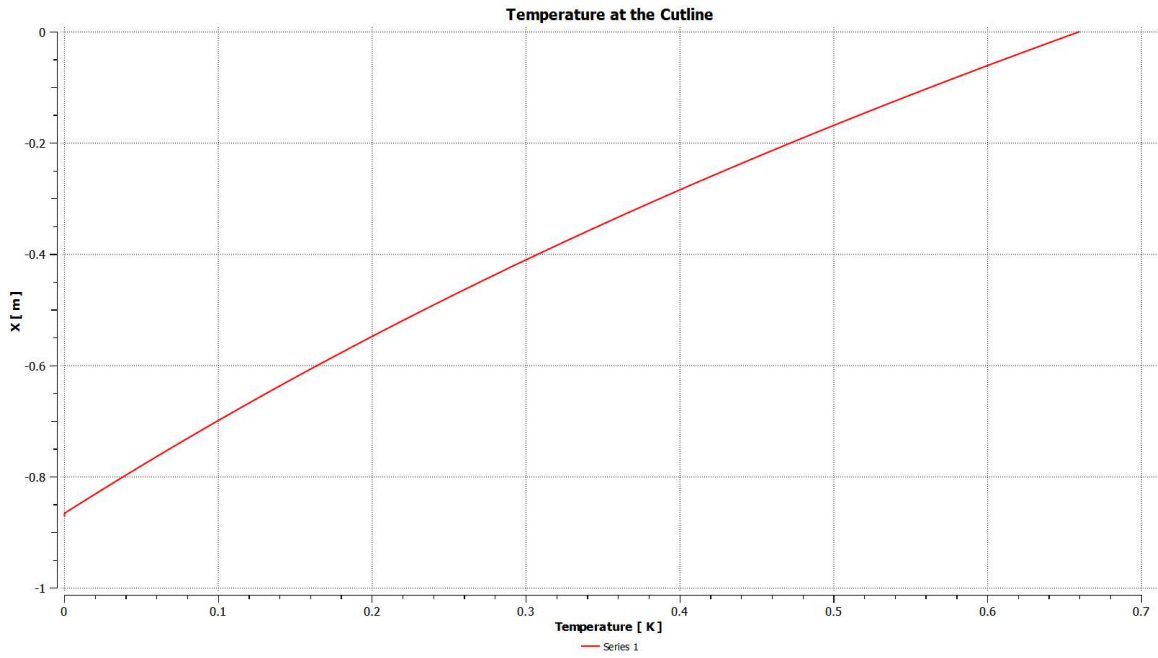


Figure B.55: Temperature at the cutline at $r^*=1$ for Exp 2.2.

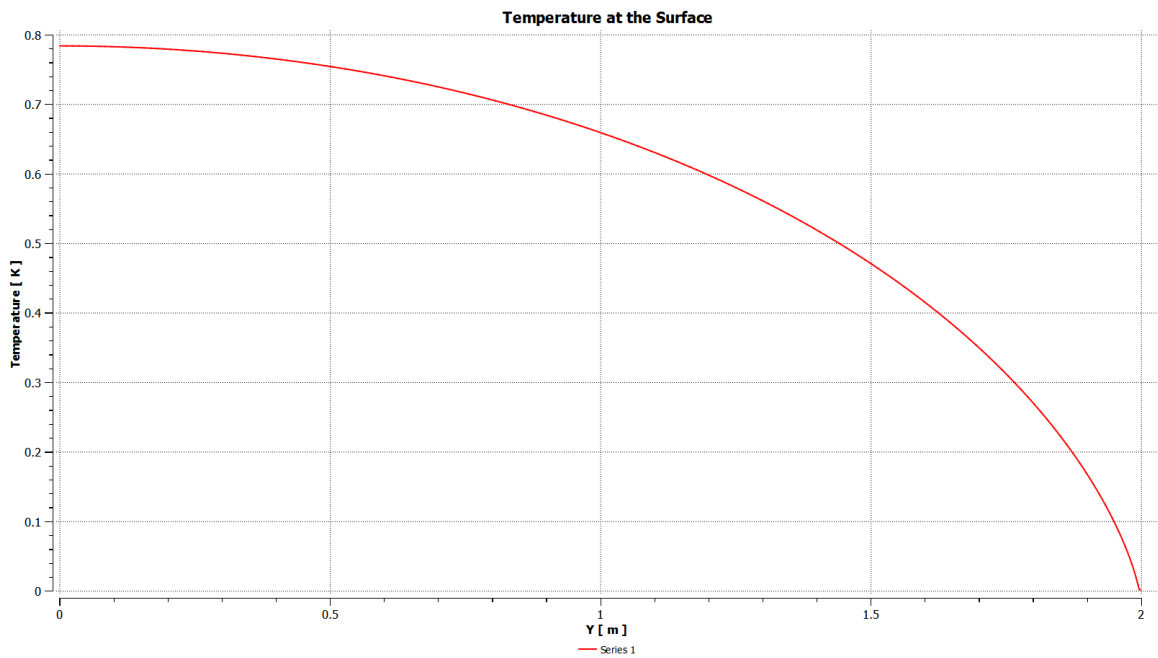


Figure B.56: Temperature at the free surface for Exp 2.2.

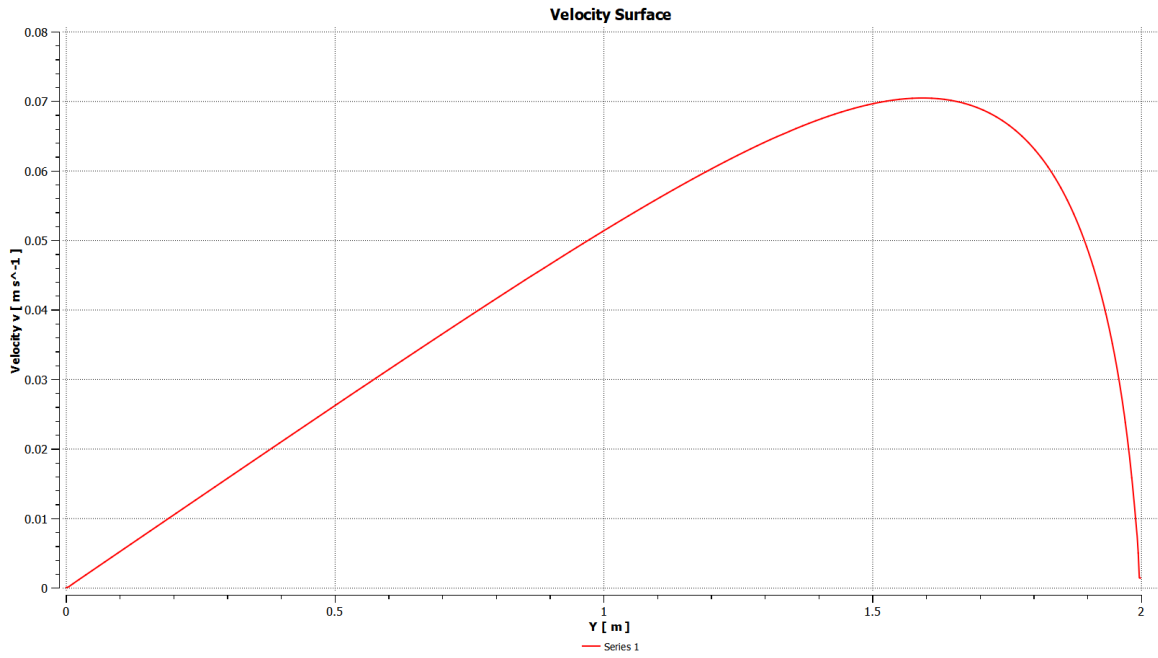


Figure B.57: Velocity at the free surface for Exp 2.2.

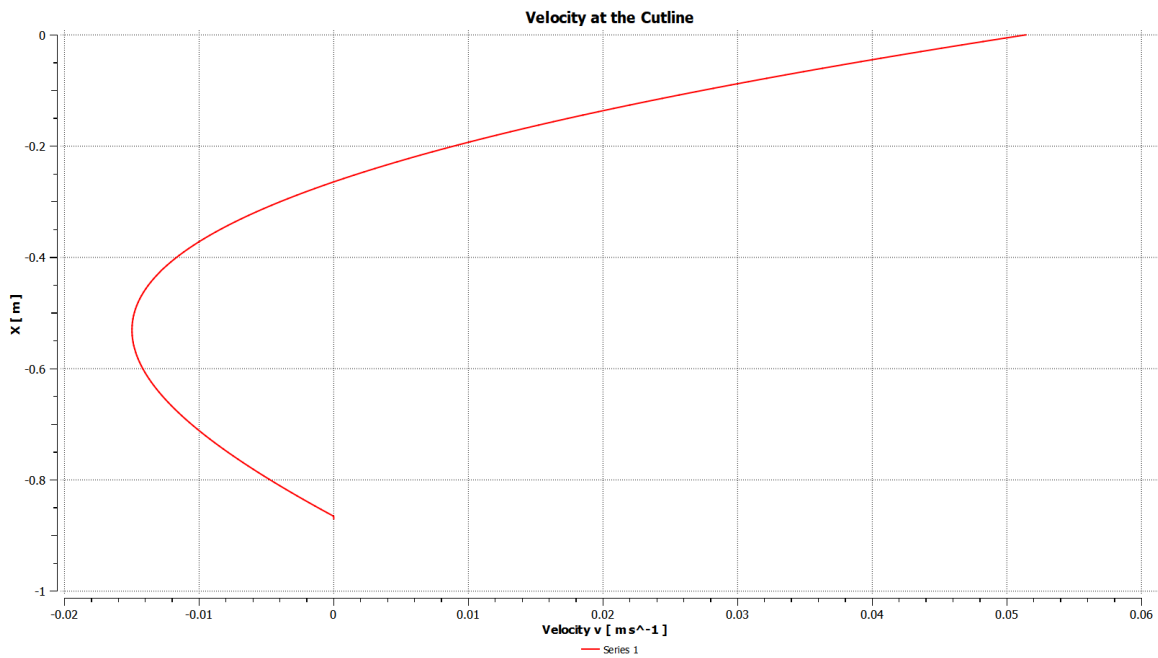


Figure B.58: Radial velocity u at the cutline at $r^*=1$ for Exp 2.2.

Exp 2.3

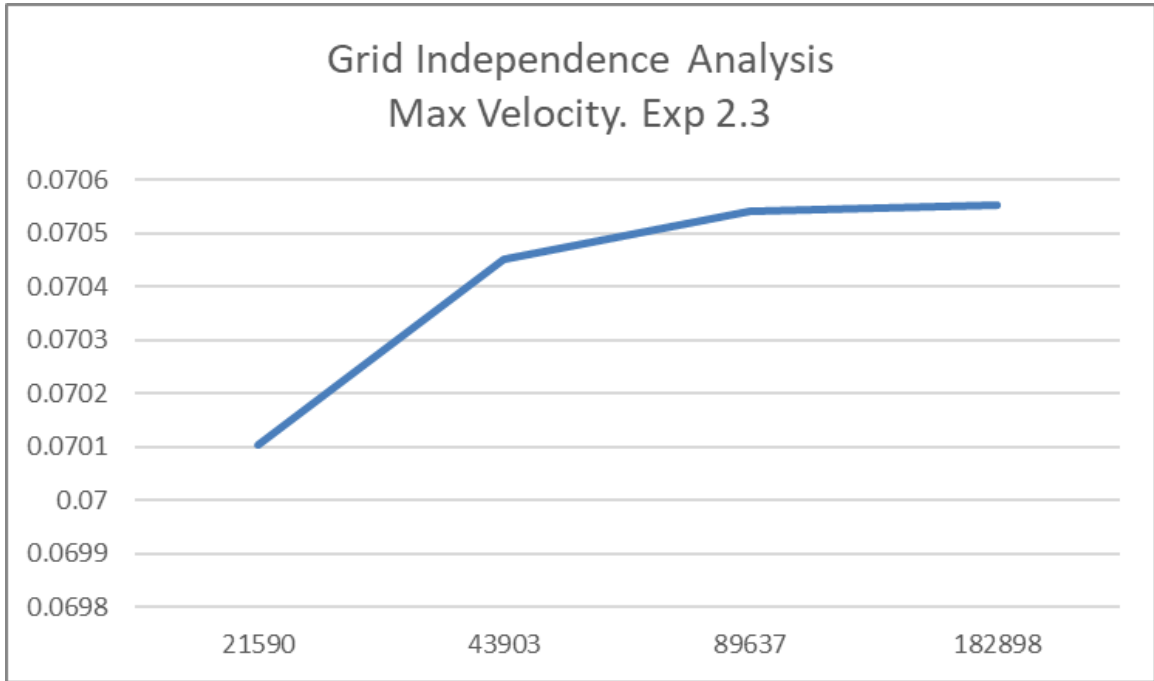


Figure B.59: Convergence for Exp 2.3: peak velocity values vs number of nodes in logarithmic scale.

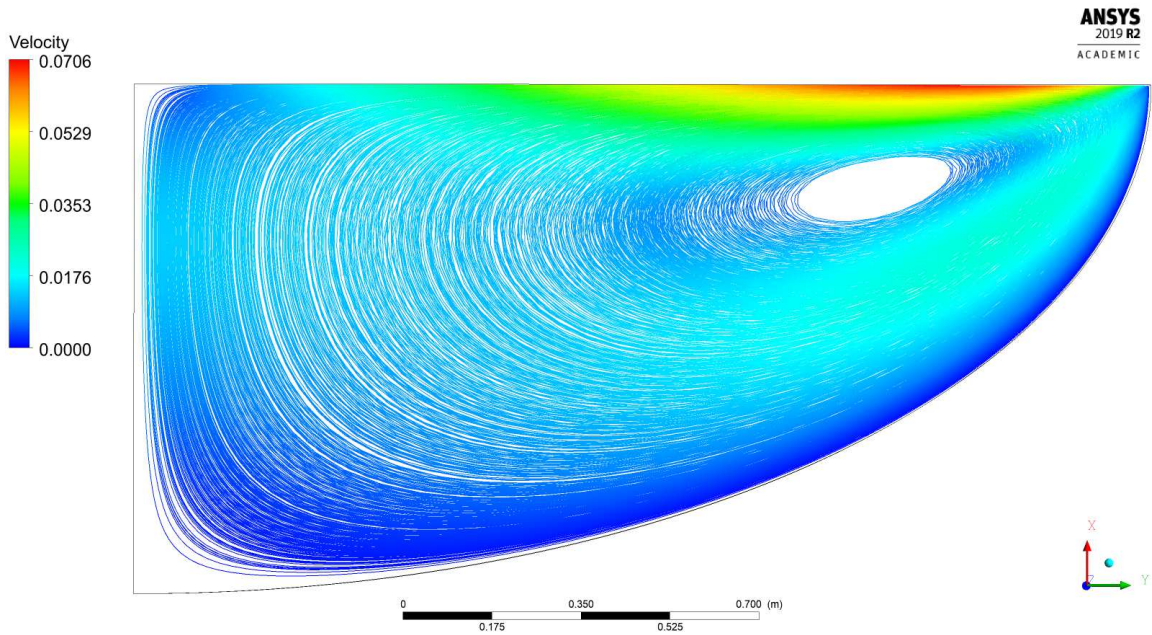


Figure B.60: Streamlines for Exp 2.3.

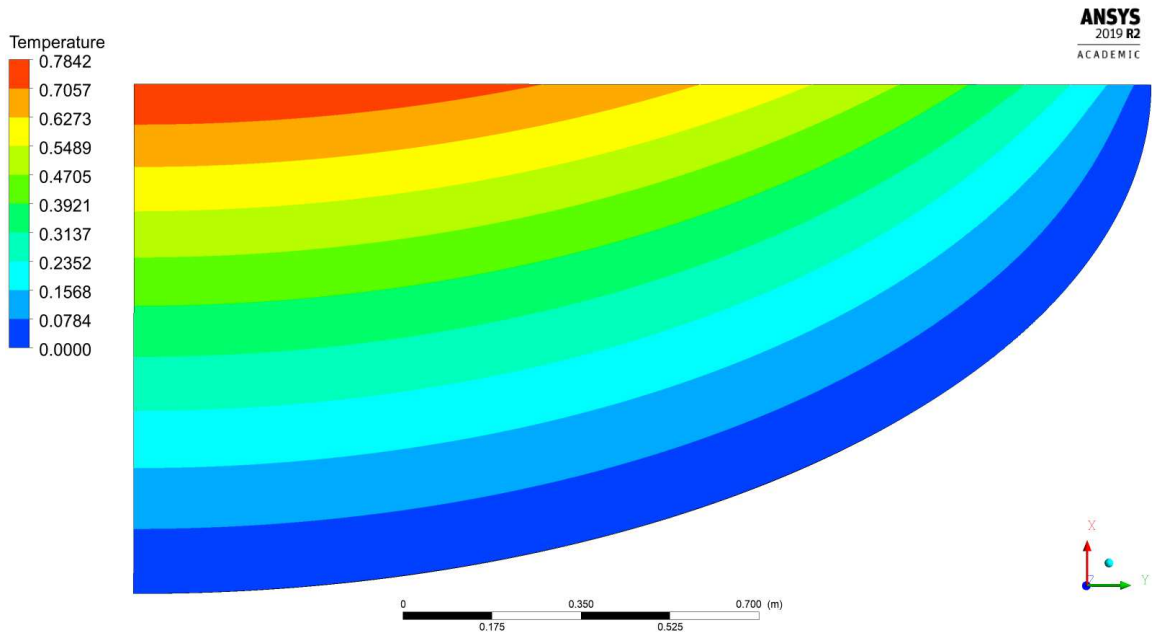


Figure B.61: Temperature field for Exp 2.3.

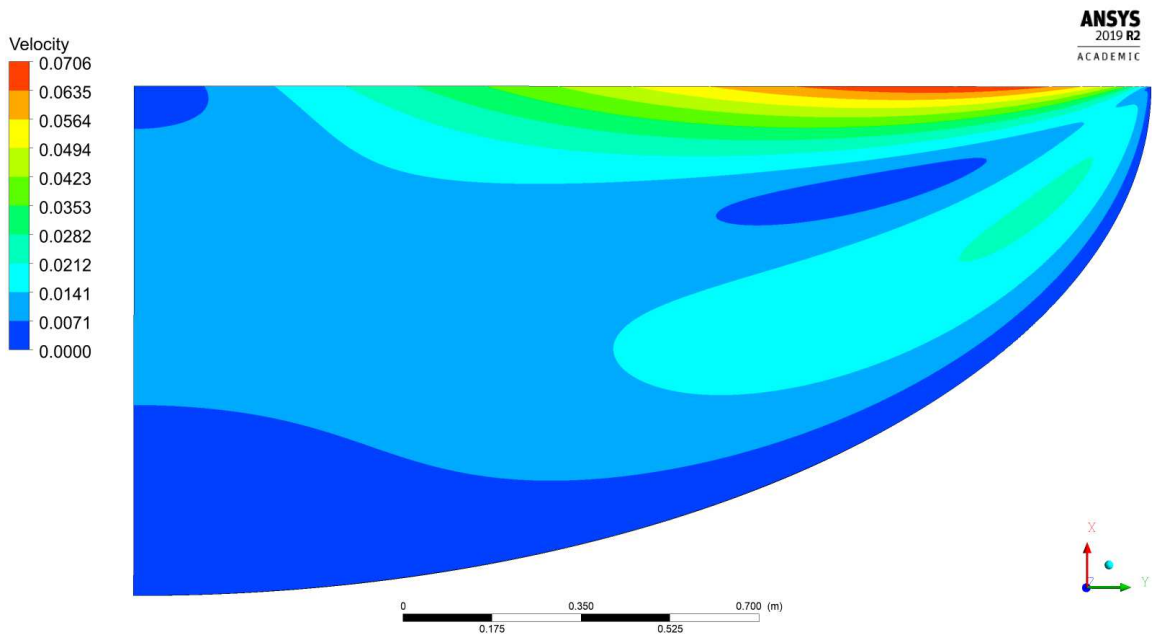


Figure B.62: Velocity magnitude contour for Exp 2.3.

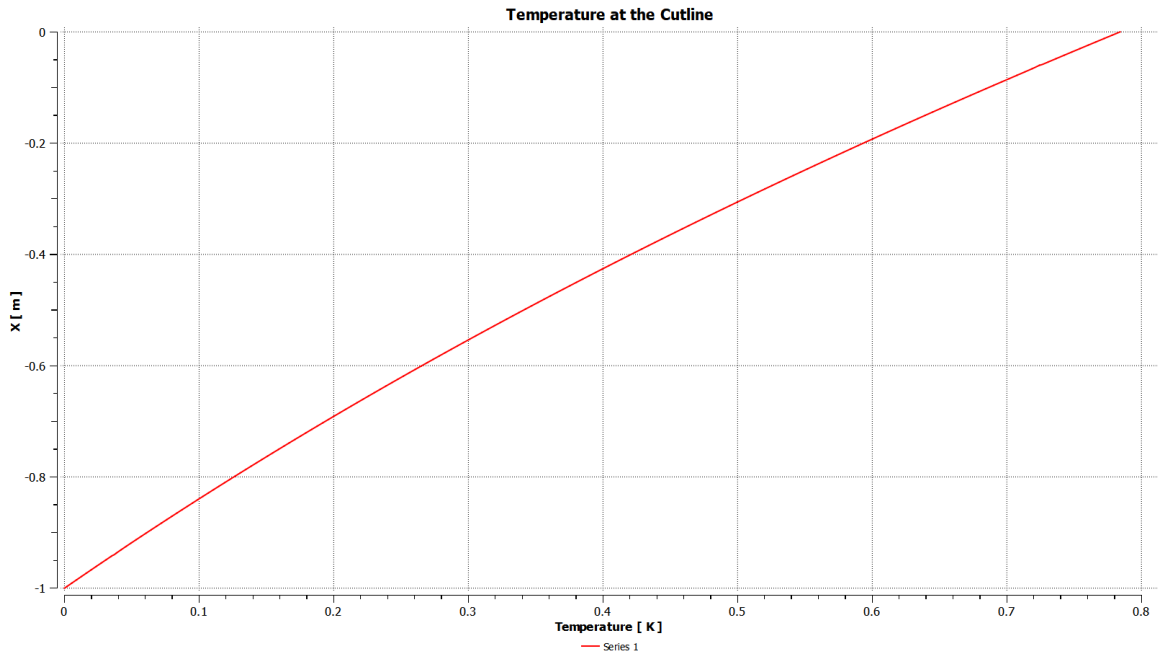


Figure B.63: Temperature at the axis of symmetry for Exp 2.3.

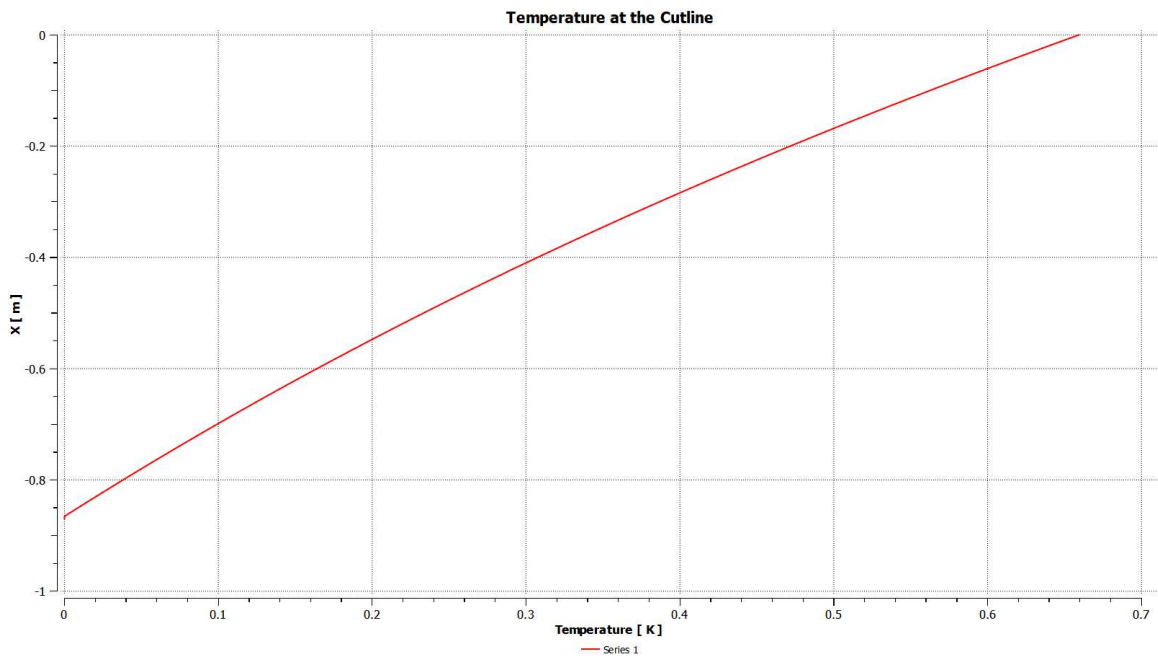


Figure B.64: Temperature at the cutline at $r^*=1$ for Exp 2.3.

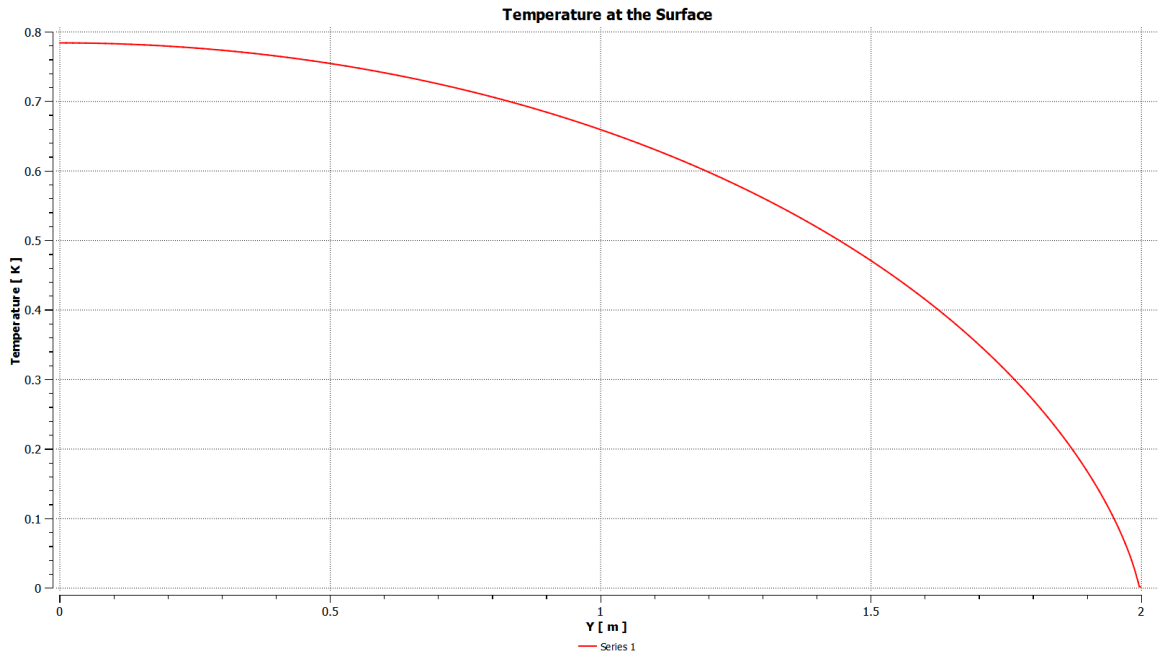


Figure B.65: Temperature at the free surface for Exp 2.3.

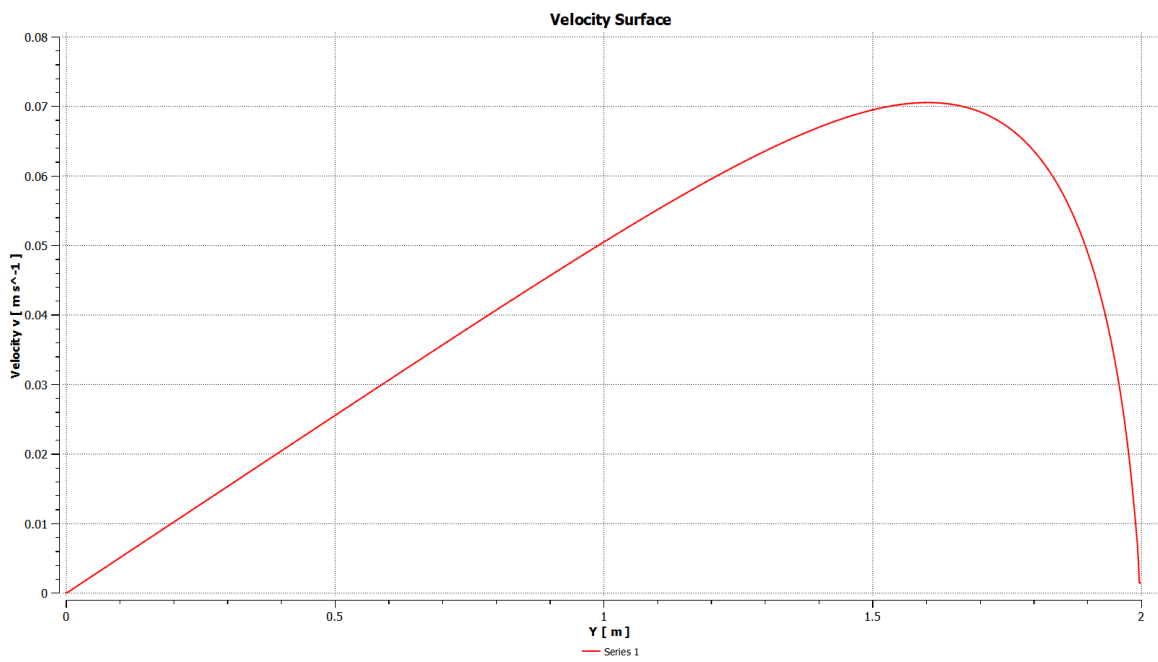


Figure B.66: Velocity at the free surface for Exp 2.3.

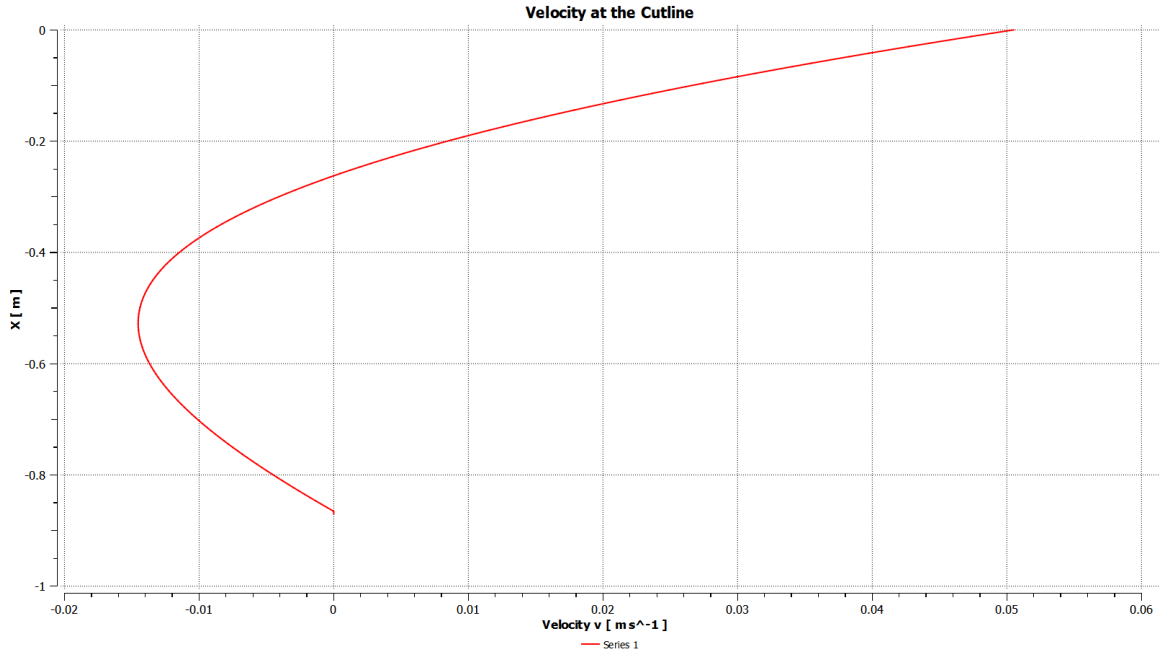


Figure B.67: Radial velocity u at the cutline at $r^*=1$ for Exp 2.3.

Exp 2.4

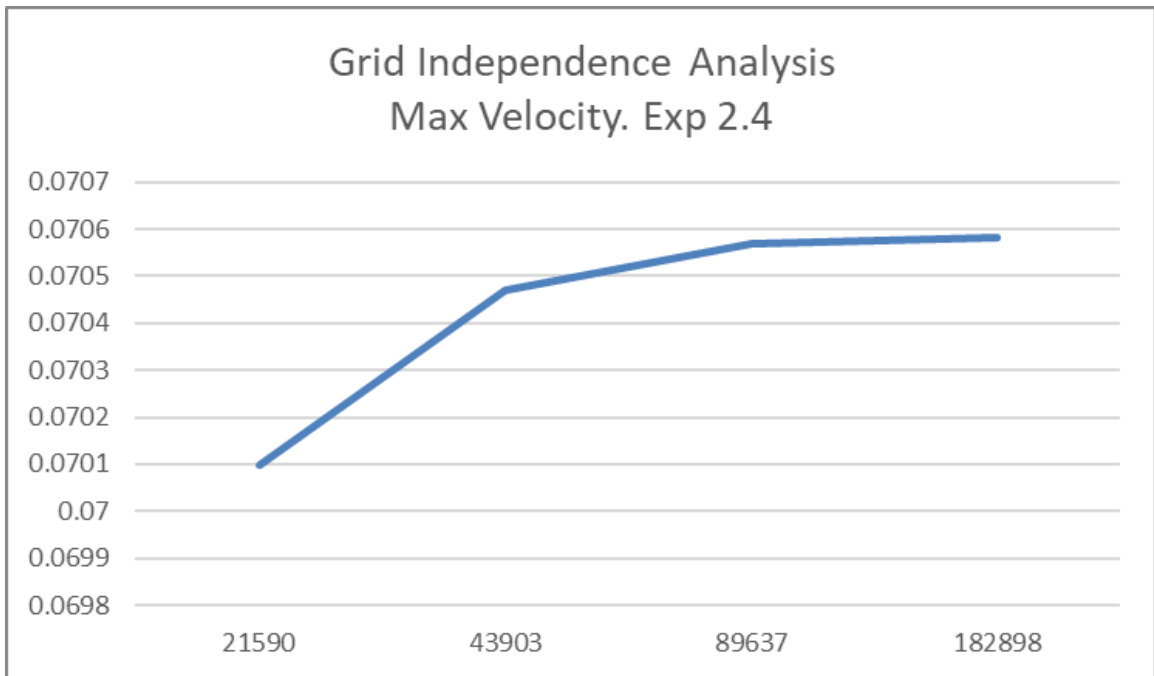


Figure B.68: Convergence for Exp 2.4: peak velocity values vs number of nodes in logarithmic scale.

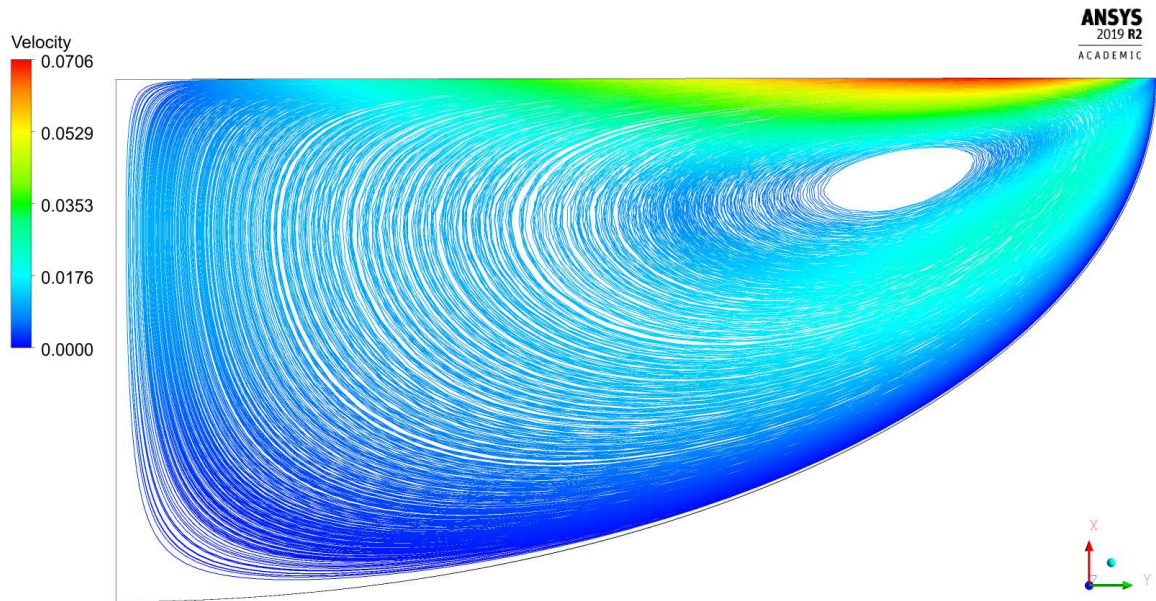


Figure B.69: Streamlines for Exp 2.4.

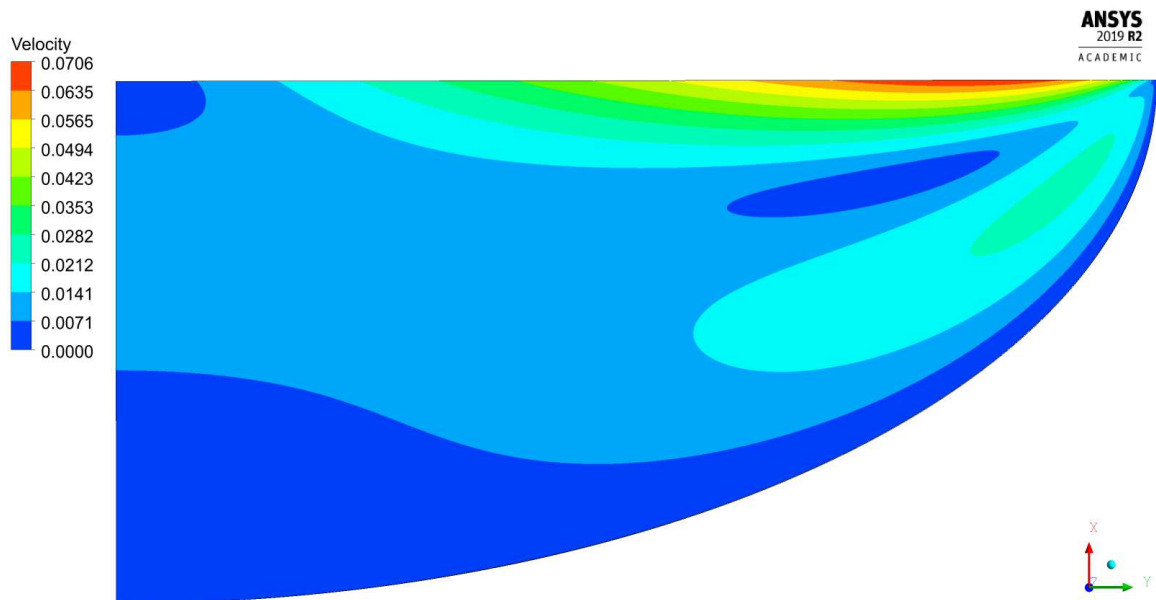


Figure B.70: Temperature field for Exp 2.4.

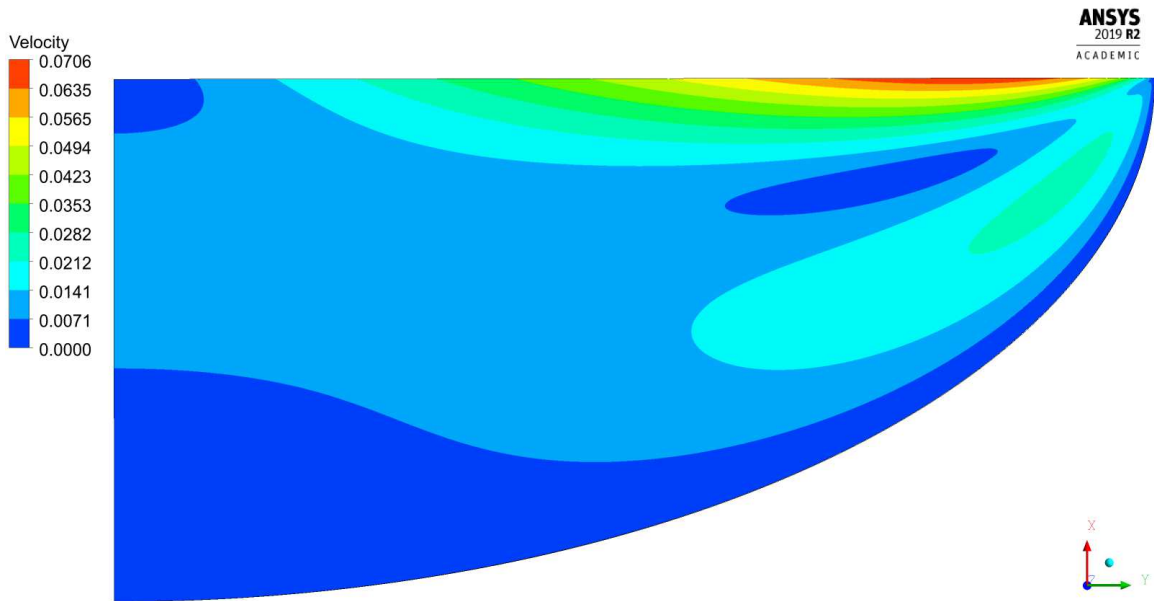


Figure B.71: Velocity magnitude contour for Exp 2.4.

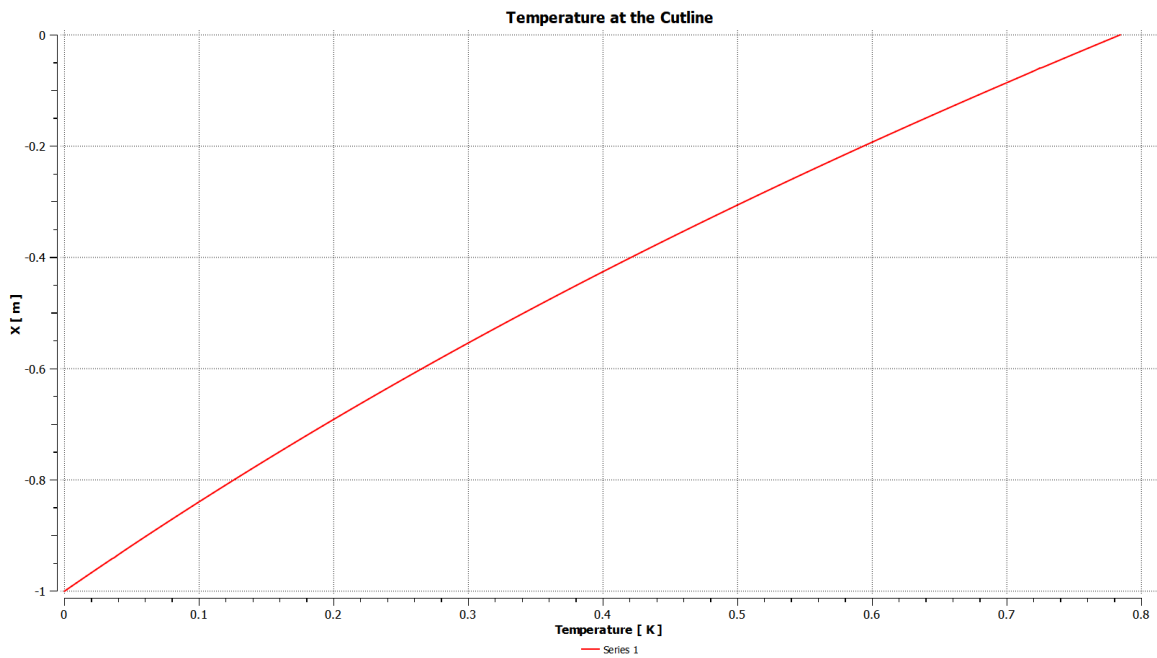


Figure B.72: Temperature at the axis of symmetry for Exp 2.4.

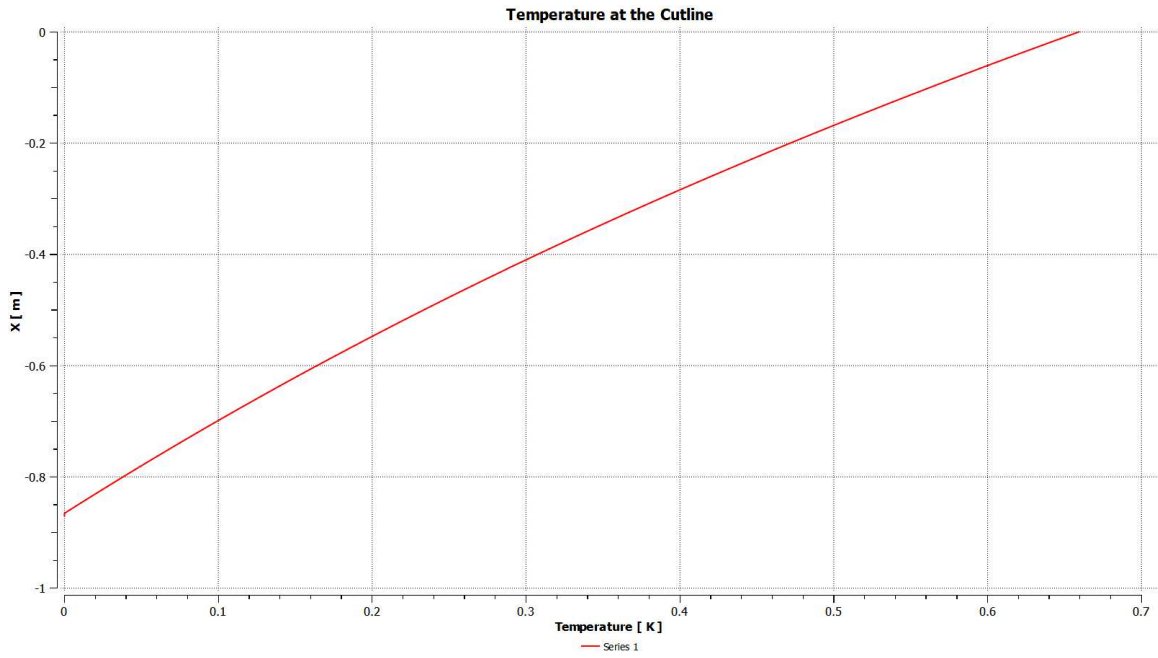


Figure B.73: Temperature at the cutline at $r^*=1$ for Exp 2.4.

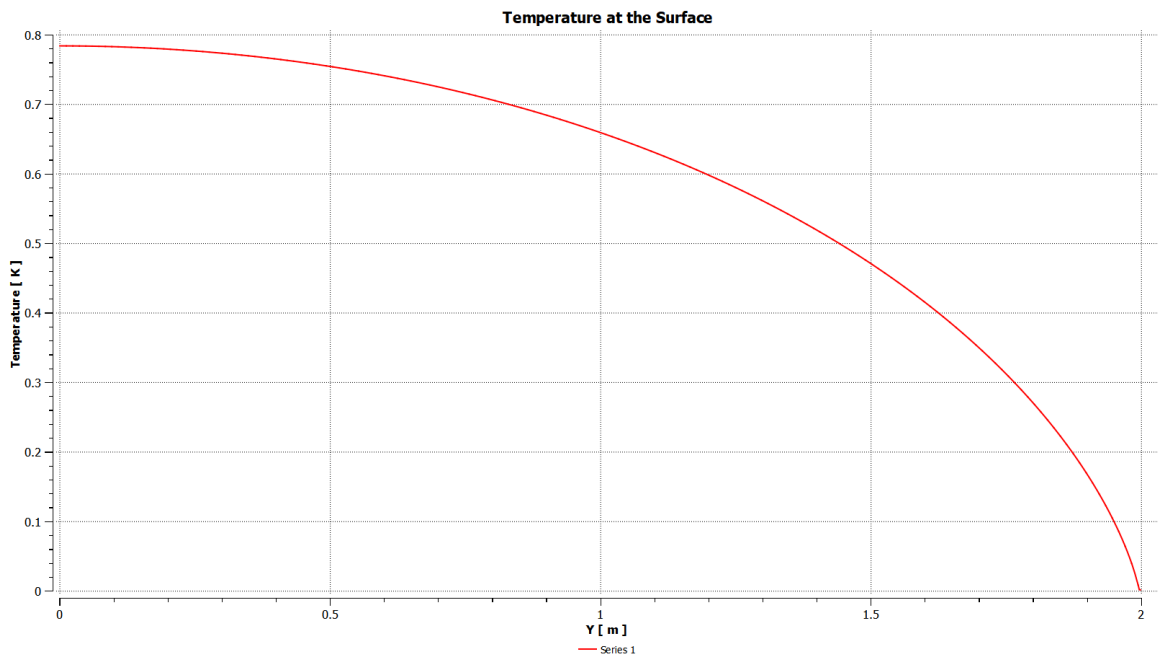


Figure B.74: Temperature at the free surface for Exp 2.4.

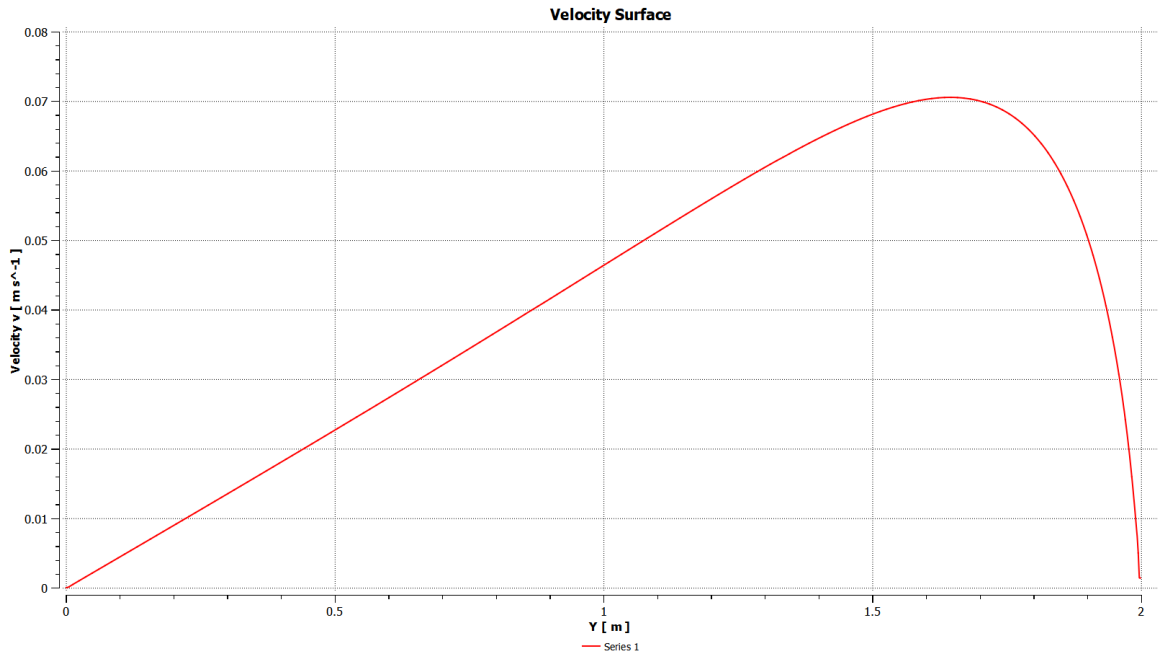


Figure B.75: Velocity at the free surface for Exp 2.4.

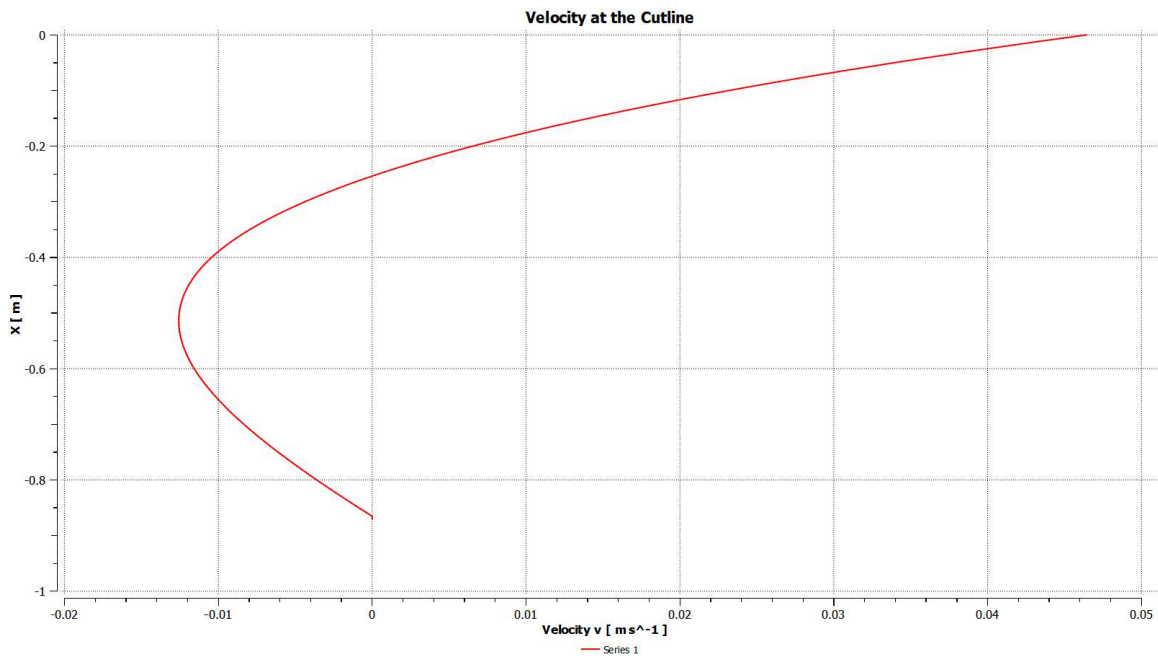


Figure B.76: Radial velocity u at the cutline at $r^*=1$ for Exp 2.4.

Exp 2.5

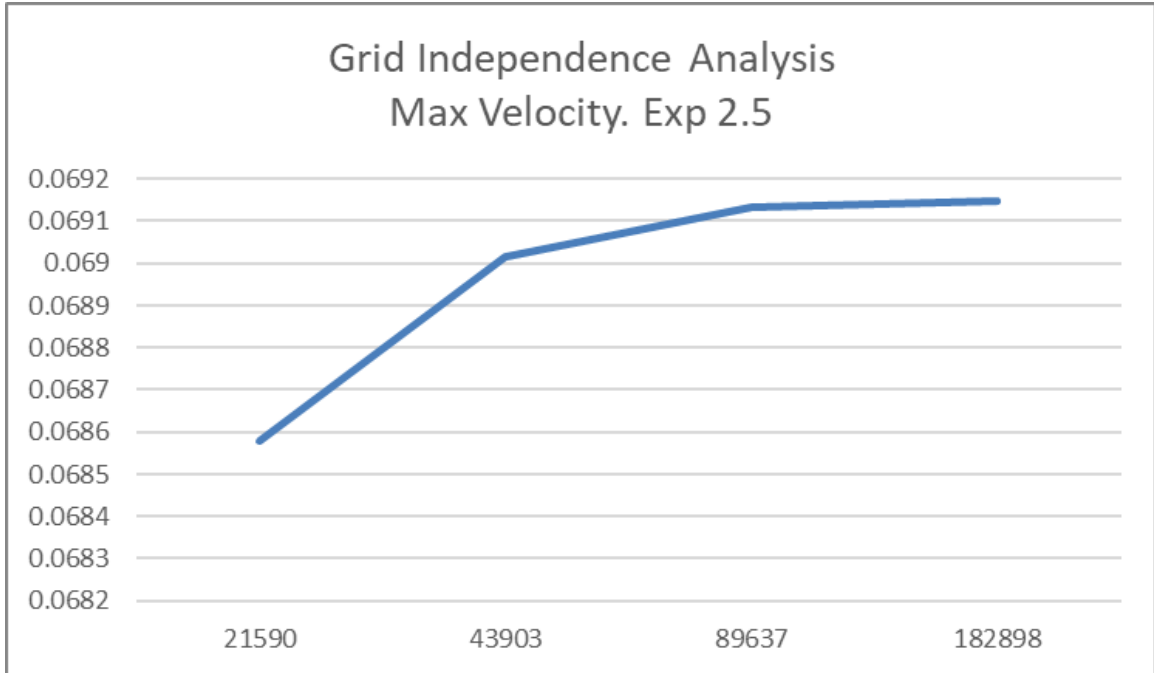


Figure B.77: Convergence for Exp 2.5: peak velocity values vs number of nodes in logarithmic scale.

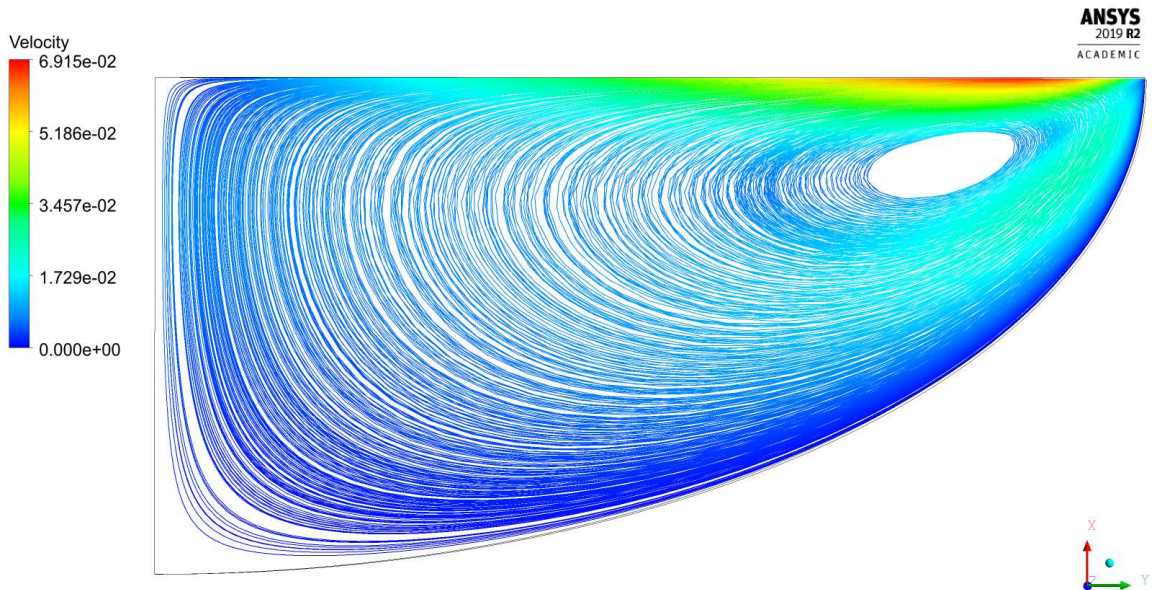


Figure B.78: Streamlines for Exp 2.5.

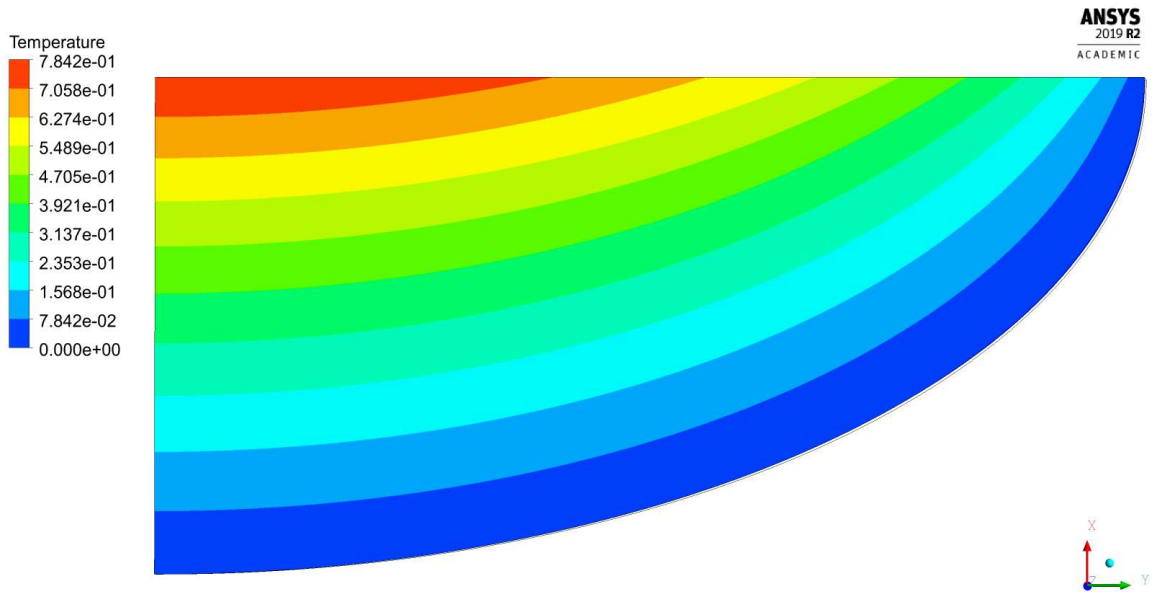


Figure B.79: Temperature field for Exp 2.5.

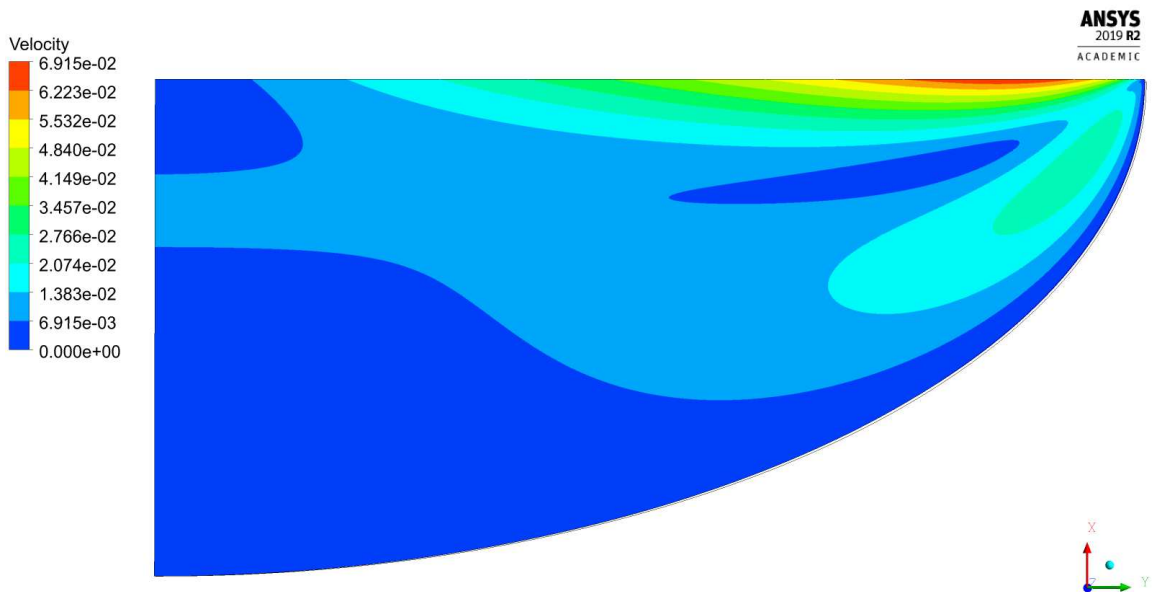


Figure B.80: Velocity magnitude contour for Exp 2.5.

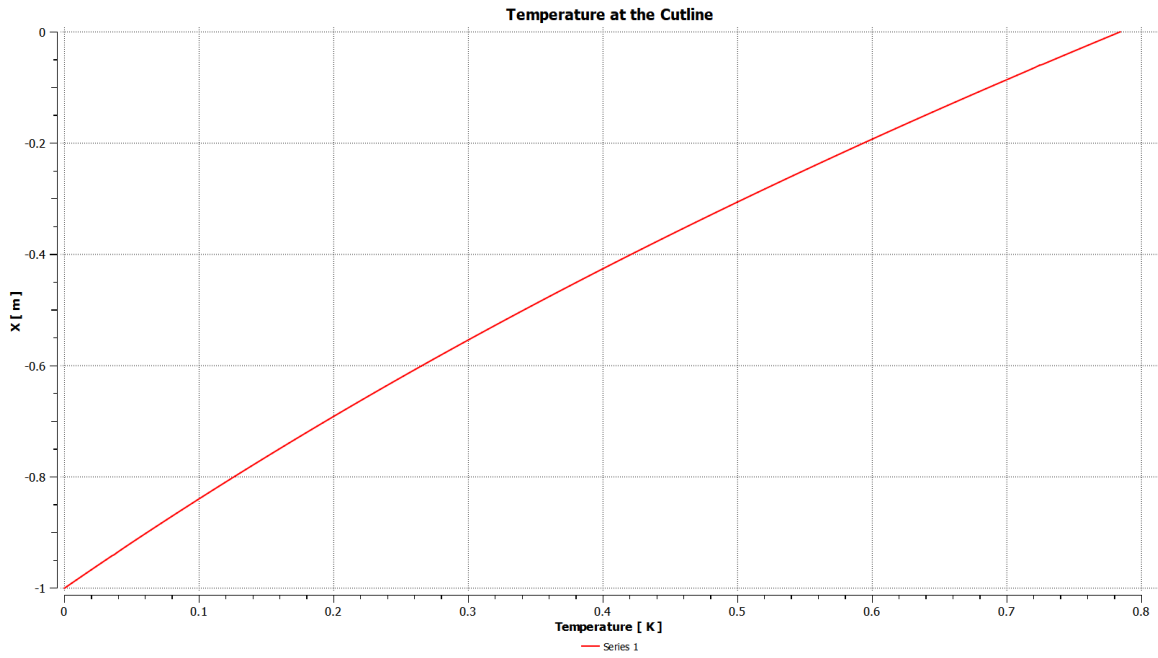


Figure B.81: Temperature at the axis of symmetry for Exp 2.5.

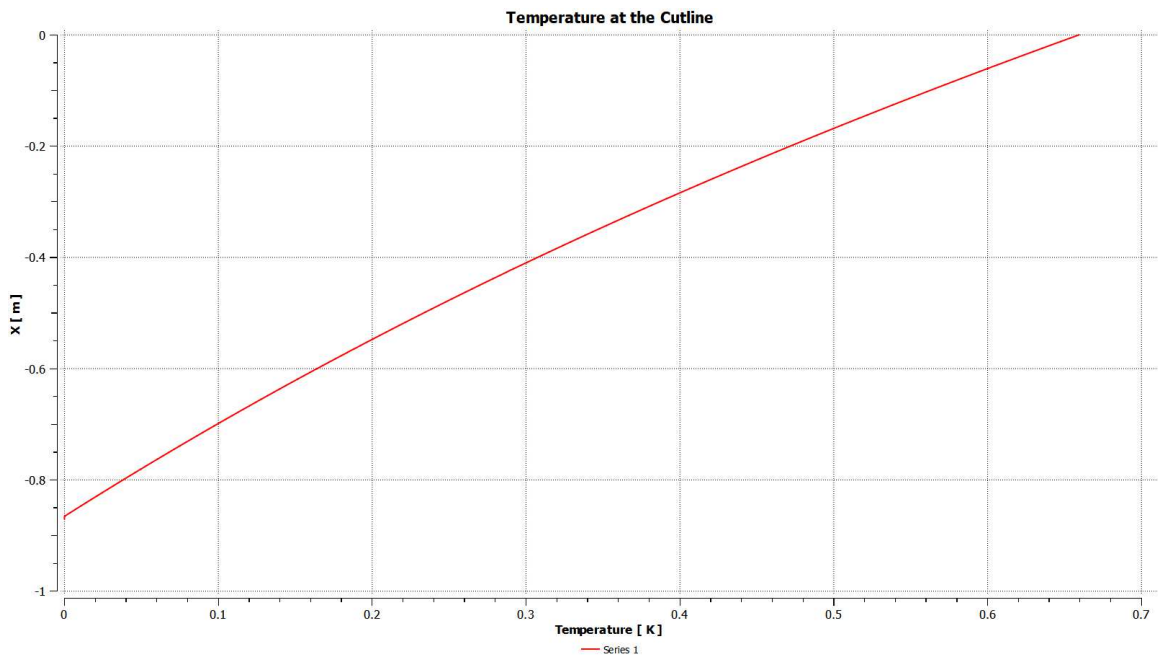


Figure B.82: Temperature at the cutline at $r^*=1$ for Exp 2.5.

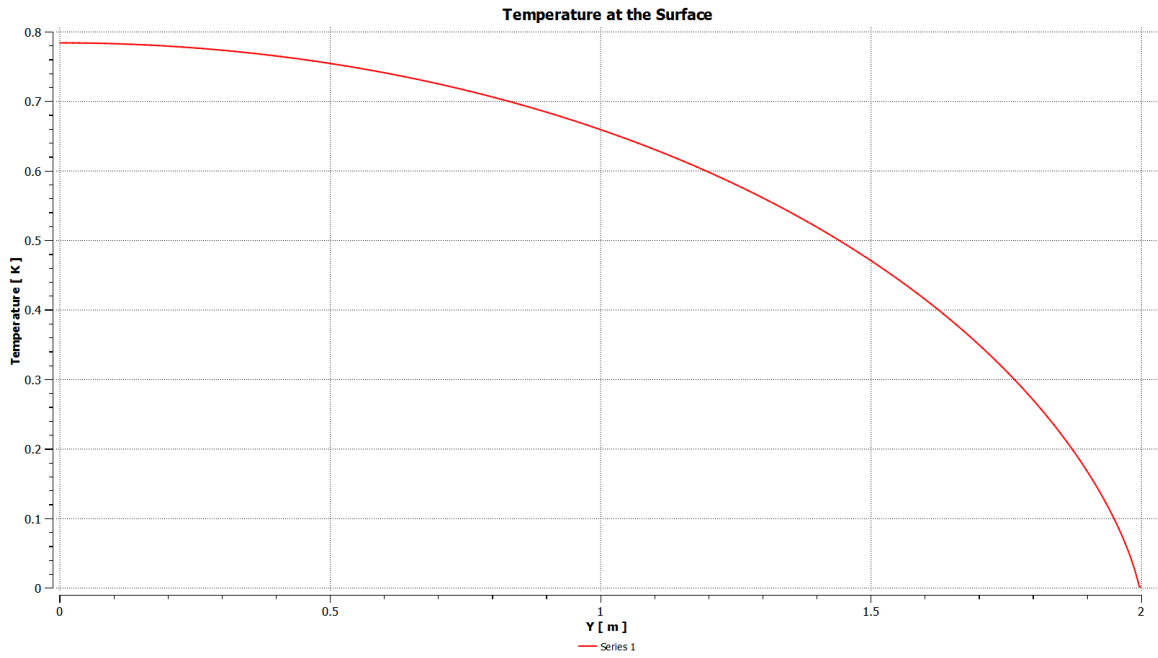


Figure B.83: Temperature at the free surface for Exp 2.5.

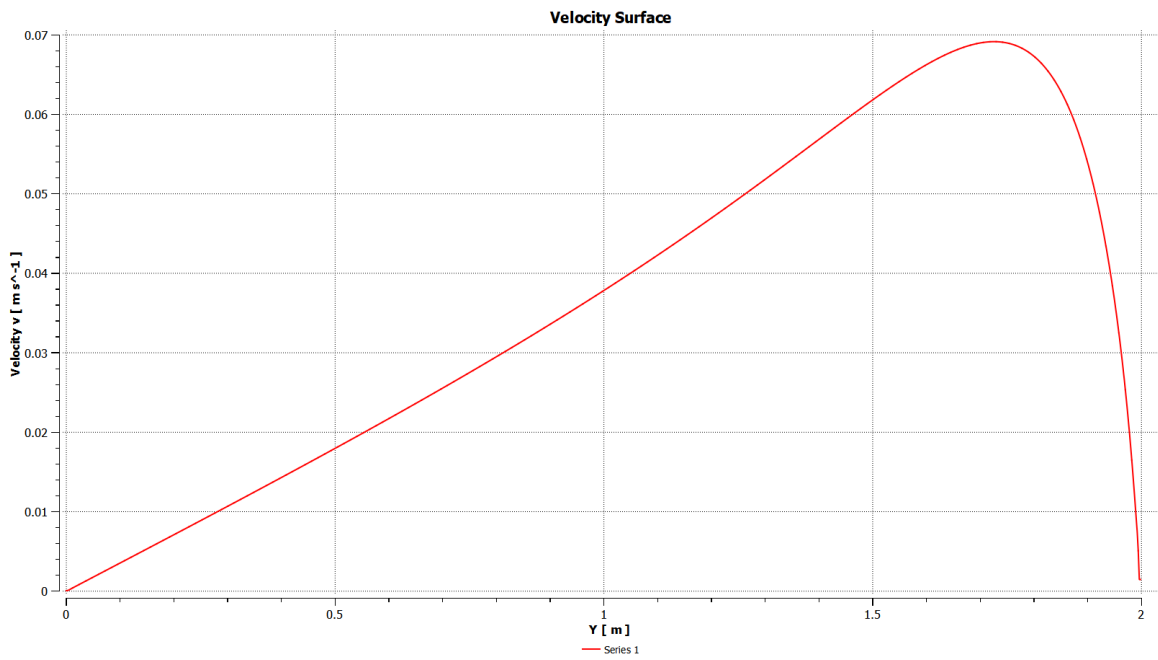


Figure B.84: Velocity at the free surface for Exp 2.5.

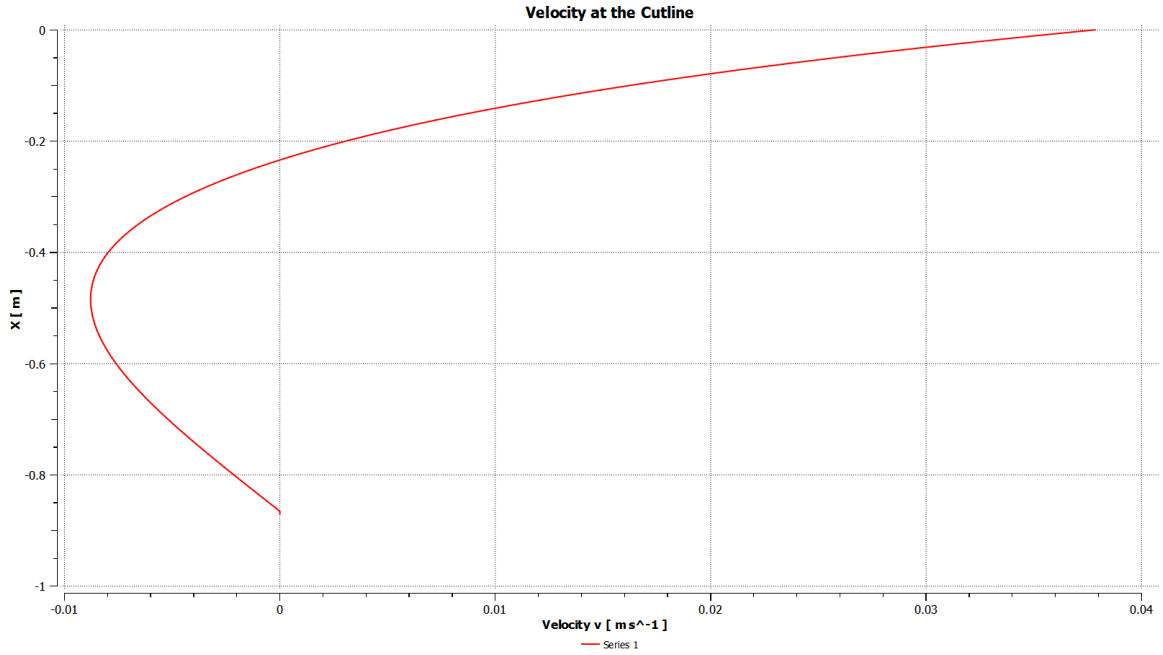


Figure B.85: Radial velocity u at the cutline at $r^*=1$ for Exp 2.5.

Exp 2.6

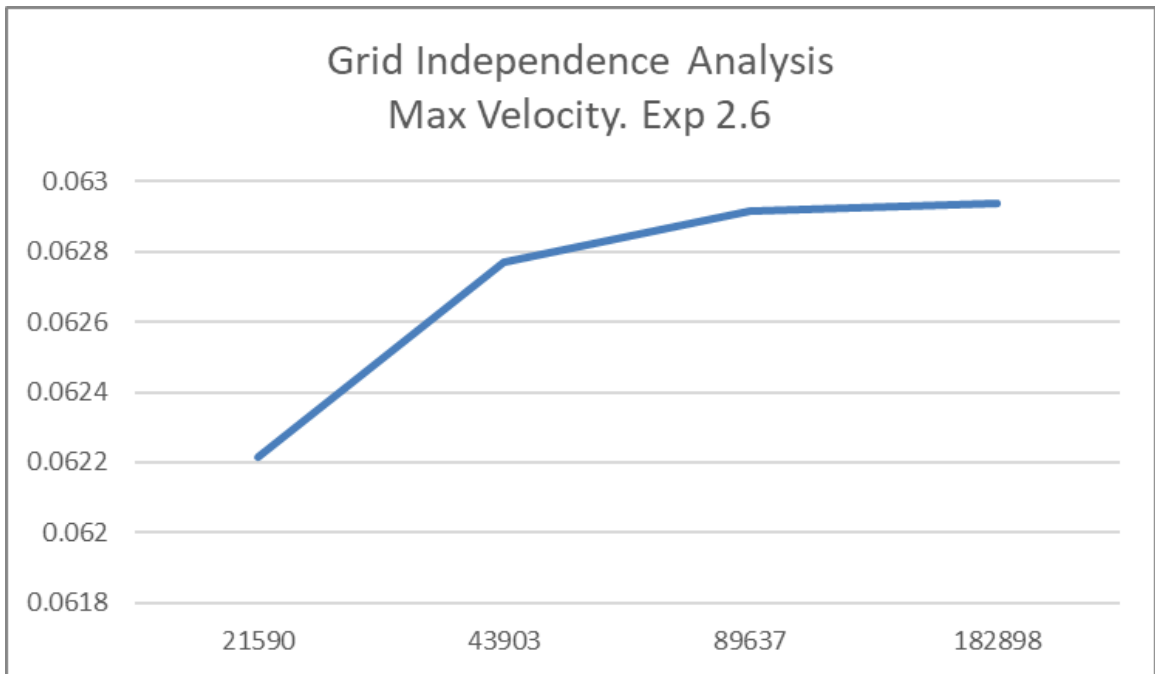


Figure B.86: Convergence for Exp 2.6: peak velocity values vs number of nodes in logarithmic scale.

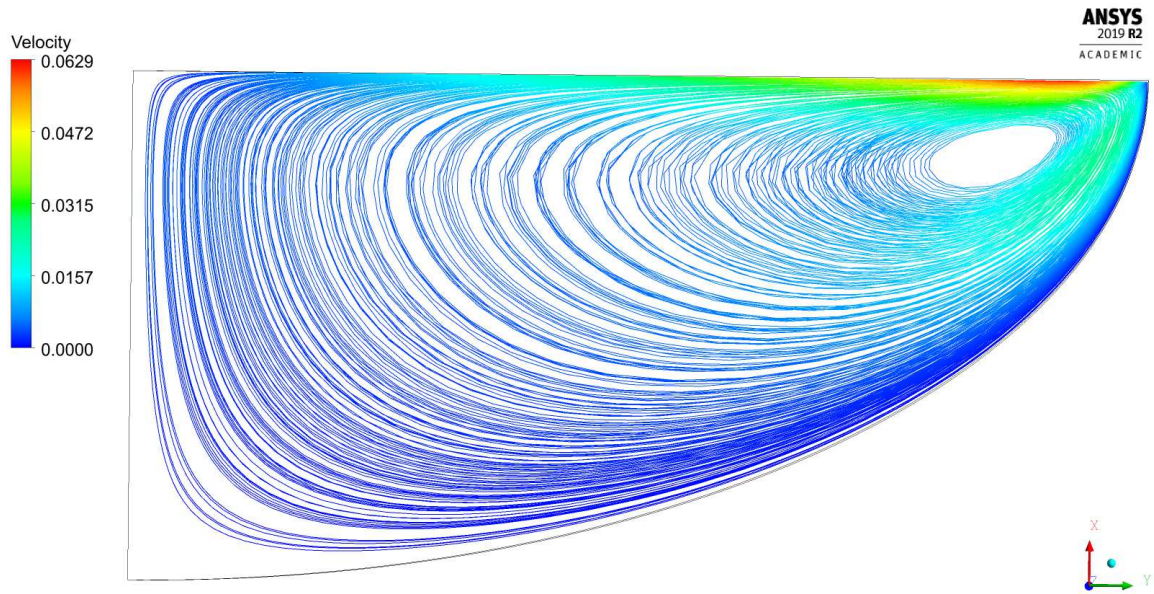


Figure B.87: Streamlines for Exp 2.6.

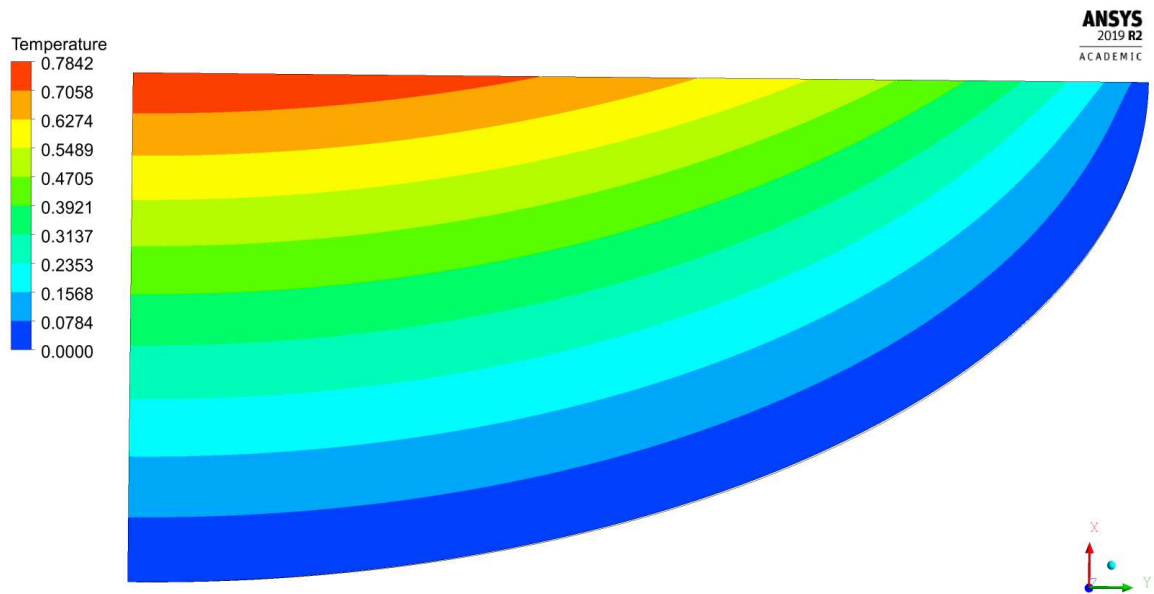


Figure B.88: Temperature field for Exp 2.6.

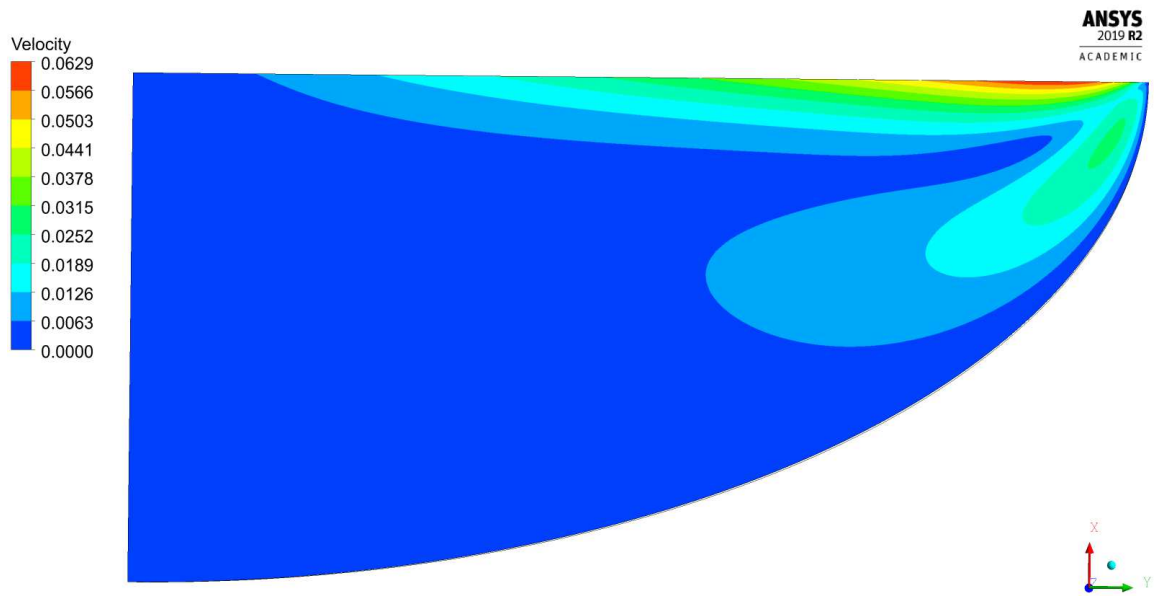


Figure B.89: Velocity magnitude contour for Exp 2.6.

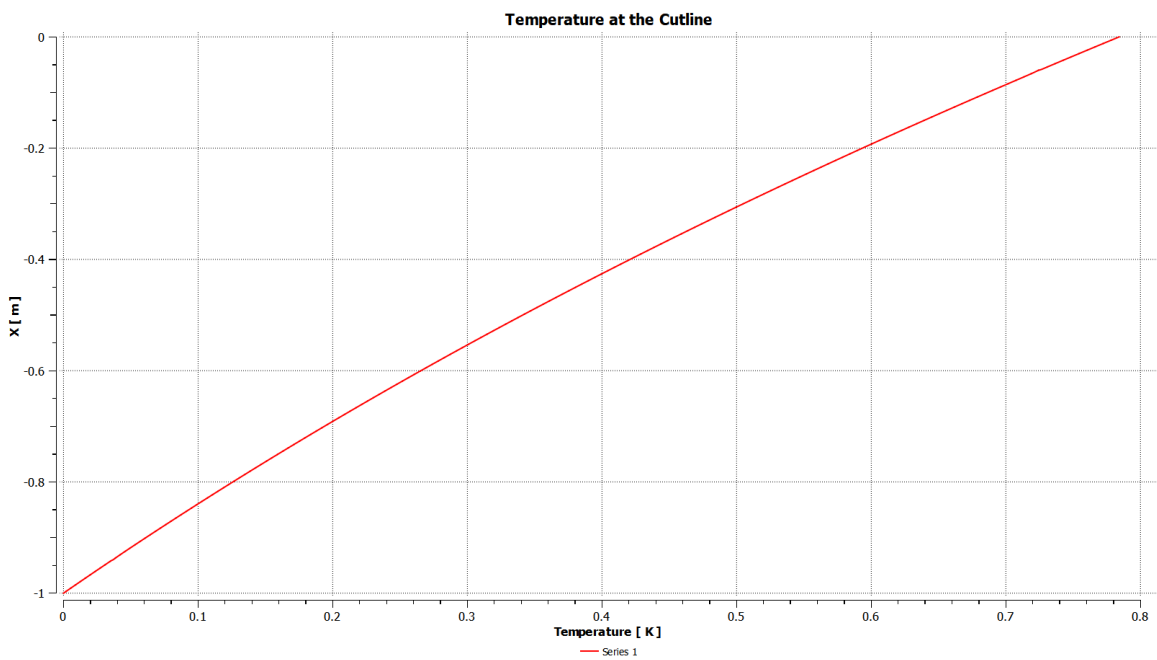


Figure B.90: Temperature at the axis of symmetry for Exp 2.6.

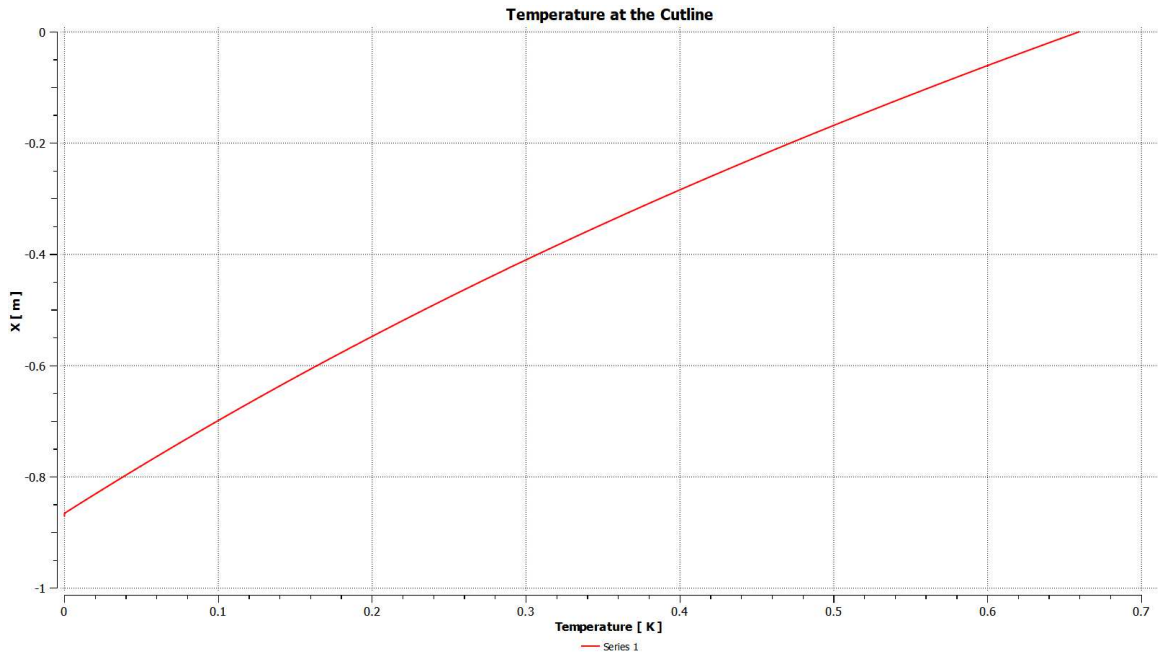


Figure B.91: Temperature at the cutline at $r^*=1$ for Exp 2.6.

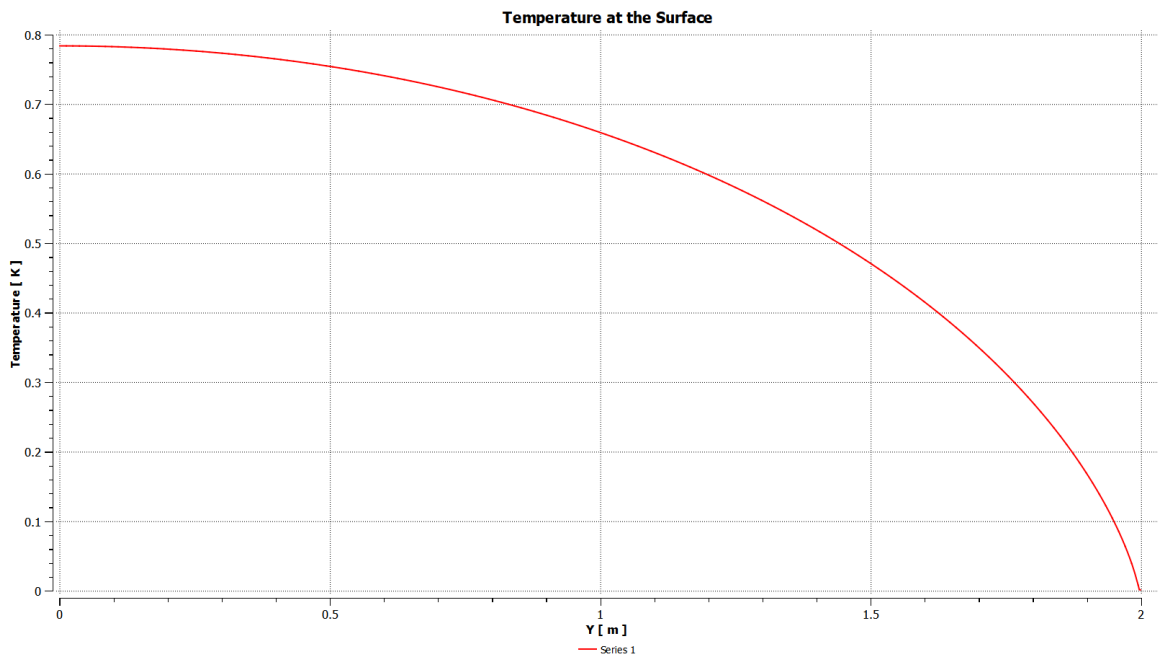


Figure B.92: Temperature at the free surface for Exp 2.6.

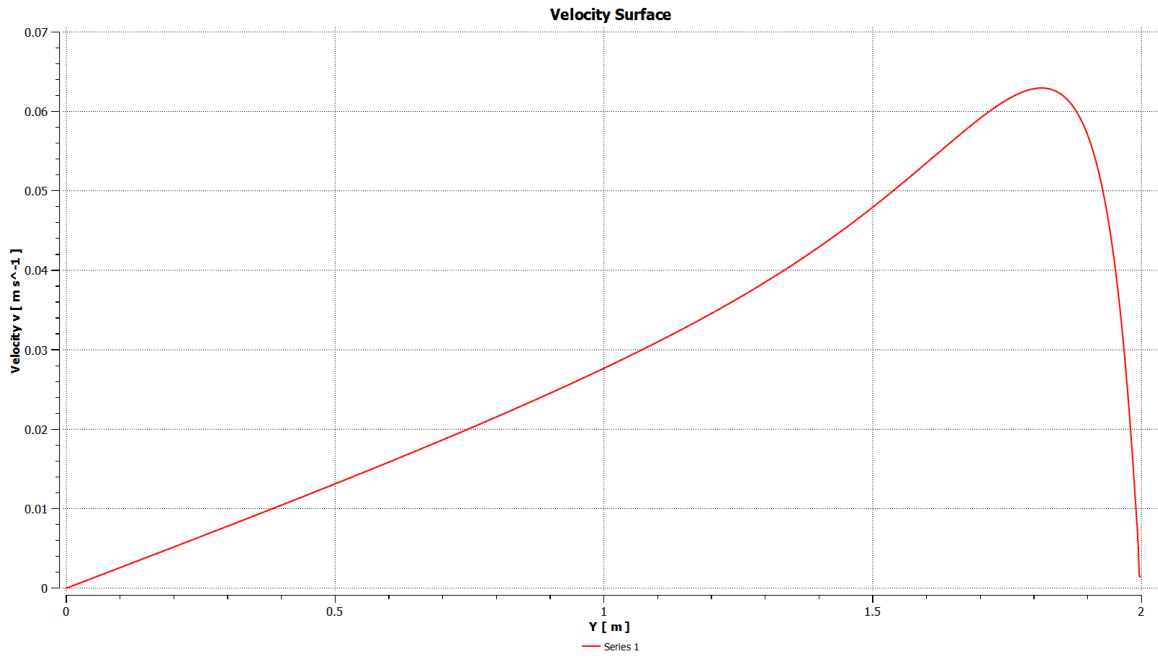


Figure B.93: Velocity at the free surface for Exp 2.6.

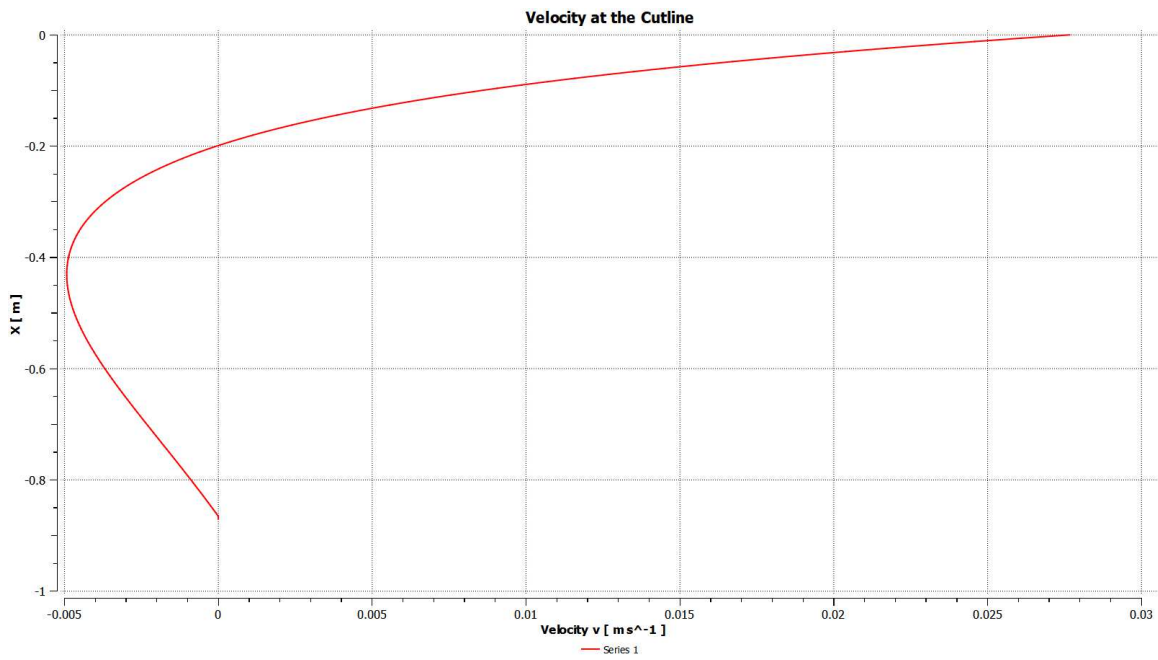


Figure B.94: Radial velocity u at the cutline at $r^*=1$ for Exp 2.6.

Exp 2.7

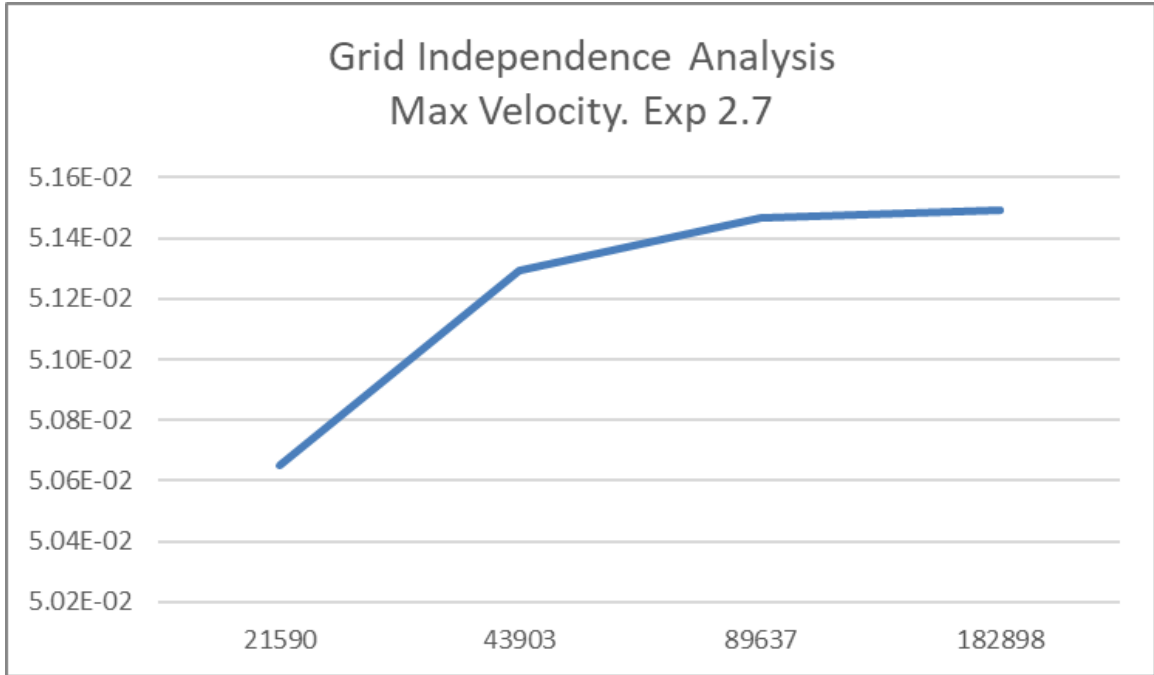


Figure B.95: Convergence for Exp 2.7: peak velocity values vs number of nodes in logarithmic scale.

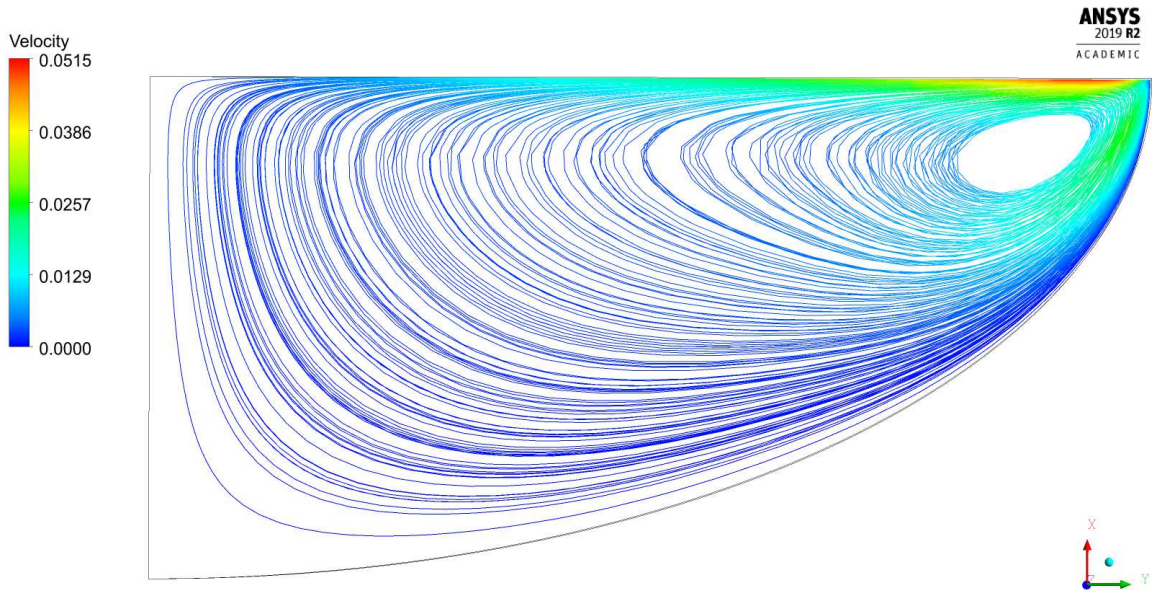


Figure B.96: Streamlines for Exp 2.7.

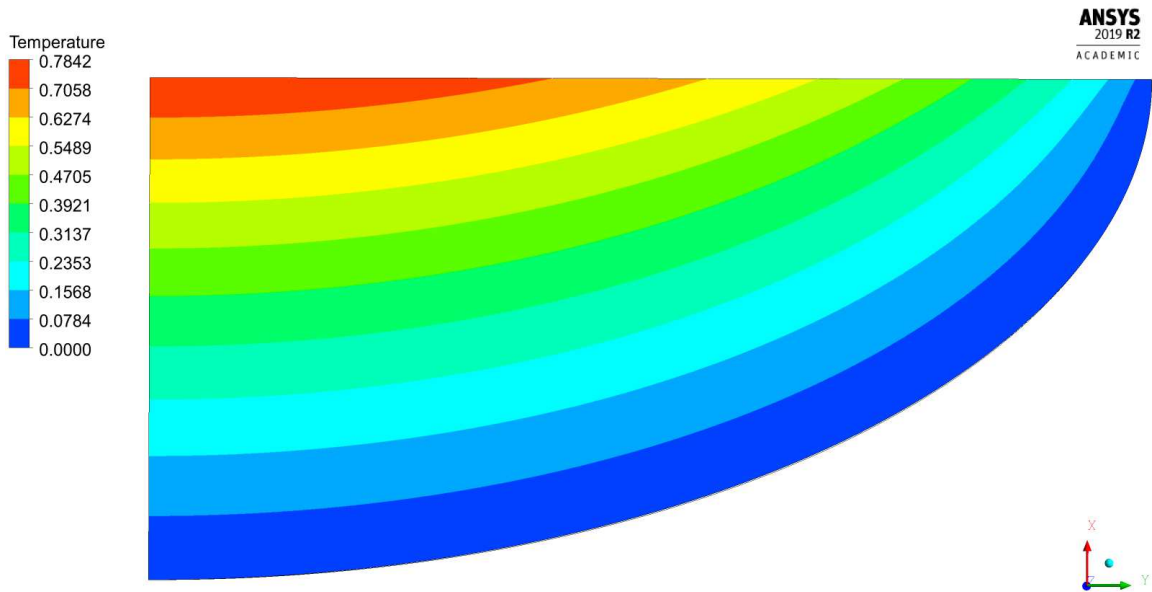


Figure B.97: Temperature field for Exp 2.7.

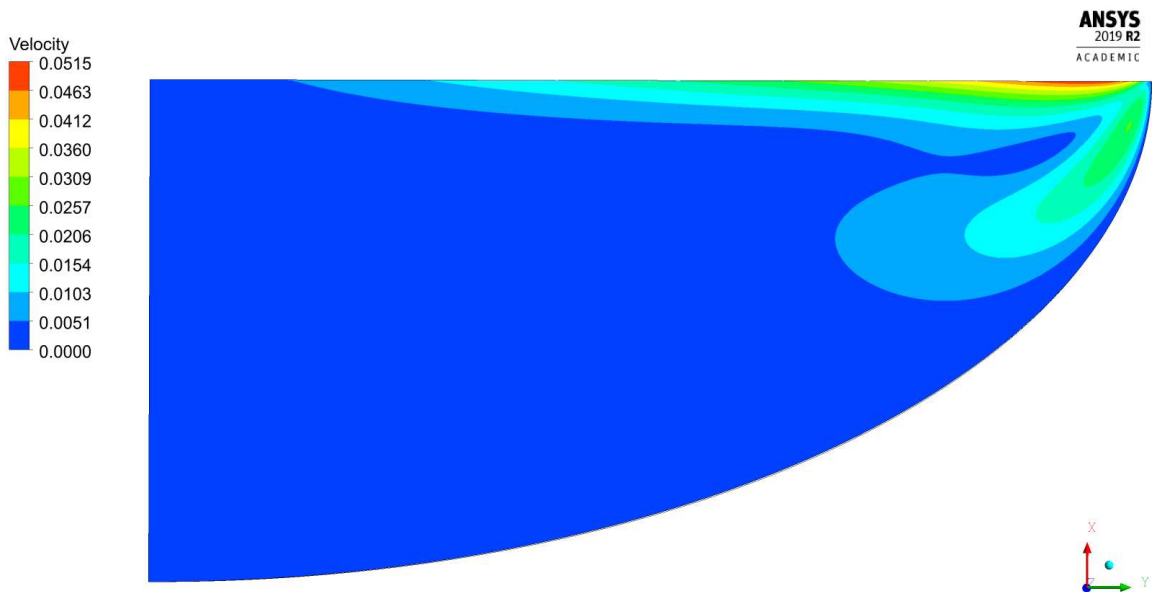


Figure B.98: Velocity magnitude contour for Exp 2.7.

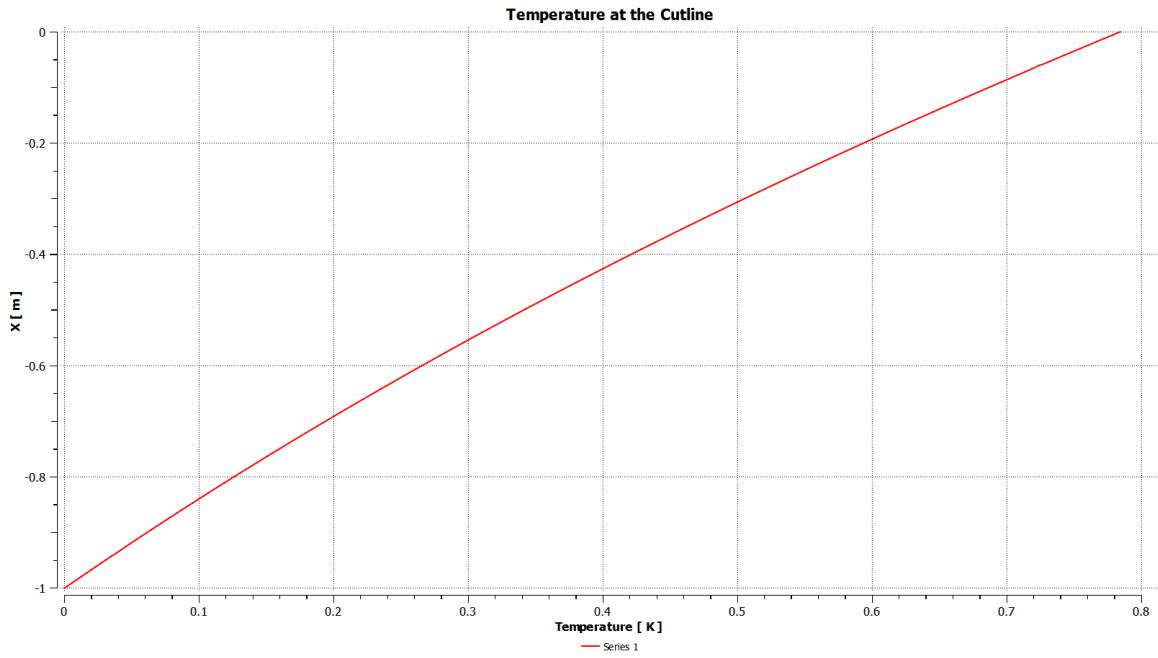


Figure B.99: Temperature at the axis of symmetry for Exp 2.7.

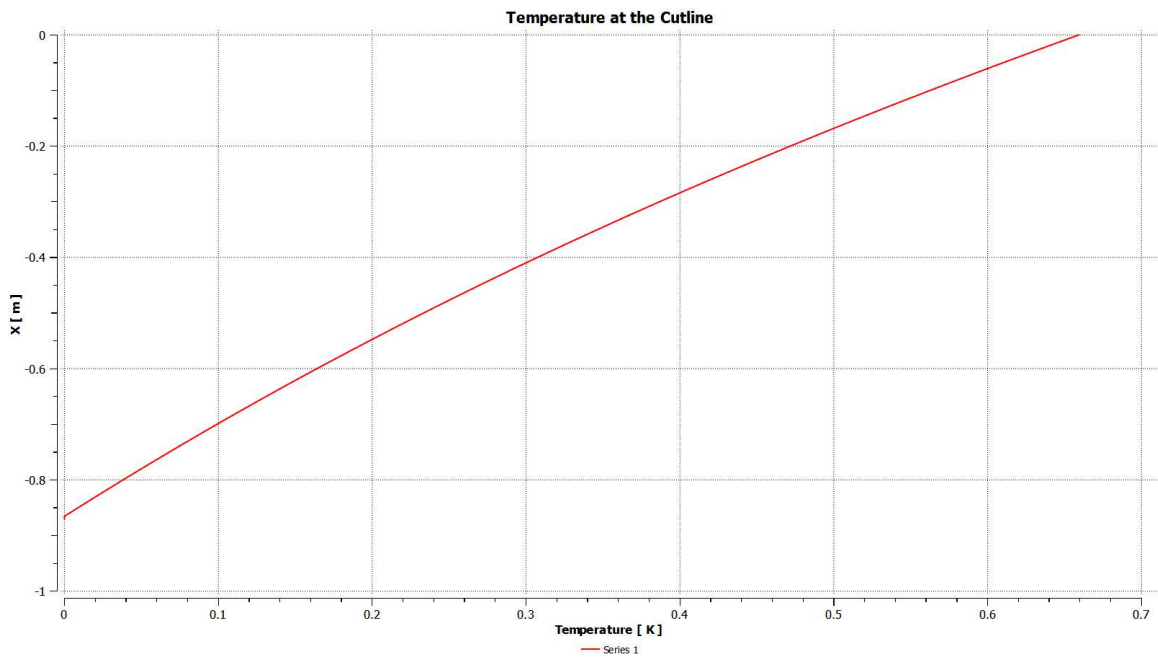


Figure B.100: Temperature at the cutline at $r^*=1$ for Exp 2.7.

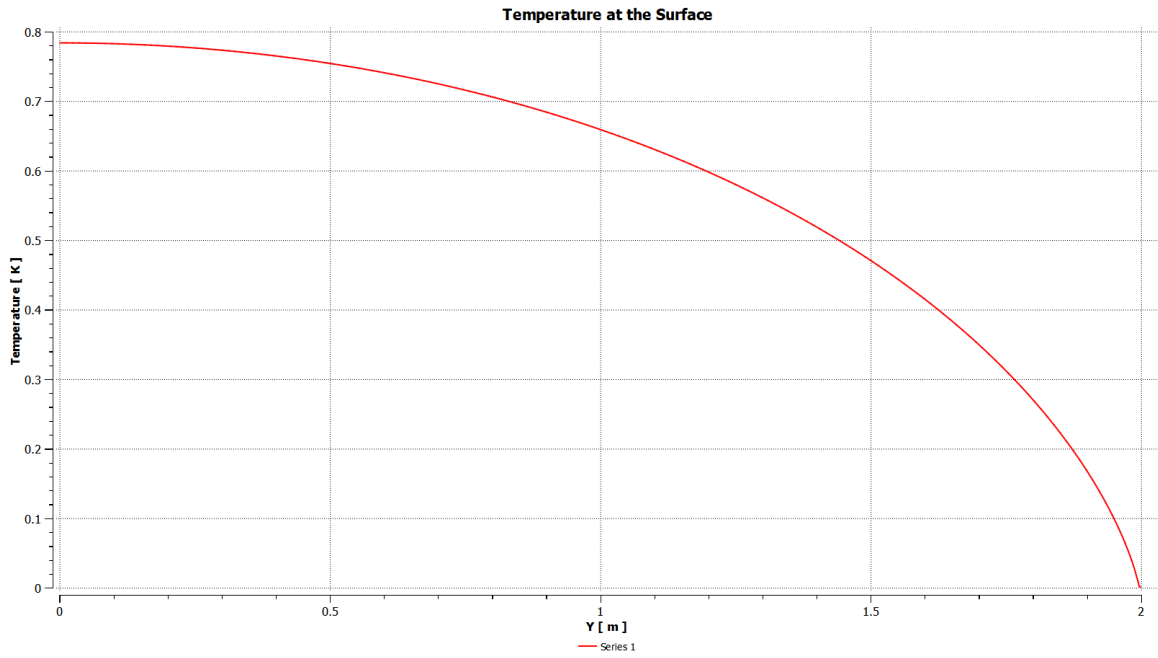


Figure B.101: Temperature at the free surface for Exp 2.7.

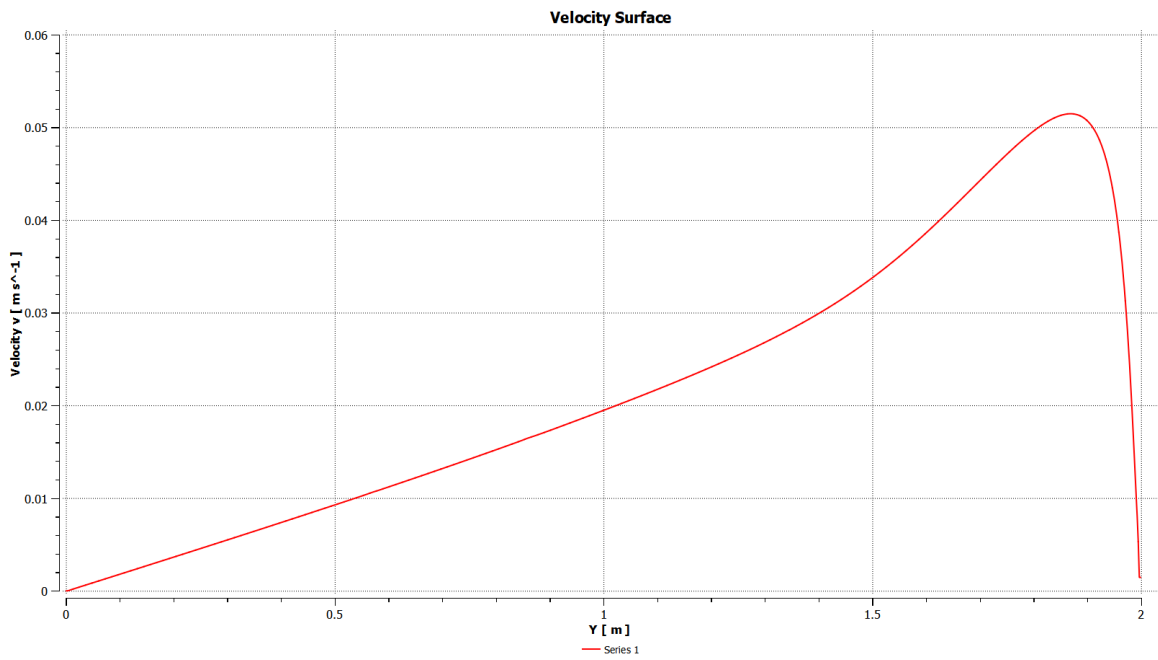


Figure B.102: Velocity at the free surface for Exp 2.7.

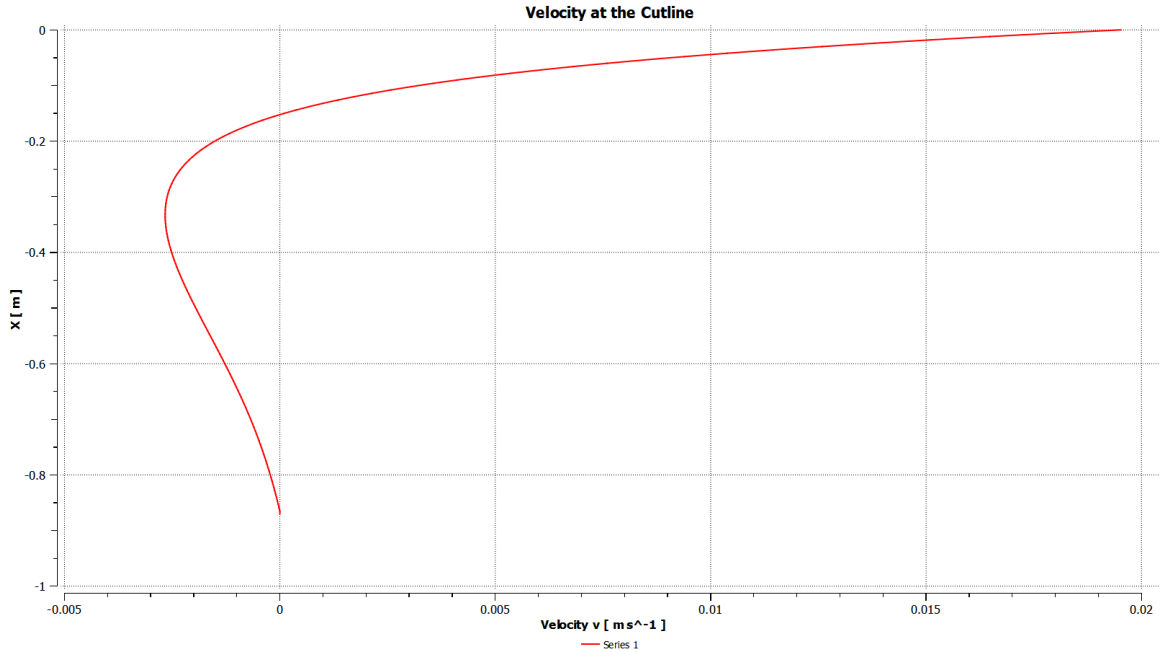


Figure B.103: Radial velocity u at the cutline at $r^*=1$ for Exp 2.7.

Exp 2.8

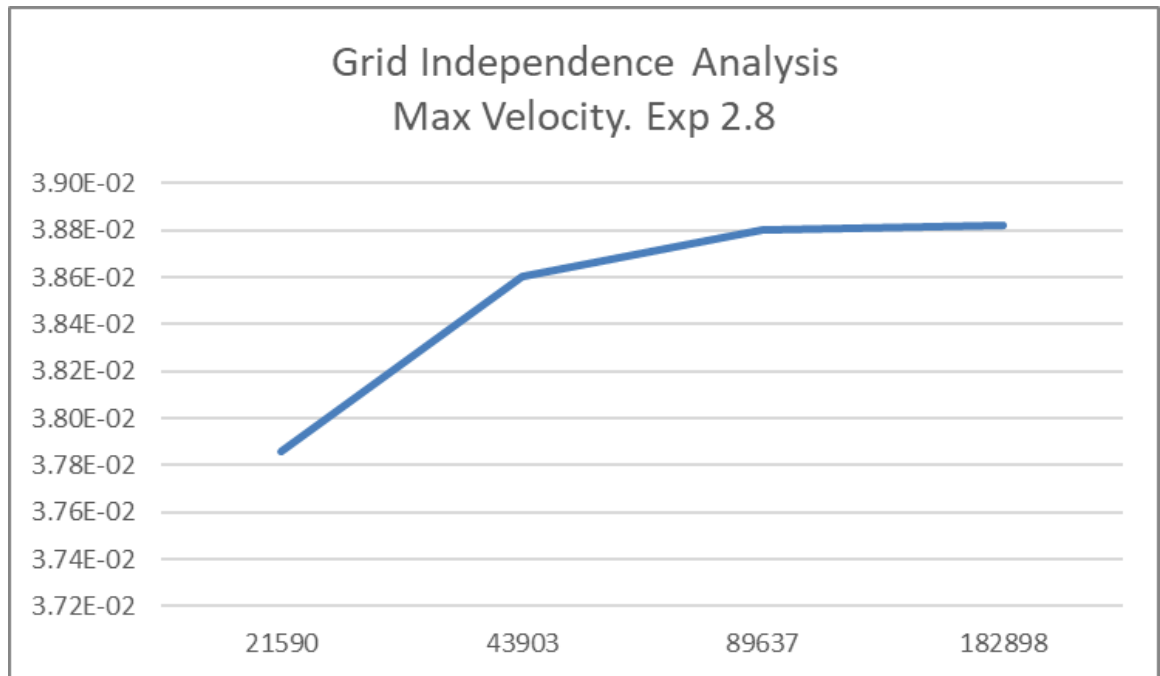


Figure B.104: Convergence for Exp 2.8: peak velocity values vs number of nodes in logarithmic scale.

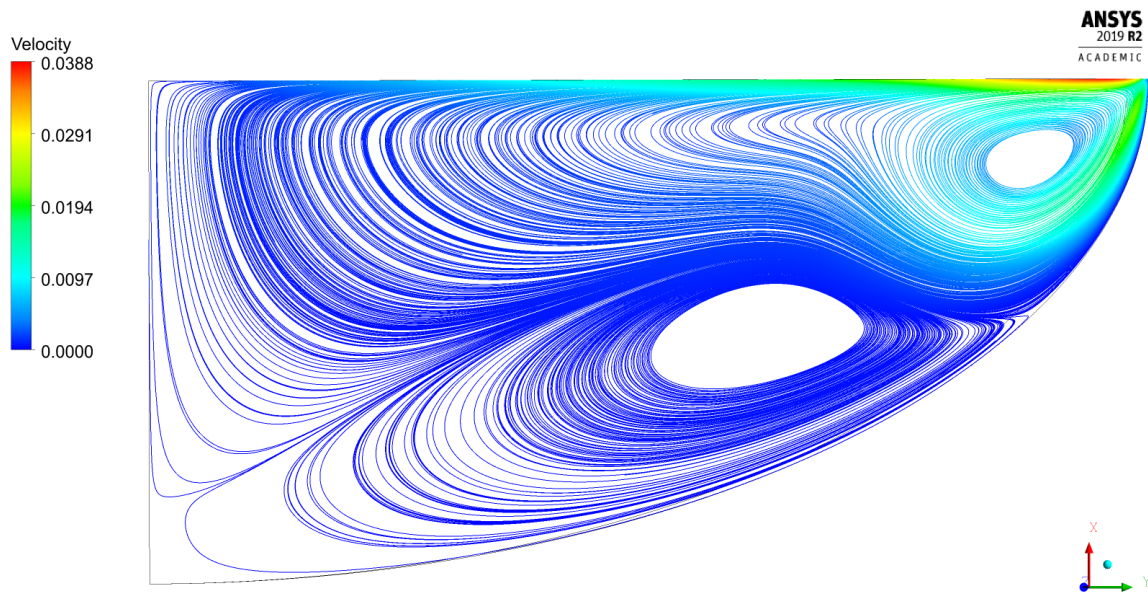


Figure B.105: Streamlines for Exp 2.8.

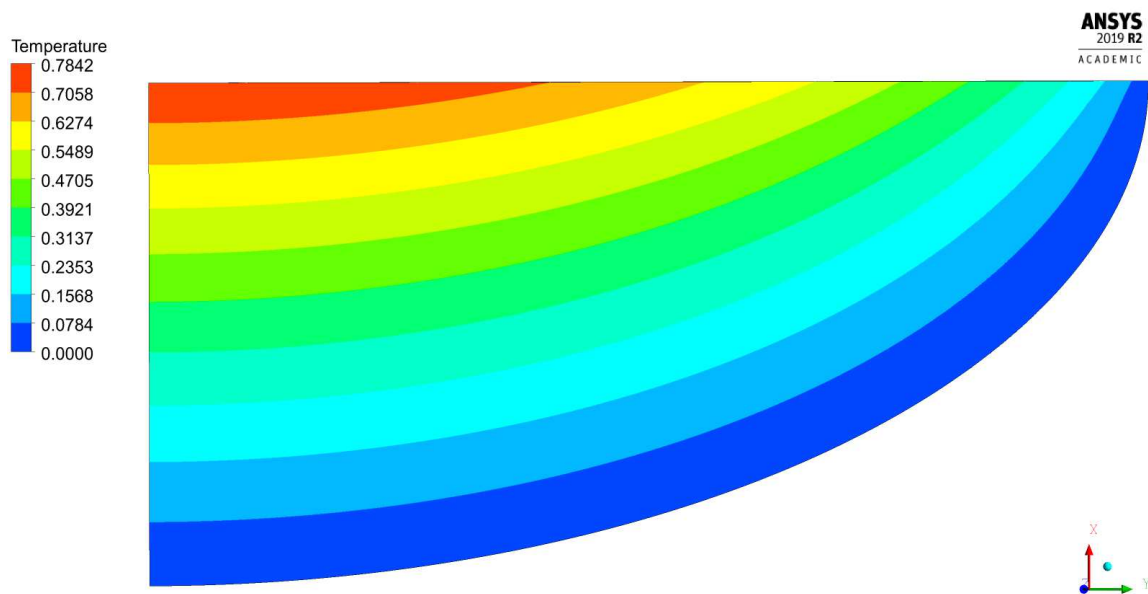


Figure B.106: Temperature field for Exp 2.8.

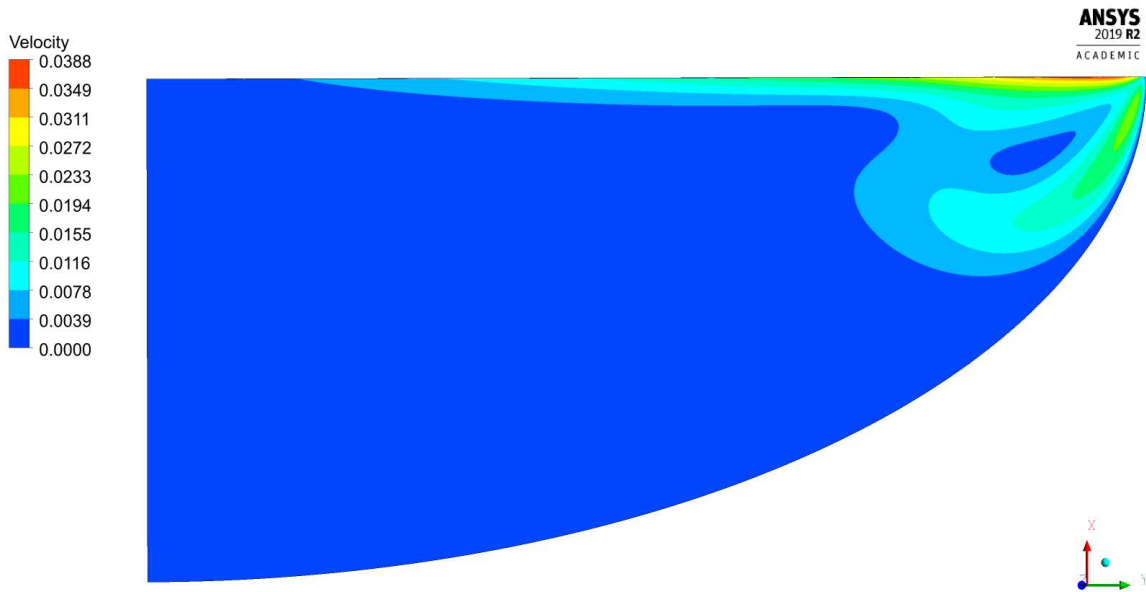


Figure B.107: Velocity magnitude contour for Exp 2.8.

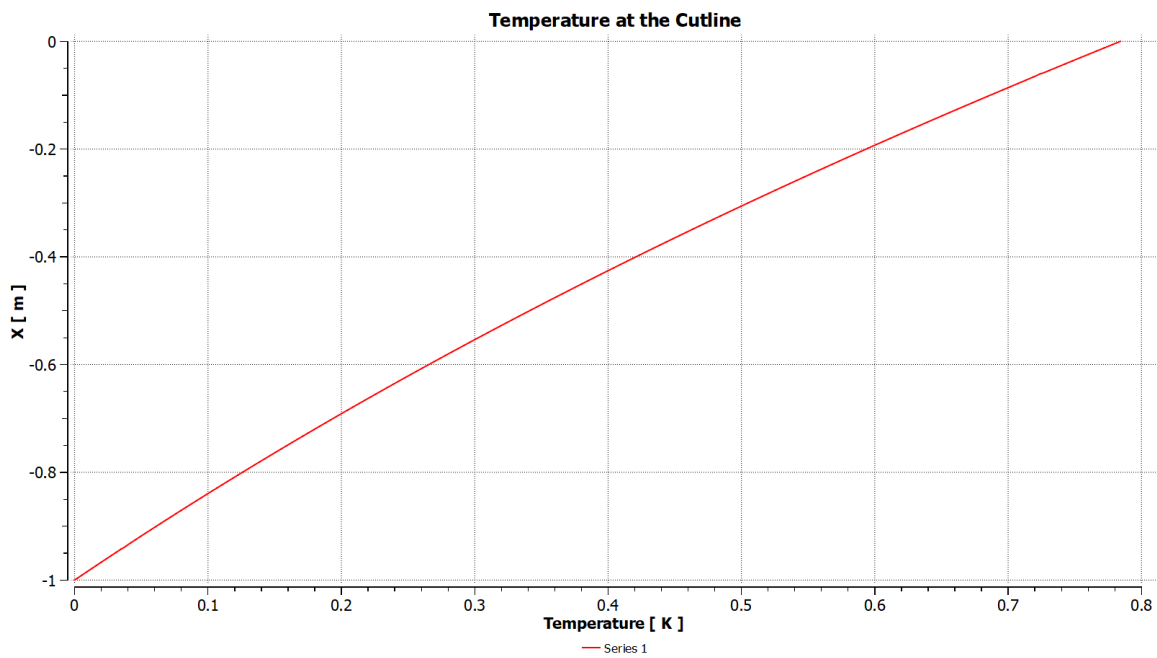


Figure B.108: Temperature at the axis of symmetry for Exp 2.8.

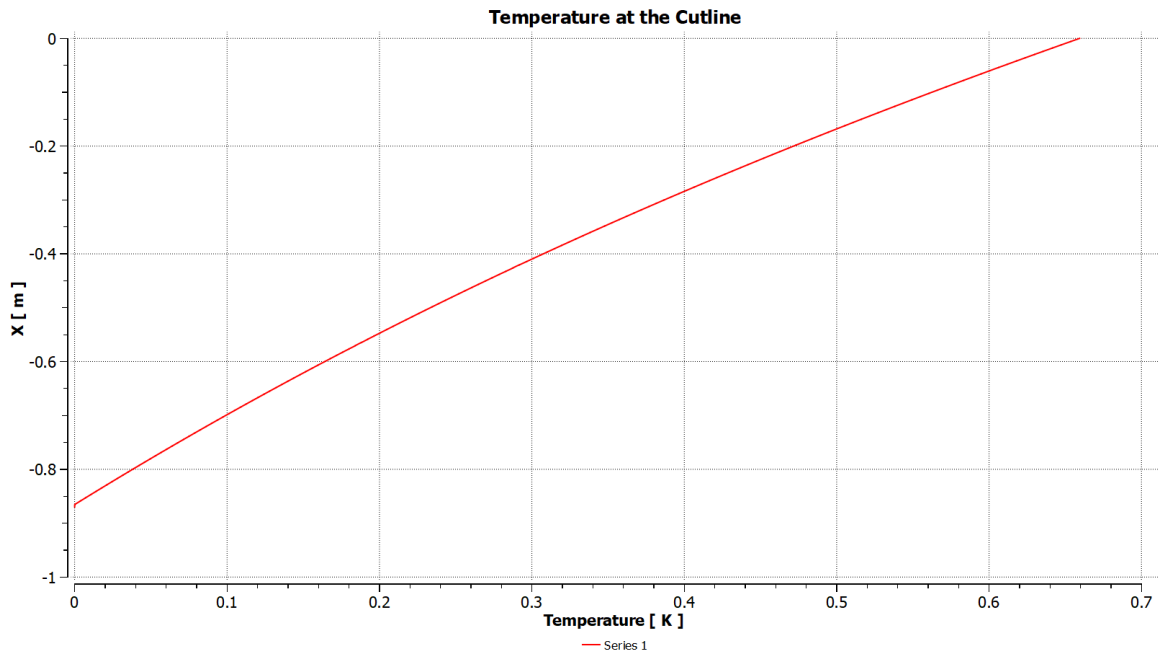


Figure B.109: Temperature at the cutline at $r^*=1$ for Exp 2.8.

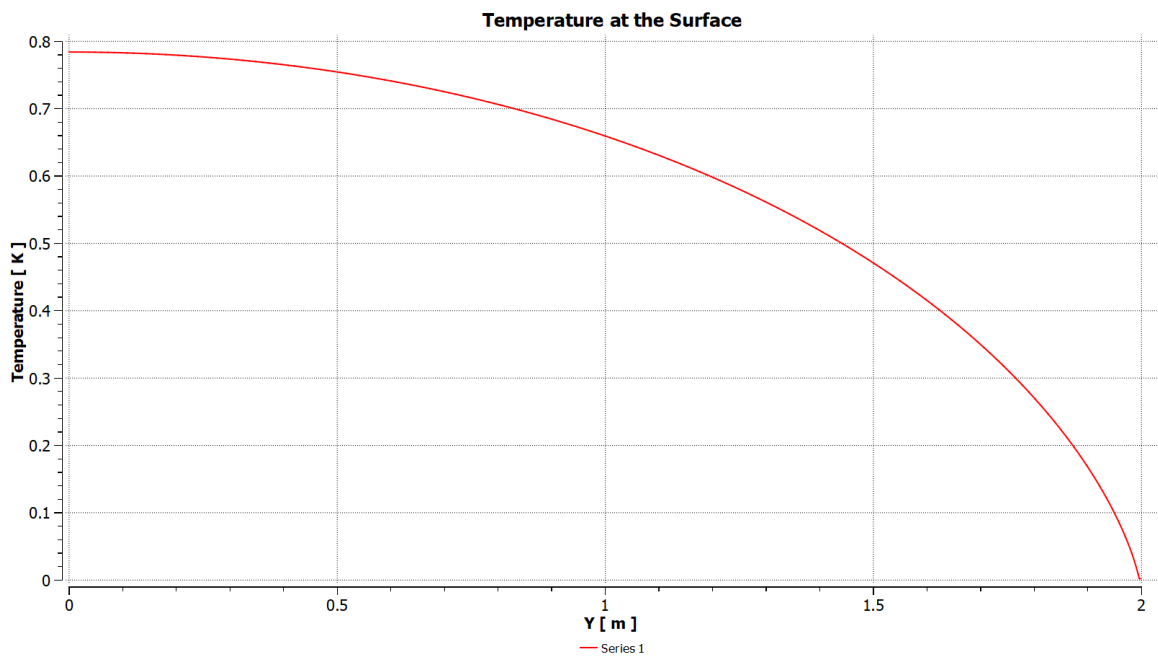


Figure B.110: Temperature at the free surface for Exp 2.8.

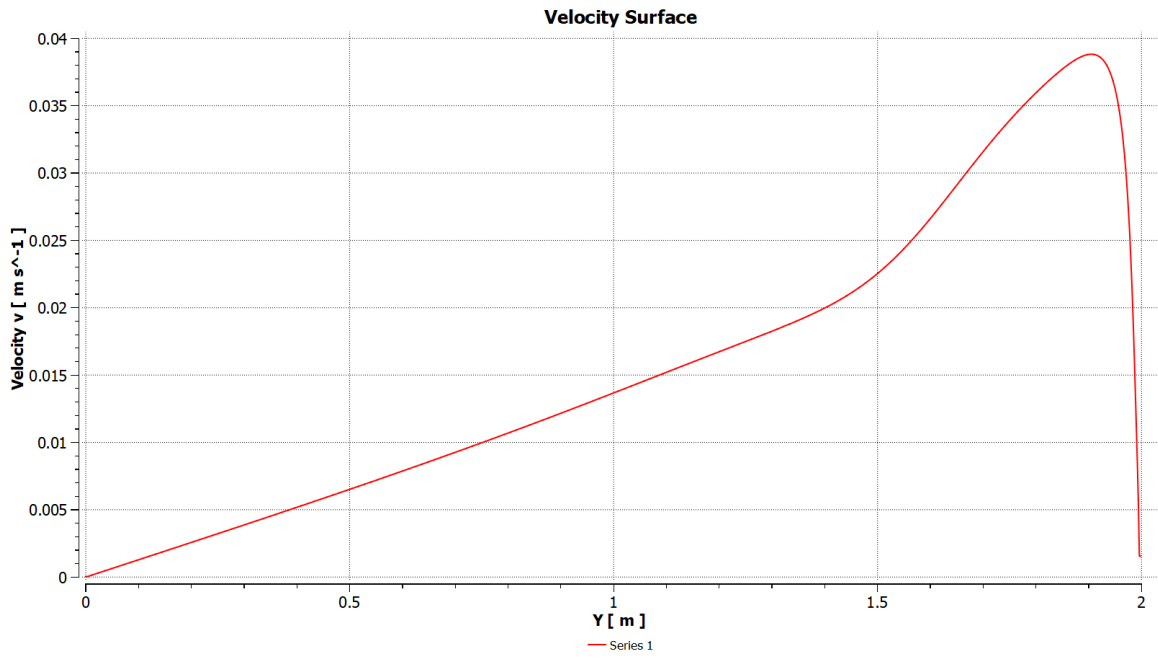


Figure B.111: Velocity at the free surface for Exp 2.8.

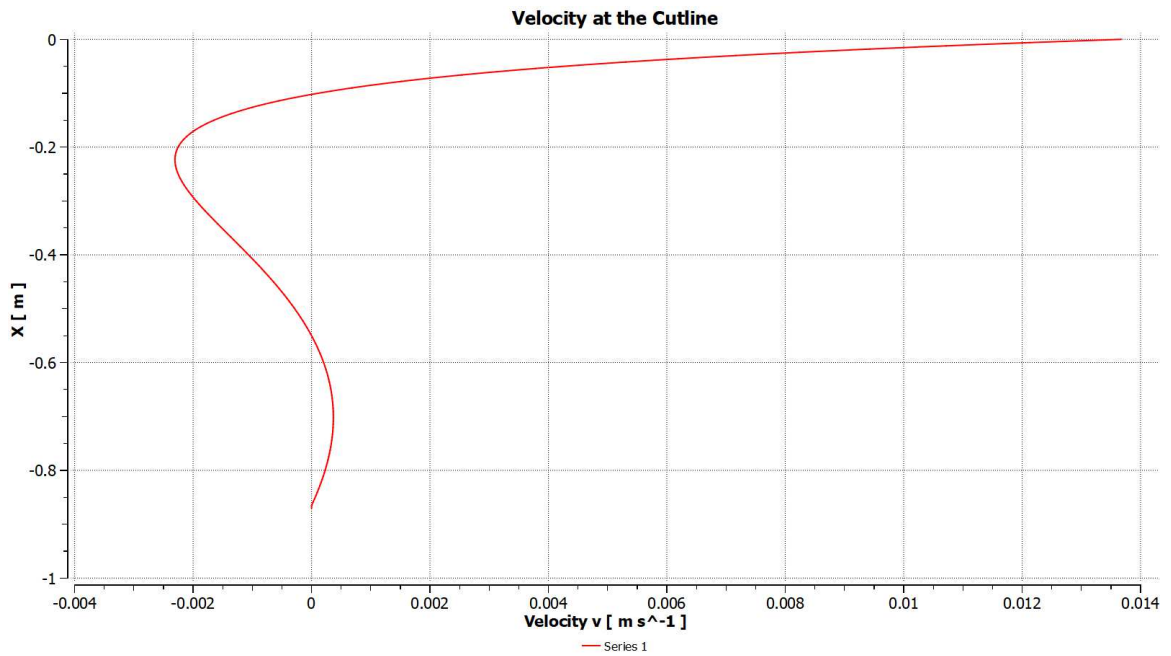


Figure B.112: Radial velocity u at the cutline at $r^*=1$ for Exp 2.8.

Exp 2.9

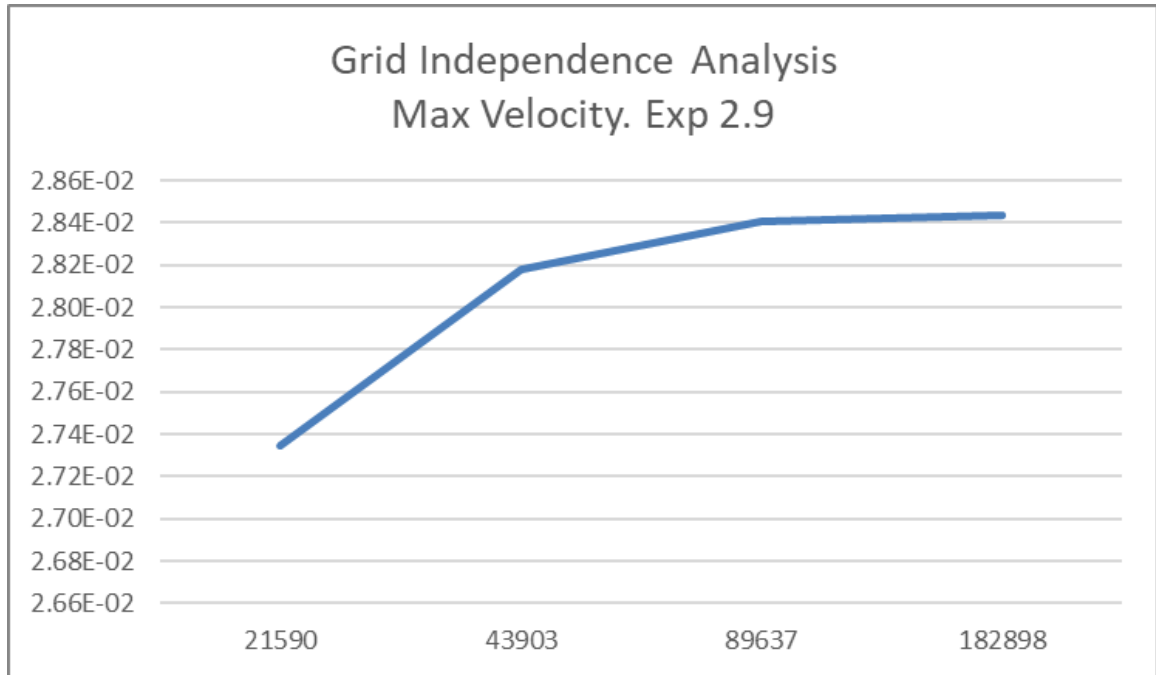


Figure B.113: Convergence for Exp 2.9: peak velocity values vs number of nodes in logarithmic scale.

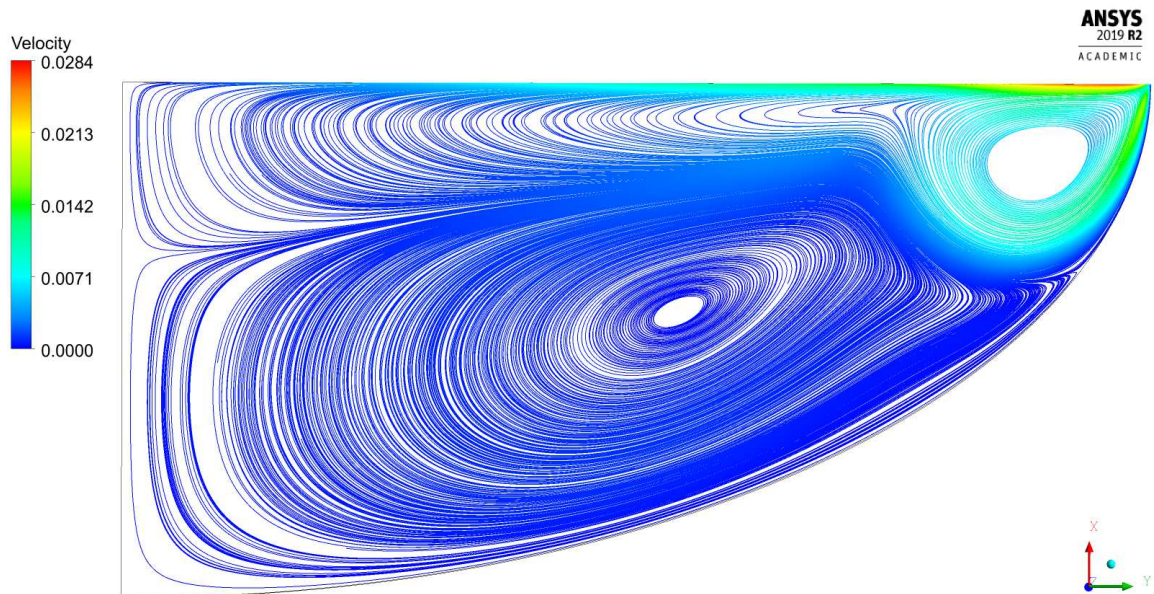


Figure B.114: Streamlines for Exp 2.9.

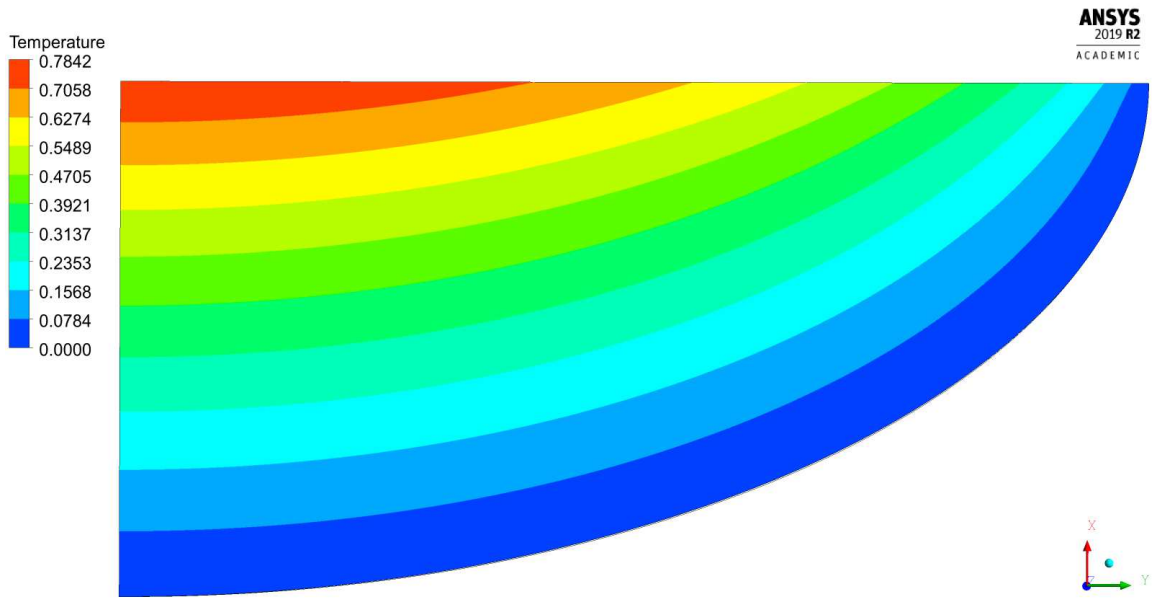


Figure B.115: Temperature field for Exp 2.9.

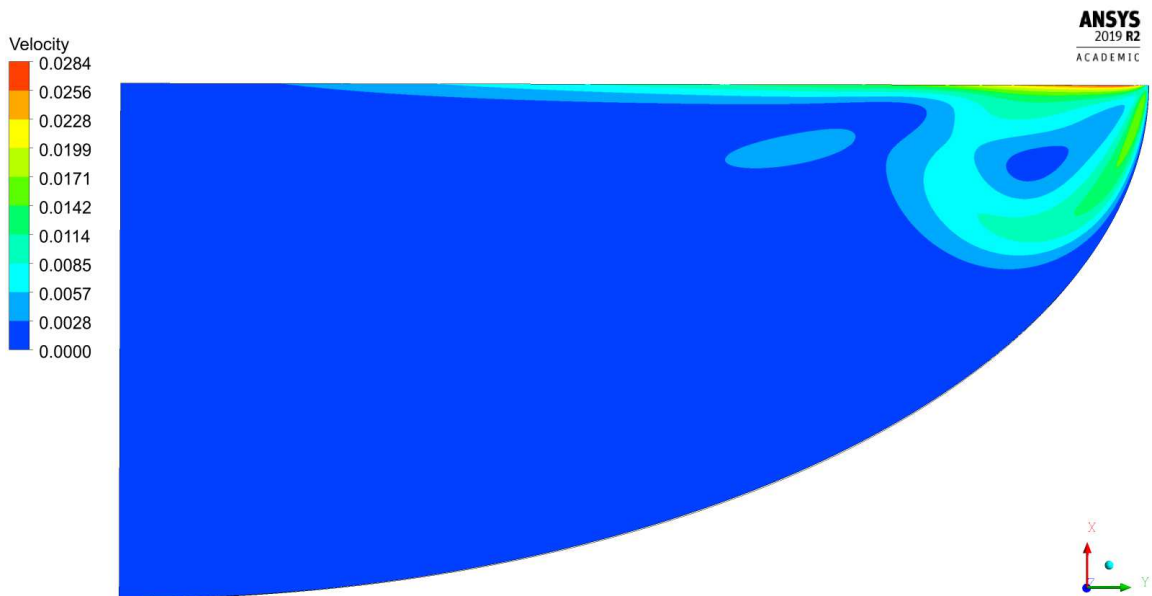


Figure B.116: Velocity magnitude contour for Exp 2.9.

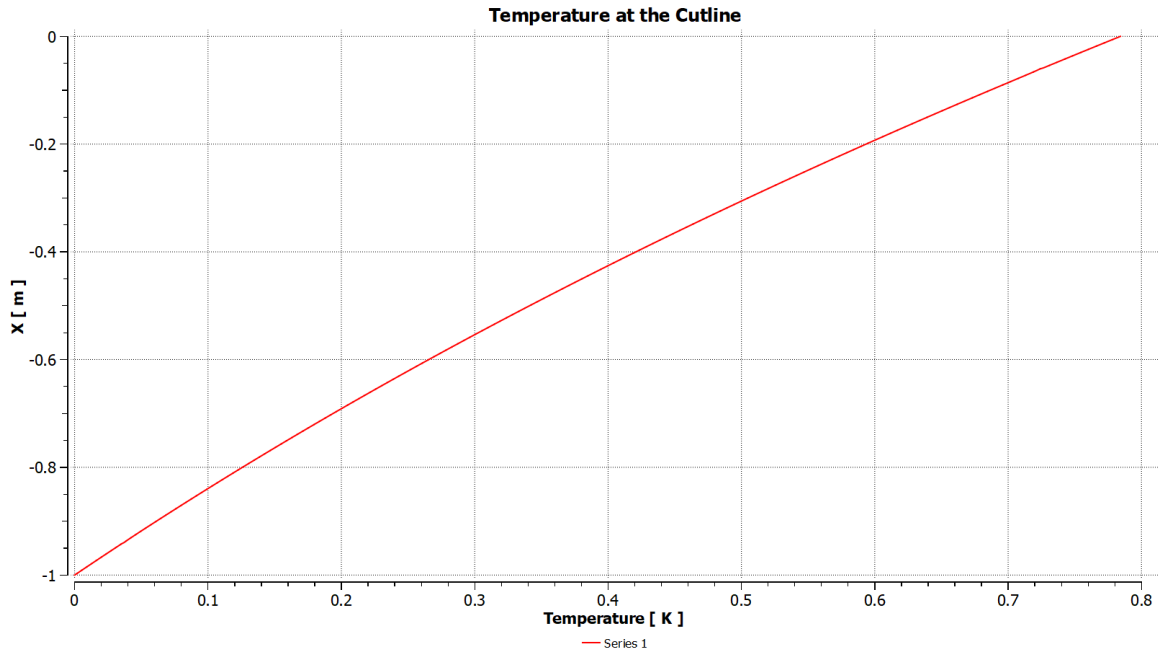


Figure B.117: Temperature at the axis of symmetry for Exp 2.9.

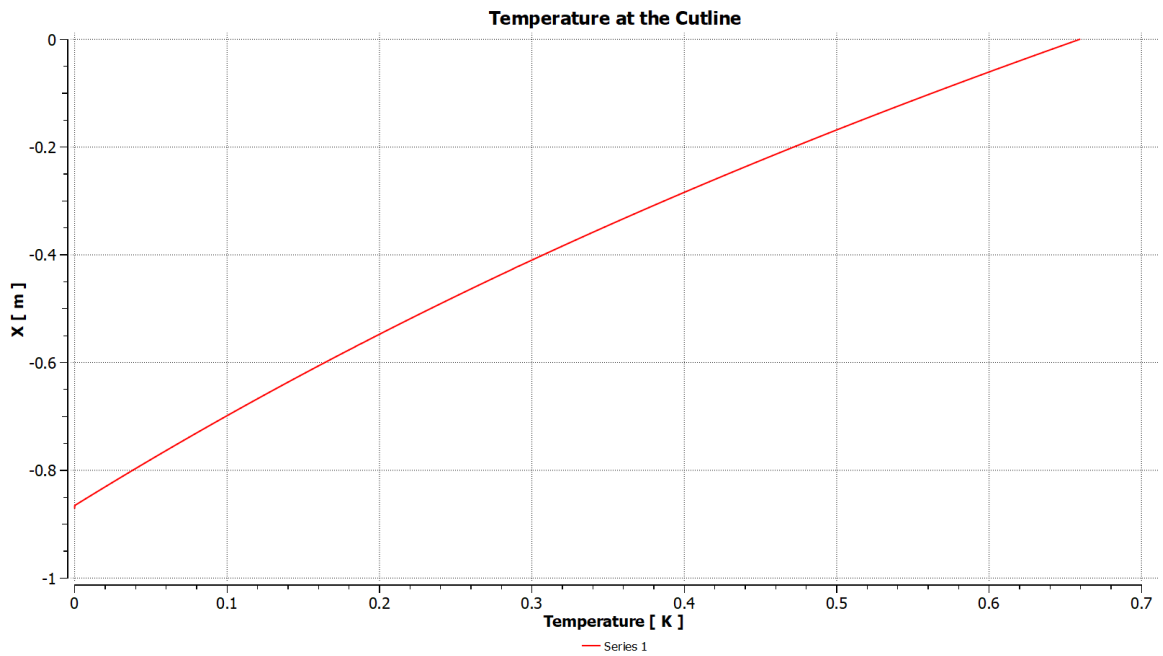


Figure B.118: Temperature at the cutline at $r^*=1$ for Exp 2.9.

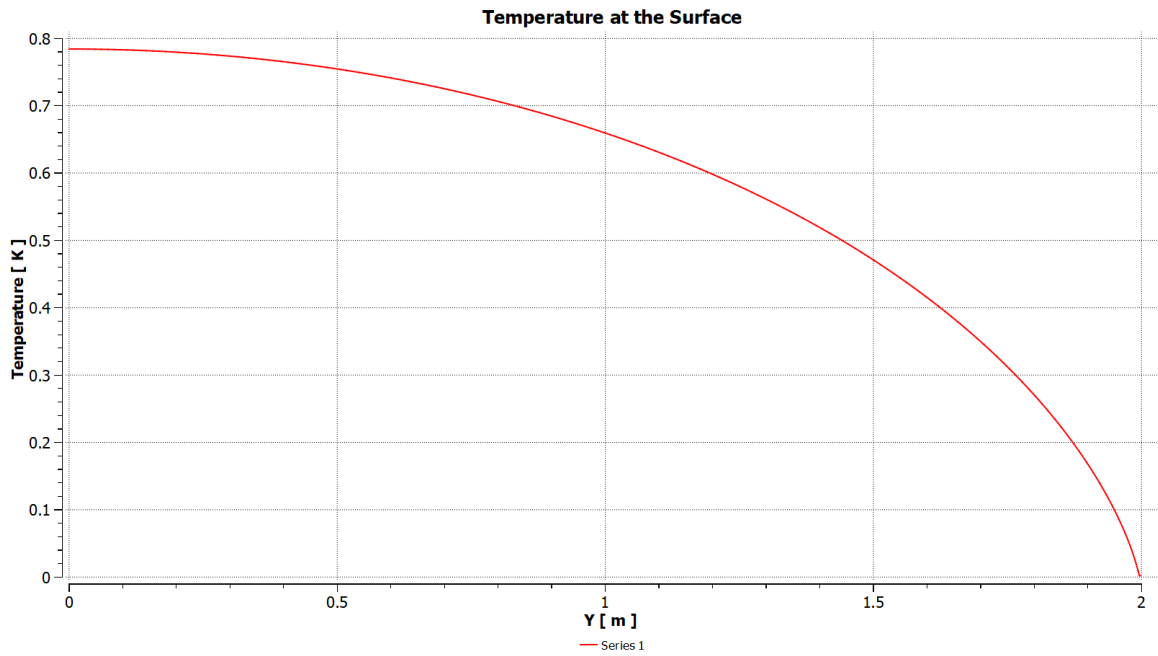


Figure B.119: Temperature at the free surface for Exp 2.9.

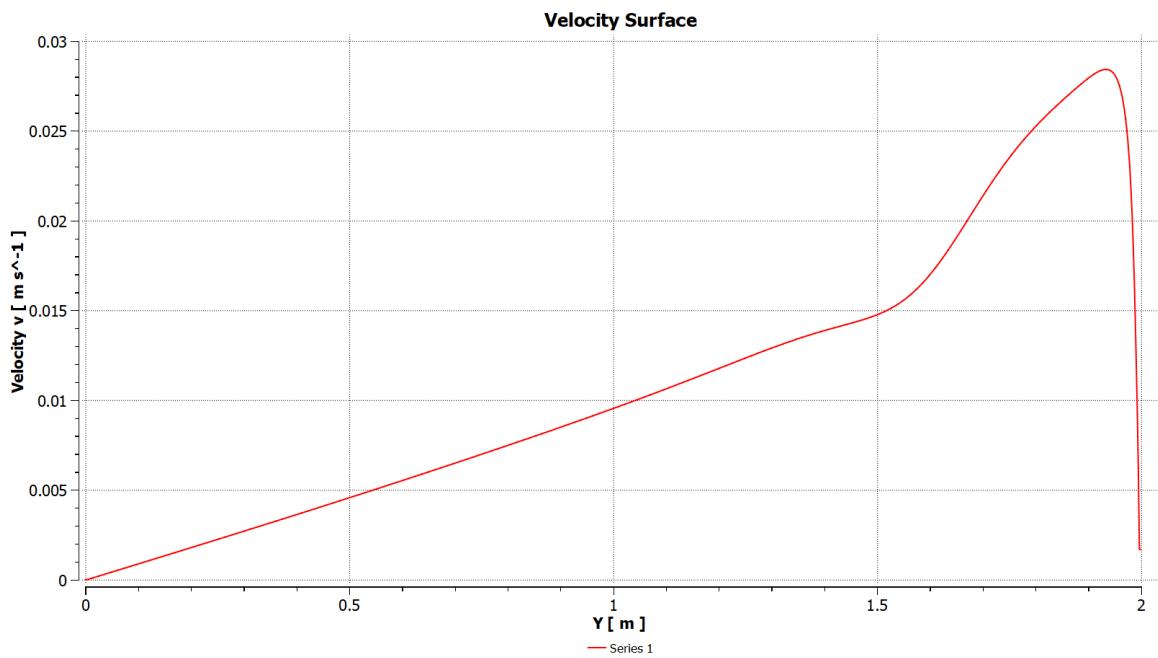


Figure B.120: Velocity at the free surface for Exp 2.9.

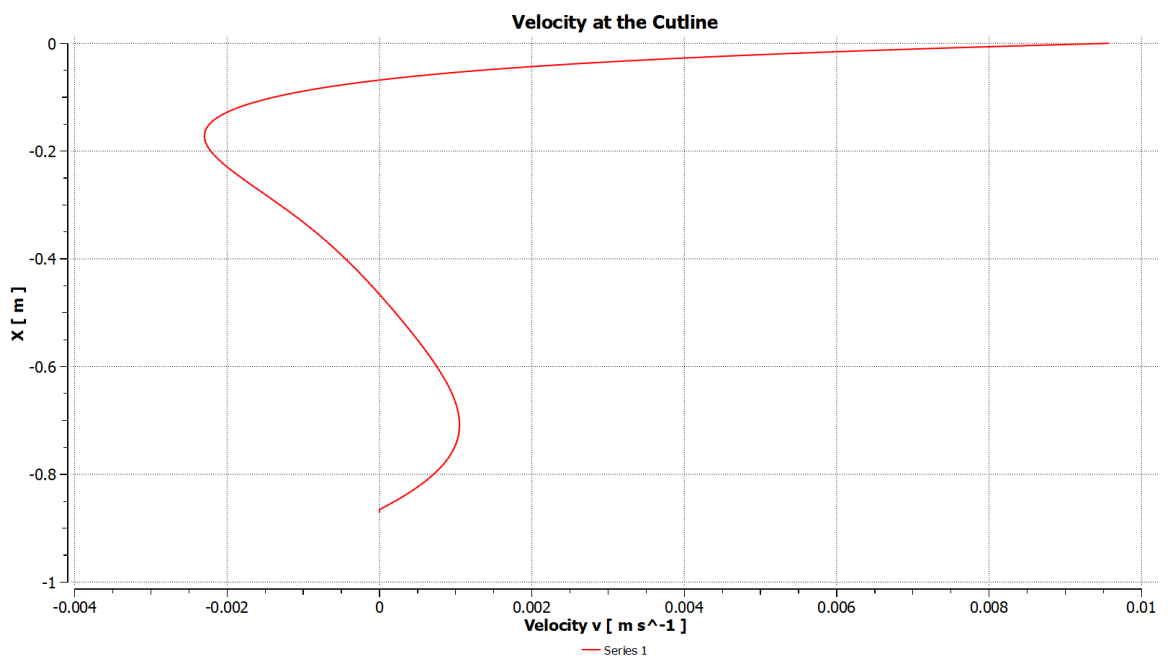


Figure B.121: Radial velocity u at the cutline at $r^*=1$ for Exp 2.9.

B.3 Regime III

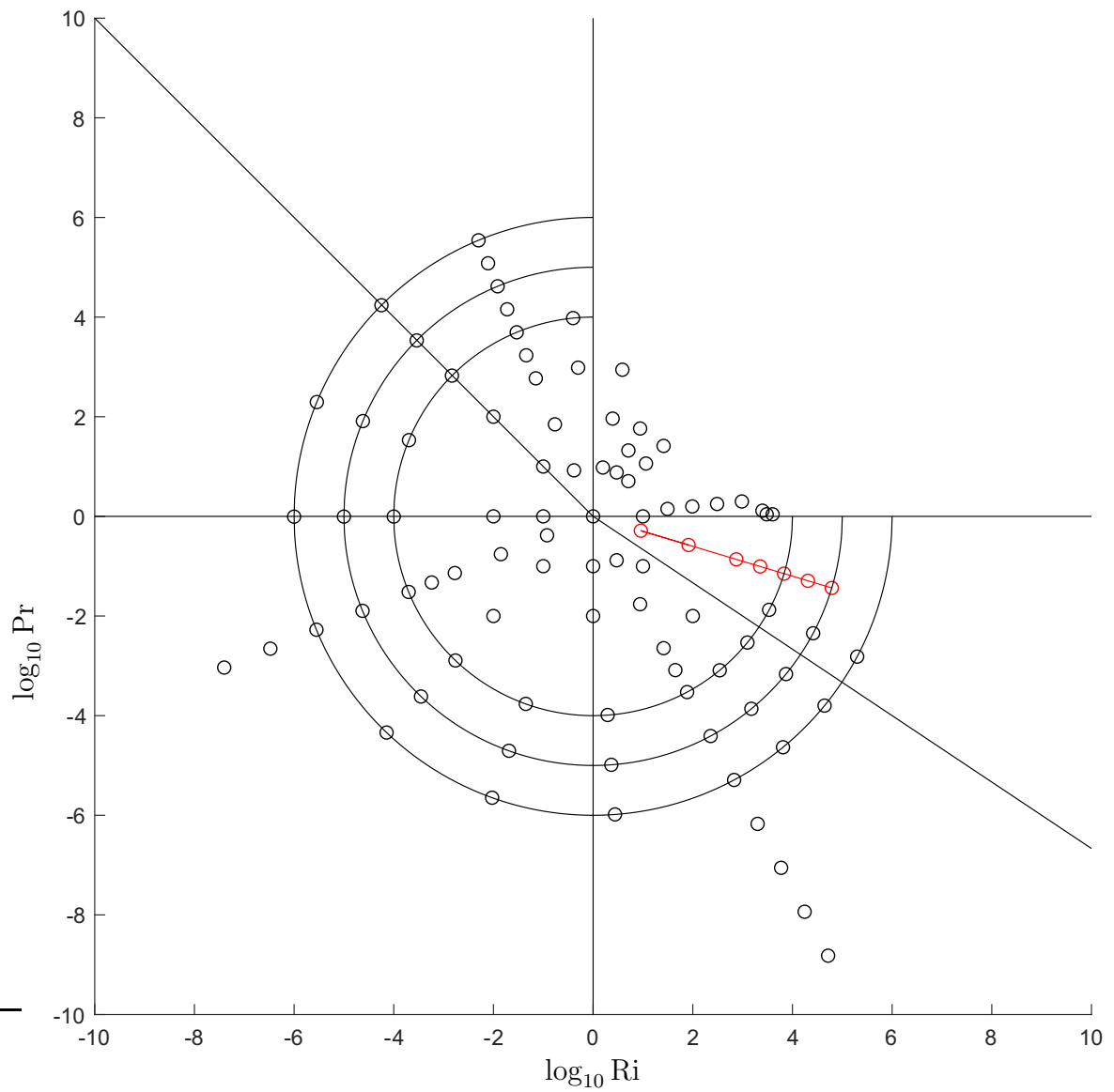


Figure B.122: Location of the dimensionless parameters for Regime III.

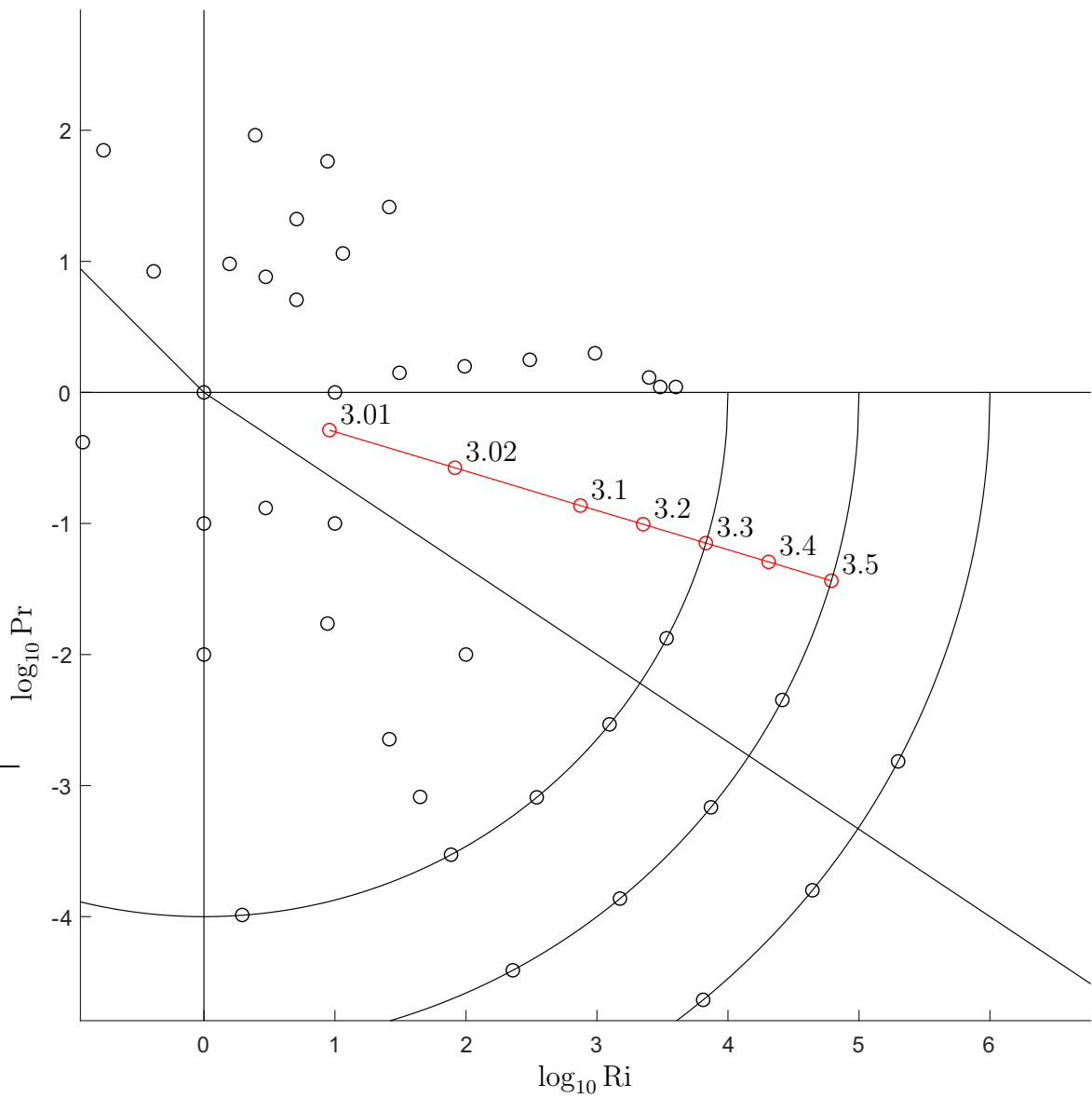


Figure B.123: Location of the dimensionless parameters for Regime III and the experiment numbers.

Exp 3.01

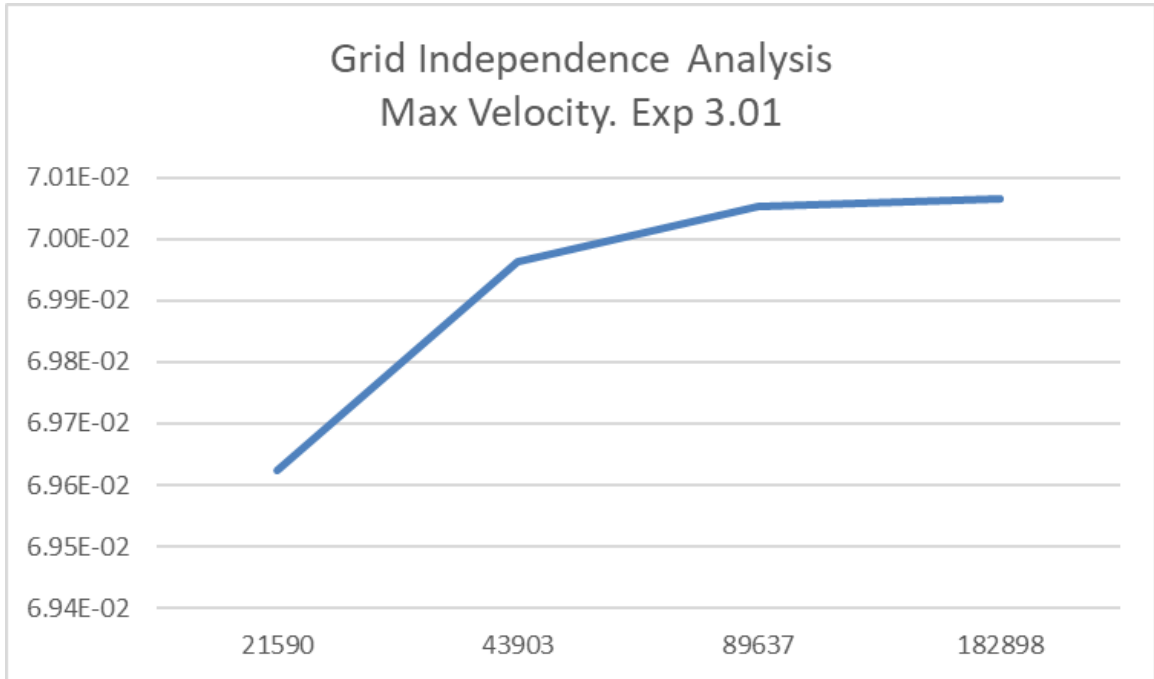


Figure B.124: Convergence for Exp 3.01: peak velocity values vs number of nodes in logarithmic scale.

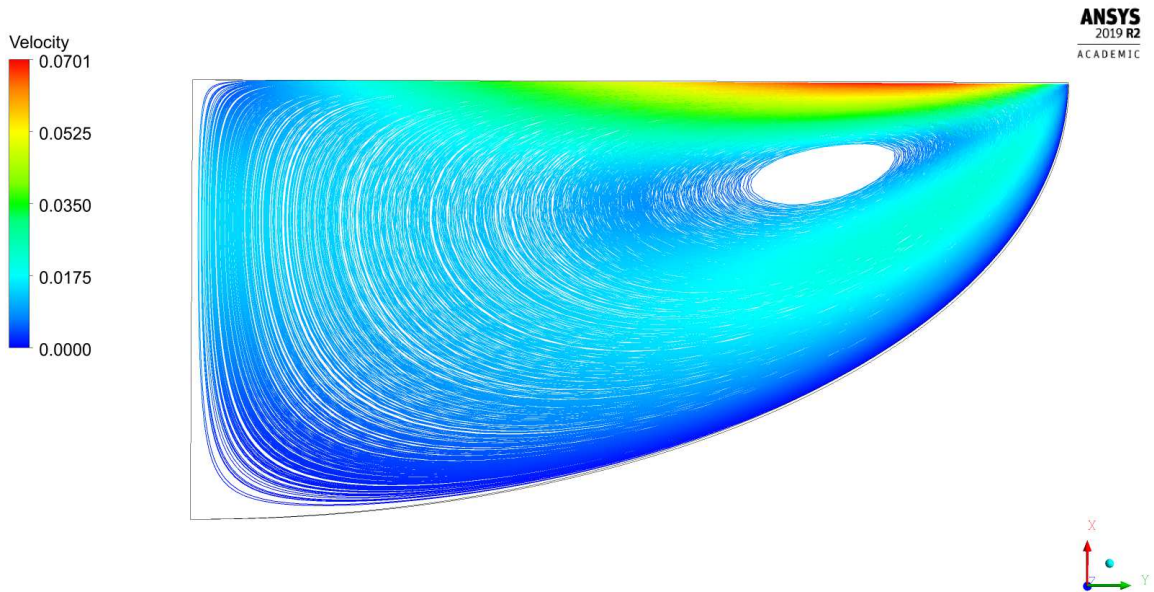


Figure B.125: Streamlines for Exp 3.01.

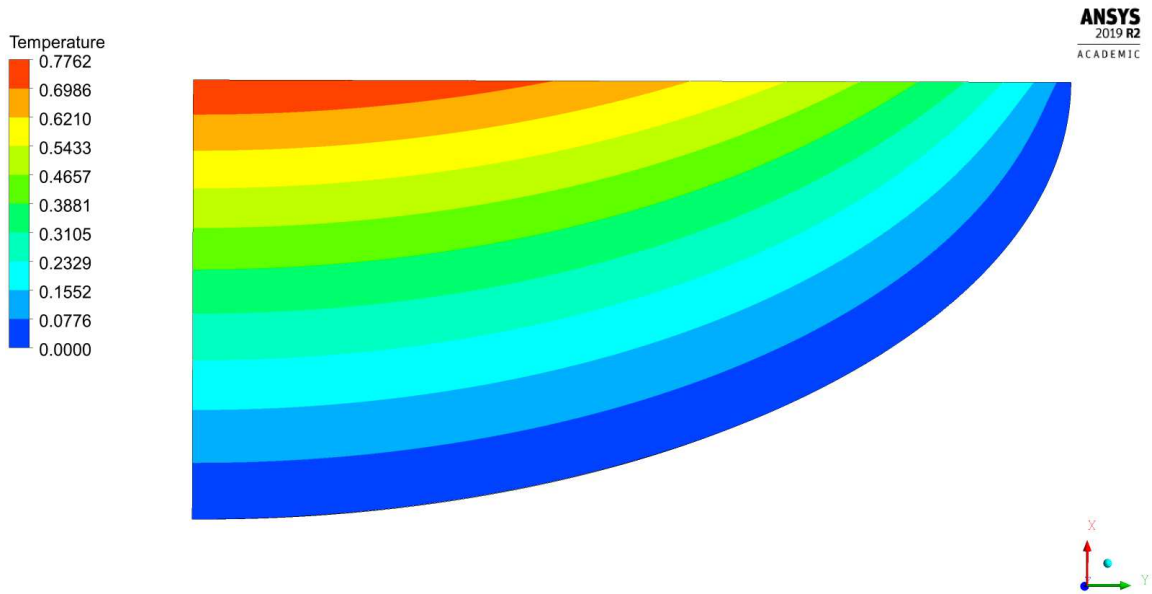


Figure B.126: Temperature field for Exp 3.01.

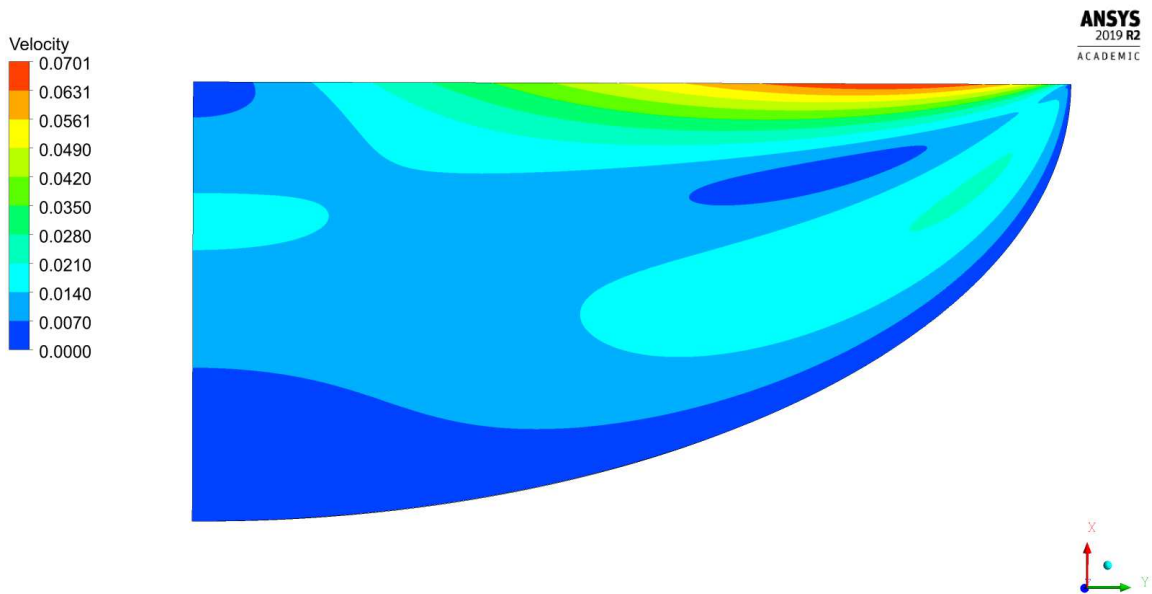


Figure B.127: Velocity magnitude contour for Exp 3.01.

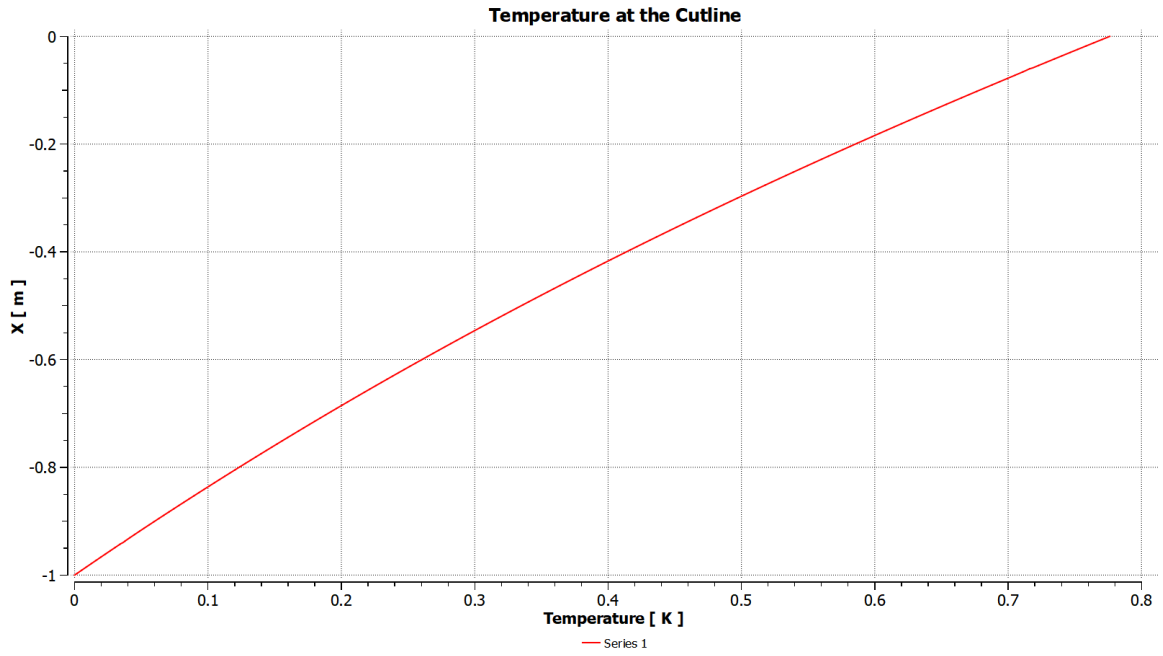


Figure B.128: Temperature at the axis of symmetry for Exp 3.01.

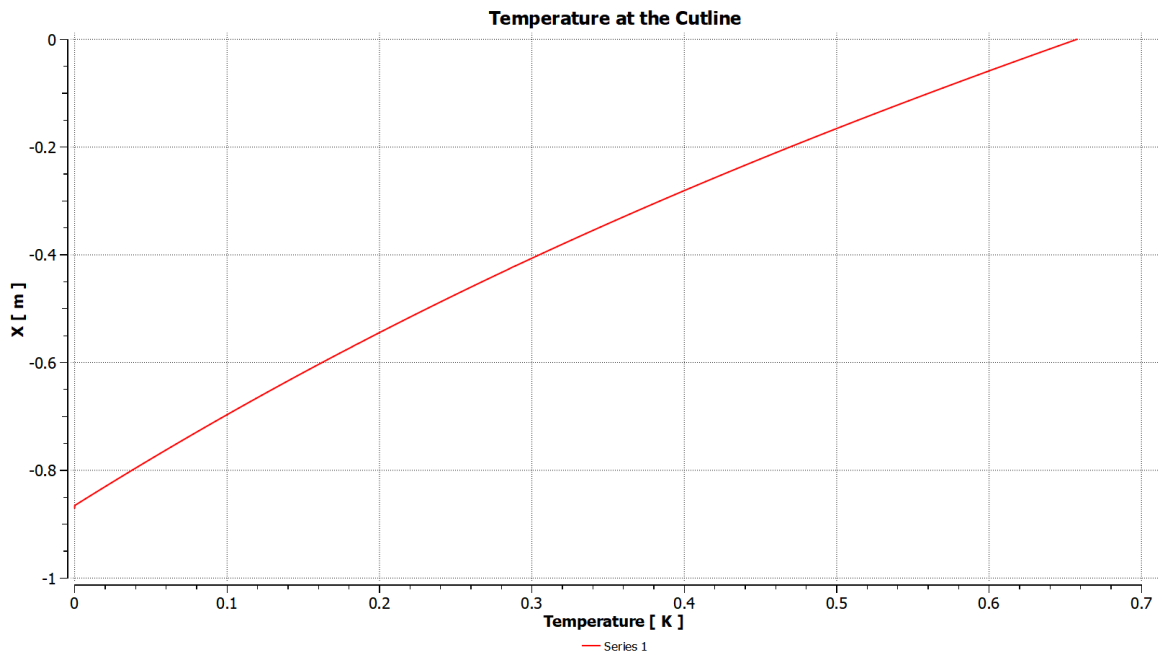


Figure B.129: Temperature at the cutline at $r^*=1$ for Exp 3.01.

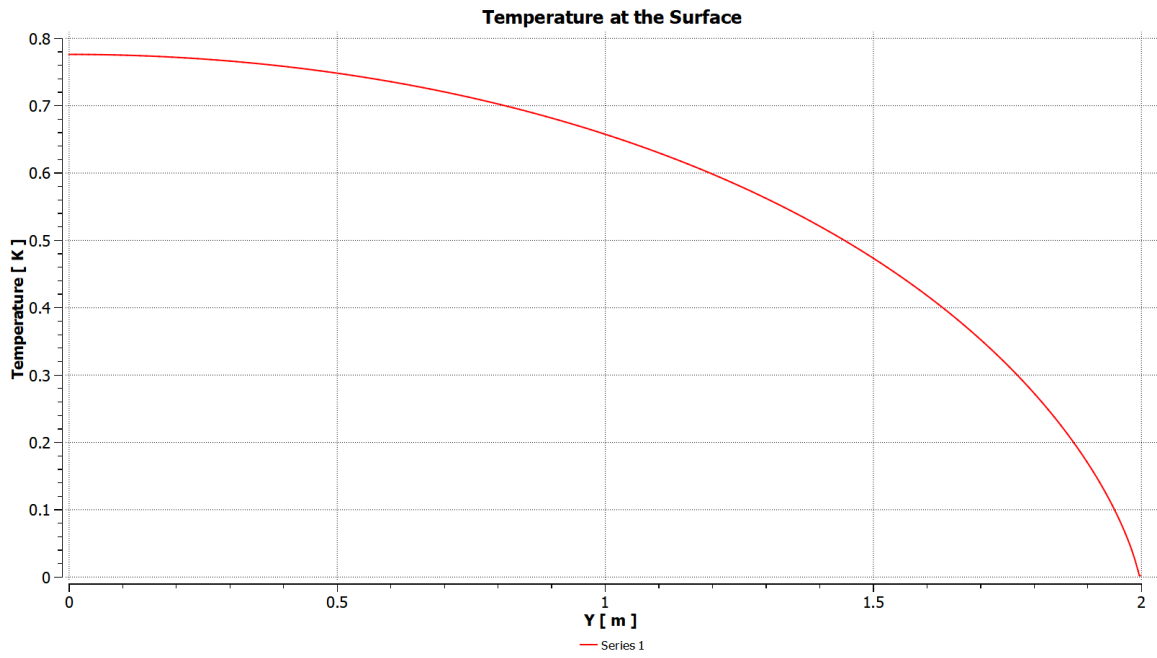


Figure B.130: Temperature at the free surface for Exp 3.01.

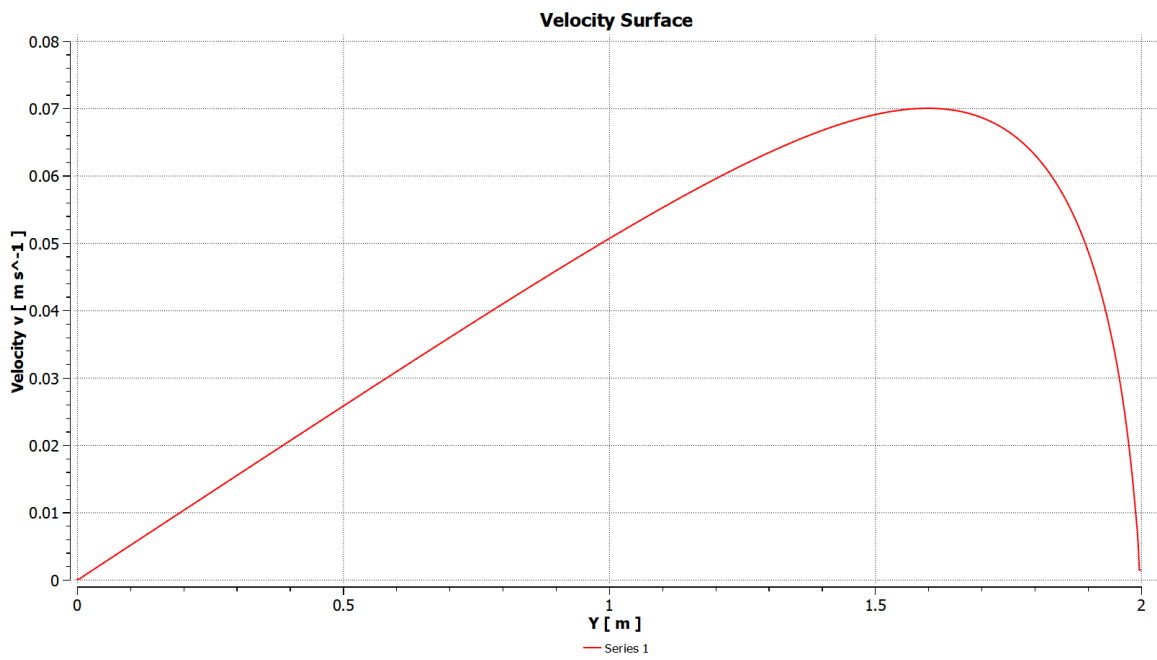


Figure B.131: Velocity at the free surface for Exp 3.01.

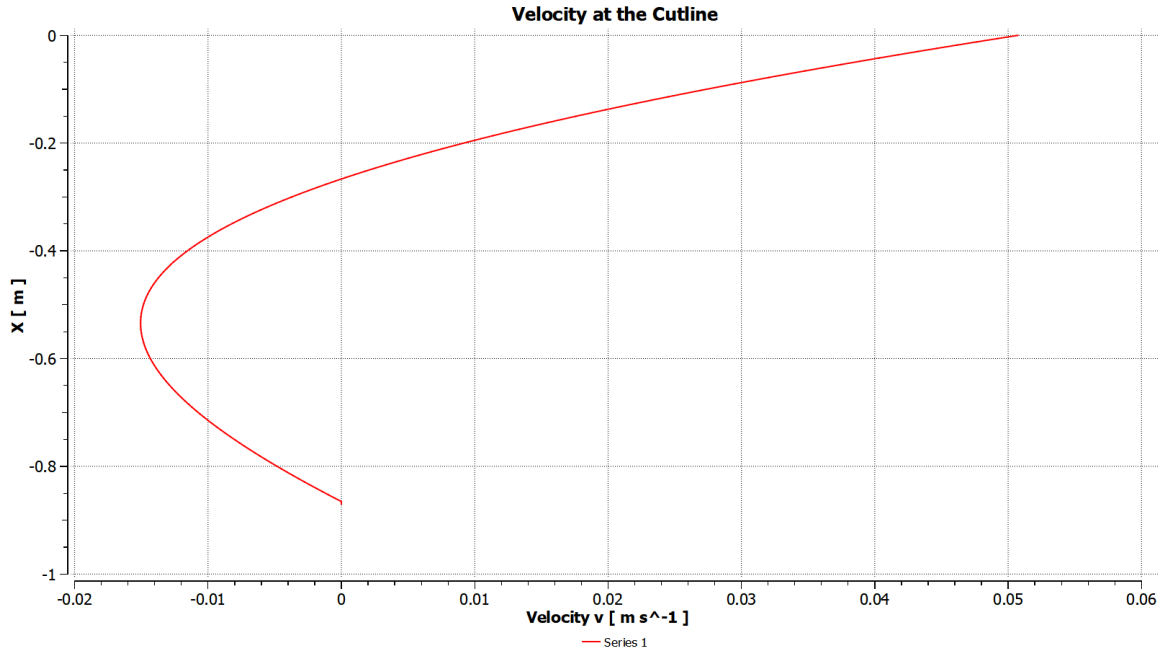


Figure B.132: Radial velocity u at the cutline at $r^*=1$ for Exp 3.01.

Exp 3.02

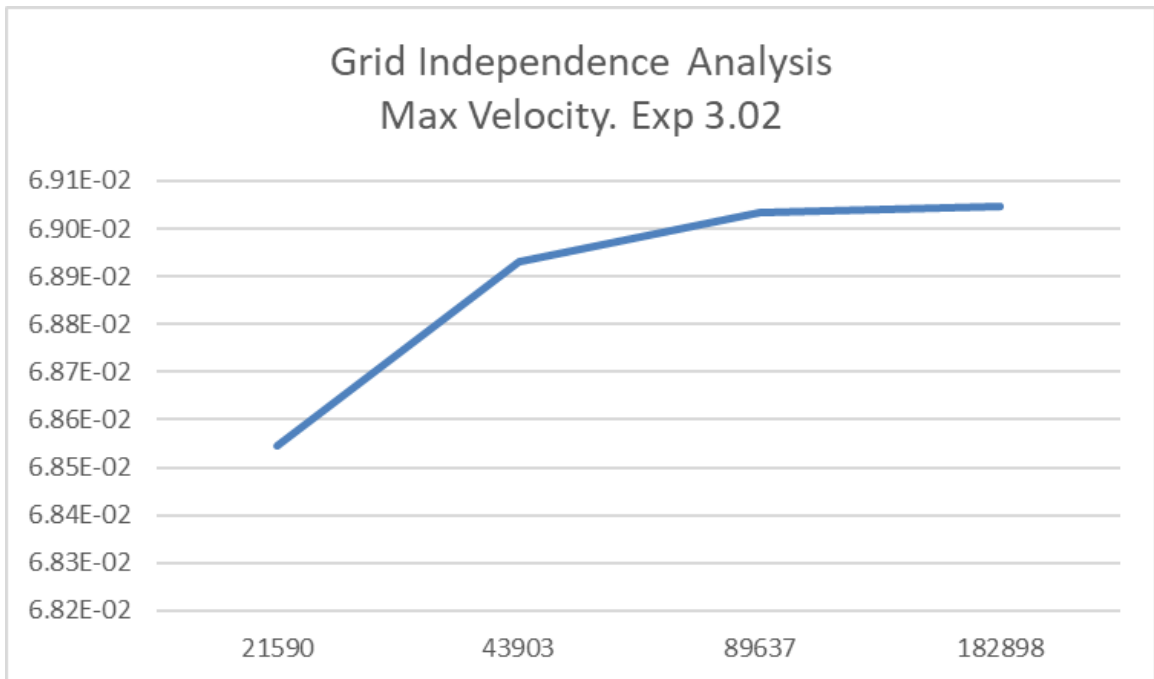


Figure B.133: Convergence for Exp 3.02: peak velocity values vs number of nodes in logarithmic scale.

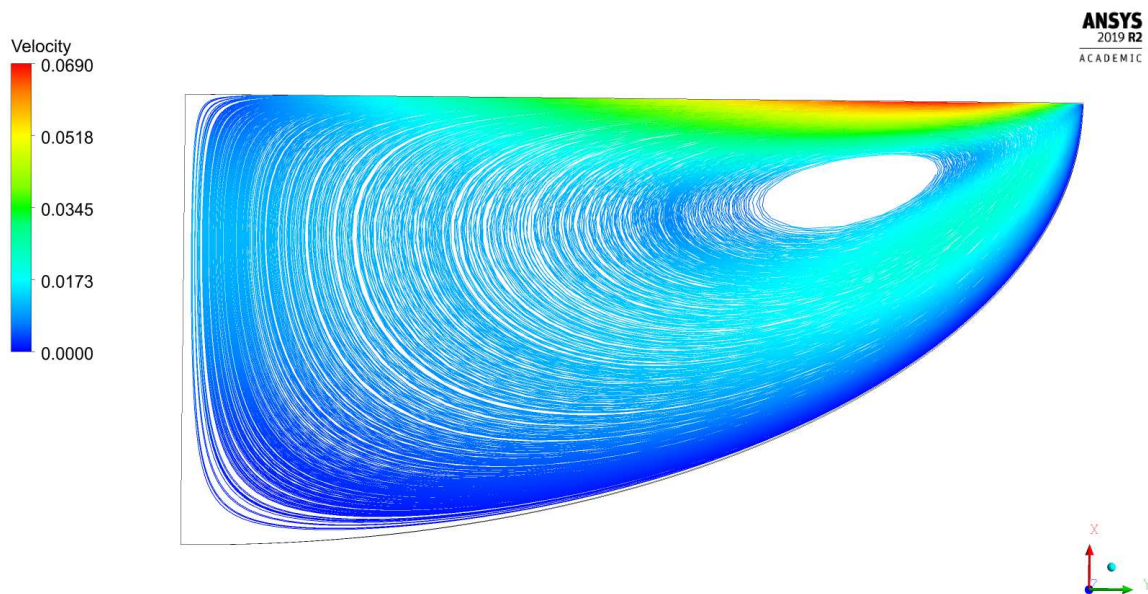


Figure B.134: Streamlines for Exp 3.02.

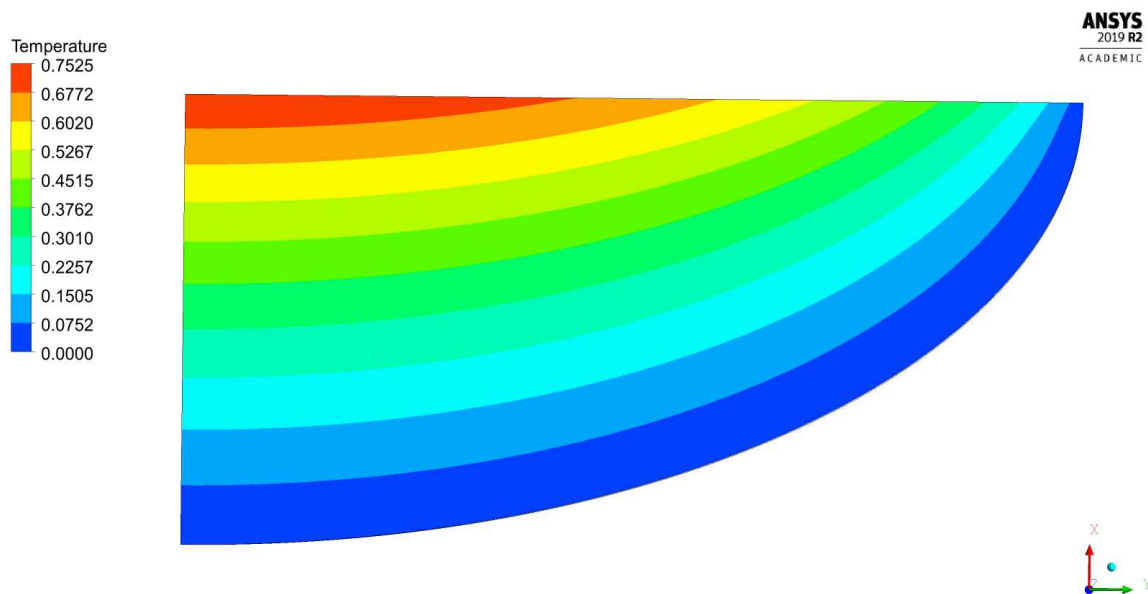


Figure B.135: Temperature field for Exp 3.02.

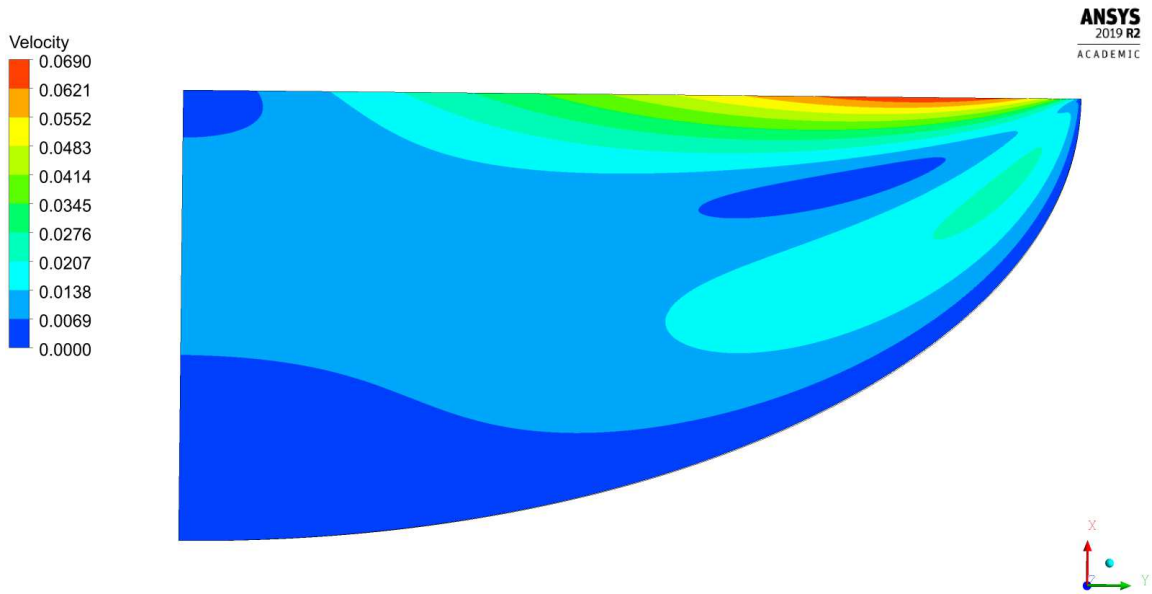


Figure B.136: Velocity magnitude contour for Exp 3.02.

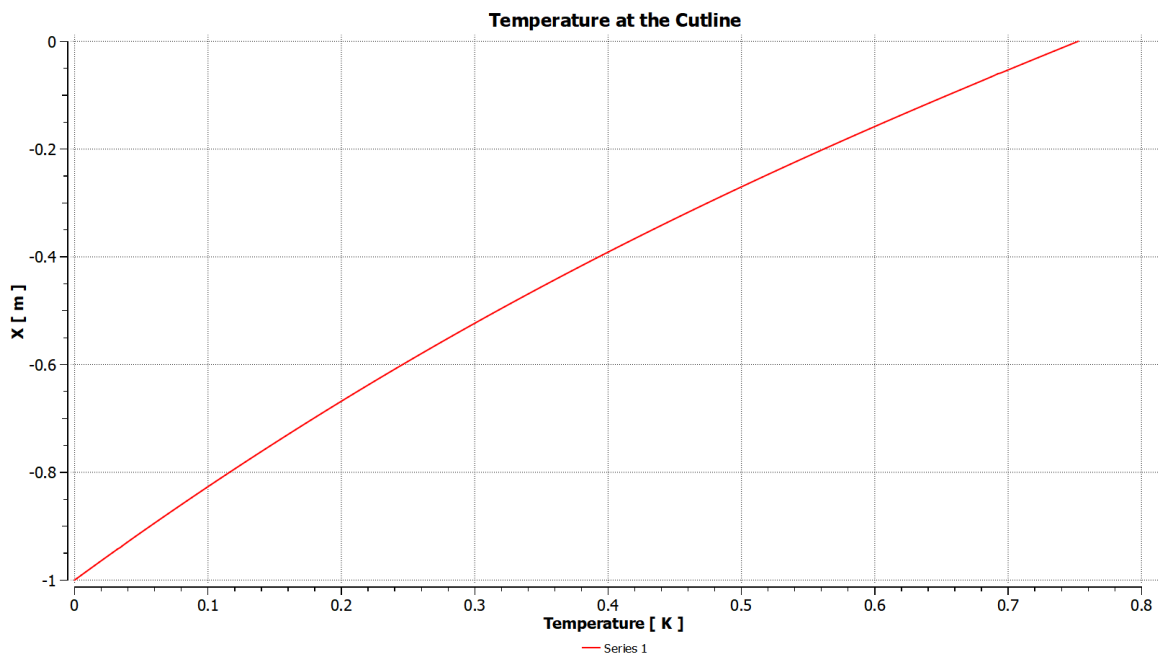


Figure B.137: Temperature at the axis of symmetry for Exp 3.02.

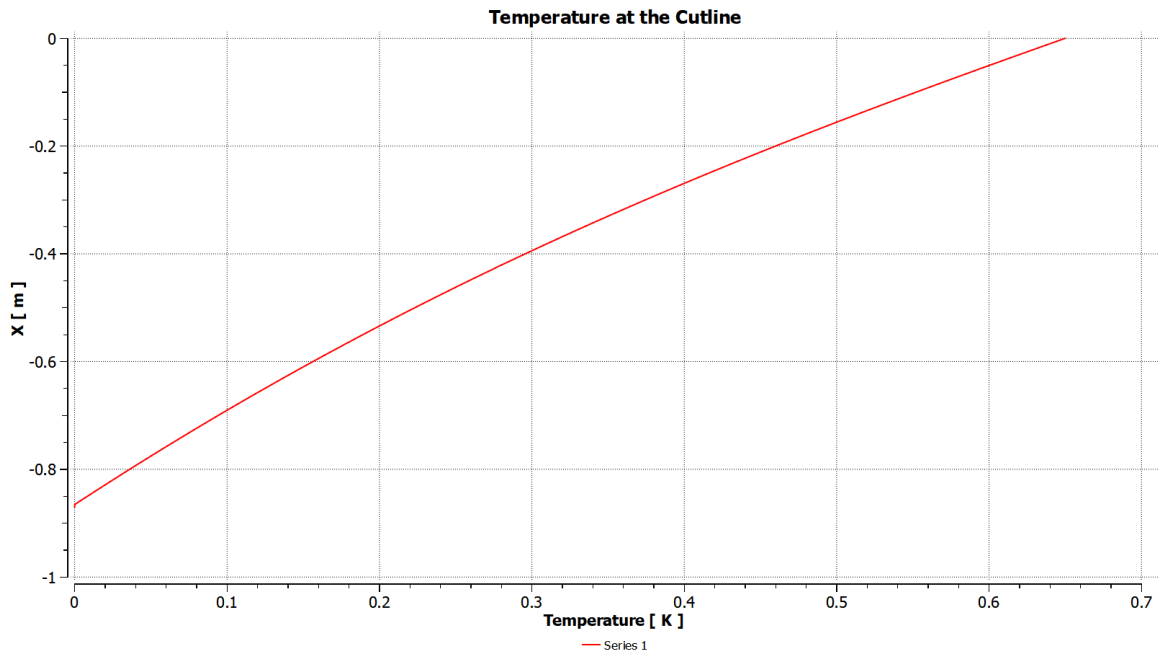


Figure B.138: Temperature at the cutline at $r^*=1$ for Exp 3.02.

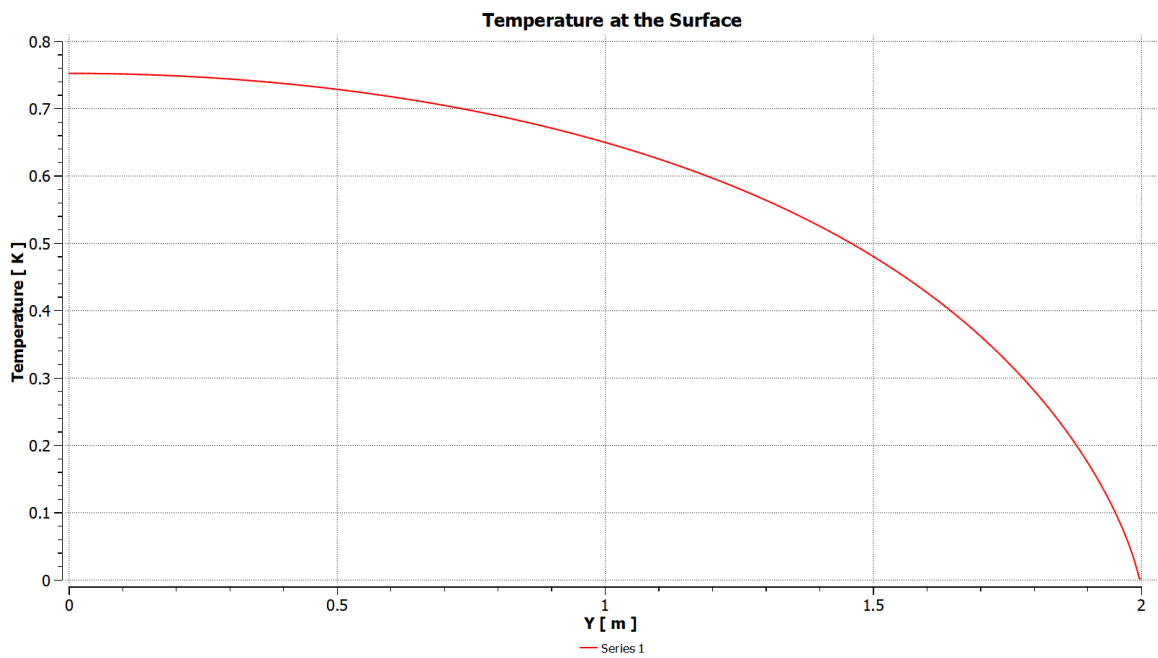


Figure B.139: Temperature at the free surface for Exp 3.02.

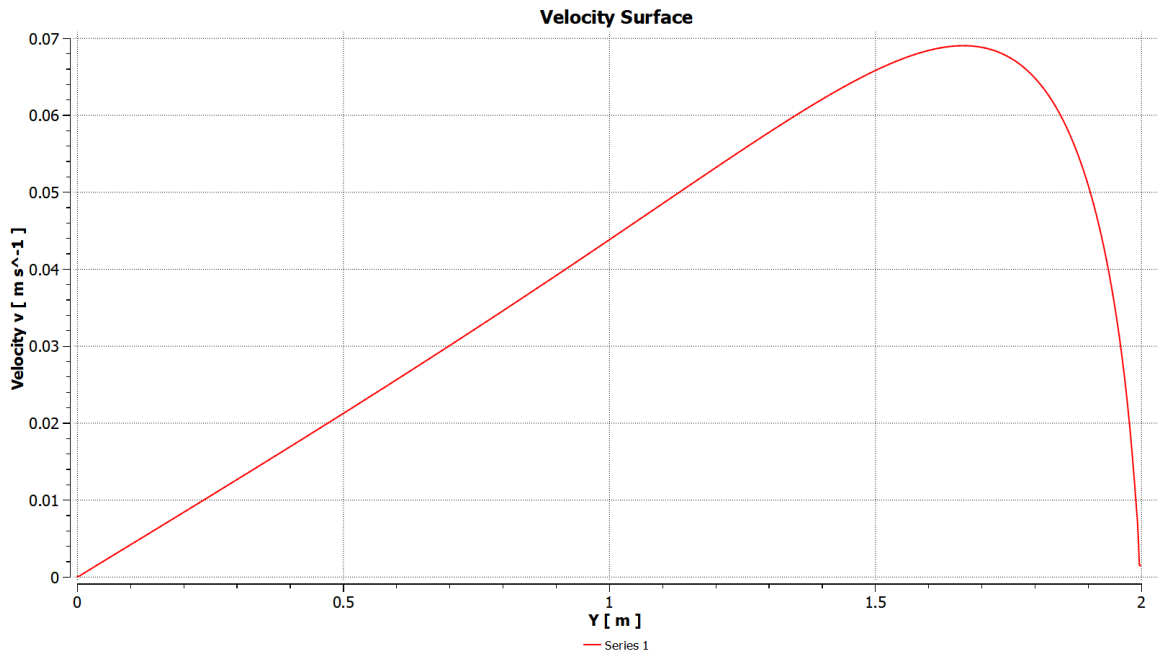


Figure B.140: Velocity at the free surface for Exp 3.02.

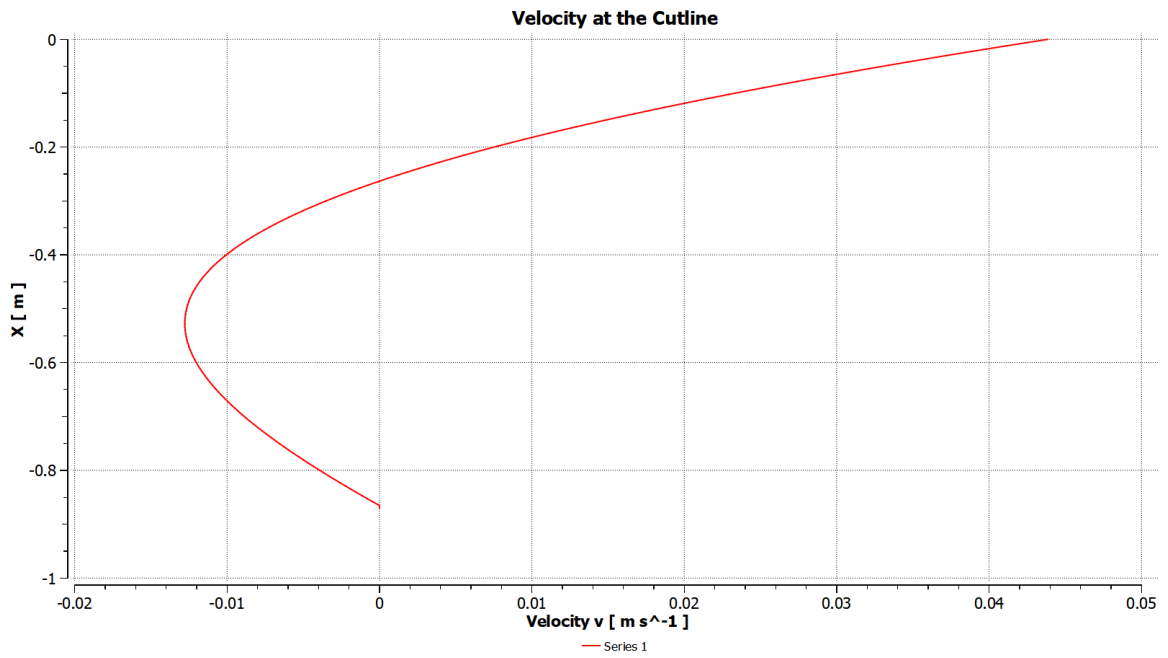


Figure B.141: Radial velocity u at the cutline at $r^*=1$ for Exp 3.02.

Exp 3.1

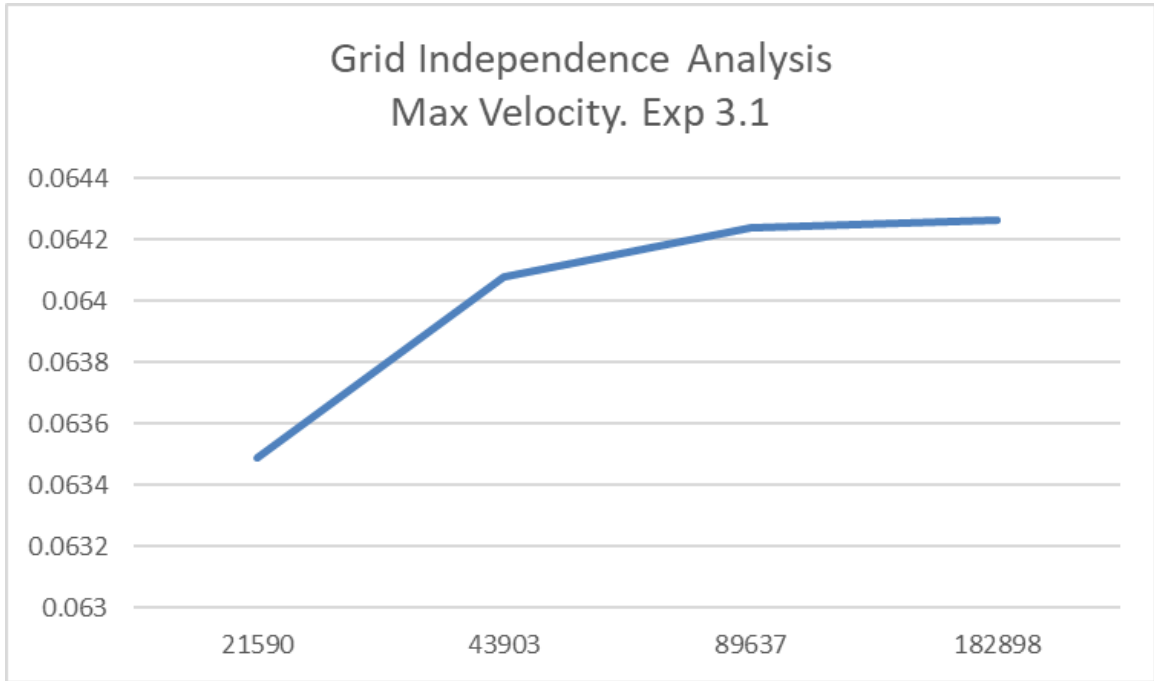


Figure B.142: Convergence for Exp 3.1: peak velocity values vs number of nodes in logarithmic scale.

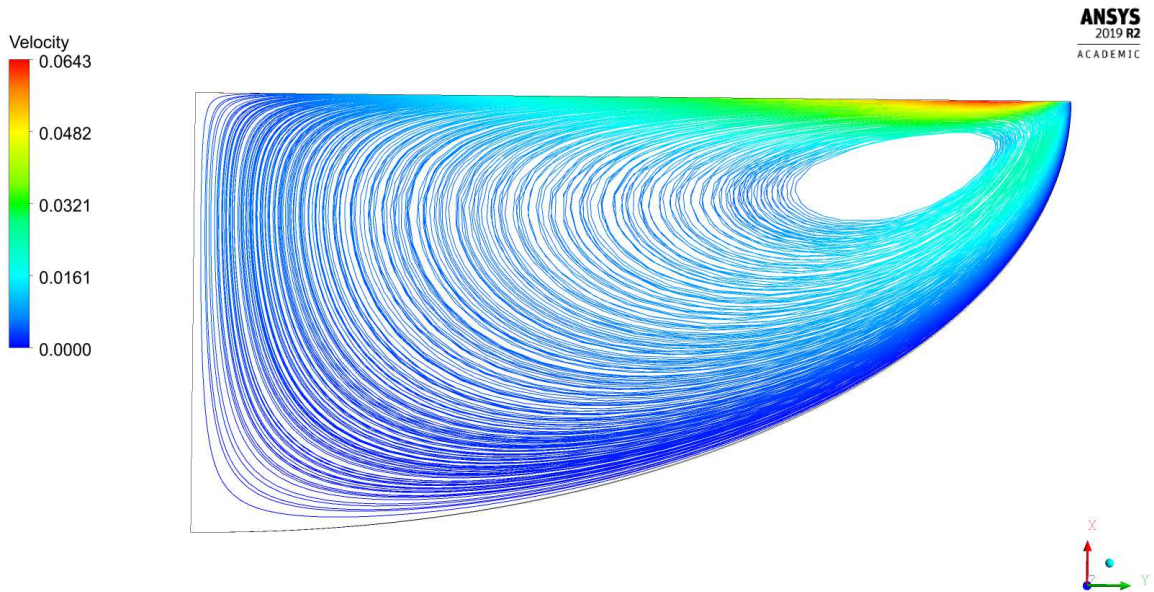


Figure B.143: Streamlines for Exp 3.1.

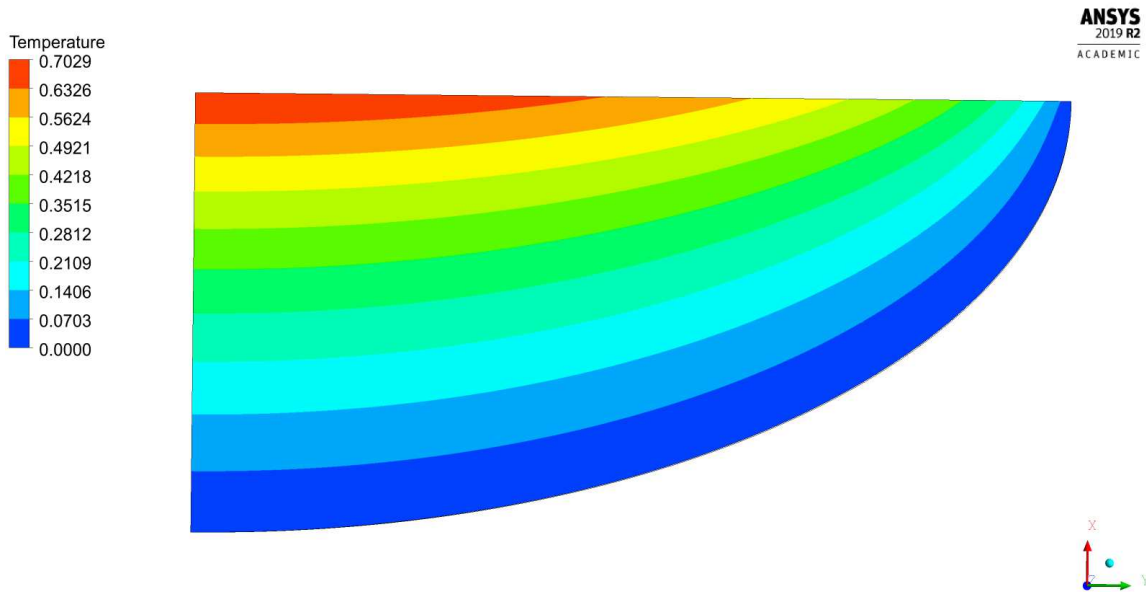


Figure B.144: Temperature field for Exp 3.1.

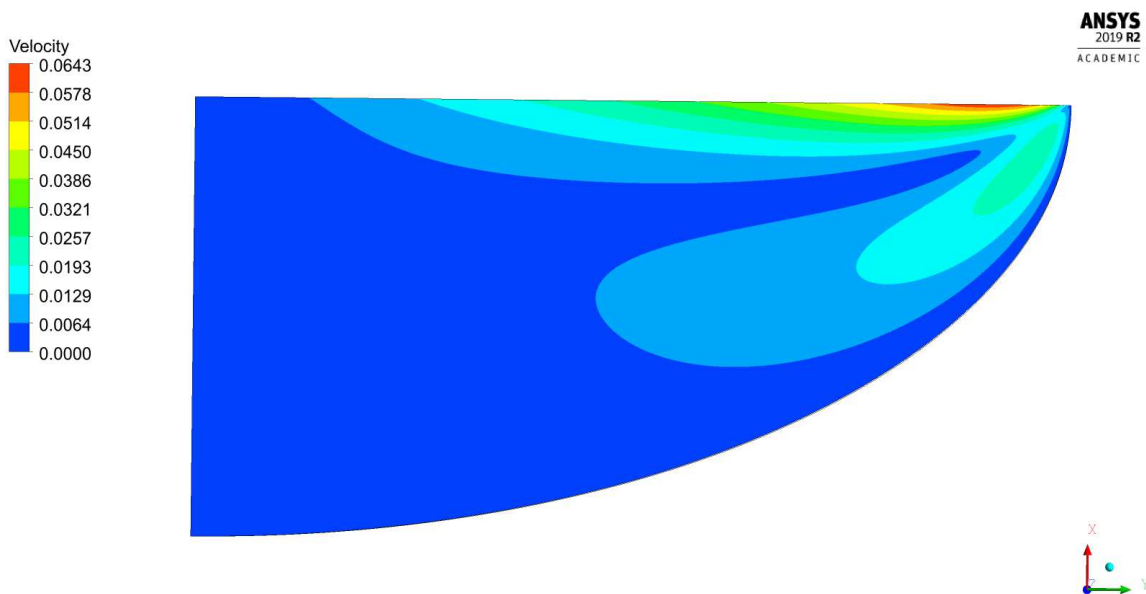


Figure B.145: Velocity magnitude contour for Exp 3.1.

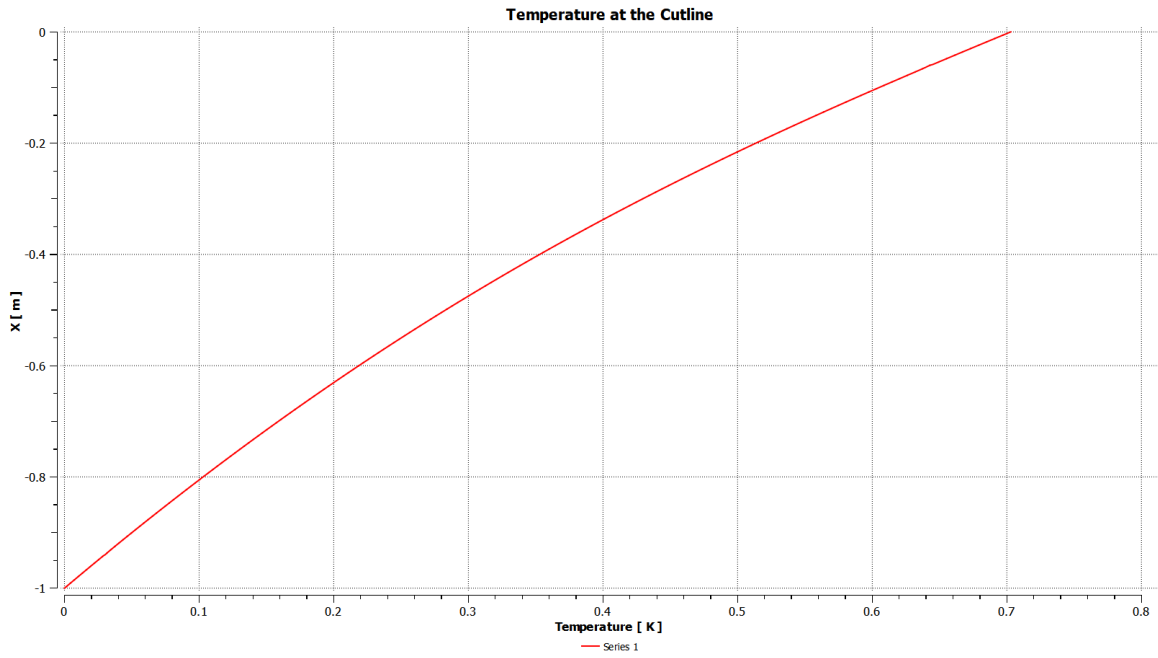


Figure B.146: Temperature at the axis of symmetry for Exp 3.1.

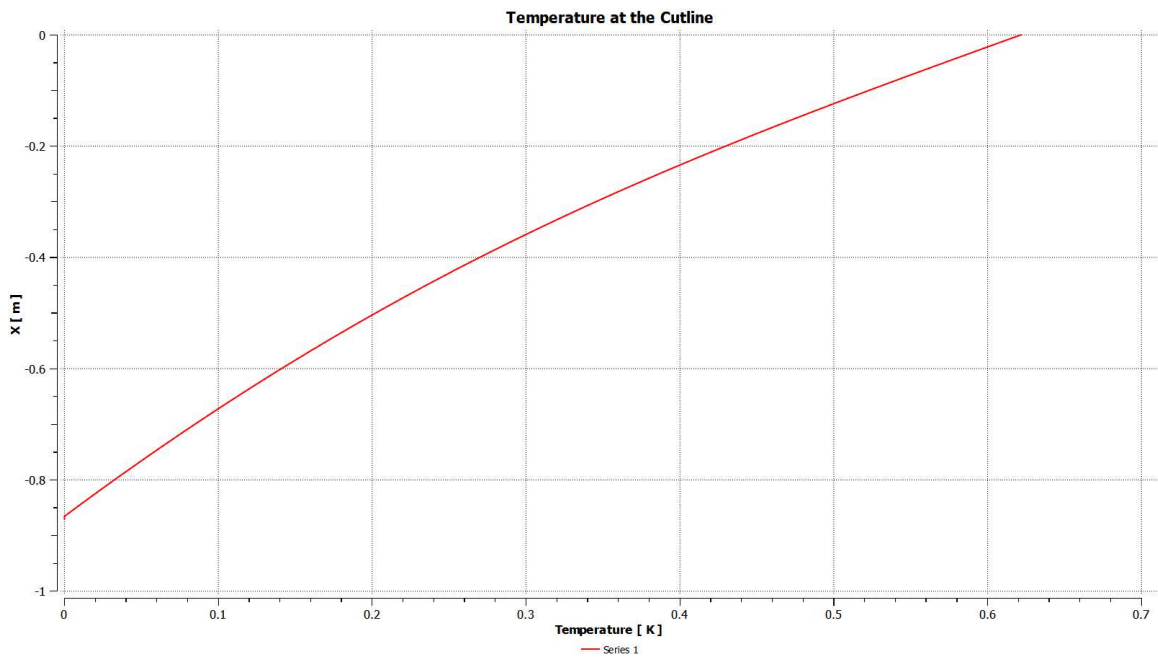


Figure B.147: Temperature at the cutline at $r^*=1$ for Exp 3.1.

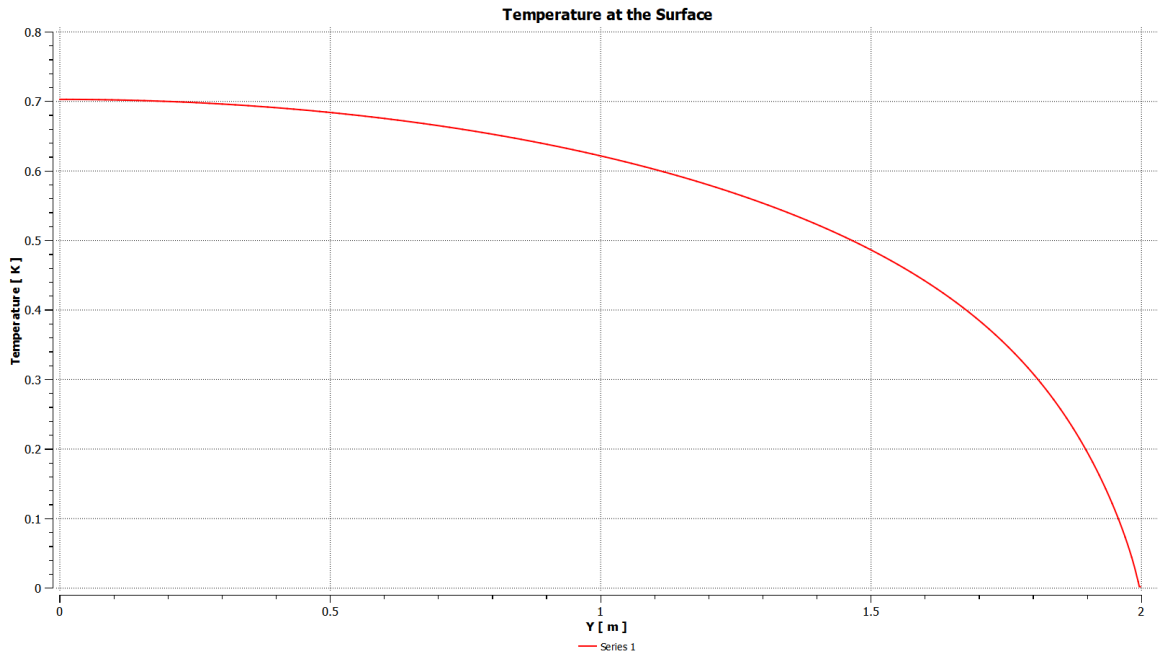


Figure B.148: Temperature at the free surface for Exp 3.1.

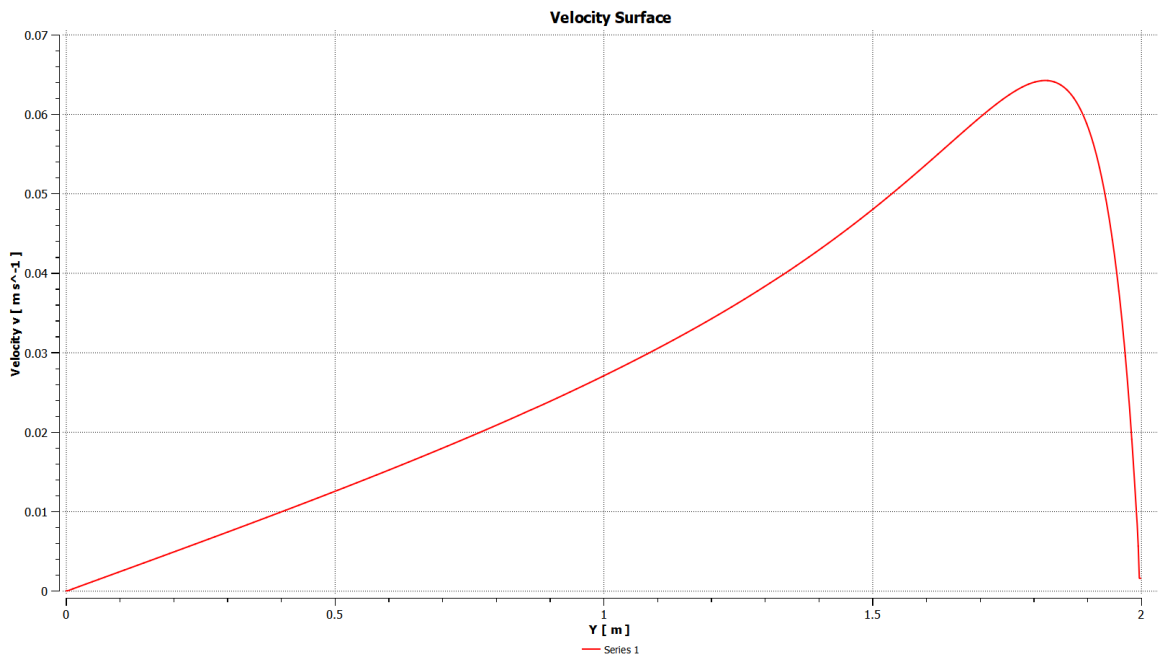


Figure B.149: Velocity at the free surface for Exp 3.1.

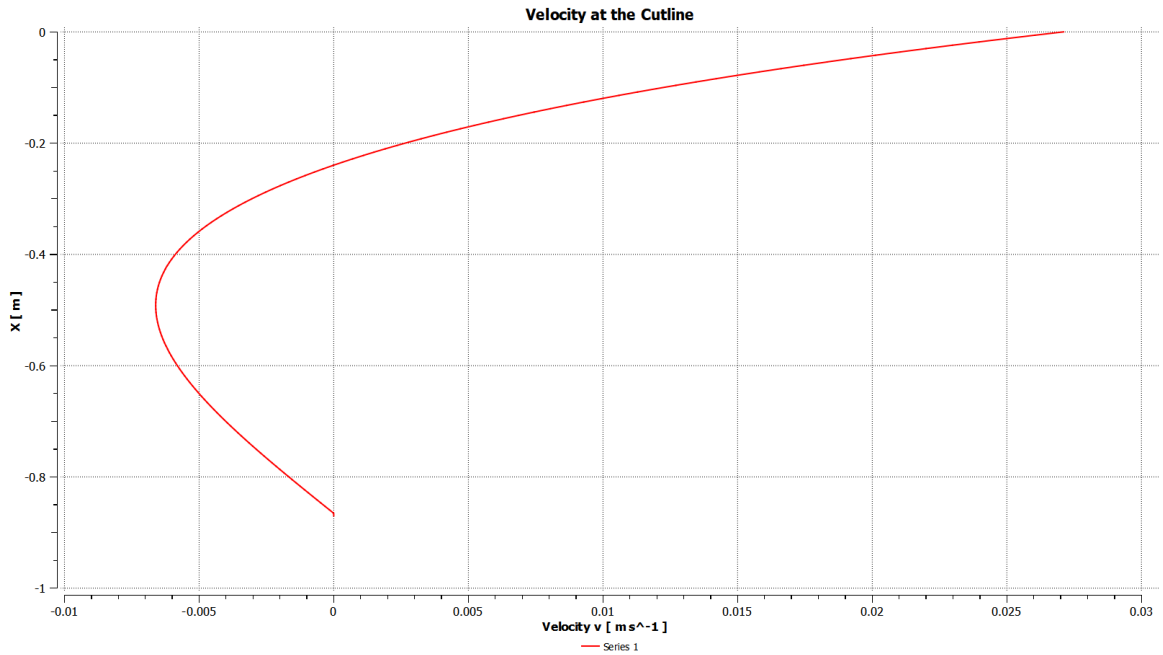


Figure B.150: Radial velocity u at the cutline at $r^*=1$ for Exp 3.1.

Exp 3.2

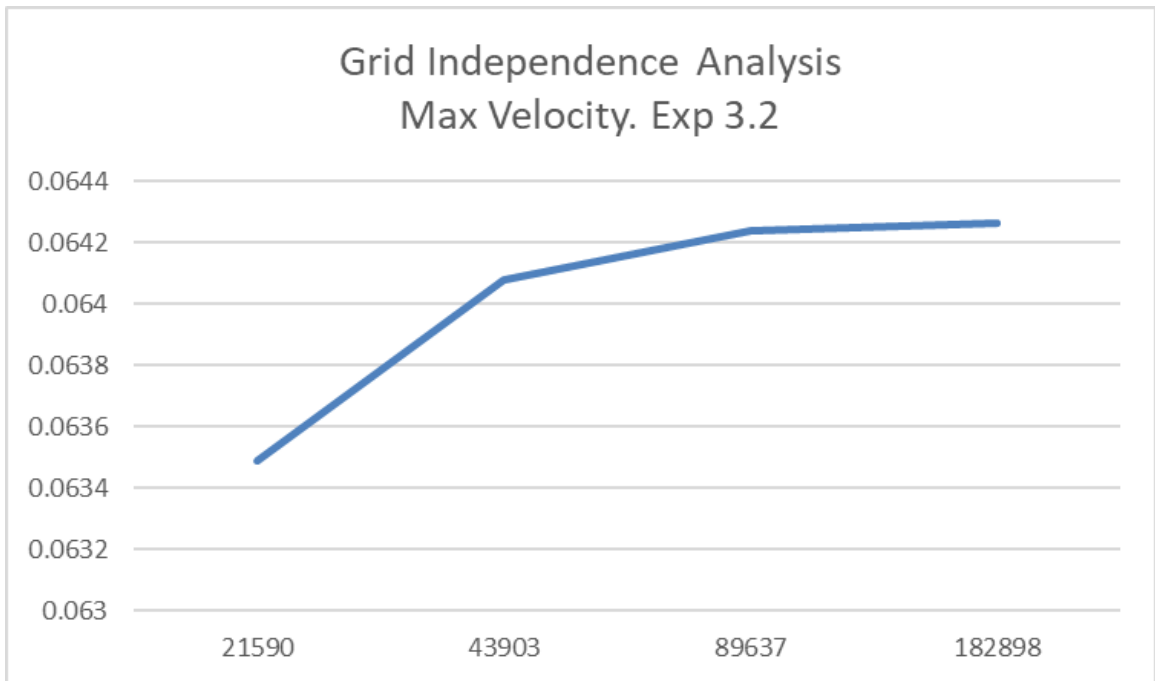


Figure B.151: Convergence for Exp 3.2: peak velocity values vs number of nodes in logarithmic scale.

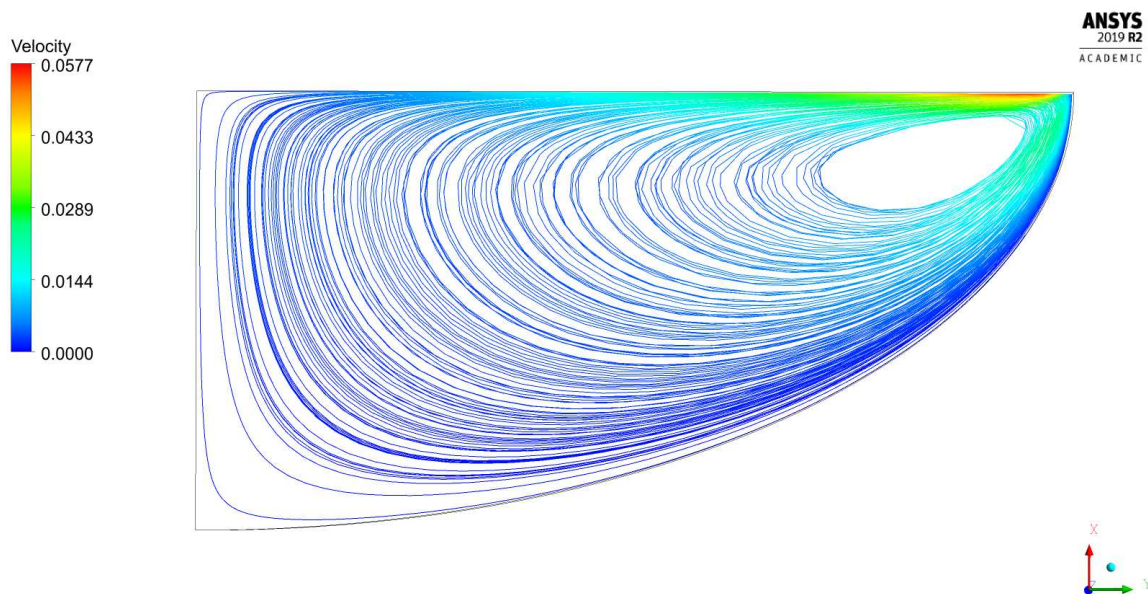


Figure B.152: Streamlines for Exp 3.2.

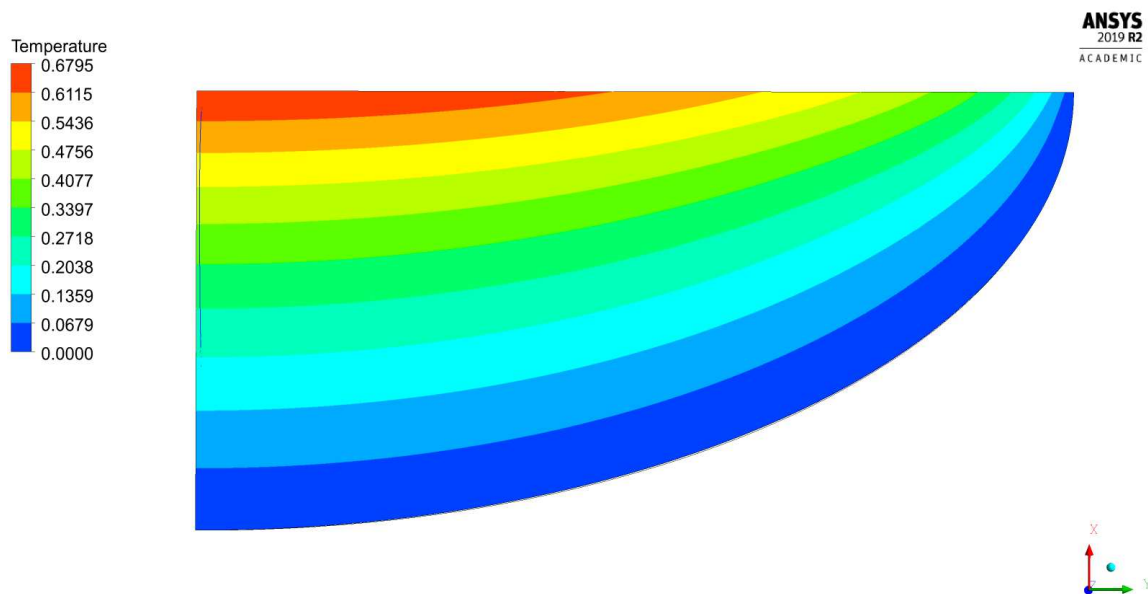


Figure B.153: Temperature field for Exp 3.2.

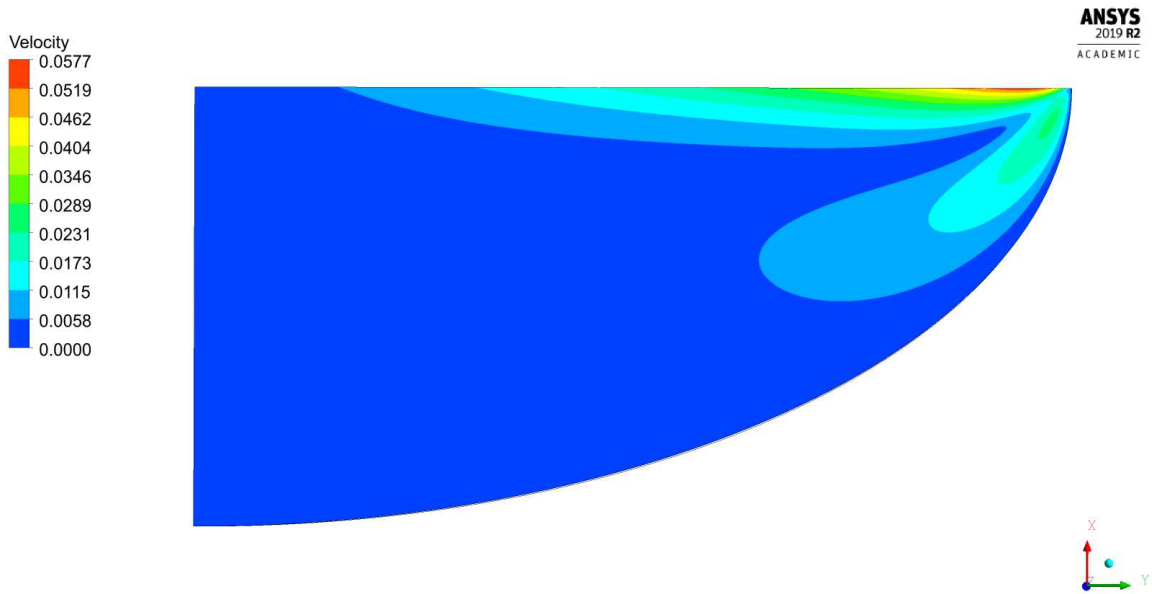


Figure B.154: Velocity magnitude contour for Exp 3.2.

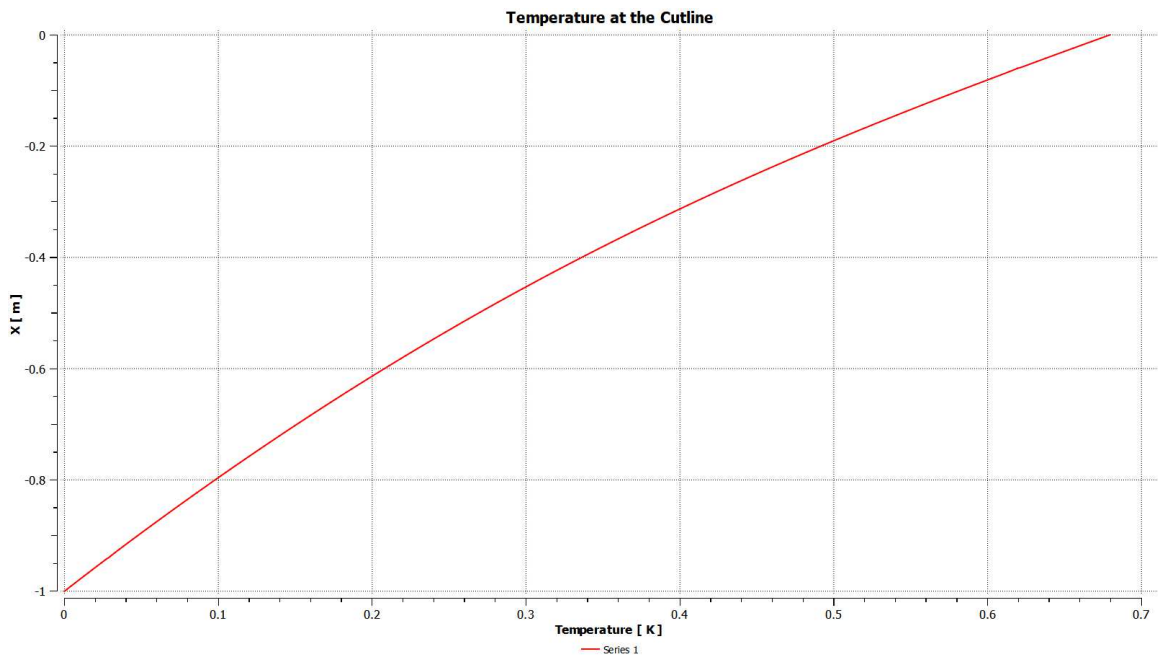


Figure B.155: Temperature at the axis of symmetry for Exp 3.2.

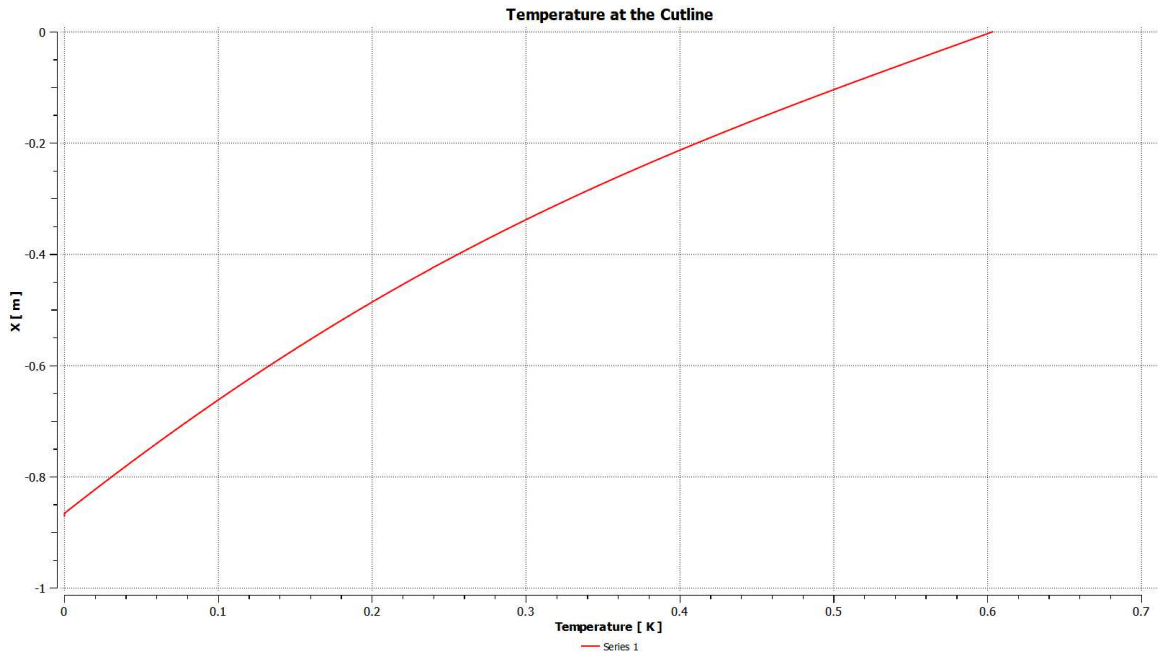


Figure B.156: Temperature at the cutline at $r^*=1$ for Exp 3.2.

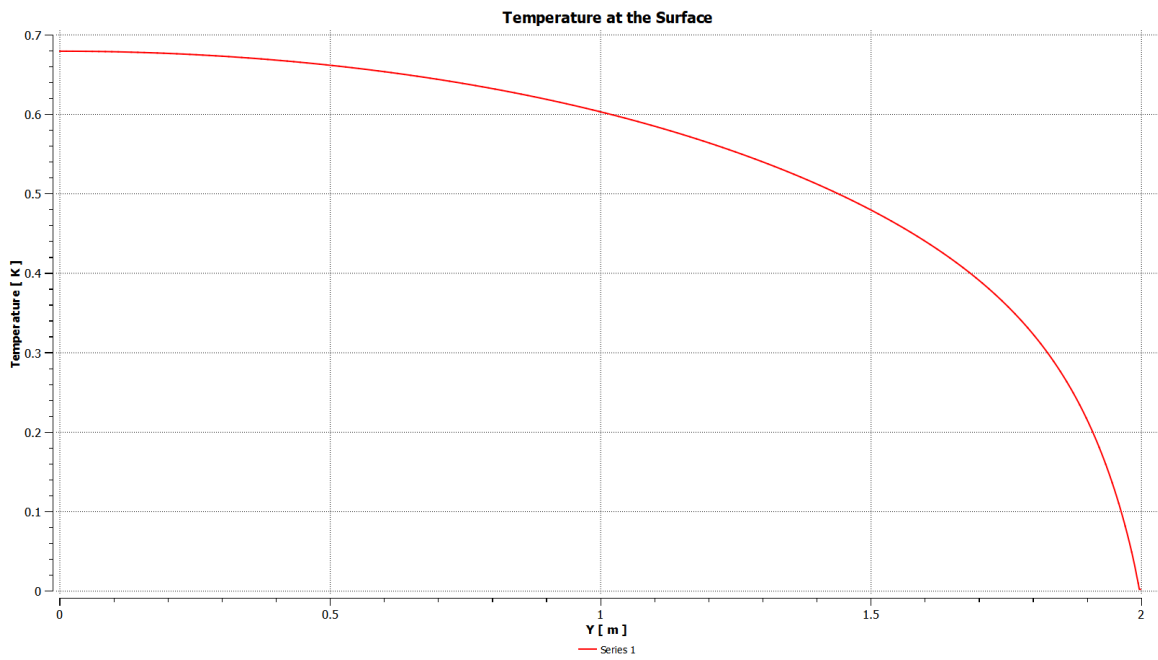


Figure B.157: Temperature at the free surface for Exp 3.2.

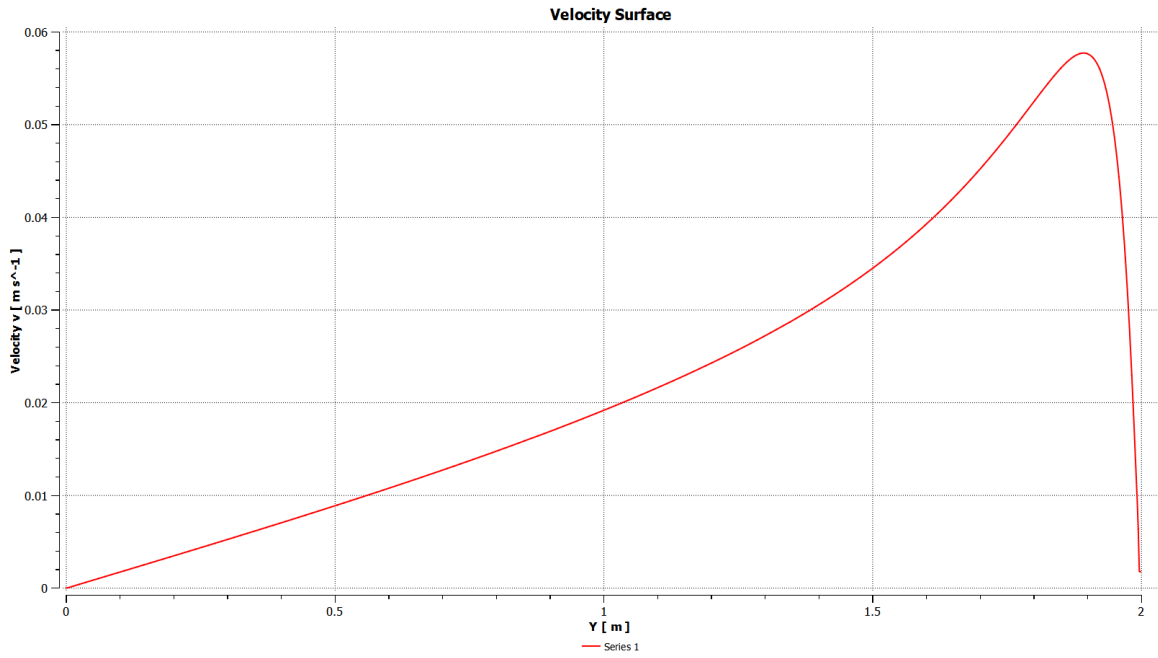


Figure B.158: Velocity at the free surface for Exp 3.2.

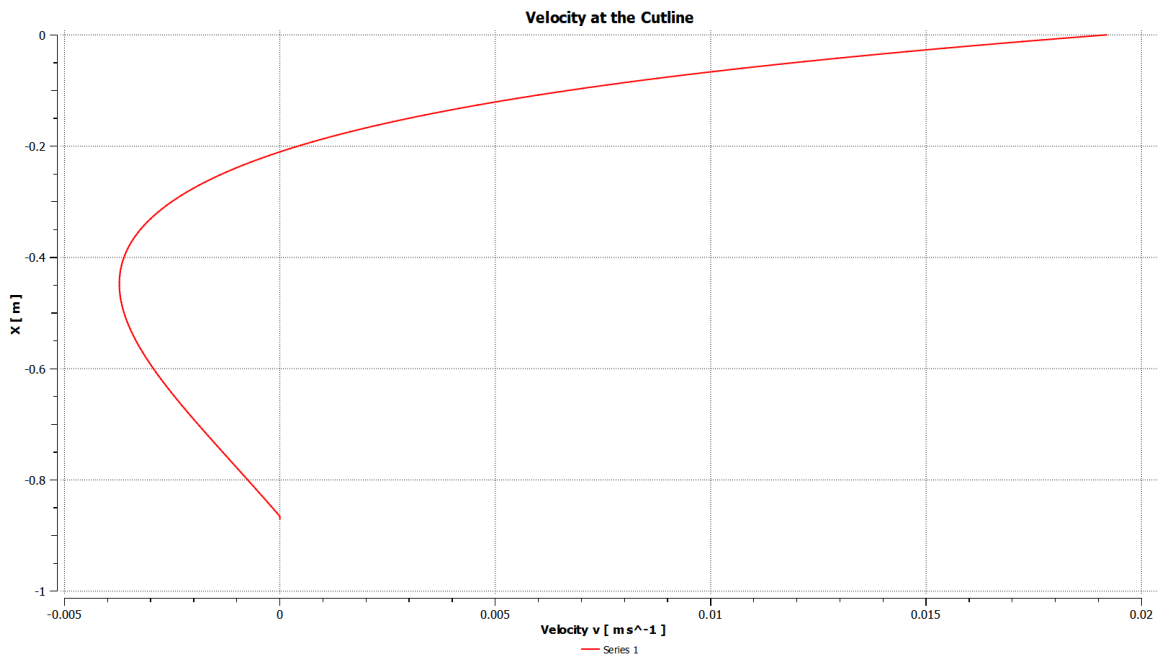


Figure B.159: Radial velocity u at the cutline at $r^*=1$ for Exp 3.2.

Exp 3.3

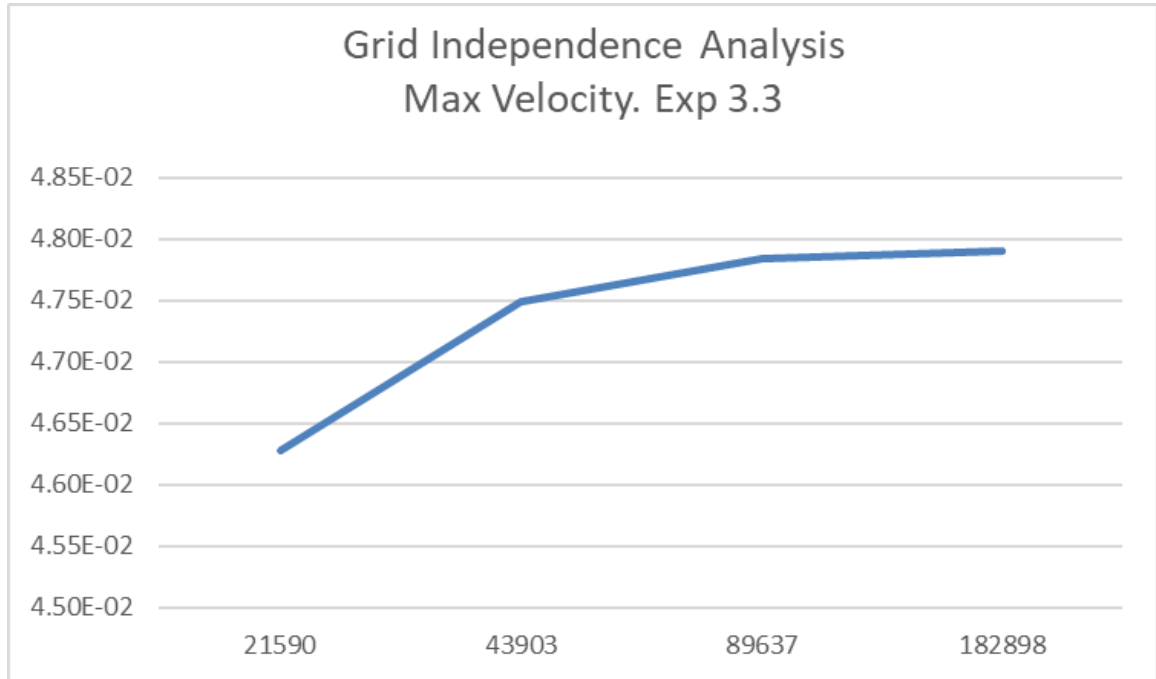


Figure B.160: Convergence for Exp 3.3: peak velocity values vs number of nodes in logarithmic scale.

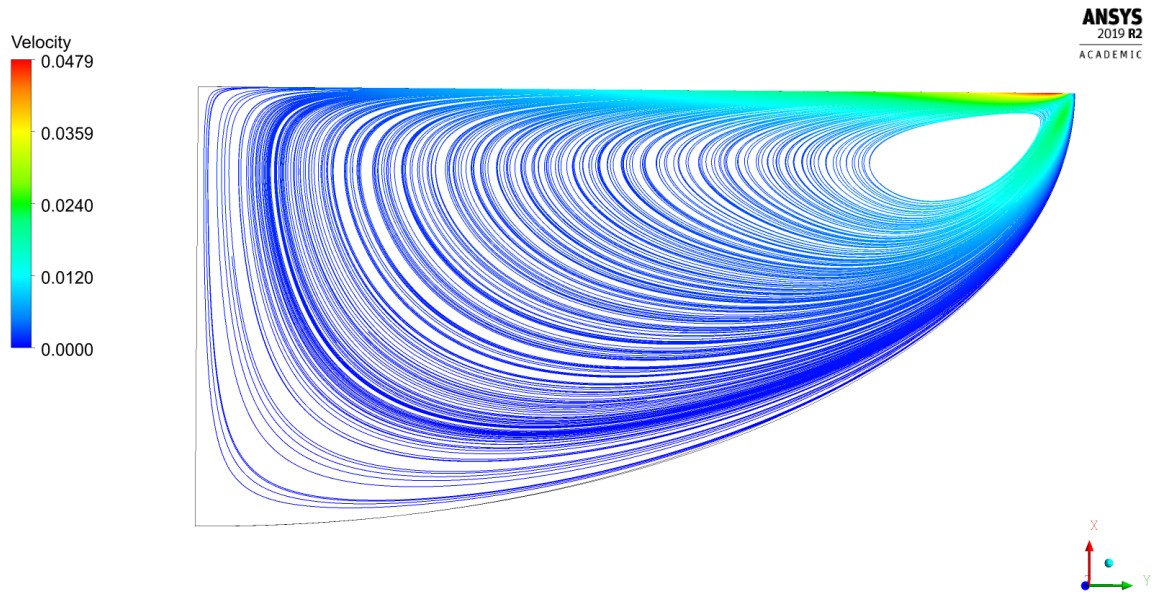


Figure B.161: Streamlines for Exp 3.3.

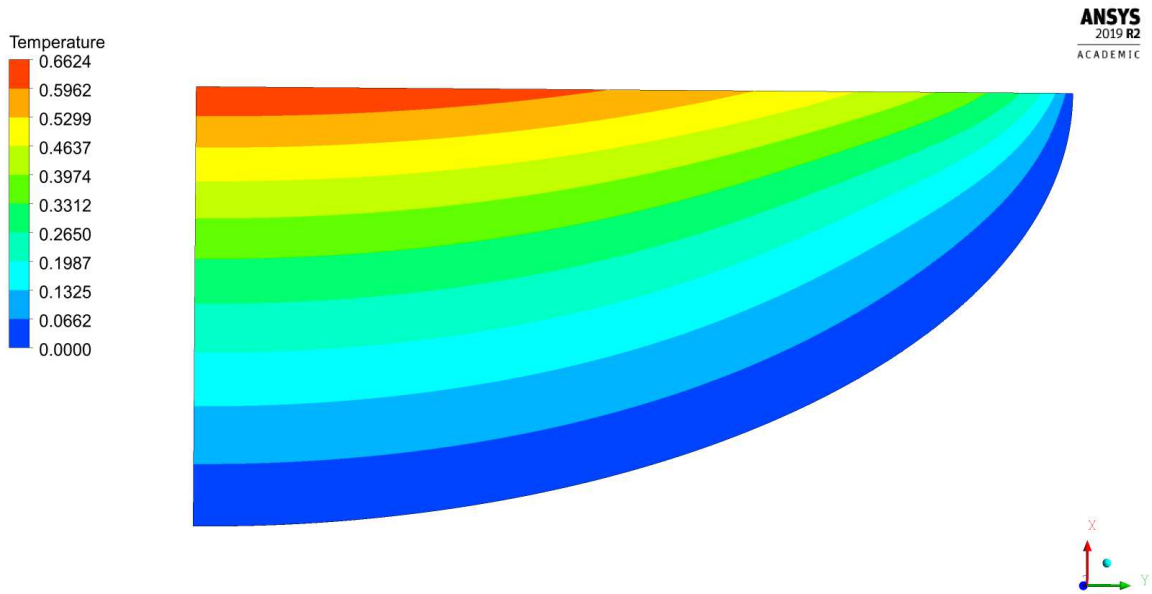


Figure B.162: Temperature field for Exp 3.3.

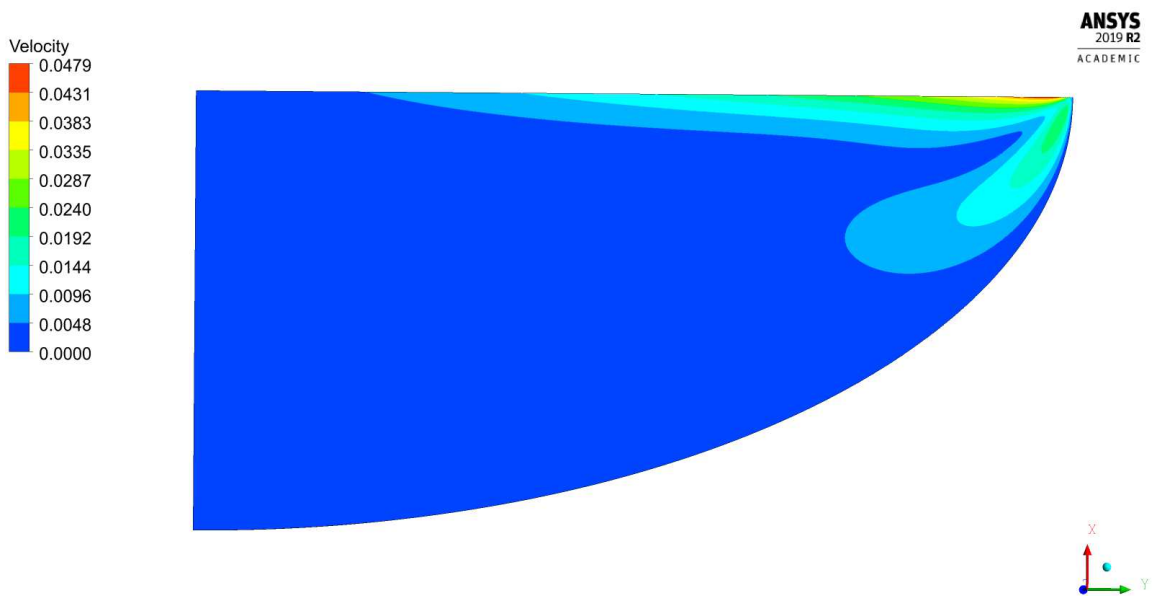


Figure B.163: Velocity magnitude contour for Exp 3.3.

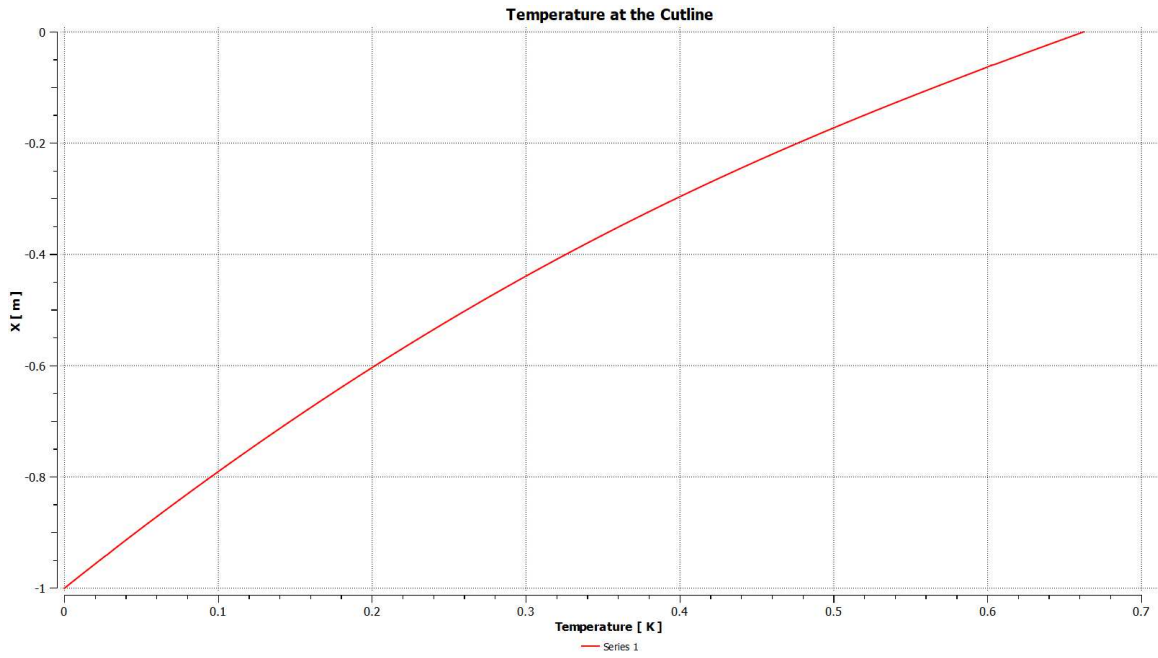


Figure B.164: Temperature at the axis of symmetry for Exp 3.3.

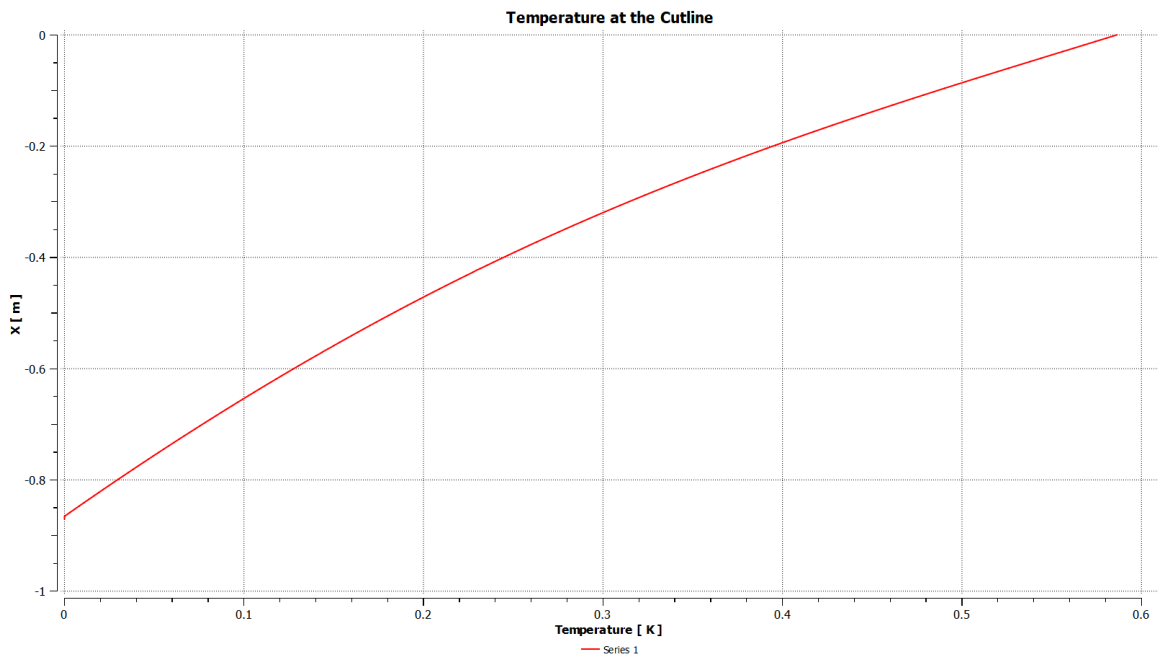


Figure B.165: Temperature at the cutline at $r^*=1$ for Exp 3.3.

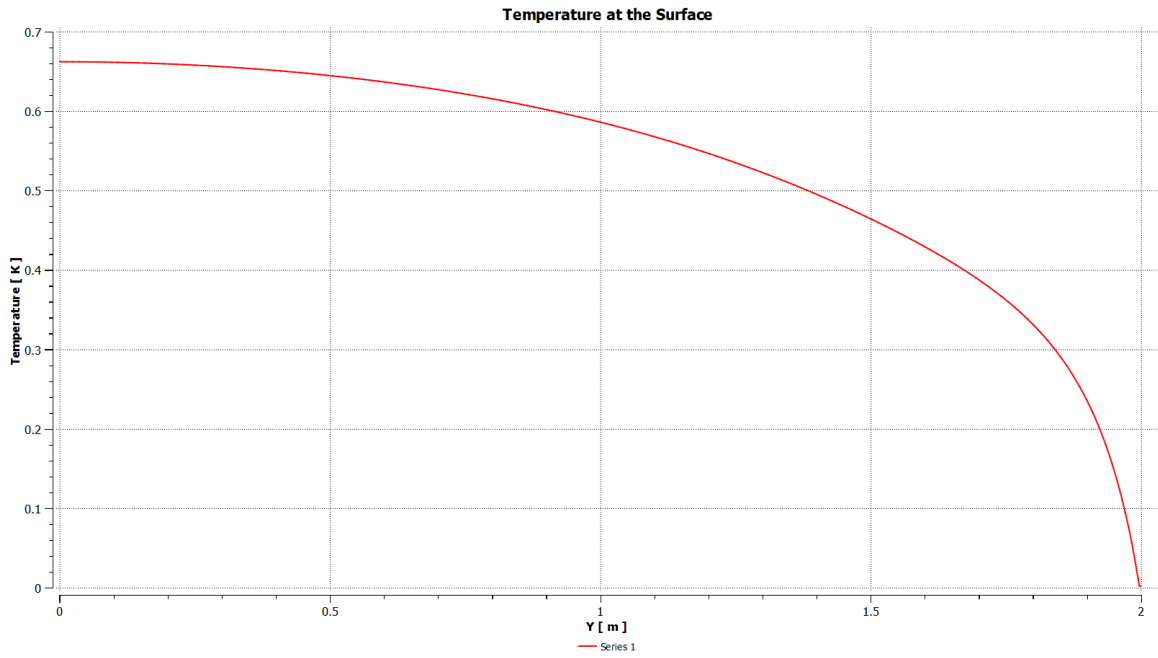


Figure B.166: Temperature at the free surface for Exp 3.3.

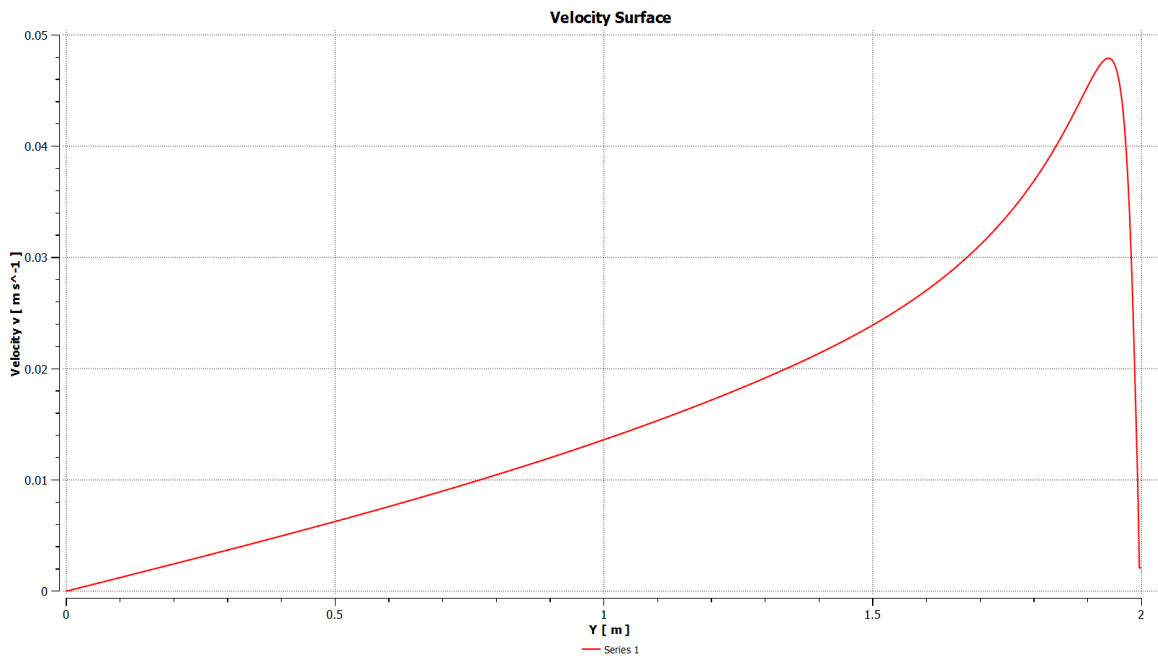


Figure B.167: Velocity at the free surface for Exp 3.3.

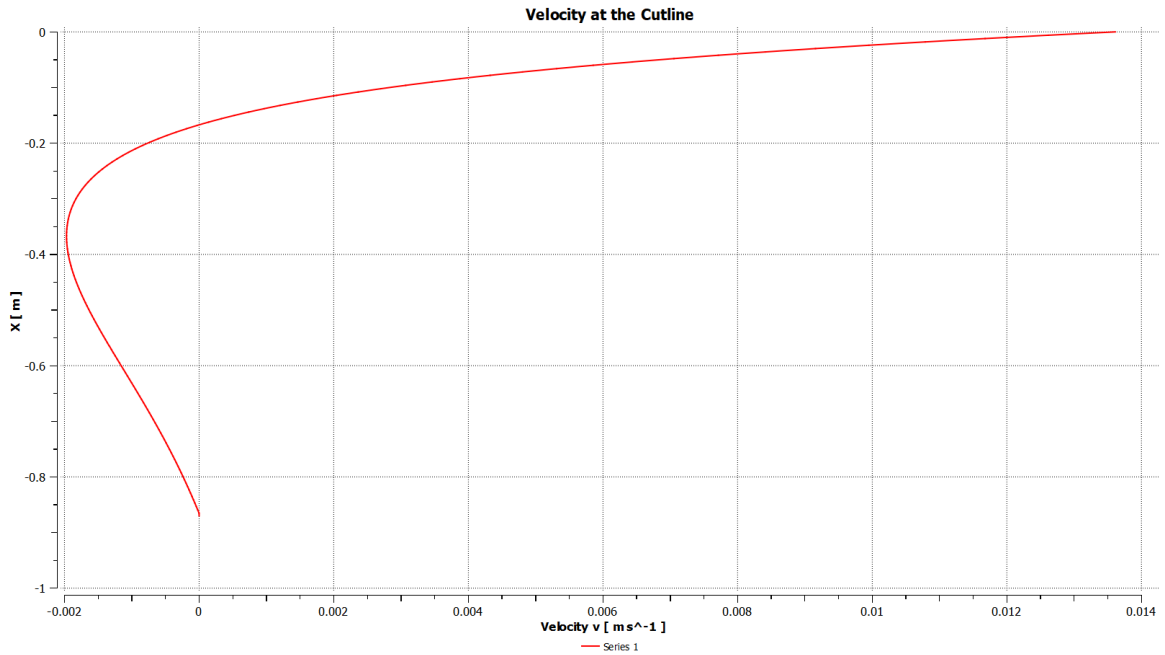


Figure B.168: Radial velocity u at the cutline at $r^*=1$ for Exp 3.3.

Exp 3.4

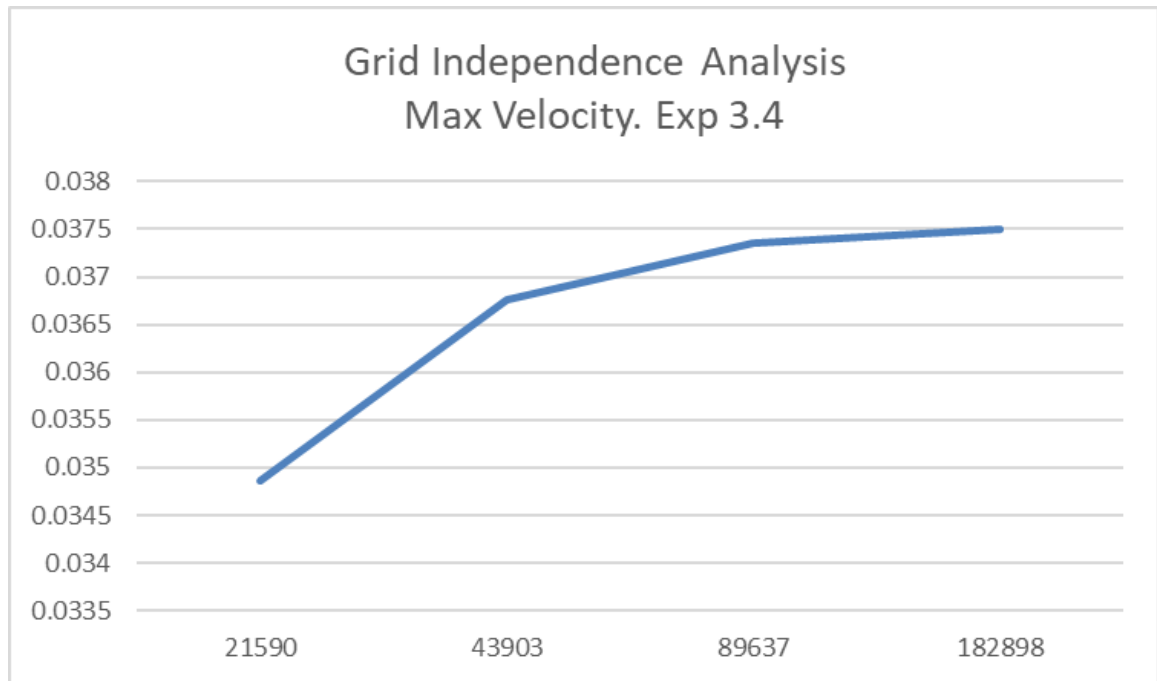


Figure B.169: Convergence for Exp 3.4: peak velocity values vs number of nodes in logarithmic scale.

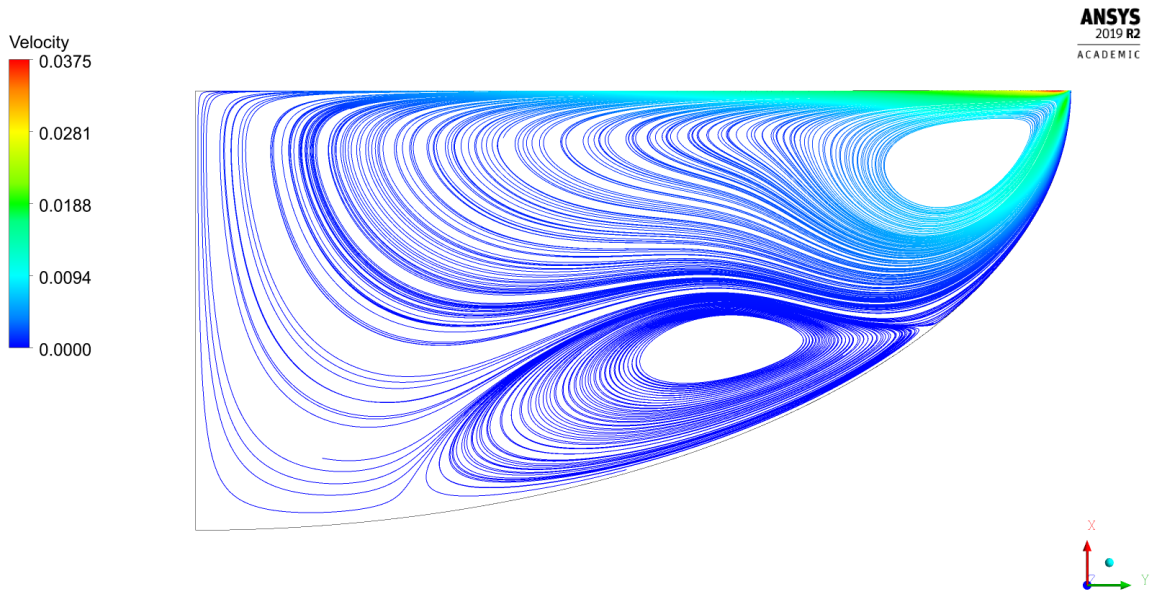


Figure B.170: Streamlines for Exp 3.4.

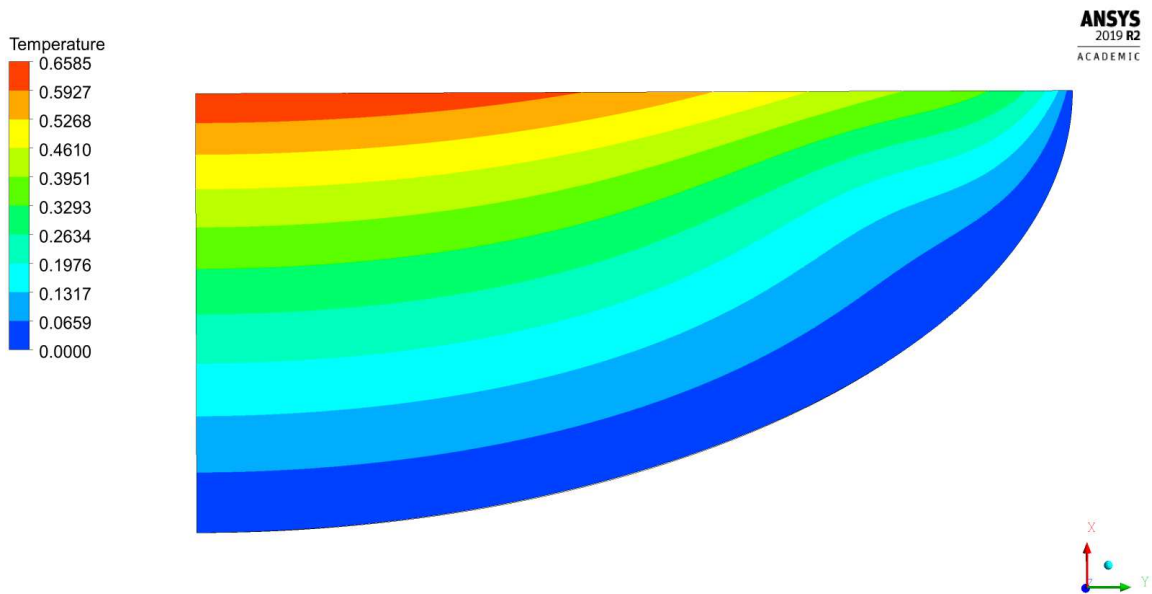


Figure B.171: Temperature field for Exp 3.4.

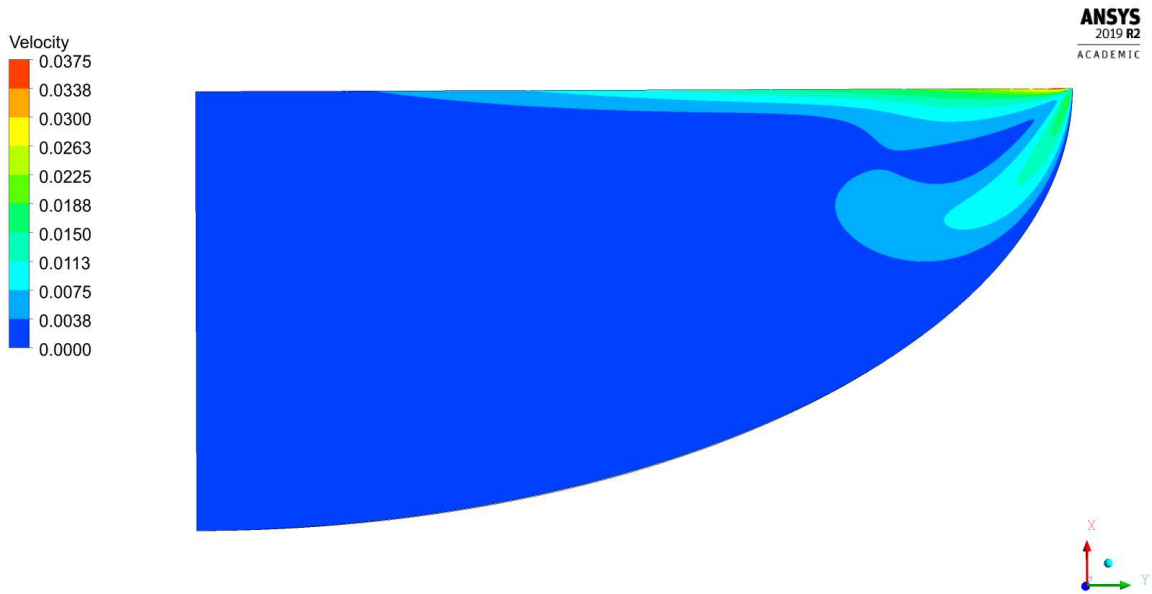


Figure B.172: Velocity magnitude contour for Exp 3.4.

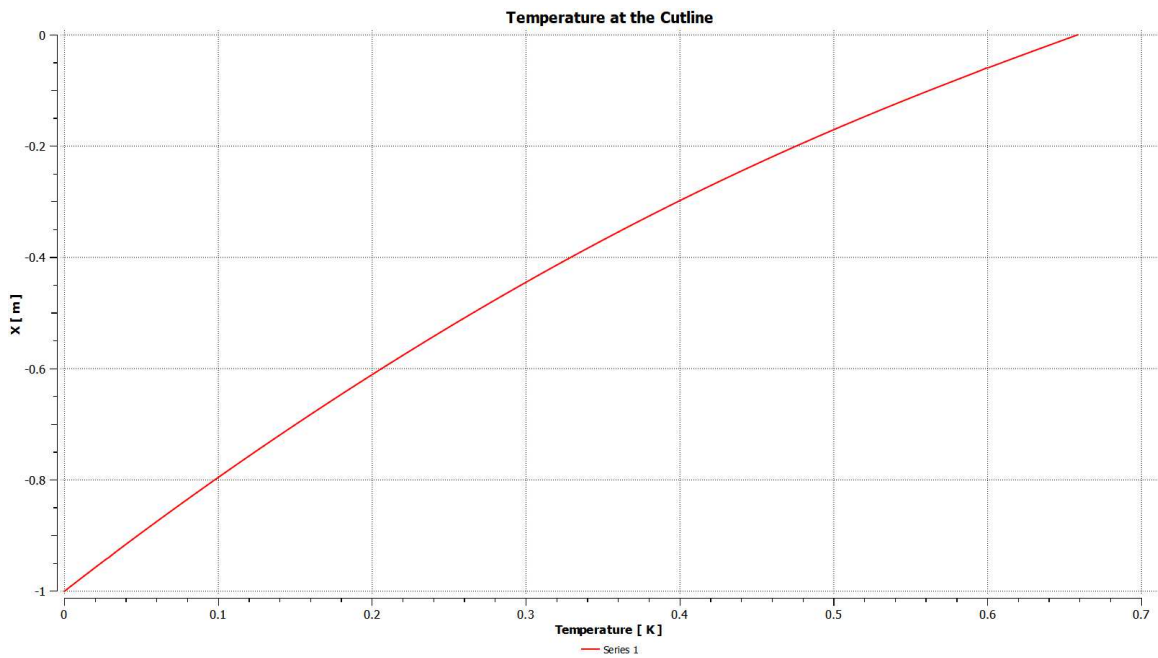


Figure B.173: Temperature at the axis of symmetry for Exp 3.4.

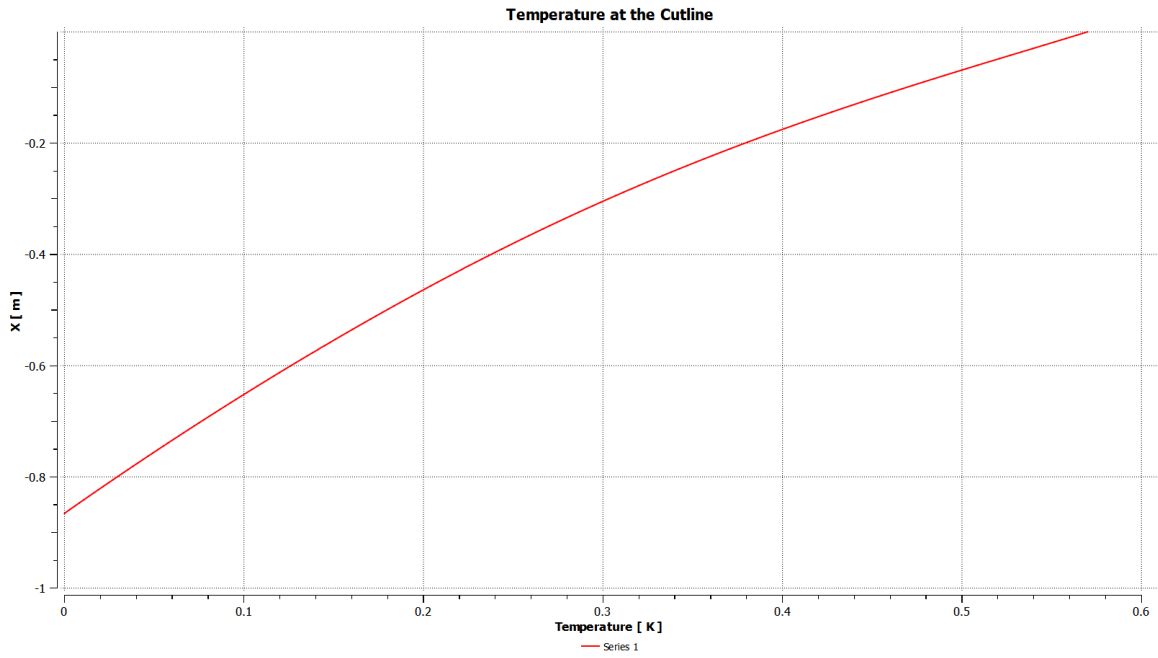


Figure B.174: Temperature at the cutline at $r^*=1$ for Exp 3.4.

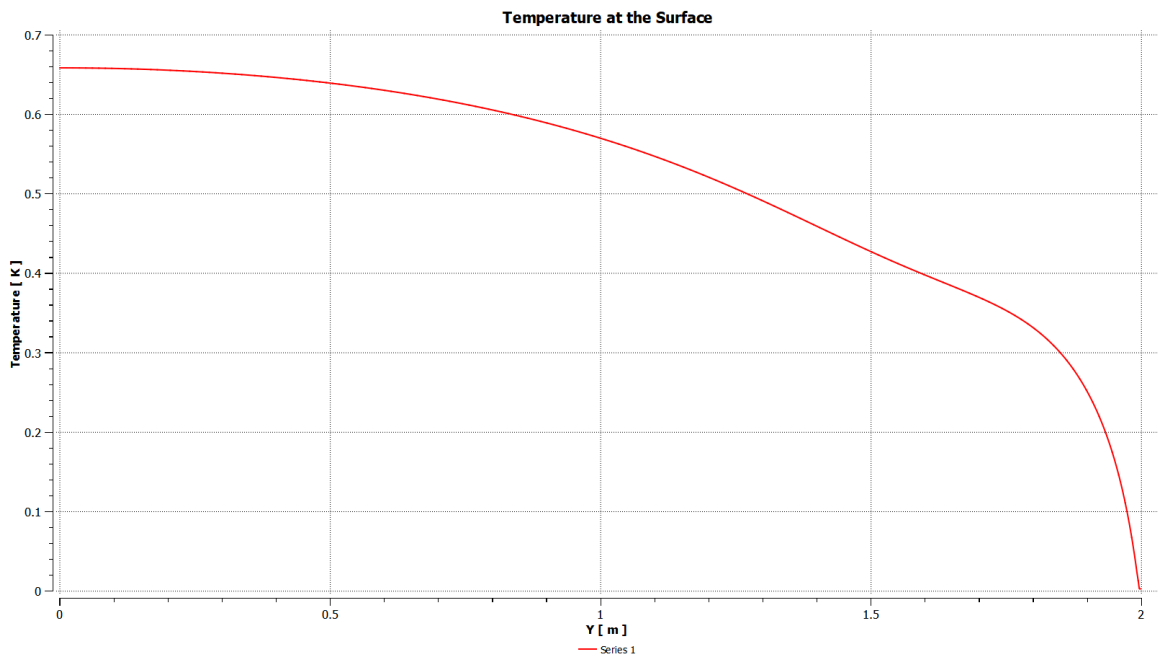


Figure B.175: Temperature at the free surface for Exp 3.4.

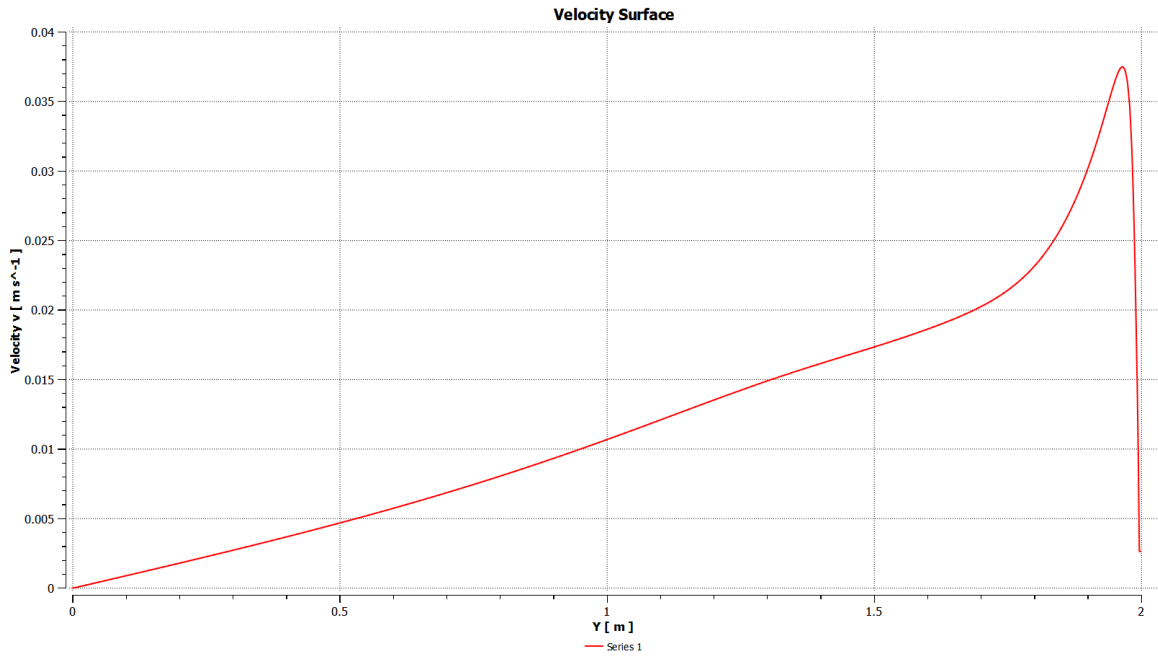


Figure B.176: Velocity at the free surface for Exp 3.4.

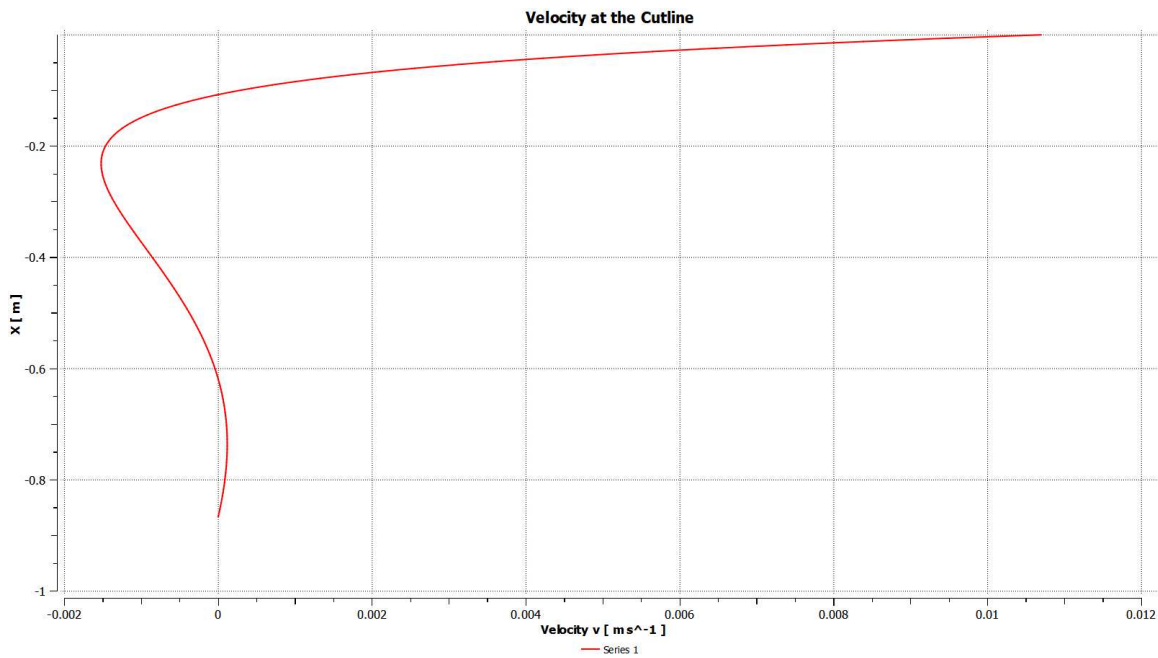


Figure B.177: Radial velocity u at the cutline at $r^*=1$ for Exp 3.4.

Exp 3.5

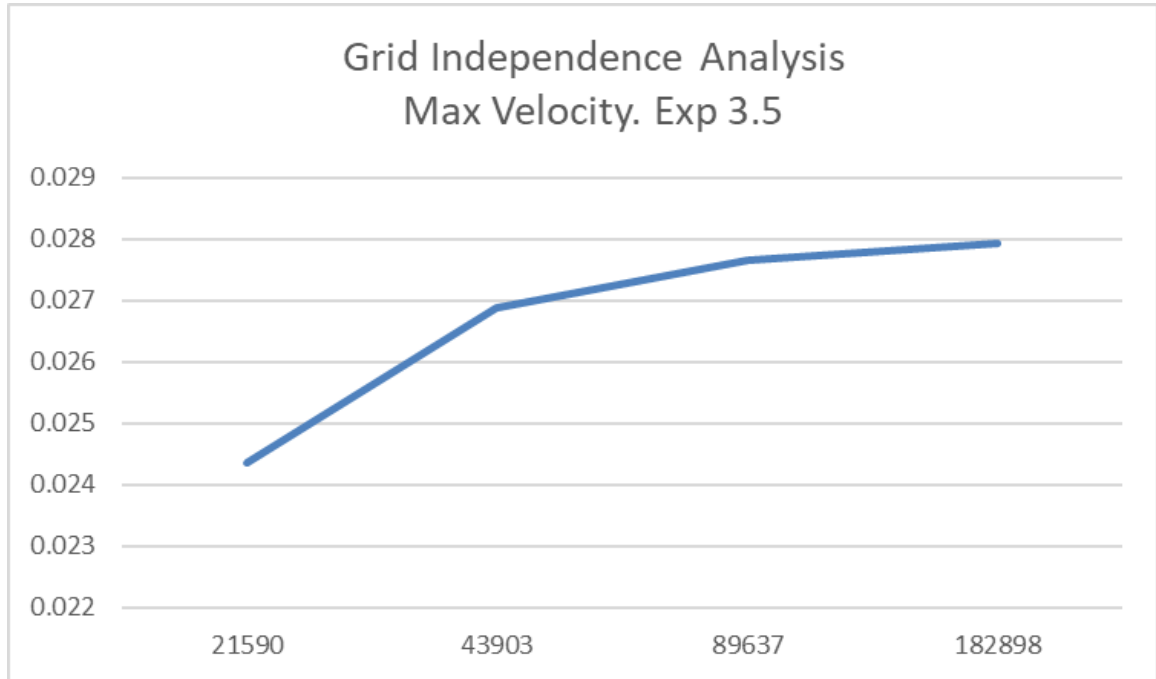


Figure B.178: Convergence for Exp 3.5: peak velocity values vs number of nodes in logarithmic scale.

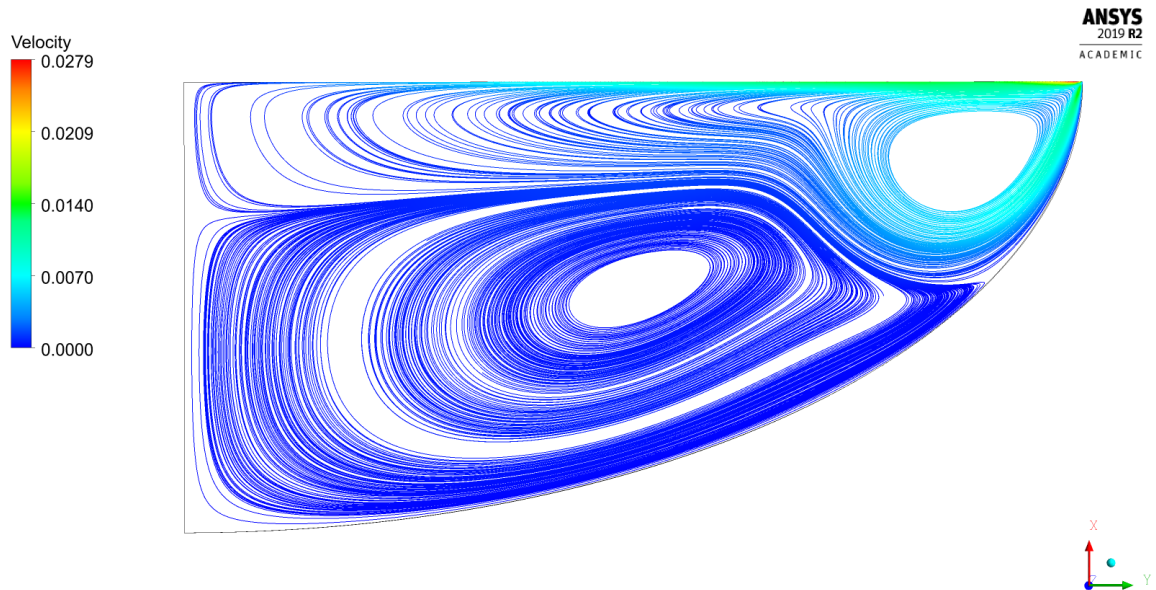


Figure B.179: Streamlines for Exp 3.5.

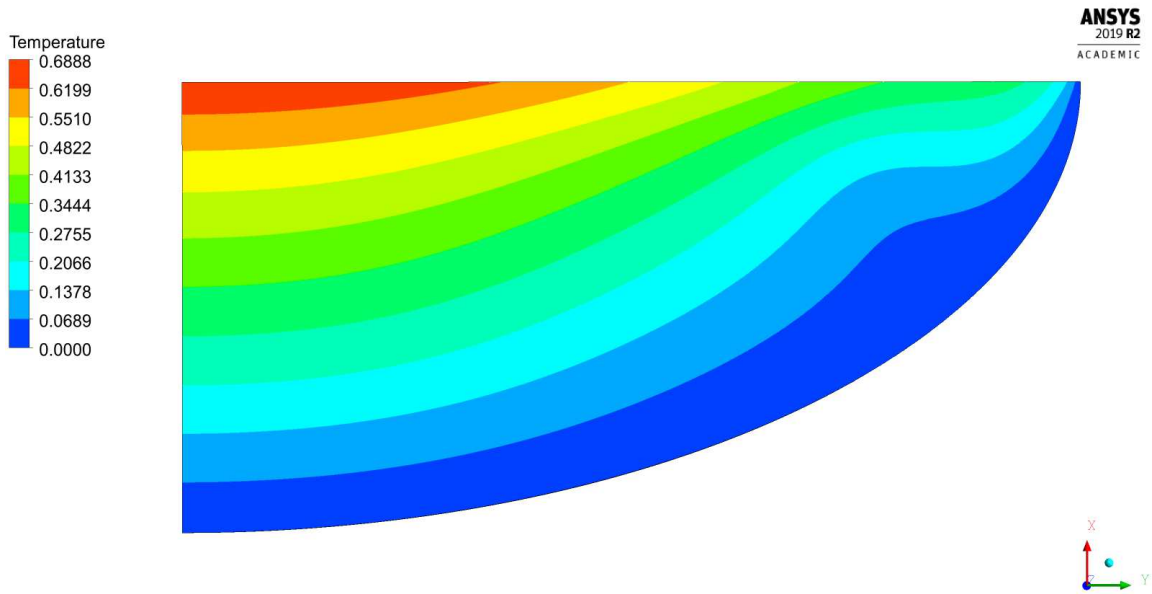


Figure B.180: Temperature field for Exp 3.5.

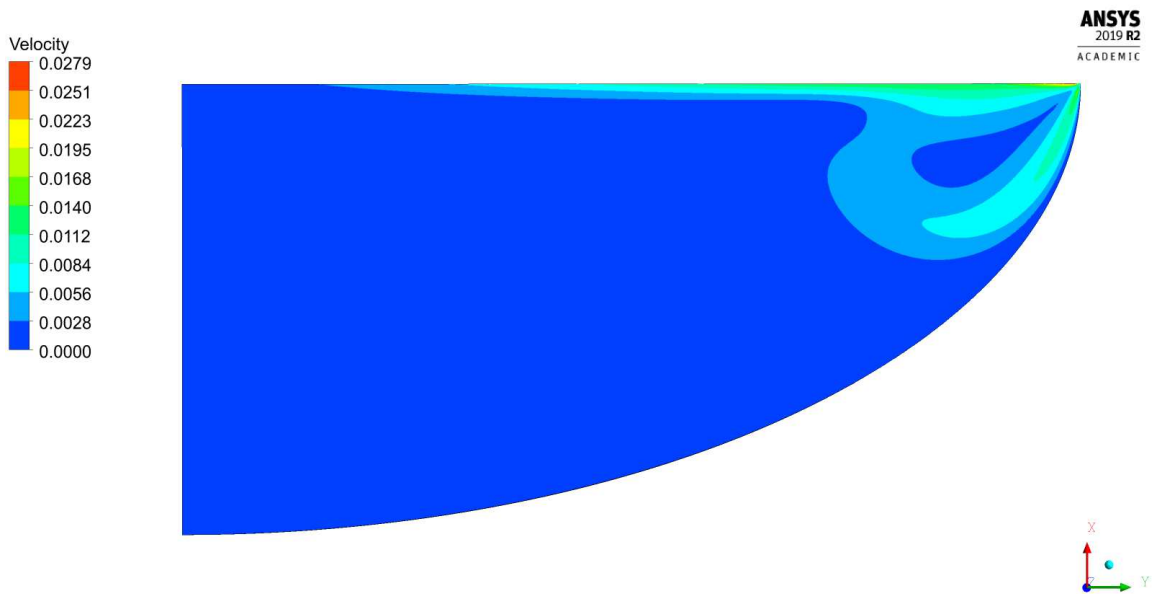


Figure B.181: Velocity magnitude contour for Exp 3.5.

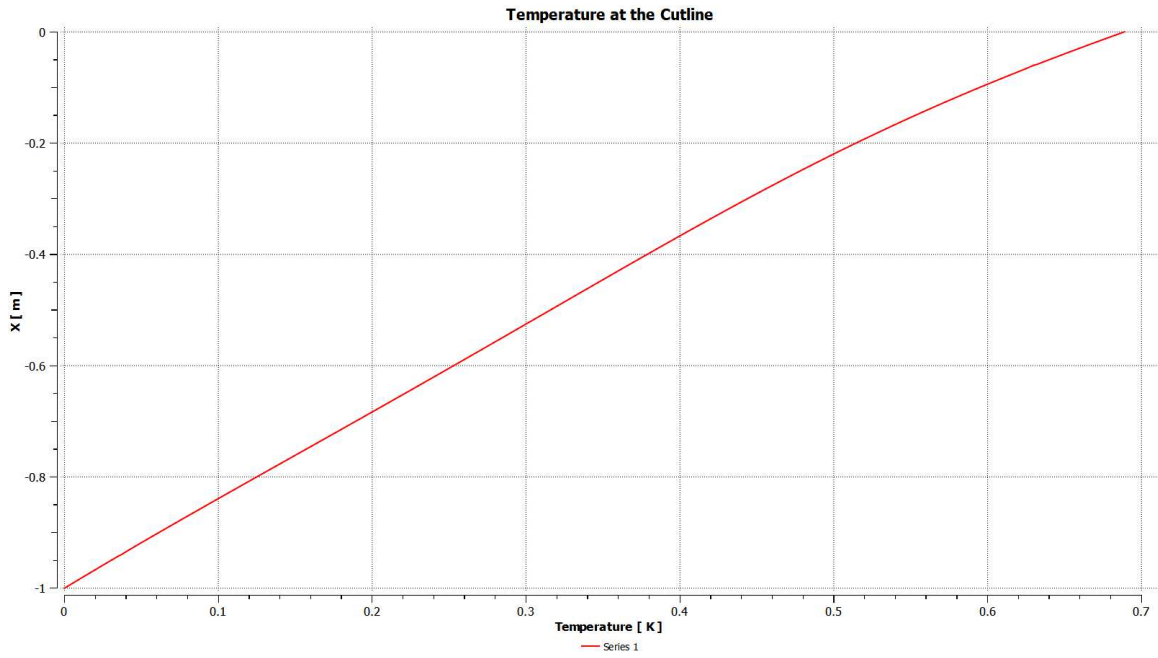


Figure B.182: Temperature at the axis of symmetry for Exp 3.5.

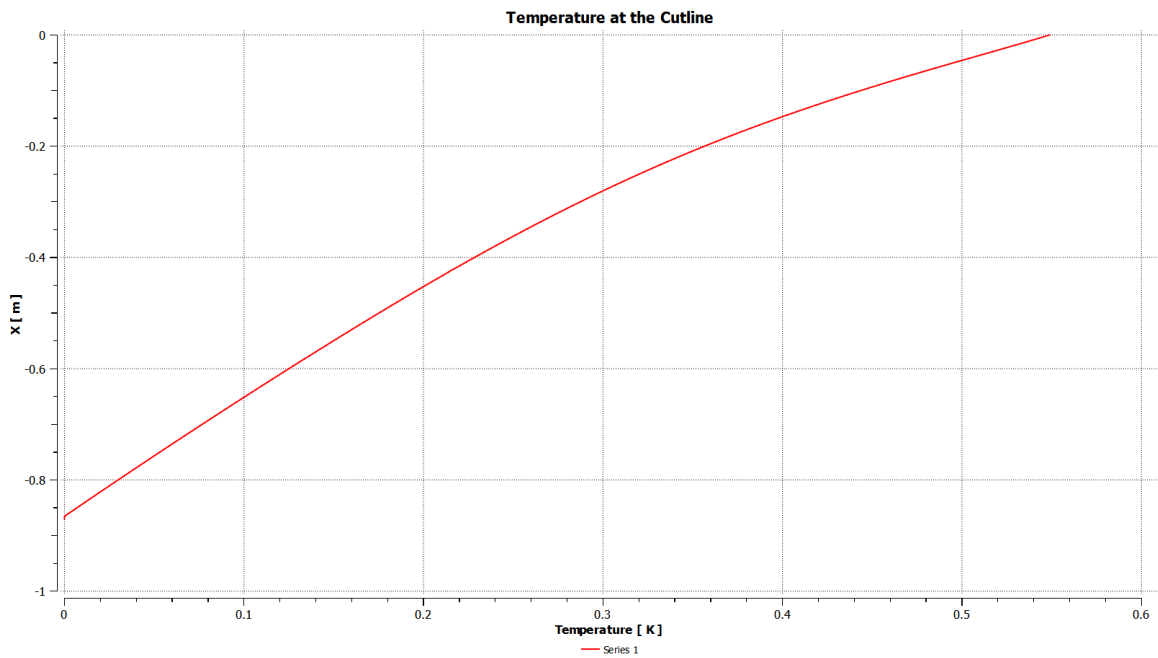


Figure B.183: Temperature at the cutline at $r^*=1$ for Exp 3.5.

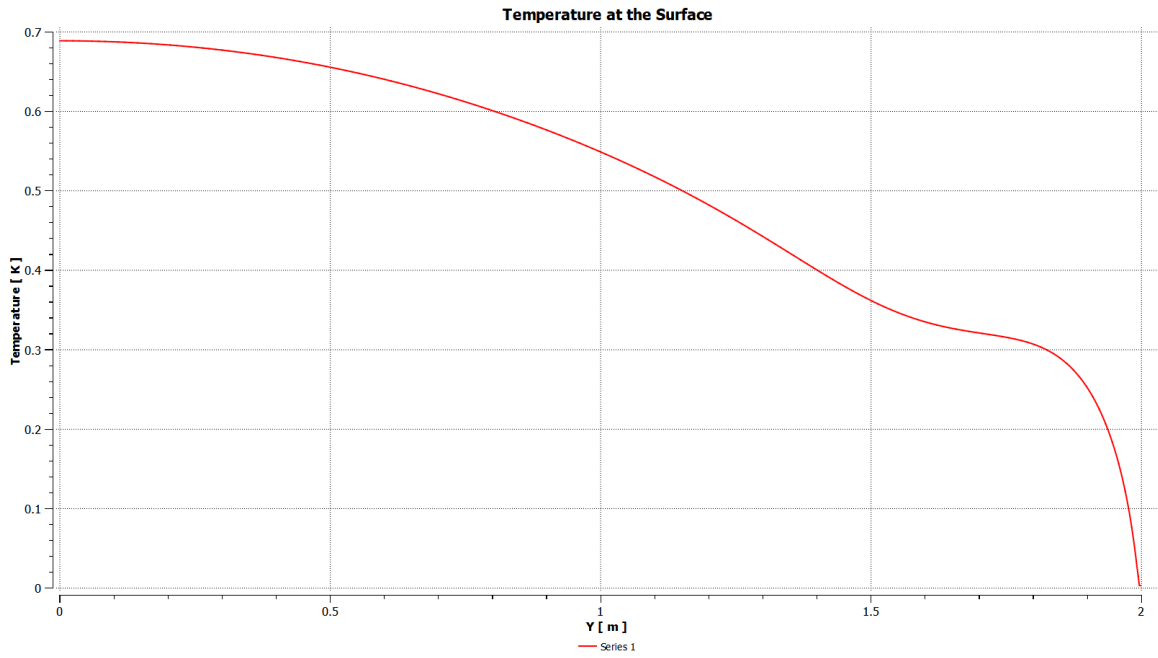


Figure B.184: Temperature at the free surface for Exp 3.5.

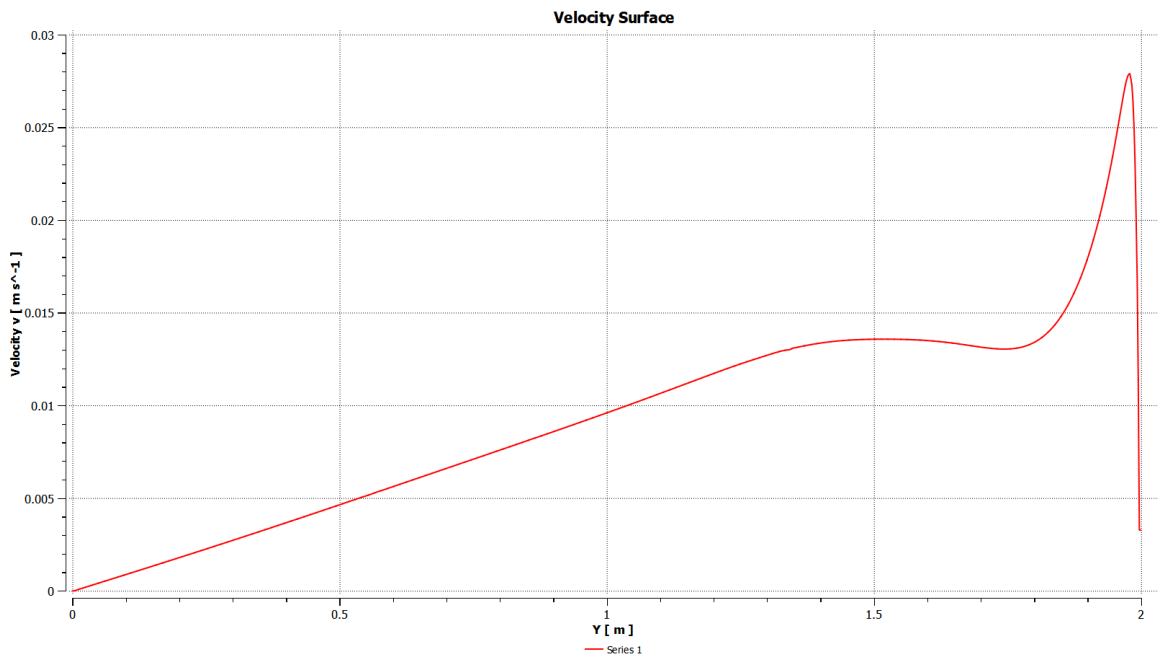


Figure B.185: Velocity at the free surface for Exp 3.5.

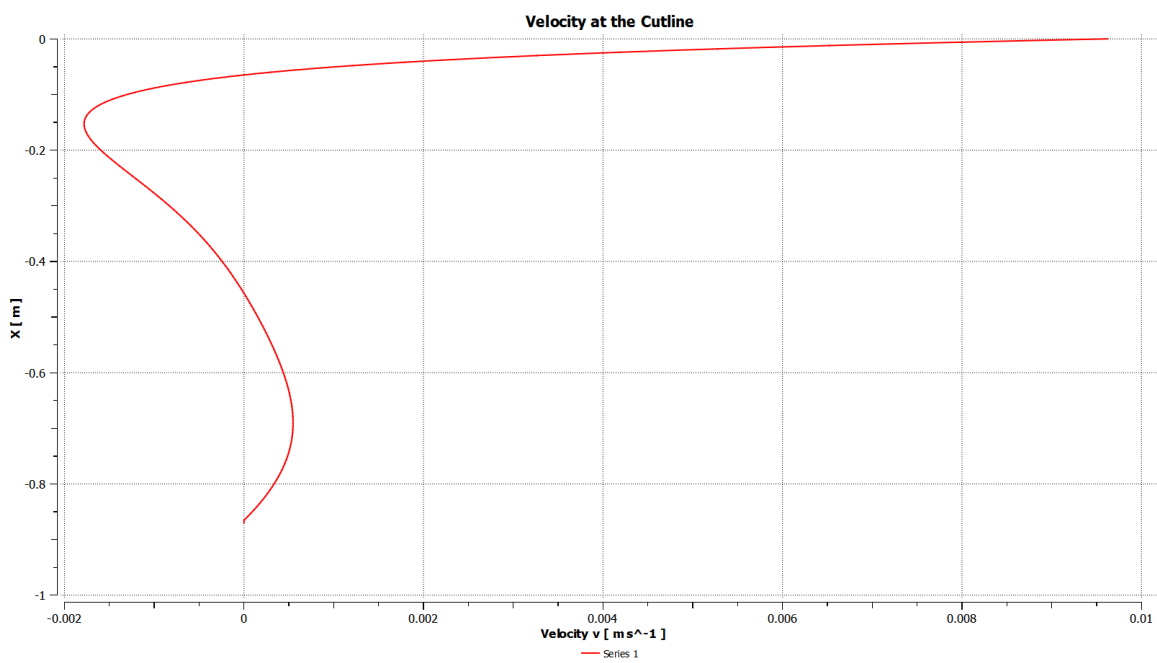


Figure B.186: Radial velocity u at the cutline at $r^*=1$ for Exp 3.5.

B.4 Regime IV

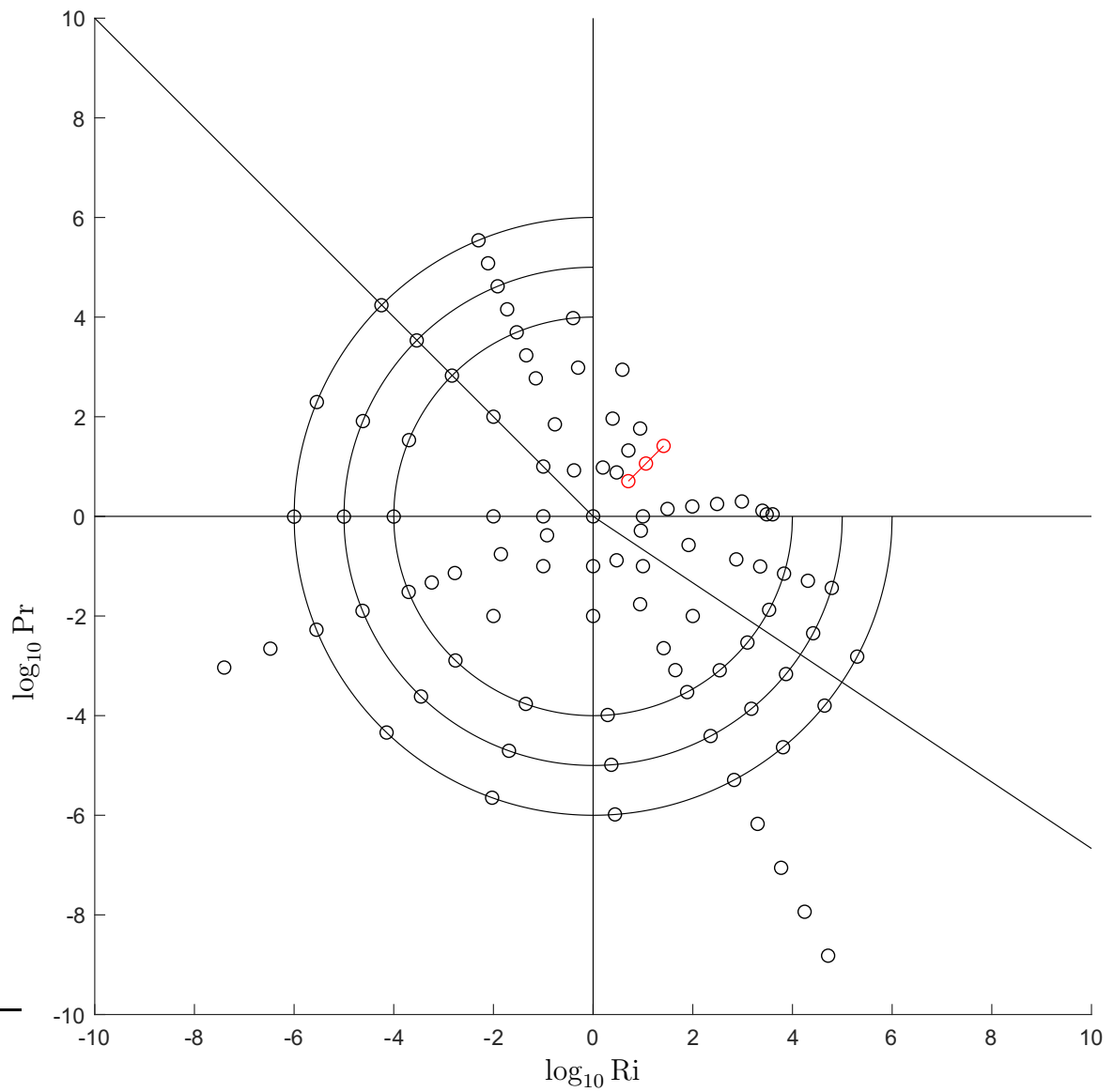


Figure B.187: Location of the dimensionless parameters for Regime IV.

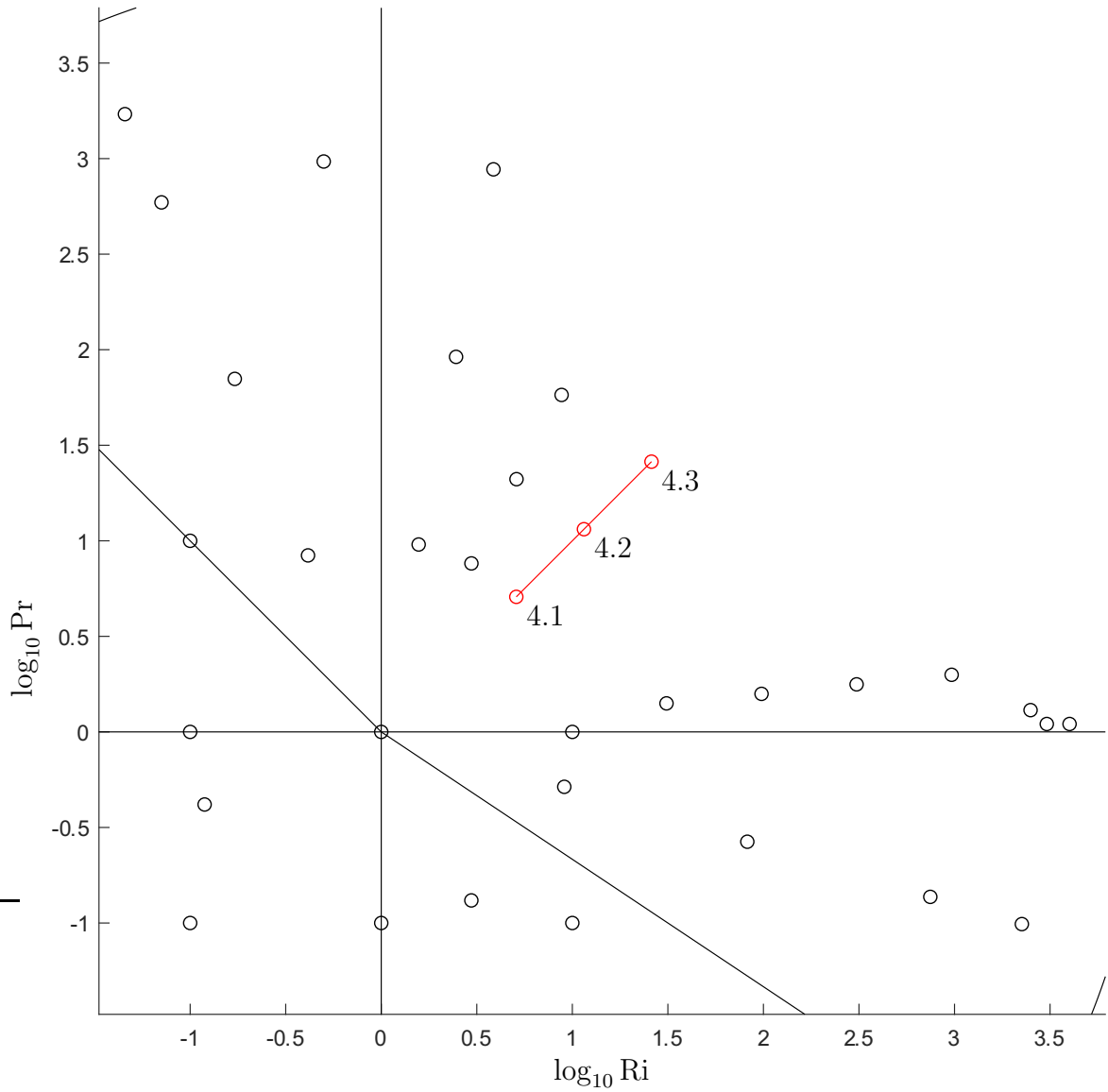


Figure B.188: Location of the dimensionless parameters for Regime IV and the experiment numbers.

Exp 4.1

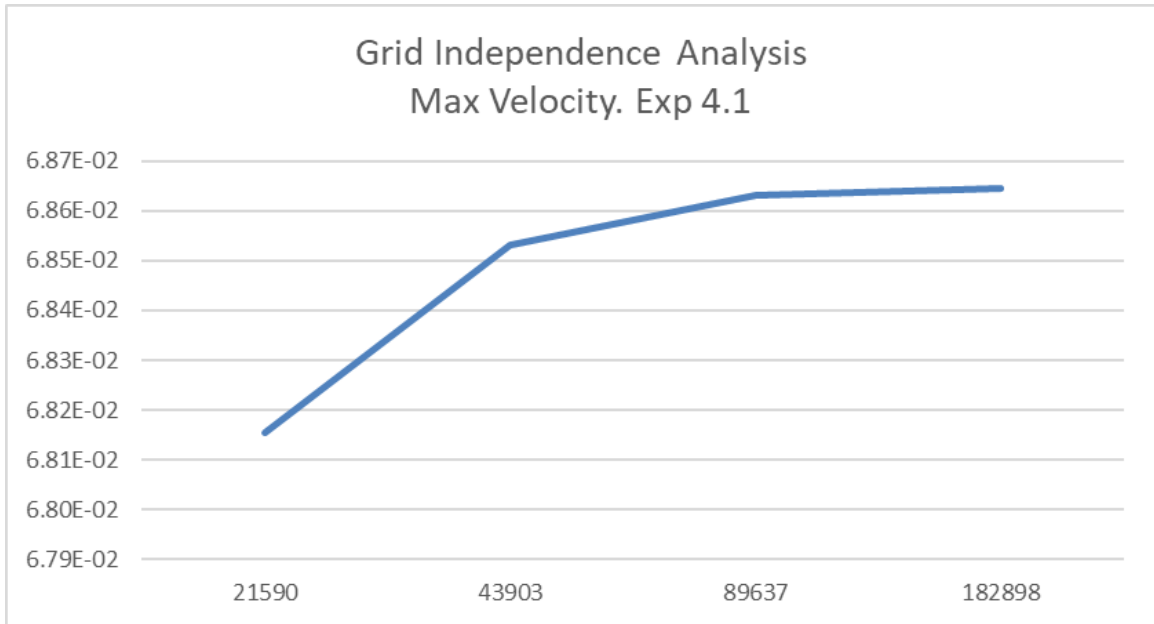


Figure B.189: Convergence for Exp 4.1: peak velocity values vs number of nodes in logarithmic scale.

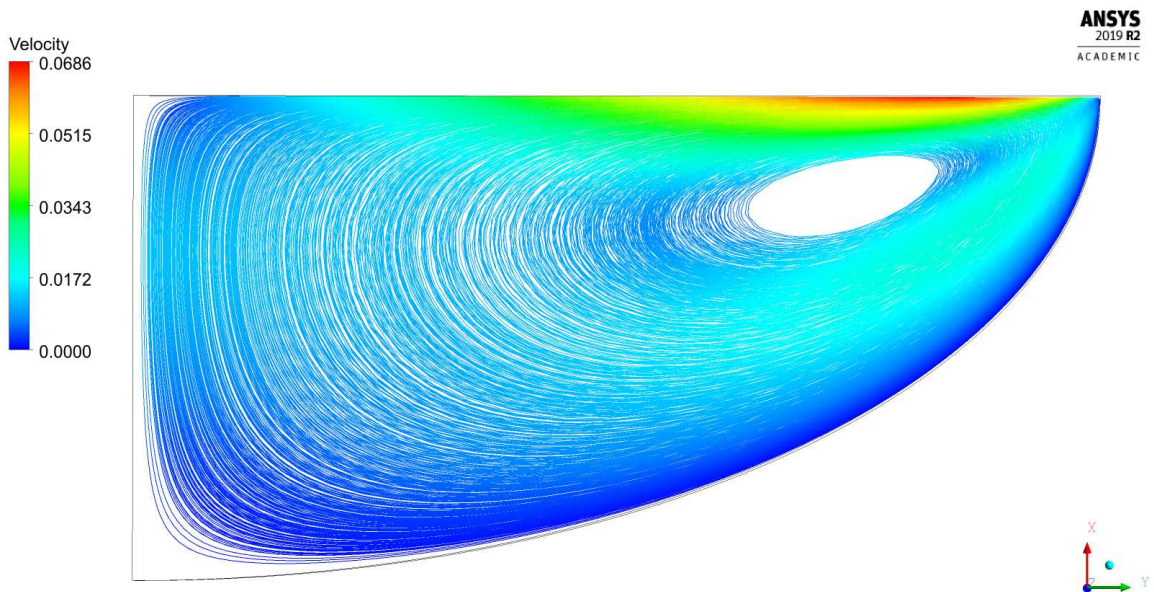


Figure B.190: Streamlines for Exp 4.1.

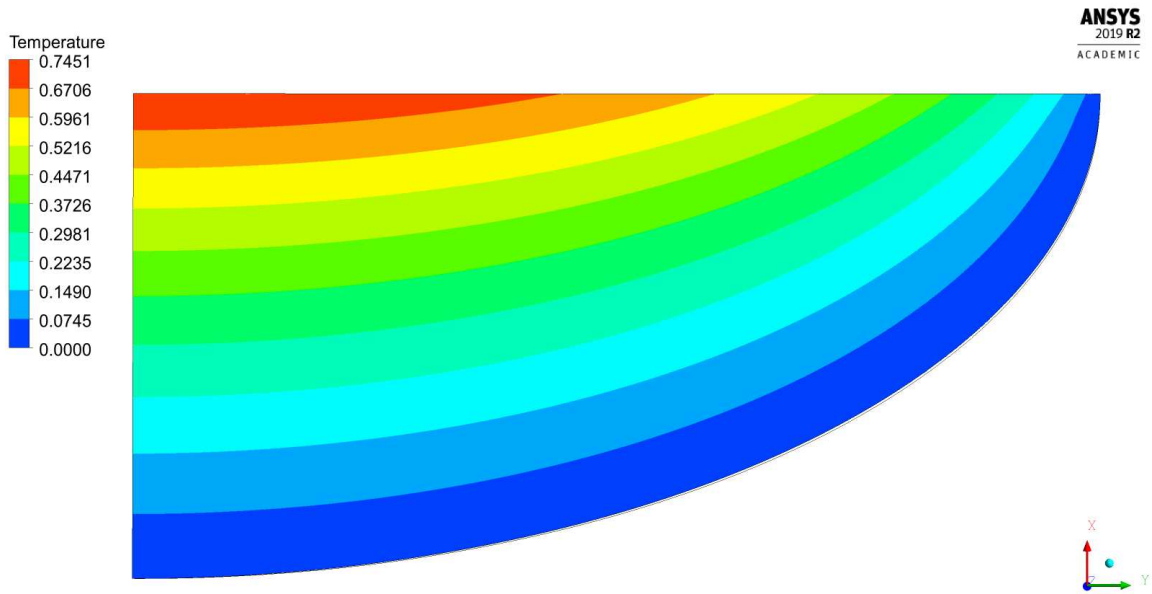


Figure B.191: Temperature field for Exp 4.1.

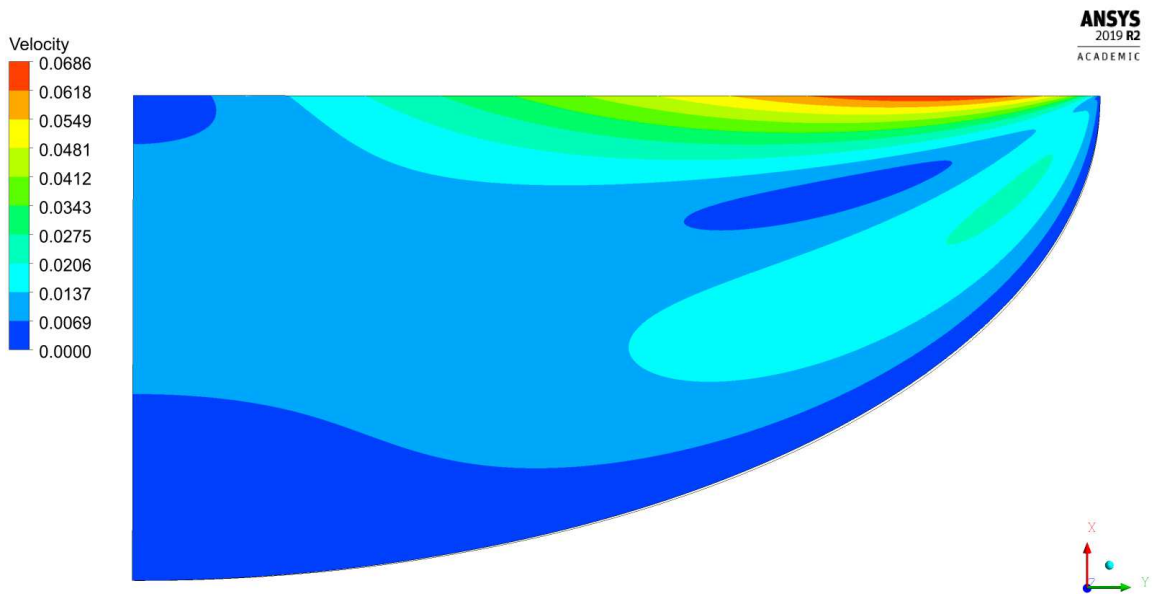


Figure B.192: Velocity magnitude contour for Exp 4.1.

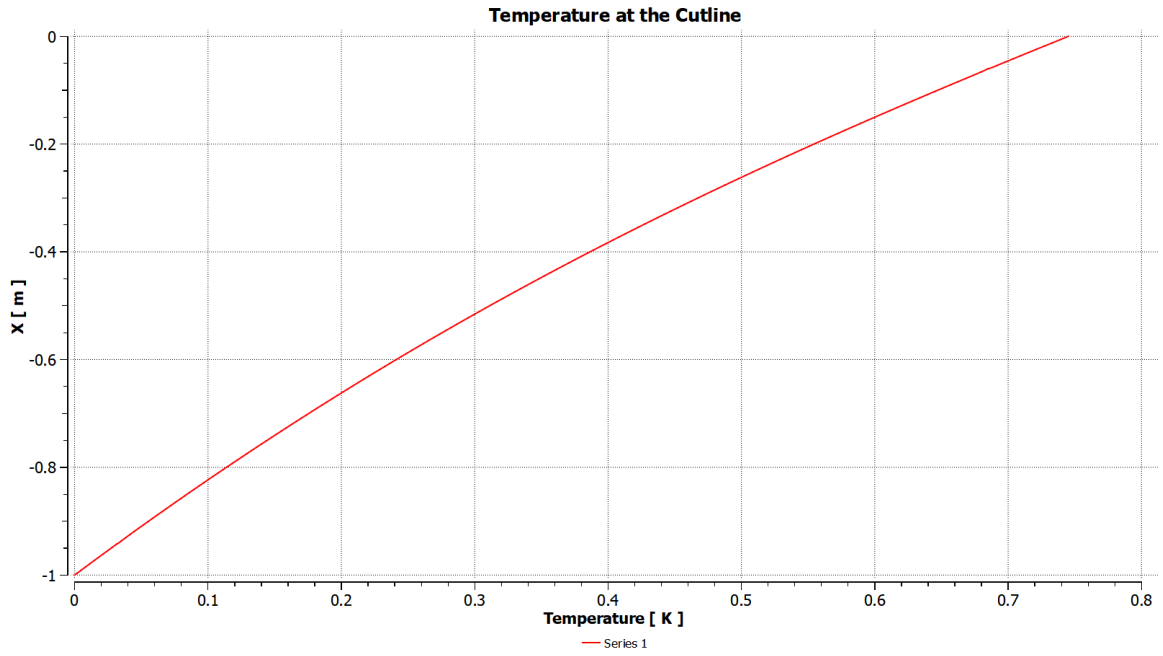


Figure B.193: Temperature at the axis of symmetry for Exp 4.1.

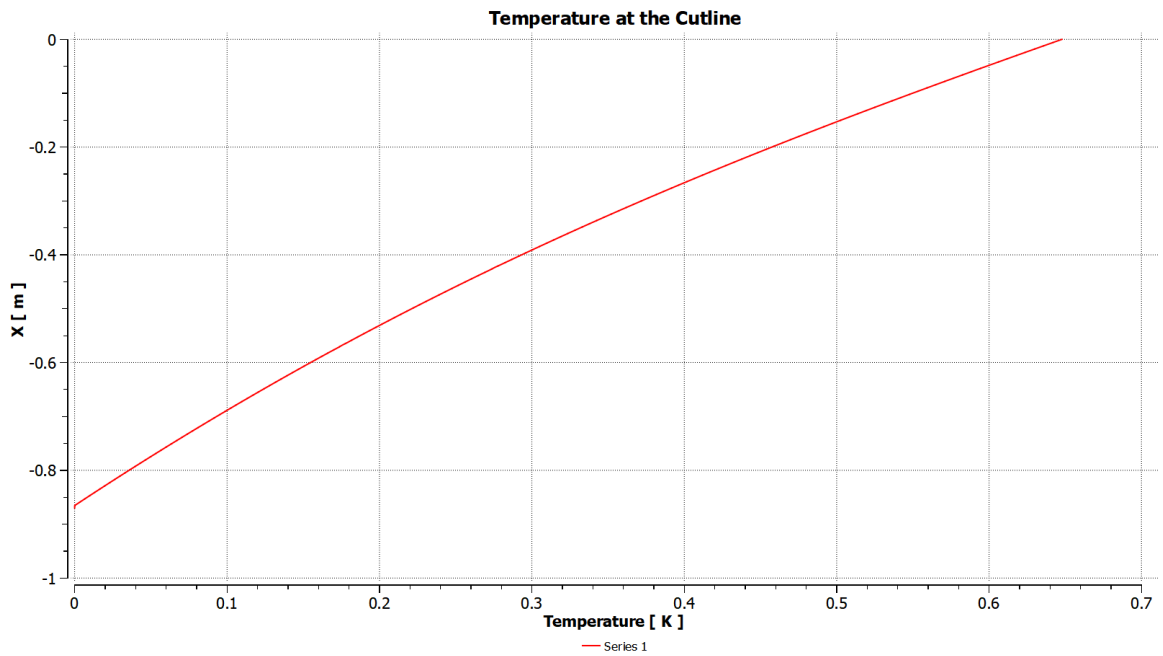


Figure B.194: Temperature at the cutline at $r^*=1$ for Exp 4.1.

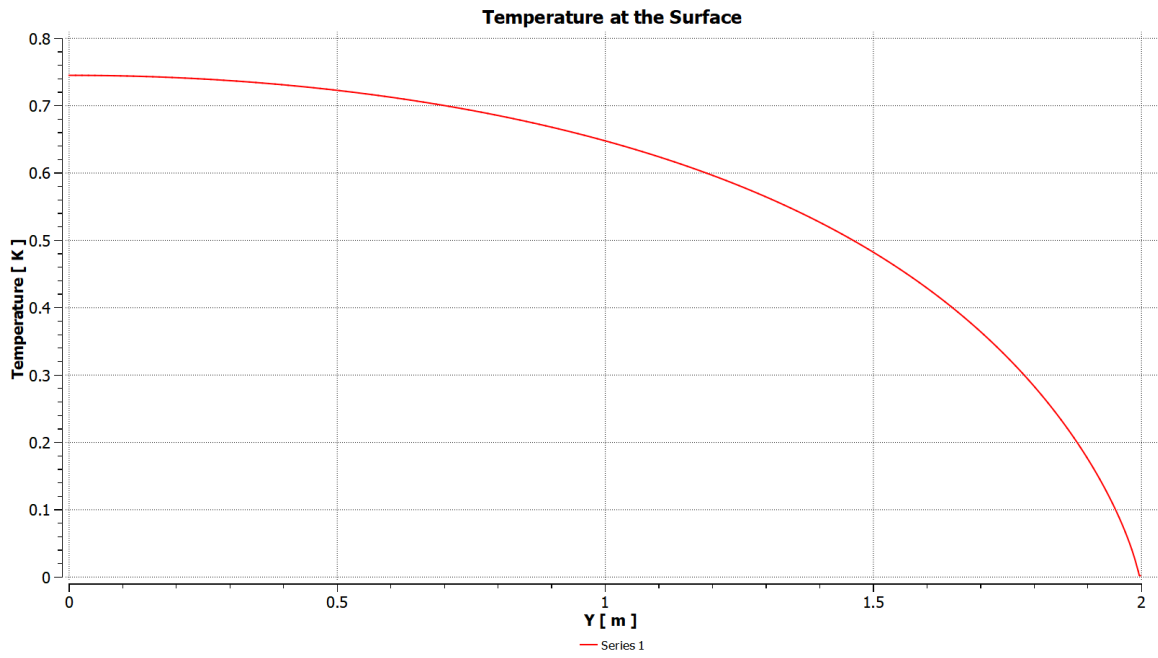


Figure B.195: Temperature at the free surface for Exp 4.1.

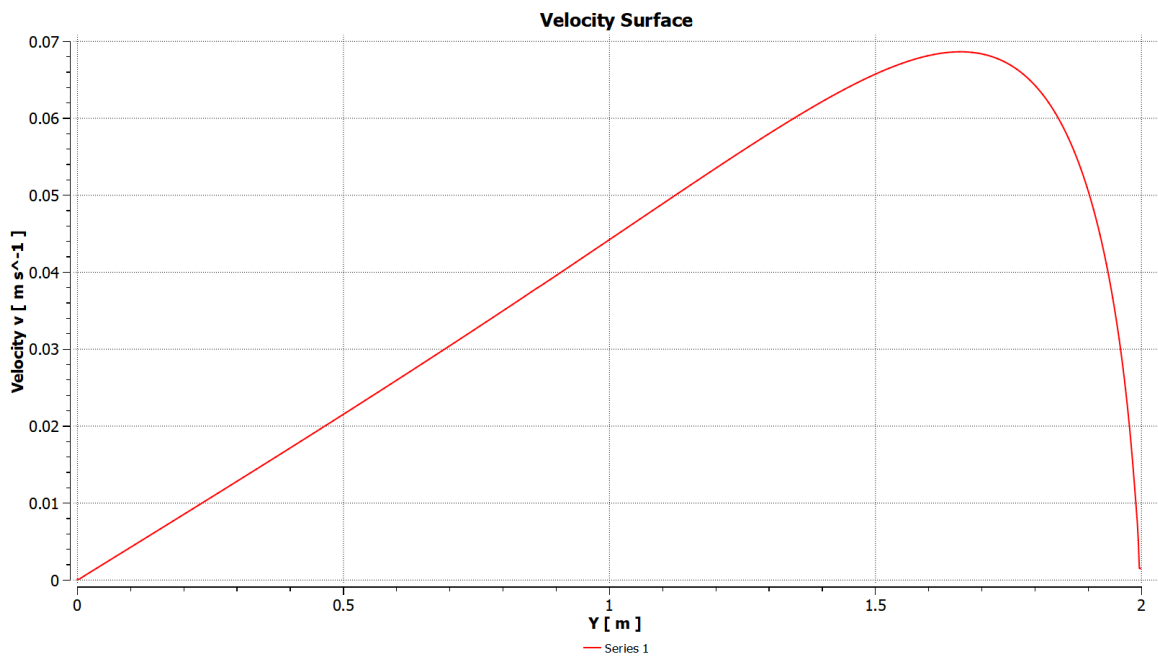


Figure B.196: Velocity at the free surface for Exp 4.1.

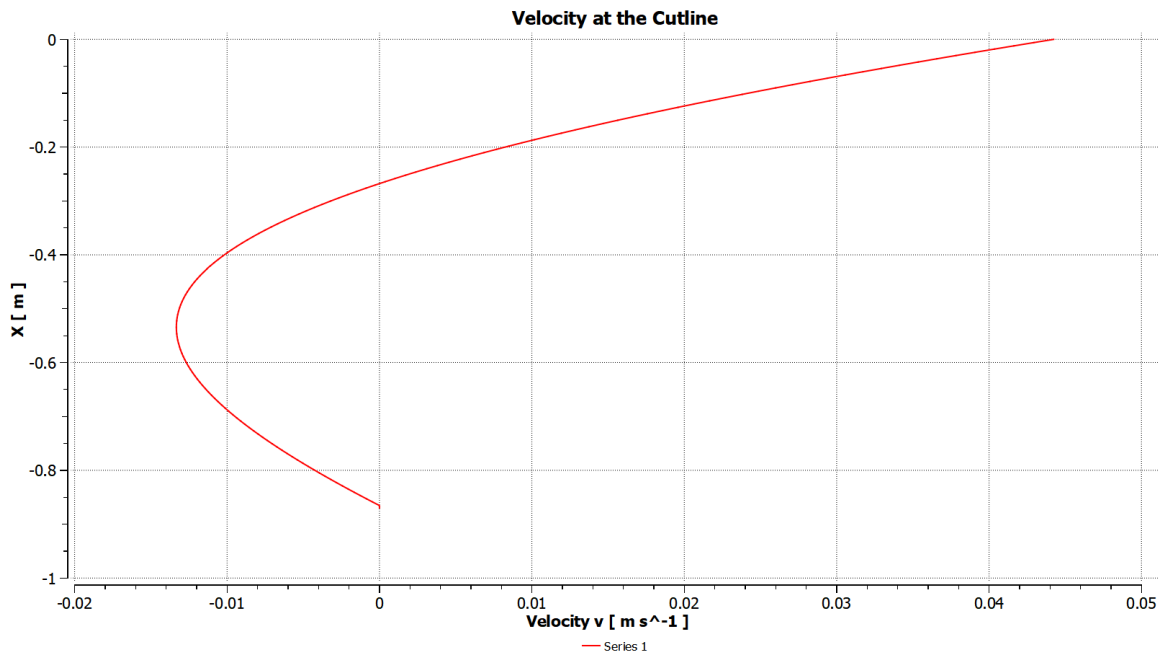


Figure B.197: Radial velocity u at the cutline at $r^*=1$ for Exp 4.1.

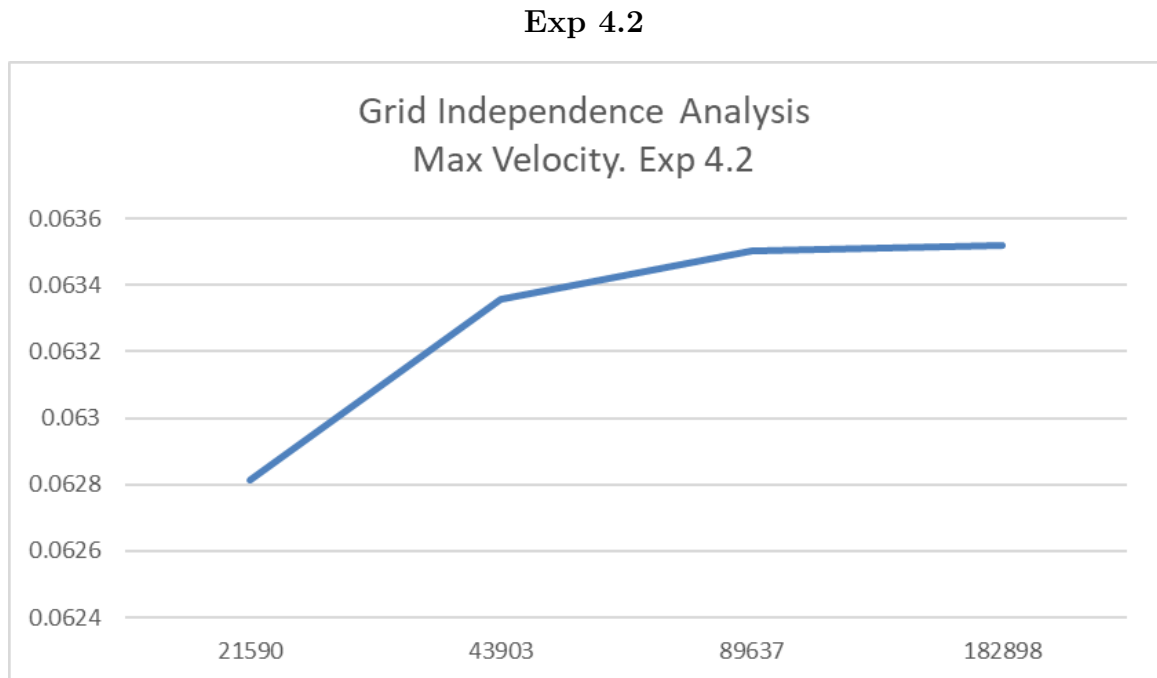


Figure B.198: Convergence for Exp 4.2: peak velocity values vs number of nodes in logarithmic scale.

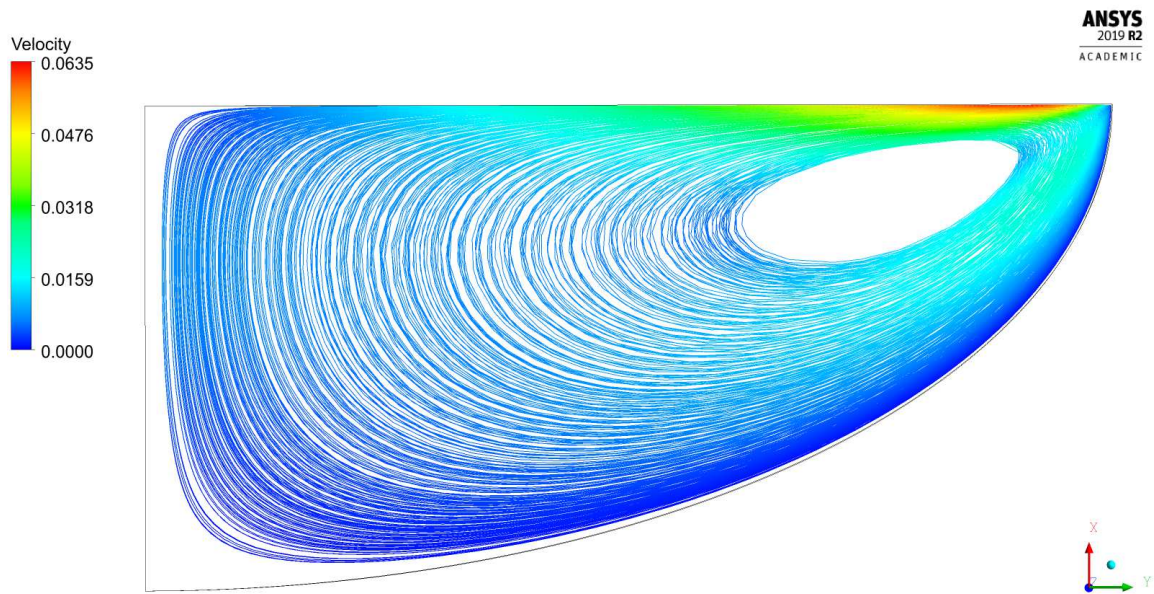


Figure B.199: Streamlines for Exp 4.2.

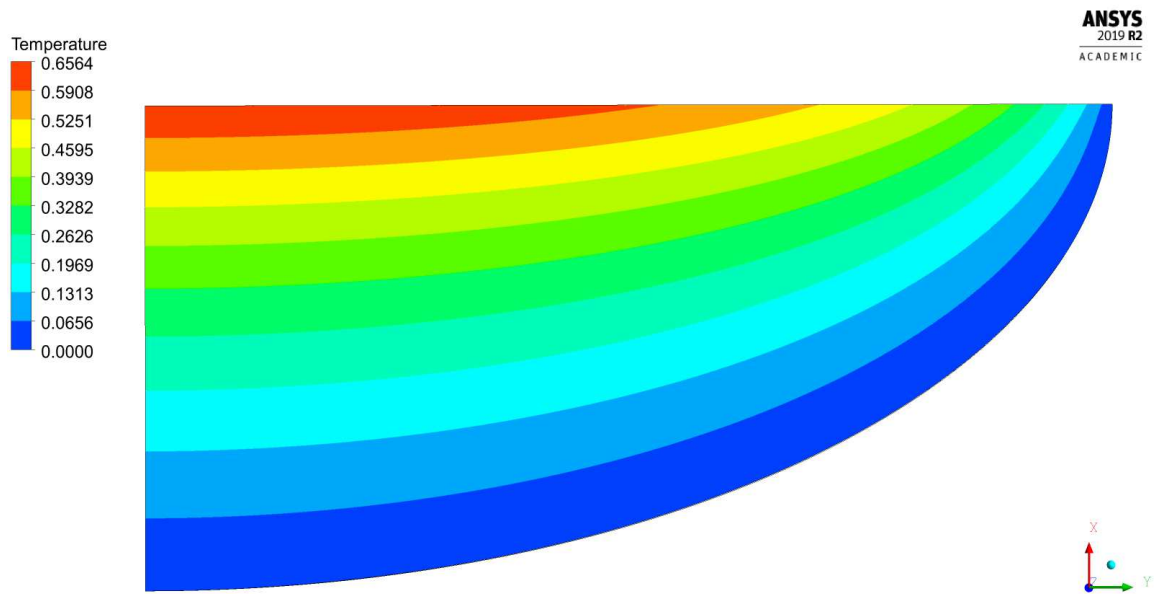


Figure B.200: Temperature field for Exp 4.2.

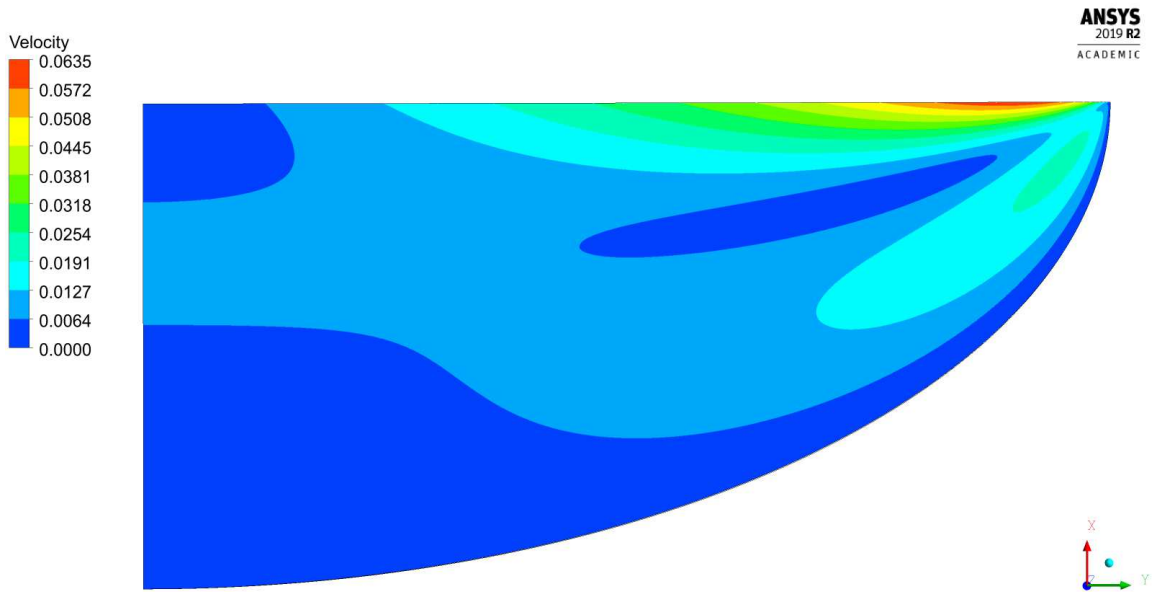


Figure B.201: Velocity magnitude contour for Exp 4.2.

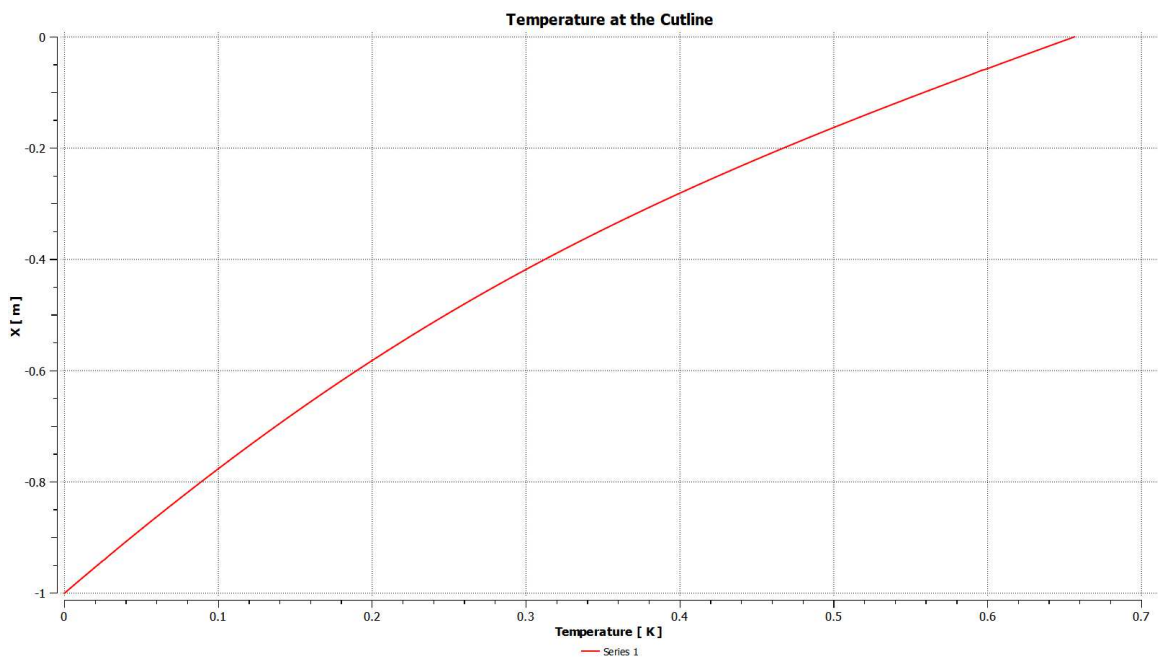


Figure B.202: Temperature at the axis of symmetry for Exp 4.2.

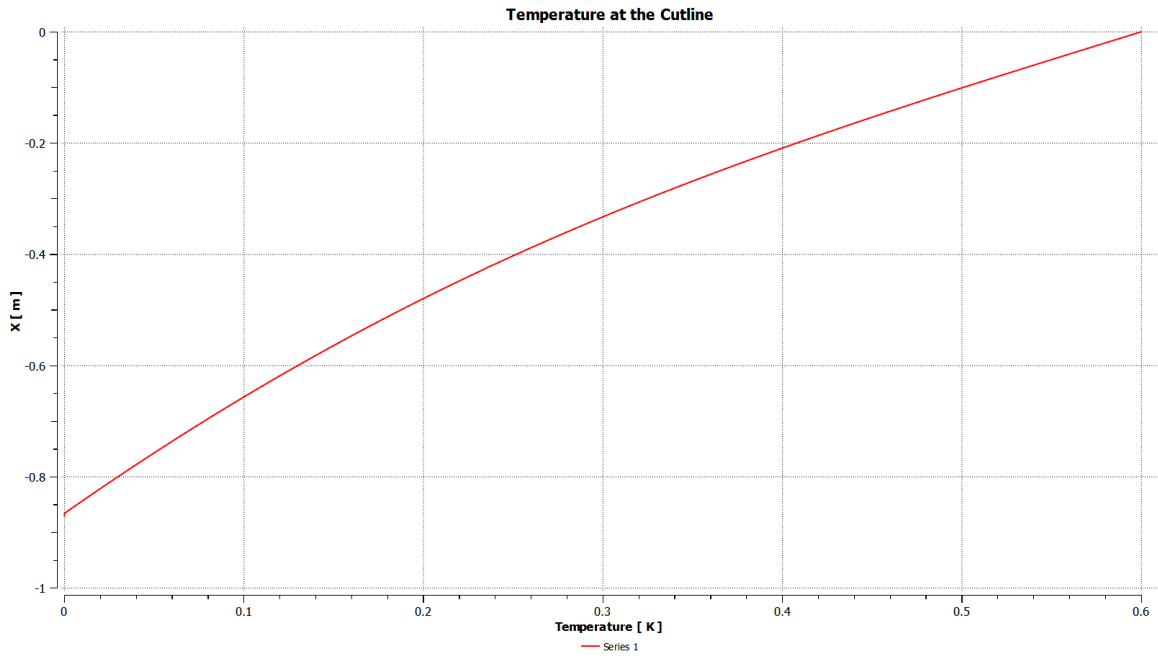


Figure B.203: Temperature at the cutline at $r^*=1$ for Exp 4.2.

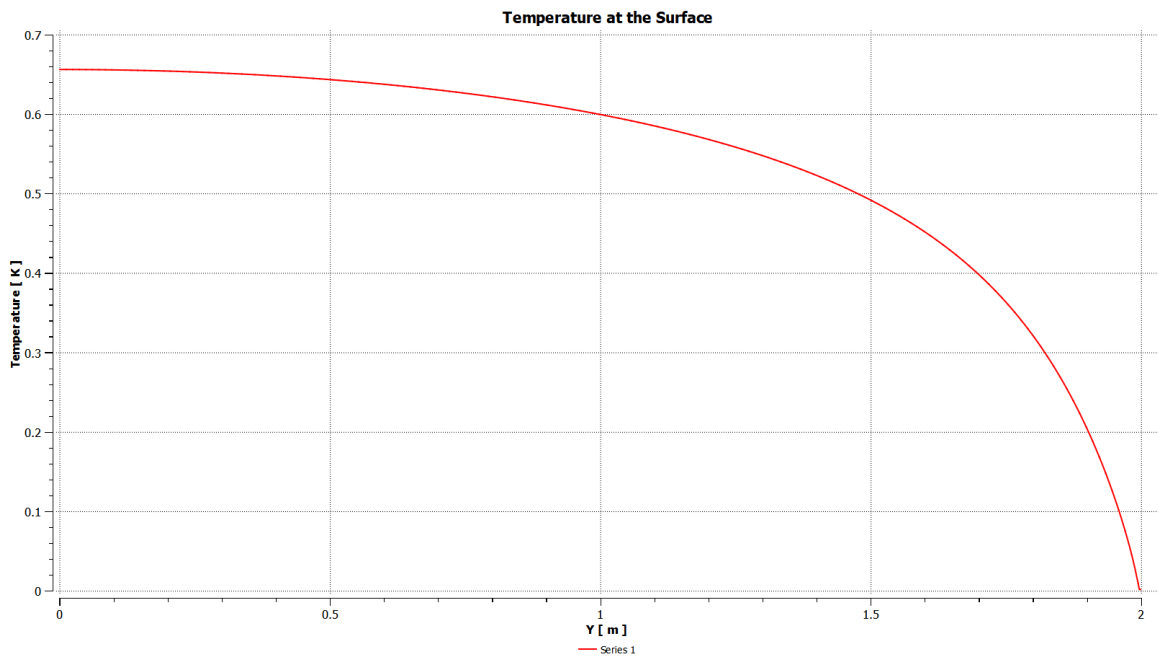


Figure B.204: Temperature at the free surface for Exp 4.2.

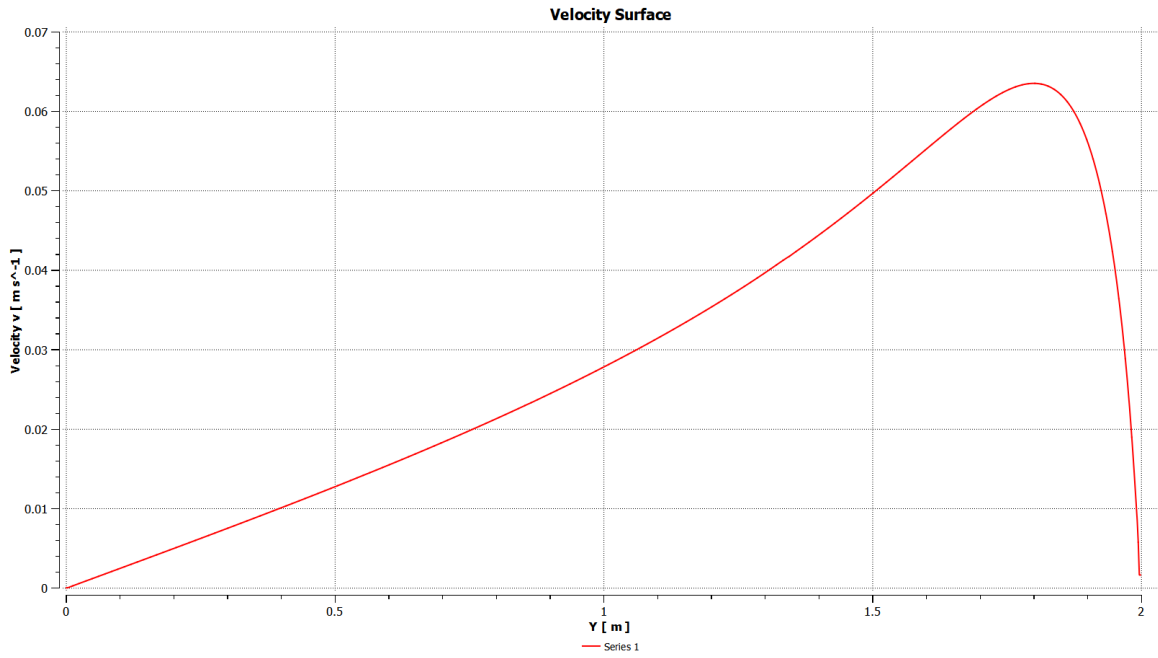


Figure B.205: Velocity at the free surface for Exp 4.2.

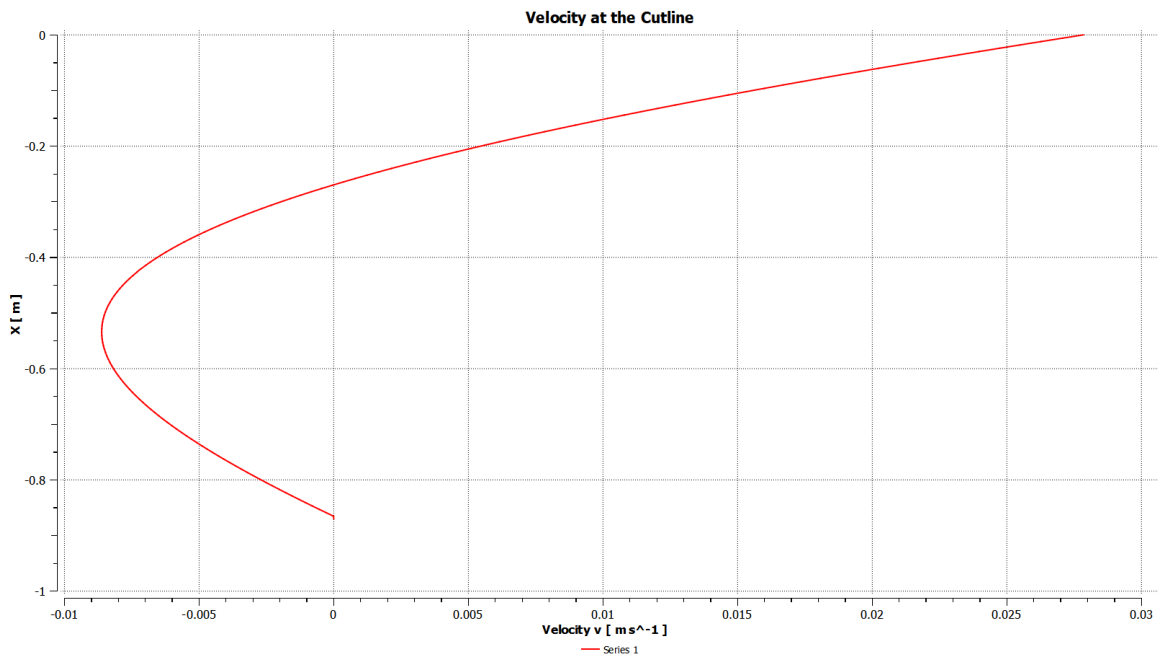


Figure B.206: Radial velocity u at the cutline at $r^*=1$ for Exp 4.2.

Exp 4.3

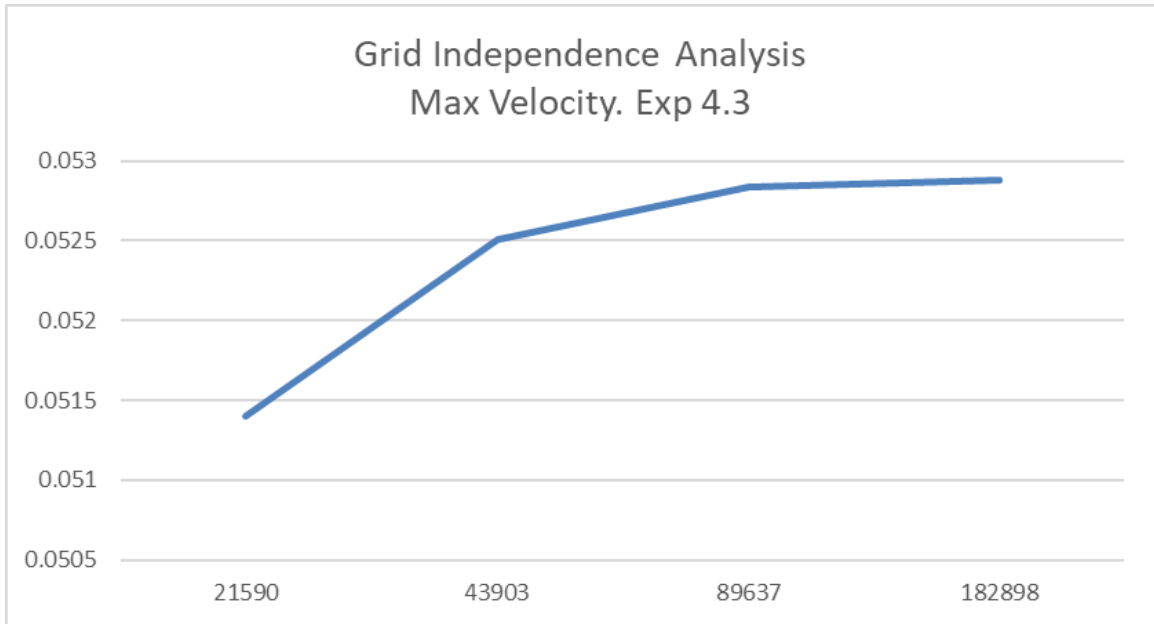


Figure B.207: Convergence for Exp 4.3: peak velocity values vs number of nodes in logarithmic scale.

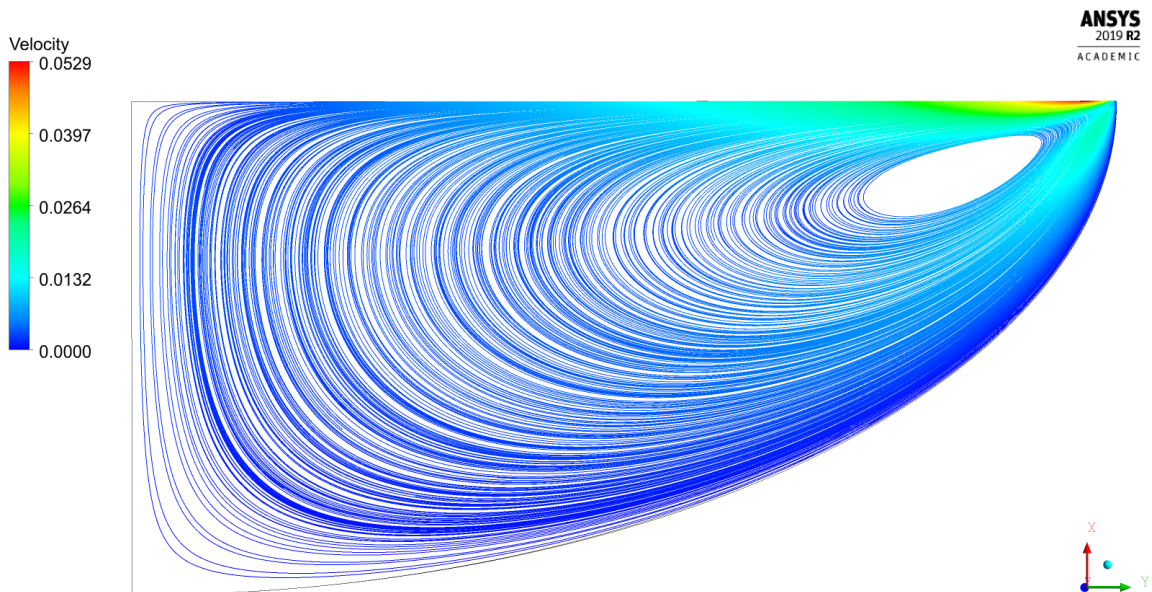


Figure B.208: Streamlines for Exp 4.3.

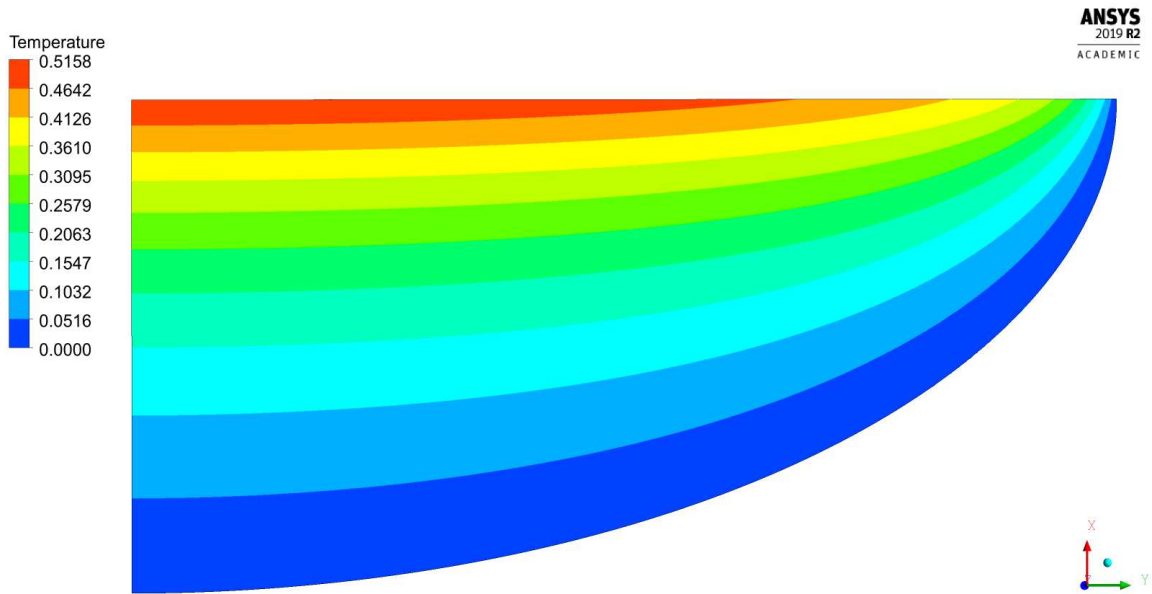


Figure B.209: Temperature field for Exp 4.3.

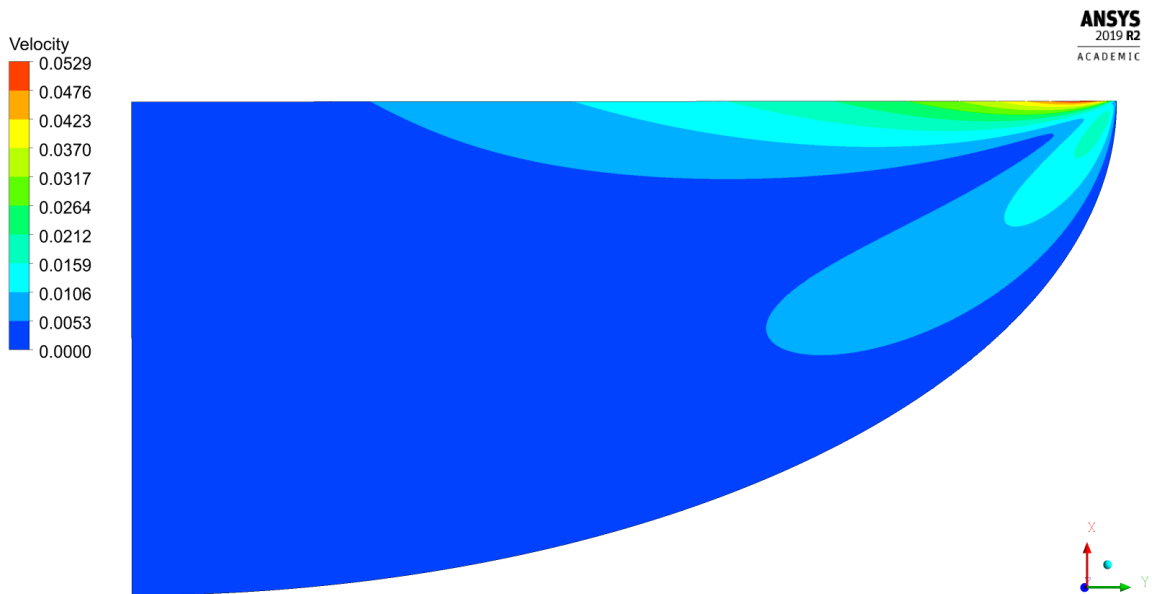


Figure B.210: Velocity magnitude contour for Exp 4.3.

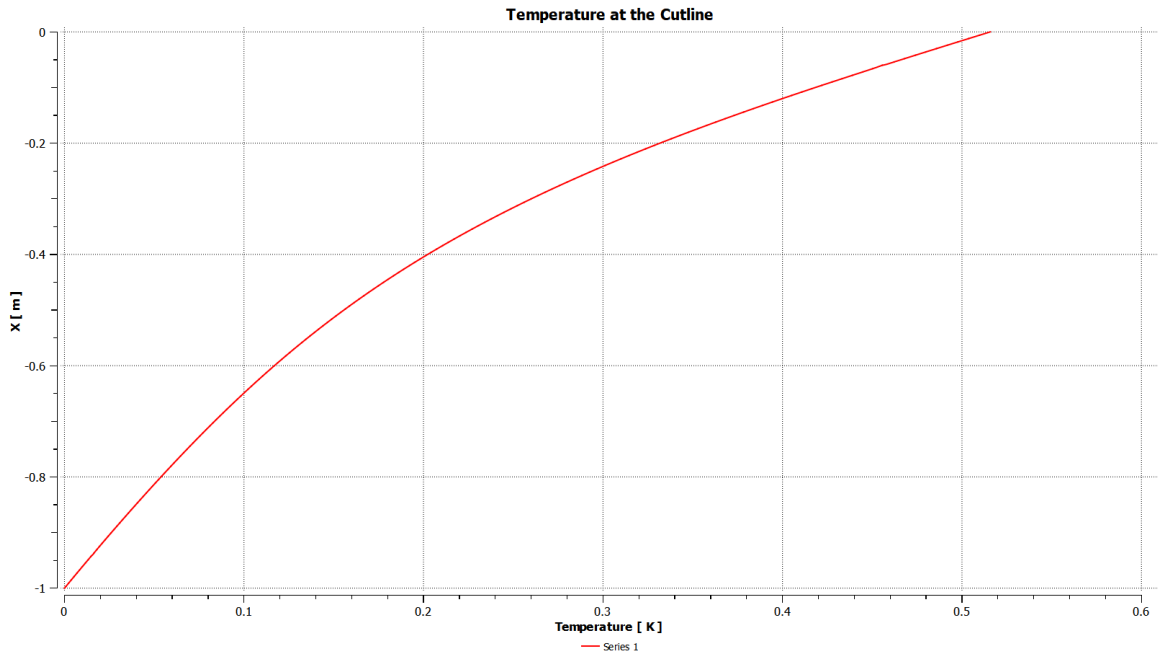


Figure B.211: Temperature at the axis of symmetry for Exp 4.3.

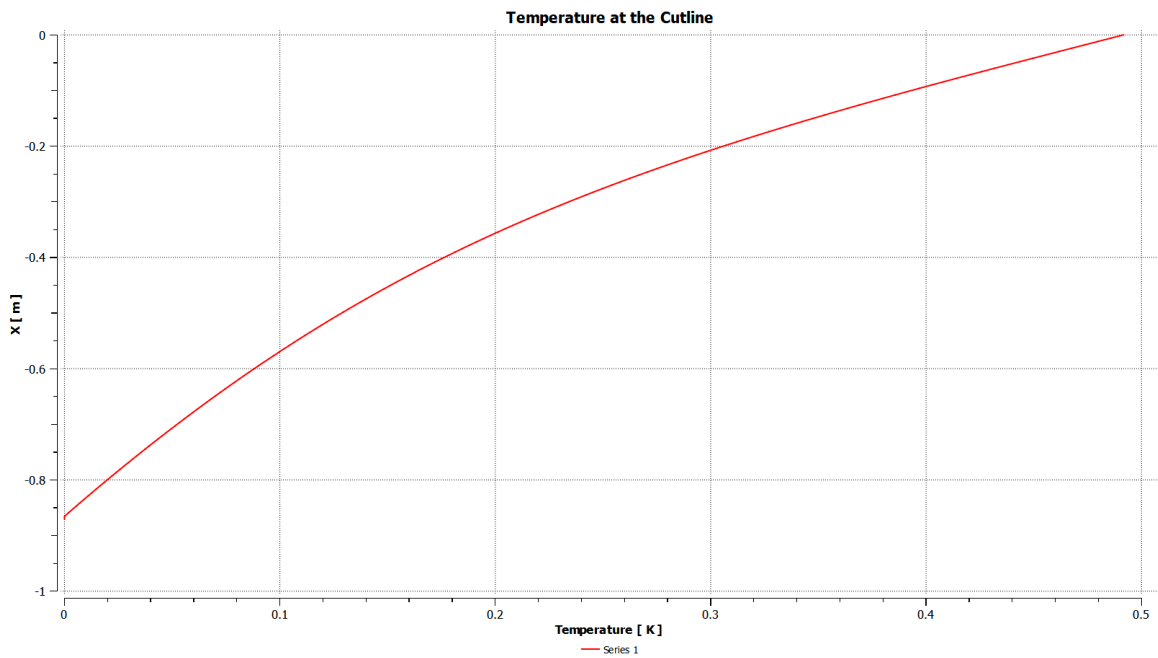


Figure B.212: Temperature at the cutline at $r^*=1$ for Exp 4.3.

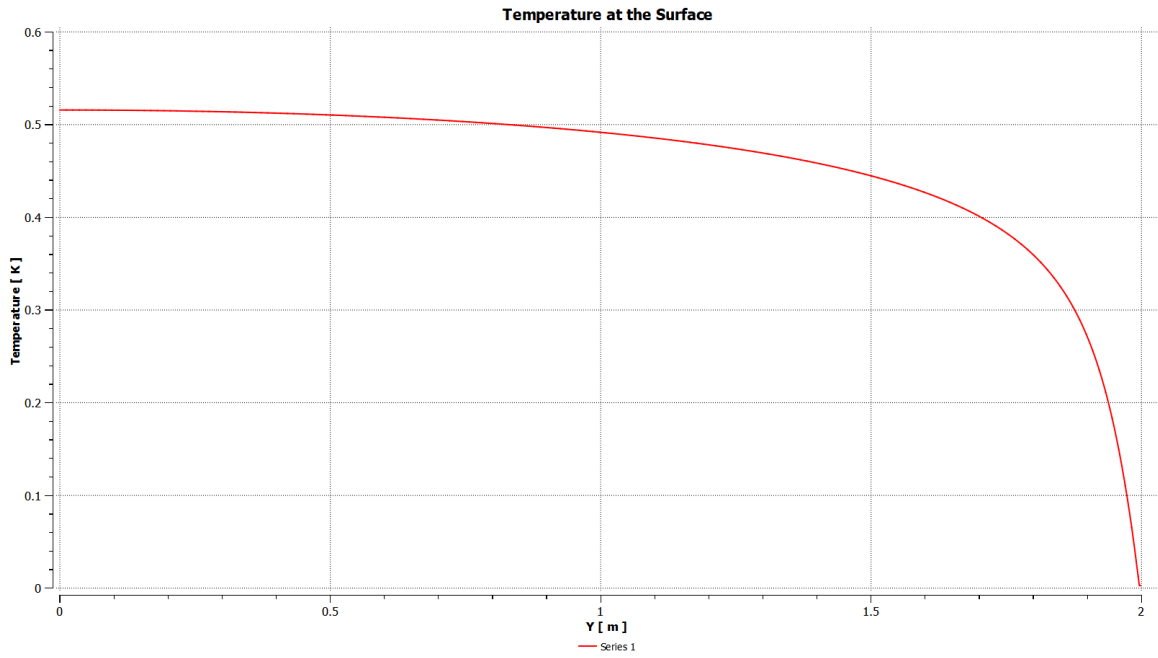


Figure B.213: Temperature at the free surface for Exp 4.3.

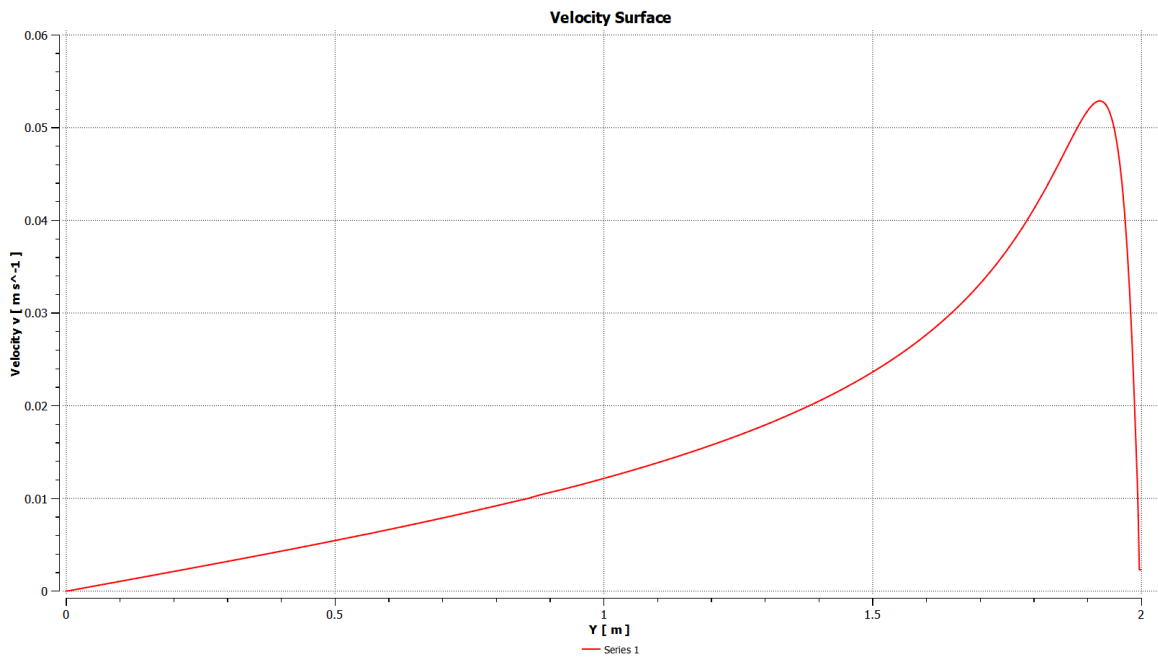


Figure B.214: Velocity at the free surface for Exp 4.3.

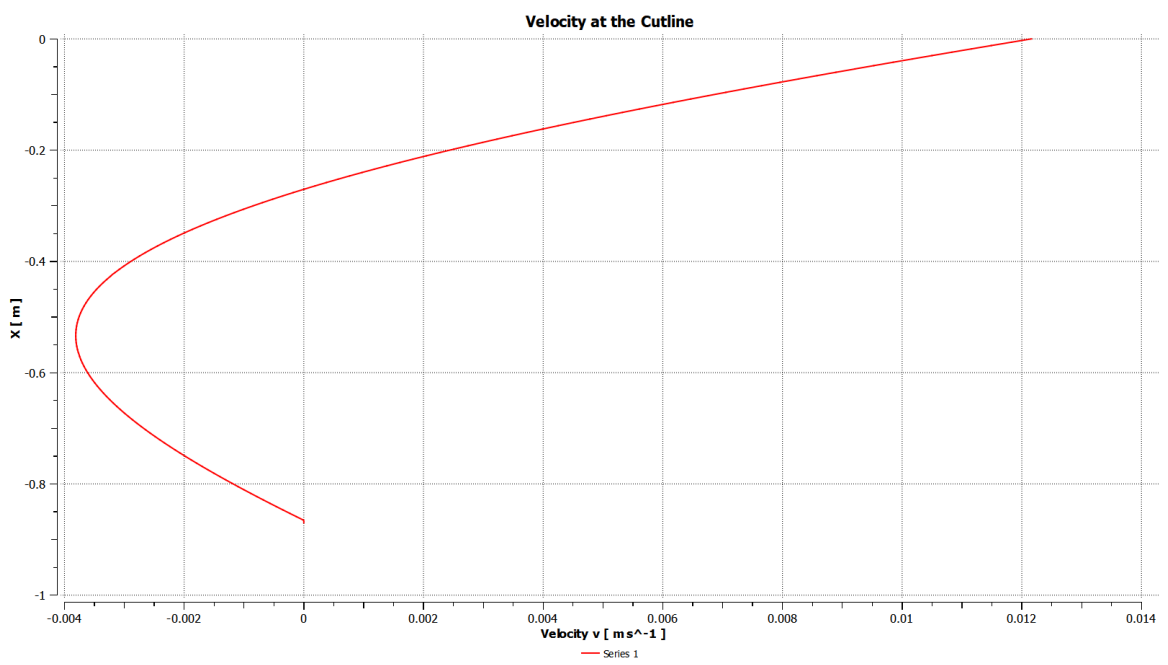


Figure B.215: Radial velocity u at the cutline at $r^*=1$ for Exp 4.3.

B.5 Regime V

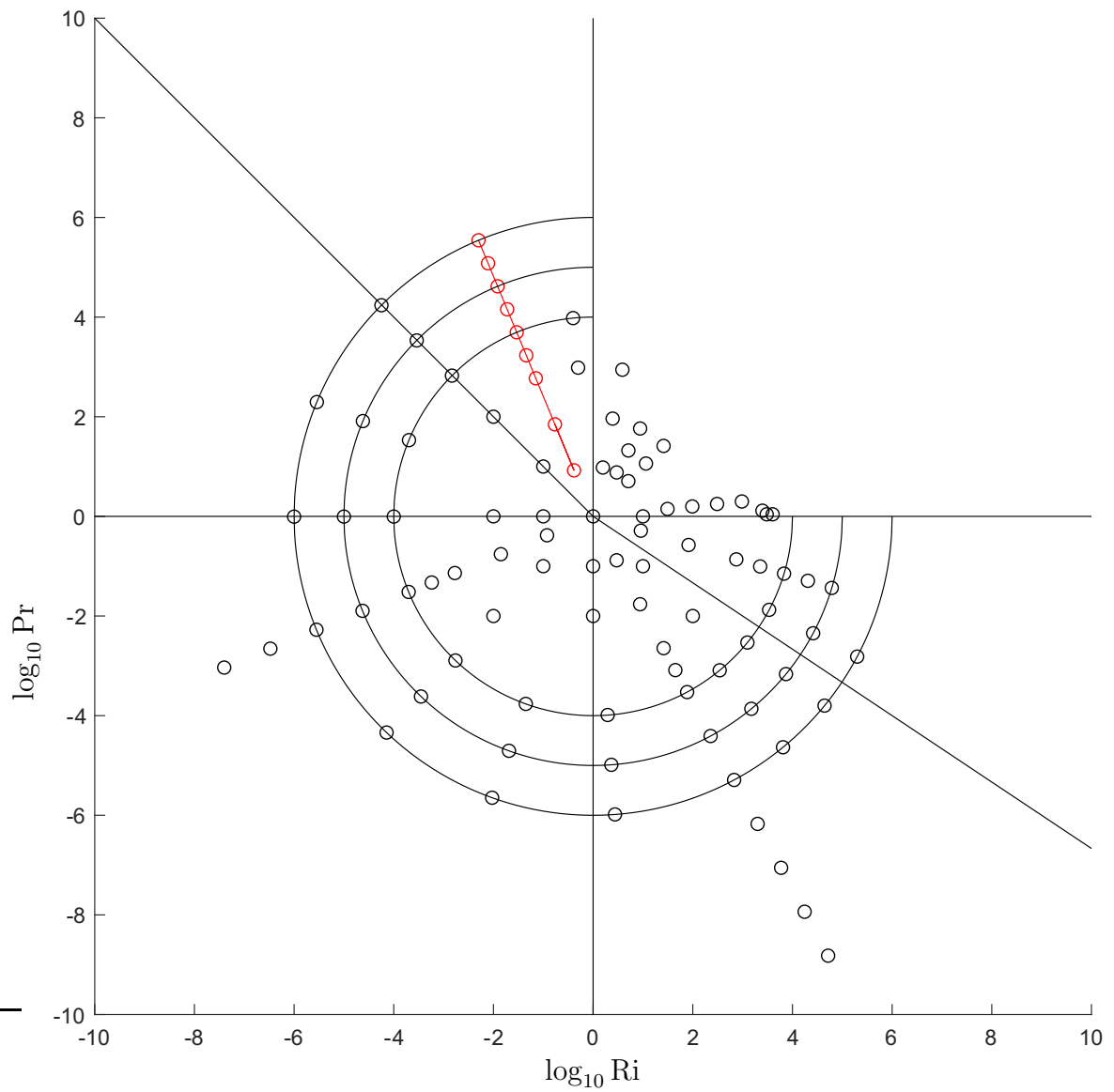


Figure B.216: Location of the dimensionless parameters for Regime V.

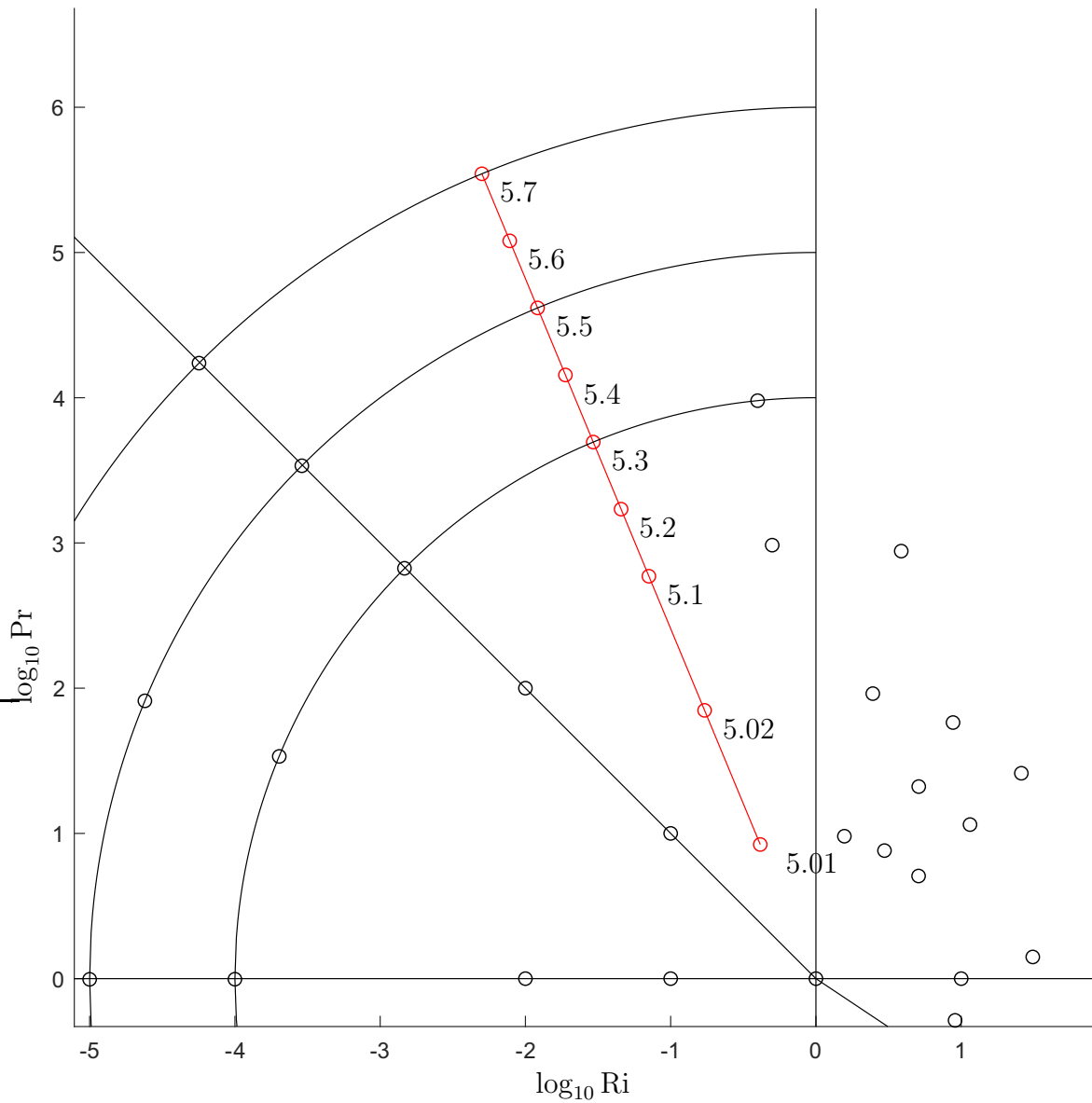


Figure B.217: Location of the dimensionless parameters for Regime V and the experiment numbers.

Exp 5.01

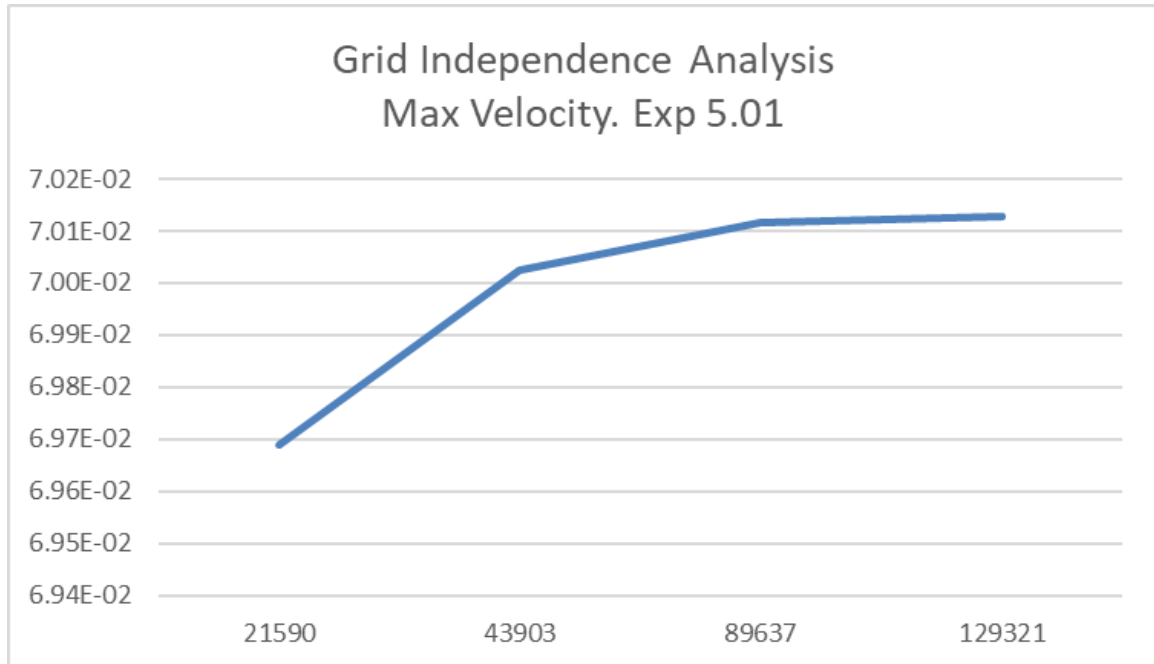


Figure B.218: Convergence for Exp 5.01: peak velocity values vs number of nodes in logarithmic scale.

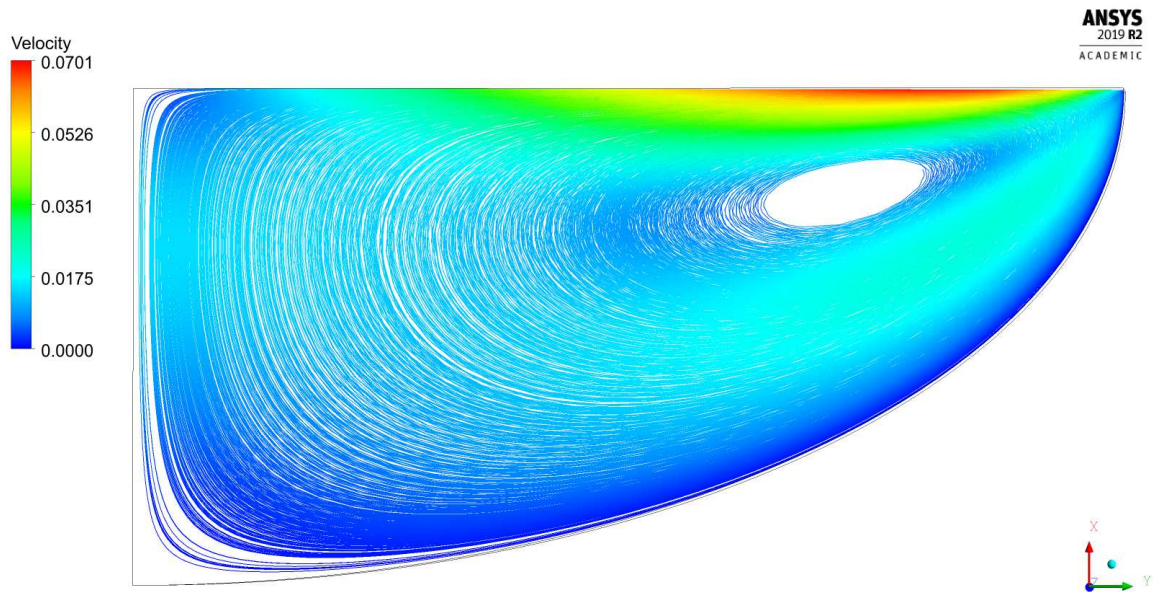


Figure B.219: Streamlines for Exp 5.01.

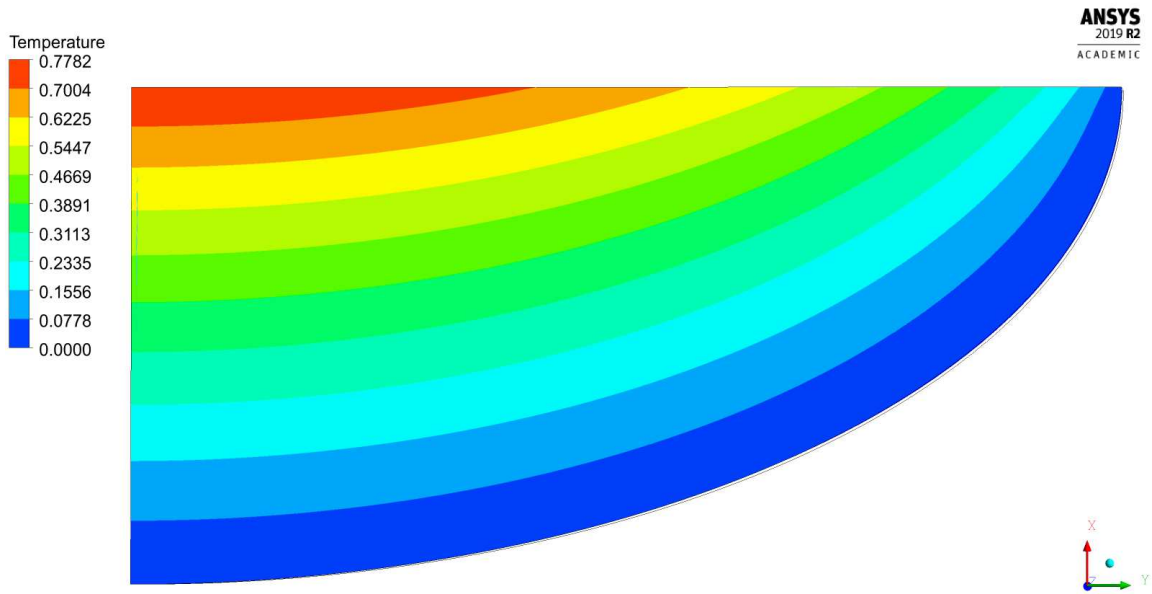


Figure B.220: Temperature field for Exp 5.01.

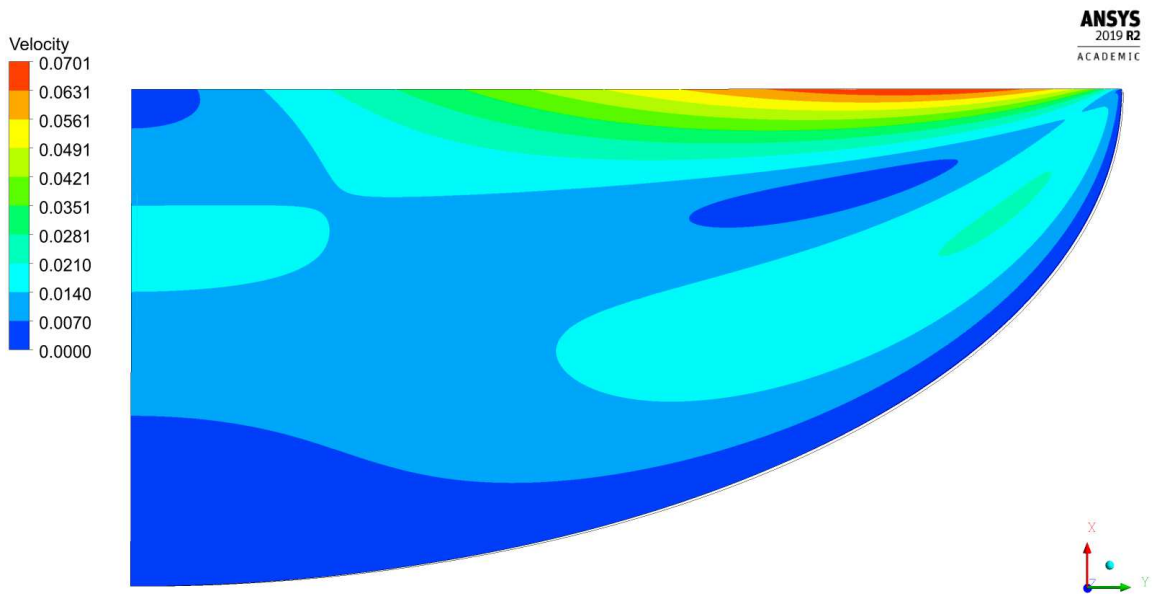


Figure B.221: Velocity magnitude contour for Exp 5.01.

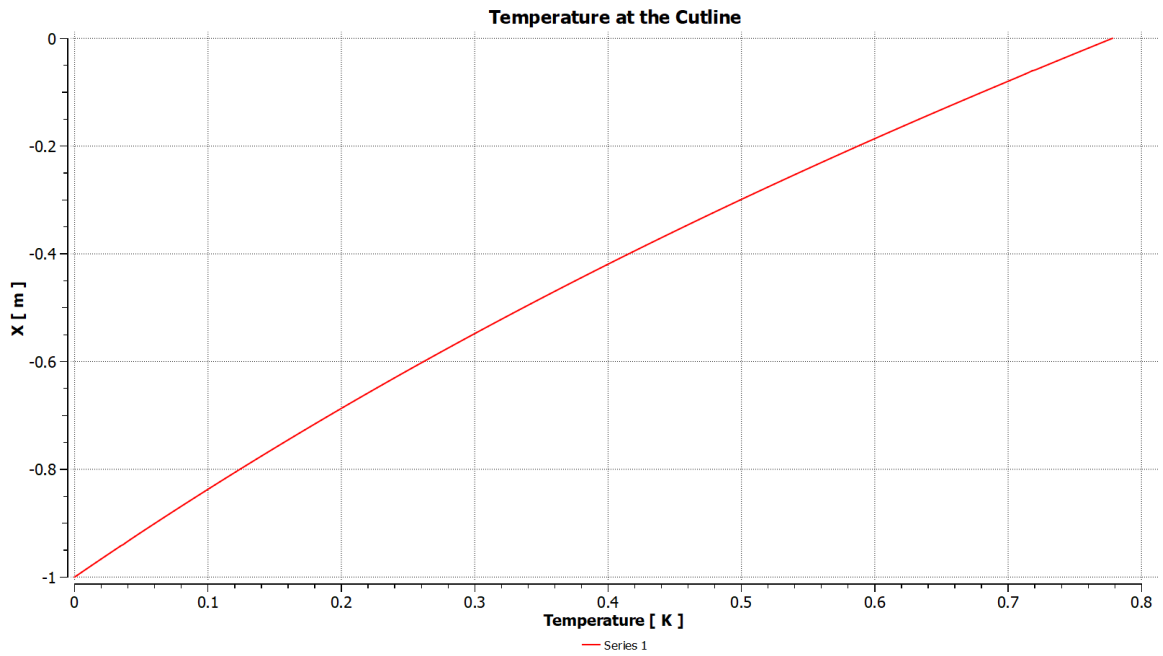


Figure B.222: Temperature at the axis of symmetry for Exp 5.01.

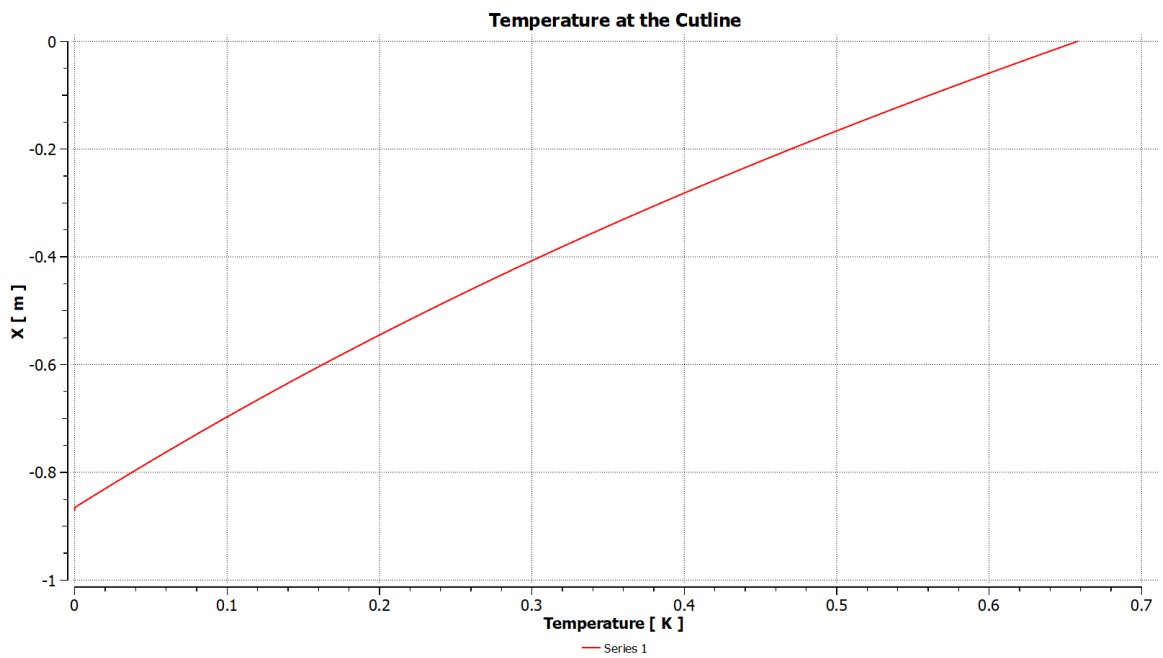


Figure B.223: Temperature at the cutline at $r^*=1$ for Exp 5.01.

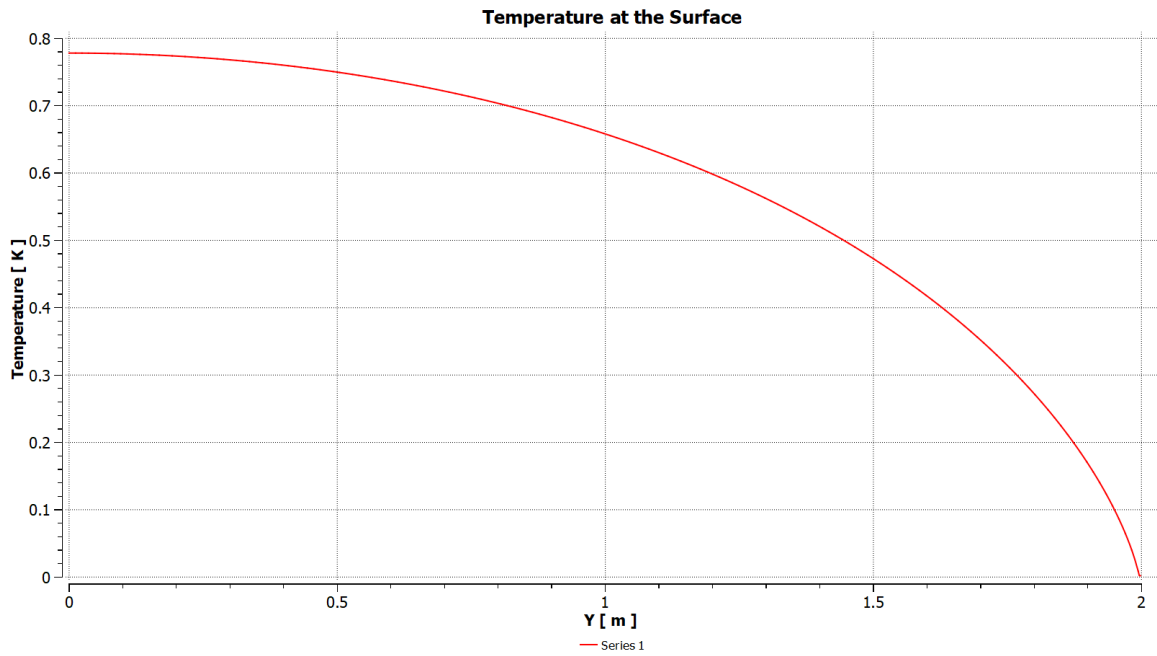


Figure B.224: Temperature at the free surface for Exp 5.01.

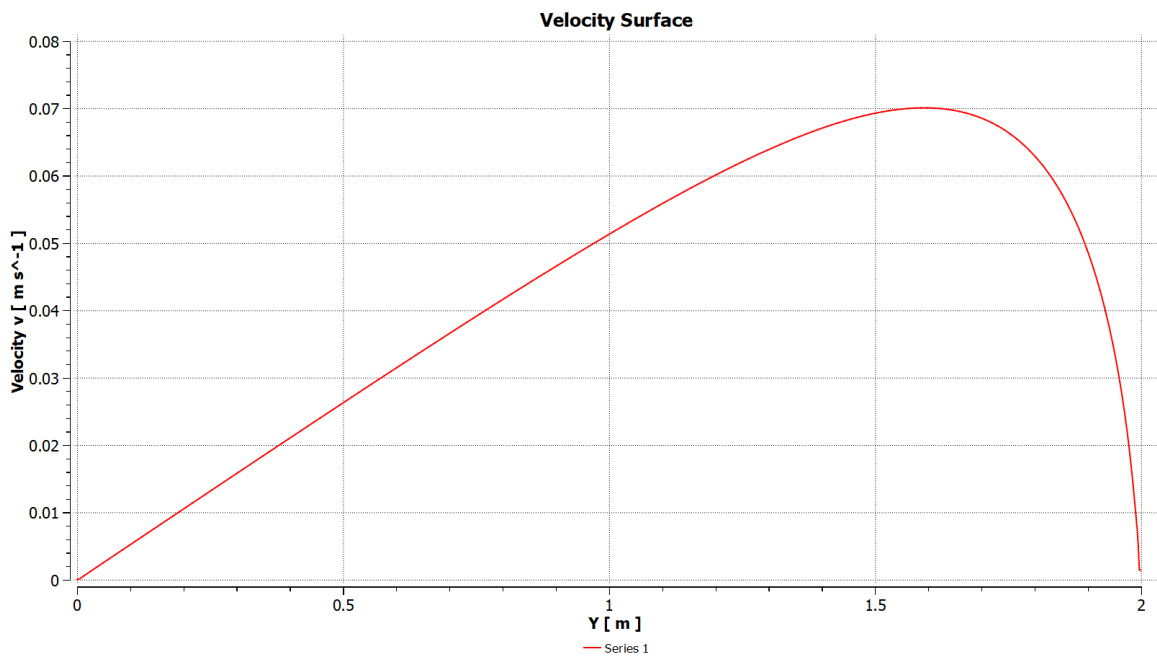


Figure B.225: Velocity at the free surface for Exp 5.01.

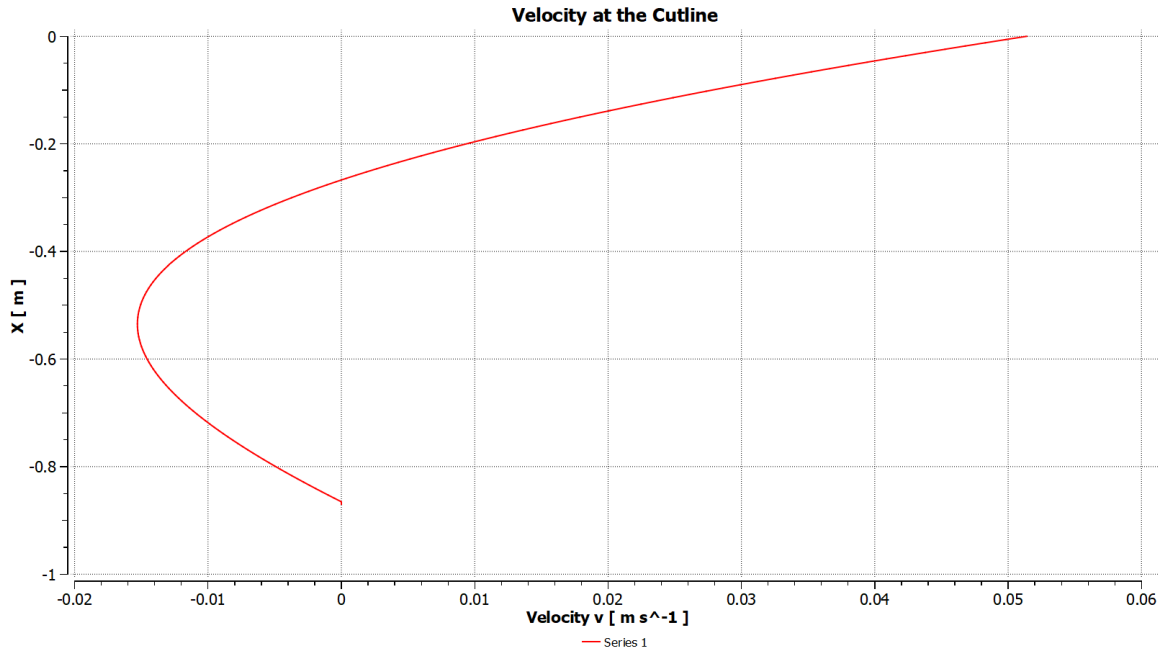


Figure B.226: Radial velocity u at the cutline at $r^*=1$ for Exp 5.01.

Exp 5.02

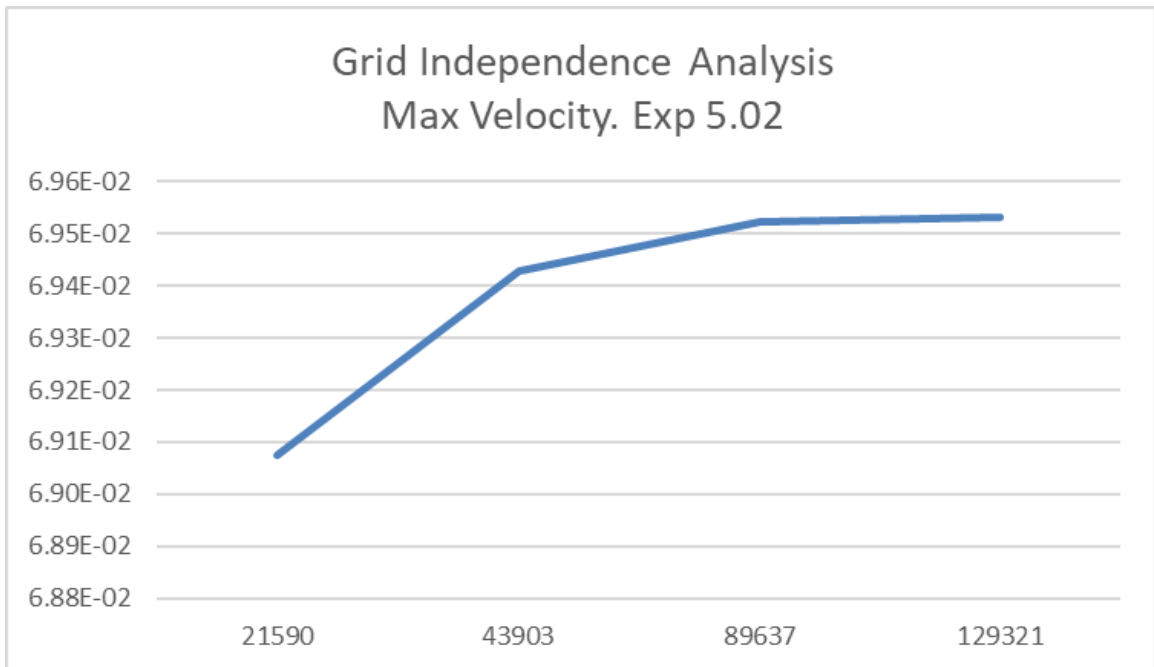


Figure B.227: Convergence for Exp 5.02: peak velocity values vs number of nodes in logarithmic scale.

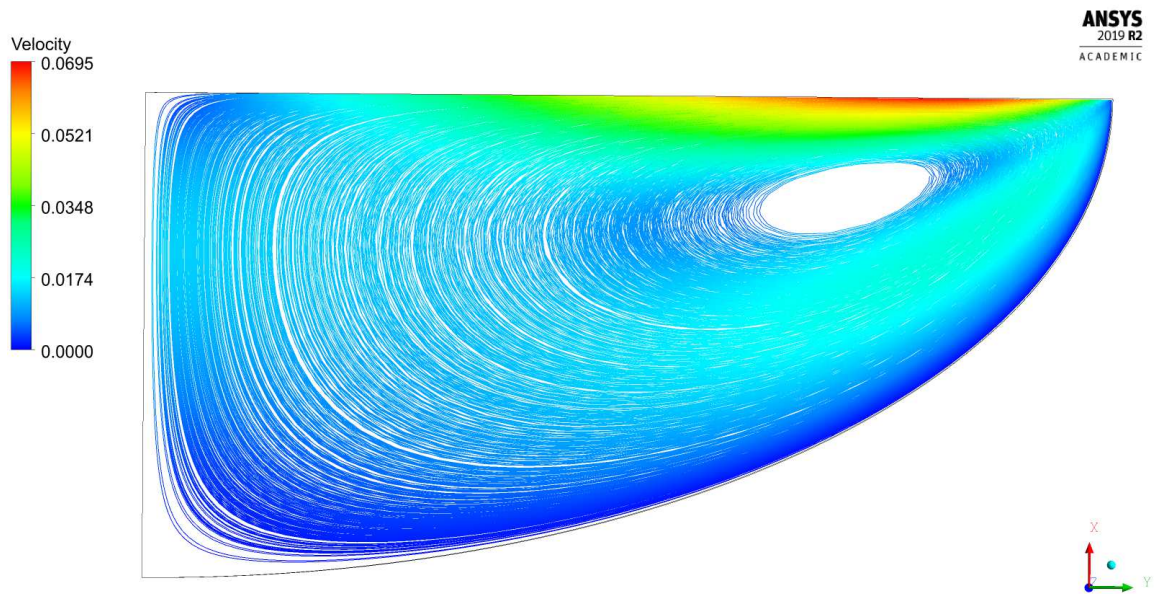


Figure B.228: Streamlines for Exp 5.02.

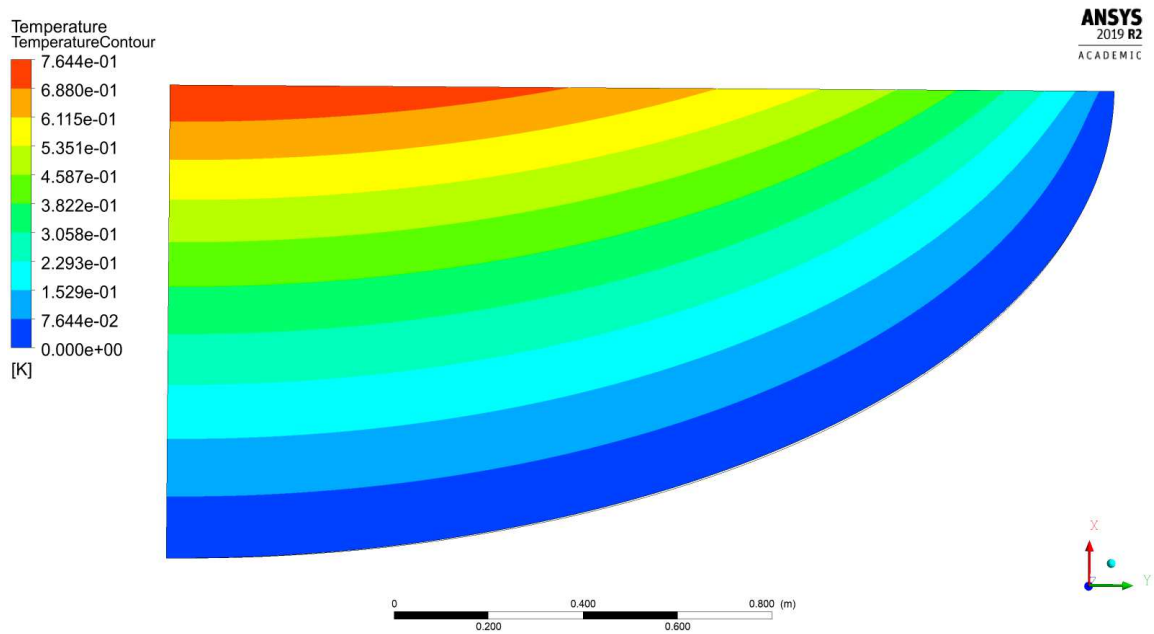


Figure B.229: Temperature field for Exp 5.02.

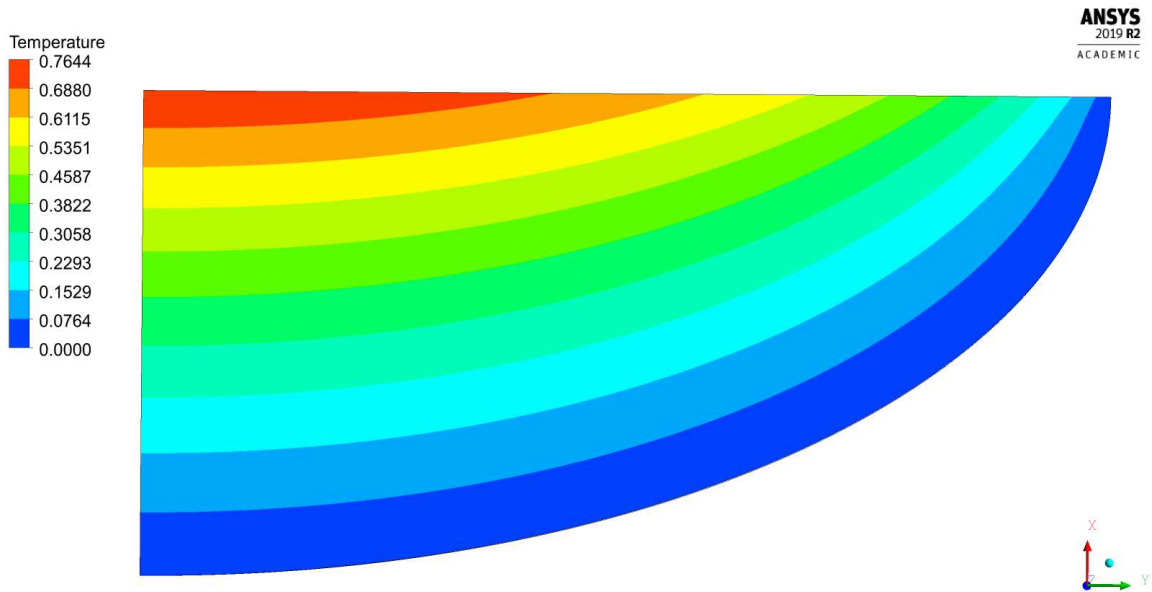


Figure B.230: Velocity magnitude contour for Exp 5.02.

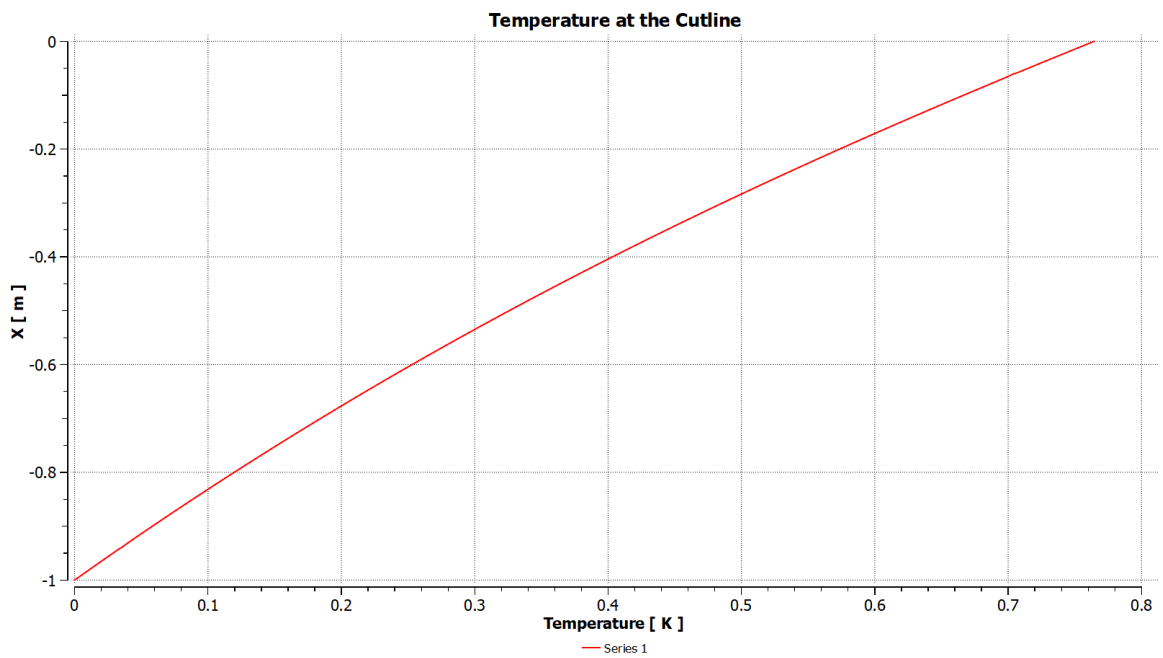


Figure B.231: Temperature at the axis of symmetry for Exp 5.02.

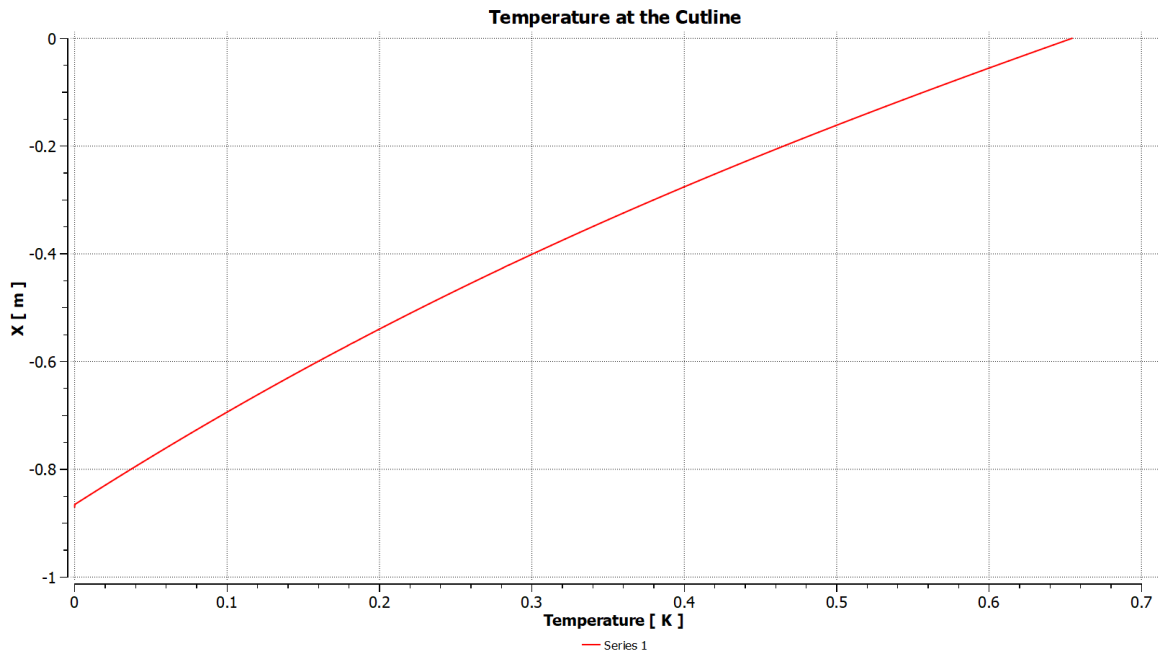


Figure B.232: Temperature at the cutline at $r^*=1$ for Exp 5.02.

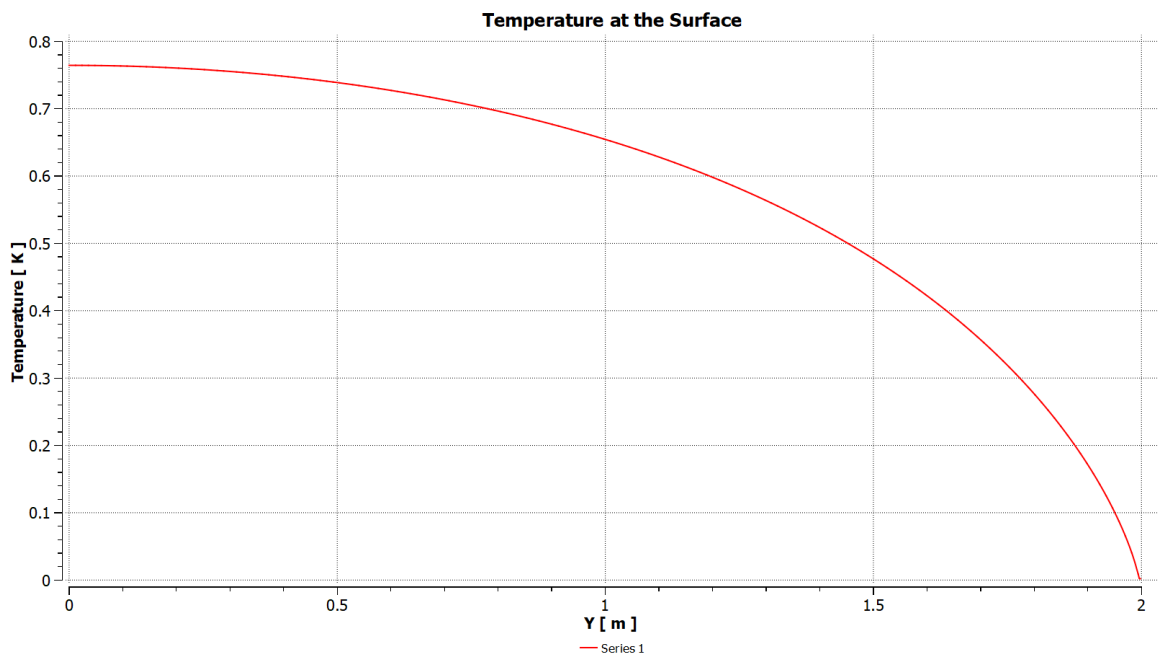


Figure B.233: Temperature at the free surface for Exp 5.02.

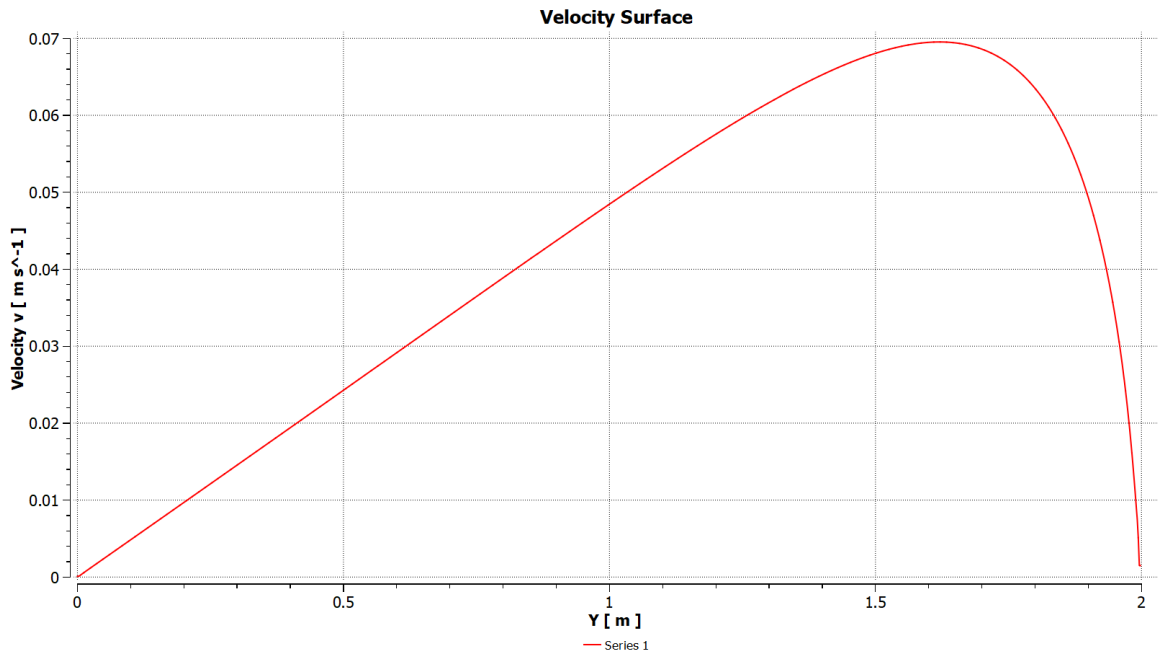


Figure B.234: Velocity at the free surface for Exp 5.02.

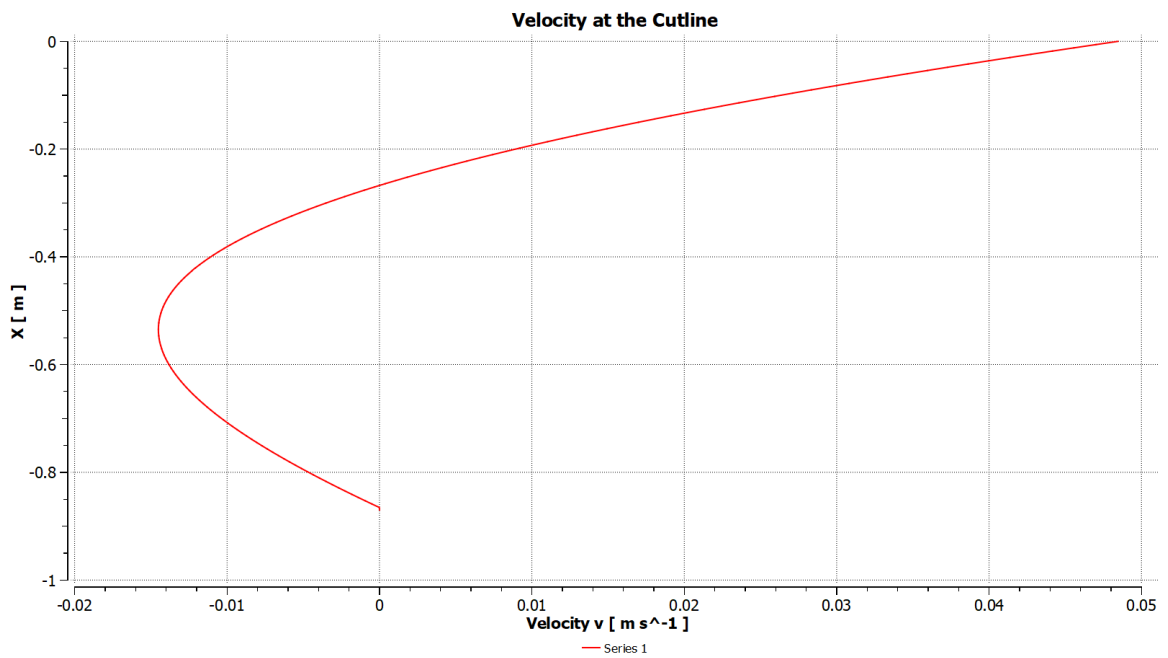


Figure B.235: Radial velocity u at the cutline at $r^*=1$ for Exp 5.02.

Exp 5.1

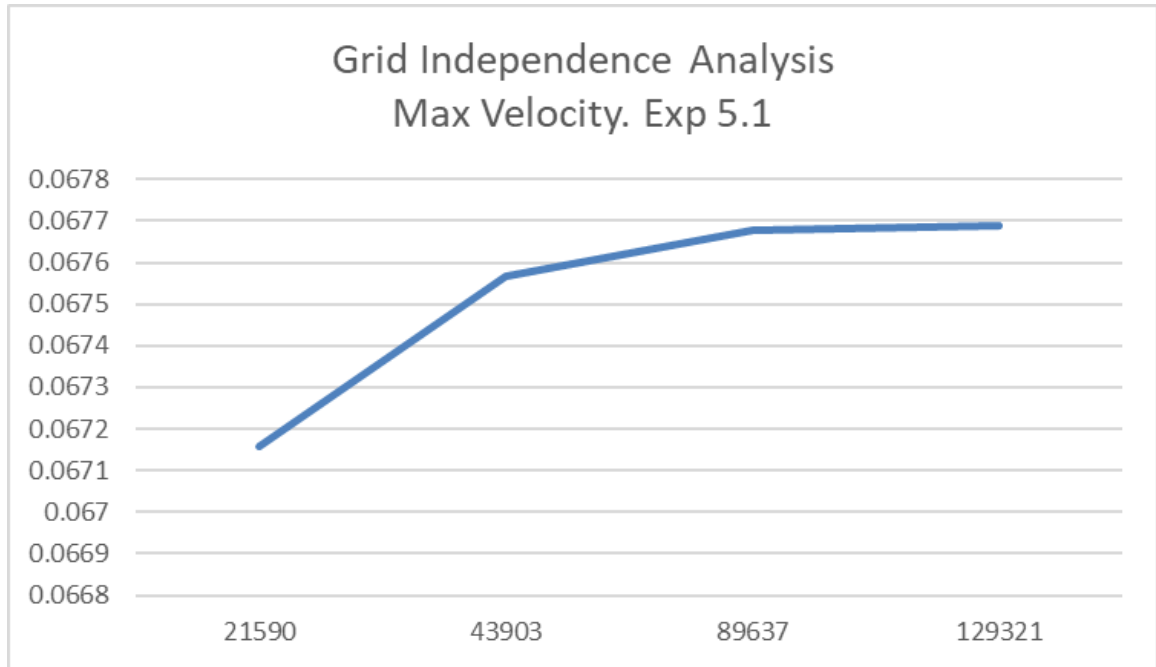


Figure B.236: Convergence for Exp 5.1: peak velocity values vs number of nodes in logarithmic scale.

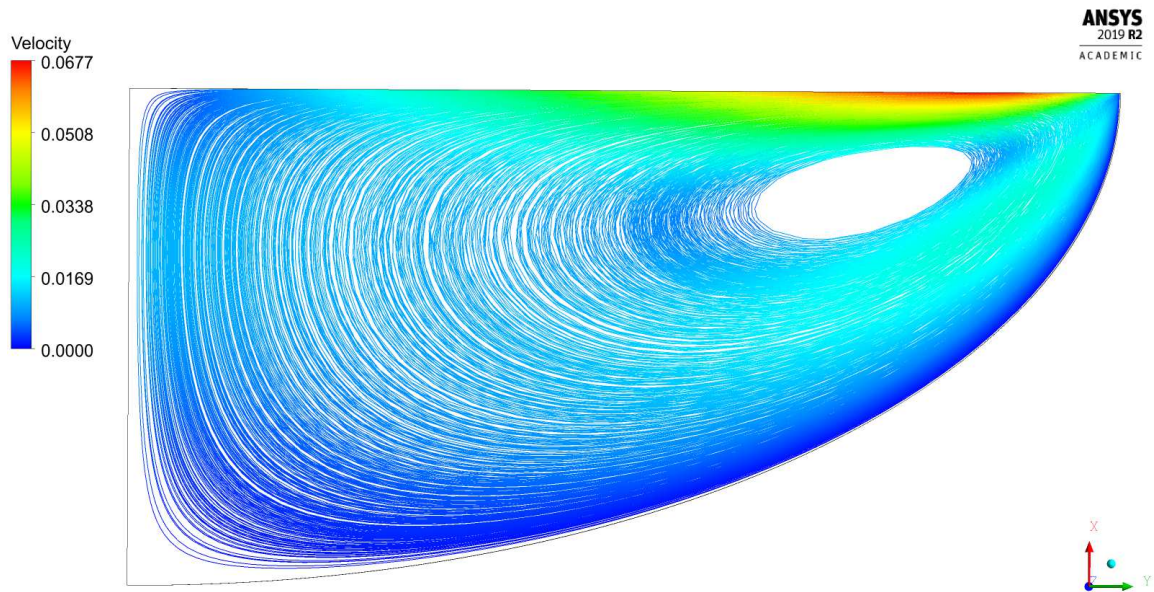


Figure B.237: Streamlines for Exp 5.1.

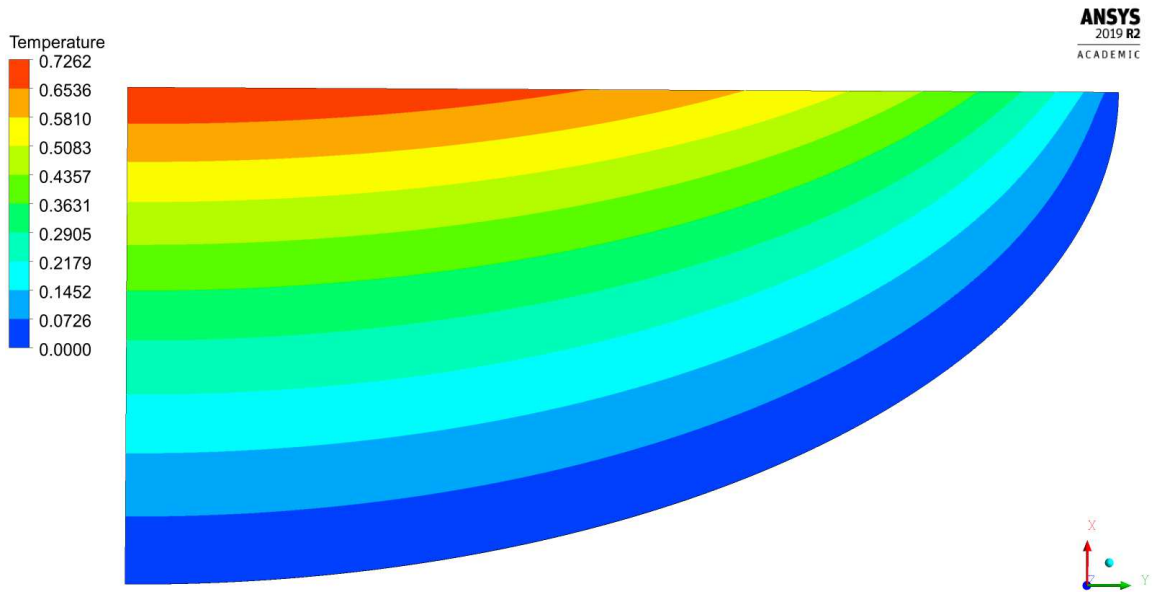


Figure B.238: Temperature field for Exp 5.1.

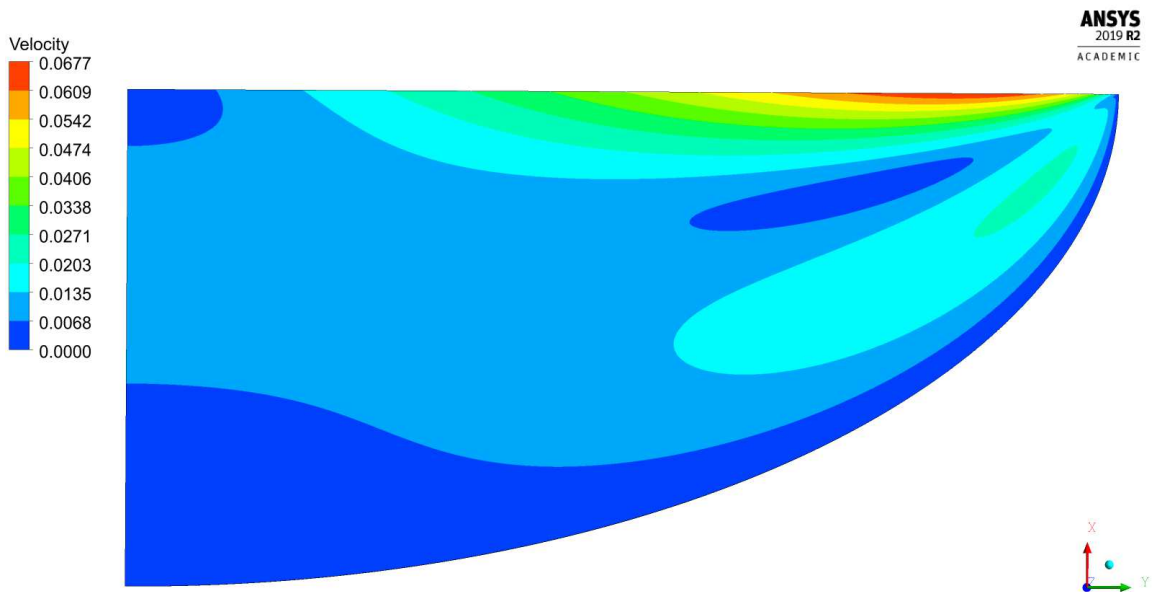


Figure B.239: Velocity magnitude contour for Exp 5.1.

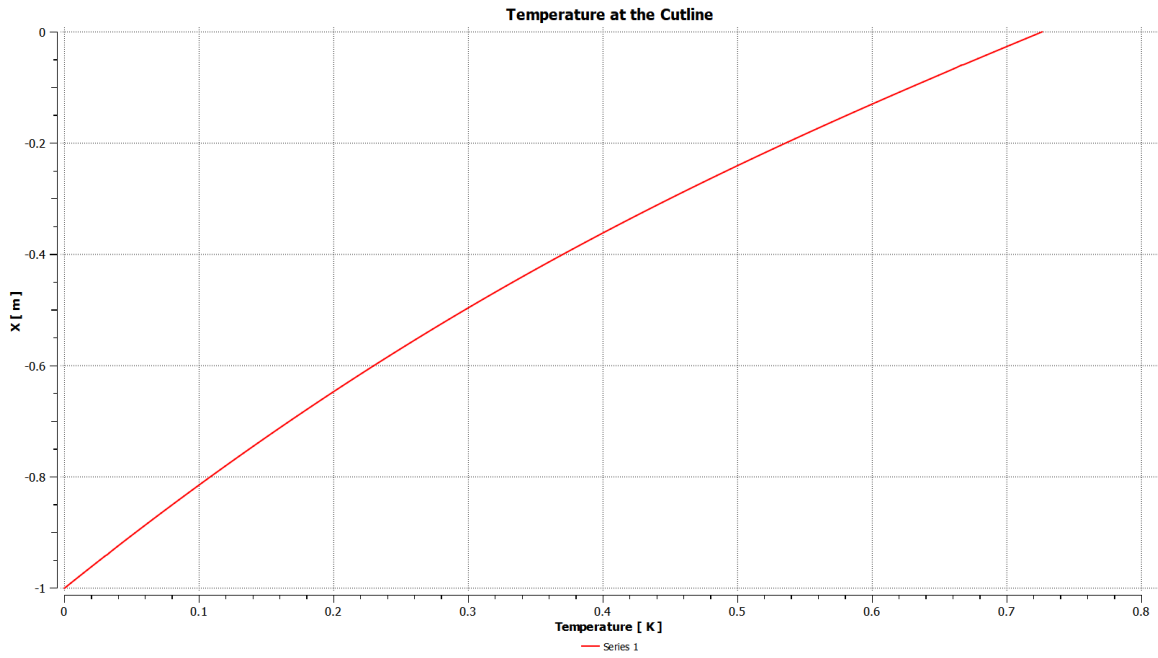


Figure B.240: Temperature at the axis of symmetry for Exp 5.1.

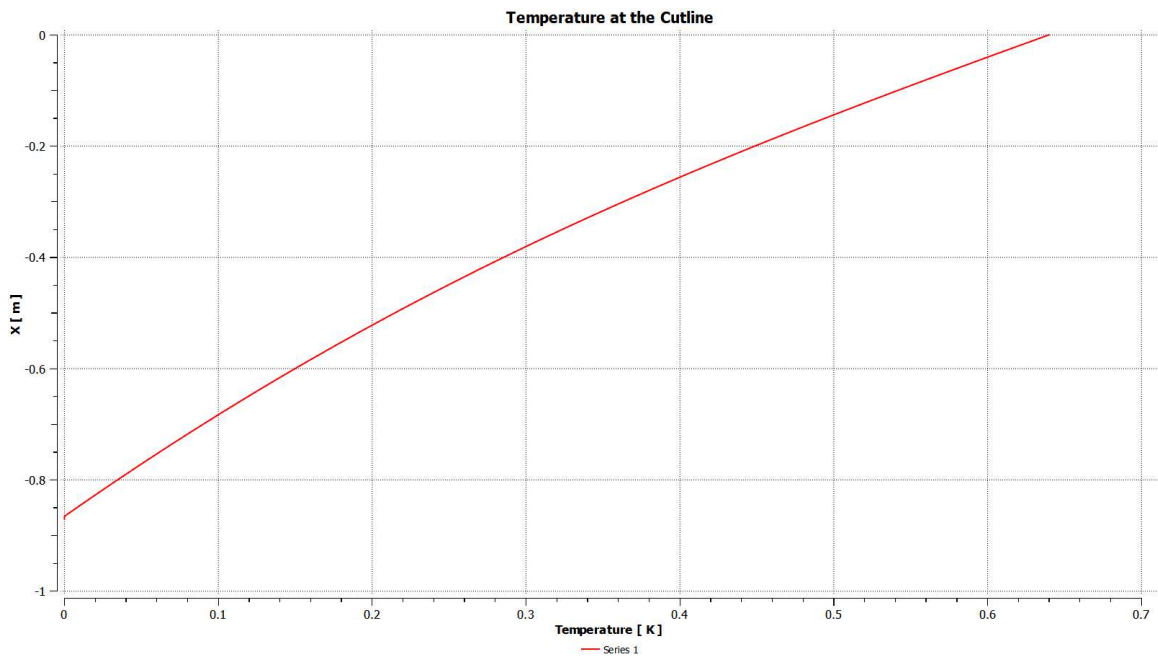


Figure B.241: Temperature at the cutline at $r^*=1$ for Exp 5.1.

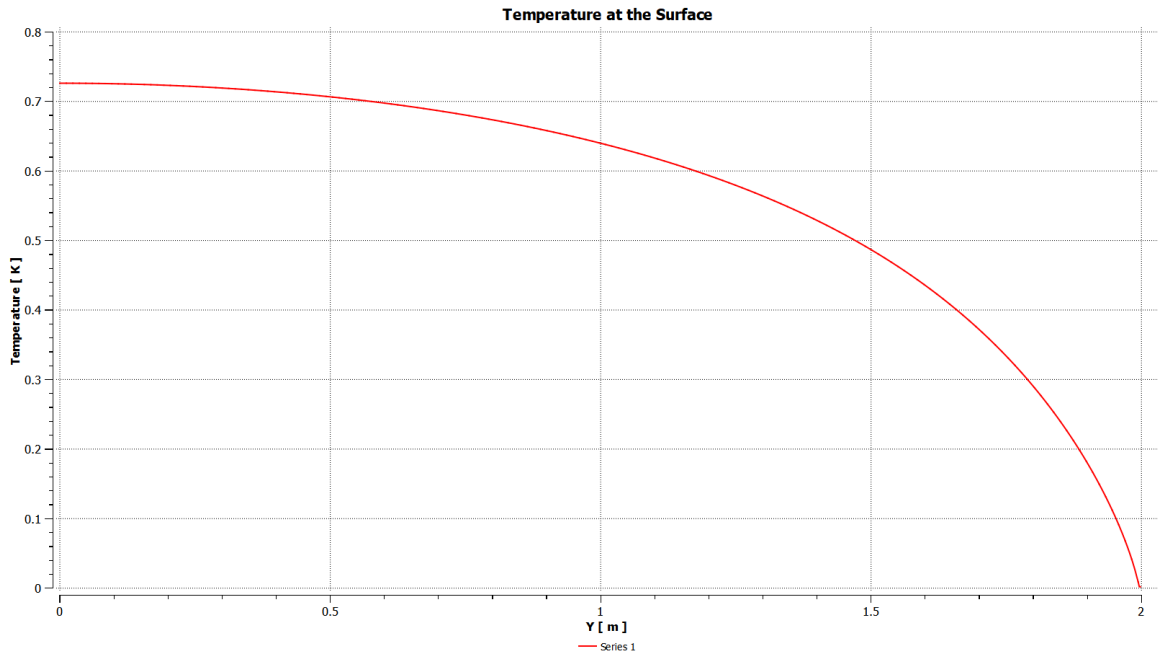


Figure B.242: Temperature at the free surface for Exp 5.1.

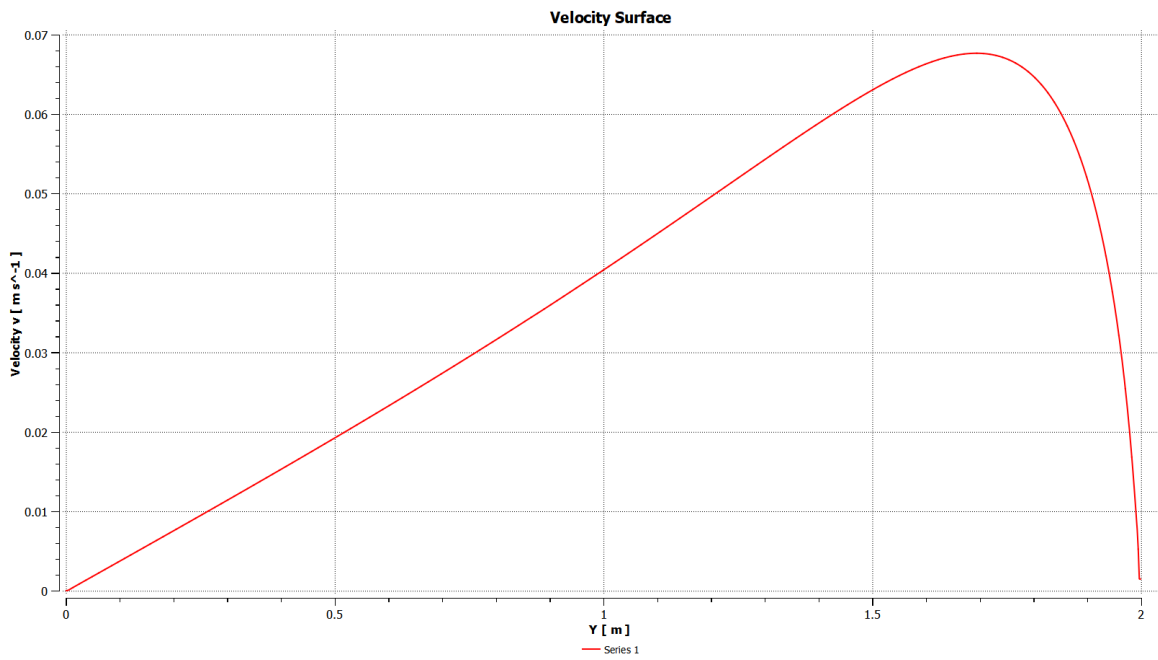


Figure B.243: Velocity at the free surface for Exp 5.1.

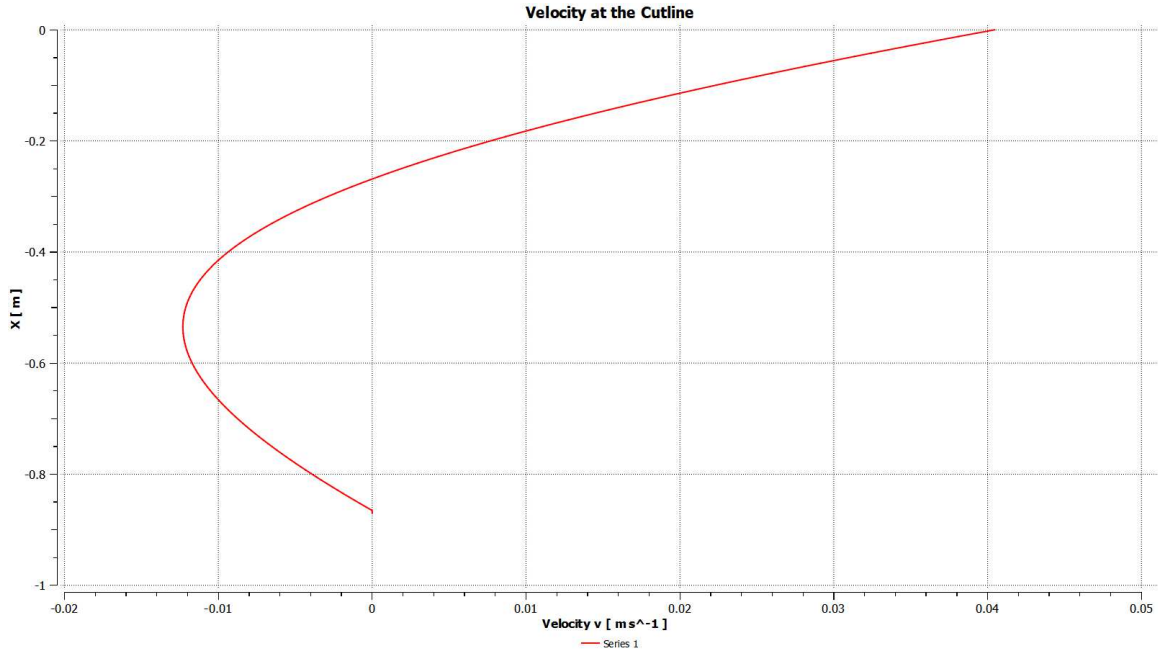


Figure B.244: Radial velocity u at the cutline at $r^*=1$ for Exp 5.1.

Exp 5.2

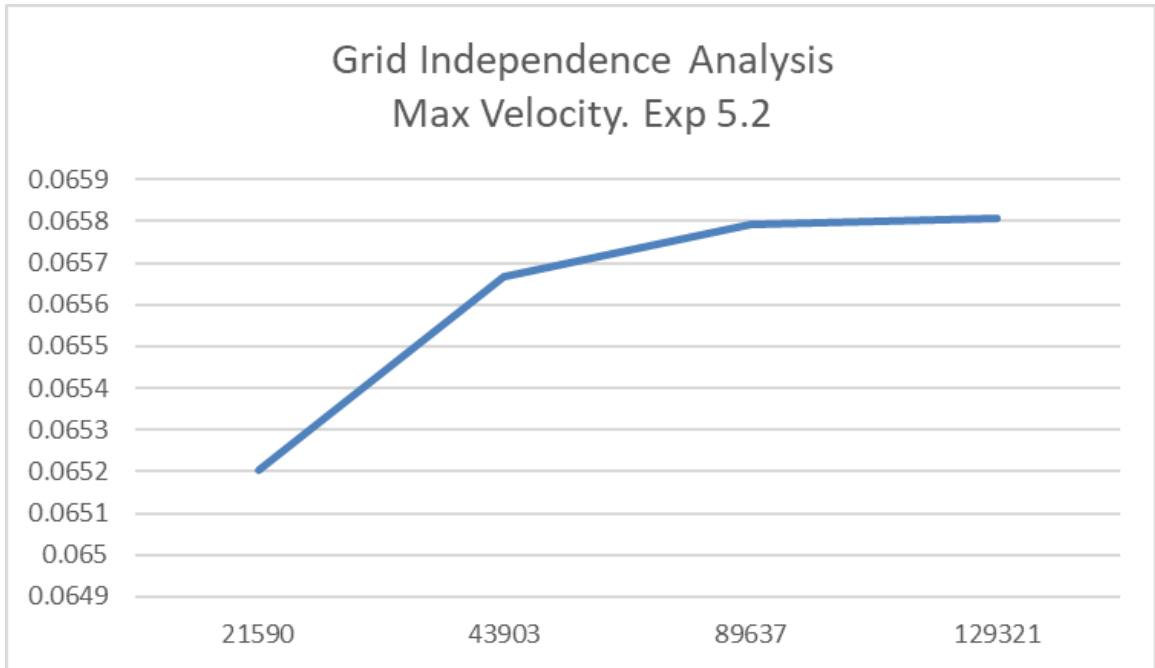


Figure B.245: Convergence for Exp 5.2: peak velocity values vs number of nodes in logarithmic scale.

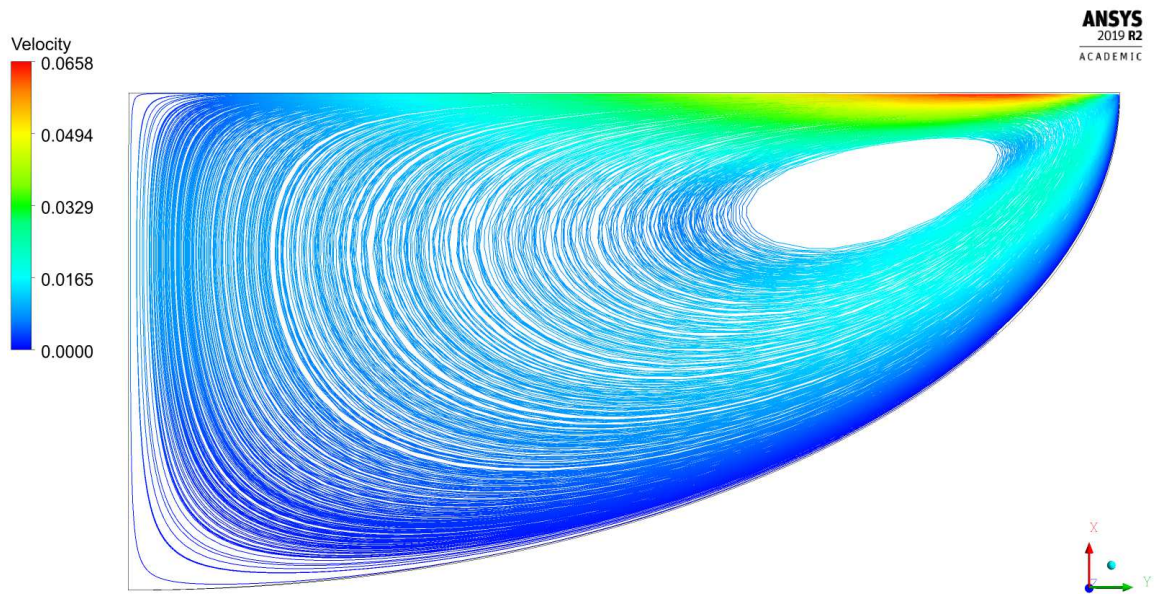


Figure B.246: Streamlines for Exp 5.2.

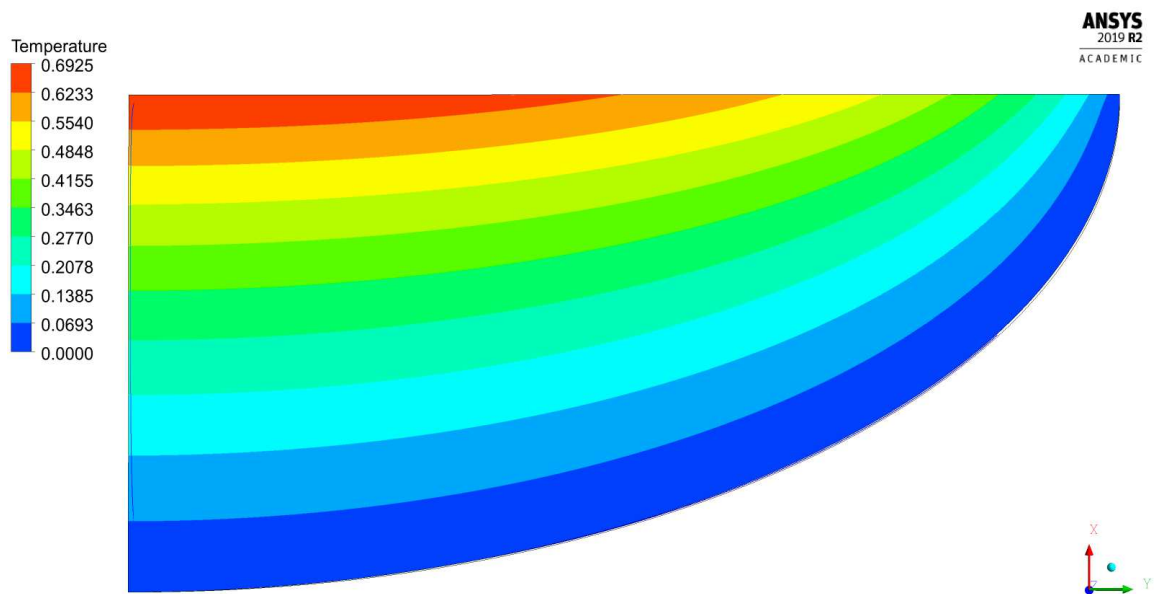


Figure B.247: Temperature field for Exp 5.2.

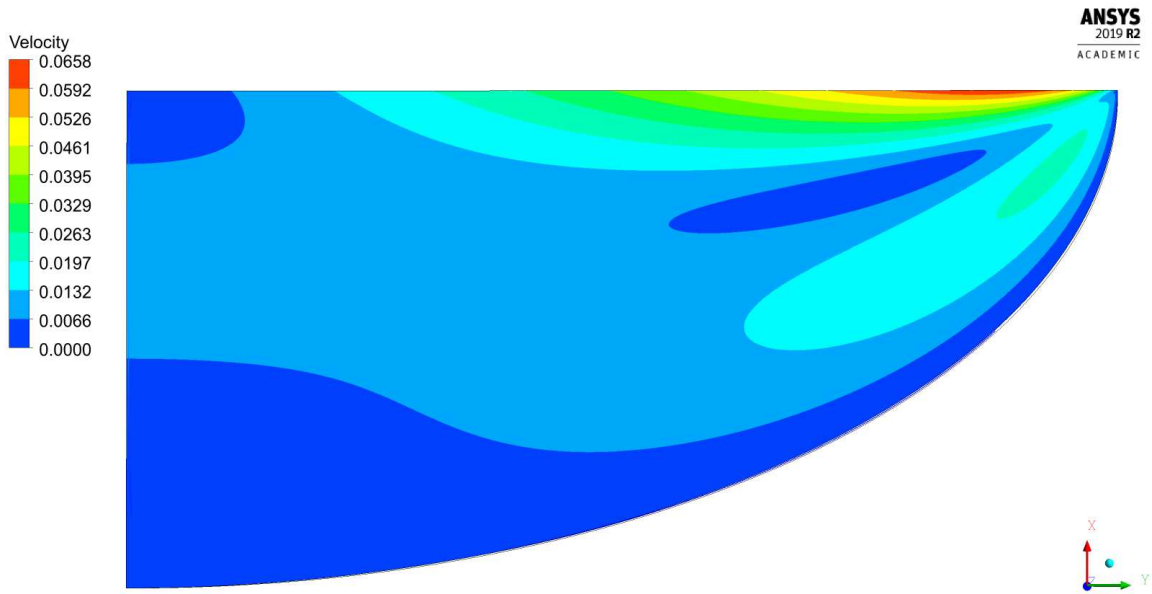


Figure B.248: Velocity magnitude contour for Exp 5.2.

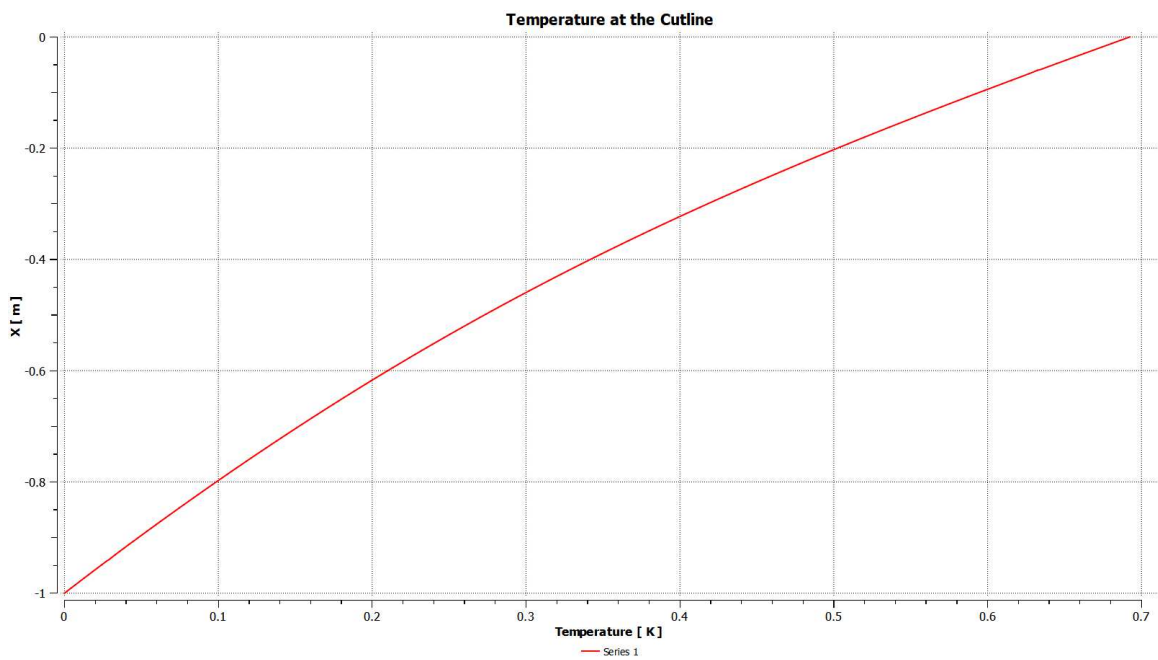


Figure B.249: Temperature at the axis of symmetry for Exp 5.2.

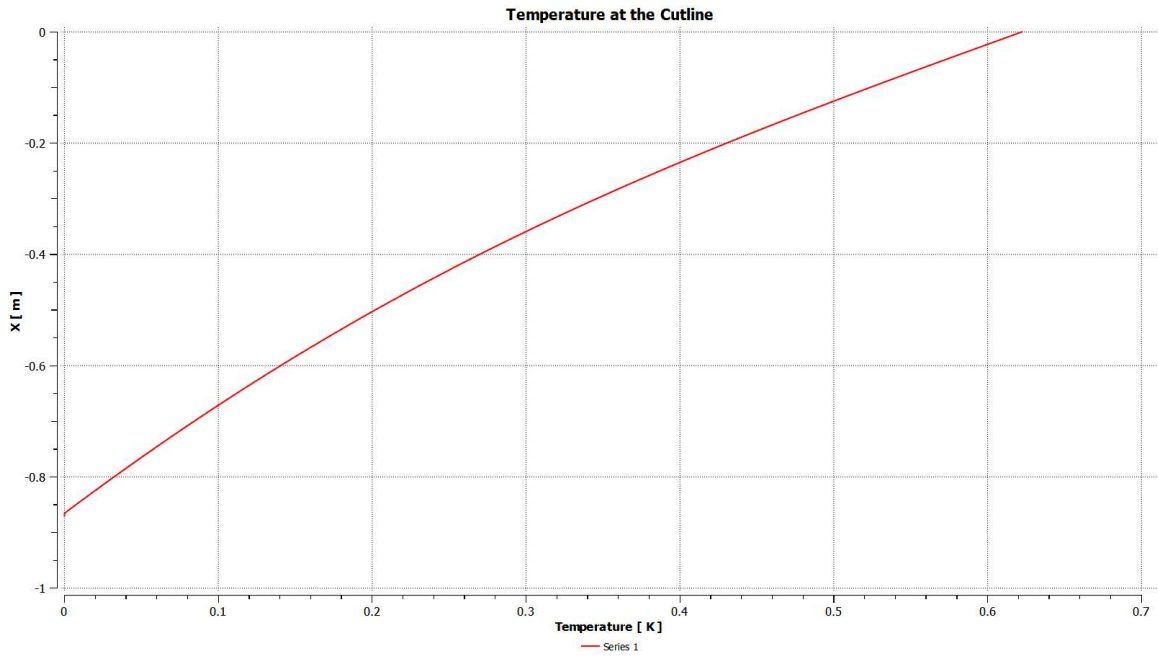


Figure B.250: Temperature at the cutline at $r^*=1$ for Exp 5.2.

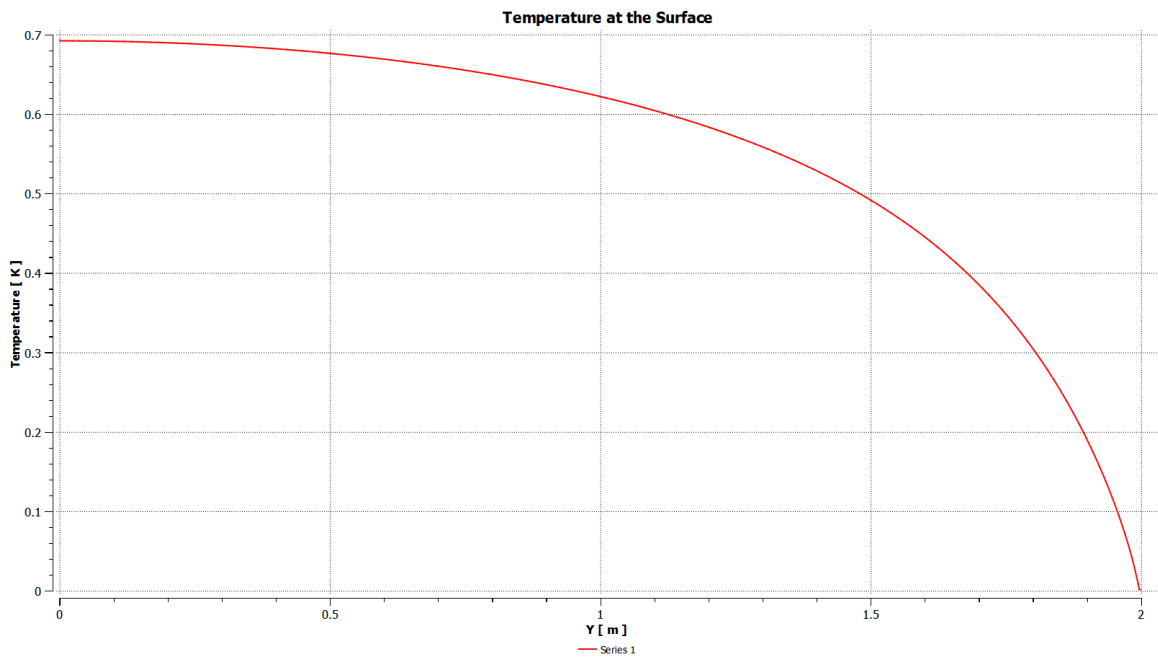


Figure B.251: Temperature at the free surface for Exp 5.2.

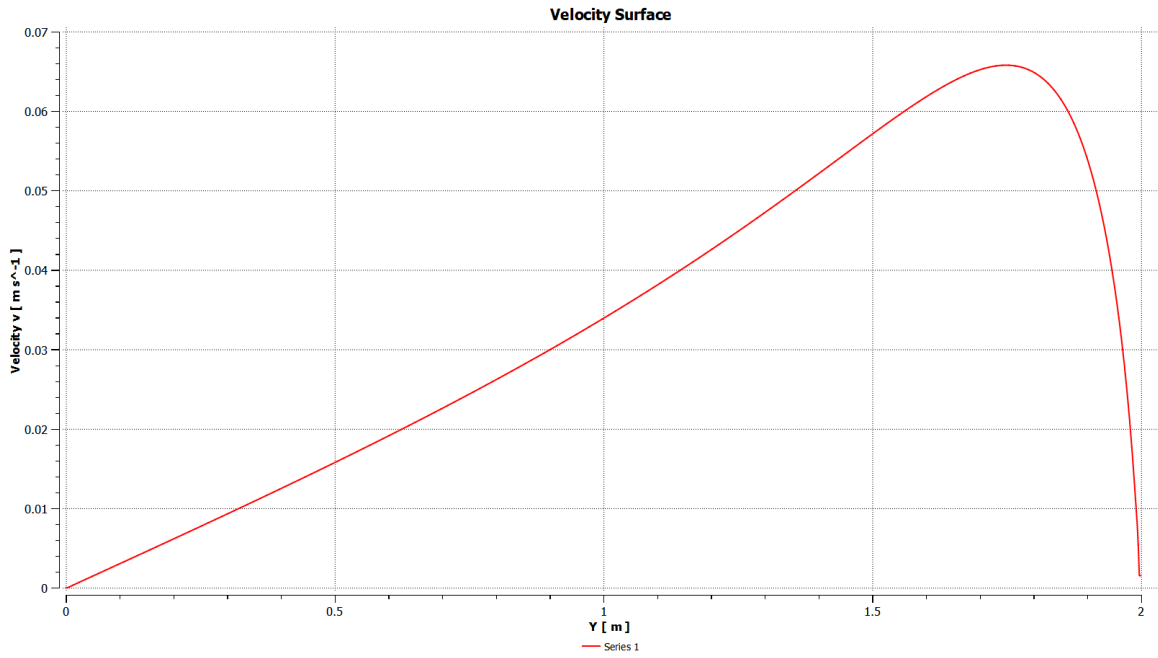


Figure B.252: Velocity at the free surface for Exp 5.2.

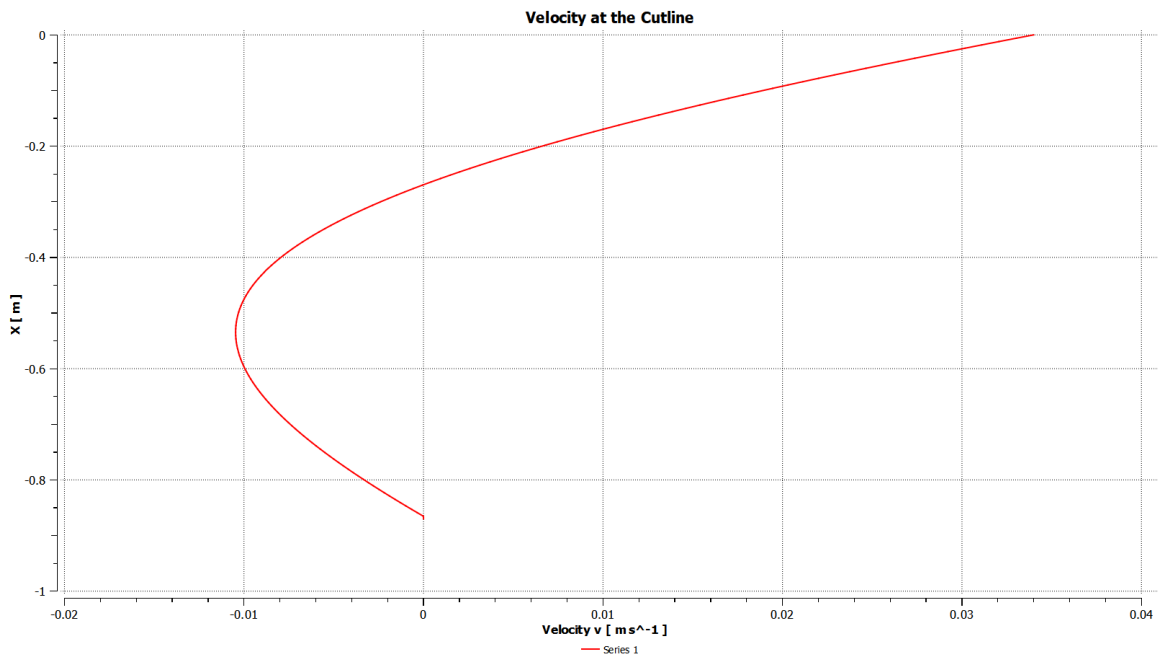


Figure B.253: Radial velocity u at the cutline at $r^*=1$ for Exp 5.2.

Exp 5.3

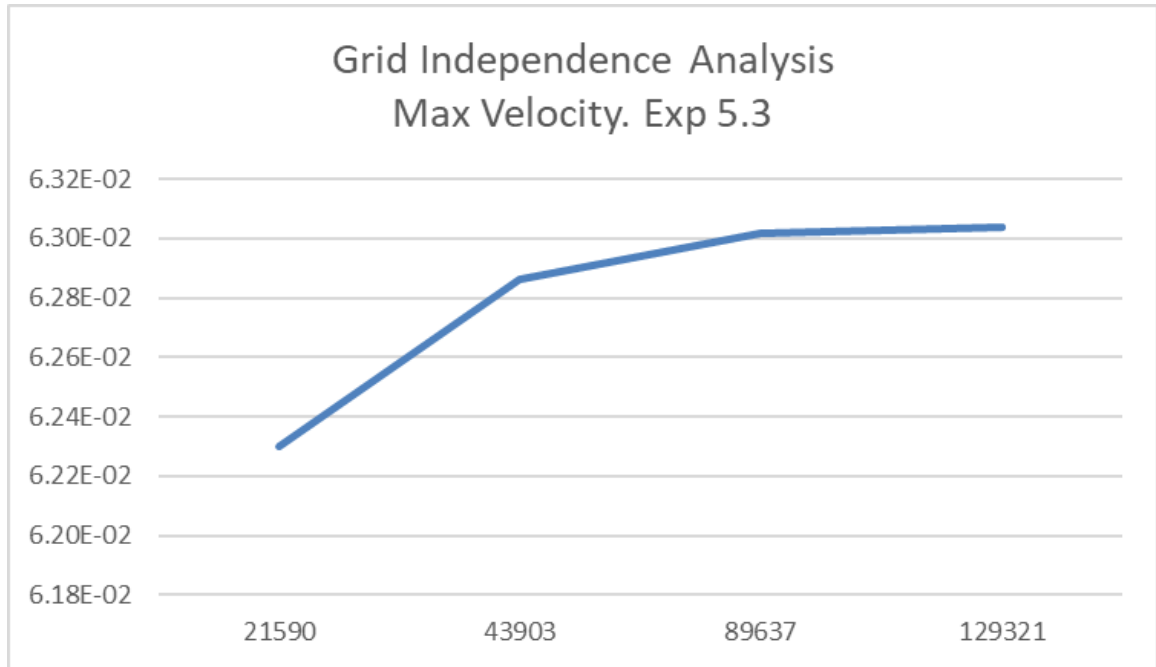


Figure B.254: Convergence for Exp 5.3: peak velocity values vs number of nodes in logarithmic scale.

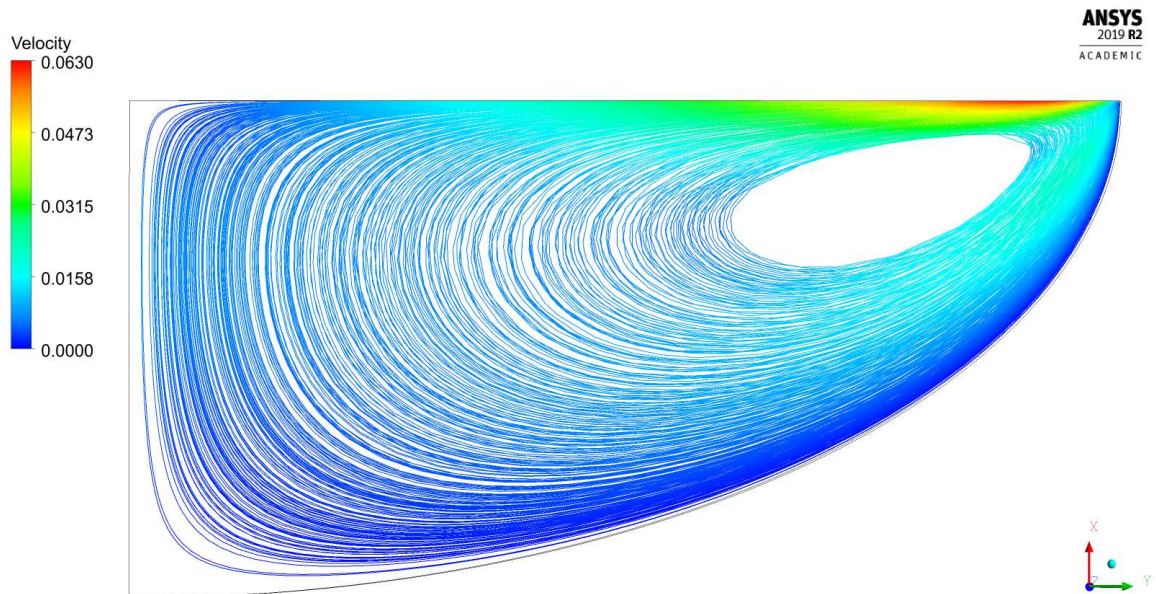


Figure B.255: Streamlines for Exp 5.3.

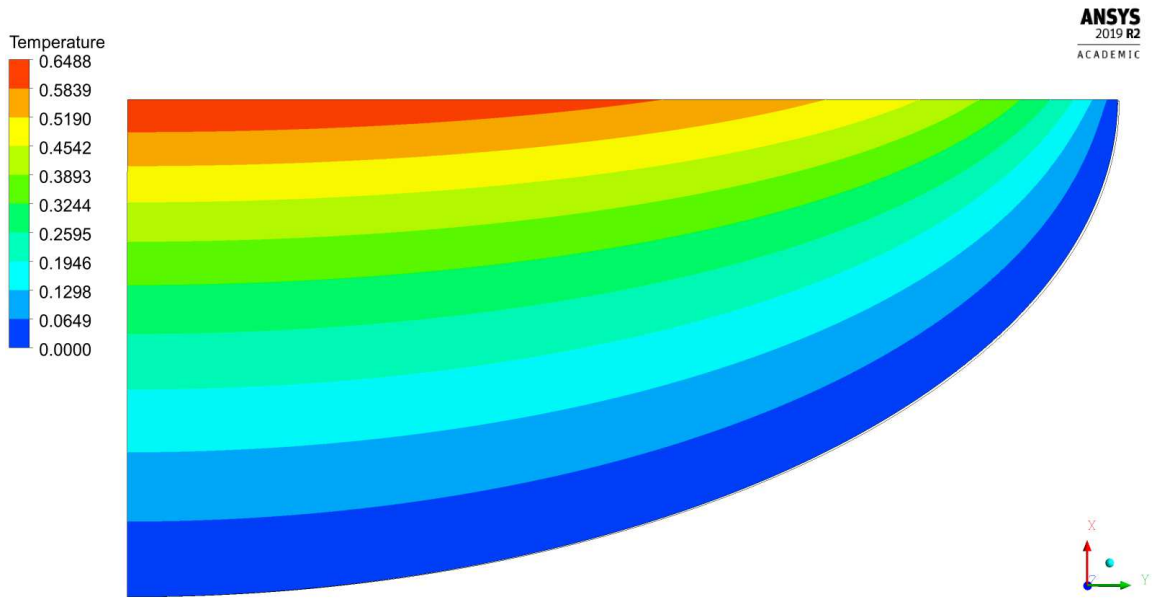


Figure B.256: Temperature field for Exp 5.3.

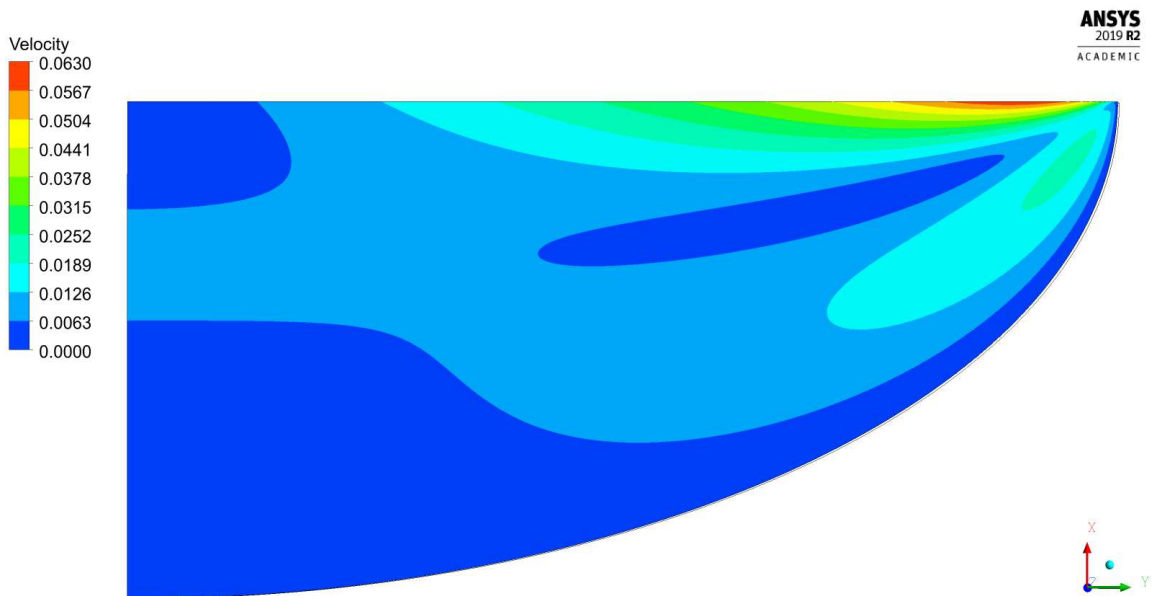


Figure B.257: Velocity magnitude contour for Exp 5.3.

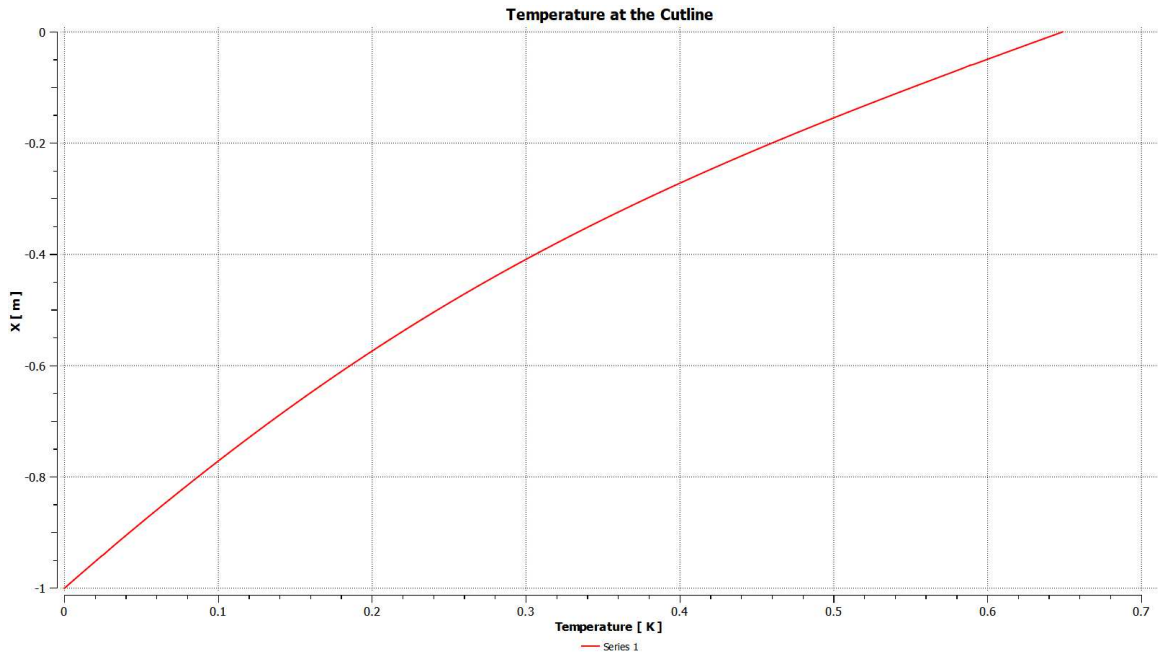


Figure B.258: Temperature at the axis of symmetry for Exp 5.3.

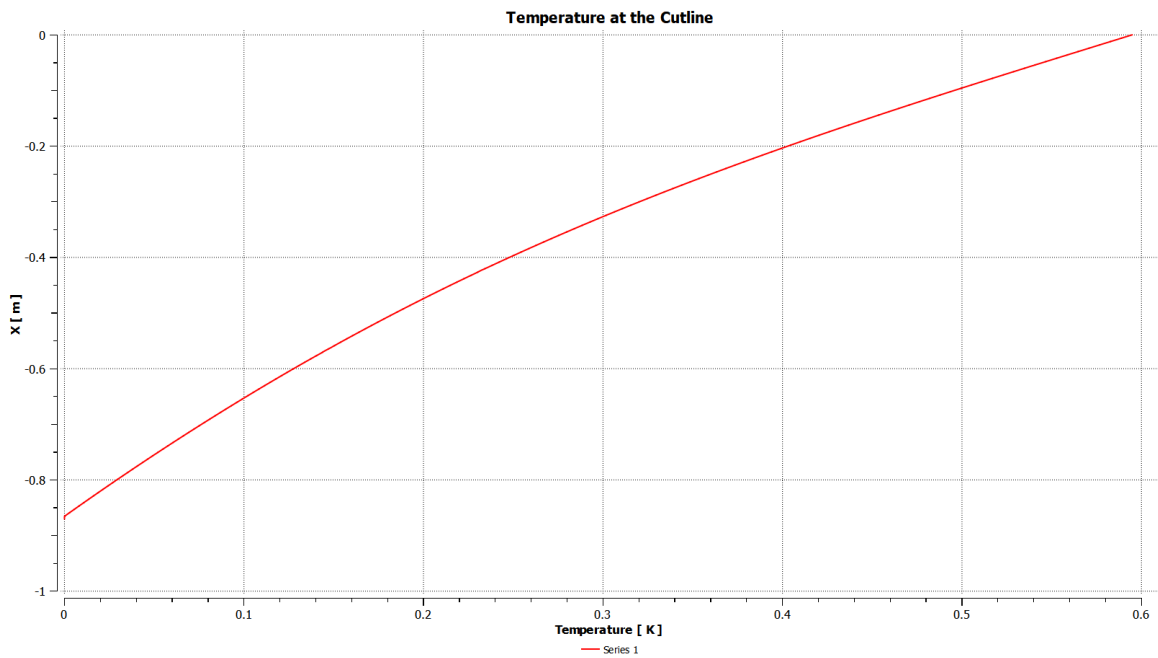


Figure B.259: Temperature at the cutline at $r^*=1$ for Exp 5.3.

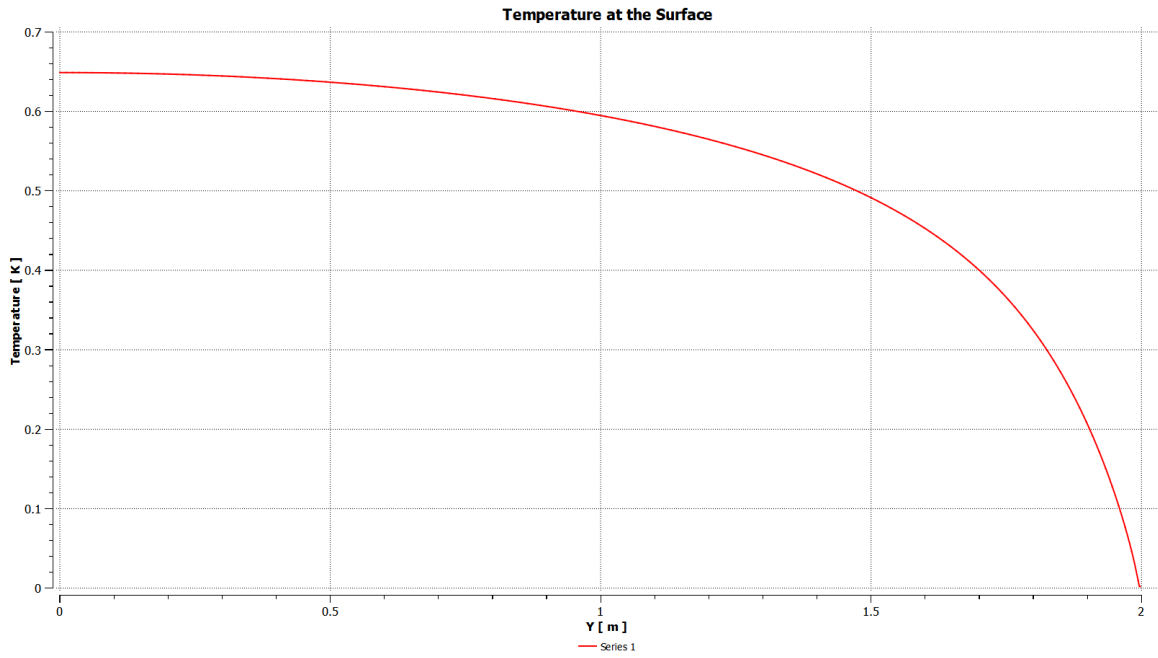


Figure B.260: Temperature at the free surface for Exp 5.3.

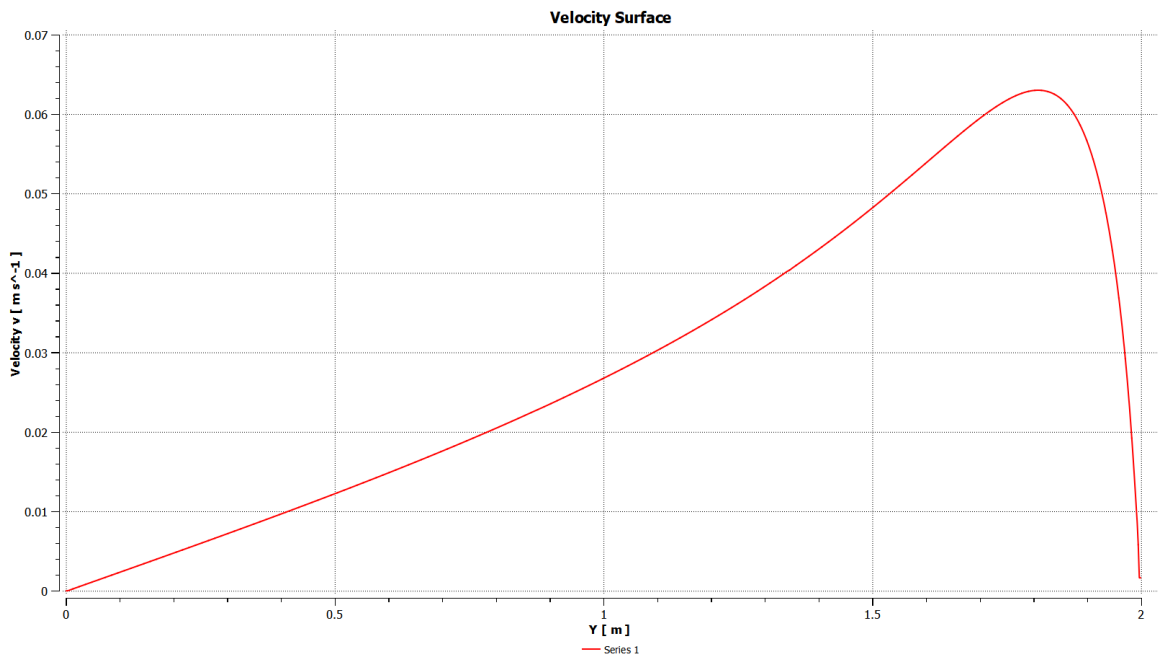


Figure B.261: Velocity at the free surface for Exp 5.3.

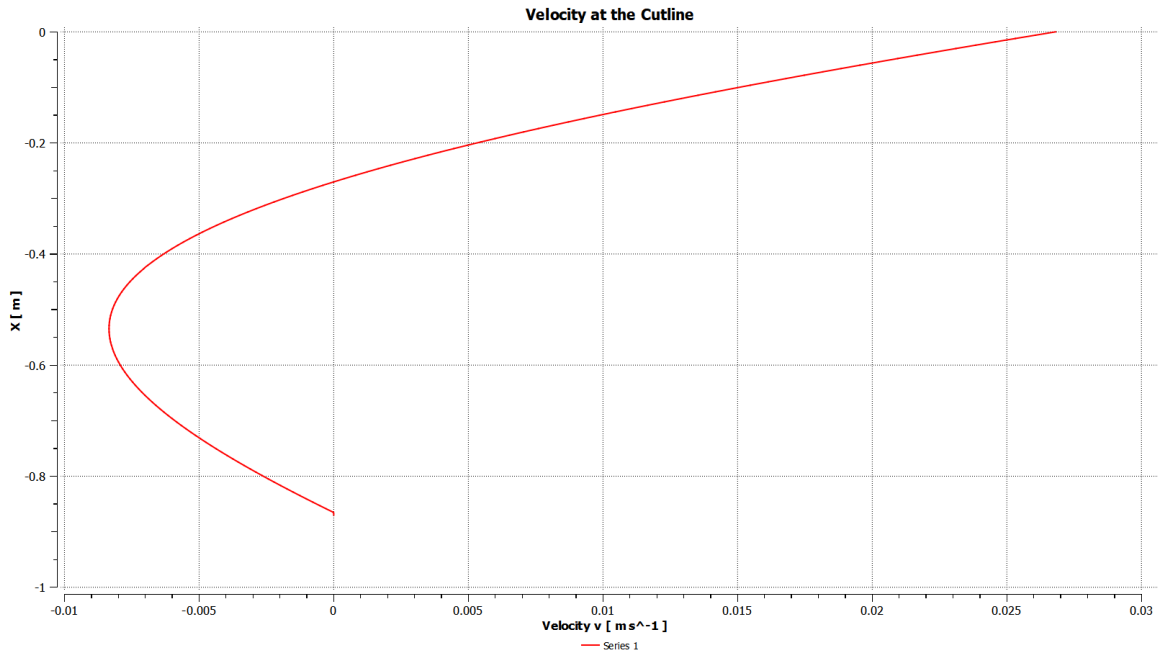


Figure B.262: Radial velocity u at the cutline at $r^*=1$ for Exp 5.3.

Exp 5.4

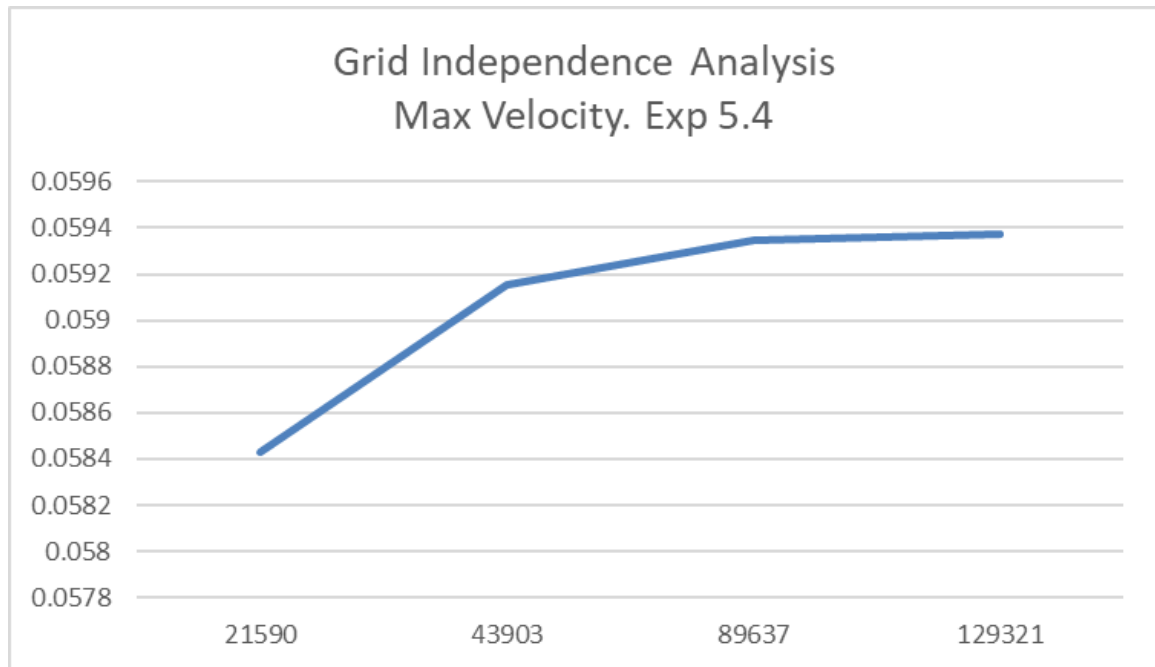


Figure B.263: Convergence for Exp 5.4: peak velocity values vs number of nodes in logarithmic scale.

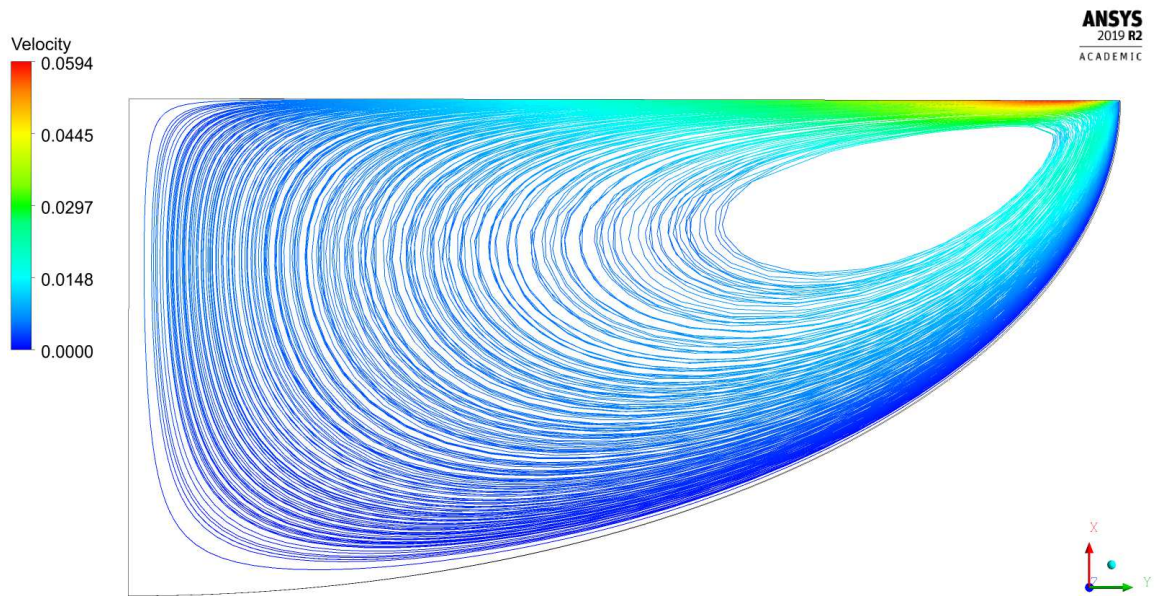


Figure B.264: Streamlines for Exp 5.4.

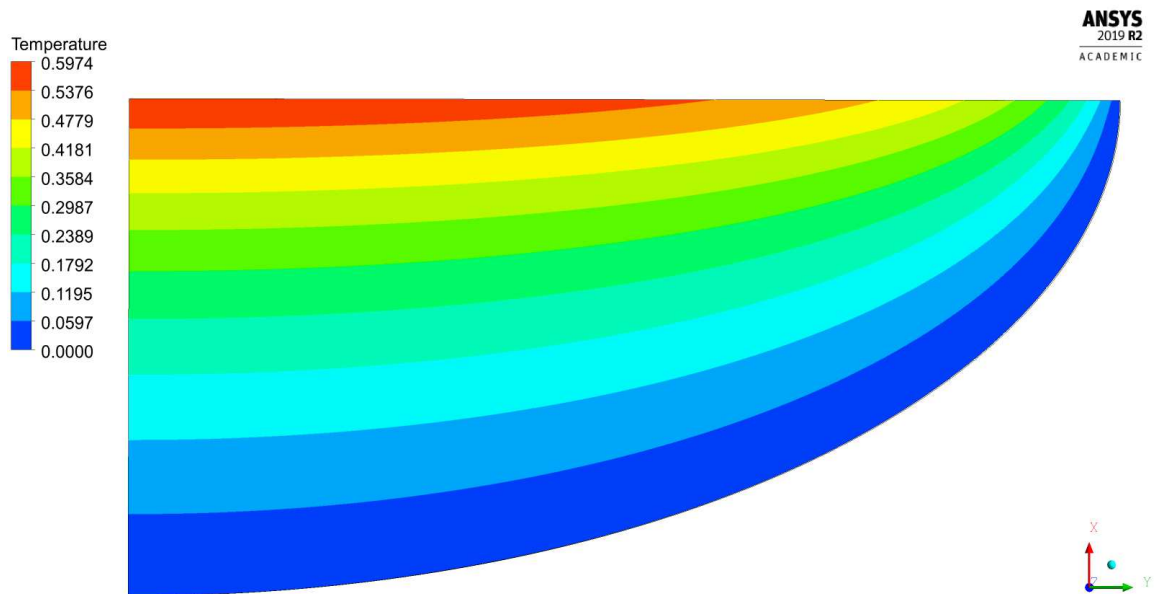


Figure B.265: Temperature field for Exp 5.4.

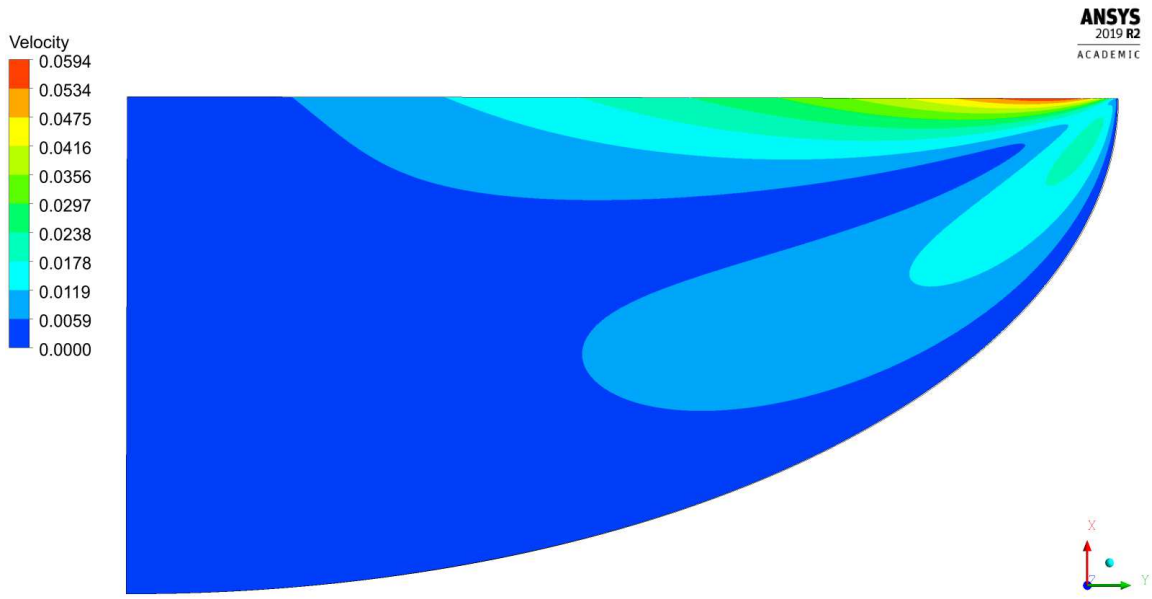


Figure B.266: Velocity magnitude contour for Exp 5.4.

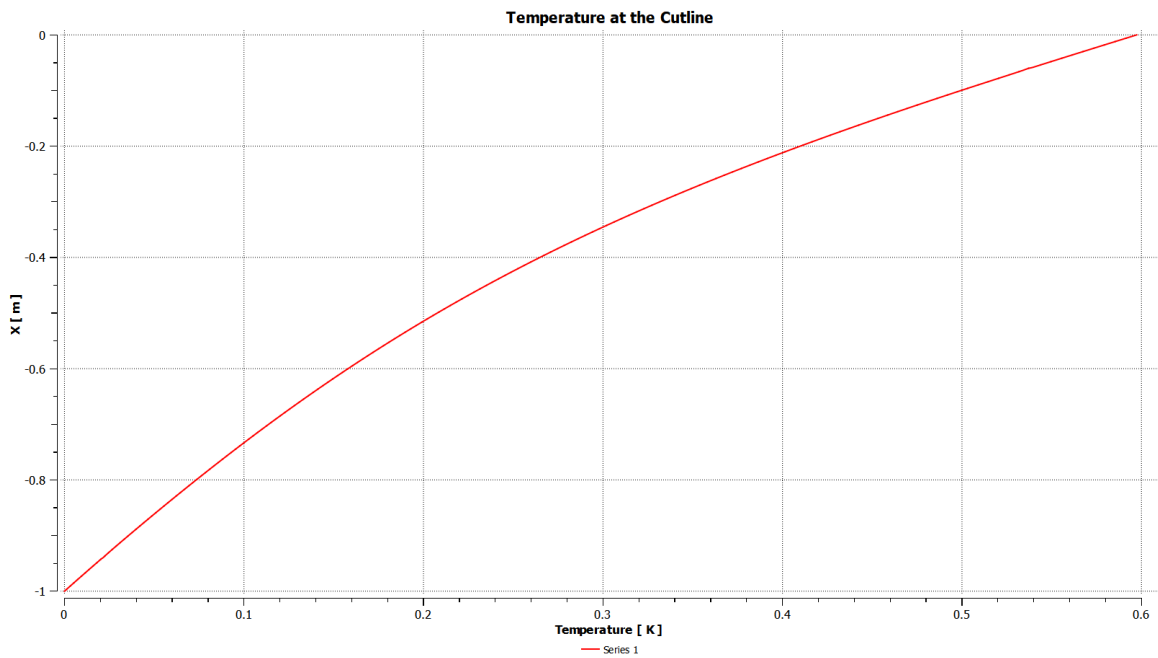


Figure B.267: Temperature at the axis of symmetry for Exp 5.4.

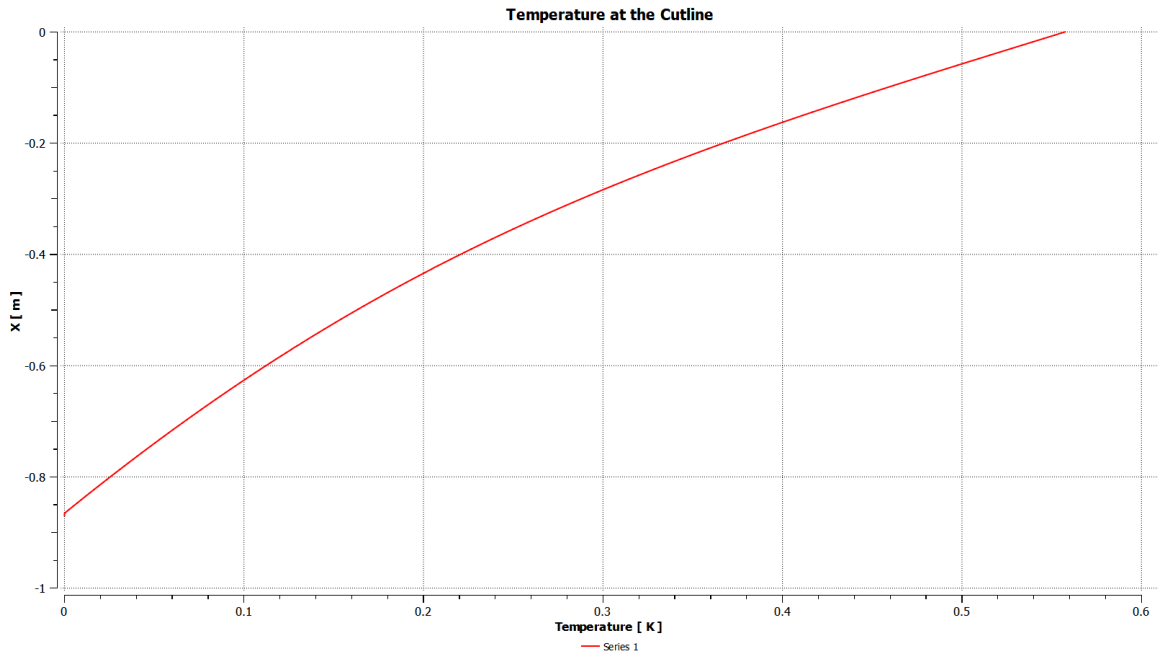


Figure B.268: Temperature at the cutline at $r^*=1$ for Exp 5.4.

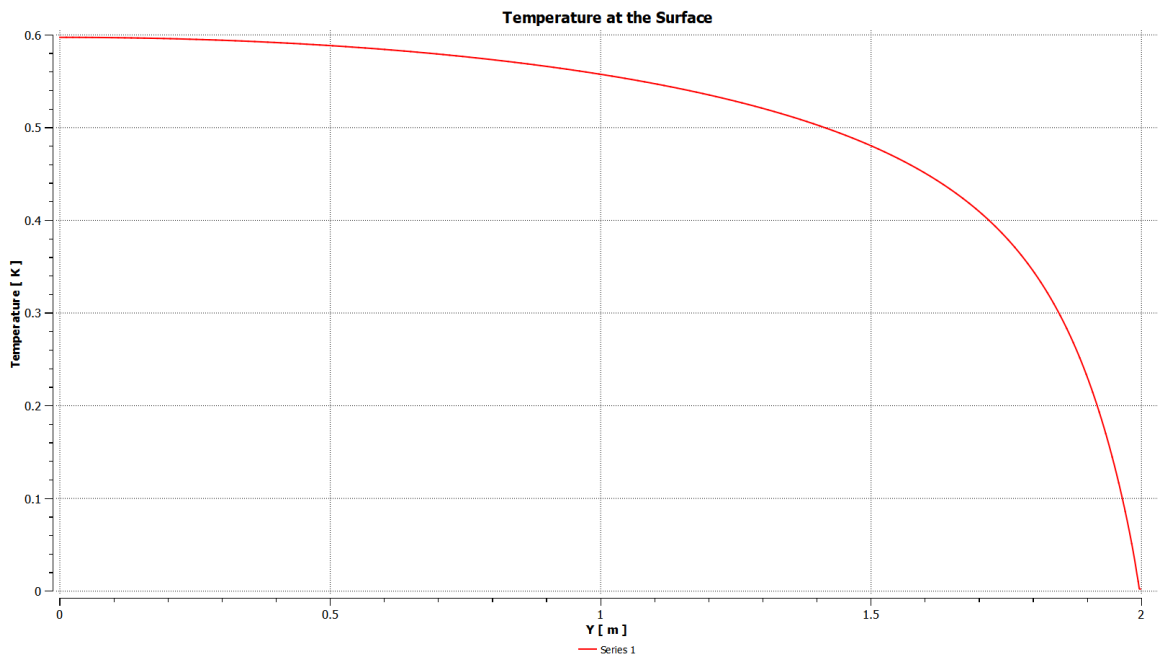


Figure B.269: Temperature at the free surface for Exp 5.4.

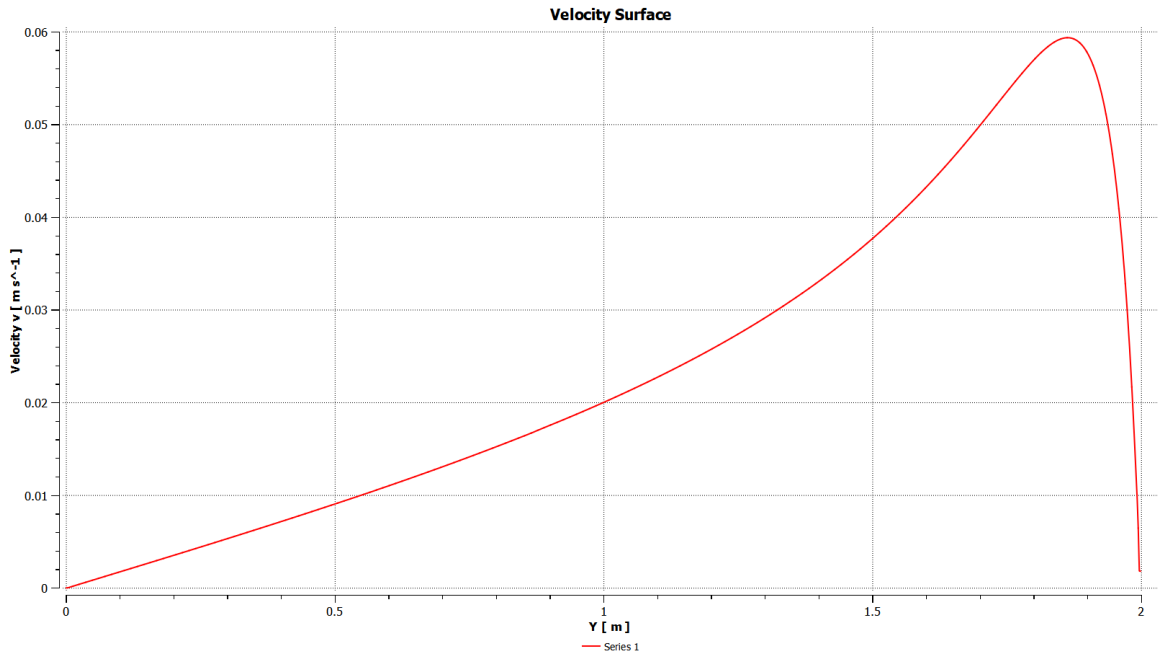


Figure B.270: Velocity at the free surface for Exp 5.4.

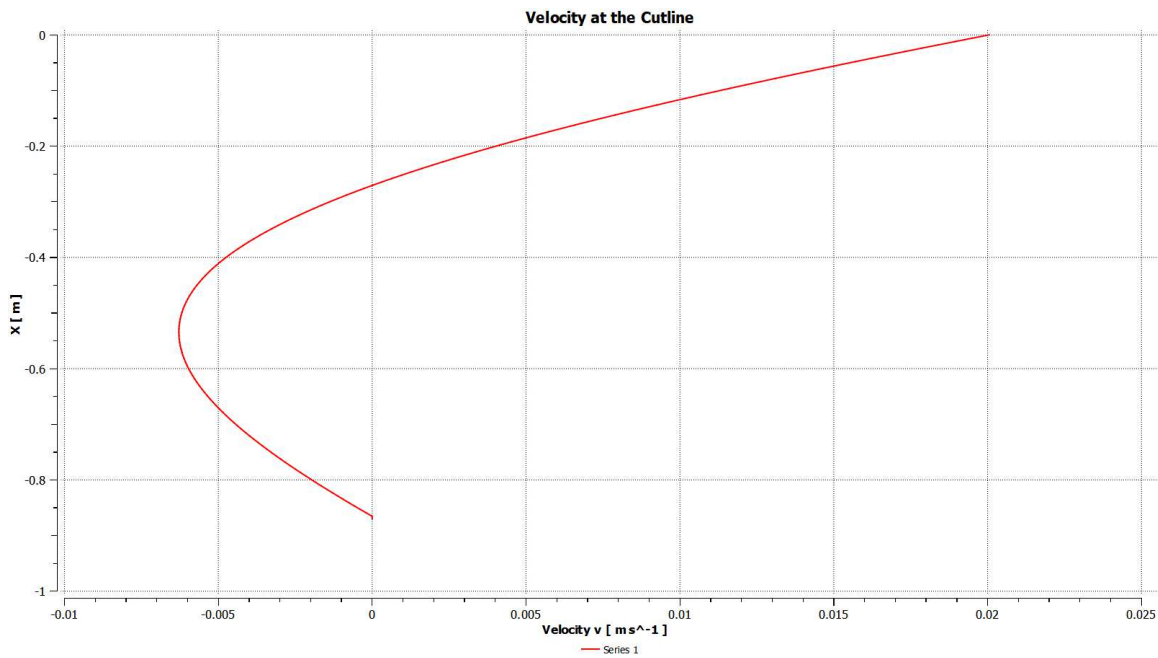


Figure B.271: Radial velocity u at the cutline at $r^*=1$ for Exp 5.4.

Exp 5.5

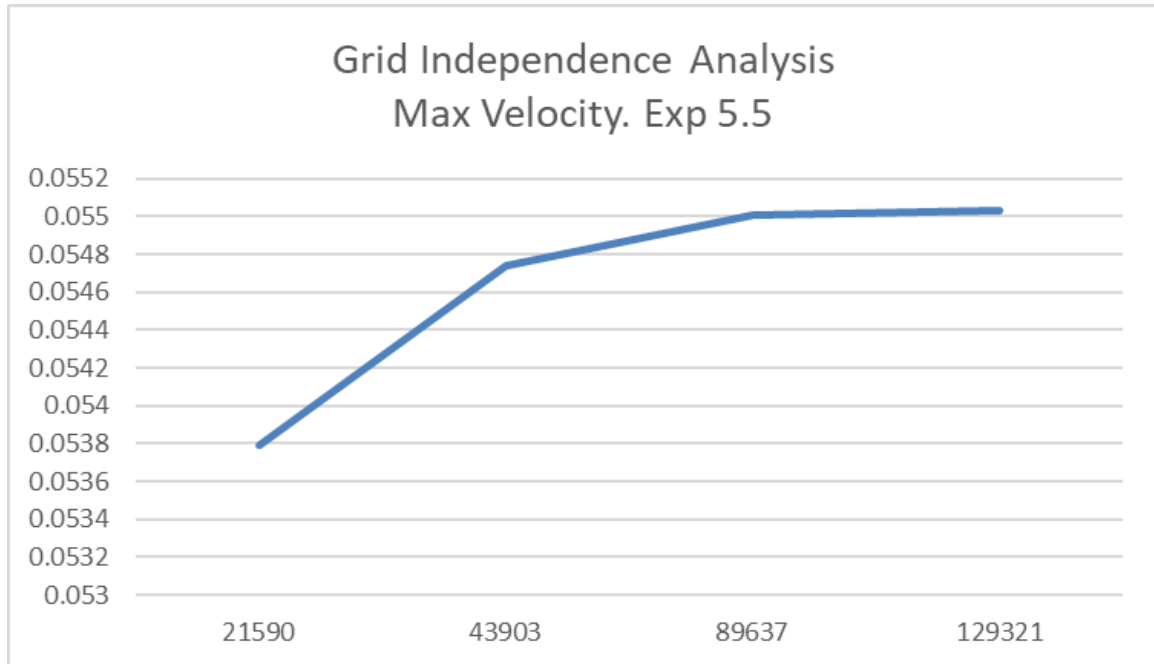


Figure B.272: Convergence for Exp 5.5: peak velocity values vs number of nodes in logarithmic scale.

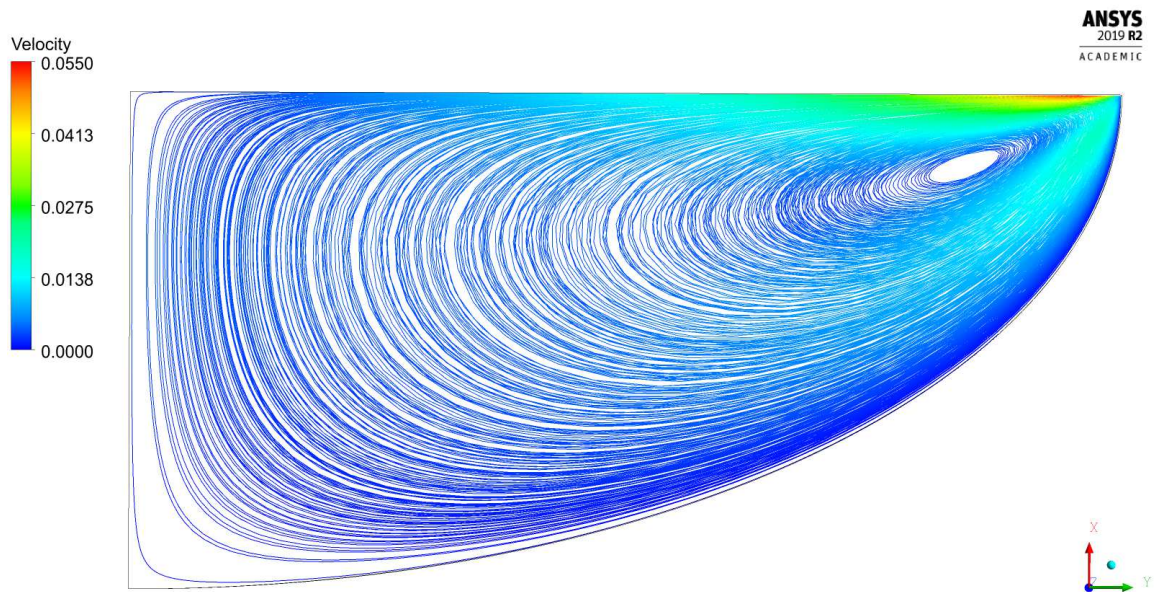


Figure B.273: Streamlines for Exp 5.5.

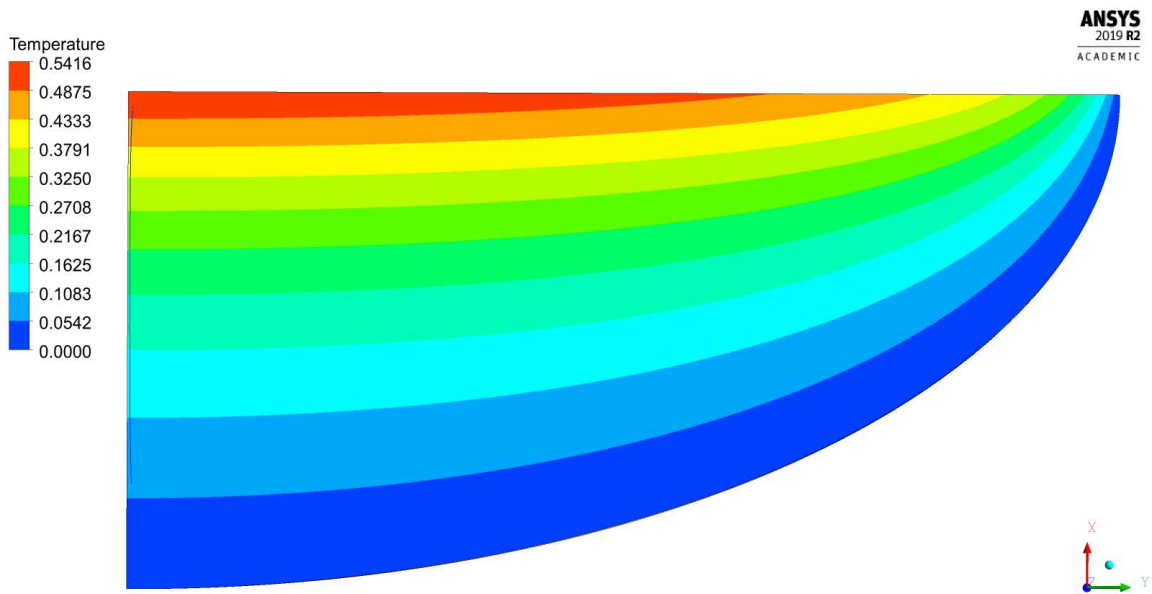


Figure B.274: Temperature field for Exp 5.5.

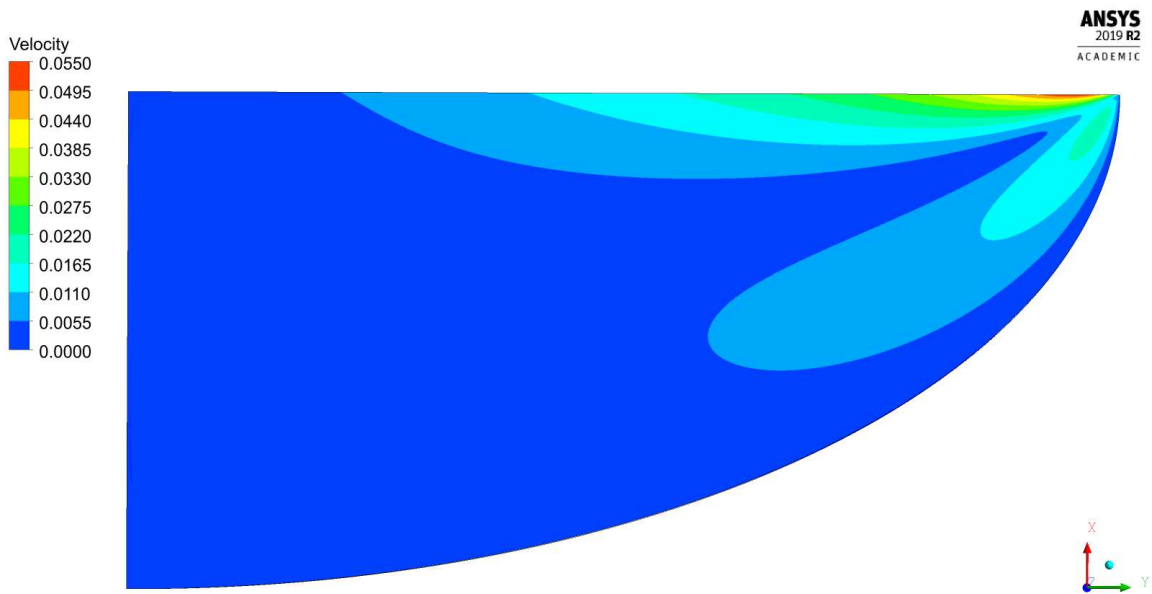


Figure B.275: Velocity magnitude contour for Exp 5.5.

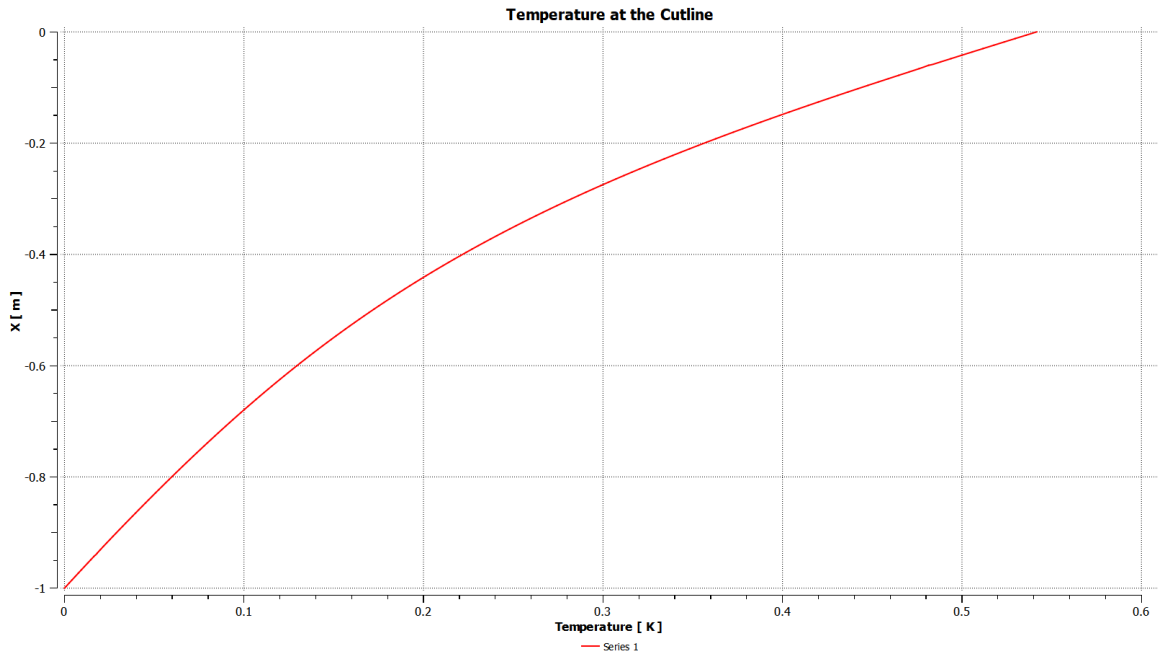


Figure B.276: Temperature at the axis of symmetry for Exp 5.5.

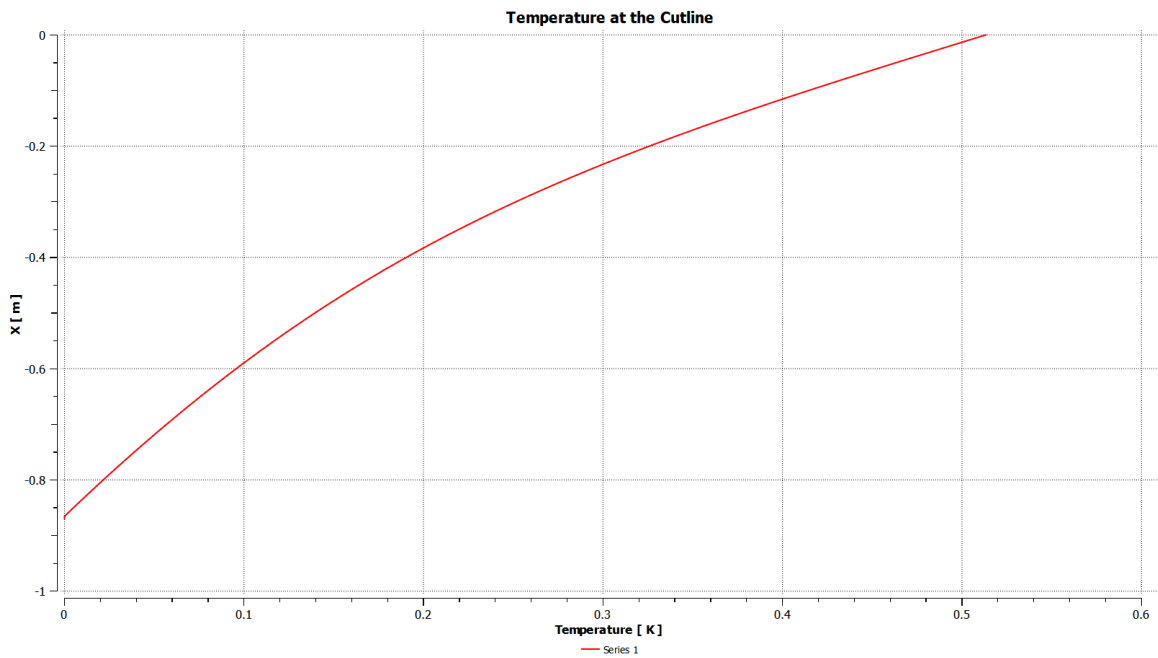


Figure B.277: Temperature at the cutline at $r^*=1$ for Exp 5.5.

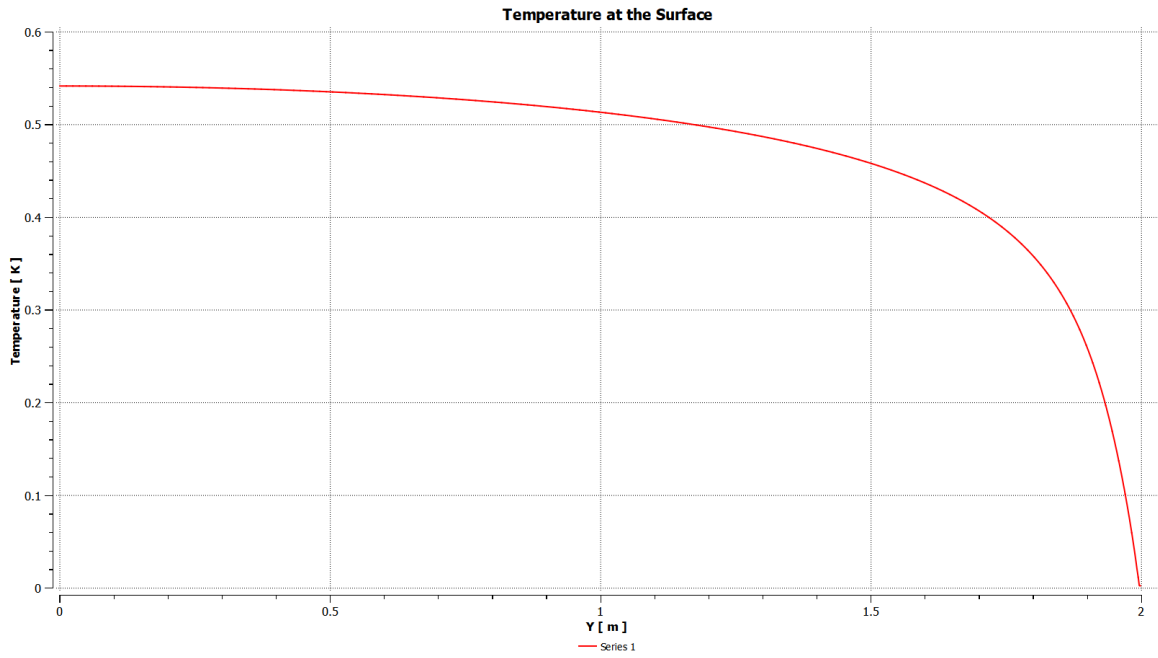


Figure B.278: Temperature at the free surface for Exp 5.5.

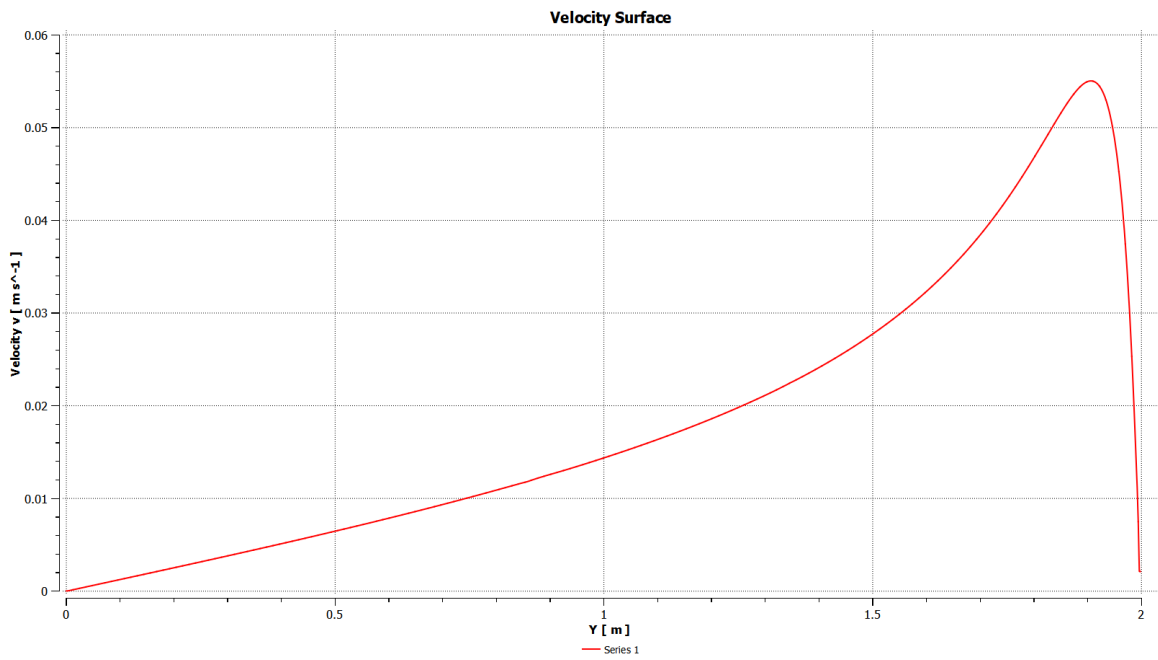


Figure B.279: Velocity at the free surface for Exp 5.5.

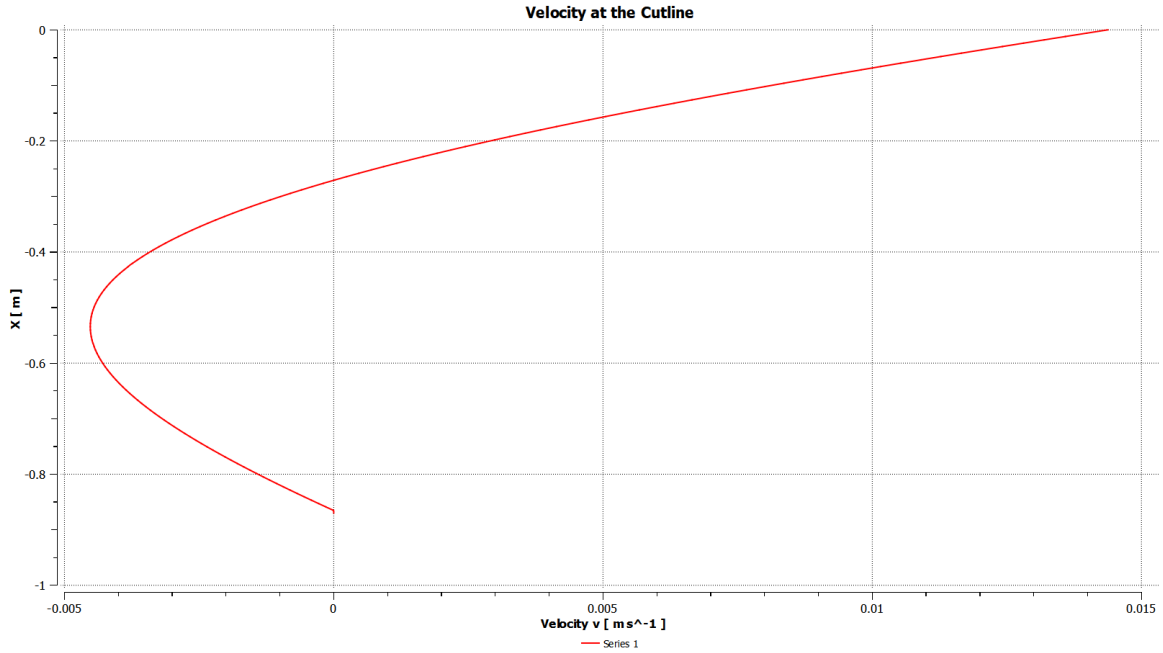


Figure B.280: Radial velocity u at the cutline at $r^*=1$ for Exp 5.5.

Exp 5.6

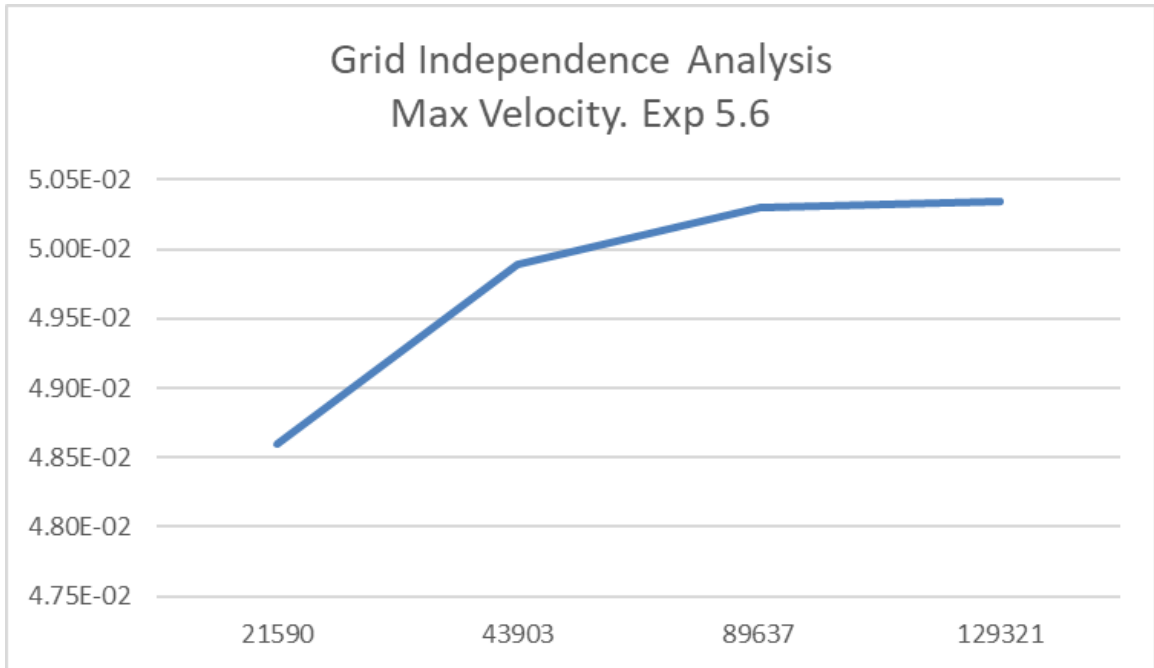


Figure B.281: Convergence for Exp 5.6: peak velocity values vs number of nodes in logarithmic scale.

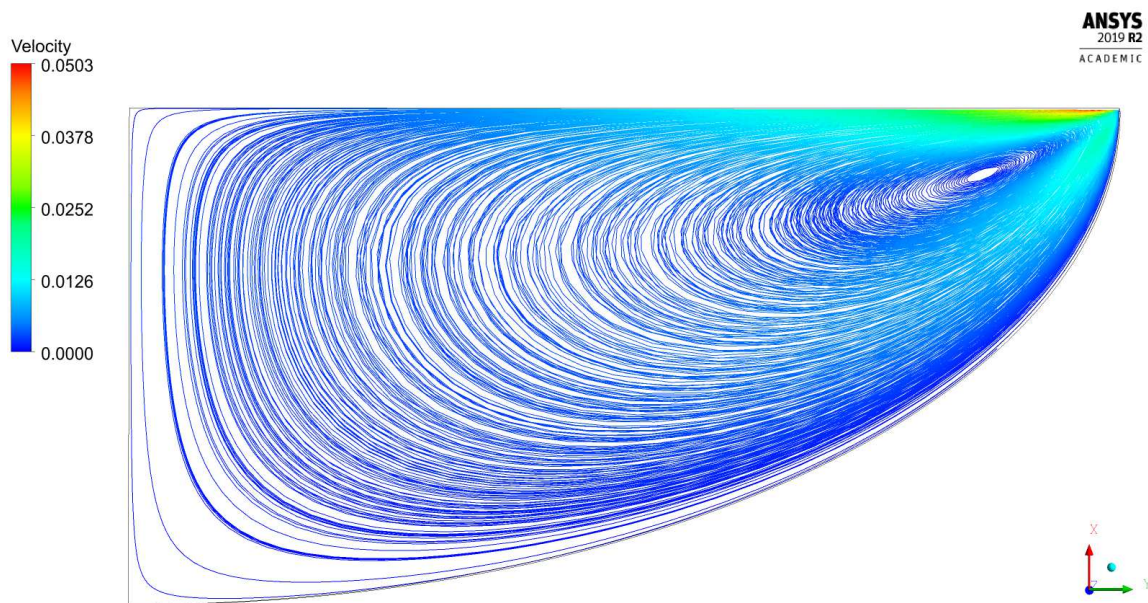


Figure B.282: Streamlines for Exp 5.6.

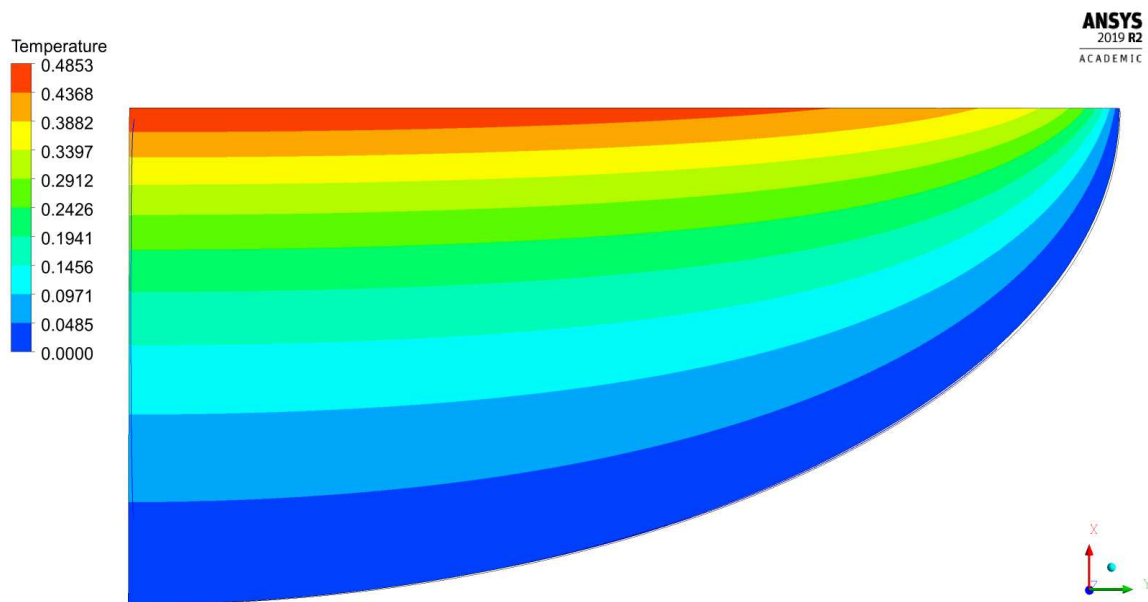


Figure B.283: Temperature field for Exp 5.6.

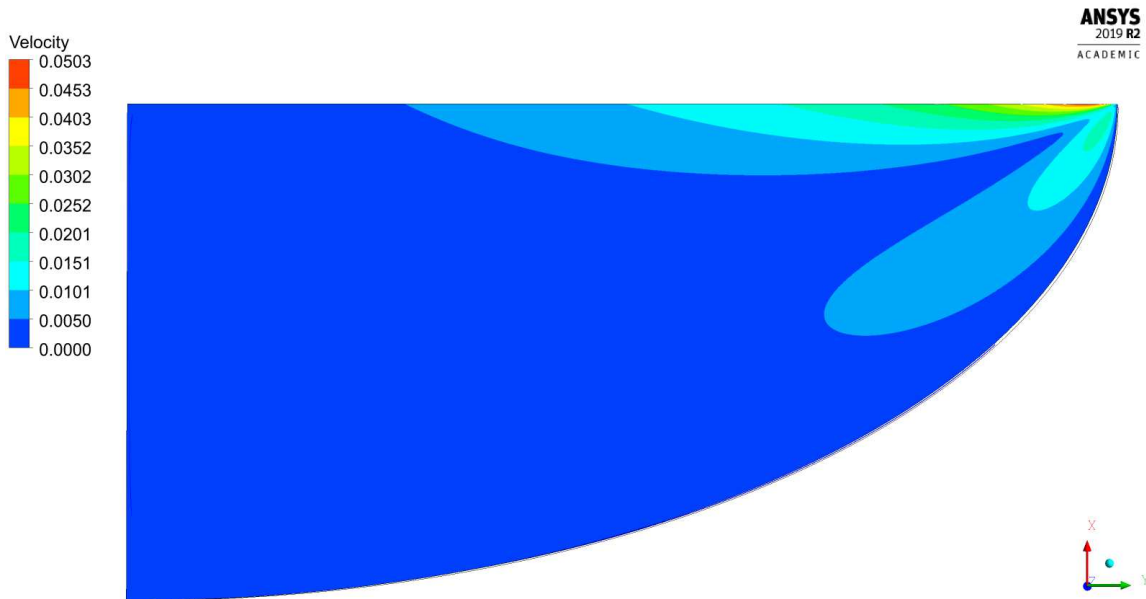


Figure B.284: Velocity magnitude contour for Exp 5.6.

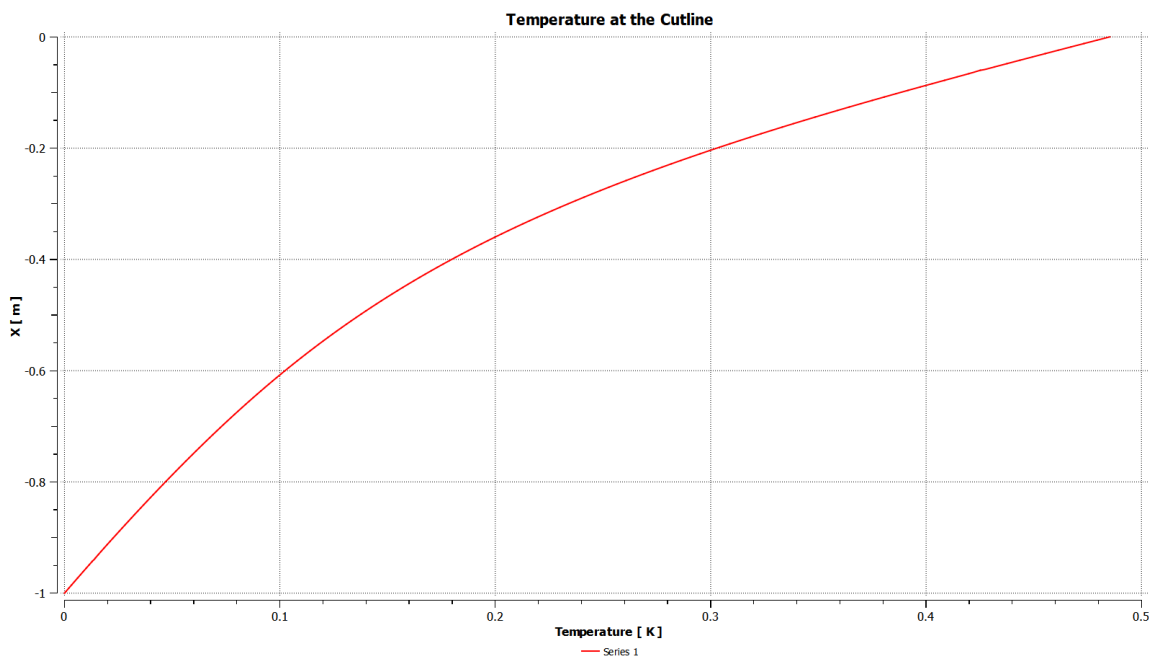


Figure B.285: Temperature at the axis of symmetry for Exp 5.6.

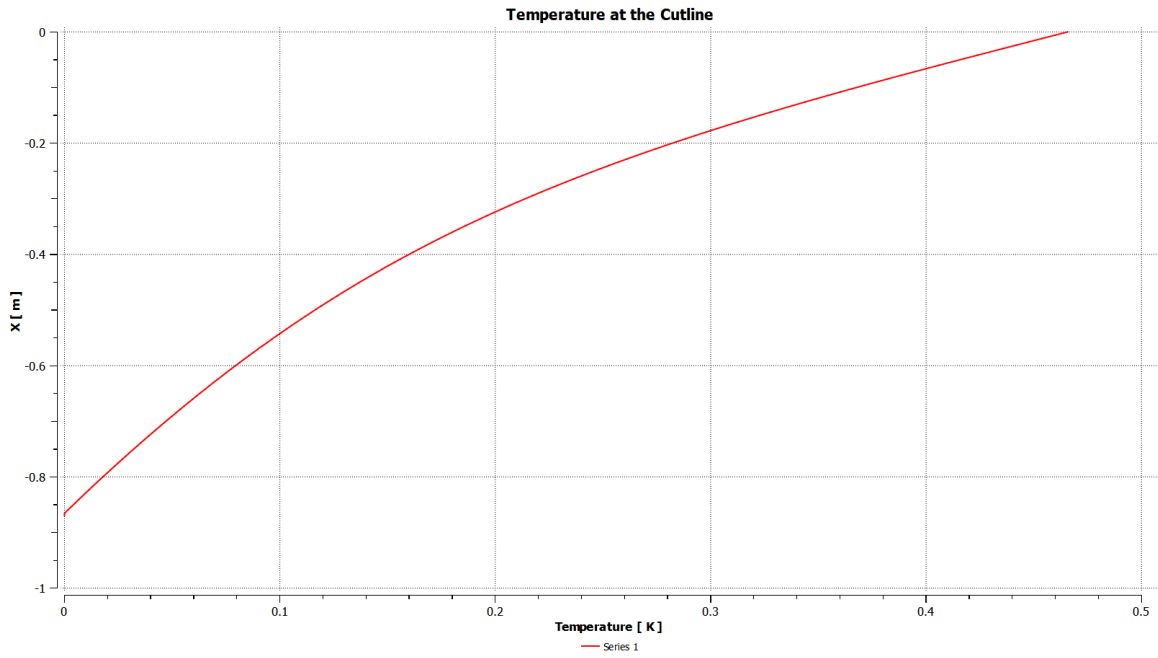


Figure B.286: Temperature at the cutline at $r^*=1$ for Exp 5.6.

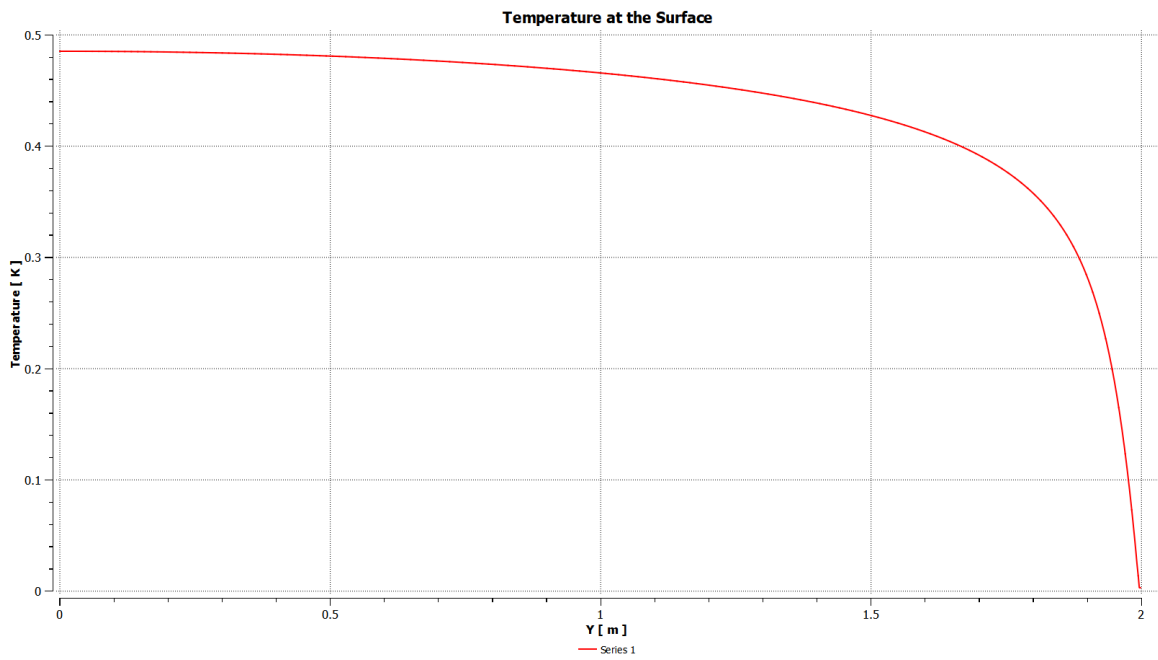


Figure B.287: Temperature at the free surface for Exp 5.6.

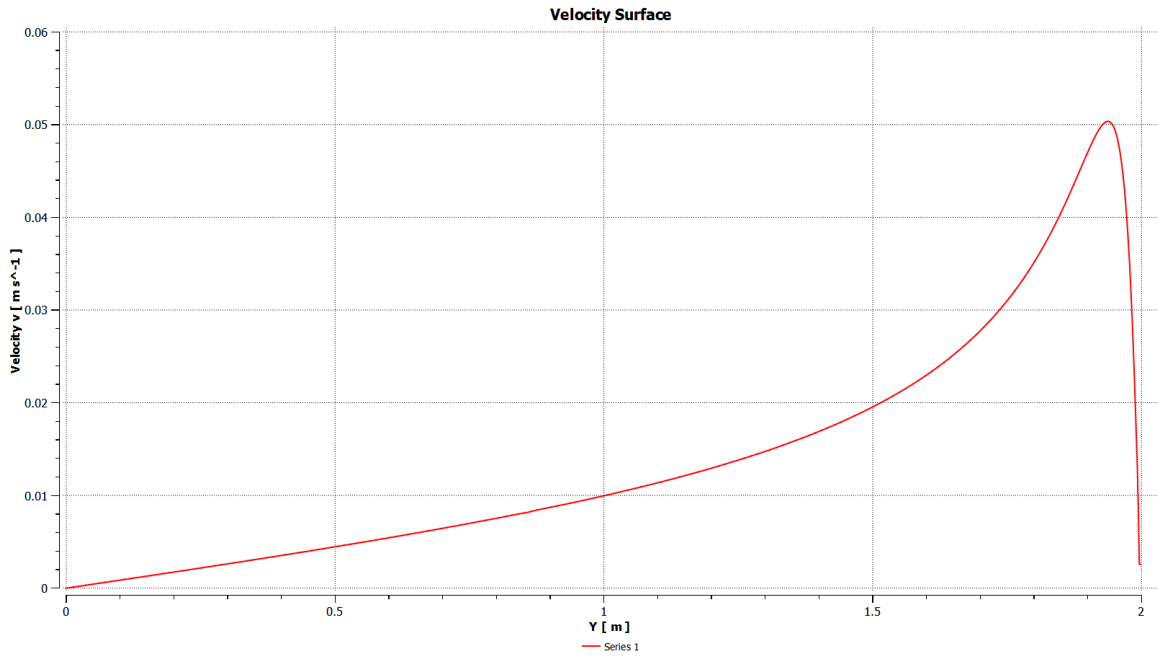


Figure B.288: Velocity at the free surface for Exp 5.6.

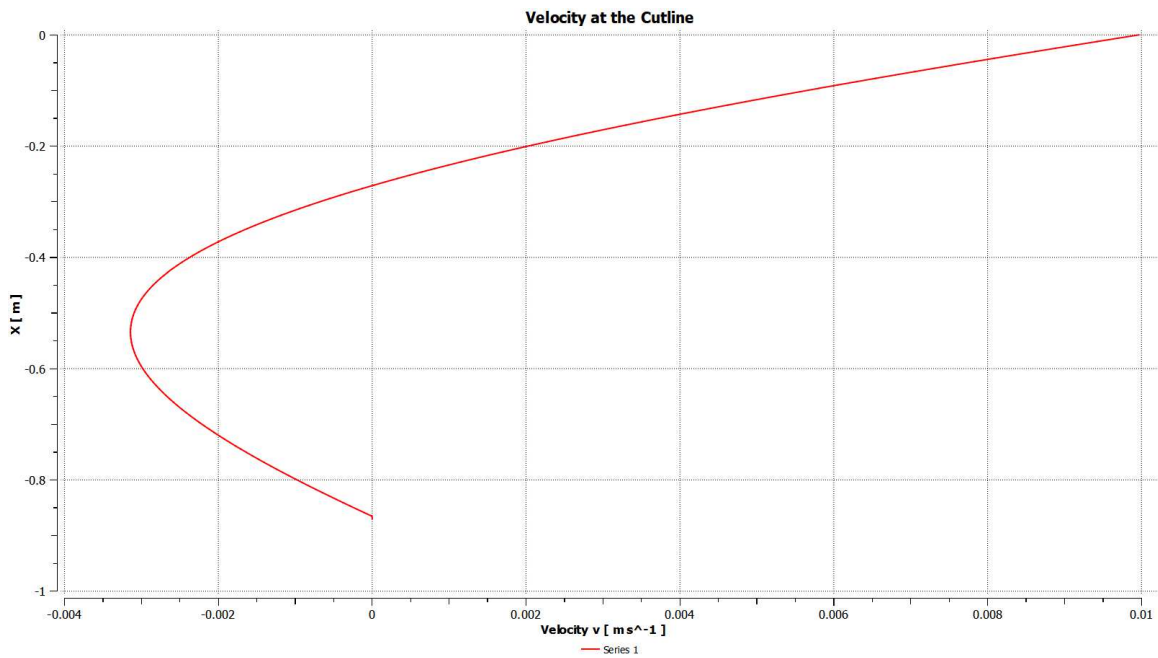


Figure B.289: Radial velocity u at the cutline at $r^*=1$ for Exp 5.6.

Exp 5.7

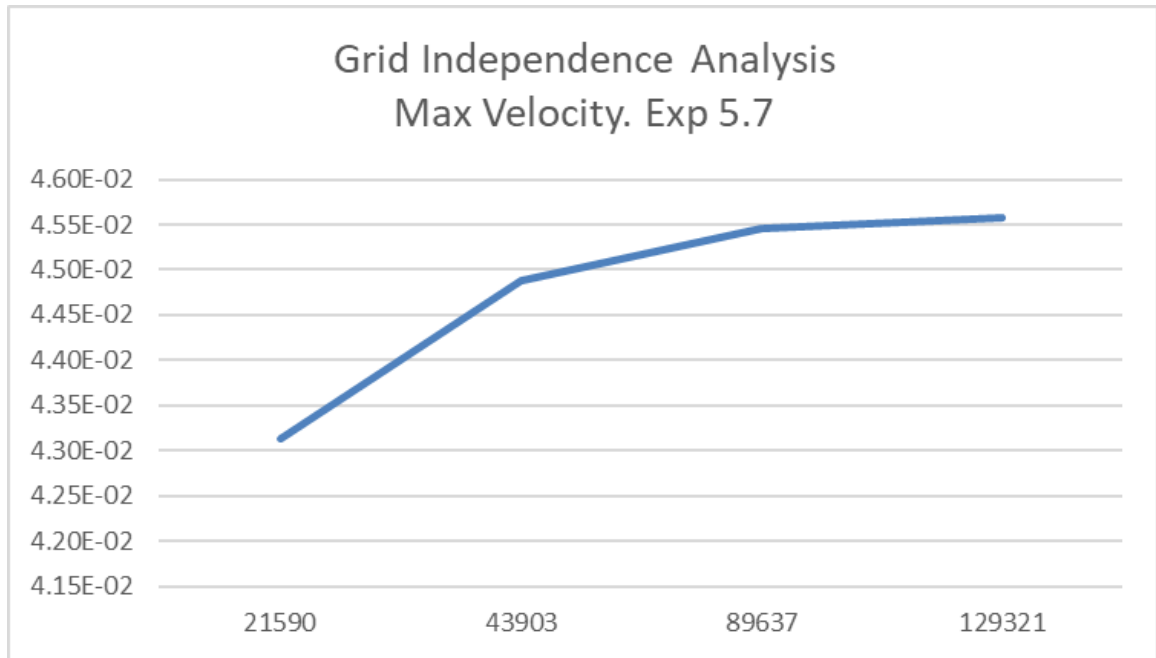


Figure B.290: Convergence for Exp 5.7: peak velocity values vs number of nodes in logarithmic scale.

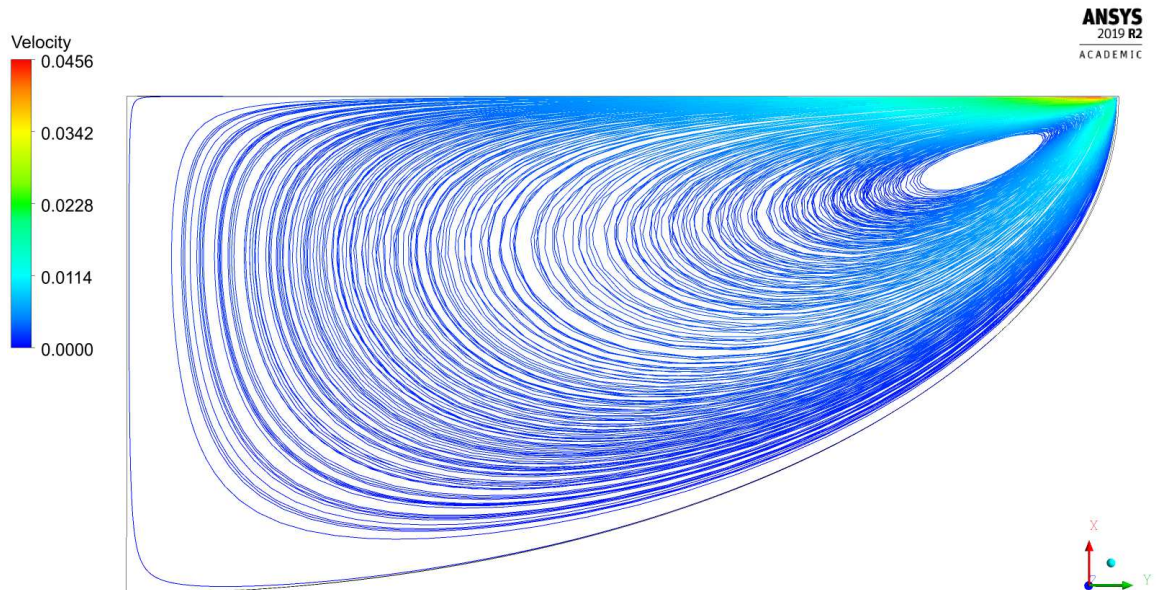


Figure B.291: Streamlines for Exp 5.7.

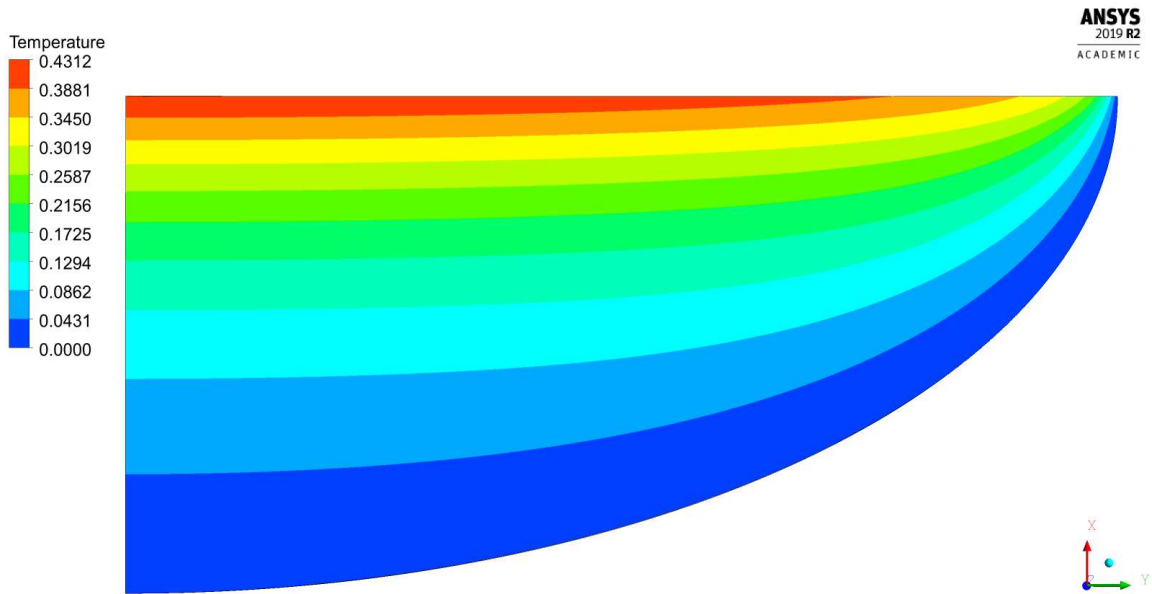


Figure B.292: Temperature field for Exp 5.7.

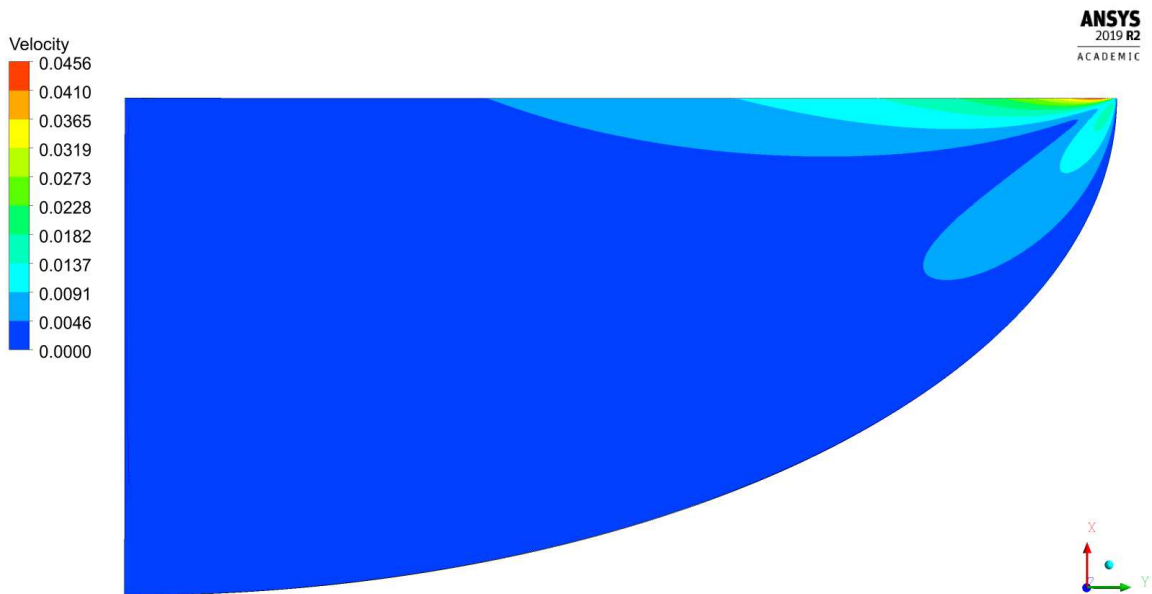


Figure B.293: Velocity magnitude contour for Exp 5.7.

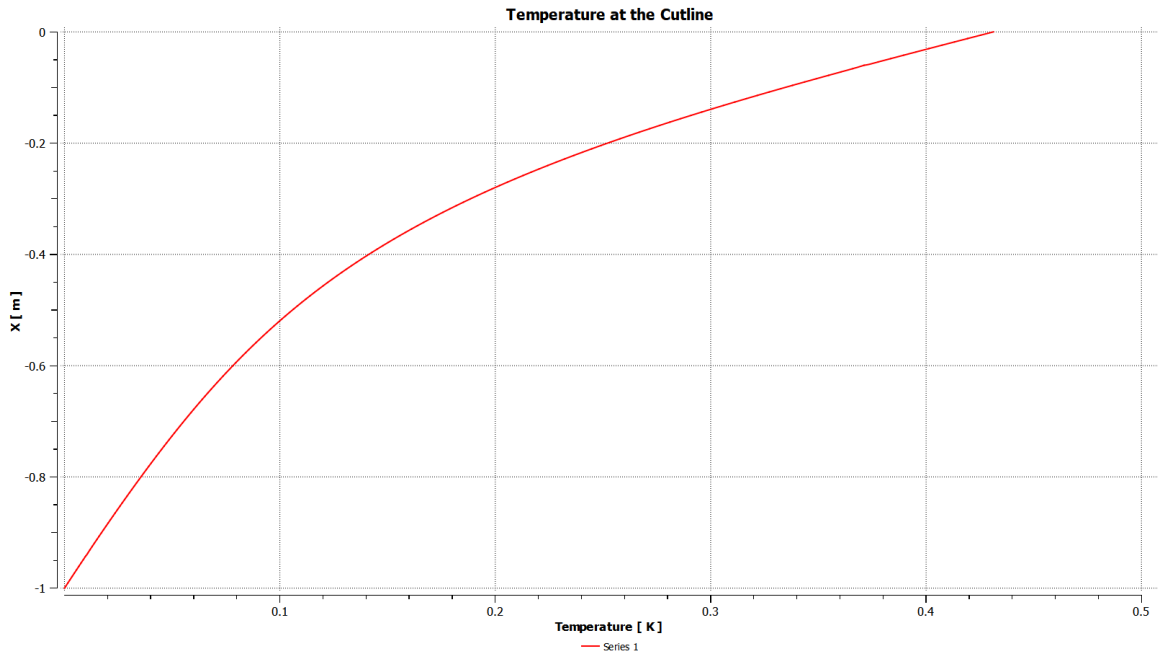


Figure B.294: Temperature at the axis of symmetry for Exp 5.7.

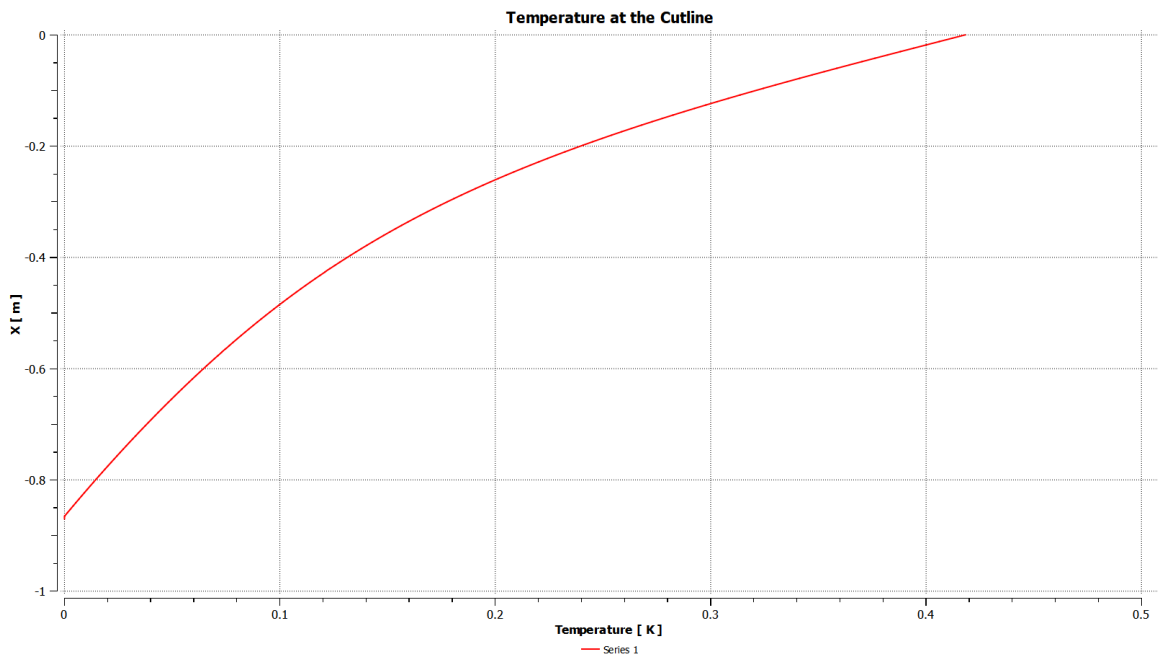


Figure B.295: Temperature at the cutline at $r^*=1$ for Exp 5.7.

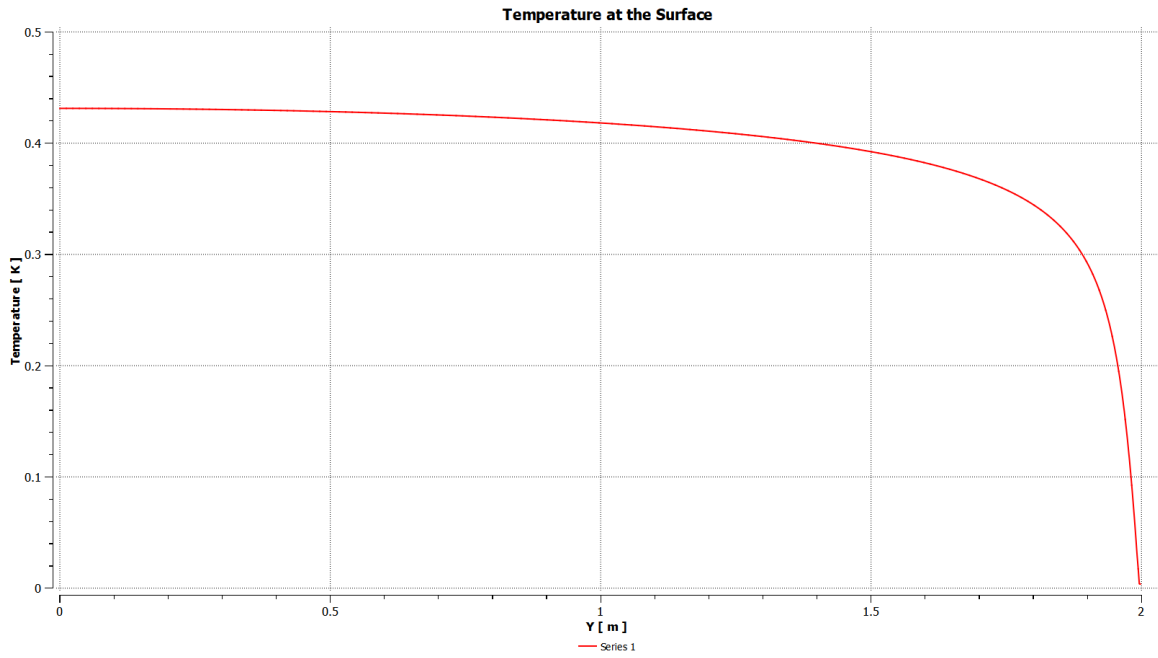


Figure B.296: Temperature at the free surface for Exp 5.7.

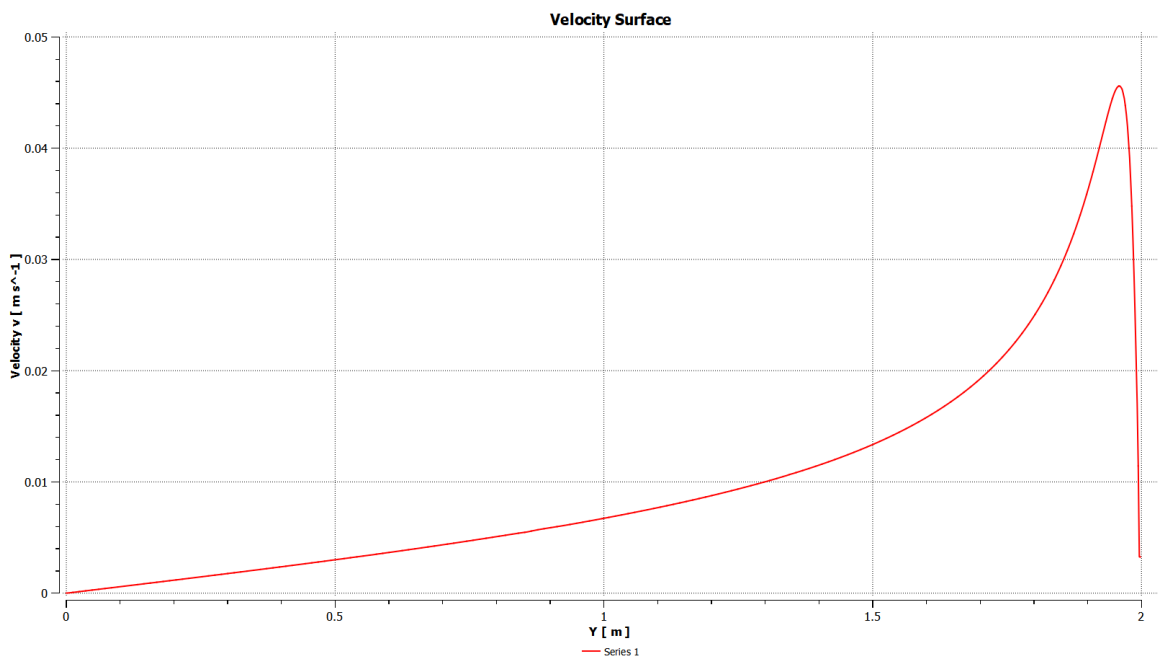


Figure B.297: Velocity at the free surface for Exp 5.7.

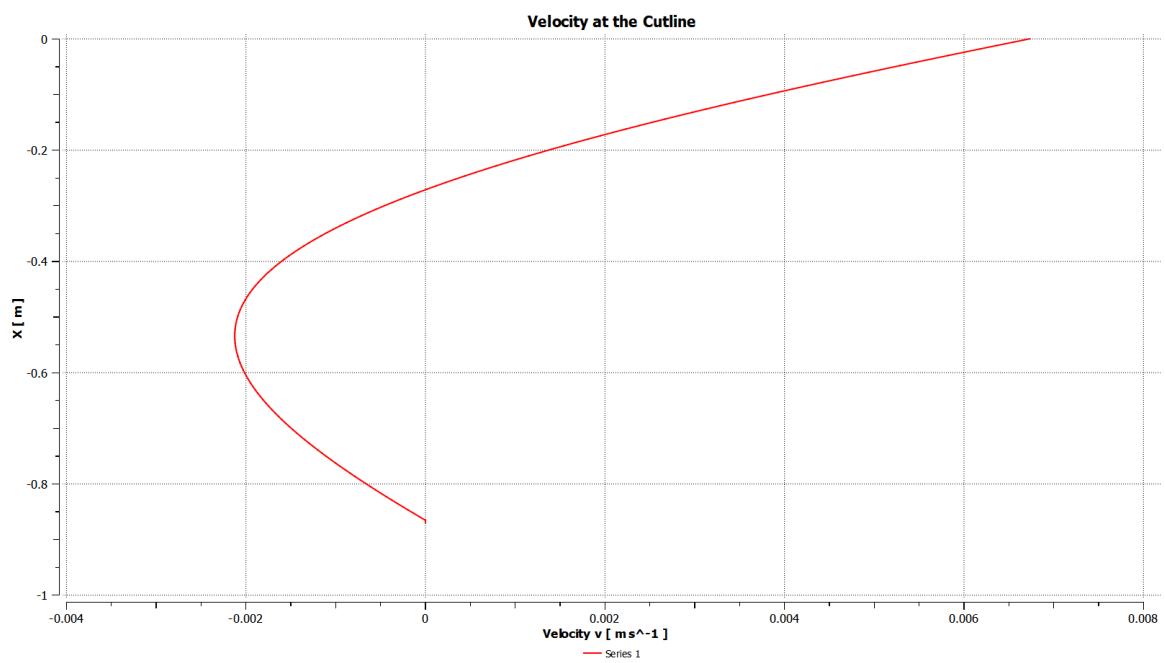


Figure B.298: Radial velocity u at the cutline at $r^*=1$ for Exp 5.7.